

FEBRUARY 2021

AJNR

VOLUME 42 • PP 213-401

AJNR

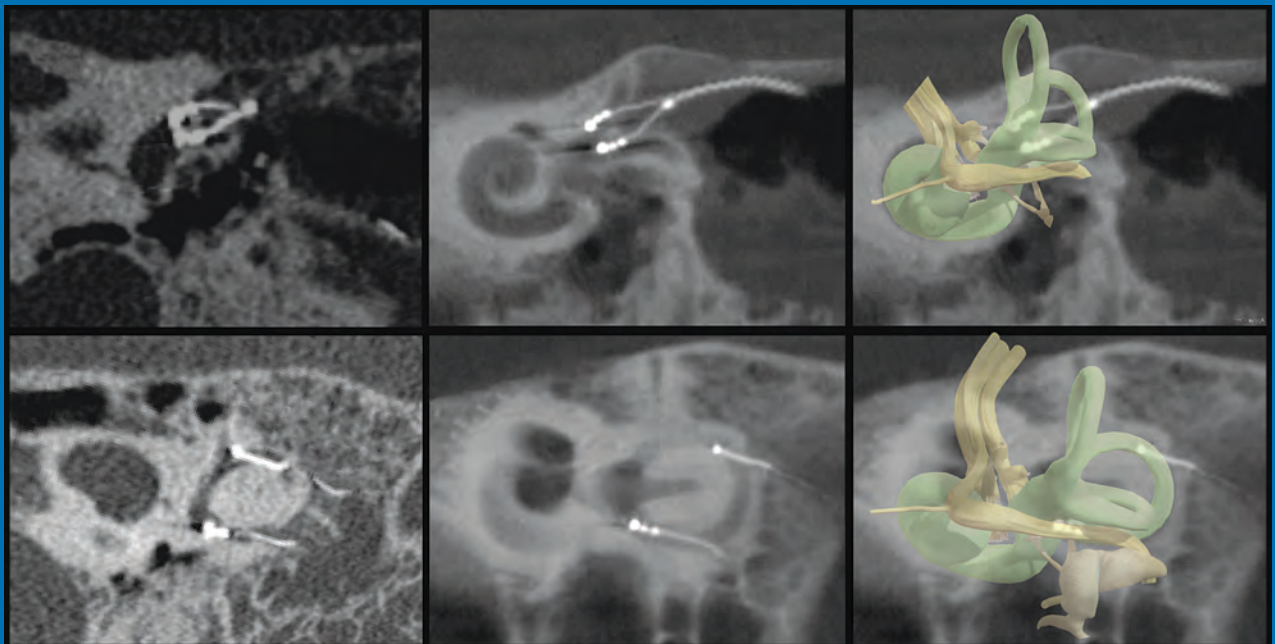
AMERICAN JOURNAL OF NEURORADIOLOGY

FEBRUARY 2021
VOLUME 42
NUMBER 2
WWW.AJNR.ORG

THE JOURNAL OF DIAGNOSTIC AND
INTERVENTIONAL NEURORADIOLOGY

Glioma grading with neural networks
Predicting outcome of large-vessel stroke with machine learning
Automated cerebral hemorrhage detection

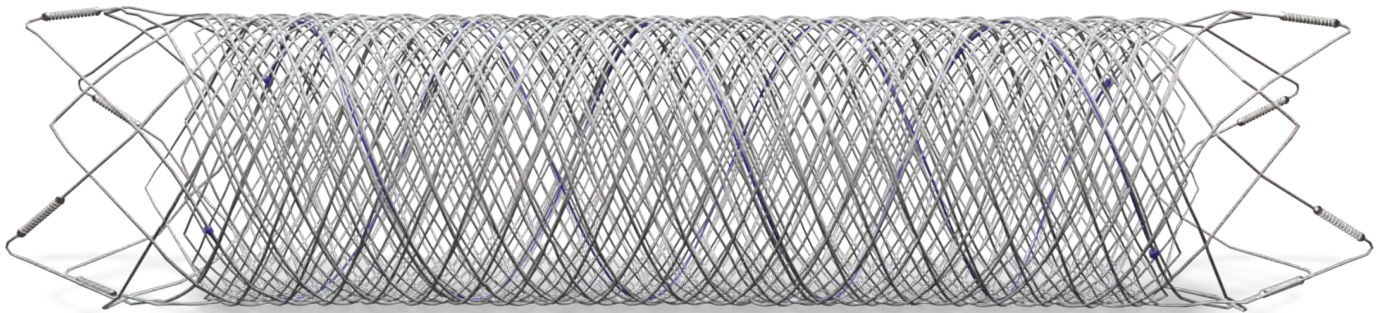
Official Journal ASNR • ASFNR • ASHNR • ASPNR • ASSR



FRED™

Flow Re-Direction
Endoluminal Device

FLOW DIVERSION.



SIMPLIFIED.



MicroVention Worldwide
Innovation Center
35 Enterprise
Aliso Viejo, CA 92656 USA
MicroVention UK Limited
MicroVention Europe S.A.R.L.
MicroVention Deutschland GmbH
Web

PH +1 714.247.8000

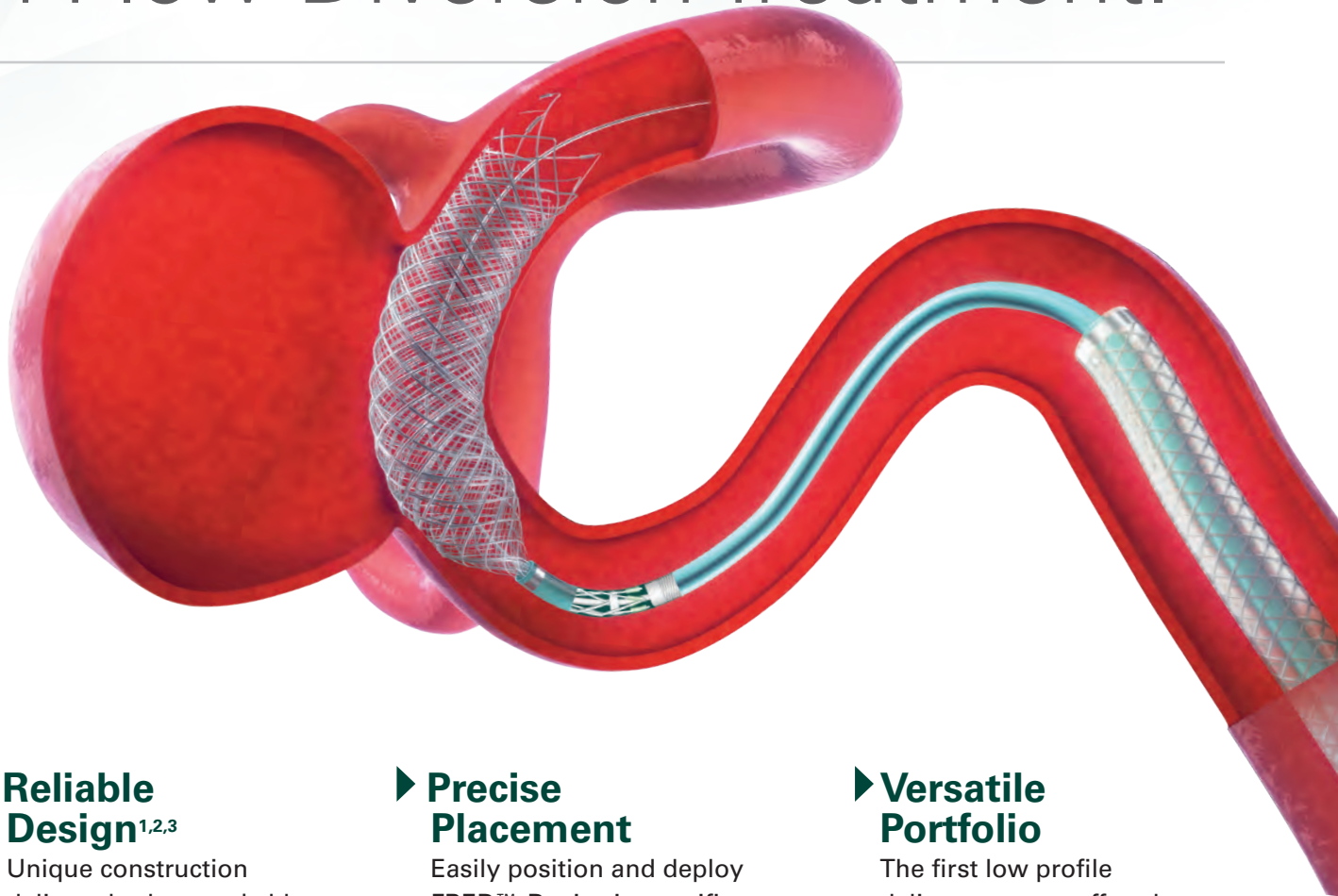
PH +1 44 (0) 191 258 6777

PH +33 (1) 39 21 77 46

PH +49 211 210 798-0

microvention.com

The New Standard of **Ease and Simplicity** in Flow Diversion Treatment.



► **Reliable Design**^{1,2,3}

Unique construction delivers both remarkable ease of use and excellent flow diversion^{1,2,3}

► **Precise Placement**

Easily position and deploy FRED™ Device in specific, targeted locations^{4,5,6}

► **Versatile Portfolio**

The first low profile delivery system offered in combination with large diameter and long length options

References:

1. TR11-211 2. TR13-171 3. TR15-055 4. TR13-192 5. TR15-072 6. TR19-145

The Flow Re-Direction Endoluminal Device (FRED™) System is indicated for use in the internal carotid artery from the petrous segment to the terminus for the endovascular treatment of adult patients (22 years of age or older) with wide-necked (neck width ≥ 4 mm or dome-to-neck ratio < 2) saccular or fusiform intracranial aneurysms arising from a parent vessel with a diameter ≥ 2.0 mm and ≤ 5.0 mm.

Use of the FRED™ System is contraindicated under these circumstances: Patients in whom anticoagulant, anti-platelet therapy, or thrombolytic drugs are contraindicated. Patients with known hypersensitivity to metal such as nickel-titanium and metal jewelry. Patients with anatomy that does not permit passage or deployment of the FRED™ System. Patients with an active bacterial infection. Patients with a pre-existing stent in place at the target aneurysm. Patients in whom the parent vessel size does not fall within the indicated range. Patients who have not received dual anti-platelet agents prior to the procedure. For complete indications, contraindications, potential complications, warnings, precautions, and instructions, see instructions for use (IFU provided in the device).

RX Only: Federal (United States) law restricts this device to sale by or on the order of a physician.

MICROVENTION™ and FRED™ are registered trademarks of MicroVention, Inc. in the United States and other jurisdictions. © 2020 MicroVention, Inc. 04/2020.



Simplify the MOC Process



Manage your CME Credits Online

CMEgateway.org

Available to Members of Participating Societies

American Board of Radiology (ABR)
American College of Radiology (ACR)
American Roentgen Ray Society (ARRS)
American Society of Neuroradiology (ASNR)
Commission on Accreditation of Medical
Physics Educational Programs, Inc. (CAMPEP)
Radiological Society of North America (RSNA)
Society of Interventional Radiology (SIR)
SNM
The Society for Pediatric Radiology (SPR)

It's Easy and Free!

Log on to CME Gateway to:

- View or print reports of your CME credits from multiple societies from a single access point.
- Print an aggregated report or certificate from each participating organization.
- Link to SAMs and other tools to help with maintenance of certification.

American Board of Radiology (ABR) participation!

By activating ABR in your organizational profile, your MOC-fulfilling CME and SAM credits can be transferred to your own personalized database on the ABR Web site.

Sign Up Today!

go to CMEgateway.org

AJNR

AMERICAN JOURNAL OF NEURORADIOLOGY

FEBRUARY 2021
VOLUME 42
NUMBER 2
WWW.AJNR.ORG

Publication Preview at www.ajnr.org features articles released in advance of print. Visit www.ajnrblog.org to comment on AJNR content and chat with colleagues and AJNR's News Digest at <http://ajnrdigest.org> to read the stories behind the latest research in neuroimaging.

213 **PERSPECTIVES** *R. Boren*

REVIEW ARTICLES

 214 **4D-DSA: Development and Current Neurovascular Applications** **INTERVENTIONAL**
K.L. Ruedinger, et al.

 221 **Multiphase CT Angiography: A Useful Technique in Acute Stroke Imaging—Collaterals and Beyond** **ADULT BRAIN**
S. Dundamadappa, et al.

RADIOLOGY-PATHOLOGY CORRELATION

228 **Optic Nerve Choristoma Mimicking a Neurenteric Cyst** **ADULT BRAIN**
J.C. Benson, et al.

GENERAL CONTENTS

    233 **Improved Glioma Grading Using Deep Convolutional Neural Networks** **ADULT BRAIN FUNCTIONAL**
S. Gutta, et al.

   240 **Prediction of Clinical Outcome in Patients with Large-Vessel Acute Ischemic Stroke: Performance of Machine Learning versus SPAN-100** **ADULT BRAIN FUNCTIONAL**
B. Jiang, et al.

 247 **Evaluation of Artificial Intelligence–Powered Identification of Large-Vessel Occlusions in a Comprehensive Stroke Center** **ADULT BRAIN FUNCTIONAL**
A. Yahav-Dovrat, et al.

255 **Commentary**
Emerging Artificial Intelligence Imaging Applications for Stroke Interventions *E. Lotan*

  257 **COVID-19 Severity and Stroke: Correlation of Imaging and Laboratory Markers** **ADULT BRAIN**
J.M. Katz, et al.

 262 **Commentary**
Time for a “Second-Wave” of COVID-19 Data
P. Nicholson

  264 **Basal Ganglia versus Peripheral Infarcts: Predictive Value of Early Fiber Alterations** **ADULT BRAIN FUNCTIONAL**
M.T. Berndt, et al.

271 **Commentary**
Diffusion Tensor Imaging for Predicting the Outcome of Large-Vessel Ischemic Stroke Treated with Mechanical Thrombectomy: Is This the Prime Time? *Y. Hannawi*

AJNR (Am J Neuroradiol ISSN 0195–6108) is a journal published monthly, owned and published by the American Society of Neuroradiology (ASNR), 800 Enterprise Drive, Suite 205, Oak Brook, IL 60523. Annual dues for the ASNR include approximately 21% for a journal subscription. The journal is printed by Intellicor Communications, 330 Eden Road, Lancaster, PA 17601; Periodicals postage paid at Oak Brook, IL and additional mailing offices. Printed in the U.S.A. POSTMASTER: Please send address changes to American Journal of Neuroradiology, P.O. Box 3000, Denville, NJ 07834, U.S.A. Subscription rates: nonmember \$410 (\$480 foreign) print and online, \$320 online only; institutions \$470 (\$540 foreign) print and basic online, \$935 (\$1000 foreign) print and extended online, \$380 online only (basic), \$825 online only (extended); single copies are \$35 each (\$40 foreign). Indexed by PubMed/MEDLINE, BIOSIS Previews, Current Contents (Clinical Medicine and Life Sciences), EMBASE, Google Scholar, HighWire Press, Q-Sensei, RefSeek, Science Citation Index, SCI Expanded, Meta/CZI, ReadCube, and Semantic Scholar. Copyright © American Society of Neuroradiology.

	273	Automated Cerebral Hemorrhage Detection Using RAPID <i>J.J. Heit, et al.</i>	ADULT BRAIN FUNCTIONAL
	279	Serial Imaging of Virus-Associated Necrotizing Disseminated Acute Leukoencephalopathy (VANDAL) in COVID-19 <i>S. Agarwal, et al.</i>	ADULT BRAIN
	285	Quantifying Tissue Properties of the Optic Radiations Using Strategically Acquired Gradient Echo Imaging and Enhancing the Contrast Using Diamagnetic Susceptibility Weighted Imaging <i>P.K. Jella, et al.</i>	ADULT BRAIN FUNCTIONAL
	288	Dural Venous Sinus Stenosis: Why Distinguishing Intrinsic-versus-Extrinsic Stenosis Matters <i>S.H. Sundararajan, et al.</i>	INTERVENTIONAL
	297	Commentary Cerebral Venous Wall Diseases: The Other Side of the Picture <i>S. Lenck, et al.</i>	
	299	Endovascular Recanalization of Symptomatic Nonacute Intracranial Internal Carotid Artery Occlusion: Proposal of a New Angiographic Classification <i>F. Gao, et al.</i>	INTERVENTIONAL
	306	Distal Vessel Imaging via Intra-arterial Flat Panel Detector CTA during Mechanical Thrombectomy <i>T. Nozaki, et al.</i>	INTERVENTIONAL
	313	Transradial Approach for Neuroendovascular Procedures: A Single-Center Review of Safety and Feasibility <i>D.T. Goldman, et al.</i>	INTERVENTIONAL
	319	Periprocedural Safety and Feasibility of the New LVIS EVO Device for Stent-Assisted Coiling of Intracranial Aneurysms: An Observational Multicenter Study <i>D.F. Vollherbst, et al.</i>	INTERVENTIONAL
	327	Outcome of Flow Diverters with Surface Modifications in Treatment of Cerebral Aneurysms: Systematic Review and Meta-analysis <i>Y.-L. Li, et al.</i>	INTERVENTIONAL
	334	WEB Device Shape Changes in Elastase-Induced Aneurysms in Rabbits <i>Y. Ding, et al.</i>	INTERVENTIONAL
	340	Assessment of 4D MR Angiography at 3T Compared with DSA for the Follow-up of Embolized Brain Dural Arteriovenous Fistula: A Dual-Center Study <i>B. Dissaux, et al.</i>	INTERVENTIONAL
	347	Applications of a Novel Microangioscope for Neuroendovascular Intervention <i>V.M. Srinivasan, et al.</i>	INTERVENTIONAL
	354	Correlation of Technical and Adjunctive Factors with Quantitative Tumor Reduction in Children Undergoing Selective Ophthalmic Artery Infusion Chemotherapy for Retinoblastoma <i>T. Abruzzo, et al.</i>	INTERVENTIONAL PEDIATRICS
	362	Cone-beam CT versus Multidetector CT in Postoperative Cochlear Implant Imaging: Evaluation of Image Quality and Radiation Dose <i>R.A. Helal, et al.</i>	HEAD & NECK
	368	MR Imaging Characteristics of Intraocular Perfluoro-n-Octane <i>M.T. Williams, et al.</i>	HEAD & NECK
	370	Vestibular Implant Imaging <i>A. Hedjoudje, et al.</i>	HEAD & NECK
	377	Assessment of the Membranous Labyrinth in Infants Using a Heavily T2-Weighted 3D FLAIR Sequence without Contrast Agent Administration <i>G. Conte, et al.</i>	PEDIATRICS
	382	Pediatric Head CT: Automated Quantitative Analysis with Quantile Regression <i>K.A. Cauley, et al.</i>	PEDIATRICS FUNCTIONAL



389 Involvement of the Spinal Cord in Primary Mitochondrial Disorders: A Neuroimaging Mimicker of Inflammation and Ischemia in Children
C.A.P.F. Alves, et al.

PEDIATRICS

397 Spinal CSF-Venous Fistulas in Morbidly and Super Obese Patients with Spontaneous Intracranial Hypotension
W.I. Schievink, et al.

SPINE

ONLINE FEATURES

LETTERS

E1 Seeing What We Expect to See in COVID-19 *A. Mamourian*

E2 Reply *M.F.V.V. Aragão, et al.*

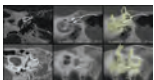
E4 COVID-19 Related Central Nervous System Vasculopathy: Beyond Vasculitis *M. Quintas-Neves*

E5 Reply *D.R. Hanafi, et al.*

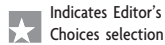
E6 **ERRATUM**

BOOK REVIEWS *R.M. Quencer, Section Editor*

Please visit www.ajnrblog.org to read and comment on Book Reviews.



From Hedjoudje, et al.: Generation of multislice CT and flat-panel CT MPR.



Indicates Editor's Choices selection



Indicates Fellows' Journal Club selection



Indicates open access to non-subscribers at www.ajnr.org



Indicates article with supplemental online table



Indicates article with supplemental online photo



Indicates article with supplemental online video



Evidence-Based Medicine Level 1



Evidence-Based Medicine Level 2

EDITOR-IN-CHIEF

Jeffrey S. Ross, MD

Professor of Radiology, Department of Radiology,
Mayo Clinic College of Medicine, Phoenix, AZ

SENIOR EDITORS

Harry J. Cloft, MD, PhD

Professor of Radiology and Neurosurgery,
Department of Radiology, Mayo Clinic College of
Medicine, Rochester, MN

Christopher G. Filippi, MD

Professor and Alice Ettinger-Jack R. Dreyfuss
Chair of Radiology,
Tufts University School of Medicine,
Radiologist-in-Chief
Tufts University Medical Center

Thierry A.G.M. Huisman, MD

Radiologist-in-Chief, Texas Children's Hospital,
Houston, TX

Yvonne W. Lui, MD

Associate Professor of Radiology,
Chief of Neuroradiology,
New York University School of Medicine,
New York, NY

C.D. Phillips, MD, FACR

Professor of Radiology, Weill Cornell Medical
College, Director of Head and Neck Imaging,
New York-Presbyterian Hospital, New York, NY

Lubdha M. Shah, MD, MS

Professor of Radiology and Director of Spine
Imaging, University of Utah Department of
Radiology and Imaging Sciences, Salt Lake City, UT

STATISTICAL SENIOR EDITOR

Bryan A. Comstock, MS

Senior Biostatistician,
Department of Biostatistics,
University of Washington, Seattle, WA

ARTIFICIAL INTELLIGENCE DEPUTY EDITOR

Peter D. Chang, MD

Assistant Professor-in-Residence,
Departments of Radiological Sciences,
Computer Sciences, and Pathology,
Director, Center for Artificial Intelligence in
Diagnostic Medicine (CAIDM),
University of California, Irvine, Irvine, CA

EDITORIAL BOARD

Ashley H. Aiken, Atlanta, GA

Lea M. Alhilali, Phoenix, AZ

Mohammed A. Almekhlafi, Calgary, Alberta,
Canada

Joachim Berkefeld, Frankfurt, Germany

Aashim Bhatia, Pittsburgh, PA

Waleed Brinjikji, Rochester, MN

Judah Burns, New York, NY

Danielle Byrne, Dublin, Ireland

Federico Cagnazzo, Montpellier, France

J. Levi Chazen, New York, NY

James Y. Chen, San Diego, CA

Gloria C. Chiang, New York, NY

Daniel Chow, Irvine, CA

Kars C.J. Compagne, Rotterdam, The Netherlands

Arturo Consoli, Suresnes, France

Seena Dehkharghani, New York, NY

Nilesh K. Desai, Houston, TX

Yonghong Ding, Rochester, MN

Birgit Ertl-Wagner, Toronto, Ontario, Canada

Clifford J. Eskey, Hanover, NH

Massimo Filippi, Milan, Italy

Nils D. Forkert, Calgary, Alberta, Canada

Ana M. Franceschi, New York, NY

Frank Gaillard, Melbourne, Australia

Joseph J. Gemmete, Ann Arbor, Michigan

Wende N. Gibbs, Phoenix, AZ

Philipp Gölitz, Erlangen, Germany

Brent Griffith, Detroit, MI

Joseph M. Hoxworth, Phoenix, Arizona

Raymond Y. Huang, Boston, MA

Gábor Janiga, Magdeburg, Germany

Christof Karmonik, Houston, TX

Timothy J. Kaufmann, Rochester, MN

Hillary R. Kelly, Boston, MA

Toshibumi Kinoshita, Akita, Japan

Alexander W. Korutz, Chicago, IL

Stephen F. Kralik, Houston, TX

Alexander Lerner, Los Angeles, CA

Yinsheng Li, Madison, WI

Franklin A. Marden, Chicago, IL

Markus A. Möhlenbruch, Heidelberg, Germany

Kambiz Nael, Los Angeles, CA

Renato Hoffmann Nunes, Sao Paulo, Brazil

Sasan Partovi, Cleveland, OH

Johannes A.R. Pfaff, Heidelberg, Germany

Laurent Pierot, Reims, France

Alireza Radmanesh, New York, NY

Prashant Raghavan, Baltimore, MD

Eytan Raz, New York, NY

Paul M. Ruggieri, Cleveland, OH

Sebastian Schafer, Madison, WI

Maksim Shapiro, New York, NY

Timothy Shepherd, New York, NY

James Shin, New York, NY

Mark S. Shiroishi, Los Angeles, CA

Bruno P. Soares, Baltimore, MD

Jason F. Talbott, San Francisco, CA

Ruth Thiex, Everett, Washington

Vincent Thijs, Melbourne, Victoria, Australia

Anderanik Tomasian, Los Angeles, CA

Fabio Triulzi, Milan, Italy

Anja G. van der Kolk, Utrecht, the Netherlands

Arastoo Vossough, Philadelphia, PA

Elysa Widjaja, Toronto, Ontario, Canada

Leonard Yeo, Singapore

Woong Yoon, Gwangju, South Korea

David M. Yousem, Evergreen, CO

Carlos Zamora, Chapel Hill, NC

Chengcheng Zhu, Seattle, WA

EDITORIAL FELLOW

Matthew D. Alvin, Baltimore, MD

SPECIAL CONSULTANTS TO THE EDITOR

AJNR Blog Editor

Neil Lall, Denver, CO

Case of the Month Editor

Nicholas Stence, Aurora, CO

Case of the Week Editors

Matylda Machnowska, Toronto, Ontario, Canada

Anvita Pauranik, Calgary, Alberta, Canada

Sapna Rawal, Toronto, Ontario, Canada

Classic Case Editor

Sandy Cheng-Yu Chen, Taipei, Taiwan

Health Care and Socioeconomics Editor

Pina C. Sanelli, New York, NY

Physics Editor

Greg Zaharchuk, Stanford, CA

Podcast Editor

Wende N. Gibbs, Phoenix, AZ

Twitter Editor

Roger Jordan, Houston, TX

Official Journal:

American Society of Neuroradiology

American Society of Functional Neuroradiology

American Society of Head and Neck Radiology

American Society of Pediatric Neuroradiology

American Society of Spine Radiology

Founding Editor

Juan M. Taveras

Editors Emeriti

Mauricio Castillo, Robert I. Grossman,

Michael S. Huckman, Robert M. Quencer

Managing Editor

Karen Halm

Assistant Managing Editor

Laura Wilhelm

Editorial Assistant

Margaret B. Sabato

Executive Director, ASNR

Mary Beth Hepp

We're Inside Every Great Neuroradiologist!

ASNR MEMBERS RECEIVE

American Journal of Neuroradiology (AJNR)

The leading neuroradiology research journal, published monthly

Neurographics

Bimonthly educational journal with CME for members

ASNR Annual Meeting

Discounts for members on the field's premier conference

eCME

Online collection of lectures and articles with SA-CME and Category 1 credit

Advocacy

Coding/reimbursement, quality standards and practice guidelines; demonstrating neuroradiology's value!

Networking

Access to 5,000 peers

... And More!

Join the leaders in neuroradiology today!

Learn more at www.asnr.org/join

ASNR

American Society of Neuroradiology

800 Enterprise Dr., Suite 205, Oak Brook, IL 60523 • (630)574-0220 • membership@asnr.org • www.asnr.org

AJNR *go green*

***AJNR* urges American Society of Neuroradiology members to reduce their environmental footprint by voluntarily suspending their print subscription.**

The savings in paper, printing, transportation, and postage directly fund new electronic enhancements and expanded content.

The digital edition of *AJNR* presents the print version in its entirety, along with extra features including:

- Publication Preview
- Case Collection
- Podcasts
- The *AJNR* News Digest
- The *AJNR* Blog

It also reaches subscribers much faster than print. An electronic table of contents will be sent directly to your mailbox to notify you as soon as it publishes.

Readers can search, reference, and bookmark current and archived content 24 hours a day on www.ajnr.org.

ASNR members who wish to opt out of print can do so by using the *AJNR* Go Green link on the *AJNR* Website (<http://www.ajnr.org/content/subscriber-help-and-services>). Just type your name in the email form to stop print and spare our ecosystem.

CALL FOR AJNR EDITORIAL FELLOWSHIP CANDIDATES

2021 Candidate Information and Requirements

ASNR and AJNR are pleased once again to join efforts with other imaging-related journals that have training programs on editorial aspects of publishing for trainees or junior staff (<5 years on staff), including Radiology (Olmsted fellowship), AJR (Figley and Rogers fellowships), JACR (Bruce J. Hillman fellowship), and Radiologia.

GOALS

- Increase interest in editorial and publication-related activities in younger individuals.
- Increase understanding and participation in the AJNR review process.
- Incorporate into AJNR's Editorial Board younger individuals who have previous experience in the review and publication process.
- Fill a specific need in neuroradiology not offered by other similar fellowships.
- Increase the relationship between "new" generation of neuroradiologists and more established individuals.
- Increase visibility of AJNR among younger neuroradiologists.

ACTIVITIES OF THE FELLOWSHIP

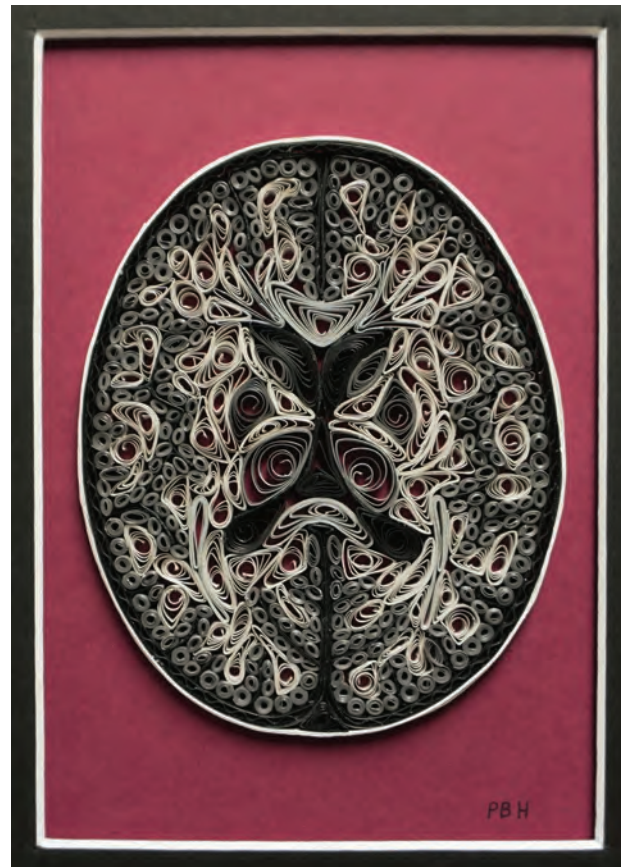
- Serve as Editorial Fellow for one year. This individual will be listed on the masthead as such.
- Review at least one manuscript per month for 12 months. Evaluate all review articles submitted to AJNR.
- Learn how electronic manuscript review systems work.
- Be involved in the final decision of selected manuscripts together with the Editor-in-Chief.
- Participate in all monthly Senior Editor telephone conference calls.
- Participate in all meetings of the Editors during the annual meetings of ASNR and RSNA and the Radiology Editors Forum as per candidate's availability. The Foundation of the ASNR will provide \$2000 funding for this activity.
- Evaluate progress and adjust program to specific needs in annual meeting or telephone conference with the Editor-in-Chief.
- Embark on an editorial scientific or bibliometric project that will lead to the submission of an article to AJNR or another appropriate journal as determined by the Editor-in-Chief. This project will be presented by the Editorial Fellow at the ASNR annual meeting.
- Recruit trainees as reviewers as determined by the Editor-in-Chief.
- Organize and host a Fellows' Journal Club podcast.
- Serve as Guest Editor for an issue of AJNR's News Digest with a timely topic.

QUALIFICATIONS

- Be a fellow in neuroradiology from North America, including Canada (this may be extended to include other countries).
- Be a junior faculty neuroradiology member (< 5 years) in either an academic or private environment.
- Be an "in-training" or member of ASNR in any other category.

APPLICATION

- Include a short letter of intent with statement of goals and desired research project. CV must be included.
- Include a letter of recommendation from the Division Chief or fellowship program director. A statement of protected time to perform the functions outlined is desirable.
- Applications will be evaluated by AJNR's Senior Editors prior to the ASNR annual meeting. The name of the selected individual will be announced at the meeting.
- Applications should be received by March 1, 2021 and sent to Ms. Karen Halm, AJNR Managing Editor, electronically at khalm@asnr.org.



Description: I am a neurologist, and my sister, a newly-retired radiologist, made this and gave it to me recently as a birthday present. The axial brain image was created using the technique of "Quilling," in which strips of paper are coiled (originally around a quill pen) and then glued together to form more complex structures. The artform can be traced to the early Renaissance, when it was practiced in convents in France and Italy to decorate reliquaries and religious manuscripts, possibly in an attempt to mimic more expensive silver and gold filigree or ivory scrollwork. Later, the craft was felt to be a "suitable pastime" for fine young ladies. (Artist: Polly Boren Hansen, MD, San Antonio, Texas)

Rance Boren, MD, Brownwood, Texas

4D-DSA: Development and Current Neurovascular Applications

 K.L. Ruedinger,  S. Schafer,  M.A. Speidel, and  C.M. Strother



ABSTRACT

SUMMARY: Originally described by Davis et al in 2013, 4D-Digital Subtraction Angiography (4D-DSA) has developed into a commercially available application of DSA in the angiography suite. 4D-DSA provides the user with 3D time-resolved images, allowing observation of a contrast bolus at any desired viewing angle through the vasculature and at any time point during the acquisition (any view at any time). 4D-DSA mitigates some limitations that are intrinsic to both 2D- and 3D-DSA images. The clinical applications for 4D-DSA include evaluations of AVMs and AVFs, intracranial aneurysms, and atherosclerotic occlusive disease. Recent advances in blood flow quantification using 4D-DSA indicate that these data provide both the velocity and geometric information necessary for the quantification of blood flow. In this review, we will discuss the development, acquisition, reconstruction, and current neurovascular applications of 4D-DSA volumes.

ABBREVIATION: TDC = time-density curve

In many clinical scenarios, multidetector CT angiography and MRA are adequate for endovascular diagnosis and treatment-planning. However, for complex vascular abnormalities such as aneurysms and AVMs/AVFs, DSA is superior to CTA and MRA due to its improved spatial and temporal resolution.^{1,2} The intracranial vessels most applicable to DSA range in size from 4 to 5 mm (internal carotid artery) to <1 mm (ie, the ophthalmic and anterior choroidal arteries, and the second-division branches and perforators of the middle cerebral artery). These vessels are tortuous and lie in very close proximity to one another; often, they overlap to such a degree that it is challenging to obtain a 2D projection or a 3D volume free of vascular overlap on the display.

In 1997, Fahrig et al³ showed the feasibility of using the projections from 2 rotational acquisitions (one to acquire a mask, the other to acquire projections containing contrast) to obtain a single 3D vascular volume (3D-DSA).⁴ Quickly, the clinical utility of 3D-DSA became apparent. The ability to view the vasculature from any desired angle and with postprocessing capabilities allowing it to be viewed either as a surface-rendered volume or as multiplanar images, offered obvious advantages over 2D projections. However,

even with these advantages, the lack of temporal information in the 3D volume still made it impossible to visualize key characteristics of some abnormalities, eg, the interior features of an AVM nidus or the sequence of blood flow entering and leaving an abnormality.

In 2013, Davis et al⁵ described a reconstruction technique that provided a series of fully time-resolved vascular volumes derived from the projections of a conventional 3D-DSA rotational acquisition. Application of this algorithm generated a time-resolved 3D-DSA, also called 4D-DSA. A 4D-DSA volume can not only be viewed at any desired angle but may also be viewed at any desired time during the passage of a contrast bolus through the vasculature. This volume is achieved using the same x-ray exposure and contrast medium dose that is required to create a single 3D-DSA volume, therefore providing more information with the same parameters.

In the following pages, we will describe and illustrate the following: 1) the development and evolution of DSA from 2D to 3D and 3D to 4D, 2) the injection and acquisition protocol used to obtain a 4D-DSA, 3) the reconstruction workflow to create a 4D vascular volume, 4) the current clinical utility of 4D-DSA, 5) the use of 4D-DSA for calculation of velocity and flow, and 6) current limitations to and helpful solutions for 4D-DSA.

Development and Evolution of 4D-DSA

In 1997, Fahrig et al³ used an image intensifier to reconstruct a 3D vascular volume from projections acquired with 2 C-arm rotations, leading to broad acceptance of the 3D-DSA technology once flat panel detectors became readily available.⁴ The increased

Received July 7, 2020; accepted after revision July 30.

From the School of Medicine and Public Health (K.L.R.) and Departments of Biomedical Engineering (K.L.R.), Medical Physics (M.A.S.), and Radiology (C.M.S.), University of Wisconsin-Madison, Madison, Wisconsin; and Siemens Healthineers (S.S.), Malvern, Pennsylvania.

Please address correspondence to Katrina Ruedinger, MS, c/o Charles Strother, Department of Radiology, WIMR, 1111 Highland Ave, Madison, WI 53705; e-mail: klrueiding@wisc.edu; @Katrina_Rued

 Indicates open access to non-subscribers at www.ajnr.org

<http://dx.doi.org/10.3174/ajnr.A6860>

size and high spatial resolution of these detectors (<0.2-mm pixel side length), in combination with intra-arterial contrast injections, allowed volumetric depiction of vascular abnormalities showing anatomic relationships to adjacent structures and visualization of implanted devices.^{6,7} Today, in clinical practice when diagnosing and treating complex cerebrovascular abnormalities, a combination of 2D- and 3D-DSA is used to depict the complex vascular abnormalities (3D) and analyze the dynamic information about the passage of contrast medium from arteries into veins (2D). In most instances though, the topography of these conditions is such that this combination still does not remove the limitations caused by vascular overlap. For example, while both 2D and 3D images typically provide excellent information about the major arteries and veins supplying an AVM, neither allow detailed assessment of the angioarchitecture of the nidus of the AVM, eg, the presence of intranidal aneurysms or direct AVFs.

Methods aimed at mitigating this limitation by combining the benefits of both 2D- and 3D-DSA have been proposed since the early 2000s. Schmitt et al⁸ developed a method encoding bolus arrival time from 2D-DSA images onto a static 3D-DSA, but each acquisition was acquired separately. Copeland et al⁹ furthered this approach by encoding the contrast passage from biplane 2D-DSA onto a 3D-DSA. Mistretta¹⁰ and Davis et al⁵ combined the above approaches, altering the 3D-DSA contrast injection protocol to that of 2D-DSA and started injections at the beginning of a 3D acquisition. Very quickly, this protocol was modified so that the contrast medium was injected 0.5–1 second after the start of an acquisition. Encoding this temporal information about the passage of a contrast bolus on the 3D-DSA allowed reconstruction of fully time-resolved 4D-DSA. This method became commercially available in 2015 (Siemens). Although the availability of a time-resolved 3D volume diminishes some of the problems caused by vascular overlap, it does not completely resolve this issue. During the rotational acquisition of a 4D-DSA, some degradation of temporal information may occur in any of the 2D projections, ie, when a ray from the source passes through opacified vessels at the same time on its way to the detector.

4D-DSA Acquisition Technique and Injection Protocol

The acquisition technique of a 4D-DSA is generalized into 2 steps: 1) a C-arm rotational acquisition without contrast injection (mask), and 2) a second acquisition with contrast injection (fill). 4D-DSA is designed to allow visualization of the passage of contrast through the 3D vasculature for inspection. For facilitating this process, a contrast-injection protocol was designed to start at the same time or just after (0.5–1 second) the start of the fill acquisition and to stop before the end of the rotation, thereby visualizing both inflow and outflow of blood/contrast. Consideration should be given to the type of vascular abnormality, eg, AVM or stenosis, as well as the patient's cardiac status, eg, normal or abnormal stroke volume.

Accurate geometric reconstruction of the vasculature for 3D-DSA requires that projections be available from about 200° of rotation. However, to ensure the accuracy of both the geometric and temporal information of a 4D-DSA, it was necessary for the angular range to be increased to at least 260° so that different parts of the vasculature, ie, arteries and veins, are all opacified for

the required 200°. In research and clinical practice, a 6- or 12-second 260° fill acquisition during contrast injection is used in accordance with a noninjection mask acquisition. The setup for contrast delivery is the same as for 2D- and 3D-DSA, with appropriate arterial access, catheters, and contrast medium. For a 4D-DSA, the contrast injection is started simultaneous with or just after the beginning of the fill acquisition, depending on the site of injection (close to or further away from the relevant vasculature). Contrast is usually injected for 8 seconds so that each vascular segment in the arterial phase and early venous phase is filled for about 200°. If the rate (milliliters/second) of a contrast medium injection is too high, there will be downstream reflux of the contrast bolus. It has been shown that this phenomenon may prevent mixing of the bolus with the nonopacified blood arriving with each systole, thereby obscuring the pulsatile waveform normally seen in the time concentration curves of the 4D projections. Without the pulsatile information from the contrast bolus mixing with nonopacified blood between systole and diastole, it would be impossible to quantify blood flow using 4D-DSA data.^{11,12} Ruedinger et al¹² reported that an injection protocol of 75% contrast (iopamidol, Isovue 370; Bracco) injected at 2.5 mL/s for 8 seconds satisfies these requirements by producing strong pulsatility in the area of interest.

After a 4D acquisition (both mask and fill acquisitions) and reconstruction, a user has a 4D-DSA vascular volume of $512 \times 512 \times 396$ voxels with resolution of 0.5 mm. It may be viewed on the software as either a movie or interactively using a slider bar to progress through the sequences of timeframes (X Workplace; Siemens). Cropping, thresholding, and dual-volume visualizations of implanted devices are available to the user as well.

4D-DSA Reconstruction Workflow

The reconstruction of 4D-DSA uses the data from a conventional 3D-DSA rotational acquisition (fill run subtracted from the mask run) to create the vasculature geometry. This is then merged with the temporal information from the 2D-DSA projection images generated in the same acquisition. Figure 1 illustrates an overview of the automated reconstruction workflow. First, a thresholded 3D-DSA reconstruction, called a constraint volume, is generated (geometry). Next, for each acquisition angle (and time point), the measured 2D-DSA image is divided by a digital forward projection of the constraint volume. The resulting ratio images describe temporal changes in x-ray intensity, relative to the constraint volume, due to the passage of contrast medium (temporal information). Finally, the temporal information, encoded in the sequence of ratio images, is individually back-projected onto the 3D constraint volume, producing a temporal sequence of 3D images. Each foreground voxel within the constraint volume is corrected by a function based on the ray-dependent ratio.

The result is a fully time-resolved 3D-DSA image (4D-DSA) of the anatomy of interest. The frame rate is identical to the acquisition frame rate (commonly 30 frames/second), and the total number of volumes is identical to the number of projection images in a rotation. For example, a 12-second acquisition rotation would have 304 frames over 260°, yielding >1 frame per degree of rotation. Ultimately, a 4D-DSA vascular volume allows viewing of the contrast bolus passage at any time and any desired viewing angle.

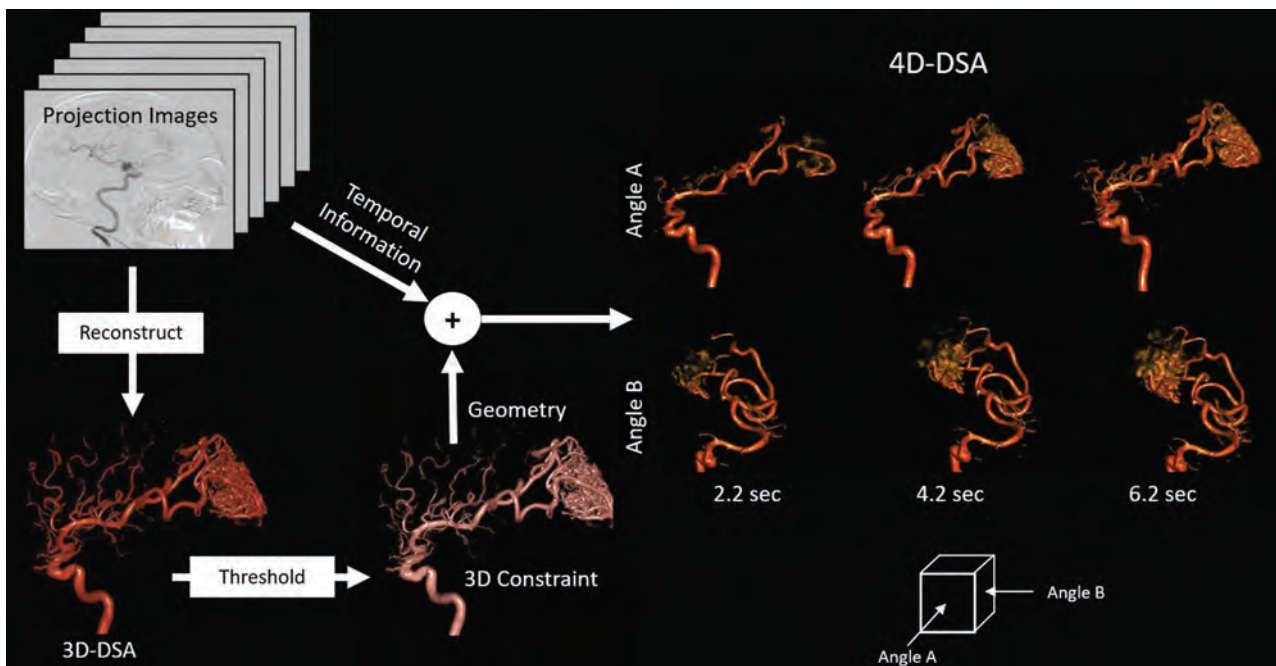


FIG 1. 4D-DSA reconstruction workflow. Starting at the upper left, projection images from a rotational acquisition are reconstructed into a 3D-DSA. Following a threshold approach, a constraint volume is generated, which provides the geometric information for the 4D-DSA. Combining the constraint volume with the angle-specific temporal information results in the volumetric, time-resolved 4D-DSA volume.

Clinical Applications of 4D-DSA

In many instances, noninvasive imaging, ie, CTA or MRA, is sufficient to establish the presence and type of cerebrovascular anomalies; however, the superior spatial resolution of 2D- and 3D-DSA enhances the user's ability to understand some of the important details of the vascular anatomy. After 4D-DSA became commercially available in 2015, it further improved this capability.

AVMs and AVFs. In a preclinical study, Sandoval-Garcia et al¹³ compared the utility and accuracy of 4D-DSA with that of 2D- and 3D-DSA in a canine model. Angiographic data of the 3 techniques, showing both the intracranial and extracranial vasculature, were scored by 3 experienced neuroradiologists for the technique's ability to do the following: 1) display a series of previously determined vascular segments, 2) determine the direction of filling of the segment (antegrade or retrograde), and 3) determine the technique they would choose for performing the previous 2 tasks. In 74% of the datasets, 4D-DSA was judged to be superior to the other methods. It was also reported that the use of the 4D-DSA reconstruction alone would have resulted in a very meaningful reduction in both contrast dose and radiation exposure.¹³

Later reports by Sandoval-Garcia et al¹⁴ and by Lescher et al¹⁵ demonstrated the value of 4D-DSA in the diagnostic evaluation of AVMs. In the 2017 study of Sandoval-Garcia et al,¹⁶ the angioarchitecture from 2D, 3D, and 4D-DSA acquisitions of 6 AVMs was compared by 4 experienced observers. By consensus, the 4D-DSA studies provided the best ability to display the presence of intranidal aneurysms, fistulas, venous obstructions, and the sequence of filling and draining, all of which are important for diagnosis.¹⁶ Figure 2 illustrates the difficulty of 3D-DSA in viewing the angioarchitecture of the nidus due to vessel overlap and the improvement when viewing the nidus with the combined spatial

and temporal features of 4D-DSA. Lescher et al¹⁵ also evaluated the utility of 2D, 3D, and 4D reconstructions for displaying these same features. In both AVMs ($n = 19$) and AVFs ($n = 9$), the 4D-DSA studies provided the best detail of the angioarchitecture at the fistulous point or the nidus. Figure 3 illustrates the improved viewing of an AVF with time-resolved 4D-DSA.

In a single-center study of 26 AVMs, Lang et al¹⁷ confirmed the ability of 4D-DSA to show details of anatomy, as well as 2D images; additionally, nidal features of the AVMs were most clearly seen in the 4D reconstructions. On the basis of their observations, they postulated that the availability of the 4D application would decrease the number of 2D studies needed, therefore decreasing the radiation dose.

In addition to diagnosis, 4D-DSA added value over conventional techniques when used to create a treatment plan for AVMs for gamma knife radiosurgery (stereotactic radiosurgery). Chen et al¹⁸ compared the original treatment plans based on MR imaging and 2D-DSA with ones based on 4D-DSA in 20 consecutive patients with AVMs ($n = 12$) or AVFs ($n = 8$) who were scheduled for gamma knife radiosurgery. The radiosurgery treatment plans were overlaid, and the registration errors were compared. The determined area for treatment created with 4D-DSA was generally smaller and more clearly demonstrated the AVM nidus (in instances when it was supplied by multiple arteries) in comparison with the areas from conventional treatment plans. This study suggests that the use of 4D-DSA for AVM radiosurgery could reduce the target volumes of irradiation, which may result in a decrease in the adverse effects of vascular radiosurgery.¹⁸

Intracranial Aneurysms. Endovascular treatment is now an option for most intracranial aneurysms. For safe and effective treatment, it is essential that both the relationship of an aneurysm

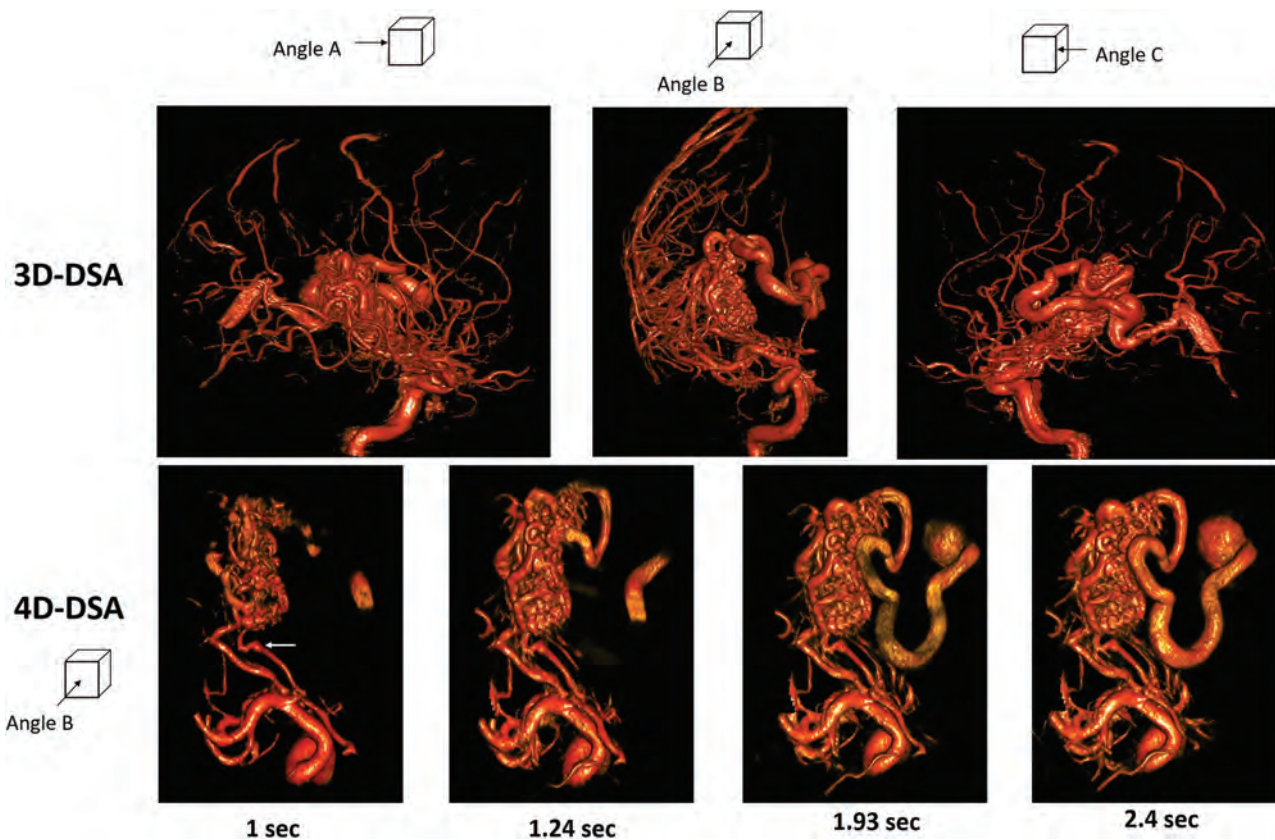


FIG 2. Three views from 3D-DSA of a patient with an AVM supplied by the lenticulostriate arteries (*upper row*). While the anatomic detail is excellent, vascular overlap in and around the nidus makes it impossible to see the angioarchitecture and to understand the sequences of blood flow into and out of the AVM. Early timeframes of the 4D-DSA (*lower row*) show details of the AVM nidus that are not visible on 3D-DSA. Note the small aneurysm on one of the lenticulostriate arteries (*white arrow*). No intranidal aneurysms are seen. Although the 4D-DSA images provided here are at 1 angle (angle B), these images may be viewed at any desired angle at any time of bolus passage.

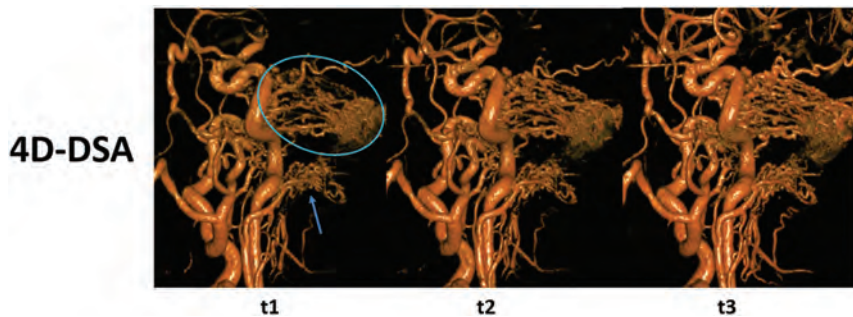


FIG 3. Three 4D-DSA images from early timeframes (t1–t3) of the filling of an AVF located along the intracranial surface of the petrous bone (*blue circle*). t1 shows several small arteries supplying the AVF (*blue arrow*). In the image from t3, acquired less than a second later, these arteries are obscured. This information is helpful when trying to plan an endovascular approach to this abnormality.

to the parent artery and to adjacent branches and the characteristics of the aneurysm be precisely defined. The accuracy of this information depends on the imaging technique chosen and the reconstruction tools used. Figure 4 illustrates a case with an intracranial aneurysm in which the spatial and temporal data obtained from 4D-DSA provide the ability to see the aneurysm in an unobstructed view, which is not possible with 3D-DSA modalities.

were performed using edge enhancement or Hounsfield unit kernels and normal or smooth image characteristics. Aneurysm volume, surface area, dome height, and minimum and maximum ostium diameter measurement were made on 5 patient-specific 3D printed aneurysm models. The actual dimensions were determined from microCT measurements of the models, and it was concluded that reconstruction parameters had very little impact on aneurysm and vessel measurements.²⁰ A subsequent article by this same group

As discussed earlier, the geometry obtained from 3D-DSA is used to create a 4D-DSA, so the geometric accuracy of the 3D-DSA reconstruction is essential for achieving accurate measurements from a 4D-DSA. Studies have shown the ability of 3D-DSA to accurately display the dimensions of intracranial vasculature, as well as intracranial aneurysm volume, with satisfactory precision.^{19,20} In an effort to further improve the precision of dimensional measurements obtained from 4D-DSA, Ruedinger et al²¹ evaluated the impact of various commercial reconstruction parameters on the accuracy of these measurements. Vessel reconstructions

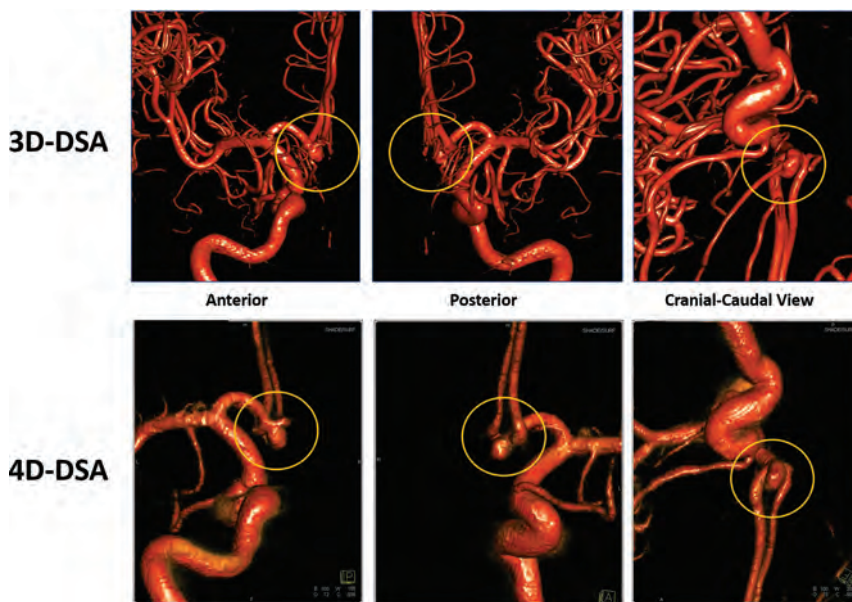


FIG 4. An anterior communicating artery aneurysm viewed from the anterior, posterior, and cranial-caudal positions of a 3D-DSA (upper row) and a 4D-DSA (lower row). The branches that obscure the view of the aneurysm (yellow circle) in the 3D-DSA are not yet filled in the 4D-DSA image, making the aneurysm neck and its relationship to adjacent branches visible. This information aids in the endovascular treatment of intracranial aneurysms.

showed that when using a proper protocol for the injection of contrast medium, both the spatial information of 3D-DSA (geometry) and the temporal information of 4D-DSA (flow) remained highly accurate.¹² Additionally, Sandoval-Garcia et al¹⁶ also found complete agreement in diagnostic characteristics in images from 2D-, 3D-, and 4D-DSA datasets. For endovascular treatment of aneurysms, it is critical that precise information on vessel sizes, ostium characteristics, and parent artery branch relationships be available.

Occlusive Disease. There are few reports about the use of 4D-DSA in the diagnosis or treatment-planning of patients with occlusive disease. However, in patients for whom stent placement or angioplasty is indicated, the ability to make measurements from images with better spatial resolution than either CTA or MRA improves the ability to select optimal stent and balloon sizes. In a series of 24 patients with ($n = 6$) and without ($n = 18$) an MCA stenosis, Kammerer et al²² compared the utility of 4D-DSA with that of 3D-DSA for displaying the anatomy of the lenticulostriate arteries. Overall, the 4D-DSA reconstructions provided a superior display of the lenticulostriate artery anatomy; in patients with a chronic MCA stenosis, the 4D images also showed connections to the collateral network. The ability to view any time point in the contrast filling of a time-resolved 3D geometry was advantageous, compared with a conventional plain 3D geometry.²²

Quantification of Blood Flow from 4D-DSA

The temporal information contained in 4D-DSA is sufficient to quantify blood velocity, and when combined with accurate vessel measurements, blood flow can be quantified.^{12,23} Flow derivation is based on identifying the time needed for a contrast bolus to pass between 2 points; this movement is captured in the time-density

curves (TDCs) of 4D-DSA (also called time-concentration curves). Each voxel contains a TDC depicting bolus inflow, steady state, and bolus outflow. As the bolus moves through the vasculature, cardiac-derived oscillation in a ratio of contrast medium to nonopacified blood is observed. This oscillation superimposes on the TDCs as a quasi-sine wave (Fig 5). Investigating the TDCs shows a position-dependent temporal shift between the contrast-arrival time and the phase of the contained quasi-sine curve. Figure 5 illustrates a simplified schematic of how blood flow is quantified using 4D-DSA.

This effect, as first identified by Waechter et al,²⁴ can be used to derive velocity and flow of the liquid. Waechter et al used a 2D representation of the contrast agent over a given vessel segment and fit virtual maps representing a given velocity and flow to the measured data. For measuring the data, the vessel centerline and radii are first determined in 3D. Subsequently, a 2D flow map is determined showing the TDC of a given centerline voxel along the y-axis and displaying each centerline voxel in directional order. Then, by means of mathematic models of the blood flow, contrast injection, and fluid mixture and propagation, a simulated flow map is determined. The final step is error minimization between the simulated and measured flow map.

Wu et al²⁵ applied a shifted least-squares analysis to time curves in a given phantom vessel segment. The vessel centerline and radii of each vessel segment of interest were determined at discrete intervals, and TDCs were recorded. Each TDC was shifted with respect to all other TDCs, and the temporal shift yielding the minimum least-squares difference was computed. A velocity for the segment was determined from temporal shift and spatial distance information with a relative root-mean-square error of 11% and a Pearson correlation coefficient with phase contrast (PC)-MR imaging of $r = 0.835$.²⁵

Shaughnessy et al²⁶ derived a similar shift from the phase signal in the Fourier domain to determine liquid velocities in a given 3D-printed, patient-specific vessel segment. In each vessel segment, the vessel centerline, discrete distances, and radii were determined. TDCs for each vessel centerline point were Fourier-transformed, and the fundamental frequency and associated phases were determined. The temporal shift of the TDC between 2 vessel centerline points was determined as the phase shift at the TDC fundamental frequency. This work yielded velocities within 10% of the ultrasonic flow meter and was extended to include a mass-preservation constraint to establish preserved flow across multiple bifurcations.^{26,27}

In a study of AVMs, Lin et al²⁸ showed the feasibility of measuring blood velocity in the angiography suite using 4D-DSA. The study used a similar approach by taking the pulsatile information

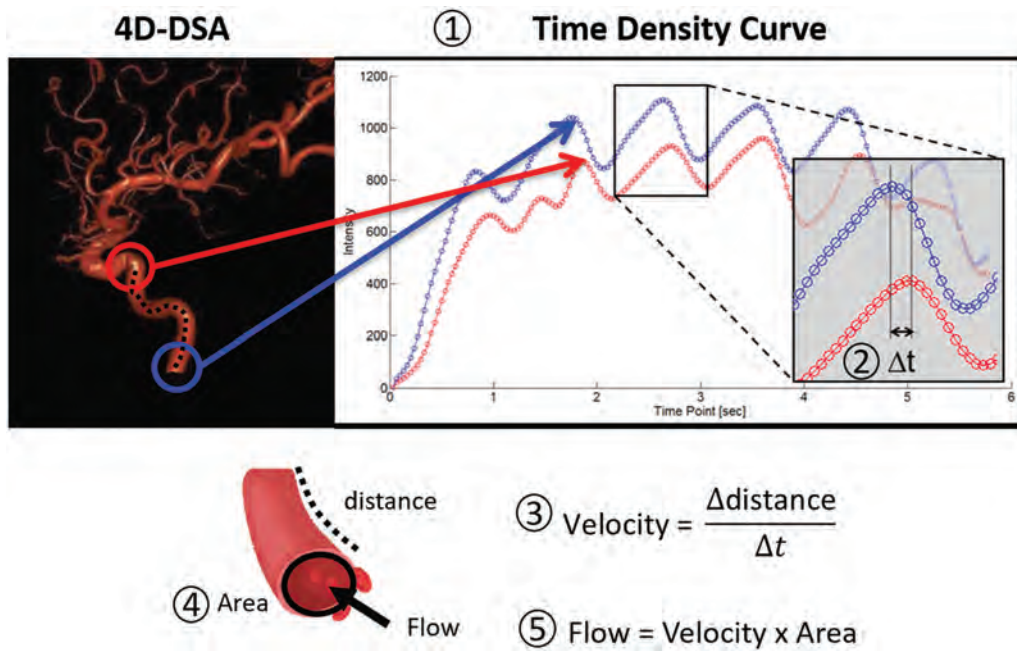


FIG 5. Simplified schematic of how flow is quantified using 4D-DSA: 1) Variations in the contrast density are due to the mixing of contrast with nonopacified blood at and downstream from the injection site with each cardiac cycle. These variations can be tracked in a time density curve (TDC) at any point along the vessel. 2) The time it takes the contrast bolus to arrive at a more distal location is quantified by the time-shift between the peak of the curves (Δt). 3) Velocity is calculated by knowing the distance and time between 2 points in the vasculature. 4) The area of the vessel is calculated from the 4D-DSA geometry. 5) The flow is quantified using the velocity and area.

of the TDC and determining the peak-to-peak distance in ICA segments. With the temporal shift, as well as distance and vessel diameter determined, the contrast/blood mixture velocity and flow were derived. Evaluation of hemorrhagic-versus-nonhemorrhagic AVMs showed an increased velocity and flow in the hemorrhagic group, albeit the results were not statistically significant. To our knowledge, it is not known how vascular overlap may affect the accuracy of flow quantification. All methods mentioned above have been evaluated in noncommercial implementations of 4D-DSA algorithms and are currently not clinically available.

Limitations and Helpful Solutions

As is the case for 3D-DSA, patient motion, improper timing of the contrast injection, and involuntary vessel and muscle movement can all degrade the spatial and temporal information contained in a 4D-DSA reconstruction. If the injection sequence is used appropriately and no patient motion occurs, Lang et al²⁹ showed that the geometry of the vasculature from a 4D-DSA is as reliable as conventional 3D-DSA. As briefly mentioned, vascular overlap may occur in ≥ 1 of the 2D projections acquired during a rotational acquisition, which may have an impact on some of the temporal information in the 4D volume of the projection. Nonetheless, the added temporal dimension in a 4D-DSA means that the clinician is no longer forced to view vasculature solely at the time of maximum contrast enhancement, as is the case in a conventional 3D-DSA. By selecting different timeframes of bolus passage and viewing angles for image display, one can separate vascular structures that fill at different time points and that would have previously been obscured by overlap on many 2D projections and 3D images.

As previously mentioned, there is a distinct overlap phenomenon, arising at specific 2D projection angles during the acquisition

when 2D images of superimposed contrast-enhanced arteries and veins are captured. Although these structures may be spatially separated in the 4D-DSA reconstruction and not visually overlapped, there is a possibility that, in some voxels, there may be mixing of temporal information at certain time points. The degree to which this affects flow quantification has not, to our knowledge, been defined. To resolve the ambiguity, Huizinga et al³⁰ detailed, in a recent publication, the use of a novel reconstruction algorithm that uses a logical flow constraint. The algorithm enforces a connectivity between filling vasculature segments, removing erroneous early filling in distal vasculature by requiring a previously filled connected vessel.

From the perspective of a clinician using 4D-DSA for diagnosis and treatment-planning, postprocessing techniques have been found useful to further reduce the limitations caused by vascular overlap. One example is when vessels from one vascular territory are, in many viewing angles, superimposed on those from another territory, eg, MCA territory on ACA territory. We refer to this type of overlap as “superimposition,” which is different from the vascular overlap that occurs when vessels in such close proximity can only be separated by viewing 4D timeframes acquired before the overlapping vessels are opacified. Superimposition can usually be resolved by simply cutting out the part of the 4D volume that is not of clinical interest, eg, the ACA territory when trying to view the details of an MCA aneurysm.

Another limitation of using a 4D-DSA volume occurs when a user thresholds an entire 4D volume. The optimal threshold for arteries will not be the same as those for veins because of the differences in contrast concentration and volume. Likewise, the optimal threshold for large arteries and veins will be different from that for

small arteries or veins. By using the postprocessing tool to cut out a small ROI from the 4D volume and then thresholding it, one can view the anatomic and blood flow features; this outcome is not possible when thresholding the entire 4D volume at once.

Summary

4D-DSA, first developed in 2013, is a commercially available angiographic technique that provides the user with a fully time-resolved 3D volume of the vasculature. The ability to see any desired viewing angle at any desired time of bolus passage adds benefit over conventional 2D- and 3D-DSAs for cerebrovascular diseases.

Disclosures: Sebastian Schafer—UNRELATED: Employment: Siemens Healthineers, Comments: I am a full-time employee. Michael A. Speidel—RELATED: Grant: National Institutes of Health, Siemens Healthineers, Comments: Partial financial support was received from National Institutes of Health grant No R01HL16567 and a sponsored research agreement with Siemens Healthineers*; UNRELATED: Grants/Grants Pending: Principal Investigator on National Institutes of Health grant No. R21EB023008 and a sponsored research agreement with Siemens Healthineers (both outside the scope of the present work)*; Patents (Planned, Pending or Issued): coinventor on US Patent 10,002,445 B2 related to 4D-DSA, and coinventor on 3 patents/patents pending that are outside the scope of the present work* *Money paid to the institution.

REFERENCES

1. Vertinsky AT, Schwartz NE, Fischbein NJ, et al. **Comparison of multidetector CT angiography and MR imaging of cervical artery dissection.** *AJNR Am J Neuroradiol* 2008;29:1753–60 CrossRef Medline
2. Veldhoen S, Schöllchen M, Hanken H, et al. **Performance of cone-beam computed tomography and multidetector computed tomography in diagnostic imaging of the midface: a comparative study on phantom and cadaver head scans.** *Eur Radiol* 2017;27:790–800 CrossRef Medline
3. Fahrig R, Fox AJ, Lownie S, et al. **Use of a C-arm system to generate true three-dimensional computed rotational angiograms: preliminary in vitro and in vivo results.** *AJNR Am J Neuroradiol* 1997;18:1507–14 Medline
4. Fahrig R, Holdsworth DW. **Three-dimensional computed tomographic reconstruction using a C-arm mounted XRII: image-based correction of gantry motion nonidealities.** *Med Phys* 2000;27:30–38 CrossRef Medline
5. Davis B, Royalty K, Kowarschik M, et al. **4D digital subtraction angiography: implementation and demonstration of feasibility.** *AJNR Am J Neuroradiol* 2013;34:1914–21 CrossRef Medline
6. Akpek S, Brunner T, Benndorf G, et al. **Three-dimensional imaging and cone beam volume CT in C-arm angiography with flat panel detector.** *Diagn Interv Radiol* 2005;11:10–13 Medline
7. Baba R, Konno Y, Ueda K, et al. **Comparison of flat-panel detector and image-intensifier detector for cone-beam CT.** *Comput Med Imaging Graph* 2002;26:153–18 CrossRef Medline
8. Schmitt H, Grass M, Suurmond R, et al. **Reconstruction of blood propagation in three-dimensional rotational x-ray angiography (3D-RA).** *Comput Med Imaging Graph* 2005;29:507–20 CrossRef Medline
9. Copeland AD, Mangoubi RS, Desai MN, et al. **Spatio-temporal data fusion for 3D+T image reconstruction in cerebral angiography.** *IEEE Trans Med Imaging* 2010;29:1238–51 CrossRef Medline
10. Mistretta CA. **Sub-Nyquist acquisition and constrained reconstruction in time resolved angiography.** *Med Phys* 2011;38:2975–85 CrossRef Medline
11. Lieber BB, Sadasivan C, Hao Q, et al. **The mixability of angiographic contrast with arterial blood.** *Med Phys* 2009;36:5064–78 CrossRef Medline
12. Ruedinger KL, Harvey EC, Schafer S, et al. **Optimizing the quality of 4D-DSA temporal information.** *AJNR Am J Neuroradiol* 2019;40:2124–29 CrossRef Medline

13. Sandoval-Garcia C, Royalty K, Aagaard-Kienitz B, et al. **A comparison of 4D DSA with 2D and 3D DSA in the analysis of normal vascular structures in a canine model.** *AJNR Am J Neuroradiol* 2015;36:1959–63 CrossRef Medline
14. Sandoval-Garcia C, Royalty K, Yang P, et al. **4D DSA: a new technique for arteriovenous malformation evaluation: a feasibility study.** *J Neurointerv Surg* 2016;8:300–04 CrossRef Medline
15. Lescher S, Gehrisch S, Klein S, et al. **Time-resolved 3D rotational angiography: display of detailed neurovascular anatomy in patients with intracranial vascular malformations.** *J Neurointerv Surg* 2017;9:887–94 CrossRef Medline
16. Sandoval-Garcia C, Yang P, Schubert T, et al. **Comparison of the diagnostic utility of 4D-DSA with conventional 2D- and 3D-DSA in the diagnosis of cerebrovascular abnormalities.** *AJNR Am J Neuroradiol* 2017;38:729–34 CrossRef Medline
17. Lang S, Göltz P, Struffert T, et al. **4D DSA for dynamic visualization of cerebral vasculature: a single-center experience in 26 cases.** *AJNR Am J Neuroradiol* 2017;38:1169–76 CrossRef Medline
18. Chen KK, Guo WY, Yang HC, et al. **Application of time-resolved 3D digital subtraction angiography to plan cerebral arteriovenous malformation radiosurgery.** *AJNR Am J Neuroradiol* 2017;38:740–46 CrossRef Medline
19. Yang P, Schafer S, Royalty K, et al. **Measurement in the angiography suite: evaluation of vessel sizing techniques.** *J Neurointerv Surg* 2016;8:965–68 CrossRef Medline
20. Bescós JO, Slob MJ, Slump CH, et al. **Volume measurement of intracranial aneurysms from 3D rotational angiography: improvement of accuracy by gradient edge detection.** *AJNR Am J Neuroradiol* 2005;26:2569–72 Medline
21. Ruedinger KL, Rutkowski DR, Schafer S, et al. **Impact of image reconstruction parameters when using 3D DSA reconstructions to measure intracranial aneurysms.** *J Neurointerv Surg* 2018;10:285–89 CrossRef Medline
22. Kammerer S, Mueller-Eschner M, Berkefeld J, et al. **Time-resolved 3D rotational angiography (4D DSA) of the lenticulostriate arteries: display of normal anatomic variants and collaterals in cases with chronic obstruction of the MCA.** *Clin Neuroradiol* 2017;27:451–57 CrossRef Medline
23. Xu J, Shaughnessy G, Schafer S, et al. **Assessing the reliability of pulsatility in four-dimensional digital subtraction angiography time concentration curves.** *Biomed Phys Eng Express* 2018;4:35021 CrossRef
24. Waechter I, Bredno J, Hermans R, et al. **Model-based blood flow quantification from rotational angiography.** *Med Image Anal* 2008;12:586–602 CrossRef Medline
25. Wu Y, Shaughnessy G, Hoffman CA, et al. **Quantification of blood velocity with 4D digital subtraction angiography using the shifted least-squares method.** *AJNR Am J Neuroradiol* 2018;39:1871–77 CrossRef Medline
26. Shaughnessy G, Schafer S, Speidel MA, et al. **Measuring blood velocity using 4D-DSA: a feasibility study.** *Med Phys* 2018;45:4510–18 CrossRef Medline
27. Shaughnessy G, Hoffman C, Schafer S, et al. Precision blood flow measurements in vascular networks with conservation constraints. In: *Medical Imaging 2018: Image-Guided Procedures, Robotic Interventions, and Modeling*. Vol 10576. International Society for Optics and Photonics; 2018;105762Q CrossRef
28. Lin CJ, Yang HC, Chien AC, et al. **In-room assessment of intravascular velocity from time-resolved rotational angiography in patients with arteriovenous malformation: a pilot study.** *J Neurointerv Surg* 2018;10:583–88 CrossRef Medline
29. Lang S, Hoelter P, Birkhold AI, et al. **Quantitative and qualitative fluid dynamics simulations in cerebral aneurysms.** *AJNR Am J Neuroradiol* 2019;40:1505–10 CrossRef Medline
30. Huizinga N, Keil F, Birkhold A, et al. **4D flat panel conebeam CTA for in vivo imaging of the microvasculature of the human cortex with a novel software prototype.** *AJNR Am J Neuroradiol* 2020;41:976–79 CrossRef Medline

Multiphase CT Angiography: A Useful Technique in Acute Stroke Imaging—Collaterals and Beyond

S. Dundamadappa, K. Iyer, A. Agrawal, and D.J. Choi



ABSTRACT

SUMMARY: Multiphase CTA offers several important advantages over the traditional single-phase CTA technique in acute ischemic stroke, including improved detection of large-vessel occlusion, improved characterization of collateral status, improved tolerance of patient motion and poor hemodynamics, and higher interrater reliability. These benefits are gleaned at little additional cost in terms of time, risk to the patient, and capital expense. Existing data suggest that there are important benefits to using multiphase CTA in lieu of single-phase CTA in the initial vessel assessment of patients with acute stroke.

ABBREVIATIONS: AIS = acute ischemic stroke; mCTA = multiphase CTA; sCTA = single-phase CTA

The introduction of IV reperfusion therapy for acute ischemic stroke (AIS) more than 20 years ago spawned an era of dramatic advances in the treatment of patients with AIS. Neuroimaging has consistently played a critical role in triaging patients with acute stroke by helping providers weigh the risks and benefits of treatment options. Important imaging findings during triage of patients with stroke have included intracranial hemorrhage, large-vessel occlusion, core infarct, penumbra, and collateral circulation status. Other less commonly used imaging findings such as thrombus length and thrombus perviousness have also assisted stroke treatment teams.

Neuroradiologists involved in the care of patients with stroke must be conversant with the diagnostic strengths and limitations of various stroke imaging modalities. The value of any imaging test should be considered in the context of its availability, acquisition and postprocessing speed, tolerance of suboptimal patient factors such as motion, and interrater reliability.

Multiple clinical trials have prompted the stroke community to recommend specific imaging modalities for various stroke scenarios, as stated in the latest 2019 American Heart Association/American Stroke Association Guidelines for Management of AIS.¹ In patients with AIS presenting within 6 hours of symptom onset and with a small core infarct on NCCT, CTA or MRA is advised to guide patient selection for mechanical thrombectomy

without the need for additional modalities such as CTP. In patients presenting in the extended 6- to 24-hour window after onset and who have a large-vessel occlusion in the anterior circulation, CTP or diffusion-weighted MR imaging with or without MR perfusion is advised, as supported by the more recent DWI or CTP Assessment with Clinical Mismatch in the Triage of Wake-Up and Late Presenting Strokes Undergoing Neurointervention with Trevo (DAWN) and Endovascular Therapy Following Imaging Evaluation for Ischemic Stroke 3 (DEFUSE 3) trials.^{2,3} The Endovascular Treatment for Small Core and Proximal Occlusion Ischemic Stroke (ESCAPE) trial⁴ and secondary analysis from the Multicenter Randomized Clinical Trial of Endovascular Treatment for Acute Ischemic Stroke in the Netherlands (MR CLEAN) trial⁵ have suggested that collateral status might also be considered when selecting patients for thrombectomy.

In patients with AIS, CTA has been the study of choice for the initial diagnosis of large-vessel occlusion and other important vascular pathology such as dissection. Multiphase CTA (mCTA) is a more recently studied, time-resolved CTA variant in which an arterial and 2 venous phases are acquired. mCTA offers several advantages over the traditional single-phase CTA technique (sCTA), including improved detection of large-vessel occlusion,⁶ higher interrater reliability, and improved characterization of collateral status.⁷ There has been increasing use of mCTA in recent clinical trials.⁴ Our institution, a comprehensive stroke center, adopted mCTA as its standard noninvasive vessel imaging technique for AIS several years ago.

In this review, we discuss the acquisition technique and interpretation of mCTA, its role in AIS patient assessment, its advantages over sCTA, and its limitations. We hope this review will help stroke providers understand the advantages of this evolving technique.

Received June 22, 2020; accepted after revision August 21.

From the Department of Radiology, University of Massachusetts Medical Center, Worcester, Massachusetts.

Please address correspondence to David Choi, MD, PhD, Department of Radiology, Room S2-824, University of Massachusetts Medical Center, 55 Lake Ave North, Worcester MA 01655; e-mail: David.Choi@umassmemorial.org

Indicates open access to non-subscribers at www.ajnr.org

<http://dx.doi.org/10.3174/ajnr.A6889>

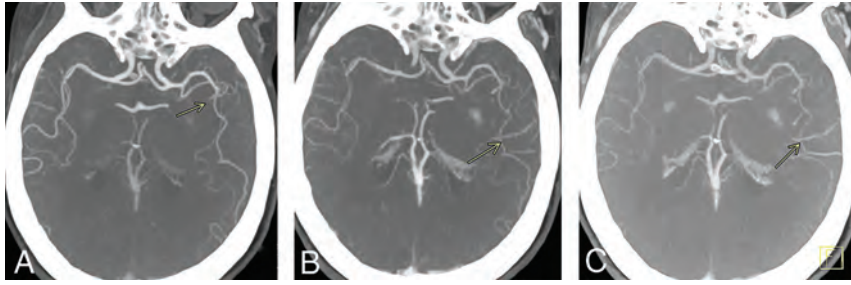


FIG 1. Delayed vessel sign. Peak arterial (A), early venous (B), and late venous (C) phase axial MIP mCTA images show occlusion of a proximal M2 segment (arrow in A) of the left MCA. The delayed vessel sign is demonstrated in the early venous and late venous phases (arrows in B and C), assisting in detection of occlusion.

METHODS

Imaging Protocol for Acute Stroke

At our institution, initial imaging for patients with AIS includes NCCT and mCTA with the goal of door-to-CT table time of less than 20 minutes. For patients presenting between 6 to 24 hours after onset of symptoms or when the time of onset is unknown, CTP is also performed. For a subset of patients (eg, those with strong contraindication to iodinated contrast or those with unclear correlation between imaging findings and neurologic signs), an abbreviated hyperacute MR imaging protocol may be performed instead (consisting of DWI, axial T2 FLAIR, and axial SWI with or without MRA).

Our mCTA protocol (Edge CT scanner; Siemens) is as follows:

- Contrast bolus of 80 cc (Omnipaque 300), at the rate of 4 mL/s followed by a saline chaser.
- First phase (peak arterial phase): Coverage extends from the aortic arch through the vertex. Image acquisition is triggered by bolus monitoring with ROI in proximal descending aorta with a trigger value of 115 HU.
- Second phase (equilibrium/peak venous phase): Coverage extends from the skull base through the vertex performed 4 seconds after completion of the peak arterial phase scan.
- Third phase (late venous phase): Coverage extends from the skull base through the vertex performed 4 seconds after completion of the second phase.

mCTA imposes little burden at postprocessing, requiring only the creation of multiplanar MIP images of the 3 phases. Such MIP images can be generated automatically within minutes using standard vendor software. In the neck, coronal and sagittal plane MIP images are created with a thickness of 5 mm and an interslice gap of 2 mm. In the head, axial plane MIP images are created with a thickness of 20 mm and an interslice gap of 3 mm; MIP images in the coronal and sagittal planes are created with a thickness of 10 mm and an interslice gap of 3 mm. On the PACS, head MIP images are best displayed for each plane with the 3 phases side by side. This arrangement facilitates appreciation of the dynamic behavior of vessel opacification over time. Collateral status is often best assessed on axial head MIP images.

Compared with sCTA, the additional time cost to acquire mCTA includes the scan time for the additional 2 phases of head CTA

(3 seconds each), the time between phases (4 seconds each), and the time required for reconstruction of the additional head MIPs (2–3 minutes). At our institution, iterative reconstruction is turned off at mCTA to shorten the reconstruction time.

Vendor software is available that can create color-coded summation maps of mCTA MIP images, such as the Faststroke package Colorviz view (GE Healthcare). This tool combines information from all 3 phases by color coding vascular segments according to their peak phase of enhancement. These

color-coded mCTA summation maps may facilitate assessment of perfusion delay, distal and multivessel occlusion, critical stenosis, and collateral flow patterns, particularly for less experienced readers.⁸ Although promising, such a tool is not required to realize the benefits of mCTA described in this review, and we have not yet adopted such a tool at our institution.

DISCUSSION

mCTA can be performed on most standard CT platforms. The technique is readily available, rapidly performed, needs no additional contrast material, requires no additional vendor package for specialized postprocessing (as is needed for CTP), and is relatively easy to interpret. mCTA is more accurate than sCTA in assessing collateral status, a useful factor for revascularization decisions in some patients with AIS. In addition, mCTA increases sensitivity for arteriovenous shunting and venous abnormalities.

Sensitivity for Vessel Occlusion

mCTA increases interrater agreement for both proximal (M1, A1 segment) and distal (M2, M3, A2 segment) vessel occlusions compared with sCTA, particularly for trainees, general radiologists, and neurologists.^{9,10} mCTA improves the detection rate of distal vessel occlusions compared with sCTA by virtue of the “delayed vessel sign”¹⁰ (Figs 1 and 2). This sign refers to the delayed enhancement of a vessel segment distal to the point of an occlusion or critical stenosis. The “delayed vessel” reaches peak enhancement at a later phase than equivalent nonoccluded vessels, which can increase the conspicuity of distal vessel occlusions. Such occlusions are sometimes difficult to detect by sCTA regardless of reader experience. It is likely that this “delayed vessel” enhancement reflects retrograde flow via pial collaterals. The delayed vessel sign is less sensitive when there are poor collaterals in the ischemic territory, in occlusions of end arteries or perforator arteries, and with small cortical infarcts.¹⁰

Endovascular intervention has become more common place for some distal vessel occlusions, such as the M2 segment. The safety profile and clinical benefits for treating some M2 occlusions approach that of M1 occlusions.^{11–13} Occlusions of the M2 segment highlight the value of the improved distal vessel detection rate by mCTA compared with sCTA. Even in patients who are not candidates for revascularization therapy, the detection of a distal

segment occlusion may provide added value to patient management, such as when there is unclear correlation between neurologic signs and imaging findings or when there is no core infarct at imaging.

Studies of the time needed for neuroradiologists, radiology trainees, and neurologists to diagnose a large-vessel occlusion by mCTA versus sCTA have favored mCTA.^{9,10} After a training period, readers on average consistently reported greater diagnostic confidence with and expended less time diagnosing large-vessel occlusion by mCTA compared with sCTA examinations. In a study of 2 radiology residents and 2 neuroradiologists, Byrne et al¹⁰ reported the average time needed for the radiology trainees to diagnose proximal M1 occlusions as 34 seconds by mCTA versus 72 seconds by sCTA. The average time for the radiology trainees to diagnose distal vessel occlusions (A2, M2, A3, M3) was 44 seconds by mCTA versus 99 seconds by sCTA. For the 2 neuroradiologists, the average time to diagnose proximal M1 occlusions was 29 seconds by mCTA versus 67 seconds by sCTA. Although the sheer number of additional source and MIP images generated by mCTA may seem discouraging at first, Byrne et al¹⁰ suggested that the diagnostic efficiency of mCTA may be related to the value of the delayed vessel sign.

Length of Occlusion

Accurate assessment of thrombus length has prognostic significance and assists in the planning and execution of thrombectomy. Thrombus burden is a predictor for infarct size, hemorrhagic transformation, and clinical outcome¹⁴ and has implications for therapy. Recanalization is unlikely for IV tPA when the thrombus

length surpasses 8 mm.¹⁵ The clot length is used to select the size of the stent retriever device at thrombectomy.

sCTA may overestimate the length of occlusion because of nonopacification of the vessel distal to the thrombus. Loss of the normal pressure gradient may also result in collapse of the vessel wall distal to the thrombus and may overestimate the length of occlusion (Figs 3 and 4). Clot length has been found to be subjectively easier to measure by mCTA than by catheter angiography even though mCTA is just as reliable.¹⁶

Assessment of Collaterals

There is often marked variability in the extent of neural damage and its clinical manifestation in patients with anterior circulation AIS, especially during the first few hours after onset.¹⁷ Studies have suggested that this variability is in part related to the quantity and quality of collateral circulation.¹⁸ In a 1989 study of 80 patients with AIS, Bozzao et al¹⁹ showed that more extensive collaterals assessed with conventional angiography correlated with smaller final infarct size and better prognosis. More robust collaterals have been linked to lower risk of hemorrhage after endovascular therapy.²⁰ In patients with AIS who do not receive reperfusion treatment, good collaterals have been strongly correlated with better clinical outcomes.²¹ Secondary analysis of CTA collateral status from the MR CLEAN randomized clinical trial showed a positive correlation between collateral score and the degree of endovascular therapy benefit. Conversely, patients with poorer collaterals were less likely to benefit.⁵ Such studies suggest that collateral status may be a useful factor in the management of some patients with AIS, as proposed by the recent 2019 American Heart Association AIS guidelines.⁵

Interest in a time-resolved CTA technique was in part initially motivated by investigators seeking a better tool for collateral status assessment. Because collateral flow to penumbral tissue tends to disperse over time, collateral status is often better assessed using information from multiple time points. Delayed filling of pial collaterals may be underestimated by a single phase. Patients with moderate or good collaterals on mCTA can be erroneously labeled as having poor collaterals

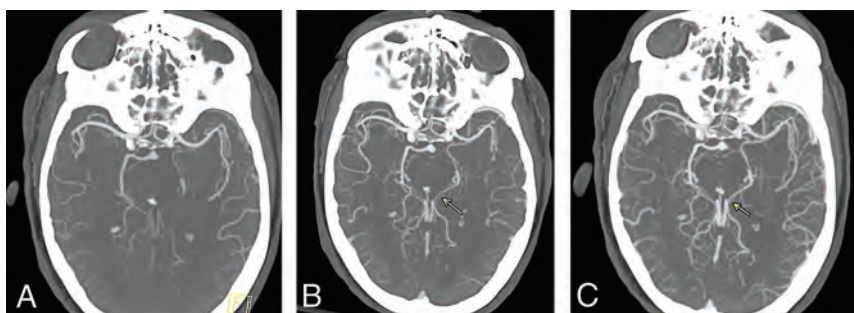


FIG 2. Axial arterial phase mCTA MIP image of a left PCA occlusion (A), which is rendered more conspicuous by delayed vessel opacification in the second and third phases (arrows in B and C).

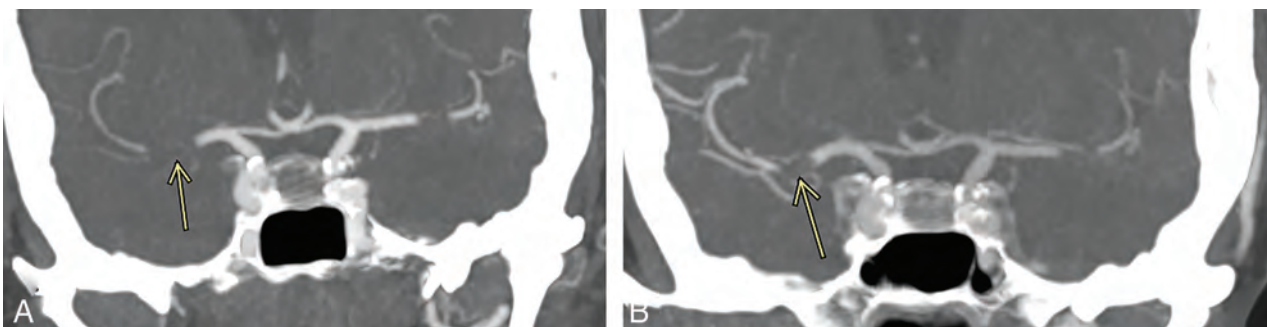


FIG 3. Coronal mCTA MIP images from the arterial phase (A) and late venous phase (B) show a right MCA M1 segment occlusion. The M1 segment thrombus length is estimated more accurately during the venous phase (7 mm in B, arrow) than in the arterial phase (11 mm in A, arrow).

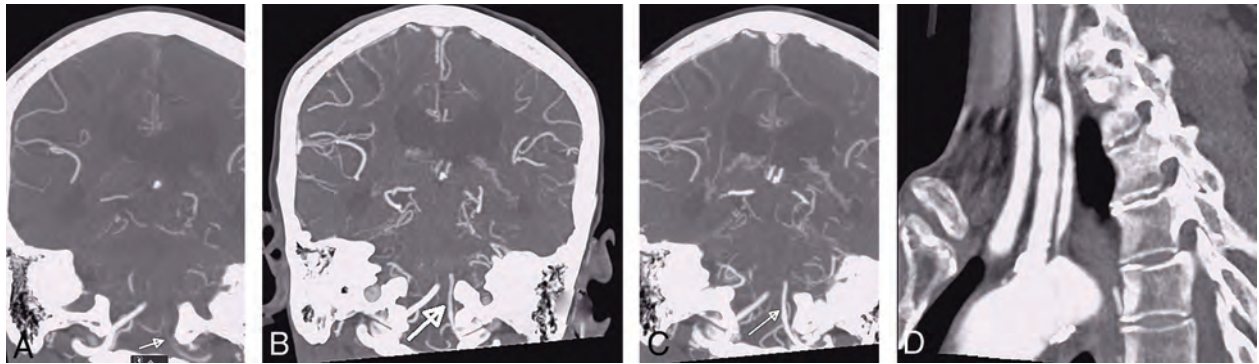


FIG 4. Pseudoocclusion of the left vertebral artery. The left vertebral artery appears occluded at its intracranial V4 segment during the arterial phase of mCTA (*arrow* in *A*). This is related to severe stenosis at its origin (*D*). The previously unopacified intracranial V4 segment is shown to enhance in the delayed phases of mCTA (*arrows* in *B* and *C*). If only single-phase CTA had been used (analogous to the arterial phase of the mCTA, *A*), a V4 segment occlusion would have been diagnosed.

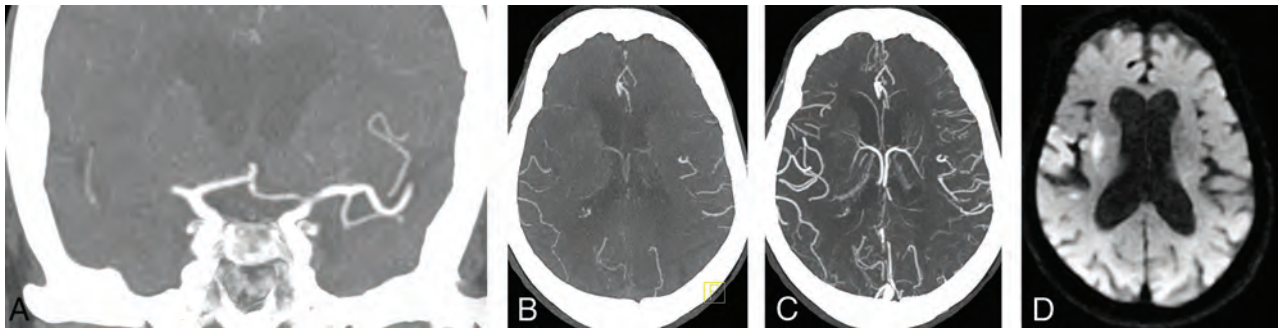


FIG 5. Coronal arterial phase mCTA MIP image demonstrates right M1 segment occlusion (*A*). Axial arterial phase mCTA MIP image (*B*) shows filling of at most 50% of distal branches. Axial delayed phase mCTA MIP image (*C*) shows filling of most distal branches. The patient underwent mechanical thrombectomy with restoration of TIC1 2c flow. Follow-up diffusion-weighted MR image shows a small infarct core. If only sCTA had been used in this case (analogous to the arterial phase of the mCTA, *B*), the collateral status would have been classified as “poor to moderate distal collaterals” instead of “good collaterals.”

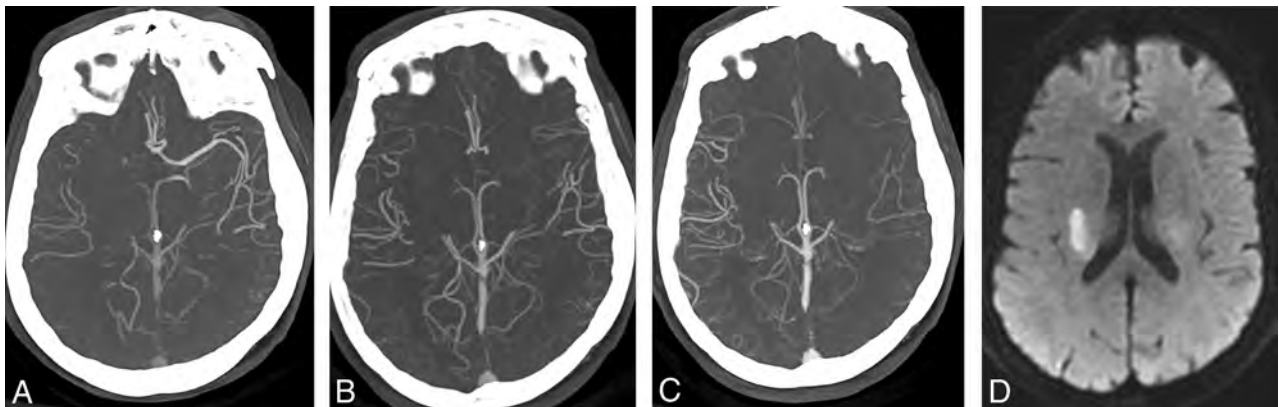


FIG 6. Right M1 segment occlusion. mCTA axial MIP images from the arterial phase (*A*), early venous phase (*B*), and late venous phase (*C*) show progressive collateral filling of distal MCA branches. The patient underwent endovascular recanalization with restoration of TIC1 3 flow. Follow-up diffusion-weighted MR image shows a small infarct core.

at sCTA⁷ (Figs 5–7). Mis-timing of acquisition with sCTA is common, given the older age and variable cardiac status typical of the AIS population. In a study by Casault et al,²² nearly 12% of sCTA

images were acquired either too early or too late, which may have resulted in mislabeling of collateral status. Pial collateral supply between PCA and MCA territories may be slower than that

between ACA and MCA territories.²² This may contribute to limited assessment of collateral status on sCTA.

Several other techniques, including MR-based techniques and processing of CT perfusion data to create dynamic CTA, have been used for assessment of collateral circulation. Although promising, these techniques have yet to reach widespread availability.²³

Ischemic Core

Rapid and accurate assessment of early infarct core and salvageable tissue is important in AIS management. Endovascular therapy has generally been considered to carry a higher risk of hemorrhage when the infarct core volume is greater than 70 to 100 mL.^{24,25} DWI is widely considered the criterion standard for core infarct assessment. However, MR imaging is not always practical in the acute stroke setting.

Perfusion studies have widely been used to estimate infarct core and penumbra volumes. Perfusion studies are typically

performed in patients with anterior circulation large-vessel occlusion who are being considered for mechanical thrombectomy in the extended time window (6–24 hours after onset). Smaller community hospitals often do not have the ability to perform these studies nor the personnel needed for postprocessing and interpretation. Although thrombectomy is not typically performed in the community hospital setting, the superior diagnostic performance of mCTA compared with sCTA may still provide added value in clinical management whether at a community hospital or at a comprehensive stroke center after patient transfer.

Reid et al²⁶ studied the potential value of mCTA in delineating the core ischemic area and detecting tissue at risk. Hypoattenuation that persisted into the venous phase of mCTA was considered better than NCCT in assessing an area of severe ischemia.²⁶ Their data suggested that hypoattenuation in the arterial phase may be useful in identifying tissue at risk for infarction²⁶ (Fig 8). Future clinical trials will be needed to define the value of mCTA in this role.

Currently, mCTA cannot be used to assess penumbra volume, though it may offer some value when penumbra imaging is not feasible, such as in the nontertiary hospital setting.

Thrombus Perviousness

Thrombus permeability (assessed by thrombus perviousness measures) was reported to be an independent predictor of clinical outcome in patients with acute stroke.²⁷ Although it seems intuitive to assume the superiority of mCTA in assessing thrombus perviousness given its temporal resolution, studies have shown little benefit of mCTA over sCTA.²⁷

Predicting Clinical Outcome

Collateral circulation status may predict clinical outcome in AIS, though this has not been consistently reproduced in studies. Menon et al⁷ found

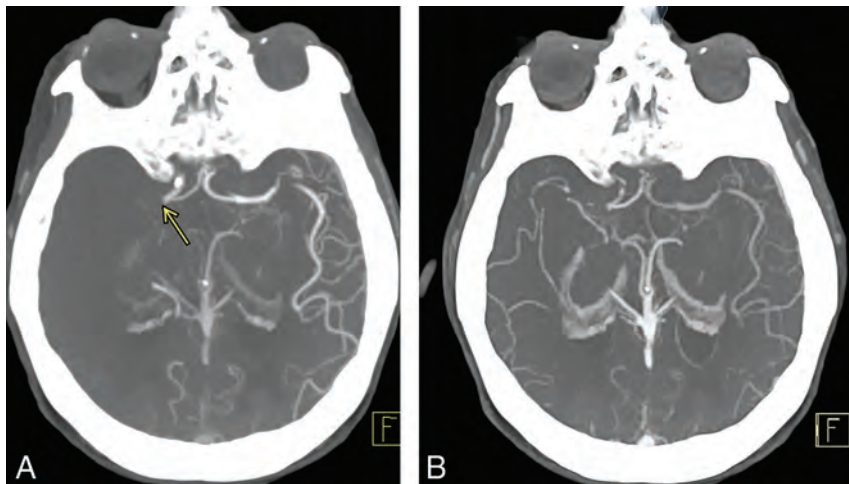


FIG 7. Multiphase CTA arterial phase axial MIP image shows occlusion of the right M1 segment (A, arrow) with no right MCA distal branches. The arterial phase of mCTA is analogous to sCTA and would have been classified as “poor collaterals” in this patient, if considered without the benefit of delayed-phase CTA images. mCTA delayed phase axial MIP in the same patient (B) shows filling of about 50% of right MCA distal branches, resulting in a more accurate assessment of collateral status.

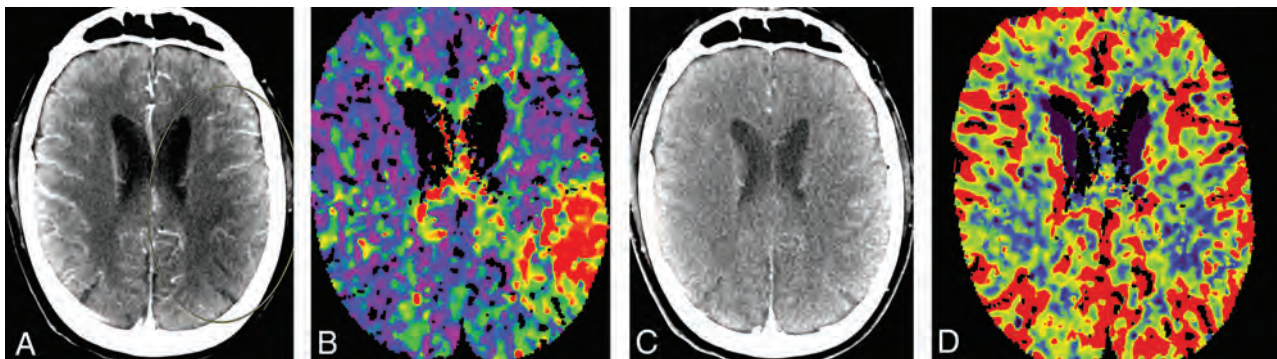


FIG 8. Correlation between mCTA and CT perfusion imaging in a patient with left MCA M2 segment occlusion. A region of hypoattenuation in an arterial phase mCTA source image (A, circled area) closely correlates with a region of delayed Tmax in a CT perfusion image (B), suggestive of tissue at risk. Absence of hypoattenuation in a delayed venous phase mCTA source image (C) is matched by preservation of cerebral blood volume in a CT perfusion image (D), suggestive of no infarct core. The patient underwent endovascular intervention with restoration of TIC1 2b antegrade flow. Subsequent diffusion-weighted MR imaging showed only small foci of acute ischemia in the frontoparietal region (not shown).

mCTA to be superior to sCTA and CTP in determining clinical outcome. In contrast, secondary analysis of data from the DEFUSE 3 randomized clinical trial by de Havenon et al²⁸ showed no correlation between good collaterals assessed by CTA and improved clinical outcome. Among the limitations cited by de Havenon et al²⁸ were the possibility of continued collateral status evolution after imaging assessment and the use of sCTA. Zhang et al²⁹ found that good collaterals are better predictors of favorable outcome in the cardioembolism stroke subtype than in the large artery atherosclerosis stroke subtype.

Radiation Dose

The mean estimated effective dose of mCTA is typically only 20% above that of sCTA compared with 70% added dose for CT perfusion.^{7,30} The added radiation dose to the eye is typically 4 times higher with CT perfusion than with mCTA.⁷

CT Perfusion and mCTA

The DAWN² and DEFUSE 3³ randomized clinical trials have shown benefit from endovascular therapy in the extended time window (6–24 hours), provided that the infarct core was small and there was a large amount of tissue at risk. The 2019 American Heart Association AIS guidelines recommend obtaining CTP or DWI with or without MR perfusion in the extended time window after anterior circulation large-vessel occlusion.¹ However, the AHA guidelines also suggest that collateral assessment may be useful in selecting some patients for mechanical thrombectomy, citing the use of mCTA collateral assessment for patient selection in the ESCAPE randomized clinical trial.⁴ Secondary analysis from the MR CLEAN trial has also supported the utility of collateral status.⁵ These initial studies have prompted increased use of mCTA in recent randomized clinical trials. Definitive recommendations on the role of mCTA in AIS management will await the completion of such trials.

The improved vessel occlusion detection rate, higher inter-rater reliability, improved measurement of thrombus length, and relatively low costs of mCTA support its use in lieu of sCTA as the standard initial vessel imaging test in the AIS setting. mCTA may be more resistant to patient motion, poor hemodynamics, and other technical factors compared with sCTA or CTP.

Limitations

As with any other test, mCTA should be interpreted in conjunction with clinical information and other available imaging, including NCCT. Flow-limiting stenosis in proximal neck vessels can potentially delay opacification of pial vessels in both ischemic and nonischemic tissue and thus lead to suboptimal assessment of collateral status. Poor hemodynamics can result in poor pial vessel opacification and thereby limit the benefits of temporal resolution at vessel imaging.

mCTA is of limited value in posterior circulation AIS, except in cases involving the posterior cerebral artery.⁷ This is likely related to the highly variable vascular anatomy of the posterior circulation and thus its poorly understood collateral supply.

CONCLUSIONS

In summary, mCTA offers several significant advantages over the traditional sCTA technique in AIS assessment, including improved detection of vessel occlusion, improved collateral status assessment, improved tolerance of suboptimal patient factors, and higher interrater reliability.²⁶ These benefits are gleaned at little additional cost in terms of time, risk to the patient, and capital expense. Although future study results will be needed to ascertain the role of mCTA in relation to perfusion techniques and DWI in the extended time window, existing data already suggest that there are important benefits to using mCTA in lieu of sCTA in the initial vessel assessment of patients with acute stroke.

REFERENCES

1. Powers WJ, Rabinstein AA, Ackerson T, et al. **Guidelines for the Early Management of Patients With Acute Ischemic Stroke: 2019 Update to the 2018 Guidelines for the Early Management of Acute Ischemic Stroke: A Guideline for Healthcare Professionals From the American Heart Association/American Stroke Association.** *Stroke* 2019;50:e344–418 CrossRef Medline
2. Nogueira RG, Jadhav AP, Haussen DC, et al. **Thrombectomy 6 to 24 hours after stroke with a mismatch between deficit and infarct.** *N Engl J Med* 2018;378:11–21 CrossRef Medline
3. Albers GW, Marks MP, Kemp S, et al. **Thrombectomy for stroke at 6 to 16 hours with selection by perfusion imaging.** *N Engl J Med* 2018;378:708–18 CrossRef Medline
4. Goyal M, Demchuk AM, Menon BK, et al. **Randomized assessment of rapid endovascular treatment of ischemic stroke.** *N Engl J Med* 2015;372:1019–30 CrossRef Medline
5. Berkhemer OA, Jansen IGH, Beumer D, et al. **Collateral status on baseline computed tomographic angiography and intra-arterial treatment effect in patients with proximal anterior circulation stroke.** *Stroke* 2016;47:768–76 CrossRef Medline
6. Yu AYY, Zerna C, Assis Z, et al. **Multiphase CT angiography increases detection of anterior circulation intracranial occlusion.** *Neurology* 2016;87:609–16 CrossRef Medline
7. Menon BK, d'Este CD, Qazi EM, et al. **Multiphase CT angiography: a new tool for the imaging triage of patients with acute ischemic stroke.** *Radiology* 2015;275:510–20 CrossRef Medline
8. Ospel JM, Volny O, Qiu W, et al. **Displaying multiphase CT angiography using a time-variant color map: practical considerations and potential applications in patients with acute stroke.** *AJNR Am J Neuroradiol* 2020;41:200–05 CrossRef Medline
9. Volny O, Cimflova P, Kadlecova P, et al. **Single-phase versus multiphase CT angiography in middle cerebral artery clot detection—benefits for less experienced radiologists and neurologists.** *J Stroke Cerebrovasc Dis* 2017;26:19–24 CrossRef Medline
10. Byrne D, Sugrue G, Stanley E, et al. **Improved detection of anterior circulation occlusions: the “delayed vessel sign” on multiphase CT angiography.** *AJNR Am J Neuroradiol* 2017;38:1911–16 CrossRef Medline
11. Tomsick TA, Carrozzella J, Foster L, et al. **Endovascular therapy of M2 occlusion in IMS III: role of M2 segment definition and location on clinical and revascularization outcomes.** *AJNR Am J Neuroradiol* 2017;38:84–89 CrossRef Medline
12. Sarraj A, Sangha N, Hussain MS, et al. **Endovascular therapy for acute ischemic stroke with occlusion of the middle cerebral artery M2 segment.** *JAMA Neurol* 2016;73:1291–96 CrossRef Medline
13. Coutinho JM, Liebeskind DS, Slater L-A, et al. **Mechanical thrombectomy for isolated M2 occlusions: a post hoc analysis of the STAR, SWIFT, and SWIFT PRIME studies.** *AJNR Am J Neuroradiol* 2016;37:667–72 CrossRef Medline
14. Puetz V, Dzialowski I, Hill MD, et al. **Intracranial thrombus extent predicts clinical outcome, final infarct size and hemorrhagic**

- transformation in ischemic stroke: the clot burden score. *Int J Stroke* 2008;3:230–36 CrossRef Medline
15. Riedel CH, Zimmermann P, Jensen-Kondering U, et al. **The importance of size: successful recanalization by intravenous thrombolysis in acute anterior stroke depends on thrombus length.** *Stroke* 2011;42:1775–77 CrossRef Medline
 16. Polito V, La Piana R, Del Pilar Cortes M, et al. **Assessment of clot length with multiphase CT angiography in patients with acute ischemic stroke.** *Neuroradiol J* 2017;30:593–99 CrossRef Medline
 17. Yeo LLL, Paliwal P, Teoh HL, et al. **Assessment of intracranial collaterals on CT angiography in anterior circulation acute ischemic stroke.** *AJNR Am J Neuroradiol* 2015;36:289–94 CrossRef Medline
 18. Liebeskind DS, Kim D, Starkman S, et al. **Collateral failure? Late mechanical thrombectomy after failed intravenous thrombolysis.** *J Neuroimaging* 2010;20:78–82 CrossRef Medline
 19. Bozzao L, Fantozzi LM, Bastianello S, et al. **Early collateral blood supply and late parenchymal brain damage in patients with middle cerebral artery occlusion.** *Stroke* 1989;20:735–40 CrossRef Medline
 20. Bang OY, Saver JL, Kim SJ, et al. **Collateral flow averts hemorrhagic transformation after endovascular therapy for acute ischemic stroke.** *Stroke* 2011;42:2235–39 CrossRef Medline
 21. Lima FO, Furie KL, Silva GS, et al. **The pattern of leptomeningeal collaterals on CT angiography is a strong predictor of long-term functional outcome in stroke patients with large vessel intracranial occlusion.** *Stroke* 2010;41:2316–22 CrossRef Medline
 22. Casault C, Al Sultan AS, Trivedi A, et al. **Collateral scoring on CT angiogram must evaluate phase and regional pattern.** *Can J Neurol Sci J Can Sci* 2017;44:503–07 CrossRef Medline
 23. Bang OY, Goyal M, Liebeskind DS. **Collateral circulation in ischemic stroke: assessment tools and therapeutic strategies.** *Stroke* 2015;46:3302–09 CrossRef Medline
 24. Lansberg MG, Thijs VN, Bammer R, et al. **Risk factors of symptomatic intracerebral hemorrhage after tPA therapy for acute stroke.** *Stroke* 2007;38:2275–78 CrossRef Medline
 25. Mlynash M, Lansberg MG, De Silva DA, et al. **Refining the definition of the malignant profile: insights from the DEFUSE-EPITHET pooled data set.** *Stroke* 2011;42:1270–75 CrossRef Medline
 26. Reid M, Famuyide AO, Forkert ND, et al. **Accuracy and reliability of multiphase CTA perfusion for identifying ischemic core.** *Clin Neuroradiol* 2019;29:543–52 CrossRef Medline
 27. Santos EMM, d’Esterre CD, Treurniet KM, et al. **Added value of multiphase CTA imaging for thrombus perviousness assessment.** *Neuroradiology* 2018;60:71–79 CrossRef Medline
 28. de Havenon A, Mlynash M, Kim-Tenser MA, et al. **Results from DEFUSE 3: good collaterals are associated with reduced ischemic core growth but not neurologic outcome.** *Stroke* 2019;50:632–38 CrossRef Medline
 29. Zhang X, Zhang M, Ding W, et al. **Distinct predictive role of collateral status on clinical outcome in variant stroke subtypes of acute large arterial occlusion.** *Eur J Neurol* 2018;25:293–300 CrossRef Medline
 30. Yang C-Y, Chen Y-F, Lee C-W, et al. **Multiphase CT angiography versus single-phase CT angiography: comparison of image quality and radiation dose.** *AJNR Am J Neuroradiol* 2008;29:1288–95 CrossRef Medline

Optic Nerve Choristoma Mimicking a Neurenteric Cyst

J.C. Benson, C. Giannini, S. Cohen Cohen, J. Van Gompel, D.K. Kim, J. Port, F. Diehn, L. Eckel, and C. Carr

ABSTRACT

SUMMARY: Optic nerve choristomas are rare entities in which a developmental focus of histologically normal tissue is abnormally located within or along a segment of the optic nerve. Although benign, choristomas may demonstrate slow growth, ultimately resulting in visual field deficits due to compression of the adjacent nerve in the few cases reported in the anterior fossa. Choristomas may have cystic components, though this has not been described in such lesions along the optic nerve. Here, a predominantly cystic optic nerve choristoma is described, with radiologic features mimicking those of an anterior cranial fossa neurenteric cyst. The case highlights the radiology-pathology correlates of choristomas and reviews the surgical approach and management of patients with such lesions.

The patient was a 64-year-old woman who presented from an outside institution with an intracranial cyst. The lesion had been discovered during a hospitalization for unrelated pulmonary emboli, when the patient underwent a head CT after revealing a multiyear history of headaches during her review of systems. On examination, the patient had trace temporal field vision loss in her left eye. A battery of pituitary function tests was completed, given the proximity of the cyst to the pituitary gland, all of which had normal findings. The patient was referred for assessment by neurosurgery, with additional imaging performed.

Imaging

CT and subsequent MR imaging demonstrated a large extra-axial cystic mass in the anterior cranial fossa (Fig 1). Most of the lesion was centered over the planum sphenoidale, with remodeling of the adjacent bone. Posteriorly, the cyst extended into the sella, slightly compressing the anterior pituitary gland and causing substantial deviation of the optic chiasm. The anterior margins of the cyst were draped around the falx cerebri, while the bifrontal cerebral gyri, corpus callosum, and distal ICAs were all displaced by the cyst. The intracystic fluid was hyperintense on both T2 and FLAIR sequences and did not restrict diffusion. A punctate T1-hyperintense focus was noted along the left optic nerve.

The appearance of the lesion was thought to have attributes of a slow-growing, benign intracranial cyst. The intralesional fluid

content was uncharacteristic of the most commonly encountered cysts: the fluid did not mimic CSF like an arachnoid cyst, did not restrict diffusion as would be expected with an epidermoid cyst, and did not have intralesional fat suggestive of a dermoid cyst. The most likely entity was thought to be a neurenteric cyst; though rarely intracranial, neurenteric cysts in the anterior cranial fossa share many of the imaging characteristics seen in this case.^{1,2} A Rathke cleft cyst and craniopharyngioma were considered much less likely because the cyst did not appear to originate from the sella.

The patient ultimately underwent surgical treatment of the cyst 6 months after presentation.

Operative Report and Subsequent Image Review

The operation was completed via a small left frontal craniotomy with a subfrontal approach. An endonasal approach was not selected because the preoperative consensus was that this was a neurenteric cyst, and the surgeon did not believe the whole capsule could be removed from the middle fossa component. The cyst was immediately identified and contained a yellowish fluid when opened. Starting on the left side, the cyst lining was carefully dissected from the olfactory nerve and the frontal lobe. However, an unexpected small granular lesion was observed along the medial surface of the left optic nerve (Fig 2). This was partially resected and sent to pathology. Examination of the surgical field found no other such lesions. The surgeons then proceeded to remove all additional remaining cyst linings before the conclusion of the procedure.

Postoperatively, images were re-reviewed to assess a correlate with the intraoperative findings. A punctate focus of T1-hyperintensity along the medial margin of the left optic nerve was

Received July 29, 2020; accepted after revision August 27.

From the Departments of Radiology (J.C.B., D.K.K., J.P., F.D., L.E., C.C.), Pathology (C.G.), and Neurosurgery (S.C.C., J.V.G.), Mayo Clinic, Rochester, Minnesota.

Please address correspondence to John C. Benson, MD, 723 6th St SW, Department of Radiology, Mayo Clinic, Rochester, MN 55902; e-mail: benson.john3@mayo.edu <http://dx.doi.org/10.3174/ajnr.A6892>

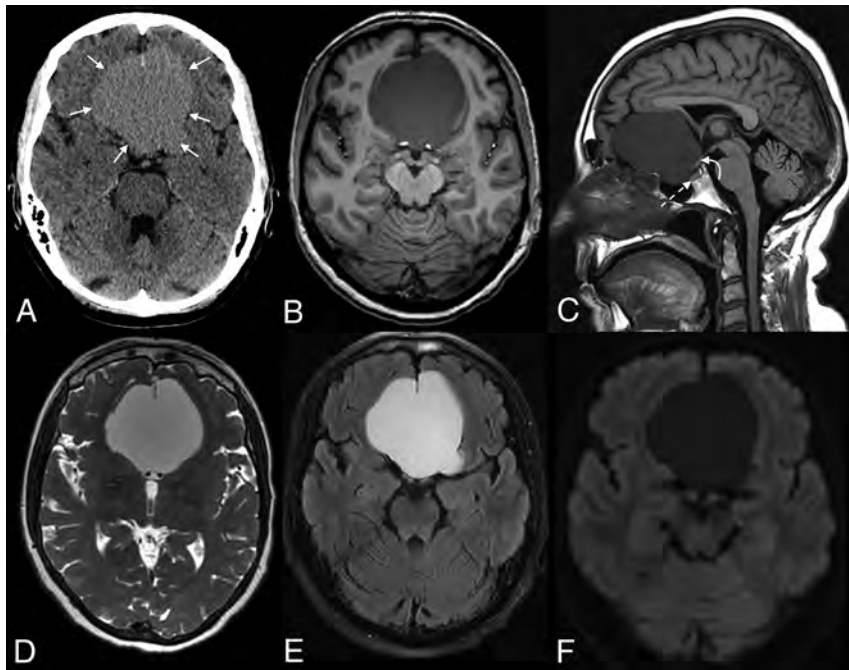


FIG 1. Preoperative CT and MR images of the lesion. Axial CT (A), axial (B) and sagittal (C) MPRAGE, and axial T2 Cube (GE Healthcare) (D), T2-FLAIR (E), and DWI (F) demonstrate an extra-axial cystic lesion in the anterior cranial fossa (between arrows, A). The cyst drapes around the anterior falx and causes substantial mass effect on the adjacent bifrontal gyri. The optic chiasm (curved arrow, C) and pituitary gland (dashed arrow, C) are deviated posteriorly. The intracystic fluid signal is slightly hyperintense to CSF on T2 Cube, does not suppress on FLAIR, and does not restrict on DWI.

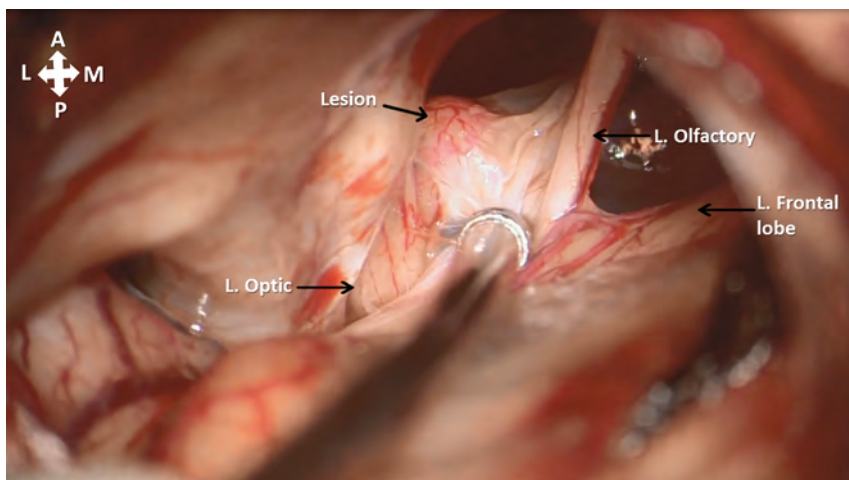


FIG 2. Intraoperative view of a left frontal craniotomy with a subfrontal approach for resection of an anterior cranial fossa cyst. A granular lesion adhering to the medial surface of the left optic nerve is shown, with adjacent structures labeled. L. indicates left.

observed, which demonstrated questionable, superimposed, associated enhancement corresponding to the small granular lesion identified intraoperatively (Fig 3).

Diagnosis

The diagnosis was benign epithelial cyst associated with an optic nerve choristoma.

Pathology

The specimen resected along the left medial optic nerve showed small glandular lobules composed predominantly of mucin-producing cells and, to a lesser extent, of serous cells associated with small ductal structures, consistent with salivary gland tissue (Fig 4). This was intermixed with adipose tissue, compatible with an optic nerve salivary gland choristoma. The cyst specimens showed a folded benign epithelial cyst wall with a double layer of cells, including a basal layer, p63-positive, as well as a superficial flattened layer, diffusely positive for anti-cytokeratin (CAM5.2) (Fig 5). There was no evidence of mucin-producing cells and no evidence of cilia, confirmed by the negative *BRAF* V600E stains.³ The cyst lining resembled, to some extent, a cystically dilated duct. It was not the lining of an enterogenous (neuroenteric) cyst, which is typically composed of a single layer of columnar cells, often ciliated and mucin-producing cells with goblet cells. The cyst lining epithelium lay over a fibrous stroma containing reactive arachnoid cells, highlighted by the progesterone receptor stain, as well as rare microcalcifications. The histopathologic findings were not those of a cystic craniopharyngioma. *BRAF* V600E and beta-catenin immunostaining, markers characteristic of papillary and adamantinomatous variants of craniopharyngioma, were performed and were negative.

DISCUSSION

Choristomas are composed of normal, mature tissue that is located in an abnormal anatomic location. They have been described throughout the body, from the head and neck to the extremities.^{4,5} Choristomas do not have a sex predilection and can present at any

age.⁶ Optic nerve choristomas, though exceedingly rare, have been previously reported.⁷⁻¹⁰ More frequently, optic nerve choristomas contain smooth-muscle and adipose tissue and, only rarely, salivary gland tissue.¹¹ The lesions often demonstrate slow progressive growth, sometimes eventually causing compressive atrophy of the optic nerve.¹¹ Nevertheless, choristomas are uniformly benign and considered to be developmental rather than neoplastic.

Radiologic descriptions of optic nerve choristomas remain predictably scarce. Adipose-rich choristomas exhibit intralesional fat density on CT and demonstrate fat signal on MR imaging with drop-out of signal on fat-suppression sequences.¹² Lesions

composed of predominantly smooth-muscle or glandular tissue, conversely, often lack such characteristic imaging findings. Both intralesional enhancement and enhancement of the adjacent optic nerve have been reported.^{11,13} The adjacent optic nerve may be enlarged due to mass effect related to the tumor or small due to compressive atrophy.⁶ An enhancing tumor involving the optic nerve (or sheath) should raise suspicion for either an optic nerve glioma or meningioma, though a dominant cyst arising from an optic nerve glioma in an adult would be atypical.¹⁴ In addition, a teratoma could be considered; such lesions are composed of all 3 germ cell layers and can appear as cystic lesions with components of intralesional fat. However, a newly diagnosed teratoma would be rare in an adult because the incidence decreases with age.¹⁵ Most teratomas also have some degree of calcification, which was lacking in this case.¹⁶

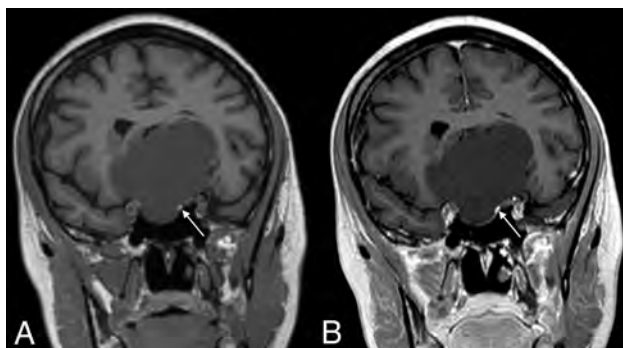


FIG 3. Re-review of preoperative coronal MPRAGE (A) and postcontrast (B) images demonstrates a T1-hyperintense focus along the left optic nerve (arrows), correlating with the surgical findings. Intrinsic T1 signal was presumably related to the intralesional fat tissue noted on subsequent histologic analysis. Although faint enhancement was seen in the adjacent tissue, it was not certain whether a component of this solid focus demonstrated definite enhancement (B).

Intracranial cysts, conversely, are not uncommon. As mentioned above, the lesion in the current case shared many features of a supratentorial neurenteric cyst: Intracystic fluid was hyperintense to CSF on FLAIR sequences (unlike arachnoid cysts, which mimic CSF) and lacked intralesional restricted diffusion (unlike epidermoid cysts).^{2,17} Thus, this case is an example of the need to closely examine the margins of all cystic foci for fat signal or pathologic enhancement.

To the best of our knowledge, this is the first reported instance of an optic nerve choristoma leading to the formation of a such a large epithelial cyst, most likely representing a very large dilated duct. Nevertheless, cystic choristomas are known entities.¹⁸⁻²⁰ Glandular tissue is found within such lesions, as was noted on histologic analysis of the current case.¹⁸ It is possible that these cysts develop from persistent excretion of fluid from intralesional glandular tissue. In the patient presented here, slow excretion of fluid would conceivably account for its insidious clinical onset and bony remodeling.

Surgical resection of choristomas is typically curative, though reports of recurrence following incomplete resection have been reported.²¹ In this case, surgical resection of the cyst wall would likely have little effect on future recurrence of the cyst because no secretory histologic components were noted in the actual cyst wall. The patient reported here is expected to make a full recovery, with resolution of her symptoms and no new neurologic deficits expected. Follow-up MRIs will be completed in 6 and 12 months to exclude recurrence of the solid tumor or re-accumulation of cystic fluid.

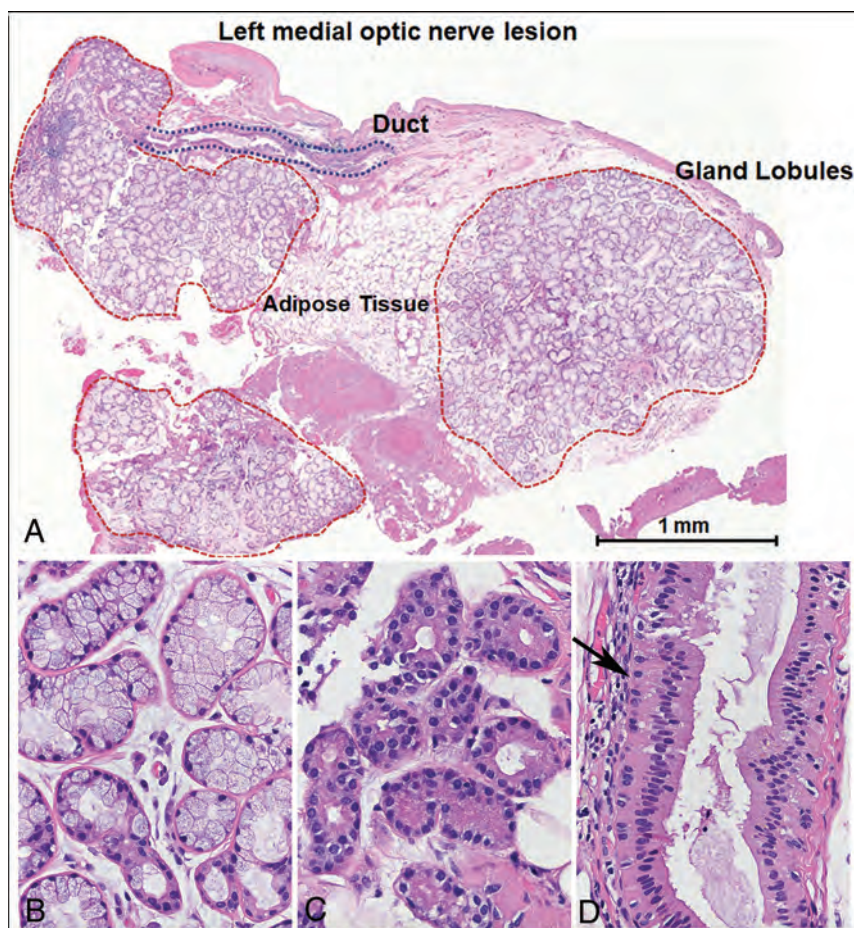


FIG 4. Optic nerve choristoma composed of adipose tissue, glandular lobules, and ducts (A), with predominant mucinous (B) and scant serous (C) glands consistent with salivary gland tissue. The duct (D) shows a typical basal cell layer (black arrow) and columnar lining.

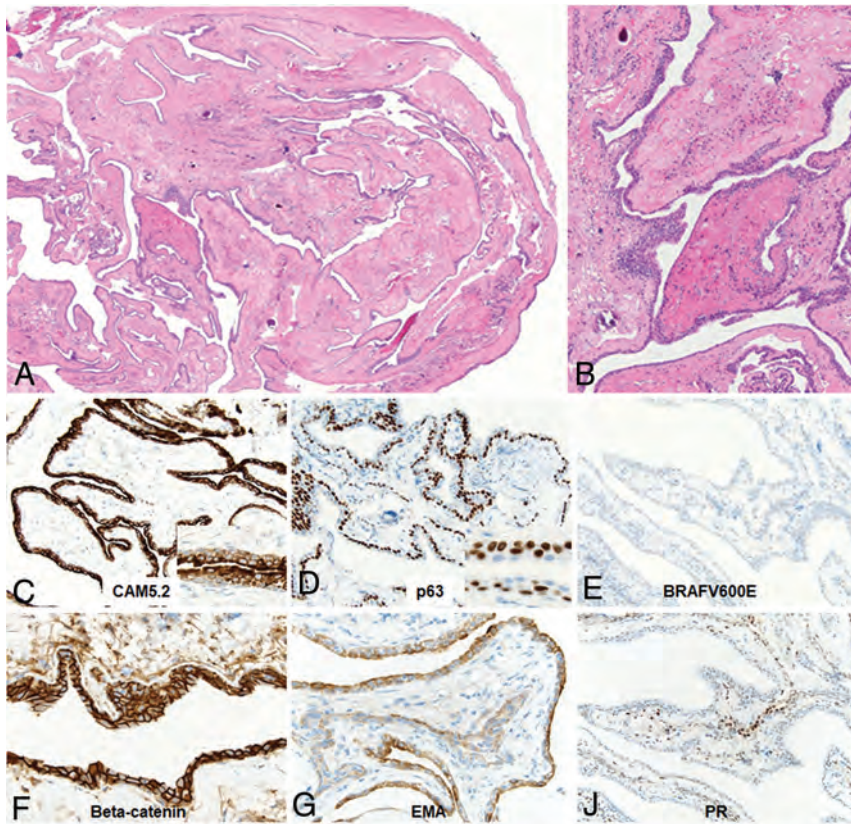


FIG 5. The collapsed cyst wall shows largely a flattened lining (A and B) bistratified positive for CAM5.2 (C), p63-positivity is limited to the basal cells of the bistratified epithelium lining the cyst wall as typically seen in duct structures (D). *BRAF V600E*, a marker of papillary craniopharyngioma, is negative (E); the stain is also typically positive in normal cilia, which were not present in the cyst lining. The cyst lining shows normal cytoplasmic beta-catenin expression (F) and also of epithelial membrane antigen (EMA) (G), while progesterone receptor (PR) stain is present in a subset of the arachnoidal cells observed in the fibrous stroma associated with the cyst wall (J).

Case Summary

- Choristomas are benign lesions, in which histologically normal tissue is located in an abnormal anatomic location
- Imaging features of choristomas vary on the basis of the histologic composition of each lesion. Adipose-rich lesions demonstrate expected features of fat tissue on CT and MR imaging; characteristics of other lesions are less specific
- Because many pathologic lesions may have cystic components, identification of any intracranial cyst should prompt close scrutiny of the margins of the lesion for T1-hyperintense or enhancing foci
- The differential diagnosis of a large cystic lesion in the anterior cranial fossa is ample and includes neurenteric cysts, arachnoid cysts, Rathke cleft cysts, teratomas, cystic pituitary adenomas, craniopharyngiomas, and epidermoid and dermoid cysts. Cystic choristoma is a very rare possibility.

Disclosures: John Port—UNRELATED: Consultancy: BioClinica, Comments: I am an imaging consultant to BioClinica; consulting fees are paid to Mayo Clinic.* *Money paid to the institution.

REFERENCES

1. Little MW, Guilfoyle MR, Bulters DO, et al. **Neurenteric cyst of the anterior cranial fossa: case report and literature review.** *Acta Neurochir (Wien)* 2011;153:1519–25 CrossRef Medline
2. Preece MT, Osborn AG, Chin SS, et al. **Intracranial neurenteric cysts: imaging and pathology spectrum.** *AJNR Am J Neuroradiol* 2006;27:1211–16 Medline
3. Jones RT, Abedalthagafi MS, Brahmandam M, et al. **Cross-reactivity of the BRAF VE1 antibody with epitopes in axonemal dyneins leads to staining of cilia.** *Mod Pathol* 2015;28:596–606 CrossRef Medline
4. Lam S, Grandhi R, Wong R, et al. **Neuromuscular hamartoma of the sciatic nerve: case report and review of the literature.** *Surg Neurol Int* 2013;4:8 CrossRef Medline
5. Arens P, Ullrich A, Olze H, et al. **Extraoral osseous choristoma in the head and neck region: case report and literature review.** *Case Rep Otolaryngol* 2019;2019:8532356 CrossRef Medline
6. Spencer A, Lee J, Prayson RA. **Optic nerve choristoma.** *Ann Diagn Pathol* 2005;9:93–95 CrossRef Medline
7. Harrison W, Pittman P, Cummings T. **Optic nerve choristoma.** *Saudi J Ophthalmol* 2018;32:90–91 CrossRef Medline
8. Zimmerman LE, Arkfeld DL, Schenken JB, et al. **A rare choristoma of the optic nerve and chiasm.** *Arch Ophthalmol* 1983;101:766–70 CrossRef Medline
9. Daxer A, Sailer U, Ettl A, et al. **Choristoma of the optic nerve: neuroimaging characteristics and association with spinal cord lipoma.** *Ophthalmologica* 1998;212:180–83 CrossRef Medline
10. Hintz EB, Yeane GA, Buchberger GK, et al. **Intracranial salivary gland choristoma within optic nerve dural sheath: case report and review of the literature.** *World Neurosurg* 2014;81:842.e1–4 CrossRef Medline
11. Giannini C, Reynolds C, Leavitt JA, et al. **Choristoma of the optic nerve: case report.** *Neurosurgery* 2002;50:1125–28 CrossRef Medline
12. Mishra A, Heathcote JG, LaRoche GR. **Optic nerve choristoma causing vision loss in an adolescent.** *Can J Ophthalmol* 2017;52:e138–40 CrossRef Medline
13. Kazim M, Kennerdell JS, Maroon J, et al. **Choristoma of the optic nerve and chiasm.** *Arch Ophthalmol* 1992;110:236–38 CrossRef Medline
14. Tailor TD, Gupta D, Dalley RW, et al. **Orbital neoplasms in adults: clinical, radiologic, and pathologic review.** *Radiographics* 2013;33:1739–58 CrossRef Medline
15. Romić D, Raguzō M, Marcōinković P, et al. **Intracranial mature teratoma in an adult patient: a case report.** *J Neurol Surg Rep* 2019;80:e14–17 CrossRef Medline
16. Abdelmuhdi AS, Almazam AE, Dissi NA, et al. **Intracranial teratoma: imaging, intraoperative, and pathologic features: AIRP best cases in radiologic-pathologic correlation.** *Radiographics* 2017;37:1506–11 CrossRef Medline

17. Opreșan A, Popescu BO. **Intracranial cysts: an imagery diagnostic challenge.** *ScientificWorldJournal* 2013;2013:172154 CrossRef Medline
18. Moon SB, Park KW, Yun WJ, et al. **Congenital cystic choristoma mimicking cervical lymphangioma.** *J Pediatr Surg* 2008;43:e5-7 CrossRef Medline
19. Herman TE, Siegel MJ. **Oropharyngeal neuroglial choristoma.** *J Perinatol* 2007;27:386-87 CrossRef Medline
20. Tepas JJ, Deen HG, McArtor R, et al. **Giant cystic choristoma of the head and neck in a neonate: successful management of a life-threatening respiratory emergency.** *J Pediatr Surg* 1982;17:184-86 CrossRef Medline
21. Mitchell A, Scheithauer BW, Ostertag H, et al. **Neuromuscular choristoma.** *Am J Clin Pathol* 1995;103:460-65 CrossRef Medline

Improved Glioma Grading Using Deep Convolutional Neural Networks

S. Gutta, J. Acharya, M.S. Shiroishi, D. Hwang, and K.S. Nayak



ABSTRACT

BACKGROUND AND PURPOSE: Accurate determination of glioma grade leads to improved treatment planning. The criterion standard for glioma grading is invasive tissue sampling. Recently, radiomic features have shown excellent potential in glioma-grade prediction. These features may not fully exploit the underlying information in MR images. The objective of this study was to investigate the performance of features learned by a convolutional neural network compared with standard radiomic features for grade prediction.

MATERIALS AND METHODS: A total of 237 patients with gliomas were included in this study. All images were resampled, registered, skull-stripped, and segmented to extract the tumors. The learned features from the trained convolutional neural network were used for grade prediction. The performance of the proposed method was compared with standard machine learning approaches, support vector machine, random forests, and gradient boosting trained with radiomic features.

RESULTS: The experimental results demonstrate that using learned features extracted from the convolutional neural network achieves an average accuracy of 87%, outperforming the methods considering radiomic features alone. The top-performing machine learning model is gradient boosting with an average accuracy of 64%. Thus, there is a 23% improvement in accuracy, and it is an efficient technique for grade prediction.

CONCLUSIONS: Convolutional neural networks are able to learn discriminating features automatically, and these features provide added value for grading gliomas. The proposed framework may provide substantial improvement in glioma-grade prediction; however, further validation is needed.

ABBREVIATIONS: CNN = convolutional neural network; GB = gradient boosting; ML = machine learning; SVM = support vector machine; RF = random forest; TICE = T1 contrast-enhanced

Primary CNS tumors originate from cells within the CNS and can be benign or malignant.¹ Malignant brain tumors require aggressive therapies and are the most challenging to treat. Gliomas are the most frequent malignant primary brain tumors in adults, with an incidence of approximately 5–10 per 100,000 in

the population every year.² Gliomas are divided into low-grade and high-grade gliomas. The prognosis for high-grade glioma is poor, despite treatment options including chemotherapy, radiation therapy, and surgery.³ The 5-year relative survival rate after diagnosis of a brain tumor is 35.8%, with the most aggressive grade IV glioblastoma multiforme having the lowest survival rate of 6.8%.⁴ In addition, treatment strategy depends on the glioma grade.^{5,6} While clinical glioma grading is still based on histopathologic methods from tissue sampling, an accurate and reliable noninvasive imaging-based determination of glioma grade is desirable.

Gliomas are classified as grades I–IV, according to the World Health Organization Classification of CNS tumors.⁷ Glioma grades were restructured in the 2016 version of the World Health Organization Classification, considering molecular information along with the histology.⁸

Recently, there have been several studies showing the potential for a noninvasive method of glioma grading using radiomic features extracted from MR images. A histogram-based texture

Received April 18, 2020; accepted after revision September 2.

From the Ming Hsieh Department of Electrical and Computer Engineering (S.G., K.S.N.), Viterbi School of Engineering, and Department of Radiology (J.A., M.S.S., D.H., K.S.N.), Keck School of Medicine, University of Southern California, Los Angeles, California.

We gratefully acknowledge grant support from the National Institutes of Health (award No. R33-CA225400, Principal Investigator: K.S. Nayak).

Please address correspondence to Sreedevi Gutta, PhD, 3740 McClintock Avenue, EEB 422, University of Southern California, Los Angeles, CA, 90089-2564; e-mail: sgutta@usc.edu

Indicates open access to non-subscribers at www.ajnr.org

Indicates article with supplemental online appendix and table.

Indicates article with supplemental online photos.

<http://dx.doi.org/10.3174/ajnr.A6882>

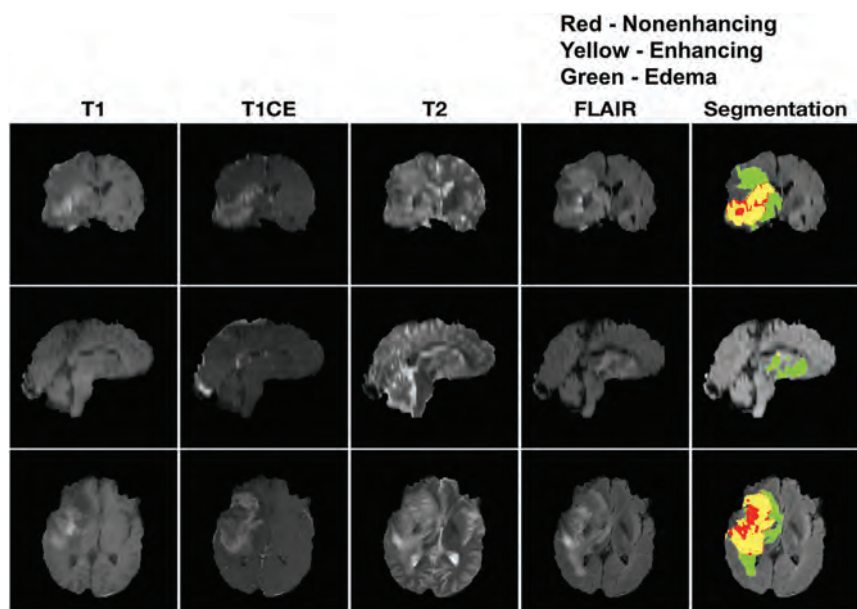


FIG 1. Representative segmentation result from one glioblastoma patient. Top row: Coronal; Middle row: Sagittal; Bottom row: Axial. T1, T1c, T2, and FLAIR are shown in the first 4 column, after being resampled to 1mm, registered, and skull-stripped. The rightmost column corresponds to the segmentation result overlapped on the FLAIR image. Segmentation was performed using cascaded convolutional networks by Wang et al. [2]. In the segmentation image, green corresponds to edema, yellow corresponds to enhancing, and red corresponds to non-enhancing regions.

analysis was performed by Skögen et al⁹ on 95 patients to differentiate low-grade from high-grade gliomas. This study reported a receiver operating characteristic area under the curve of 0.910. In another study to classify grades II–IV, Tian et al¹⁰ performed texture analysis in 153 patients using a support vector machine (SVM) model reporting an accuracy of 98%. This study also showed that the contrast-enhanced T1-weighted (T1CE) method yields the best sequence for grade prediction. Xie et al¹¹ were able to differentiate grade III and IV and grade II and III gliomas using entropy and inverse difference moment of model-free and dynamic contrast-enhanced MR imaging.

These prior MR imaging–based glioma grading studies used hard-coded features that are straightforward to extract. We hypothesized that such an approach limits the use of rich information embedded in the multicontrast MR images. The premise of this work is that rich imaging information beyond simple changes in image contrast/intensity is the following; 1) deeply embedded in pre- and postcontrast enhanced MR imaging, 2) potentially valuable in glioma grading, and 3) learned from labeled training data using deep learning techniques.

In recent years, convolutional neural networks (CNNs) have shown superior performance in numerous visual object-recognition and image-classification studies.¹² They also accelerated the development of medical image analysis,¹³ including applications for tumor diagnosis.¹⁴ With a CNN, a hierarchy of features can be learned from a low to high level in a layer-by-layer manner.¹⁵ Recently, CNNs¹⁵ have also been used for glioma classification. Ertosun and Rubin¹⁶ proposed a CNN to classify glioma grades (II, III, and IV) and low-grade-versus-high-grade gliomas,

obtaining accuracies of 71% and 96%, respectively. Anaraki et al¹⁷ proposed a CNN and genetic algorithm to classify glioma grades (II, III, and IV), obtaining an accuracy of 90.9%. Yang et al¹⁸ explored a transfer-learning approach for glioma grading, obtaining 90% test accuracy. However, all of these studies lacked a sufficiently large dataset from which features could be learned.

In this study, we propose a CNN to predict glioma grade from pre- and post-contrast-enhanced MR images. We automatically learn features by training a supervised deep network. The learned features are used for classification and are compared using machine learning (ML) approaches that are trained using radiomic features alone.

MATERIALS AND METHODS

Imaging Dataset

Clinical data were obtained from patients with a diagnosis of glioma who received standard of care brain MR imaging with and without a gadolinium-based contrast agent at the Keck

Medical Center of the University of the Southern California from May 2007 to January 2019. Retrospective data were obtained under a protocol approved by the University of Southern California institutional review board (protocol HS-19-00019). The patients were imaged by using a 3T MR imaging scanner (GE Healthcare). The imaging acquisition protocol was the same for all patients and included the following sequences: T1-weighted (TR = 700 ms; TE = 10 ms; flip angle = 90°; section thickness = 5 mm; spacing between slices = 7 mm), T1CE (TR = 500 ms; TE = 19 ms; flip angle = 90°; section thickness = 5 mm; spacing between slices = 7 mm), T2-weighted (TR = 5000 ms; TE = 100 ms; flip angle = 90°; section thickness = 5 mm; spacing between slices = 7 mm), and T2-weighted/FLAIR (TR = 8802 ms; TE = 158 ms; flip angle = 90°; section thickness = 5 mm; spacing between slices = 7 mm).

Preprocessing

The dataset contained 366 adult patients with a total of 1154 scans. Because of poor image quality or unknown pathology, 65 patients were excluded from the study. The remaining 301 patients with 887 scans qualified for the study. First, all images were resampled to 1-mm³ isotropic resolution using BrainSuite software (<http://brainsuite.org/>).¹⁹ Second, the 4 volumes were coregistered using the FSL (<http://www.fmrib.ox.ac.uk/fsl>) toolbox.²⁰ Third, images were skull-stripped using BrainSuite software.¹⁹ Forty-two patients were excluded due to skull-stripping failure, leaving 259 patients' scans to undergo further segmentation.

A fully-automated brain tumor segmentation tool was used to identify lesion regions (enhancing tissue, nonenhancing tissue, and edema) from the skull-stripped multimodal images. This

algorithm was one of the top-performing tools as evaluated in the international 2017 Multimodal Brain Tumor Segmentation challenge.²¹ It uses a cascade of CNNs and decomposes the multiclass segmentation task into 3 sequential binary segmentation tasks.

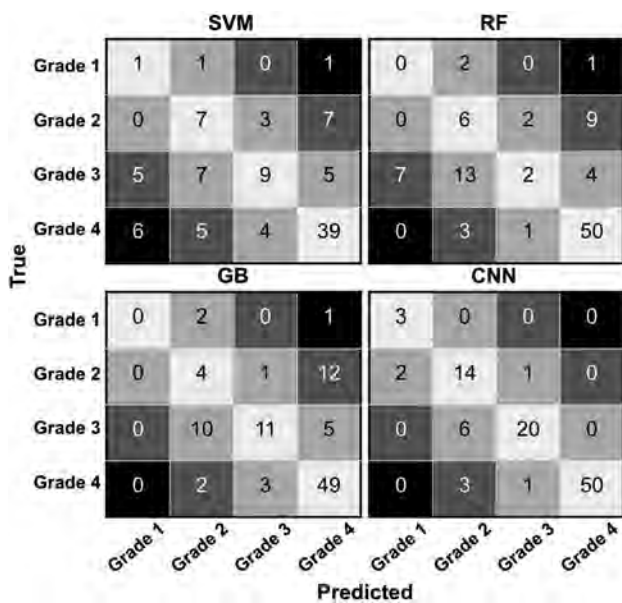


FIG 2. Confusion matrices of the candidate methods (SVM, RF, GB, and CNN). Top left: SVM; Top right: RF; Bottom left: GB; Bottom right: CNN. Each row corresponds to the true grade and column corresponds to the predicted grade. The main diagonal shown in light grey represents the number of data points that were classified correctly. The off-diagonal numbers are the number of data points that were mis-classified. CNN outperforms the machine learning models by a 23% improvement in accuracy.

Complete details of the network architecture and the training can be found in Wang et al.²¹ More details on how each dataset was preprocessed can be found in Online Fig 2.

One representative segmentation result for a grade IV tumor. All segmentations were visually checked by a board-certified neuroradiologist with 9 years of experience. The radiologist was not given the opportunity to alter the segmentations because this would have been extremely time-consuming. The radiologist was simply asked to approve or reject the automatic segmentation result. Segmentation was deemed satisfactory if the regions qualitatively correlated to the respective areas: enhancing tissue, non-enhancing tissue, and edema. The areas of tissue enhancement and nonenhancement were assessed by reviewing the T1 post-contrast sequence and comparing it with the segmented dataset. The edema assessment was performed by comparing the T2 and FLAIR sequences with the segmentation data. If the segmentation corresponded to the specified source data sequence, it was determined to be appropriately segmented. Due to segmentation failure, data from 22 patients were excluded. The other 237 cases with 660 scans approved by the radiologist were included for the remainder of this work. Of the 237 patients, 17 patients had a grade I tumor, 59 had a grade II tumor, 46 had a grade III tumor, and 115 had a grade IV tumor. The total data were randomly divided into training, validation, and testing with the ratios being 70%, 15%, and 15%, respectively. The test data were set aside to evaluate the performance of the model. The splitting of data is performed on the number of patients, and the detailed split is given in the Online Appendix. Tumors were graded by a fellowship-trained neuropathologist. Grade I tumors primarily include pilocytic astrocytoma; grade II includes diffuse astrocytoma, oligodendroglioma, and oligoastrocytoma; grade III includes anaplastic astrocytoma, anaplastic oligodendroglioma, and anaplastic oligoastrocytoma; and grade IV includes glioblastoma.

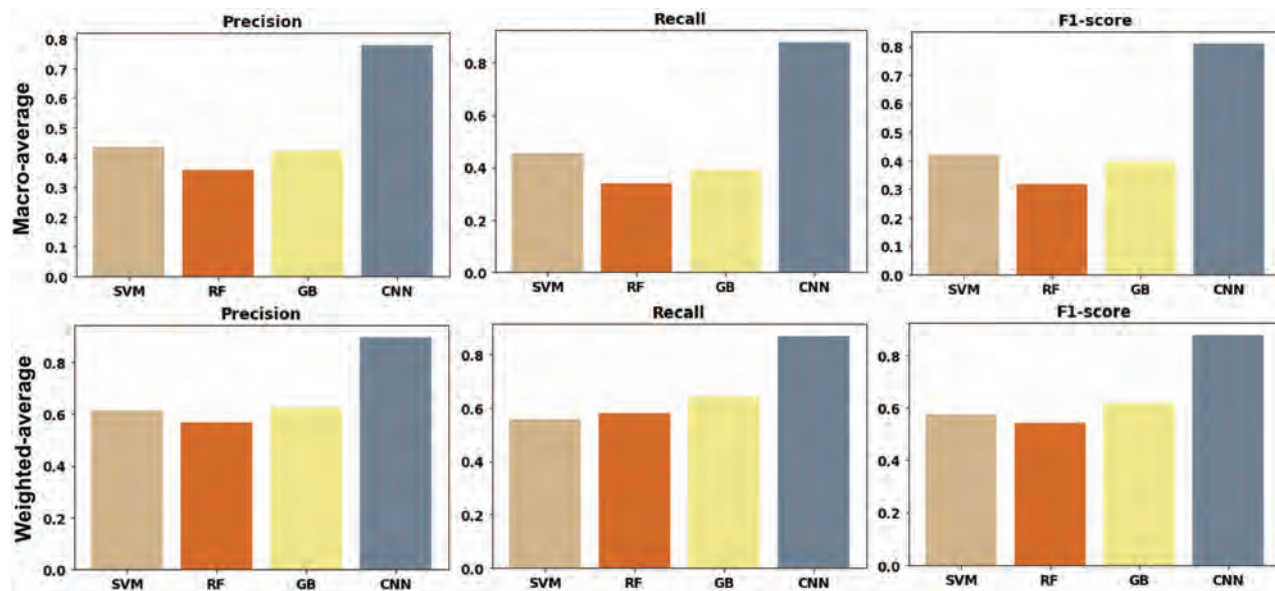


FIG 3. Comparison of the candidate methods (SVM, RF, GB, and CNN) using three performance metrics. Left: Precision; Middle: Recall; Right: F1-score. The top row corresponds to macro-averaged metrics and the bottom row corresponds to weighted average metrics. Macro-averaging computes the score for each grade and then averages without accounting for class imbalance. On the other hand, weighted average accounts for class imbalance by weighting the metric of each class with the number of samples in that specific class. CNN performs superior to the other models in all of the metrics examined.

Standard Feature Extraction

PyRadiomics (<https://pypi.org/project/pyradiomics/>),²² an open-source platform, was used for the extraction of radiomic features from the tumors. A total of 107 features were extracted for each sequence. These included first-order statistics, shape-based features, and other commonly used texture features: specifically, first-order (16 features), shape-based (16 features), gray-level co-occurrence matrix (24 features), gray-level run length matrix (16 features), gray-level size zone matrix (16 features), neighboring gray tone difference matrix (5 features), and gray-level dependence matrix (14 features). Complete details about the extracted features can be found in the image biomarker Standardisation Initiative reference manual.²³ Each dataset, therefore, had 1284 ($107 \times 4 \times 3$) features extracted: 4 corresponded to the total number of sequences, and 3 corresponded to the enhancing component, nonenhancing component,

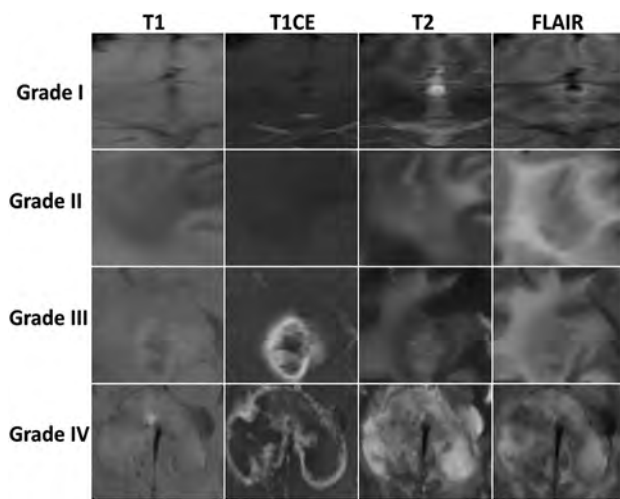


FIG 4. Representative activation maps generated by the proposed CNN (one example per grade). Each row corresponds to a particular grade (I to IV) and each column corresponds to a sequence (T1, T1CE, T2, and FLAIR). Activation by T1CE images was significant for grades III and IV. Activation by FLAIR was most significant for grade II. There was a gradual increase in activation based on T2 images from grades I to IV. T1CE and FLAIR were the most significant sequences for differentiation of low grade (I and II) and high grade (III and IV) gliomas. FLAIR, T1CE, and T2 images produced the strongest activation for grades II, III, and IV respectively.

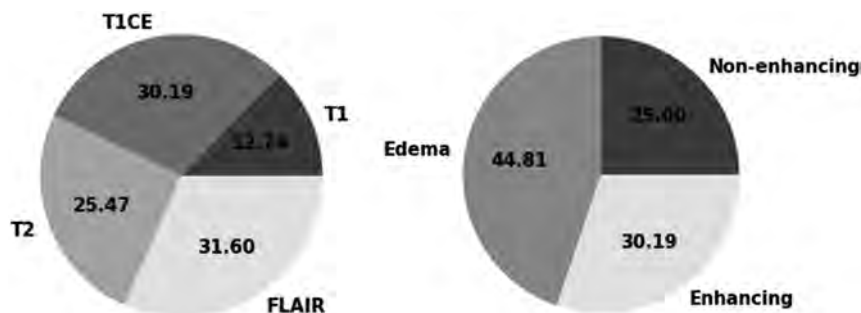


FIG 5. Sequence and tumor component significance was determined using a gradient boosting algorithm. The results obtained here comply with the findings of CNN. T1CE and FLAIR were most significant, followed by T2. Edema that is seen in FLAIR plays an important role for classification of different grades.

and edema associated with the tumor. To handle the large number of features, we performed a feature-selection step on the training data alone on the basis of the importance score obtained from the gradient boosting algorithm. A total of 45 features were selected by evaluating performance on the validation dataset. These features extracted from 3D tumors were given to the ML models: SVM, random forest (RF), and gradient boosting (GB) to predict the grade of the tumor.

Proposed Convolutional Network

CNNs are an extension of the traditional artificial neural network architecture, in which banks of convolutional filter parameters and nonlinear activation functions act as a mapping function to transform a multidimensional input image into a desired output.²⁴ Network overview and details are provided in the Online Appendix.

The input to the proposed network is a 150×150 region (corresponding to 15 cm^2) that is centered on the centroid of the entire segmented tumor (edema, enhancing, and nonenhancing). We considered slices that contain at least 100 pixels of tumor (which corresponds to 1 cm^2). The proposed framework was compared with the ML approaches trained with only radiomic features. To determine the final grade of the tumor, we applied the proposed network to all of the slices and chose most common grade among all predictions.

The performance was measured using the confusion matrix and accuracy. Precision, recall, and the F_1 score were also used for evaluating the models. Macro averaging calculates metrics for each grade and finds their unweighted mean. Thus, it does not take class imbalance into account. Weighted averaging computes the metrics for each class and finds their average, weighted by the number of scans in each class. This alters the macro score and accounts for class imbalance.

Gradient-Weighted Class Activation Mapping (Grad-CAM)²⁵ was used for visualizing the features learned by the CNN to understand which parts of an input image were important for a classification decision. Complete details of the method to generate these maps can be found in Selvaraju et al.²⁵

RESULTS

The hyperparameters of ML methods and CNN were selected on the basis of performance on the validation dataset: SVM = radial basis function kernel; degree = 3; $C = 1$; RF = 10,000 trees; Gini index to determine the quality of split; GB = maximum depth 4; 100 sequential trees; CNN = learning rate $1e-3$; batch size = 64; epochs = 30; Adam optimizer; cross-entropy loss function.

Figure 2 contains the confusion matrices for all of the discussed methods: SVM, RF, GB, and CNN. It can be seen that the CNN is superior to the machine learning methods that are trained with radiomic features alone. The accuracy of SVM, RF, GB, and CNN are 56%, 58%, 64%, and 87% respectively. Among the machine learning models, GB performs better

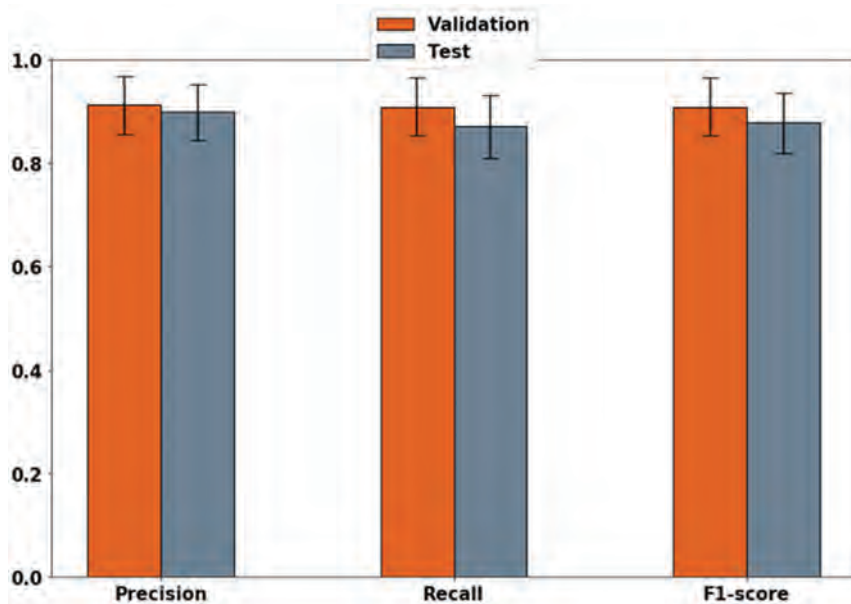


FIG 6. Weighted average precision, recall, and F1-score for the validation (red) and test (gray) dataset for proposed CNN method. The performances of CNN are consistent in both datasets, indicating robustness of the proposed method.

than SVM and RF. CNN outperforms the best performing model with an improvement in accuracy by 23%.

Figure 3 contains a comparison of the discussed methods using performance metrics: precision, recall, and F1-score. There is a significant improvement in performance by the proposed CNN method, suggesting that the learned features are valuable in predicting tumor grade.

Figure 4 contains the activation maps from one representative case for each tumor grade. T1CE images are more strongly activated for high grade (III and IV) compared to low grade (I and II) gliomas. There is a gradual increase in activation of T2 images from grades I to IV. FLAIR images are most strongly activated for grade II. Based on activation maps for the proposed CNN, we infer that T1CE, T2, and FLAIR are the most valuable for identification of grades II to IV respectively. There was no significant activation observed in any of the grade I images. These interpretations were made based on visual inspection of all scans of each grade.

Figure 5 contains the sequence significance and tumor component significance determined by using the GB algorithm. Among the sequences considered for grading, T1CE and FLAIR were most important, followed by T2. Edema was the most significant tumor component for classification, followed by the enhancing and non-enhancing regions.

Figure 6 contains the comparison between validation and test data using weighted average precision, recall, and F1-score to test robustness of the proposed CNN. The error bar corresponds to the 95% confidence interval. Validation data was used to determine the hyperparameters of the network and test data was used to evaluate the performance of the proposed CNN with these hyperparameters. We observed that the performances of the proposed method between validation and test data are consistent, indicating robustness of the proposed method.

DISCUSSION

In this study, we used a convolutional network to classify glioma grades, based on pre- and post-contrast-enhanced MR images, and compared performance against 3 established ML methods. We were able to implement the entire preprocessing pipeline from resampling to tumor segmentation automatically. A neuroradiologist was required only to validate the segmentations. We have leveraged convolutional networks to extract learned spatial features and have used these features to improve prediction of glioma grade from multicontrast MR imaging. This is in contrast to most of the previous studies that rely on radiomic features alone.

The ML methods have poor prediction of grade I compared with the proposed CNN. All of the misclassified grade II tumors were predicted as a higher grade by ML methods. Moreover, at least 70% of the misclassified grade II tumors were predicted as grade IV: SVM = 7/10, RF = 9/11, GB = 12/13. The proposed CNN incorrectly classified grade II as grades I and III. A large proportion of misclassified grade III tumors were predicted as grade II: SVM = 7/17, RF = 13/24, GB = 10/15, CNN = 6/6. All of the methods, except SVM, which had a misclassification rate of 28%, performed well in predicting grade IV tumors with a misclassification rate below 10%. Overall, the methods except GB tended to bias predictions toward a lower grade. SVM overclassified 17 and underclassified 27, RF overclassified 18 and underclassified 24, GB overclassified 21 and underclassified 15, and CNN overclassified 1 and underclassified 12. Distinguishing grades II and III is clinically important for treatment planning. For all the methods, a higher percentage of grade III tumors was predicted as grade II than grade II predicted as grade III. Moreover, most of the errors in ML techniques were due to misclassification of lower grade tumors (Fig 2). This may, in part, be due to the inherent class imbalance of the training set.

Essential to the proposed network was the use of drop-out to prevent overfitting and batch normalization, improving the performance of the network through adjusting and scaling the activations. The results presented in Figs 2 and 3 correspond to test data, which were unseen by the model during training and were used to evaluate the final performance of the network. We observed no difference in performance between the validation and test data (Fig 6), suggesting the robustness of the proposed method.

There are several limitations to this study. First, we did not consider molecular information of the tumors. This was a practical limitation because only a small subset of the cases had molecular information on file. This would be a worthwhile extension if this work were to be replicated with a larger dataset. Second, we considered only structural MR imaging data for this work. In the future, we plan to include additional sequences such as diffusion, perfusion,

and susceptibility-weighted images, which may improve the model performance. Third, the experiments in this study were performed on 237 patients with 660 scans, all from a single center. This number is large compared with previous glioma-grading studies¹⁰ but is small compared with nonmedical domains.¹² Substantially larger datasets will enable one to fully harness the potential of deep learning for prediction of glioma grade. Further testing is also required to evaluate the potential of the proposed algorithm in a multicenter setting, to analyze the effect of scanner systems and acquisition settings on the learned features. Fourth, this study did not consider demographic information of the included population (eg, patient age), which may provide additional discriminatory value. Fifth, a unique biopsy was not performed for every MR image. We assumed that the grade from the biopsy applied to all the scans of that particular patient. Sixth, there could be bias in the patient selection due to rejection of data on the basis of automatic skull-stripping and segmentation failures. This warrants further investigation to determine any specific structural characteristics unique to these tumors. It is worth noting that the state-of-the-art skull-stripping and segmentation are improving at a rapid pace, and we expect a failure rate of these preprocessing modules to diminish with time. Seventh, the number of patients with grade I was very small, creating a data imbalance. This is because patients with grade I tumor are less likely to be referred for surgical biopsy for confirmation. This feature makes it difficult to evaluate the performance of grade I detection; however, in clinical practice, grade I neoplasms tend to be monitored with imaging across time to assess change without necessarily requiring surgical resection. Eighth, about 50% of the scans were excluded either due to poor image quality or failures in skull-stripping and segmentation. These problems must be overcome for broad clinical applicability of automated glioma grading.

This study was performed entirely using 2D slices. A natural extension would be to adapt the proposed network architecture to process the entire 3D tumor volume. This change would substantially increase the number of parameters and reduce the dataset size. Overfitting would become a major concern, even with regularization. We believe a 3D solution would require a dramatic increase in the sample size through ≥ 1 of the following: 1) access to a larger reference dataset, 2) data augmentation, 3) use of combination approaches that feature-extract using a trained network and classify using ML that are robust to small data sizes,²⁶ and 4) adapting a transfer learning approach.¹⁸

There is substantial clinical value in accurate prediction of glioma grade. Direct tissue biopsy is inherently associated with a risk to the patient, has the potential for sampling error, and has a substantial cost in resources. Accurate differentiation between low-grade gliomas (grades I and II) and high-grade gliomas (grades III and IV) has important treatment ramifications and is particularly valuable if this can be done noninvasively and accurately. Because these training data are applied to larger datasets, further ability to differentiate the tumor grade may be more apparent. Ultimately, earlier detection of disease grade using this noninvasive method may be safer and more cost efficient and permit a more timely treatment implementation.

With the availability of appropriate training data, the same or a similar technique can be adapted to other classification tasks, such

as prediction of genetic mutations in gliomas²⁷ and classifying a glioblastoma as recurrent disease versus pseudoprogression.²⁸

CONCLUSIONS

We have demonstrated the feasibility of deep learning, specifically deep convolutional networks, to learn relevant spatial features from multimodal MR images. The proposed network that incorporated the learned features was compared against traditional ML approaches (SVM, RF, and GB) and was found to be superior on the basis of precision, recall, and the F_1 score. Thus, CNN-based approaches are an effective alternative for accurate prediction of glioma grade and may ultimately optimize efficient diagnosis and treatment planning with the goal of improved health care management in patients with gliomas.

ACKNOWLEDGMENTS

We thank Anand Joshi for help with the use of BrainSuite software and Andrew Yock for proofreading the manuscript.

Disclosures: Krishna S. Nayak—RELATED: Grant: National Institutes of Health.*
*Money paid to the institution.

REFERENCES

- Lapointe S, Perry A, Butowski NA. **Primary brain tumours in adults.** *Lancet* 2018;6736:1–15 CrossRef Medline
- Progress M, Wen PY, Kesari S. **Malignant gliomas in adults.** *N Engl J Med* 2008;359:492–507 CrossRef Medline
- Behin A, Hoang-Xuan K, Carpentier AF, et al. **Primary brain tumours in adults.** *Lancet* 2003;361:323–31 CrossRef Medline
- Ostrom QT, Cioffi G, Gittleman H, et al. **CBTRUS statistical report: primary brain and other central nervous system tumors diagnosed in the United States in 2012–2016.** *Neuro Oncol* 2019;21(Supple 5):v1–100 CrossRef Medline
- Cairncross G, Wang M, Shaw E, et al. **Phase III trial of chemoradiotherapy for anaplastic oligodendroglioma: long-term results of RTOG 9402.** *J Clin Oncol* 2013;31:337–43 CrossRef Medline
- Weller M, van den Bent M, Tonn JC, et al; European Association for Neuro-Oncology (EANO) Task Force on Gliomas. **European Association for Neuro-Oncology (EANO) guideline on the diagnosis and treatment of adult astrocytic and oligodendroglial gliomas.** *Lancet Oncol* 2017;18:e315–29 CrossRef Medline
- Louis DN, Ohgaki H, Wiestler OD, et al. **The 2007 WHO Classification of Tumours of the Central Nervous System.** *Acta Neuropathol* 2007;114:97–109 CrossRef Medline
- Wesseling P, Capper D. **WHO 2016 Classification of Gliomas.** *Neuropathol Appl Neurobiol* 2018;44:139–50 CrossRef Medline
- Skögen K, Schulz A, Dormagen JB, et al. **Diagnostic performance of texture analysis on MRI in grading cerebral gliomas.** *Eur J Radiol* 2016;85:824–29 CrossRef Medline
- Tian Q, Yan LF, Zhang X, et al. **Radiomics strategy for glioma grading using texture features from multiparametric MRI.** *J Magn Reson Imaging* 2018;48:1518–28 CrossRef Medline
- Xie T, Chen X, Fang J, et al. **Textural features of dynamic contrast-enhanced MRI derived model-free and model-based parameter maps in glioma grading.** *J Magn Reson Imaging* 2018;47:1099–111 CrossRef Medline
- Lecun Y, Bottou L, Bengio Y, et al. **Gradient-based learning applied to document recognition.** *Proceedings of the IEEE* 1998;86:2278–2324 CrossRef
- Shen D, Wu G, Suk H, et al. **Deep learning in medical image analysis.** *Annu Rev Biomed Eng* 2017;19:221–48 CrossRef Medline

14. Spanhol L, Oliveira FA, Petitjean LS, et al. **Breast cancer histopathological image classification using convolutional neural networks.** In: *Proceedings of the 2016 International Joint Conference on Neural Networks*, Vancouver, British Columbia, Canada. July 25–29, 2016:2560–67 CrossRef
15. Lecun Y, Bengio Y, Hinton G. **Deep learning.** *Nature* 2015;521:436–44 CrossRef Medline
16. Ertosun MG, Rubin DL. **Automated grading of gliomas using deep learning in digital pathology images: a modular approach with ensemble of convolutional neural networks.** In: *Proceedings of the American Medical Informatics Association Annual Symposium*, San Francisco, California. November 14–18, 2015:1899–1908
17. Anaraki AK, Ayati M, Kazemi F. **Magnetic resonance imaging-based brain tumor grades classification and grading via convolutional neural networks and genetic algorithms.** *Biocybernetics and Biomedical Engineering* 2019;39:63–74 CrossRef
18. Yang Y, Yan LF, Zhang X, et al. **Glioma grading on conventional MR images: a deep learning study with transfer learning.** *Front Neurosci* 2018;12:804–14 CrossRef Medline
19. Dogdas B, Shattuck DW, Leahy RM. **Segmentation of skull and scalp in 3-D human MRI using mathematical morphology.** *Hum Brain Mapp* 2005;26:273–85 CrossRef Medline
20. Smith SM, Jenkinson M, Woolrich MW, et al. **Advances in functional and structural MR image analysis and implementation as FSL.** *Neuroimage* 2004;23(Supple 1):208–19 CrossRef Medline
21. Wang G, Li W, Ourselin S, et al. **Automatic brain tumor segmentation based on cascaded convolutional neural networks with uncertainty estimation.** *Front Comput Neurosci* 2019;13:56 CrossRef Medline
22. van Griethuysen JJ, Fedorov A, Parmar C, et al. **Computational radiomics system to decode the radiographic phenotype.** *Cancer Res* 2017;77:e104 CrossRef Medline
23. Zwanenburg A, Leger S, Vallières M. **The image biomarker standardisation initiative.** <https://arxiv.org/abs/1612.07003>. Accessed April 10, 2020
24. LeCun Y, Bengio Y. Convolutional networks for images, speech, and time series. In: Arbib MA, ed. *The Handbook of Brain Theory and Neural Networks*. MIT Press; 1998:255–58
25. Selvaraju RR, Cogswell M, Das A, et al. **Grad-CAM: visual explanations from deep networks via gradient-based localization.** In: *Proceedings of the IEEE International Conference on Computer Vision*, Venice, Italy. October 22–29, 2017:618–26
26. Nie D, Lu J, Zhang H, et al. **Multi-channel 3D deep feature learning for survival time prediction of brain tumor patients using multi-modal neuroimages.** *Sci Rep* 2019;9:1–14 CrossRef Medline
27. Chang P, Grinband J, Weinberg BD, et al. **Deep-learning convolutional neural networks accurately classify genetic mutations in gliomas.** *AJNR Am J Neuroradiol* 2018;39:1201–07 CrossRef Medline
28. Jang B, Jeon SH, Kim IH, et al. **Prediction of pseudoprogression versus progression using machine learning algorithm in glioblastoma.** *Sci Rep* 2018;8:12516 CrossRef Medline

Prediction of Clinical Outcome in Patients with Large-Vessel Acute Ischemic Stroke: Performance of Machine Learning versus SPAN-100

B. Jiang, G. Zhu, Y. Xie, J.J. Heit, H. Chen, Y. Li, V. Ding, A. Eskandari, P. Michel, G. Zaharchuk, and M. Wintermark



ABSTRACT

BACKGROUND AND PURPOSE: Traditional statistical models and pretreatment scoring systems have been used to predict the outcome for acute ischemic stroke patients (AIS). Our aim was to select the most relevant features in terms of outcome prediction on the basis of machine learning algorithms for patients with acute ischemic stroke and to compare the performance between multiple models and the Stroke Prognostication Using Age and National Institutes of Health Stroke Scale (SPAN-100) index model.

MATERIALS AND METHODS: A retrospective multicenter cohort of 1431 patients with acute ischemic stroke was subdivided into recanalized and nonrecanalized patients. Extreme Gradient Boosting machine learning models were built to predict the mRS score at 90 days using clinical, imaging, combined, and best-performing features. Feature selection was performed using the relative weight and frequency of occurrence in the models. The model with the best performance was compared with the SPAN-100 index model using area under the receiver operating curve analysis.

RESULTS: In 3 groups of patients, the baseline NIHSS was the most significant predictor of outcome among all the parameters, with relative weights of 0.36~0.69; ischemic core volume on CTP ranked as the most important imaging biomarker with relative weights of 0.29~0.47. The model with the best-performing features had a better performance than the other machine learning models. The area under the curve of the model with the best-performing features was higher than SPAN-100 model and reached statistical significance for the total ($P < .05$) and the nonrecanalized patients ($P < .001$).

CONCLUSIONS: Machine learning–based feature selection can identify parameters with higher performance in outcome prediction. Machine learning models with the best-performing features, especially advanced CTP data, had superior performance of the recovery outcome prediction for patients with stroke at admission in comparison with SPAN-100.

ABBREVIATIONS: AIS = acute ischemic stroke; CBS = clot burden score; GBM = Gradient Boosting Machine; IQR = interquartile range; NECT = non-contrast-enhanced CT; SPAN = Stroke Prognostication Using Age and National Institutes of Health Stroke Scale; TIMI = Thrombolysis in Myocardial Infarction; XGB = Extreme Gradient Boosting; AUC = area under the receiver operating curve

Ischemic stroke still ranks as the fifth leading cause of death and the second leading cause of disability in the United States.¹ Although recent reports show a trend toward a decreasing incidence of ischemic stroke for individuals 65 years of age or older, the incidence remains stable for individuals

18~65 years of age.¹ Revascularization therapies such as endovascular thrombectomy have extended the treatment window up to 16–24 hours after symptom onset as demonstrated in selected patients in Endovascular Therapy Following Imaging Evaluation for Ischemic Stroke (DEFUSE 3)² and Clinical Mismatch in the Triage of Wake Up and Late Presenting Strokes Undergoing Neurointervention with Trevo (DAWN) trials.³ However, up to 55% of patients in the endovascular therapy group and 83% in the medical therapy group remained functionally dependent, with 90-day mRS scores of >2.² Therefore, physicians taking care of patients with acute ischemic stroke (AIS) not only need to predict the individual benefit of endovascular treatment but should also be able to estimate prognosis in both treated and untreated patients and to select patients for acute treatment, inform all involved persons about the prognosis, and plan for rehabilitation and long-term care.⁴

Received April 24, 2020; accepted after revision September 12.

From the Department of Radiology, Neuroradiology Section (B.J., G.Z., Y.X., J.J.H., H.C., Y.L., G.Z., M.W.), Stanford University School of Medicine, Palo Alto, California; Department of Medicine (V.D.), Quantitative Sciences Unit, Stanford University, Stanford, California; and Neurology Service (A.E., P.M.), Centre Hospitalier Universitaire Vaudois and Lausanne University, Lausanne, Switzerland.

Please address correspondence to Max Wintermark, MD, Stanford University, Department of Radiology, Neuroradiology Division, 300 Pasteur Dr, Room 5047, Stanford, CA 94305-5105; e-mail: max.wintermark@gmail.com

 Indicates article with supplemental online tables.

 Indicates article with supplemental online photos.

<http://dx.doi.org/10.3174/ajnr.A6918>

Many publications have addressed the issues of predicting outcome in patients with acute large-vessel ischemic stroke. These include (but are not limited to) traditional logistic regression statistical models and pretreatment scoring systems such as the DRAGON score (Dense cerebral artery sign/early infarct signs on admission CT scan, prestroke modified Rankin Scale, Age, Glucose level at baseline, Onset-to-treatment time, and baseline National Institutes of Health Stroke Scale score),⁵⁻⁷ the Stroke Prognostication Using Age and National Institutes of Health Stroke Scale (SPAN-100) index,^{8,9} the Acute Stroke Registry and Analysis of Lausanne (ASTRAL) score,⁷ the Pittsburgh Response to Endovascular Therapy (PRE) score,¹⁰ the Total Health Risks in Vascular Events (THRIVE) score,¹¹ the Houston Intra-Arterial Therapy (HIAT) score, and the HIAT2 score.¹² The components considered in these predicting scoring systems were either clinical parameters only such as age and the NIHSS or non-contrast-enhanced CT (NECT) parameters such as ASPECTS. None of these models take into account advanced imaging parameters. In addition, these models were built on the basis of the hypothesis of a linear relationship between the parameters and the outcome, but some studies have highlighted a nonlinear correlation.^{13,14}

In comparison with traditional modeling methods, machine learning algorithms have much higher scalability, allowing large numbers of features and parameters to be incorporated into the models. Machine learning models have been trained not only for outcome prediction following intravenous thrombolysis¹⁵ and intra-arterial therapy^{16,17} after AIS but also for subtype classification,¹⁸ hemorrhagic transformation,¹⁹ and clot-characteristic identification.²⁰ All the above-mentioned models use clinical features as input; 2 studies also used baseline NECT^{14,16} or MR imaging gradient recalled-echo sequence features,²⁰ and 1 study used MR perfusion.¹⁹

The hypothesis of our study was that machine learning algorithms can help select the most powerful features in outcome prediction, and the model with features from advanced perfusion CTP data would have more robust prognostic ability in comparison with the other machine learning models and SPAN-100 model.⁹

MATERIALS AND METHODS

Study Population

This retrospective study was conducted using a registry of 1782 patients with AIS from January 2008 to December 2018 at the Lausanne University Hospital (1310 patients) and Stanford University (472 patients). Institutional review board approval was obtained from both institutional review boards, with a waiver of informed consent due to the retrospective nature of the study. Inclusion criteria were the following: 18 years of age or older; clinical examination and baseline CT imaging confirming acute ischemic infarction with the infarct area within the ICA/MCA territory; availability of complete clinical (onset-to-baseline time; baseline NIHSS; glucose, lipid, and blood pressure levels at admission; history of cardiac disease, statin use, smoking status; stroke mechanism according to the Trial of Org 10172 in Acute Stroke Treatment [TOAST] trial;²¹ and treatment and 90-day mRS) and imaging parameters (baseline NECT, CTP, and CTA;

early [<72 hours from baseline] recanalization CTA). Patients with subacute, chronic, remote, and/or hemorrhagic infarctions were excluded from this study. The type of revascularization treatment (intravenous thrombolysis and endovascular treatment) was recorded if performed on the basis of the treating physician's decision.

Initial Clinical and Imaging Data

All the clinical and imaging parameters assessed in our study are summarized in Online Table 1. The 90-day mRS was dichotomized into favorable (mRS 0–2) and unfavorable outcome (mRS 3–6).

NECT, CTP, and CTA data were collected at admission as baseline studies. A blinded neuroradiologist evaluated the imaging features for all of the imaging studies. Features including the ASPECTS and hyperdense middle cerebral artery sign were extracted from the NECT. CTP datasets were processed on a workstation (Brain Perfusion, Version 6.0.0; Philips Healthcare). Automatic segmentation of ischemic core and penumbra volumes was performed on the basis of previously published thresholds.²² The sidedness of cerebral ischemia was evaluated as well. The site of occlusion, Thrombolysis in Myocardial Infarction (TIMI) score, and collateral status were interpreted on the MIP CTA images. The TIMI²³ score was assessed as follows: 0, complete occlusion; 1, subocclusion with no distal branch filling; 2, subocclusion with incomplete or slow distal branch filling; and 3, completely open artery. A previously reported scoring system²⁴ was used for grading the collaterals into 4 levels in comparison with the normal side on baseline CTA. In addition, the clot burden score²⁵ (CBS), reflecting the extent of intracranial clot, and degree of stenosis of the carotid bifurcation according to the NASCET criteria were assessed on baseline CTA images. The total cohort was divided into 2 subgroups depending on the recanalization status. A TIMI score of ≥ 2 on recanalization studies was considered recanalization, while < 2 was considered persistent arterial occlusion.

Model Construction

Our dataset had 2 distinctive characteristics: low dimensionality with < 100 features and high nonlinearity for both qualitative and quantitative clinical/imaging features. We, therefore, decided to use Extreme Gradient Boosting (XGB), which is a specialized Gradient Boosting Machine (GBM), for our dataset. There are 2 core elements of the GBM. The first is a decision tree, which is the approach to generate and approximate non-linear-relationship mapping between input features and final outcome. The second is boosting. Initially raised by the authors of Adaptive Boosting (AdaBoost),²⁶ the concept of boosting consists of first creating many weaker, simpler machine learning classifiers during training. Then, the final model is constructed by pooling the results from all weaker models and creating a fine-tuned, stronger classifier. XGB was developed on the basis of the GBM with superiority of performance in multiple data science contests, and its multicore algorithms allow multiple computations to run simultaneously in parallel, thus enabling the algorithm to scale to large datasets.²⁷

A previous study²⁸ using GBM demonstrated that machine learning methods with decision tree and boosting algorithms were capable of predicting patient outcomes after AIS. In that study, both XGB and GBM were used, and XGB was found to have a relatively better performance when the cohort was divided into subgroups. XGB was also shown to perform very well in another study when segmenting stroke infarct regions using both clinical and imaging features.²⁹

Sixteen clinical and 11 imaging parameters were introduced in our models (Online Table 1). The dataset was broken down into 5 groups with a relatively equal number of patients in each group for 5-fold cross-validations. Data of each patient were randomly enrolled into 1 of the 5 folds as a testing set. In the remaining 4 folds, the patient data were used as a training set. For each model's training and testing phase, 5 identical models were trained, each using 1 group as the test set, with the remaining 4 groups as a training set. Then the overall model performance was evaluated on the basis of results from all 5 models on 5 test sets. At first, 3 types of feature group combinations, clinical features, imaging features, and clinical plus imaging features, were used in the XGB models to predict the 90-day mRS of the entire cohort and recanalized and nonrecanalized subgroups, respectively, creating 9 total combinations. To improve the performance of the machine learning models, we selected a subset of clinical and imaging features from all the predictors according to their contributions to the models. Features were selected on the basis of the following criteria: They had a relative weight of ≥ 0.2 or a relative weight of ≥ 0.1 and were in the top 5 highest weights in the 9 above-mentioned models. The SPAN-100 XGB model was built by introducing age and the NIHSS at admission based on the definition.

Statistical Analysis

Overall and by recanalization status, continuous characters were summarized as medians and interquartile ranges (IQRs) and as counts and percentages for categoric characters. For each of the 3 cohorts, measures of prediction sensitivity, specificity, accuracy, and area under the receiver operating curve (AUC) were estimated for the machine learning models, as well as for the reference SPAN-100 index model, with SPAN-100 defined as the sum of patient age and the NIHSS score.⁹ The machine learning model with the highest AUC was then compared with the SPAN-100 index model, with the DeLong test of pair-wise AUCs assessed using the pROC R package (<https://www.rdocumentation.org/packages/pROC/versions/1.16.2>).^{30,31}

Finally, confusion matrices for 90-day mRS prediction were constructed, by cohort, for all models on the basis of 7-fold cross-validation and visualized as heatmaps. All analyses were conducted in the R statistical computing framework,³² Version 3.6 (<http://www.r-project.org/>), and statistical significance was assessed at the .05 α level.

RESULTS

There were 1431 patients included in this study, including 899 patients with recanalization and 532 patients with no recanalization (Online Fig 1). Online Table 1 illustrates the clinical and

imaging characteristics for the total cohort and for the 2 subgroups.

Feature Selection with Machine Learning

Among the clinical and imaging parameters, the baseline NIHSS was the most important predictor of outcome for the whole cohort, as well as in the recanalized and nonrecanalized groups, with relative weights ranging from 0.36 to 0.69. Age and glucose levels at admission ranked as the next most important parameters in both the model using only clinical parameters and the model using all the clinical and imaging parameters (Online Table 2). The NIHSS and age are both components of the SPAN-100 scoring system.

Among the imaging parameters, ischemic core volume on CTP came in first place for all 3 groups of patients, with relative weights of 0.29~0.47 (Online Table 2). The CTA-CBS score, penumbra volume on CTP, and infarct side were the second strongest imaging predictors in the full cohort, the recanalized patients, and the nonrecanalized patients, respectively.

Clinical features such as baseline NIHSS score and age outweighed all the imaging features in importance in all 3 groups. Glucose level at admission appeared to be the third most important clinical biomarker in the total cohort and in recanalized patients, but not in nonrecanalized patients. In the nonrecanalized group, infarct and penumbra volume on CTP and time from onset to the baseline study came before the glucose level. Accordingly, the model with the best-performing features (total of 6 features) was built by including 3 clinical features (baseline NIHSS, age, glucose at admission) and 3 imaging features (ischemic core volume on CTP, penumbra volume on CTP, and CTA-CBS) (Online Table 3).

Model Performance in the Full Cohort and Recanalized and Nonrecanalized Cohorts

The sensitivity, specificity, accuracy, AUC, and heatmap of each model in the full cohort, as well as in the recanalized and the nonrecanalized subgroups are demonstrated in the Table, Figure, and Online Fig 2. The models with both imaging and clinical features performed better than those with only clinical or imaging input. The model with 6 features performed better than models with clinical features only, models with imaging features only, and models with both clinical and imaging features. This finding was true in all 3 groups of participants, with the highest AUC value of 0.83 for the nonrecanalized patients.

Comparison between Machine Learning Models and the SPAN Scoring Model

Our best model, the model with the best-performing features, was compared with the SPAN-100 index (Figure and Online Fig 2). The AUCs for the machine learning models with the 6 best-performing features in the total cohort and recanalized and nonrecanalized groups were 0.80, 0.79, and 0.82, respectively. The AUCs for SPAN-100 were 0.78, 0.76, and 0.78, respectively. The optimal cutoff values of SPAN-100 were 85, 94, and 64 for the total, recanalized, and nonrecanalized cohorts, respectively. The AUCs of the XGB models with the 6 best-performing features were higher than those of SPAN-100 and reached the

Performance of machine learning models and the SPAN-100 index in 3 cohorts

Cohorts/Models	Sensitivity (%)	Specificity (%)	Accuracy (%)	AUC
Full cohort				
Clinical features only (16 features)	78.1	65.5	73.5	0.77
Imaging features only (11 features)	53.5	79.9	63.2	0.69
Both clinical and imaging features (27 features)	74.4	69.8	72.8	0.79
Best-performing clinical and imaging features (6 features)	72.2	74.0	72.8	0.80 ^a
SPAN-100	80.6	64.3	73.5	0.78
Recanalized				
Clinical features only (16 features)	73.1	70.4	71.9	0.76
Imaging features only (11 features)	53.7	69.4	60.9	0.61
Both clinical and imaging features (27 features)	74.5	68.9	72.0	0.77
Best-performing clinical and imaging features (6 features)	76.9	69.9	73.8	0.79 ^a
SPAN-100	78.8	63.8	71.9	0.76
Nonrecanalized				
Clinical features only (16 features)	80.0	65.8	74.1	0.78
Imaging features only (11 features)	63.3	67.8	64.3	0.70
Both clinical and imaging features (27 features)	71.3	80.5	73.3	0.81
Best-performing clinical and imaging features (6 features)	81.9	75.4	80.5	0.82 ^a
SPAN-100	65.5	77.1	68.1	0.78

^a Model with the highest AUC value.

statistical significance for the total cohort ($P < .05$) and the nonrecanalized patients ($P < .001$). In the recanalized group, the difference was not significant ($P = .05$).

DISCUSSION

Our study shows that machine learning models trained with best-performing clinical and imaging features, including advanced CTP parameters, can predict the outcome of patients with stroke more accurately than a conventional scoring system.

Bacchi et al³³ used deep learning models to predict the outcome in patients with AIS who underwent intravenous thrombolysis. The combined convolutional-plus-artificial neural network model based on both clinical and imaging data performed best in predicting patient outcomes. Heo et al³⁴ attempted to predict favorable outcome in a large group of 2043 patients with stroke using 3 machine learning models. By incorporating 38 demographic/clinical variables into their models, they found that the deep neural network model performed better than the other 2 models (random forest and logistic regression) and the ASTRAL score, while the performance of the deep neural network did not differ significantly from the ASTRAL score when trained on only the same 6 variables used for calculating the ASTRAL score. Nishi et al¹⁷ built 9 models, including 5 previously reported scoring models, 1 logistic regression statistical model, and 3 machine learning models to predict the clinical outcome in a cohort of 387 patients with stroke who underwent endovascular treatment. Machine learning models were superior to the other models. These above-mentioned models used ASPECTS as the only imaging variable to make the outcome prediction, and the overwhelming clinical variables in these models seemed not quite practical in an emergency scenario because a physician has to input many variables to get valuable prognostic information. Our models with the best-performing features were trained on more advanced imaging data such as CTP and CTA parameters, which provide improved accuracy compared with models using only parameters from the NECT. Furthermore, clinical features are

important predictors, but when they are broken down into recanalized and nonrecanalized groups, CTP imaging data were a more potent contributor, especially for those nonrecanalized patients.

The commonly used machine learning models in cerebrovascular diseases include random forest, support-vector machines, the neural network, decision trees, and logistic regression. In this study, we used a supervised XGB model, which is a decision tree-based machine learning method. Previous publications^{28,29,35} highlighted the adaptability of XGB in dealing with redundant and nonlinear datasets. Compared with other machine learning models, XGB makes more powerful predictions with less chance of overfitting, especially in predictions of binary outcomes.

Our modeling filtered 6 parameters that best predicted the 90-day mRS score. Baseline NIHSS, age, and glucose on admission are clinical components of most of the conventional pre-treatment prognostic systems developed for patients with stroke.⁵⁻¹² Previous studies have shown that baseline NIHSS and age are strongly associated with prognosis.^{13,36,37} Hyperglycemia on admission is known to be an independent predictor of worse outcome because of its association with lactic acidosis and accelerated conversion of penumbra to infarct.^{38,39} The relevant imaging features (CTP ischemic core volume, penumbra volume, and CTA-CBS) are also well-established stroke imaging biomarkers.¹³ Collateral scores and the CBS have been reported to be equally important in outcome prediction.⁴⁰ In our study, collaterals played an important role in the recanalized group, but not in the nonrecanalized group.

It is beneficial to have a simple model because it makes clinical deployment faster and easier. A model requiring few features to yield a useful prediction is also less prone to overfitting. In addition, the 3 imaging features used in our model can be automatically extracted within a machine learning pipeline embedded in the daily workflow. It is practical for our best-performing model to provide a prompt outcome prediction.

The SPAN-100 index has been shown to have the ability to predict patient outcome and the risk of complications after endovascular therapy in several stroke cohorts.^{9,13} Möbius et al⁸ found

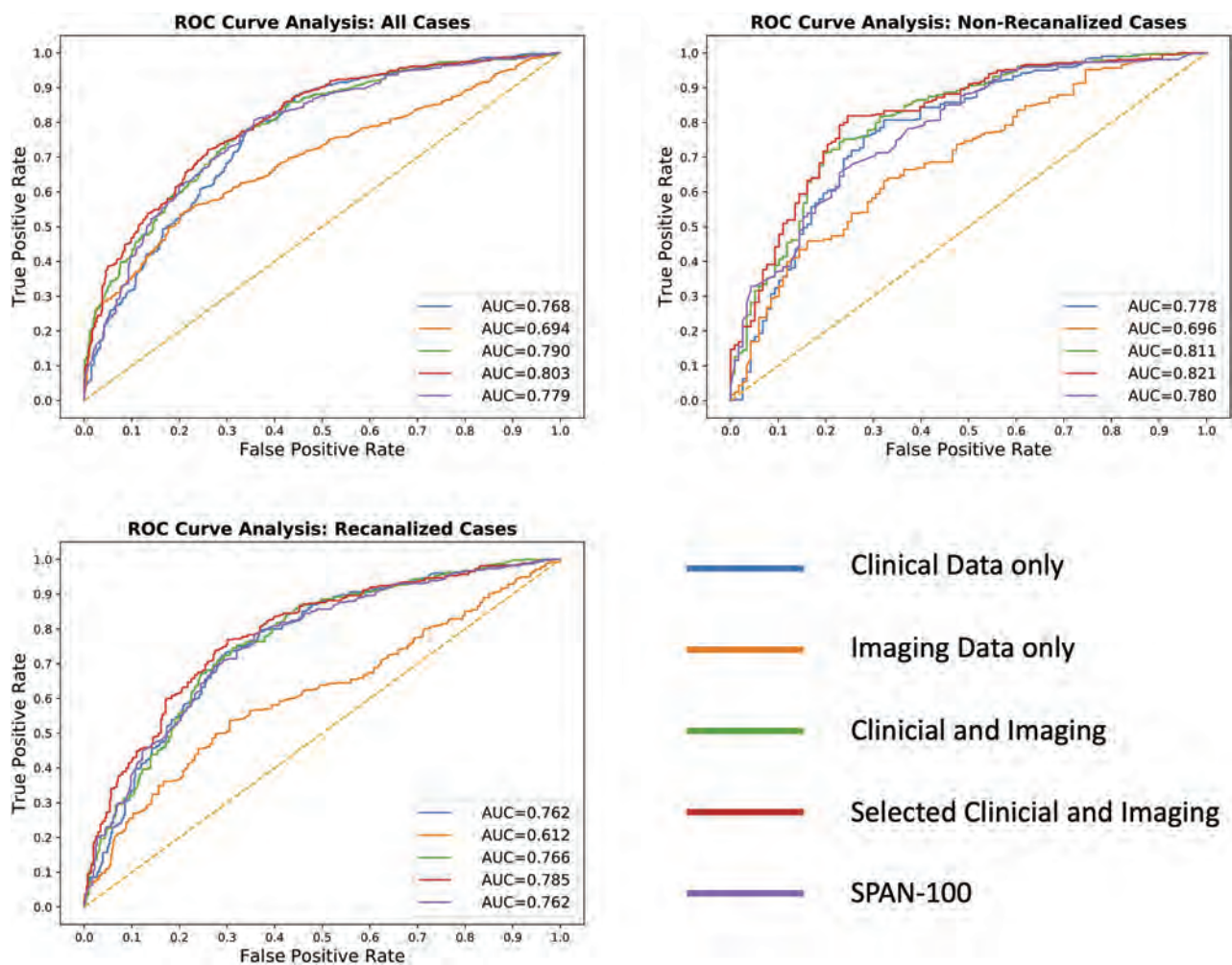


FIGURE. Receiver operating characteristics (ROCs) of XGB prediction models with clinical features, imaging features, both clinical and imaging features, best-performing features, and SPAN-100 for predicting a 90-day mRS score of >2. For all patients and recanalized and nonrecanalized patients, the AUCs of models with the best-performing features were higher than those in SPAN-100, and statistical significance was reached in the total and nonrecanalized groups. The AUCs for machine learning models with the 6 best-performing features in the total cohort and recanalized and nonrecanalized groups were 0.80, 0.79, and 0.82, respectively. The AUCs for SPAN-100 were 0.78, 0.76, and 0.78, respectively. The AUCs of XGB models with the best-performing features were higher than those in SPAN-100 and reached statistical significance for the total cohort ($P < .05$) and the nonrecanalized patients ($P < .001$). In the recanalized group, the difference was not significant ($P = .05$).

that the patients positive on the basis of SPAN-100 demonstrated a 9-fold increase in the odds ratio of poor outcome compared with those negative on the basis of SPAN-100, with an AUC of 0.74. The NIHSS ranked as the most highly relevant parameter among all of the clinical and imaging biomarkers in our study, while age was the second-best predictor in nonrecanalized patients and the third-best predictor in all and recanalized patients. When combined with imaging features, the ability of outcome prediction improved from 0.78, 0.76, and 0.78 to 0.80, 0.79, and 0.82 for all and recanalized and nonrecanalized patients. The major limitation of SPAN-100 is its inapplicability to younger patients, for it cannot reach a positive status because of the age component. However, our model overcomes this limitation and is applicable to any patient with AIS older than 18 years of age.

There are several limitations to this study. First, this was a retrospective study, and our model will need to be validated

prospectively. Second, we used only XGB models in this machine learning study, and other machine learning algorithms need to be considered in future study designs. Third, prognostic models other than the SPAN-100 may have superior long-term predictive values for handicap and mortality, which will be incorporated into our future study design.⁴¹

CONCLUSIONS

Machine learning-based feature selection can identify parameters with higher performance in long-term recovery-outcome prediction for patients with stroke at admission, while removing redundant and less predictive parameters. Moreover, the models with input from the best-performing features had better predictive value than the other models using clinical features only, imaging features only, both clinical and imaging features, and the SPAN-100 index. Finally, the prognostic

ability of machine learning models with advanced imaging features such as CTP data can be improved, especially for nonrecanalized patients.

Disclosures: Yuan Xie—UNRELATED: Employment: Subtle Medical Inc; Stock/Stock Options: Subtle Medical Inc. Jeremy J. Heit—UNRELATED: Board Membership: iSchemaView, Comments: Medical and Scientific Advisory Board member; Consultancy: Medtronic and MicroVention. Patrik Michel—RELATED: Grant: Swiss National Science Foundation, Swiss Heart Foundation*; Consulting Fee or Honorarium: Medtronic*; Other Relationships: Steering Committees/Data Safety and Monitoring Board of BASICS, ELAN, International PFO Consortium PROMISE, CLOSE (no payments); Greg Zaharchuk—UNRELATED: Board Membership: Subtle Medical Inc; Consultancy: Subtle Medical Inc; Grants/Grants Pending: various National Institutes of Health projects, GE Healthcare, Bayer AG*; Royalties: Cambridge University Press; Stock/Stock Options: Equity, Subtle Medical Inc. Max Wintermark—UNRELATED: Consultancy: MORE Health, Magnetic Insight, Subtle Medical Inc, icometrix, Nous. *Money paid to the institution.

REFERENCES

1. Benjamin EJ, Muntner P, Alonso A, et al; American Heart Association Council on Epidemiology and Prevention Statistics Committee and Stroke Statistics Subcommittee. **Heart disease and stroke statistics-2019 update: a report from the American Heart Association.** *Circulation* 2019;139:e56–528 CrossRef Medline
2. Albers GW, Marks MP, Kemp S, et al; DEFUSE 3 Investigators. **Thrombectomy for stroke at 6 to 16 hours with selection by perfusion imaging.** *N Engl J Med* 2018;378:708–18 CrossRef Medline
3. Nogueira RG, Jadhav AP, Haussen DC, et al; DAWN Trial Investigators. **Thrombectomy 6 to 24 hours after stroke with a mismatch between deficit and infarct.** *N Engl J Med* 2018;378:11–21 CrossRef Medline
4. Winzeck S, Hakim A, McKinley R, et al. **ISLES 2016 and 2017-benchmarking ischemic stroke lesion outcome prediction based on multispectral MRI.** *Front Neurol* 2018;9:679 CrossRef Medline
5. Turc G, Apoil M, Naggara O, et al. **Magnetic resonance imaging-dragon score: 3-month outcome prediction after intravenous thrombolysis for anterior circulation stroke.** *Stroke* 2013;44:1323–28 CrossRef Medline
6. Strbian D, Seiffge DJ, Breuer L, et al. **Validation of the dragon score in 12 stroke centers in anterior and posterior circulation.** *Stroke* 2013;44:2718–21 CrossRef Medline
7. Cooray C, Mazya M, Bottai M, et al. **External validation of the astral and dragon scores for prediction of functional outcome in stroke.** *Stroke* 2016;47:1493–99 CrossRef Medline
8. Möbius C, Blinzler C, Schwab S, et al. **Re-evaluation of the Stroke Prognostication Using Age and NIH Stroke Scale index (SPAN-100 index) in IVT patients: the-SPAN 100(65) index.** *BMC Neurol* 2018;18:129 CrossRef Medline
9. Saposnik G, Guzik AK, Reeves M, et al. **Stroke prognostication using age and NIH Stroke Scale: SPAN-100.** *Neurology* 2013;80:21–28 CrossRef Medline
10. Rangaraju S, Aghaebrahim A, Streib C, et al. **Pittsburgh Response to Endovascular Therapy (PRE) score: optimizing patient selection for endovascular therapy for large vessel occlusion strokes.** *J NeuroIntervent Surg* 2015;7:783–88 CrossRef Medline
11. Flint AC, Faigeles BS, Cullen SP, et al; VISTA Collaboration. **Thrive score predicts ischemic stroke outcomes and thrombolytic hemorrhage risk in VISTA.** *Stroke* 2013;44:3365–69 CrossRef Medline
12. Sarraj A, Albright K, Barreto AD, et al. **Optimizing prediction scores for poor outcome after intra-arterial therapy in anterior circulation acute ischemic stroke.** *Stroke* 2013;44:3324–30 CrossRef Medline
13. Jiang B, Ball RL, Michel P, et al. **Factors influencing infarct growth including collateral status assessed using computed tomography in acute patients with stroke with large artery occlusion.** *Int J Stroke* 2019;14:603–12 CrossRef Medline
14. Hakimelahi R, Vachha BA, Copen WA, et al. **Time and diffusion lesion size in major anterior circulation ischemic strokes.** *Stroke* 2014;45:2936–41 CrossRef Medline
15. Bentley P, Ganesalingam J, Carlton Jones AL, et al. **Prediction of stroke thrombolysis outcome using CT brain machine learning.** *Neuroimage Clin* 2014;4:635–40 CrossRef Medline
16. Asadi H, Dowling R, Yan B, et al. **Machine learning for outcome prediction of acute ischemic stroke post intra-arterial therapy.** *PLoS One* 2014;9:e88225 CrossRef Medline
17. Nishi H, Oishi N, Ishii A, et al. **Predicting clinical outcomes of large vessel occlusion before mechanical thrombectomy using machine learning.** *Stroke* 2019;50:2379–88 CrossRef Medline
18. Garg R, Oh E, Naidech A, et al. **Automating ischemic stroke subtype classification using machine learning and natural language processing.** *J Stroke Cerebrovasc Dis* 2019;28:2045–51 CrossRef Medline
19. Yu Y, Guo D, Lou M, et al. **Prediction of hemorrhagic transformation severity in acute stroke from source perfusion MRI.** *IEEE Trans Biomed Eng* 2018;65:2058–65 CrossRef Medline
20. Chung JW, Kim YC, Cha J, et al. **Characterization of clot composition in acute cerebral infarct using machine learning techniques.** *Ann Clin Transl Neurol* 2019;6:739–47 CrossRef Medline
21. Adams HP Jr, Bendixen BH, Kappelle LJ, et al. **Classification of subtype of acute ischemic stroke: definitions for use in a multicenter clinical trial—TOAST. Trial of Org 10172 in Acute Stroke Treatment.** *Stroke* 1993;24:35–41 CrossRef Medline
22. Wintermark M, Flanders AE, Velthuis B, et al. **Perfusion-CT assessment of infarct core and penumbra: receiver operating characteristic curve analysis in 130 patients suspected of acute hemispheric stroke.** *Stroke* 2006;37:979–85 CrossRef Medline
23. TIMI Study Group. **The Thrombolysis in Myocardial Infarction (TIMI) trial: Phase I findings.** *N Engl J Med* 1985;312:932–36 CrossRef Medline
24. Tan JC, Dillon WP, Liu S, et al. **Systematic comparison of perfusion-CT and CT-angiography in acute patients with stroke.** *Ann Neurol* 2007;61:533–43 CrossRef Medline
25. Puetz V, Dzialowski I, Hill MD, et al; Calgary CTA Study Group. **Intracranial thrombus extent predicts clinical outcome, final infarct size and hemorrhagic transformation in ischemic stroke: the clot burden score.** *Int J Stroke* 2008;3:230–36 CrossRef Medline
26. Freund Y. **An adaptive version of the boost by majority algorithm.** *Machine Learning* 2001;43:293–18. file:///C:/Users/mrudi/Downloads/Freund2001_Article_AnAdaptiveVersionOfTheBoostByM.pdf. Accessed January 18, 2019
27. Chen T, Guestrin C. **Xgboost: a scalable tree boosting system.** In: *KDD '16: Proceedings of the 22nd Association for Computing Machinery Special Interest Group for Knowledge Discovery from Data International Conference on Knowledge Discovery and Data Mining*. San Francisco, California; August 2016:785–94
28. Xie Y, Jiang B, Gong E, et al. **Journal club: use of Gradient Boosting Machine learning to predict patient outcome in acute ischemic stroke on the basis of imaging, demographic, and clinical information.** *AJR Am J Roentgenol* 2019;212:44–51 CrossRef Medline
29. Livne M, Boltdsen JK, Mikkelsen IK, et al. **Boosted tree model reforms multimodal magnetic resonance imaging infarct prediction in acute stroke.** *Stroke* 2018;49:912–18 CrossRef Medline
30. DeLong ER, DeLong DM, Clarke-Pearson DL. **Comparing the areas under two or more correlated receiver operation characteristic curves: a nonparametric approach.** *Biometrics* 1988;44:837 CrossRef Medline
31. Xavier Robin NT, Hainard A, Tiberti N, et al. **Proc: An open-source package for R and S+ to analyze and compare roc curves.** *BMC Bioinformatics* 2011;12:77 CrossRef
32. The R Core Team. *A Language and Environment for Statistical Computing.* R Foundation for Statistical Computing; 1999–2012
33. Bacchi S, Zerner T, Oakden-Rayner L, et al. **Deep learning in the prediction of ischaemic stroke thrombolysis functional**

- outcomes: a pilot study.** *Acad Radiology* 2019;27:e19–23 CrossRef Medline
34. Heo J, Yoon JG, Park H, et al. **Machine learning-based model for prediction of outcomes in acute stroke.** *Stroke* 2019;50:1263–65 CrossRef Medline
35. Torlay L, Perrone-Bertolotti M, Thomas E, et al. **Machine learning-XGBoost analysis of language networks to classify patients with epilepsy.** *Brain Inform* 2017;4:159–69 CrossRef Medline
36. Adams HP Jr, Davis PH, Leira EC, et al. **Baseline NIH stroke scale score strongly predicts outcome after stroke: a report of the Trial of Org 10172 in Acute Stroke Treatment (TOAST).** *Neurology* 1999;53:126–31 CrossRef
37. Hankey GJ, Spiesser J, Hakimi Z, et al. **Rate, degree, and predictors of recovery from disability following ischemic stroke.** *Neurology* 2007;68:1583–87 CrossRef Medline
38. Weir CJ, Murray GD, Dyker AG, et al. **Is hyperglycaemia an independent predictor of poor outcome after acute stroke? Results of a long-term follow-up study.** *BMJ* 1997;314:1303–06 CrossRef Medline
39. Parsons MW, Barber PA, Desmond PM, et al. **Acute hyperglycemia adversely affects stroke outcome: a magnetic resonance imaging and spectroscopy study.** *Ann Neurol* 2002;52:20–28 CrossRef Medline
40. Tan IY, Demchuk AM, Hopyan J, et al. **CT angiography clot burden score and collateral score: correlation with clinical and radiologic outcomes in acute middle cerebral artery infarct.** *AJNR Am J Neuroradiol* 2009;30:525–31 CrossRef Medline
41. Quinn TJ, Singh S, Lees KR, et al; VISTA Collaborators. **Validating and comparing stroke prognosis scales.** *Neurology* 2017;89:997–1002 CrossRef Medline

Evaluation of Artificial Intelligence–Powered Identification of Large-Vessel Occlusions in a Comprehensive Stroke Center

A. Yahav-Dovrat, M. Saban, G. Merhav, I. Lankri, E. Abergel, A. Eran, D. Tanne, R.G. Nogueira, and R. Sivan-Hoffmann



ABSTRACT

BACKGROUND AND PURPOSE: Artificial intelligence algorithms have the potential to become an important diagnostic tool to optimize stroke workflow. Viz LVO is a medical product leveraging a convolutional neural network designed to detect large-vessel occlusions on CTA scans and notify the treatment team within minutes via a dedicated mobile application. We aimed to evaluate the detection accuracy of the Viz LVO in real clinical practice at a comprehensive stroke center.

MATERIALS AND METHODS: Viz LVO was installed for this study in a comprehensive stroke center. All consecutive head and neck CTAs performed from January 2018 to March 2019 were scanned by the algorithm for detection of large-vessel occlusions. The system results were compared with the formal reports of senior neuroradiologists used as ground truth for the presence of a large-vessel occlusion.

RESULTS: A total of 1167 CTAs were included in the study. Of these, 404 were stroke protocols. Seventy-five (6.4%) patients had a large-vessel occlusion as ground truth; 61 were detected by the system. Sensitivity was 0.81, negative predictive value was 0.99, and accuracy was 0.94. In the stroke protocol subgroup, 72 (17.8%) of 404 patients had a large-vessel occlusion, with 59 identified by the system, showing a sensitivity of 0.82, negative predictive value of 0.96, and accuracy of 0.89.

CONCLUSIONS: Our experience evaluating Viz LVO shows that the system has the potential for early identification of patients with stroke with large-vessel occlusions, hopefully improving future management and stroke care.

ABBREVIATIONS: ICA-T = ICA terminus; ICC = intraclass correlation coefficient; LVO = large-vessel occlusion; PPV = positive predictive value

Acute ischemic stroke caused by large-vessel occlusion (LVO) contributes disproportionately to stroke-related disability and death.^{1,2} It requires emergent detection and treatment ideally by an endovascular approach. Management has changed dramatically during the past few years, most notably due to the numerous clinical trials published in 2015 that indicated that endovascular treatment is superior to tPA alone in the treatment of LVO acute ischemic stroke.^{3,4} One of the major contributors to this revolutionary result was the proper selection of eligible patients.⁵ As opposed to earlier trials,^{6,7} patients in recent studies

were selected primarily by CTA scans. These trials demonstrated the efficacy of mechanical thrombectomy in patients with a limited ischemic core in the setting of moderate-to-severe clinical deficits, which designated such patients as ideal candidates for revascularization therapy. The window for treatment was further extended at the beginning of 2018 to 24 hours,⁸ following 2 trials that demonstrated the efficacy of endovascular treatment for selected patients in timeframes of 6–16 hours⁹ and 6–24 hours.¹⁰ The immediate consequence was an increase in the number of patients eligible for transfer from primary and secondary hospitals to comprehensive stroke centers for endovascular treatment. Thus, fast and accurate recognition of pathology on CT scans has become crucial.

Artificial intelligence algorithms, particularly deep learning, have demonstrated remarkable progress in image-recognition tasks. Methods ranging from convolutional neural networks to variational autoencoders have found great application in the medical image-analysis field, pushing it forward at a rapid pace. Deep learning has the potential to revolutionize entire industries, and given the centrality of neuroimaging in the diagnosis and treatment of neurologic disease,

Received April 13, 2020; accepted after revision September 13.

From the Department of Radiology (A.Y.-D., G.M., A.E., R.S.-H.), Unit of Interventional Neuroradiology (E.A., R.S.-H.), and Stroke and Cognition Institute (D. T.), Rambam Health Care Campus, Haifa, Israel; Faculty of Social Health and Welfare (M.S.), Haifa University, Haifa, Israel; Faculty of Medicine (I.L.), Technion Israel Institute of Technology, Haifa, Israel; Neuroendovascular Service (R.G.N.), Marcus Stroke and Neuroscience Center, Grady Memorial Hospital, Atlanta, Georgia; and Departments of Neurology, Neurosurgery, and Radiology (R.G.N.), Emory University School of Medicine, Atlanta, Georgia.

Please address correspondence to Rotem Sivan-Hoffmann, MD, Rambam Health Care Campus, HaAliya HaShniya St 8, Haifa, Israel. 3109601; e-mail: otemsivan3@gmail.com

<http://dx.doi.org/10.3174/ajnr.A6923>

deep learning will likely affect neuroradiologists most profoundly.^{11,12}

Viz LVO (Viz.ai) is a medical product leveraging a convolutional neural network designed to detect LVOs on CTA scans and notify a neurointerventional specialist within minutes via a dedicated mobile application.

Our aim was to evaluate the detection accuracy of the Viz LVO in real clinical practice at a comprehensive stroke and trauma center.

MATERIALS AND METHODS

A retrospective study was conducted. Viz LVO was installed at the Rambam Health Care Campus in January 2018 for this study. All CTA scans obtained from January 2018 to March 2019 were scanned by the system, including nonacute ischemic stroke cases. The scans were analyzed by the Viz LVO Algorithm, Version 4.1.3, a convolutional neural network using deep learning to detect occlusions from the ICA terminus (ICA-T) to the Sylvian fissure. Analysis of this area would include all occlusions of the M1 segment of the MCA and possibly proximal M2 segment occlusions. Posterior circulation arteries are not assessed by the system.

The results of the system were compared with the formal CTA reading documented in the patients' files. Each CTA reading was performed by a single reader. The readers were 4 senior neuroradiologists, with 7–25 years of experience. A separate designated pool of 15 examinations was used for evaluating interrater and intrarater reliability among 4 raters. No variation was found between the results given for each CTA examination (intraclass correlation coefficient [ICC] > 0.99).

LVO was considered as either an ICA-T or MCA-M1 occlusion. A second analysis included M2, which was further divided into proximal and distal occlusions using the curve into the Sylvian fissure as an anatomic landmark (Fig 1).

Other major pathologies reported in the formal neuroradiologist read were also documented, including cerebral hemorrhage, tumors, and intracranial arterial stenosis. Arterial stenosis was defined as a decrease of more than that in the arterial cross-sectional area calculated by the NASCET formula for ICA or MCA reported in the formal CTA read.

Examinations with metal artifacts ($n = 7$) as well as those with severe motion or incomplete skull scanning ($n = 6$) were excluded from the analysis a priori because they are automatically not analyzed by the algorithm. Such examinations are transferred to the server and the mobile application by the system, marked as technically inadequate and classified as negative for LVO. This process is further explained in the Algorithm Description segment and illustrated in Figs 2 and 3.

Algorithm Description

The LVO-detection algorithm involves several steps. First, applicable CTA series are identified by inspecting the DICOM metadata. Once an applicable series is identified, the next step is to verify the existence of contrast. The soft matter is extracted by creating a mask of all bone voxels, based on Hounsfield unit thresholding, dilation, and connected component analysis, and removing the bone mask and all voxels

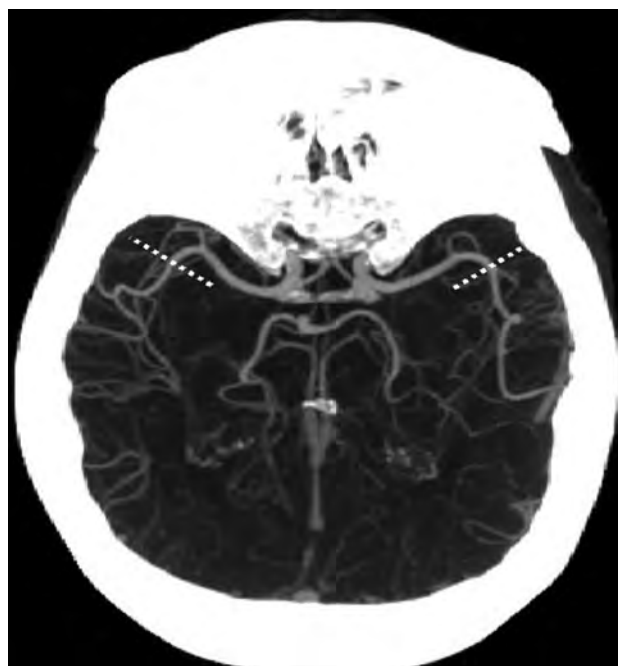


FIG 1. Division of the M2 segment of the MCA into proximal and distal segments at the curve of the artery into the Sylvian fissure (marked bilaterally by the dashed lines).

external to it. Once the soft matter is extracted, it is inspected for the existence of contrast by counting the total number of voxels with Hounsfield unit values consistent with iodine contrast (100–800 HU). If no contrast is identified, the scan is flagged as a suspected missed bolus and no further processing is conducted.

In the selected examinations, 3D registration of the brain is performed followed by cropping of a 3D cuboid, with dimensions determined so that the ICA-T, M1, and M2 regions are contained within the cuboid. The cuboid is inspected for the presence of metal by looking for voxels with Hounsfield unit values of >3000. If such voxels are identified, the scan is flagged as suspected of containing metallic artifacts and no further processing is conducted. Scans that were not processed due to bad bolus timing or metal artifacts are still available for viewing but are marked by a red frame to notify the user that the algorithm rejected the series. Examples are given in Fig 2, and an illustration of the process is provided in Fig 3.

The 3D cuboid is fed through a 3D segmentation convolutional neural network inspired by the U-Net architecture.¹³ The output of the network is a 3D cuboid of the same dimension as the input, whereby each voxel is assigned a number between 0 and 1 by the network, describing the probability (as estimated by the network) that this voxel is part of the ICA-T or M1 segments. The network was trained on hundreds of manual segmentations of the ICA-T and M1 regions.

Next, the lengths of the left and right segmentations are compared. This step is to identify cases in which due to an ICA occlusion and no retrograde filling, the ICA-T and M1 segments are not visible in the scan. If one of the sides is significantly shorter than the other, an LVO is detected and the system triggers an alert.

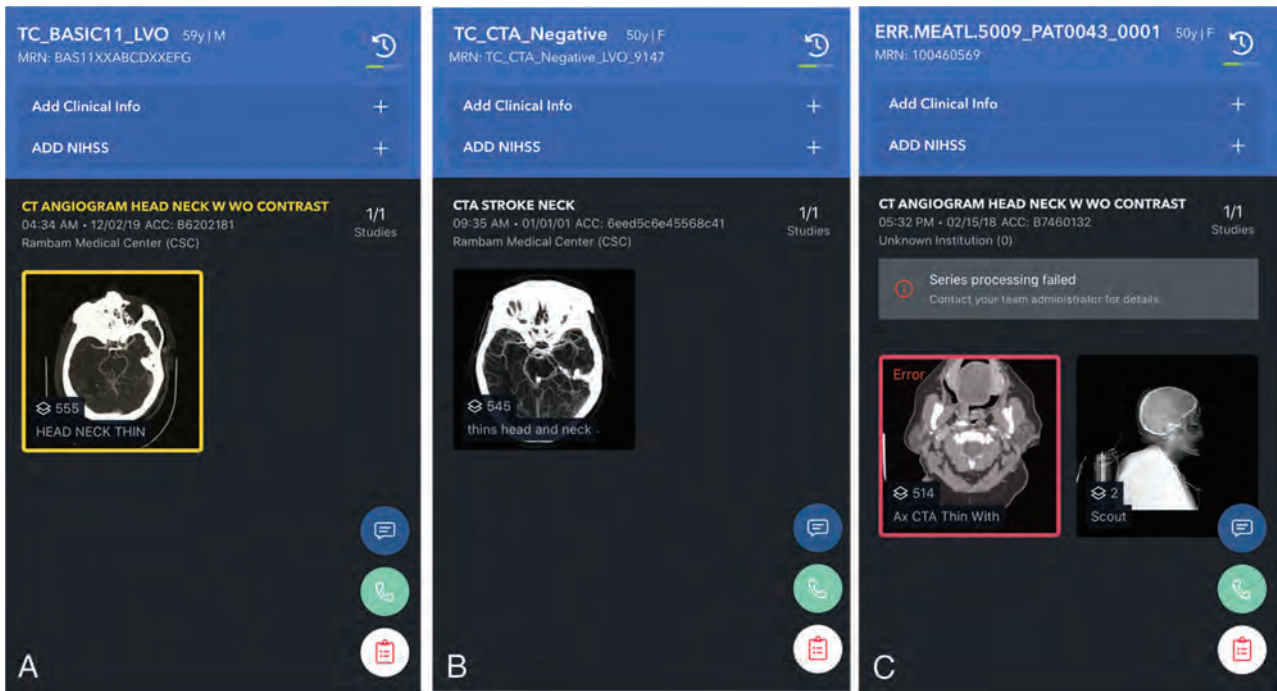


FIG 2. Alerts as they appear on the user end of the mobile application, showing the overview screen of examinations with (A) and without (B) a suspected LVO. An overview screen of failed processing is shown in C, in this case, due to metallic artifacts.

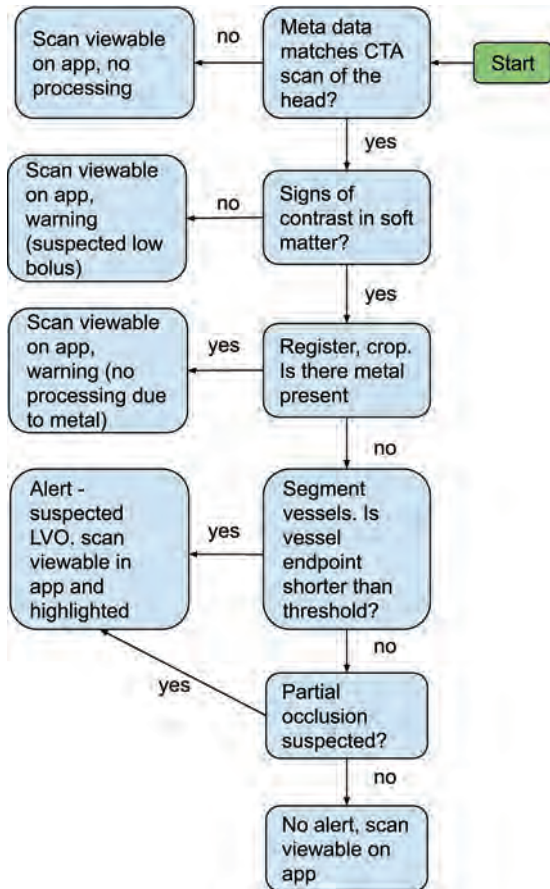


FIG 3. Flow diagram delineating the various steps of the algorithm. App indicates mobile application.

If, however, sizable segmentations are available on both sides, these segmentations are extended using another segmentation convolutional neural network of similar architecture that was trained to segment all vessels (not just ICA-T and M1 vessels). The combination of the outputs of both networks is refined to generate the MCA vessel tree. Following this step, end points of the MCA vessels are identified. If the total distance between the ICA-T and the end point is below a predefined threshold, an LVO is detected and the system triggers an alert. The threshold was determined on the basis of the receiver operating characteristic curve to yield approximately equal sensitivity and specificity on the suspected-stroke population and corresponds, roughly, to the beginning of the Sylvian fissure. The process is visualized in Fig 4.

If no end point on either side is shorter than the threshold, the algorithm looks for partial occlusions. This is done by computing the centerline of the segmentation and inspecting the average Hounsfield unit value in the vicinity of the centerline. The algorithm is looking for a pattern of a drop in Hounsfield units, followed by an increase (Fig 5). If such a case is identified, an LVO is detected and the system triggers an alert.

Examples of system identification of both partial and complete occlusions and the matching images sent to the end user by the application during an alert are provided in Fig 6.

Statistical Analysis

Statistical analyses were performed using descriptive data analysis, including ranges, means, medians, SDs, and interquartile ranges for continuous variables and frequencies and percentages for categorical variables.

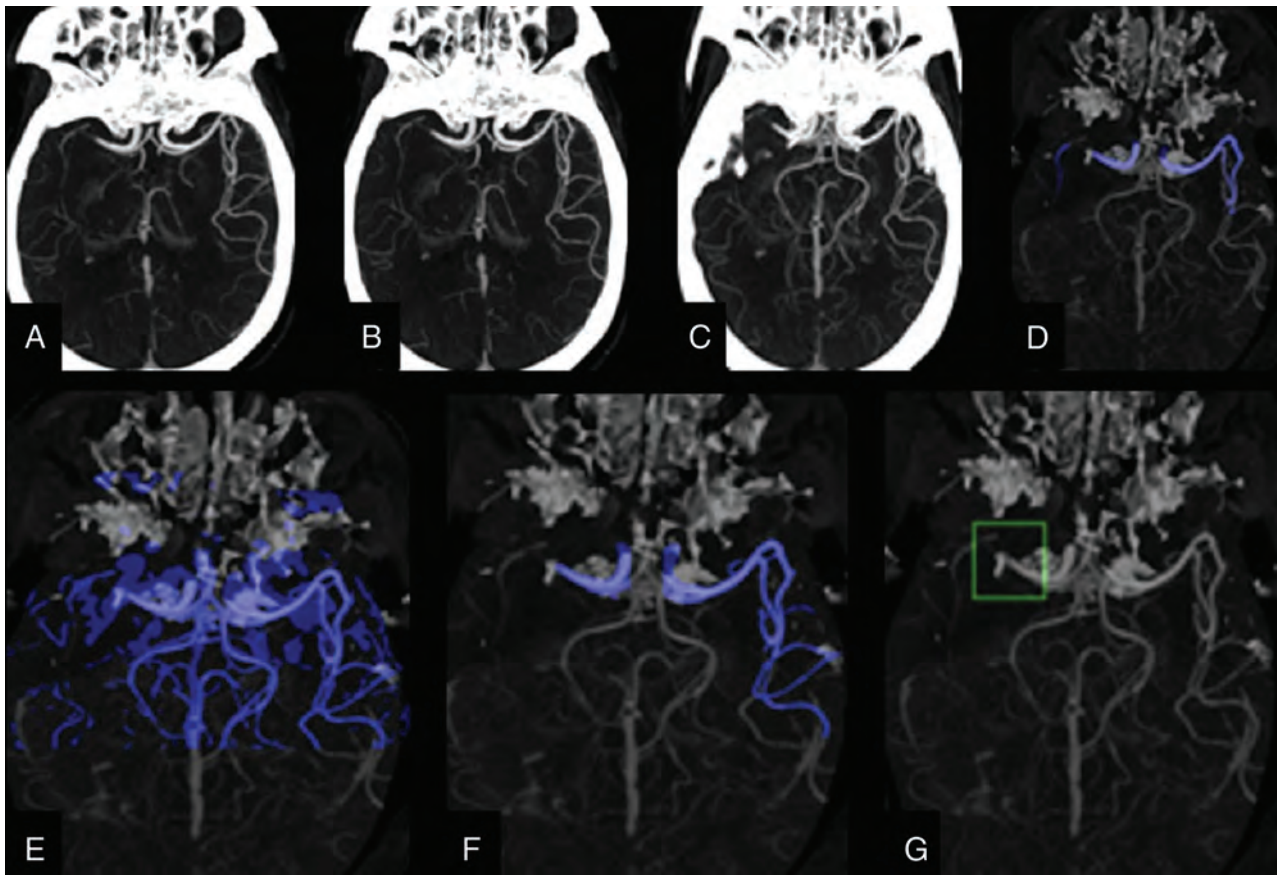


FIG 4. Overview of the algorithm steps. *A*, Identification of an applicable scan based on metadata. *B*, Cropping the head region. Registration (*C*) and segmentation (*D*) of ICA-T/MI regions. *E*, Additional segmentation of all vessels. Refinement of the segmentations to include only the MCA branches (*F*) and detection of suspected LVO based on vessel length (*G*).

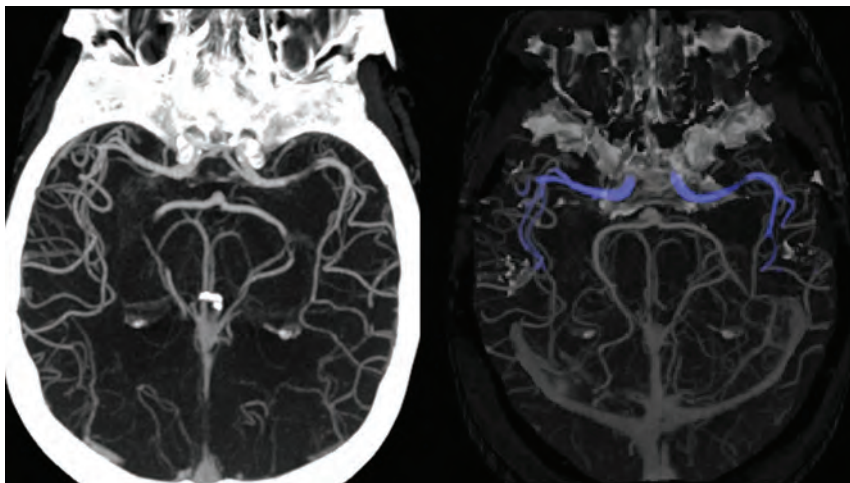


FIG 5. Algorithm processing of a partial occlusion. The cropped scan on the left visualizes a left MI partial occlusion. The segmentation (*on the right*) extends through the partial occlusion. However, the average Hounsfield unit value decreases and then increases and a notification is triggered, even though the length of the segmentation exceeds the threshold.

Interrater reliability between system results and the formal read was quantified using an ICC model, namely 2-way random effects, absolute agreement, and single measurement. This model was selected because all ratings were performed by a different set

of raters,¹⁴ a scenario that would be expected in routine clinical settings. Thus, this model can be considered a realistic estimate of reliability for this scenario. The interrater ICCs were calculated between the model predictions and senior radiologist reports.

Measures of system performance were examined using sensitivity, specificity, positive predictive value (PPV), negative predictive value, and total accuracy.

In addition, logistic regression models were performed to predict the effect of each factor category—age, sex, and identification of LVO by the Viz LVO system—on LVO detection. ORs and 95% CIs were estimated for each predictor.

To test the additive value of each factor, we entered the variables into receiver operating characteristic (area under the curve) curves one at a time: patient characteristics (age, sex) followed by Viz LVO results. When a logistic regression is fit, receiver operating characteristic curves are

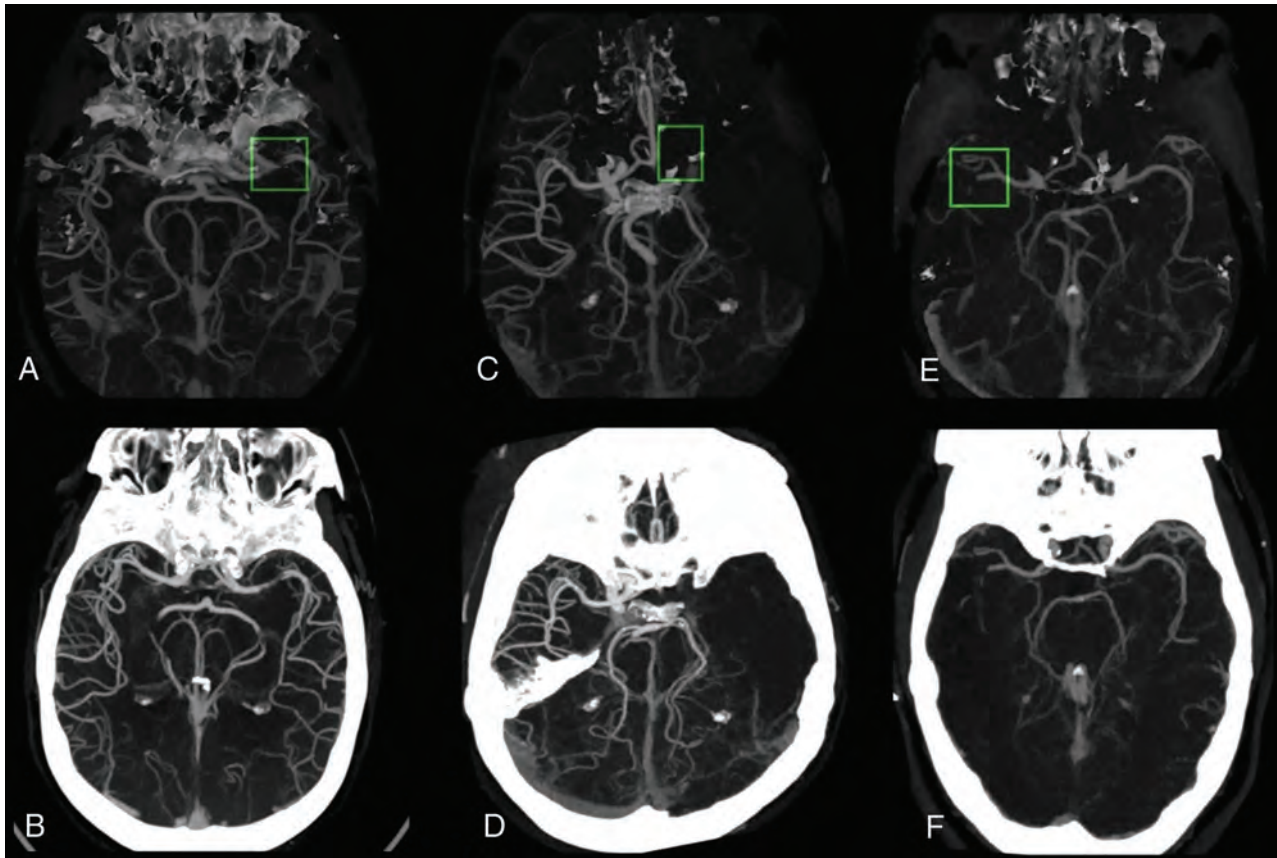


FIG 6. System identification illustration demonstrates stenosis of the M1 segment of the left MCA (A), occlusion of the M1 segment of the left MCA (C), and occlusion of the proximal M2 segment of the right MCA (E), as they appear as preliminary convolutional neural network outcomes (green boxes represent original annotations by the Viz LVO system during identification). The images on the lower row (B, D, and F, respectively) match processed images sent by the system via the application and received by the viewer during an alert.

routinely used to summarize the model fit and to determine the best cutoff value for predicting whether a new observation is a failure (0) or a success (1).

The receiver operating characteristic curve is the sensitivity or recall as a function of fall-out. Overall, if the probability distributions for both detection and false-positives are known, the curve can be generated by plotting the cumulative distribution function (area under the probability distribution from infinity to the discrimination threshold) of the detection probability in the y-axis versus the cumulative distribution function of the false-positive probability on the x-axis. Ideal prediction produces an area under the curve of 1.00; area under the curve values of 0.70 and higher would be considered strong effects.¹⁵

The level of significance for all statistical analyses was 5%. We analyzed the data using the SPSS, Version 25.0 (IBM). This study was approved by the local Helsinki committee at Rambam Health Care Campus (IRB 0417-17).

RESULTS

A total of 1180 CTAs were scanned by the system and sent to the server and the mobile application during the study period. Thirteen cases had been flagged by the system as technically inadequate and were excluded a priori because they were not

Table 1: Descriptive statistics of the study sample^a

Patients (n = 1167)		
Age (mean) [SD]	62.2	19.6
Male	689	59
Stenosis (50%>)	66	5.7
Extracranial ICA	43	3.7
Intracranial	23	2.0
Stroke protocol	404	34.6
Hemorrhage	80	6.8
Tumor	12	1.0
LVO	75	6.4
LVO location (n = 75)		
Carotid terminus	28	37.3
M1	47	62.6
Distal occlusion (non-LVO) (n = 44)		
Proximal M2	21	47.7
Distal M2-3	23	52.3

^aData are number and percentage unless otherwise indicated.

analyzed by the algorithm. Of the 1167 cases included in the study, 404 were stroke protocols, with others performed due to trauma, suspected stenosis, and other miscellaneous reasons (Table 1).

The interrater ICC for all cases was 0.83 (95% CI, 0.725–0.867). For stroke protocol only, the ICC was higher (0.86; 95% CI, 0.837–0.892). Of 1167 patients, 75 had an LVO as per a senior neuroradiologist's formal read, representing 6.4% of the cases.

Sixty-one of these cases were detected by the system, leaving 14 cases of false-negative results.

The system alerted a possible LVO in 117 examinations, 56 of which did not show occlusion of the ICA-T or MCA M1, defined

Table 2: Pathologies detected in false-positive cases

Pathology	No.	%
Stenosis (>50%)	9	16.1
Distal occlusions	12	21.4
Proximal M2	8	14.3
Distal M2/M3	4	7.14
Hemorrhage	12	21.4
Tumor	4	7.14
No revealed pathology	19	33.9
Overall	56	100

Table 3: Prediction of LVO by the Viz LVO system—logistic regression (adjusted for age and sex)

Variable	OR	SE	Sig	95% CI	
				Lower	Upper
Suspected LVO	51.75	0.298	.000	28.84	92.84
Age	1.030	0.009	.001	1.013	1.048
Sex	1.474	0.295	.188	0.828	2.626

Note:—SE indicates standard error; Sig, significance.

in our study as an LVO. Nevertheless, in 12 of these false-positive cases an occlusion of a more distal part of the MCA (M2 or M3) was detected. Additionally, 25 more of the false-positive alerts had different major pathologies, such as hemorrhage, tumors, or intracranial stenosis, defined as a decrease of <50% in the arterial cross-sectional area (Table 2).

Measures of system performance for the entire group were a sensitivity of 0.81 (95% CI, 0.74–0.91), negative predictive value of 0.99 (95% CI, 0.98–0.99), PPV of 0.65 (95% CI, 0.55–0.74), and accuracy of 0.94 (95% CI, 0.92–0.96).

Logistic regression analysis adjusted for age and sex showed that Viz LVO strongly predicts LVO (OR = 51.75; 95% CI, 28.84–92.84) (Table 3). Further receiver operating characteristic analysis demonstrated an area under the curve of 0.91 (Fig 7).

In the stroke protocol subgroup, 72 (17.8%) of 404 patients had an LVO acute ischemic stroke. Of the 72 cases, 59 LVOs were identified by the system. Thirteen false-negative cases were encountered. Sensitivity was 0.82 (95% CI, 0.71–0.89); PPV, 0.64 (95% CI, 0.53–0.73); negative predictive value, 0.96 (95% CI, 0.93–0.98); and accuracy, 0.89 (95% CI, 0.86–0.94). Measures of system performance are summarized in Table 4.

Three non-stroke protocol cases were found to have LVOs and were detected by the system: An elderly lady brought in as

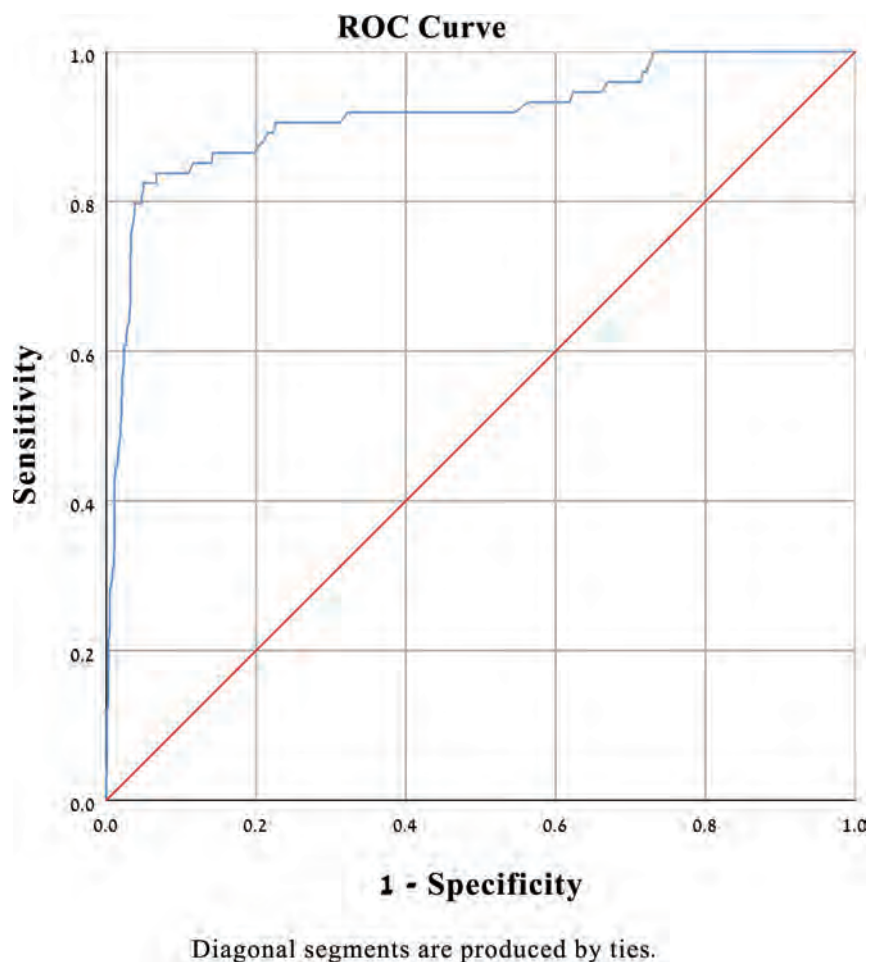


FIG 7. Prediction of LVO logistic regression (adjusted for age and sex). The area under the curve is shown to be 0.91. ROC indicates receiver operating characteristic.

Table 4: Prediction of LVO by the Viz LVO system

System LVO Detection	Sensitivity	95% CI	Specificity	95% CI	NPV	95% CI	PPV	95% CI	Accuracy	95% CI
Entire cohort (n = 1167)	0.81	0.74–0.91	0.96	0.95–0.97	0.99	0.98–0.99	0.65	0.55–0.74	0.94	0.92–0.96
Stroke protocol subgroup (n = 404)	0.82	0.71–0.89	0.90	0.86–0.93	0.96	0.93–0.98	0.64	0.53–0.73	0.89	0.86–0.94

Note:—NPV indicates negative predictive value.

a trauma patient due to an automobile collision, a 41-year-old patient referred from another hospital with a suspect mass found to be an infarct, and a man suspected of having carotid artery stenosis, who was found to have complete occlusion of the ICA-T. In all cases, the system alerted the team by identifying an LVO.

DISCUSSION

Computer-aided detection and diagnosis performed using machine learning algorithms can be an important tool in helping physicians interpret medical imaging findings and reducing interpretation times.¹⁶ Imaging analysis has been shown to be the main artificial intelligence medical flagship, with especially promising results in the field of neuroradiology.¹¹ This pairs well with stroke care, in which both timeliness and precision are needed.^{17,18} Various artificial intelligence-based systems have been developed for emergent detection of acute ischemic stroke, with Viz LVO being the first to include automatic direct LVO detection from CTA data.¹⁹ Evaluation of the accuracy and sensitivity of the system on a large patient population is imperative for future implementation into common clinical practice. In Rambam Health Care Center, about 150 cases of endovascular treatment for acute ischemic stroke are performed annually, allowing rapid evaluation of the system on a sizeable cohort.

In this retrospective single-center study, we found the Viz LVO detection system to be highly accurate. Similar results were previously reported by Chatterjee et al²⁰ in a study performed using an older version of the software (Viz.ai-Algorithm, Version 4.1.2) exclusively on patients with stroke. A recent study by Barreira et al²¹ showed a sensitivity of 0.90 and accuracy of 0.86 using the Viz.ai Algorithm, Version 4.1.3. Both studies focused on stroke-activation protocols and, therefore, showed high rates of LVOs, 30% of the cohort in the former and 49% in the latter, in contrast to our results of 18% for the stroke protocols and 7% for the entire cohort, regardless of the scan indication.

The system encountered 56 false-positive results, 37 (66%) of which had major pathologies and 19 that had no identified pathology. The high prevalence of pathologic examinations being accidentally flagged as LVOs is related to tissue distortion, resulting in vessels being pushed and changing their course. These results, including identification of 12 M2/3 occlusion cases and 9 cases of stenosis, are difficult to interpret because the inner working of deep learning systems is not completely understood. Future improvements to the algorithms are needed to enable higher accuracy of subtler pathologies on the one hand and exclusion of nonrelevant ones on the other.

The main advantage of using artificial intelligence software in medical analysis is that it can accelerate decision-making, a feature that is especially valuable in situations that demand quick action as in LVO stroke. The system showed suboptimal sensitivity, which prevents it from being used as a diagnostic tool to date. The PPV in our cohort was 0.65. A high PPV is essential to avoid an unacceptable burden on the application end-users due to multiple false-positive alerts.

The main advantage of the system in the clinical setting of acute stroke at this point relies on its ability to accelerate decision-making in cases positive for LVO stroke. This may show great significance in environments in which interventional neuroradiology consultants are less accessible, such as in prehospital advanced imaging used in mobile stroke units, which is a fast-evolving field,²² and in primary care centers.

The study was conducted in the setting of routine clinical practice, unlike previous studies. The patients were not preselected, and the neuroradiologists involved were not notified of the evaluation performed. This feature allowed analysis and assessment of the performance of the system for everyday patients in the emergency department. It accounts for the low rate of LVO acute ischemic stroke in our patient population and the lower PPV found compared with previous publications in stroke-only series. Because the system is being installed currently in multiple medical centers, some without dedicated stroke protocols, it could provide a better reflection of the real impact of the system on the diagnostic and therapeutic flow of patients.

The system uncovered 3 LVOs in patients with a non-stroke protocol that could have been easily missed due to low clinical suspicion. Such alerts could accelerate proper care in this scenario.

This study has several limitations. First, it is not an interventional study. The system was assessed without changing the treatment provided to patients in real-time, due to ethical limitations, thus preventing concrete discussion of improved time and cost with use of the system. Further research is already planned.

Furthermore, the criterion standard for LVO detection relied on a single neuroradiologist read per examination. Although the ICC showed no variation among readers, such evaluation is still subject to mistakes. Data were collected by radiology residents and assessed for possible discrepancies in follow-up examinations and the general clinical course of the patient to minimize such errors. In any case of inconsistency, examinations were marked and reread by a second senior neuroradiologist.

Another point is the exclusion of 13 examinations rejected by the system as technically inadequate, as described above. These examinations were not included in the study

because they were not processed by the algorithm for LVO detection.

This study was conducted in a single comprehensive stroke center. One of the most fundamental future applications of the system is in improving notification, assessment, and treatment times for patients arriving at primary stroke centers. Thus, the next step in the evaluation of the system will need to be a multicenter study, comparing treatment timelines.

CONCLUSIONS

Our experience evaluating Viz LVO shows that the system has real potential for early, accurate identification of patients with stroke, hopefully improving workflow and patient care.

Disclosures: Raul G. Nogueira—RELATED: Consulting Fee or Honorarium: Viz.ai Physician Advisory Board consulting fees; UNRELATED: Stock/Stock Options: Viz.ai; OTHER RELATIONSHIPS: Stryker Neurovascular (DAWN Trial Principal Investigator, no compensation; TREVO Registry Steering Committee, no compensation; consultant, significant); Cerenovus/Neuravi (ENDOLOW Trial Principal Investigator, no compensation; EXCELLENT Registry Principal Investigator, no compensation; ARISE-2 trial Steering Committee, no compensation; Physician Advisory Board, modest); phenox (PROST Trial Principal Investigator, Physician Advisory Board, modest); Anaconda (Physician Advisory Board, modest); Genentech (Physician Advisory Board, modest); Biogen (CHARM Trial Steering Committee; Physician Advisory Board, modest); Prolong Pharmaceuticals (Physician Advisory Board, modest); Stock/Stock Options: Brainomix (Physician Advisory Board); Viz.ai (Physician Advisory Board); Corindus Vascular Robotics (Physician Advisory Board); Vesalio (Physician Advisory Board); Ceretrieve (Physician Advisory Board); Astrocyte (Physician Advisory Board); Cerebrotech (Physician Advisory Board); Imperative Care (Imperative Trial Principal Investigator, modest). Rotem Sivan-Hoffmann—RELATED: Support for Travel to Meetings for the Study or Other Purposes: VIZ.ai, Comments: supported my participation in ASNR meeting in Boston, May 2019; UNRELATED: Board Membership: CVAid Medical, Comments: Founder and Chief Medical Officer, member of the board; Patents (Planned, Pending or Issued): CVAid Medical. Eitan Abergel—UNRELATED: Grants/Grants Pending: Viz.ai, Comments: grant for multicenter study.* *Money paid to the institution.

REFERENCES

1. Malhotra K, Gornbein J, Saver JL. **Ischemic strokes due to large-vessel occlusions contribute disproportionately to stroke-related dependence and death: a review.** *Front Neurol* 2017;8:1–5 CrossRef Medline
2. Smith WS, Lev MH, English JD, et al. **Significance of large vessel intracranial occlusion causing acute ischemic stroke and TIA.** *Stroke* 2009;40:3834–40 CrossRef Medline
3. Berkhemer OA, Fransen PSS, Beumer D, et al; MR CLEAN Investigators. **A randomized trial of intraarterial treatment for acute ischemic stroke.** *N Engl J Med* 2015;372:11–20 CrossRef Medline
4. Jovin TG, Chamorro A, Cobo E, et al; REVASCAT Trial Investigators. **Thrombectomy within 8 hours after symptom onset in ischemic stroke.** *N Engl J Med* 2015;372:2296–306 CrossRef Medline
5. Malhotra K, Liebeskind D. **Imaging in endovascular stroke trials.** *J Neuroimaging* 2015;25:517–27 CrossRef Medline
6. Broderick JP, Palesch Y, Demaerschalk B, et al; Interventional Management of Stroke (IMS) III Investigators. **Endovascular therapy after intravenous t-PA versus t-PA alone for stroke.** *N Engl J Med* 2013;368:893–903 CrossRef Medline
7. Saver JL, Jahan R, Levy EI, et al. **Solitaire Flow Restoration Device versus the Merci Retriever in Patients with Acute Ischaemic Stroke (SWIFT): a randomised, parallel-group, non-inferiority trial.** *Lancet* 2012;380:1241–49 CrossRef Medline
8. Powers WJ, Rabinstein AA, Ackerson T, et al; American Heart Association Stroke Council. **Guidelines for the Early Management of Patients with Acute Ischemic Stroke: A Guideline for Healthcare Professionals From the American Heart Association/American Stroke Association.** *Stroke* 2018;49:e46–e110 CrossRef Medline
9. Albers GW, Marks MP, Kemp S, et al. **Thrombectomy for stroke at 6 to 16 hours with selection by perfusion imaging.** *N Engl J Med* 2018;378:708–18 CrossRef Medline
10. Nogueira RG, Jadhav AP, Haussen DC, et al. **Thrombectomy 6 to 24 hours after stroke with a mismatch between deficit and infarct.** *N Engl J Med* 2018;378:11–21 CrossRef Medline
11. Zaharchuk G, Gong E, Wintermark M, et al. **Deep learning in neuroradiology.** *AJNR Am J Neuroradiol* 2018;39:1776–84 CrossRef Medline
12. Hosny A, Parmar C, Quackenbush J, et al. **Artificial intelligence in radiology.** *Nat Rev Cancer* 2018;18:500–10 CrossRef Medline
13. Ronneberger O, Fischer P, Brox T. **U-net: convolutional networks for biomedical image segmentation.** 2015. <https://arxiv.org/pdf/1505.04597.pdf>. Accessed November 19, 2019
14. Shrout PE, Fleiss JL. **Intraclass correlations: uses in assessing rater reliability.** *Psychol Bull* 1979;86:420–28 CrossRef Medline
15. Rice ME, Harris GT. **Comparing effect sizes in follow-up studies: ROC area, Cohen's d, and r.** *Law Hum Behav* 2005;29:615–20 CrossRef Medline
16. Erickson BJ, Korfiatis P, Akkus Z, et al. **Machine learning for medical imaging.** *Radiographics* 2017;37:505–15 CrossRef Medline
17. Lee EJ, Kim YH, Kim N, et al. **Deep into the brain: artificial intelligence in stroke imaging.** *J Stroke* 2017;19:277–85 CrossRef Medline
18. Hinman JD, Rost NS, Leung TW, et al. **Principles of precision medicine in stroke.** *J Neurol Neurosurg Psychiatry* 2017;88:54–61 CrossRef Medline
19. Murray NM, Unberath M, Hager GD, et al. **Artificial intelligence to diagnose ischemic stroke and identify large vessel occlusions: a systematic review.** *J Neurointerv Surg* 2020;12:156v64 CrossRef Medline
20. Chatterjee A, Somayaji N, Kabakis IM. **Abstract WMP16: artificial intelligence detection of cerebrovascular large vessel occlusion: nine month, 650 patient evaluation of the diagnostic accuracy and performance of the Viz.ai LVO algorithm.** *Stroke* 2019;50 (Suppl 1) CrossRef
21. Barreira CM, Bouslama M, Al-Bayati AR, et al. **E-108 Aladin study: automated large artery occlusion detection in stroke imaging: a multicenter analysis.** *J Neurointerv Surg* 2018(Suppl 2):101–02 CrossRef
22. Lima FO, José F, Mont A, et al. **Pre-hospital assessment of large vessel occlusion strokes: implications for modeling and planning stroke systems of care.** *Front Neurol* 2019;10:955 CrossRef Medline

Emerging Artificial Intelligence Imaging Applications for Stroke Interventions

Stroke is the most frequent cause of acquired disability and the fifth most frequent cause of death in the United States. Treatment options for acute ischemic stroke (AIS) caused by large-vessel occlusion (LVO) are rapid recanalization of the occluded large vessels using IV thrombolysis with alteplase (recombinant tissue plasminogen activator) within 4.5 hours and mechanical thrombectomy (MT) within 6 hours.¹ In either treatment, identifying a substantial and salvageable ischemic penumbra is essential for a patient to be eligible for therapy. Recent randomized controlled trials—Clinical Mismatch in the Triage of Wake Up and Late Presenting Strokes Undergoing Neurointervention with Trevo (DAWN),² Endovascular Therapy Following Imaging Evaluation for Ischemic Stroke 3 (DEFUSE-3),³ and Efficacy and Safety of MRI-based Thrombolysis in Wake-up Stroke (WAKE-UP)⁴—that revolutionized the management of patients with LVO stroke laid the foundation for a further revolution in the selection of patients eligible for late MT, up to 24 hours, regardless of whether they receive IV alteplase for the same ischemic stroke event. An ongoing phase III trial (Tenecteplase in Stroke Patients Between 4.5 and 24 Hours; TIMELESS) is investigating the efficacy of tenecteplase in an extended time window from 4.5 to 24 hours.⁵ Because of rapid changes in the evidence, the American Heart Association/American Stroke Association updated their acute stroke guidelines from 2018, which replaced the 2013 guidelines.^{6,7} In this context, a transition takes place from the concept of a “temporal therapeutic window” to that of a “cerebral tissue window” accounting for the degree of collateral perfusion, incorporating advanced neuroimaging methods, such as CT perfusion and MR imaging with FLAIR, diffusion, and perfusion-weighted imaging, for the assessment ischemic core (irreversibly damaged tissue) and of ischemic penumbra (potentially reversible ischemic tissue).⁸ The best method for the correct selection of such patients is still a matter of debate. Nevertheless, because the benefit of reperfusion therapy decreases over time, it is critical to treat patients as quickly as possible before cell death ensues.

However, several challenges may limit the widespread clinical use of LVO stroke interventions, specifically MT. Indeed, only 13,000 MTs were performed in the United States as of 2016 (<2% of total AIS cases).⁹ First, only an estimated 10% of patients with AIS have a proximal LVO in the anterior circulation and present

early enough to qualify for MT within 6 hours,^{10,11} but approximately 9% of patients presenting in the 6- to 24-hour time window may qualify for MT.¹² Second, after the patient arrives at a medical center, urgent imaging, either CT or MR imaging, is performed and must be promptly analyzed by qualified radiologists to determine if MT is required. However, image interpretation is subject to inconsistent local expertise and time delays and varies between institutions. Third, because of increasing centralization of acute stroke care at specialist facilities, only a few stroke centers have sufficient advanced neuroimaging and neurointerventional resources and expertise to deliver this therapy,¹³ which make it necessary to transfer eligible patients from a primary stroke center to a comprehensive stroke center, many times after initiation of thrombolysis, a strategy called “drip and ship.”¹⁴ Even at experienced facilities, activation of interhospital communication for LVO triage and transport to a thrombectomy center can be operationally challenging.

To address this need, artificial intelligence (AI) tools using machine learning algorithms are being developed as a rapid clinical decision support system for complete assessment and identification of LVO. These tools can automatically generate quantitative measures, such as a patient’s Alberta Stroke Program Early CT Score calculated on noncontrast CT, process perfusion maps and determine salvageable brain tissue on CT or MR perfusion imaging, and detect LVO on CT angiography. Thereafter, the resultant data are automatically delivered with email or text notifications on a cell-phone application to the relevant emergency department and stroke team members, aiming to achieve faster onset-to-treatment time in fibrinolytic-eligible patients and MT-eligible patients. Additional outputs can be sent as DICOM images or to a web browser user interface.

Over the past several years, a few software platforms have been commercialized, of which some of the most popular are RapidAI (iSchemaView), e-Stroke-Suite (Brainomix Ltd) in collaboration with Olea Sphere (Olea Medical Solutions), and VIZ.ai (Viz.ai). Other similar solutions from different companies are being developed with different stages of pending European CE mark or FDA approval. The applications share the same concept but have variations regarding the algorithm and available features.

Initial clinical data focus mainly on accuracy and compare AI performance and precision with the interpretation of experienced radiologists. Albers et al¹⁵ evaluated the performance of automatically generated RapidAI ASPECTS relative to scores determined by experienced radiologists and showed similar or even better relative accuracy of the automatic ASPECTS after comparison with matched DWI. Similar results were achieved using the e-ASPECTS software (Brainomix).^{16,17} With regard to LVO detection in CTA, a recent study found sensitivity, specificity, and negative predictive value of 0.94, 0.76, and 0.98, respectively, using RapidAI software.¹⁸ Recently, e-CTA software (Brainomix) was assessed for automated measurement of collateral score in 98 patients with LVO eligible for MT with sensitivity and specificity for identifying favorable collateral flow of 0.99 and 0.94, respectively.¹⁹

In the current *AJNR* issue, automatic AI-driven detection of LVO with Viz.LVO software was assessed on all head CTAs in a single comprehensive stroke center for 14 months. Sixty-one of 75 LVO cases were identified by the software (sensitivity = 0.81), with additional positive predictive value, negative predictive value, and accuracy of 0.65, 0.99, and 0.94, respectively. In stroke CTAs, subgroup results for sensitivity, positive predictive value, negative predictive value, and accuracy were 0.82, 0.64, 0.96, and 0.89, respectively.²⁰ As a screening tool, future versions of the software's algorithm should be oriented for higher sensitivity with an acceptable price of lower specificity and higher false-positive rates. The suboptimal sensitivity of Viz.LVO currently prevents it from being used as a diagnostic tool; however, early evidence supports its utility in reduction in time to treatment and improved clinical outcomes. Recently, the Centers for Medicare & Medicaid Services has granted Viz.ai the first New Technology Add-on Payment for AI software, up to \$1040 per use in Medicare patients with suspected strokes.

To conclude, recent years have seen a substantial increase in the fraction of patients whose AIS can be treated with reperfusion therapy. Future development of AI applications that integrate software platforms intended for automatic rapid imaging review and provide a communication platform and optimized workflow to multidisciplinary teams will undoubtedly play a key role in more rapid and efficient identification of eligible candidates for reperfusion therapy, resulting in better neurologic outcomes.

REFERENCES

- Goyal M, Menon BK, van Zwam WH, et al. **Endovascular thrombectomy after large-vessel ischaemic stroke: a meta-analysis of individual patient data from five randomised trials.** *Lancet* 2016;387:1723–31 CrossRef Medline
- Nogueira RG, Jadhav AP, Haussen DC, et al. **Thrombectomy 6 to 24 hours after stroke with a mismatch between deficit and infarct.** *N Engl J Med* 2018;378:11–21 CrossRef Medline
- Albers GW, Marks MP, Kemp S, et al. **Thrombectomy for stroke at 6 to 16 hours with selection by perfusion imaging.** *N Engl J Med* 2018;378:708–18 CrossRef Medline
- Thomalla G, Simonsen CZ, Boutitie F, et al. **MRI-guided thrombolysis for stroke with unknown time of onset.** *N Engl J Med* 2018;379:611–22 CrossRef Medline
- ClinicalTrials.gov. Tenecteplase in Stroke Patients Between 4.5 and 24 Hours (TIMELESS). <https://clinicaltrials.gov/ct2/show/nct03785678>. Accessed September 14, 2020
- Powers WJ, Rabinstein AA, Ackerson T, et al. **Guidelines for the early management of patients with acute ischemic stroke: a guideline for healthcare professionals from the American Heart Association/American Stroke Association. [published corrections appear in *Stroke* 2018;49:e138 and *Stroke* 2018;49:e233–234].** *Stroke* 2018;49:e46–e99 CrossRef Medline
- Powers WJ, Rabinstein AA, Ackerson T, et al. **Guidelines for the early management of patients with acute ischemic stroke: 2019 update to the 2018 guidelines for the early management of acute ischemic stroke: a guideline for healthcare professionals from the American Heart Association/American Stroke Association [published correction appears in *Stroke* 2019;50:e440–e441].** *Stroke* 2019;50:e344–e418 CrossRef Medline
- Rocha M, Jovin TG. **Fast versus slow progressors of infarct growth in large vessel occlusion stroke: clinical and research implications.** *Stroke* 2017;48:2621–27 CrossRef Medline
- Saber H, Navi BB, Grotta JC, et al. **Real-world treatment trends in endovascular stroke therapy.** *Stroke* 2019;50:683–89 CrossRef Medline
- Chia NH, Leyden JM, Newbury J, et al. **Determining the number of ischemic strokes potentially eligible for endovascular thrombectomy: a population-based study.** *Stroke* 2016;47:1377–80 CrossRef Medline
- Vanacker P, Lambrou D, Eskandari A, et al. **Eligibility and predictors for acute revascularization procedures in a stroke center.** *Stroke* 2016;47:1844–49 CrossRef Medline
- Jadhav AP, Desai SM, Kenmuir CL, et al. **Eligibility for endovascular trial enrollment in the 6- to 24-hour time window: analysis of a single comprehensive stroke center.** *Stroke* 2018;49:1015–17 CrossRef Medline
- Josephson SA, Kamel H. **The acute stroke care revolution: enhancing access to therapeutic advances.** *JAMA* 2018;320:1239–40 CrossRef Medline
- Sheth KN, Smith EE, Grau-Sepulveda MV, et al. **Drip and ship thrombolytic therapy for acute ischemic stroke: use, temporal trends, and outcomes.** *Stroke* 2015;46:732–39 CrossRef Medline
- Albers GW, Wald MJ, Mlynash M, et al. **Automated calculation of Alberta Stroke Program Early CT Score: validation in patients with large hemispheric infarct.** *Stroke* 2019;50:3277–79 CrossRef Medline
- Seker F, Pfaff J, Nagel S, et al. **CT reconstruction levels affect automated and reader-based ASPECTS ratings in acute ischemic stroke.** *J Neuroimaging* 2019;29:62–64 CrossRef Medline
- Sundaram VK, Goldstein J, Wheelwright D, et al. **Automated ASPECTS in acute ischemic stroke: a comparative analysis with CT perfusion.** *AJNR Am J Neuroradiol* 2019;40:2033–38 Medline
- Amukotuwa SA, Straka M, Smith H, et al. **Automated detection of intracranial large vessel occlusions on computed tomography angiography: a single center experience.** *Stroke* 2019;50:2790–98 CrossRef Medline
- Grunwald IQ, Kulikovski J, Reith W, et al. **Collateral automation for triage in stroke: evaluating automated scoring of collaterals in acute stroke on computed tomography scans.** *Cerebrovasc Dis* 2019;47:217–22 CrossRef Medline
- Anat Y-D, Mor S, Goni M, et al. **Evaluation of artificial intelligence-powered identification of large vessel occlusions in a comprehensive stroke center.** *AJNR Am J Neuroradiol* 2021 in press

© E. Lotan

Department of Radiology
NYU Grossman School of Medicine
New York, New York

<http://dx.doi.org/10.3174/ajnr.A6902>

COVID-19 Severity and Stroke: Correlation of Imaging and Laboratory Markers

J.M. Katz, R.B. Libman, J.J. Wang, C.G. Filippi, P. Sanelli, A. Zlochower, M. Gribko, S.V. Pacia, R.I. Kuzniecky, S. Najjar, and S. Azhar



ABSTRACT

BACKGROUND AND PURPOSE: Coronavirus disease 2019 (COVID-19) appears to be an independent risk factor for stroke. We hypothesize that patients who develop stroke while hospitalized for severe COVID-19 will have higher inflammatory markers and distinct stroke imaging patterns compared with patients positive for COVID-19 with out-of-hospital stroke onset and milder or no COVID-19 symptoms.

MATERIALS AND METHODS: This is a retrospective case series of patients positive for COVID-19 on polymerase chain reaction testing with imaging-confirmed stroke treated within a large health care network in New York City and Long Island between March 14 and April 26, 2020. Clinical and laboratory data collected retrospectively included complete blood counts and creatinine, alanine aminotransferase, lactate dehydrogenase, C-reactive protein, ferritin, and D-dimer levels. All CT and MR imaging studies were independently reviewed by 2 neuroradiologists who recorded stroke subtype and patterns of infarction and intracranial hemorrhage.

RESULTS: Compared with patients with COVID-19 with outside-of-hospital stroke onset and milder or no COVID-19 symptoms ($n = 45$, 52.3%), patients with stroke already hospitalized for severe COVID-19 ($n = 41$, 47.7%) had significantly more frequent infarctions (95.1% versus 73.3%, $P = .006$), with multivascular distributions (56.4% versus 33.3%, $P = .022$) and associated hemorrhage (31.7% versus 4.4%, $P = .001$). Patients with stroke admitted with more severe COVID-19 had significantly higher C-reactive protein and ferritin levels, elevated D-dimer levels, and more frequent lymphopenia and renal and hepatic injury (all, $P < .003$).

CONCLUSIONS: Patients with stroke hospitalized with severe COVID-19 are characterized by higher inflammatory, coagulopathy, and tissue-damage biomarkers, supporting proposed pathogenic mechanisms of hyperinflammation activating a prothrombotic state. Cautious balancing of thrombosis and the risk of hemorrhagic transformation is warranted when considering anticoagulation.

ABBREVIATIONS: COVID-19 = coronavirus disease 2019; SARS-CoV-2 = Severe Acute Respiratory Syndrome coronavirus 2

First reported as a respiratory illness in Wuhan, China, in December 2019,¹ coronavirus disease 2019 (COVID-19), caused by the novel coronavirus Severe Acute Respiratory Syndrome coronavirus 2 (SARS-CoV-2), has become a global pandemic. As of the end of August 2020, there were >33 million infections and >1 million deaths globally, including >7 million infections and >206,000 deaths in the United States alone.² While many patients infected

with the SARS-CoV-2 virus have mild or asymptomatic disease,³ a sizeable number of patients require hospitalization and frequently develop multiorgan dysfunction secondary to a heightened immune response.^{4,5} Either due to this cytokine storm or direct viral or immune-mediated endothelial injury, some patients with COVID-19 develop prothrombotic and coagulopathic states, often simultaneously, and these phenomena may underlie the observed association between COVID-19 and stroke.⁵⁻¹¹

In a previous study, we showed that COVID-19 is a strong independent risk factor for stroke in hospitalized patients.¹² In this study, we compare patients positive for COVID-19 with out-of-hospital stroke onset who had mild or no COVID-19 symptoms with patients diagnosed with stroke while already hospitalized for severe COVID-19. We hypothesize that patients with stroke with severe COVID-19 will have significantly higher levels of inflammatory (C-reactive protein and ferritin) and coagulopathic markers (D-dimers) and distinctive stroke imaging patterns. Our aim is to

Received July 29, 2020; accepted after revision October 2.

From the Departments of Neurology (J.M.K., R.B.L., M.G., S.V.P., R.I.K., S.N., S.A.), and Radiology (C.G.F., P.S., A.Z.), Donald and Barbara Zucker School of Medicine at Hofstra/Northwell, Hempstead, New York; and Feinstein Institute for Medical Research at Northwell Health (J.J.W.), Manhasset, New York.

Please address correspondence to Christopher G. Filippi, MD, Donald and Barbara Zucker School of Medicine at Hofstra/Northwell, 500 Hofstra Blvd, Hempstead, NY 11549; e-mail: cfilippi@northwell.edu; @sairaallapeikko

 Indicates open access to non-subscribers at www.ajnr.org

 Indicates article with online supplemental data.

<http://dx.doi.org/10.3174/ajnr.A6920>

provide evidence that a hyperinflammatory and prothrombotic state, such as seen in patients with severe SARS-CoV-2 infection, underlies the mechanism linking COVID-19 and stroke.

MATERIALS AND METHODS

This is a retrospective study of patients with COVID-19 concurrently diagnosed with stroke, admitted between March 14 and April 26, 2020, to 11 different Northwell Health hospitals in New York City and Long Island. Northwell Health is the largest health care network in New York, with multiple tertiary teaching hospitals and community hospitals. The institutional review board approved this Health Insurance Portability and Accountability Act-compliant study as minimal risk and waived the requirement for informed consent. Additional methods, as well as demographic, clinical, and outcome details of this cohort, have been reported elsewhere.¹² Study inclusion required the following: 1) polymerase chain reaction-proved SARS-CoV-2 infection, 2) imaging-confirmed stroke, 3) documented stroke-symptom onset during a COVID-19 illness, or 4) the onset of COVID-19 symptoms or SARS-CoV-2 polymerase chain reaction positivity, within 14 days of stroke-symptom onset. The last criterion was meant to capture patients who tested positive for SARS-CoV-2 infection post-stroke hospitalization, applying the standard definition used in clinical care in terms of the potential latency between infection and symptom onset. Using this criterion, we captured 6 likely patients with initially false-negative results on polymerase chain reaction testing with a delay from COVID-19 ($n = 4$) or stroke ($n = 2$; 2- and 3-day delay) symptom onset to polymerase chain reaction positivity. Three additional patients who met this criterion possibly acquired COVID-19 while in the hospital, but this cannot be established with any certainty; therefore, these patients are included in our analysis. Clinical and laboratory data were collected by retrospective chart review. Only laboratory variables with at least 75% complete data were included in our analysis. Two neuroradiologists with Certificates of Added Qualification characterized the neuroimaging findings, blinded to clinical and laboratory data; in cases of disagreement, consensus was reached.

In-hospital stroke onset was defined as a new-onset focal neurologic deficit or altered mental status after hospital admission for COVID-19 and imaging confirmation of cerebral infarction or intracranial hemorrhage. During the pandemic peak, only patients with severe COVID-19 complications were hospitalized, and patients with less severe symptoms related to COVID-19 were treated at home. Although hospitals in our system did not mandate the use of specific hard criteria, in general, oxygen saturation $<90\%$ or 92% or other signs of severe respiratory distress or severe systemic illness such as sepsis were used as guiding criteria for COVID-19 admission during the crisis. Laboratory data included complete blood count and coagulation profile at hospital admission or in-hospital stroke onset, lowest lymphocyte count, signs of noncerebral end-organ damage (elevated creatinine level >1.3 mg/dL), twice the normal alanine aminotransferase level >90 U/L and lactate dehydrogenase level >484 U/L), and the highest hospitalization inflammatory (C-reactive protein and ferritin) and coagulopathy markers (D-dimer). Diagnosis of coexistent deep vein thrombosis was recorded. Neuroimaging findings were based on brain CT or MR imaging findings, including stroke

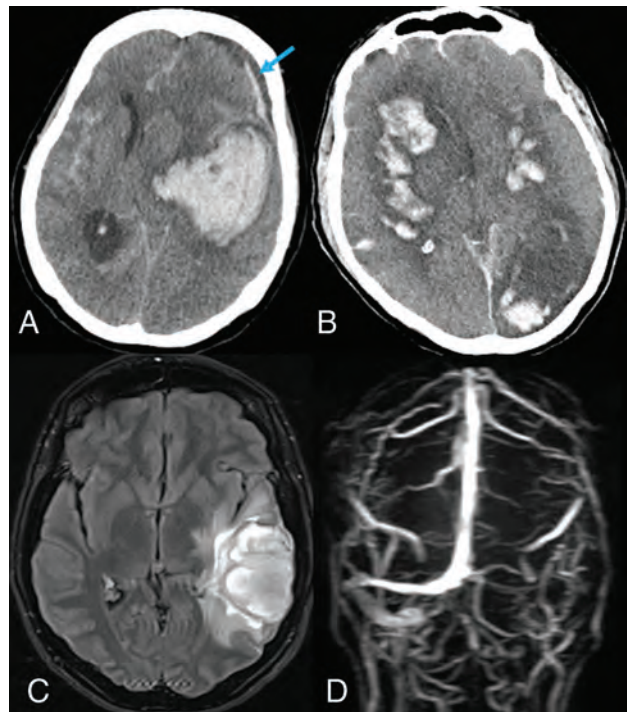


FIG 1. Cerebral hemorrhage in patients with COVID-19. *A*, Noncontrast CT of the head shows a large left basal ganglia intraparenchymal hemorrhage, with diffuse subarachnoid and left frontal subdural (blue arrow) hemorrhages in a woman with asymptomatic COVID-19. *B*, Noncontrast CT of the head showing extensive bilateral multifocal cerebral infarctions with hemorrhagic conversion in a comatose man with multiorgan failure. *C*, Brain MR imaging FLAIR and *D*, MR venogram show hemorrhagic venous infarction in the left temporal lobe (*C*) secondary to thrombosis of left transverse and sigmoid sinuses and internal jugular vein (*D*) in a young woman presenting with seizures.

subtype, infarction pattern, and the presence of hemorrhagic transformation and simultaneous infarction and hemorrhage.

Statistical Analysis

A bivariate analysis of imaging and laboratory findings dichotomized by inpatient or outpatient stroke-onset location as a surrogate for COVID-19 severity was performed. Only laboratory variables with at least 75% complete data were included in our study. Statistical analyses were performed using the Wilcoxon rank sum test for continuous variables and the χ^2 test for most categorical variables. The Fisher exact test was used when the cell number was <5 . Statistical significance was considered for P values $< .05$. All statistical analyses were performed in SAS Version, 9.4 (SAS Institute).

RESULTS

Between March 14 and April 26, 2020, eighty-six patients (48 men, 38 women) with mean age of 67.4 years (range, 25–94 years) met the inclusion criteria with imaging-confirmed infarction (83.7%) or pure intracranial hemorrhage (16.3%) (Fig 1A). Associated intracranial hemorrhage (Fig 1B) was found in 20.8% of 72 patients with infarction, including 9 with simultaneous hemorrhage and infarction and 6 with hemorrhagic transformation, including 1 hemorrhagic venous infarction secondary to

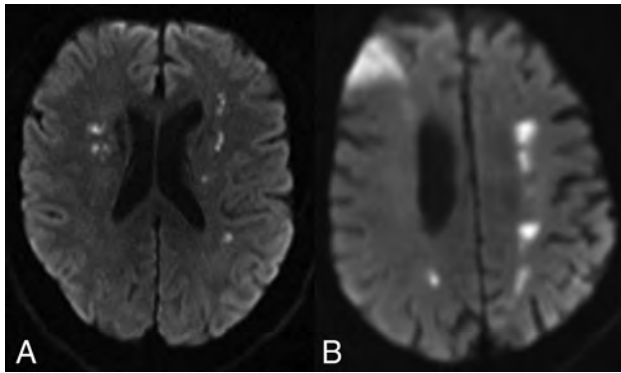


FIG 2. Multivascular territory infarctions in COVID-19. MR imaging of the brain diffusion-weighted imaging demonstrates watershed-pattern infarctions in a 52-year-old man with mild COVID-19 symptoms, who awoke at home with left hemiparesis (A) and an 86-year-old woman admitted for hypoglycemia, dehydration, and COVID-19 pneumonia (B) and found to have new-onset atrial fibrillation; 8 days into her hospitalization, she developed lethargy, left hemiparesis, expressive aphasia, and dysphagia.

dural venous sinus thrombosis (Fig 1C, -D). Multivascular territory infarction (33/72 patients; 45.8%) predominated, including 12 with a watershed pattern (Fig 2), followed by single vascular territory infarction (29/72 patients, 40.3%) and solitary small-vessel occlusion (10/72 patients, 13.9%).

Forty-one patients (47.7%) were already hospitalized at stroke onset, whereas 45 patients (52.3%) developed out-of-hospital neurologic deficits, with ongoing mild or asymptomatic COVID-19 infection. In-hospital stroke onset was associated with more frequent mechanical ventilation (56.1% versus 33.3%, $P = .034$), admission tachypnea (respiratory rate, >20 breaths per minute; 61.0% versus 33.3%, $P = .016$), and discharge to a rehabilitation facility (51.2% versus 22.2%, $P = .011$), supporting our hypothesis that these patients had more severe COVID-19 infection.

Supplemental Table 1 summarizes the bivariate analysis of imaging and laboratory findings dichotomized by patient location at stroke onset (see Supplemental Table 2 for analysis of laboratory values as continuous variables). In-hospital stroke onset was significantly associated with ischemic stroke (95.1% versus 73.3%, $P = .006$), particularly multivascular distribution (56.4% versus 33.3%, $P = .022$) and associated hemorrhagic transformation or simultaneous intracranial hemorrhage (31.7% versus 4.4%, $P = .001$). These patients also had more frequent deep vein thrombosis (29.3% versus 2.2%, $P = .001$). For those with laboratory values available, patients with in-hospital stroke onset had more frequent leukocytosis (61.0% versus 26.7%, $P = .001$) and lymphopenia (90.2% versus 55.6%, $P = .001$), abnormal creatinine levels (79.0% versus 43.8%, $P = .001$), and severely elevated D-dimer (92.5% versus 54.8%, $P = .001$), C-reactive protein (79.0% versus 43.8%, $P = .002$), ferritin (79.0% versus 31.1%, $P < .001$), lactate dehydrogenase (73.0% versus 42.9%, $P = .014$), and alanine aminotransferase levels (78.1% versus 39.5%, $P < .001$).

DISCUSSION

Patients hospitalized for severe COVID-19 infection who develop stroke in the hospital demonstrate substantial differences compared

with other patients with COVID-19 infection who develop stroke as an outpatient with milder or no COVID-19 symptoms. Although we are unable, in a retrospective study, to prove that our findings are exclusively related to COVID-19, as opposed to other intensive care unit-related variables, patients hospitalized with severe COVID-19 had distinct stroke imaging patterns and even more abnormal laboratory biomarkers, which support a potential pathophysiologic link underpinning our previous finding that COVID-19 is a strong independent risk factor for stroke in hospitalized patients.¹² Patients with severe manifestations of COVID-19 had significantly more frequent ischemic strokes with multivascular territory distributions, hemorrhagic transformation, and simultaneous infarction and intracranial hemorrhage. While many patients with COVID-19 and stroke had elevated serum inflammatory markers (C-reactive protein and ferritin), lymphocytopenia, thrombocytopenia, and coagulopathy (elevated D-dimer levels and international normalized ratio), those with severe consequences of COVID-19 had significantly higher serum markers of inflammation, with more frequent levels of ferritin >4 times normal and C-reactive protein levels more than twice normal. These patients also had significantly higher markers of hypercoagulability with D-dimer levels more frequently >4 times normal. Furthermore, patients with severe COVID-19 and stroke had significant associations with greater frequencies of leukocytosis, lymphopenia, and cytotoxicity (measured by lactate dehydrogenase), hepatic and renal dysfunction, and deep vein thrombosis.

In a series of 214 patients hospitalized with COVID-19 from Wuhan, China, acute cerebrovascular disease was first reported in 6 patients (2.8%) and was associated with severe pulmonary infection, older age, stroke risk factors, elevated inflammatory markers, and end-organ damage.⁸ Evidence of a concomitant prothrombotic state was proposed by others who describe a series of 6 patients with COVID-19 and ischemic stroke who had infarctions suggesting large-artery occlusion.⁹ In that study, all cases had significantly elevated D-dimer levels, 2 had venous thromboembolic disease, and 2 developed large-artery occlusion despite therapeutic anticoagulation. One patient had antiphospholipid antibodies. Very high median D-dimer and C-reactive protein levels were also reported in a larger retrospective study of 32 patients with COVID-19 with ischemic stroke in the New York metropolitan area.¹⁰ In a study by others in the same region of 31 patients with COVID-19 with ischemic stroke, higher D-dimer levels and erythrocyte sedimentation rates were reported compared with concurrent patients with COVID-19 without stroke and with a historical sample of patients with influenza.¹³ In that study, when one adjusted for demographics, vascular risk factors, and critical care admission, COVID-19 still nearly quintupled the odds of ischemic stroke compared with influenza infection.

Our experience, like that of other centers,^{9-11,13,14} suggests that a hypercoagulable-prothrombotic state is a prevalent homeostatic complication among patients with COVID-19 and particularly in those with severe illness. Under these conditions, in which sepsis is common, ineffective host defense mechanisms to limit crosstalk between coagulation and hyperinflammation can increase tissue injury, worsen organ dysfunction, and promote thrombogenesis.^{15,16} Hyperinflammation can activate coagulation pathways via several mechanisms. These include promoting

Supplemental Table 1: Bivariate analysis of imaging and laboratory findings in patients with COVID-19 dichotomized by location at stroke onset

Variable	Median (IQR)	In-Hospital (No.) (%)	Out-of-Hospital (No.) (%)	P Value
Patients (No.)	86	41	45	
Age (yr)				
20–69 years of age	68 (60–76)	20 (48.8)	26 (57.8)	.403
Sex, male		26 (63.4)	22 (48.9)	.176
Imaging				
Ischemic stroke		39 (95.1)	33 (73.3)	.006
Infarction, no hemorrhage		26 (63.4)	31 (68.9)	.001
Infarction with HT		5 (12.2)	1 (2.2)	
Infarction and ICH		8 (19.5)	1 (2.2)	
Pure ICH, no infarction		2 (4.9)	12 (26.8)	
Multivasculature territory infarction (<i>n</i> = 72)		22 (56.4)	11 (33.3)	.022
Deep vein thrombosis		12 (29.3)	1 (2.2)	.001
Laboratory values				
White blood cell ^a				
≥10.5 K/uL	9.7 (7.2–14.7)	25 (61.0)	12 (26.7)	.001
Lymphocytes ^b				
<1.00 K/uL	0.6 (0.31–1.05)	37 (90.2)	25 (55.6)	.001
Hemoglobin ^a				
<11.5 g/dL	12.3 (9.7–13.8)	19 (46.3)	16 (35.6)	.309
Platelets ^a				
<150 K/uL	247 (152–335)	9 (22.0)	10 (22.2)	.976
aPTT ^{a,c}				
>36.3 seconds	30.9 (28.4–36.1)	13 (32.5)	7 (17.1)	.108
INR ^{a,c}				
>1.20	1.17 (1.07–1.31)	19 (48.7)	17 (39.5)	.403
D-dimer, ^c 4 × nl				
>920 ng/mL	3060 (1064–24,211)	37 (92.5)	17 (54.8)	.001
C-reactive protein, ^c 2 × nl				
>10.0 mg/L	17.5 (6.4–28.8)	30 (79.0)	14 (43.8)	.002
Ferritin, ^c 4 × nl				
>1200 ng/mL	1382 (706–2424)	30 (79.0)	10 (31.1)	<.001
LDH, ^c 2 × nl				
>484 U/L	536 (357–815)	27 (73.0)	12 (42.9)	.014
ALT, ^c 2 × nl				
>90.0 U/L	50 (29–136)	32 (78.1)	17 (39.5)	<.001
Creatinine ^c				
>1.30 mg/dL	1.30 (0.93–2.81)	28 (70.0)	15 (34.1)	.001

Note:—HT indicates hemorrhagic transformation; ICH, intracranial hemorrhage; nl, upper limit of the normal value; aPTT, activated partial thromboplastin time; INR, international normalized ratio; LDH, lactate dehydrogenase; ALT, alanine aminotransferase; IQR, interquartile range.

^a White blood cell count, hemoglobin, platelets, activated aPTT, and INR are from admission or at the time of consultation for stroke. Remaining laboratory values (except lymphocyte count) are the maximum level during the hospitalization.

^b Lowest lymphocyte count during admission.

^c Variable has missing values. The number and percentage (No.) (%) of patients with missing laboratory values are the following: aPTT (*n* = 5, 5.8%), INR (*n* = 4, 4.7%), D-dimer (*n* = 16, 18.6%), C-reactive protein (*n* = 16, 18.6%), ferritin (*n* = 16, 18.6%), LDH (*n* = 21, 24.4%), ALT, (*n* = 2, 2.3%), and creatinine (*n* = 2, 2.3%). All other variables have no missing values.

endothelial activation, increasing tissue factor expression on vascular endothelial and circulating inflammatory cells such as monocytes, and downregulating the efficiency of the protein C–protein S thrombomodulin system to regulate the increased thrombogenesis associated with consumptive coagulation.^{14,17,18} Specifically, surges in proinflammatory cytokines and mediators, related to an exaggerated innate immune response and extensive tissue damage associated with severe COVID-19, can downregulate the expression and function of thrombomodulin, an endogenous protein with potent anticoagulant and anti-inflammatory properties pivotal in preventing vascular occlusion.^{19,20}

Moreover, an autoimmune hypercoagulable state associated with antiphospholipid antibodies, such as anti-cardiolipin and anti-β₂-glycoprotein-1 antibodies, can contribute to the pathophysiology of a subset of strokes associated with COVID-19.²¹ As shown in the peripheral vasculature,²² direct SARS-CoV-2

infection of cerebrovascular endothelia expressing angiotensin-converting enzyme 2, causing endotheliitis and vascular injury, is postulated and may result in both ischemic and hemorrhagic stroke, though this mechanism remains unproven. Finally, a potential downregulation of neurovascular endothelial angiotensin-converting enzyme 2 expression in response to its binding to SARS-CoV-2 may also be relevant to ischemic stroke pathogenesis, though this too is theoretic.

Our study has several strengths and limitations. As we previously reported,¹² our series likely undercounted the actual COVID-19-stroke burden during this timeframe. Many potential patients with stroke with normal initial brain imaging did not undergo repeat imaging because of clinical instability or concerns for spreading infection while transporting patients with COVID-19 off quarantined wards. For similar reasons, MR imaging use was limited at numerous centers, especially earlier on in the local

epidemic. Therefore, some patients with smaller and more acute infarctions were not included in our study, and our results should be interpreted as only relevant to patients with COVID-19 who have imaging-confirmed stroke.

A relative strength to our approach was the inclusion of patients with primary and secondary intracranial hemorrhage, allowing, for the first time, the demonstration of a frequent hemorrhagic component to infarctions seen in patients with severe COVID-19. Independent neuroradiologic review of the imaging-enabled confirmation of stroke diagnoses and characterization of imaging findings were blinded and uniform. As a retrospective study, some laboratory values were missing in a proportion of patients. To mitigate this issue, we analyzed only variables with at least 75% complete data. Consequently, some commonly cited laboratory abnormalities associated with COVID-19 are not included, such as fibrinogen, antiphospholipid antibodies, and interleukin levels. In addition, given our small sample size, we were unable to perform an adjusted analysis. Nevertheless, the number of cases of COVID-19 stroke in our series permitted a comprehensive analysis of neuroimaging and laboratory biomarkers, reinforcing potential pathophysiologic mechanisms supporting the association between COVID-19 and stroke.

CONCLUSIONS

Compared with those with mild or asymptomatic COVID-19 at stroke onset, patients who have strokes while hospitalized with severe manifestations of COVID-19 have significantly more inflammation, multiorgan dysfunction, and coagulopathy, including deep vein thrombosis. These findings support proposed pathophysiologic mechanisms linking these diagnoses, though we cannot definitively state that our findings are specific to SARS-CoV-2 infection as opposed to the critical illness associated with severe COVID-19. Infarctions with concurrent hemorrhage are also more frequent. Given the associated hypercoagulability, clinical-treatment algorithms for patients hospitalized with COVID-19 have shifted toward widespread use of full- or prophylactic-dose anticoagulation to prevent thromboembolic complications, though the benefits of this approach remain unproven because it is based solely on observational data.²³ In patients with COVID-19 with stroke, anticoagulation may be of benefit, but the approach may have to be more nuanced, given the risks of associated cerebral hemorrhage, mandating a more cautious balancing of the risks of thrombosis and hemorrhage.

Disclosures: Christopher G. Filippi—UNRELATED: Consultancy: Guerbet, Syntactx; Grants/Grants Pending: Foundation of the American Society of Neuroradiology grant and National MS Society grant*; Payment for Manuscript Preparation: article on topics in MRI journal (April 2020); Stock/Stock Options: minority stakeholder in start-up Avicenna. Pina Sanelli—UNRELATED: Grants/Grants Pending: Siemens, Harvey L. Neiman Sanell Health Policy Institute, Comments: research partnership.* Souhel Najjar—UNRELATED: Employment: Full-time and Chair of Neurology at Northwell Health. *Money paid to the institution.

REFERENCES

- Zhu N, Zhang D, Wang W, et al; China Novel Coronavirus Investigating and Research Team. **A novel coronavirus from patients with pneumonia in China, 2019.** *N Engl J Med* 2020;382:727–33 CrossRef Medline
- COVID-19 dashboard by the Center for Systems Science and Engineering at Johns Hopkins University.** <https://publichealthupdate.com/jhu/>. Accessed October 1, 2020
- Mizumoto K, Kagaya K, Zarebski A, et al. **Estimating the asymptomatic proportion of coronavirus disease 2019 (COVID-19) cases on board the Diamond Princess cruise ship, Yokohama, Japan, 2020.** *Euro Surveill* 2020;25:2000180 CrossRef Medline
- Richardson S, Hirsch JS, Narasimhan M, et al. **Presenting characteristics, comorbidities and outcomes among 5700 patients hospitalized with COVID-19 in the New York City area.** *JAMA* 2020;323:2052–59 CrossRef Medline
- Mehta P, McAuley DF, Brown M, et al; HLH Across Speciality Collaboration, UK. **COVID-19: consider cytokine storm syndromes and immunosuppression.** *Lancet* 2020;395:1033–34 CrossRef Medline
- Tang N, Li D, Wang X, et al. **Abnormal coagulation parameters are associated with poor prognosis in patients with novel coronavirus pneumonia.** *J Thromb Haemost* 2020;18:844–47 CrossRef Medline
- Cao W, Li T. **COVID-19: towards understanding of pathogenesis.** *Cell Res* 2020;30:367–69 CrossRef Medline
- Mao L, Jin H, Wang M, et al. **Neurologic manifestations of hospitalized patients with coronavirus disease 2019 in Wuhan, China.** *JAMA Neurol* 2020;77:683 CrossRef Medline
- Beyrouti R, Adams ME, Benjamin L, et al. **Characteristics of ischemic stroke associated with COVID-19.** *J Neurol Neurosurg Psychiatry* 2020;91:889–91 CrossRef Medline
- Yaghi S, Ishida K, Torres J, et al. **SARS2-CoV-2 and stroke in a New York healthcare system.** *Stroke* 2020;51:2002–11 CrossRef Medline
- Arachchilage DR, Laffan M. **Abnormal coagulation parameters are associated with poor prognosis in patients with novel coronavirus pneumonia.** *J Thromb Haemost* 2020;18:1233–34 CrossRef Medline
- Katz JM, Libman RB, Wang JJ, et al. **Cerebrovascular complications of COVID-19.** *Stroke* 2020;51:e227–31 CrossRef Medline
- Merkler AE, Parikh NS, Mir S, et al. **Risk of ischemic stroke in patients with coronavirus 2019 (COVID-19) vs patients with influenza.** *JAMA Neurol* 2020 Jul 2. [Epub ahead of print] CrossRef Medline
- Lillicrap D. **Disseminated intravascular coagulation in patients with 2019-nCoV pneumonia.** *J Thromb Haemost* 2020;18:786–87 CrossRef Medline
- Foley JH, Conway EM. **Cross talk pathways between coagulation and inflammation.** *Circ Res* 2016;118:1392–1408 CrossRef Medline
- Levi M, van der Poll T. **Coagulation and sepsis.** *Thromb Res* 2017;149:38–44 CrossRef Medline
- Amiral J, Seghatchian J. **Revisiting the activated protein C-protein S-thrombomodulin ternary pathway: impact of new understanding on its laboratory investigation.** *Transfus Apher Sci* 2019;58:538–44 CrossRef Medline
- Bode M, Mackman N. **Regulation of tissue factor gene expression in monocytes and endothelial cells: thromboxane A2 as a new player.** *Vascul Pharmacol* 2014;62:57–62 CrossRef Medline
- Ikezoe T. **Thrombomodulin/activated protein C system in septic disseminated intravascular coagulation.** *J Intensive Care* 2015;3:1 CrossRef Medline
- Joseph L, Fink LM, Hauer-Jensen M. **Cytokines in coagulation and thrombosis: a preclinical and clinical review.** *Blood Coagul Fibrinolysis* 2002;13:10–16 CrossRef Medline
- Zhang Y, Xiao M, Zhang S, et al. **Coagulopathy and antiphospholipid antibodies in patients with COVID-19.** *N Engl J Med* 2020;382:e38 CrossRef Medline
- Varga Z, Flammer AJ, Steiger P, et al. **Endothelial cell infection and endotheliitis in COVID-19.** *Lancet* 2020;395:1417–18 CrossRef Medline
- Nadkarni GN, Lala A, Bagiella E, et al. **Anticoagulation, mortality, bleeding and pathology among patients hospitalized with COVID-19: a single health system study.** *J Am Coll Cardiol* 2020 Aug 24. [Epub ahead of print] CrossRef Medline

Time for a “Second Wave” of COVID-19 Data



Lenin supposedly said, “There are decades when nothing happens, and there are weeks when decades happen.”¹ Although likely apocryphal, the statement is nonetheless a good summary for what 2020 has felt like. The early days of the first wave of the coronavirus disease 2019 (COVID-19) pandemic simultaneously seems like a few months ago and many years ago. In March and April, our community was dealing with the rapidly growing body of literature regarding neuroimaging findings in these patients and trying to tie this into our developing knowledge regarding the pathophysiology of this novel pathogen. By now, though, we are familiar with the common imaging appearances of some critically ill patients with COVID-19.

As a group, we have responded admirably to the pandemic in other ways, too. In addition to providing front-line services for both diagnostic and interventional neuroradiology, neuroradiologists have, during a few short months, come together to share valuable information with each other. Rather than retreating inward, the advent (and wide normalization) of regular webinars has meant that we can now attend more conferences than ever and catch up with talks later if they occur at an inconvenient time. Thanks to a plethora of communication tools, from WhatsApp groups and Twitter to mailing lists and American Society of Neuroradiology chat forums, we have come together and shared information on topics ranging from COVID-19 neuroimaging to personal protective equipment protocols and remote working tips. Thus, while we see each other less and less, in ways we are working closer than ever.

Keeping up to date with medical literature in general is a daunting task, though, and this problem has been magnified many times over when trying to keep current with COVID-19-related articles, which sometimes feels like drinking from a firehose. The first wave of such literature with regard to neuroimaging consisted of mainly single-center, retrospective case series (including contributions from our own center²), which were followed by larger retrospective, sometimes multicenter series.³ As experience has grown, some patterns are beginning to emerge. For example, it is now clear that a certain subset of critically patients with COVID-19 can present with diffuse white matter changes, thromboses (either large-vessel occlusions or microvascular thromboses), and

even hemorrhage. This information is thanks to the many published series so far.

However, even in times of an urgent need for more information about this new virus, we must not let our hunger for answers overcome our desire to seek better, higher-quality data. In the “gold rush” of articles that have come forth following the emergence of this new disease, we as a community can often eagerly rush to extrapolate an overriding story or narrative from limited or early data. One example of this came earlier this year, when a few small-denominator case reports suggested that there was a higher rate of stroke due to large-vessel occlusion (LVO) in younger patients with COVID-19. These reports received widespread media coverage, but the media did not widely report the multiple subsequent larger series that showed that, in fact, the number of LVO presentations was much less during the pandemic.

We, thus, need to try to distinguish the signal from the noise, and the truth is that there are many things that we do not yet know. We do not know how many asymptomatic patients with COVID-19 will show changes on their imaging studies or how many patients will show such changes but only demonstrate mild symptoms. We do not know how many patients who would have been admitted before the pandemic but were, instead, sent home had neurologic changes as a result of the virus. We also do not know whether some of the imaging findings we are seeing, microhemorrhages, for example, are related to their critical illness/intensive care unit syndrome or are unique to patients with COVID-19. Finally, and perhaps most important, we do not yet know the natural history of these imaging findings and how they may relate to the patient’s clinical course. What about the neurologic and neuroimaging findings in patients with so-called “long COVID” or patients who have recovered from the disease but still have the sequelae?

Much of the data we have thus far are poor-quality and retrospective in nature. This is not a criticism, but rather an observation. Such is the nature of figuring out an emerging new illness, and these case reports and case series provided very useful information at a time when it was badly needed. However, the answer to this problem is not to collate the data we have and run it through the “meta-analysis machine.” It is, instead, time for us to look forward to a second wave of

COVID-19 data, a wave of prospective, multicenter, and more long-term studies. Many such studies are ongoing, and we eagerly look forward to the results.

REFERENCES

1. O'Toole G. **Days into Which 20 Years Are Compressed. Quote Investigator.** 2020. <https://quoteinvestigator.com/2020/07/13/decades-weeks/>. Accessed December 14, 2020
2. Nicholson P, Alshafai L, Krings T. **Neuroimaging findings in patients with COVID-19.** *AJNR Am J Neuroradiol* 2020;41:1380–83 CrossRef Medline
3. Mahammedi A, Saba L, Vagal A, et al. **Imaging of neurologic disease in hospitalized patients with COVID-19: an Italian multicenter retrospective observational study.** *Radiology* 2020;297:E270–73 CrossRef Medline

 P. Nicholson

 T. Krings

Division of Neuroradiology
Joint Department of Medical Imaging
Toronto Western Hospital
University Health Network
University of Toronto
Toronto, Ontario, Canada

<http://dx.doi.org/10.3174/ajnr.A7020>

Basal Ganglia versus Peripheral Infarcts: Predictive Value of Early Fiber Alterations

M.T. Berndt, D. Pürner, C. Maegerlein, S. Wunderlich, B. Friedrich, C. Zimmer, D. Sepp, J. Kaesmacher, and T. Boeckh-Behrens



ABSTRACT

BACKGROUND AND PURPOSE: Impairment of fiber integrity of the corticospinal tract in the subacute and chronic phases after ischemic stroke has been linked to poor motor outcome. The aim of the study was an assessment of fiber integrity in the acute poststroke phase and an evaluation of its association with the clinical course dependent on the infarction pattern (subtypes: peripheral versus basal ganglia infarction).

MATERIALS AND METHODS: All patients who underwent mechanical recanalization of a large-vessel occlusion in the anterior circulation and postinterventional DTI were included ($n = 165$). The fractional anisotropy index of the patient-specific corticospinal tract within the posterior limb of the internal capsule was correlated to clinical parameters (NIHSS scores/mRS at 90 days), and the interaction of stroke subtype (peripheral infarcts versus basal ganglia infarction) was tested in a moderation analysis.

RESULTS: The fractional anisotropy index was reduced in the acute poststroke phase with a correlation to clinical presentation, especially in case of peripheral infarcts (eg, with the NIHSS motor subscore: $r = -0.4$, $P < .001$). This correlation was absent for basal ganglia infarction ($r = -0.008$, $P > .05$). There was a significant association between the fractional anisotropy index and clinical outcome (mRS after 90 days, $P < .01$), which is moderated by stroke subtype with significant effects only for peripheral infarcts.

CONCLUSIONS: Corticospinal tract abnormalities can be observed in the early stage after mechanical recanalization and have prognostic capacity. This finding increases the clinical value of early DTI imaging parameters. Because the effects observed were limited to peripheral infarcts, further and longitudinal evaluation of fiber integrities within basal ganglia infarction is required.

ABBREVIATIONS: BGI = basal ganglia infarction; CST = corticospinal tract; FA = fractional anisotropy; IQR = interquartile range; mNIHSS = motor subindex scores of NIHSS; mNIHSS-AL = sum of arm (A) and leg (L) symptom values of the affected side; mNIHSS-ALF = the sum of arm (A), leg (L) and facial (F) symptoms value of the affected side; mTICI = modified TICI; PED = cerebral peduncle; PLIC = posterior limb of the internal capsule

In most cases, ischemic stroke caused by acute occlusions of a large intracranial vessel of the anterior circulation leads to motor impairment, resulting in major disability and poor quality of life.¹ Early prediction of functional motor outcome is essential for clinical stroke management, rehabilitation, and related research.² The prediction of functional recovery is challenging due to high interindividual variability,³ influenced by a variety of biologic and environmental factors.⁴ Studies are notably missing

for the rapidly rising entity of basal ganglia infarction (BGI), which emerges from high rates of successful reperfusion due to mechanical recanalization.

Several variables are valid predictors of motor recovery, such as the grade of initial motor deficit, site of infarction, stroke volume, age, demographics, comorbidities, and stroke subtype.^{2,5-11} Most patients are discharged from stroke units within several days after treatment, making early prediction of outcome difficult even for experienced clinicians.¹² They would benefit from biomarkers that could easily be assessed in the acute poststroke phase. Imaging can provide parameters about tissue integrity that have a promising value for outcome prediction beyond the existing ones. The integrity of the corticospinal tract (CST) has already proved to be an essential factor for motor outcome.^{13,14} Macrostructural analyses are important, but they can give only limited information, eg, about specific tissue integrity. This can be better assessed by microstructural imaging, eg, patient-specific fiber analyses with DTI, providing more information about functional structures.

Received March 31, 2020; accepted after revision September 7.

From the Departments of Neuroradiology (M.T.B., C.M., B.F., C.Z., D.S., T.B.-B.) and Neurology (D.P., S.W.), Klinikum Rechts der Isar, School of Medicine, Technical University of Munich, Munich, Germany; and Department of Neuroradiology (J.K.), Inselspital, University Hospital Bern, University Bern, Bern, Switzerland.

Please address correspondence to Maria Berndt, MD, Department of Neuroradiology, Klinikum Rechts der Isar, School of Medicine, Technical University of Munich, Ismaninger Str 22, 81675 Munich, Germany; e-mail: maria.berndt@tum.de

 Indicates article with supplemental online appendix and tables.

 Indicates article with supplemental online photo.

<http://dx.doi.org/10.3174/ajnr.A6886>

Currently, evaluation of fiber integrity using DTI is well-established.¹⁵ Microstructural damage of CST fibers has previously been analyzed in different phases after stroke, mostly in subacute and chronic stages, and the potential to predict motor outcome has been shown.¹⁶⁻¹⁹ A previous study used neuroimaging acquired during the acute stroke work-up, which has been able to predict motor recovery by macrostructural injury of the CST.²⁰ However, this study did not use individual mapping of the corticospinal tract, which is mandatory for an accurate investigation of DTI metrics, especially in cases of concomitant ischemia and edema. Therefore, the present study aimed to analyze the microstructural integrity of the patient-specific CST within the posterior limb of the internal capsule (PLIC) in the acute poststroke phase for a large patient collective. The central question was whether these integrity abnormalities are associated with clinical outcome parameters. A subanalysis was performed depending on the extent of infarction (peripheral infarcts versus BGI only) and was used to evaluate effects on outcome prediction.

MATERIALS AND METHODS

Patient Characteristics

The whole study cohort consisted of 439 consecutive patients with ischemic stroke with acute occlusions of a large intracranial vessel of the anterior circulation (middle cerebral artery or carotid-T) who underwent mechanical recanalization at a single comprehensive stroke center (Klinikum Rechts der Isar, School of Medicine, Technical University of Munich) between April 2016 and December 2018. The prospectively collected clinical and imaging data were retrospectively analyzed. Basic demographic, clinical, and interventional data of patients were gathered. The NIHSS score as well as the motor subindex scores (mNIHSS), defined as the sum of arm and leg symptom values of the affected side (mNIHSS-AL) (0–8 points) and the sum of arm (A), leg (L) and facial (F) symptoms value of the affected side (mNIHSS-ALF) (0–11 points), were assessed by NIHSS-certified neurologists at admission and at the MR imaging acquisition. The mRS score was used to measure disability at day 90 assessed by experienced neurologists, either on a routinely scheduled clinical visit or by a structured telephone interview. Good clinical outcome was defined as an mRS score of ≤ 2 according to large clinical trials.^{21,22}

The modified TIC1 (mTIC1) score²³ was determined by 2 experienced neurointerventionalists (C.M., B.F.) in consensus. Successful recanalization was defined as mTIC1 2b–3. Time to groin puncture, time of the reperfusion, and corresponding procedure times were taken from the existing data base. Recanalization time was defined as the difference between the time to groin puncture and reperfusion. In cases in which recanalization was not successful (mTIC1, <2b), the control series after the last maneuver was used as the end time point.

After we applied specific exclusion criteria (see flow chart, Fig 1), the final study cohort consisted of 165 patients who underwent MR imaging in the acute poststroke phase after mechanical thrombectomy (median, 3 days; interquartile range [IQR], 3–4 days; maximum, 7 days) including DTI and structural T1-weighted imaging.

On the basis of the infarction in the MR imaging acquisition, the stroke subtype of all patients was unanimously determined by consensus of 2 experienced neuroradiologists. It was graduated into BGI without relevant infarction of cortical structures, and peripheral infarcts, which were further divided into infarction severity. The severity assessment originates from DWI-ASPECTS (involvement of cortical regions M1–M6,^{24,25}) and is modified by estimating the volume ratio that reflects, more importantly, the extent of peripheral infarcts (mild, below one-third; middle, between one-third and two-thirds; and high, above two-thirds of the peripheral infarct territory).

This study was approved by the local ethics committee of the Klinikum Rechts der Isar (School of Medicine, Technical University of Munich, Germany) (vote number 250/17 S), and the need for patient consent was waived.

MR Imaging Data Acquisition

MR imaging data were acquired on a 3T scanner (Achieva; Philips Healthcare) with a standard 8-channel head coil using consistent sequences and parameter settings.

Diffusion tensor images were acquired using a single-shot spin-echo echo-planar imaging sequence, resulting in 1 non-diffusion-weighted image ($b = 0 \text{ s/mm}^2$) and 15 diffusion-weighted images ($b = 800 \text{ s/mm}^2$ in 15 noncolinear gradient directions) covering the whole brain with the following parameters: TE = 55 ms, flip angle = 90°, FOV = 224 × 224 × 146 mm, 73 transverse slices, section thickness = 2 mm, 0-mm interslice gap, voxel size = 2 × 2 × 2 mm.

A whole-head, high-resolution 3D gradient-echo T1-weighted image was acquired using the following parameters: TE = 4 ms, TR = 9 ms, flip angle = 8°, FOV = 240 × 252 × 200.25 mm, 267 sagittal slices, section thickness = 1 mm, 0-mm interslice gap, voxel size = 1 × 1 × 1 mm.

DTI Data Processing

DTI data were processed using FSL (written mainly by members of the Analysis Group, FMRIB, Oxford, UK²⁶) applying the following steps: DTI preprocessing, DTI data quality check, and probabilistic tractography of the bilateral CST (seed, cerebral peduncle [PED], and target [precentral gyrus], ROI-based). In a next step, the individual CST was characterized within the PLIC and PED (atlas-based ROIs, transformed from standard to individual diffusion space) through an analysis of fractional anisotropy (FA) values. FA is commonly used to measure the integrity of white matter tracts by assessing the anisotropy.

The individual FA indices for PLIC and PED were calculated to get quantitative values of FA alterations of the infarcted CST (I) in comparison with the healthy, nonaffected CST (H) (Fig 2). FA index = $(FA_I - FA_H)/(FA_I + FA_H)$. The FA index was used to characterize the microstructural integrity of the CST within the PLIC and PED. More detailed descriptions can be found in the Online Appendix.

Statistical Analysis

The mean value comparison of the FA index among the different infarction groups was performed by means of a 2-sample *t* test

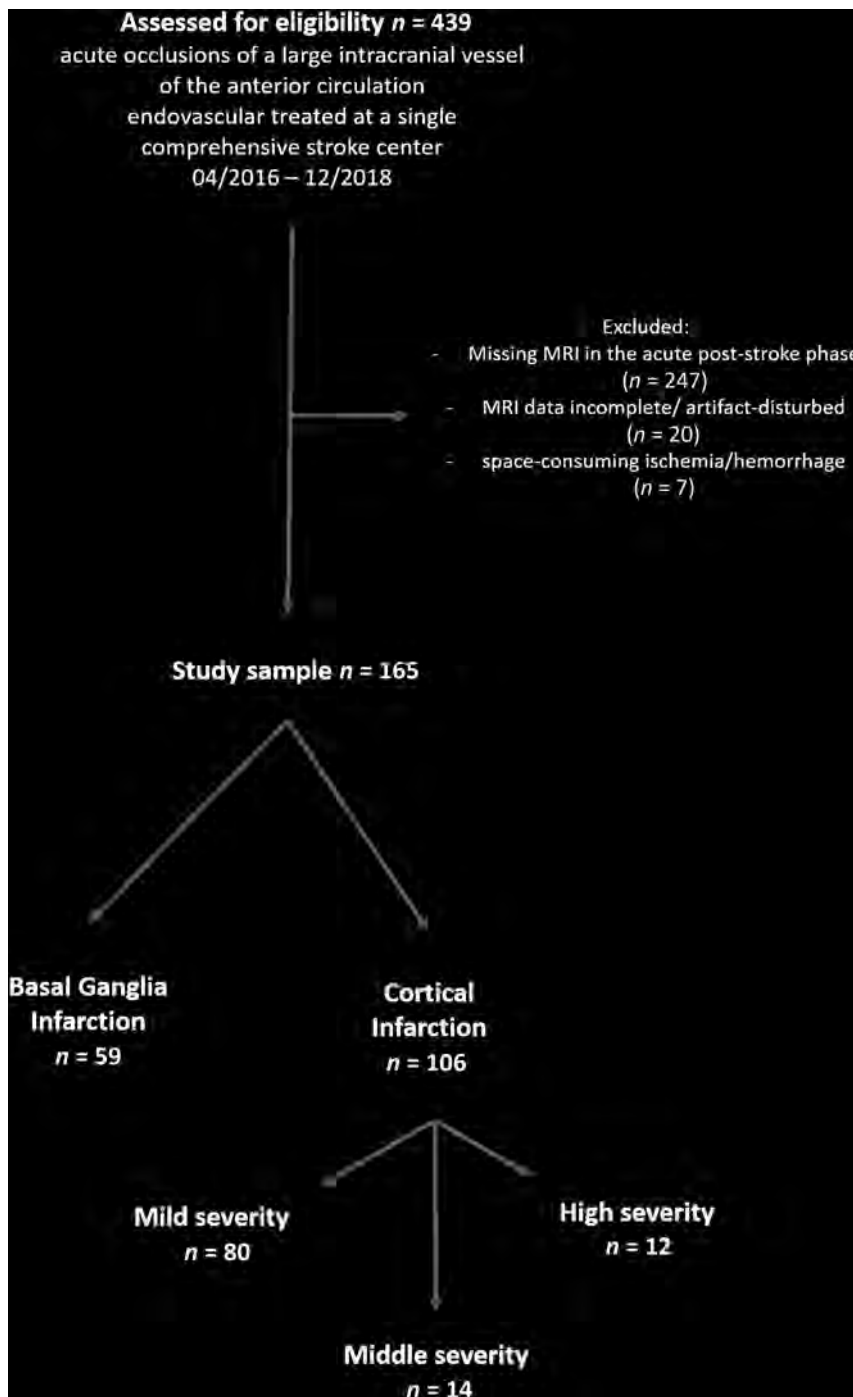


FIG 1. Flow diagram explaining the study sample.

for independent samples. Wilcoxon rank sum tests were used for comparison of NIHSS and mRS values among the different infarction groups.

To explore the relevance of the FA index for clinical presentation, we tested the relationships between the FA index and NIHSS score as well as the mNIHSS (at MR imaging date and the percentage improvement compared with admission) using the following procedure: Partial correlation analyses were performed between the FA index and NIHSS-/mNIHSS at the time of MR imaging as well as with their percentage improvement. The

analyses were corrected for age, sex, time between recanalization and MR imaging, and recanalization time.

In a multivariate logistic regression model, the association of the FA index (CST-PLIC) and further variables such as age, sex, time between recanalization and MR imaging, and recanalization time with good clinical outcome (mRS after 90 days, ≤ 2) was tested by means of a stepwise forward variable selection method. To check the interaction of stroke subtype (BGI versus peripheral infarcts) on the association of the FA index and the mRS after 90 days, we performed moderation analysis under consideration of the same covariates, age, sex, time between recanalization and MR imaging, and recanalization time.

For details of the mediation analysis see the Online Appendix.

All statistical analyses were performed using SPSS Statistics (Version 25; IBM).

RESULTS

Patient Characteristics

In total, 165 patients met the required inclusion criteria. Online Table 1 provides an overview of demographic, clinical, and interventional data of patients as well as their stroke subtypes assessed on the MR imaging examination.

Microstructural Integrity Changes of the CST within the PLIC

The distributions of the FA index of the CST within the PLIC are plotted in Fig 3 for the different stroke subtypes. The FA indices presented mostly negative values, meaning a loss of CST-FA values within the PLIC for the affected side. The subgroup of BGI showed FA indices (mean, -0.050 [SD, 0.098]) similar to those of peripheral infarcts in general (mean, -0.039 [SD, 0.076], $P = .46$). Within the group of peripheral infarcts, those of mild infarction severity (mean, -0.020 , [SD, 0.058]) showed significantly higher FA indices than those of middle infarction severity (mean, -0.091 [SD, 0.108], $P < .001$) or of high infarction severity (mean -0.101 [SD, 0.079], $P < .001$).

To estimate how specific the CST alterations are for the PLIC in the acute poststroke phase, we added additional analyses of the FA index within the PED. For both stroke subgroups, a weak tendency toward negative FA indices (for BGI: mean, -0.013

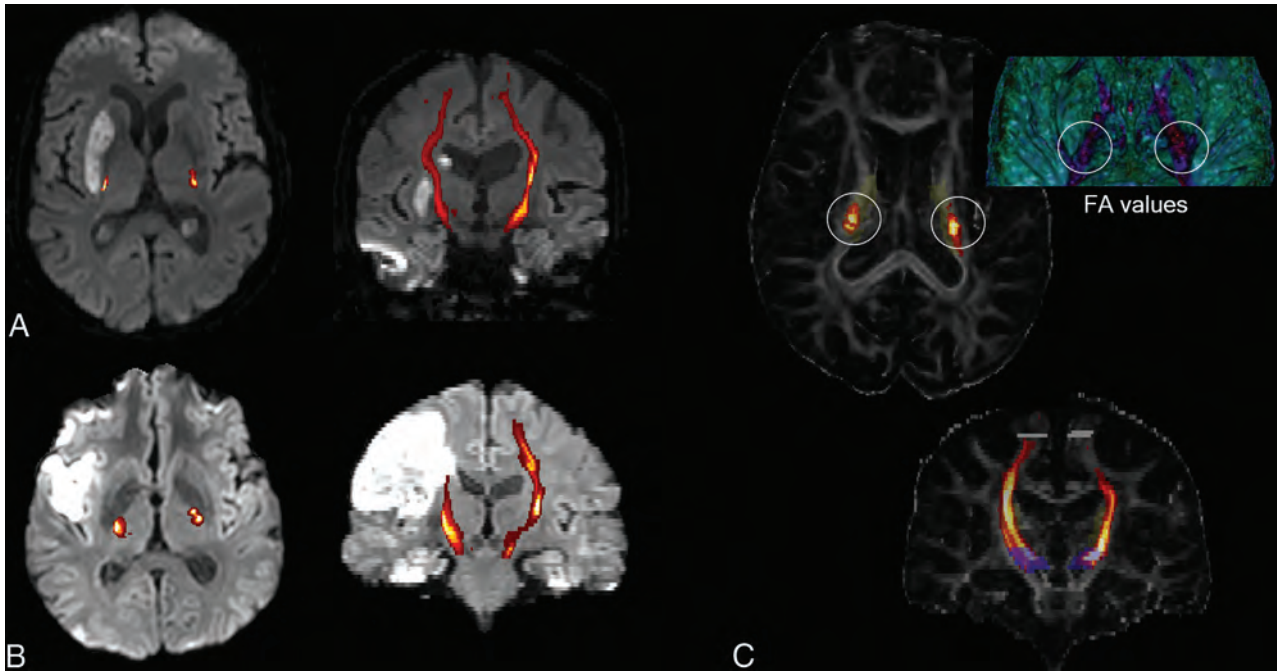


FIG 2. Examples of 2 patients 3 days after mechanical recanalization of a right middle cerebral artery occlusion and consecutive basal ganglia infarction (A, patient 1)/peripheral infarct (B, patient 2). The CST, reconstructed by probabilistic fiber tracking (C, demonstrated on FA maps, blue seed ROI, gray target ROI, yellow posterior limb of the internal capsule) is overlaid on the reconstructed DWI trace picture in A and B (CST connectivity values, increasing probability from red to yellow before CST thresholding). For both patients, lower FA values of the CST within the posterior limb of the internal capsule are found for the infarcted right side in comparison with the healthy, nonaffected left side (C, illustrated using 3D Slicer; <http://www.slicer.org>).

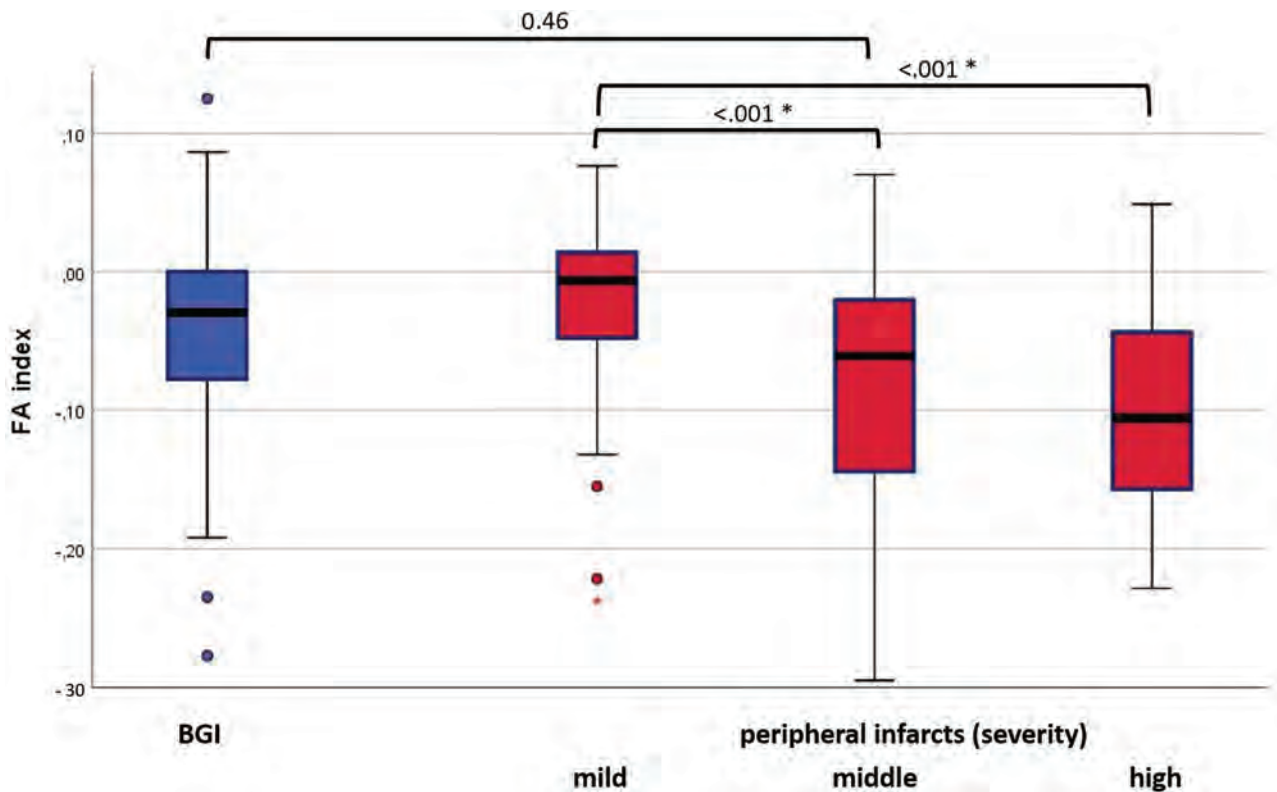


FIG 3. Distribution of the FA index of the corticospinal tract within the posterior limb of the internal capsule. Boxplots for the different stroke subtypes (BGI versus peripheral infarcts, which were further divided according to infarction severity). The asterisk indicates a statistically significant difference between the subgroups.

[SD, 0.047]; for peripheral infarcts: mean -0.003 [SD, 0.062]) was found, possibly suggesting real white matter alterations of the CST on the affected side in general, not only locally in the PLIC in the acute poststroke phase.

Correlations of Microstructural CST Integrity Changes with Clinical Presentation

For the whole study cohort, the FA index of PLIC showed weak negative correlations to the NIHSS at the time of MR imaging ($r = -0.246, P = .002$), mNIHSS-AL ($r = -0.278, P = .001$), and mNIHSS-ALF ($r = -0.284, P < .001$). The analyses were corrected for age, sex, time between recanalization and MR imaging, and recanalization time.

The FA indices of the additional PED testing showed no significant association with NIHSS/mNIHSS-AL/mNIHSS-ALF ($r = -0.110/-0.028/-0.047; P = .183, .733, .566$).

Subgroup of BGI. The analyses to test an association of the FA index of the PLIC with the clinical presentation were repeated within the subgroup of BGI ($n = 59$). None of the correlation analyses with NIHSS/mNIHSS-AL/mNIHSS-ALF at the time of MR imaging as well as with the percentage improvement of these parameters from pretreatment to time of MR imaging showed significant results ($P > .05$, respectively) (Online Table 2).

Subgroup of Peripheral Infarcts with Impact of Infarction Severity. The analyses to test an association of the FA index of the PLIC with the clinical presentation were repeated within the subgroup of peripheral infarcts with mild-to-middle infarction severity ($n = 94$, 12 patients with high severity were excluded to get a more homogeneous sample). All analyses showed statistically significant associations with higher correlation coefficients than in the analyses within the whole study cohort (Online Table 2). The mNIHSS-AL is moderately correlated to the FA index ($r = -0.40, P < .001$) under consideration of all above-mentioned covariates. It shows that a greater motor impairment is associated with a microstructural integrity loss of the corresponding CST.

Correlation coefficients differed significantly between the 2 subgroups (peripheral infarcts versus BGI) in most cases, as shown by the use of the Fisher-Z test (Online Table 2).

Association of Microstructural CST Integrity Changes with Clinical Outcome

In a logistic regression analysis, the FA index (CST-PLIC) was associated with good clinical outcome (mRS after 90 days, ≤ 2 ; regression coefficient, 10.3, standard error, 3.8, $P < .01$). Age was inversely associated with good clinical outcome (regression coefficient, -0.12 ; standard error, 0.04; $P < .01$); the other covariates showed no significant effect (excluded with stepwise forward variable selection method).

In a second step, the impact of the FA index on the mRS (after 90 days) was tested depending on the moderator variable stroke subtype under consideration of the same covariates. Due to the interaction of this moderator variable, a significant change in R^2 (.05) was shown ($P < .001$). The conditional effect of the FA index on clinical outcome at the 2 different moderator values was as follows: No significant effect could be seen for the stroke subgroup BGI (effect, -0.9 ; 95% CI containing 0 [$-4.4-2.6$], $P =$

.61), but for peripheral infarcts, a strong effect of the FA index on clinical outcome existed (effect, -11.0 ; 95% CI, 5.2 to -6.8 , $P < .0001$).

Impact of Microstructural CST Integrity on the Effect between Infarction Severity and Clinical Outcome

The 2 groups of mild and middle infarction severity differed not only in their FA indices (see above), with lower values for higher infarction severity, but also in their clinical parameters showing higher affection (NIHSS/mRS) for the higher infarction severity subgroup ($P < .001, .002$).

In a mediation analysis (Online Figure), the effect of group (mild or middle infarction severity) on clinical outcome (mRS after 90 days) (total effect $c = 1.10 \pm 0.35, P = .003$) was still present but reduced when controlling for the FA index (direct effect $c' = 0.89 \pm 0.36, P = .014$); critically, the bootstrapped 95% confidence interval for the indirect effect (ie, mediation: total-direct effect) was different from zero (95% CI, 0.02–0.58), indicating that the FA index significantly mediated the relationship between infarction severity and clinical outcome.

DISCUSSION

When we integrated the whole cohort of patients with large intracranial vessel occlusions of the anterior circulation, structural patient-specific CST abnormalities were found in the acute poststroke phase after mechanical recanalization. Reduced FA indices indicate a loss of CST integrity within the PLIC. These structural alterations were associated with the clinical presentation, especially for peripheral infarcts. The level of integrity was negatively correlated to symptom severity (NIHSS/mNIHSS values) and positively correlated to the percentage improvement of symptom severity from the onset to the date of MR imaging. CST integrity within the PLIC was also associated with good clinical outcome after 90 days, as measured by the mRS, suggesting that impairment of the CST fiber integrity within the PLIC has a negative impact on clinical presentation in general.

Beside the previously shown prediction capacity of macrostructural CST injury in the acute poststroke phase,²⁰ the present study is powered with an adequate patient number, enabling us to detect individual microstructural CST integrity changes within the PLIC, also suggesting an impact on the clinical presentation and outcome. However, occlusions of the anterior circulation result in different infarction patterns, especially since the establishment of mechanical recanalization of intracranial large-vessel occlusions with high rates of successful reperfusion and, consequently, an increasing occurrence of isolated basal ganglia infarction. To adequately address these different subgroups of infarction patterns and severity, we performed subgroup analyses.

The association of CST integrity with clinical outcome was predominantly based on the subgroup of peripheral infarcts. For BGIs, which are increasingly common in the era of mechanical recanalization, this relation could not be observed. Within the subgroup of peripheral infarcts, a further subdivision based on infarction severity was made, showing a nearly linear impairment of CST integrity and clinical presentation in relation to infarction severity as expected. Furthermore, the impact of infarction severity on the clinical outcome at day 90 was mediated by the FA index,

shown by a statistically significant reduction of the association between infarction severity and outcome. It implies that CST integrity changes within the PLIC can partially explain this relationship, but the still visible effect of infarction severity on mRS suggests that the FA index is not the only mediator. Possibly other structural integrity changes, eg, within the extrapyramidal system,¹⁹ could also have an influence, requiring further research in this field.

Several studies exist that aim to examine the role of DTI in predicting motor recovery after stroke, inspired by the limitations of using clinical scores alone.¹⁶ Conventional imaging does not have the potential to detect CST damage accurately, especially when the CST is not apparently infarcted. Thus, most studies used DTI with FA calculations to characterize microstructural fiber integrity.^{17,18,27-33} Identifying the voxels of the individual CST fibers by probabilistic fiber-tracking is accurate. This technique was used in the present study in combination with FA assessment within a specific tract section (PLIC), which was atlas-based. The FA index that is equivalent to the FA asymmetry as part of the predicting recovery potential was used as a most popular predictor variable in previous DTI studies and showed a good association to clinical parameters,^{16,29,34} providing the rationale for applying it in the present study.

Most previous studies about CST integrity were performed in the subacute or chronic stage of stroke and showed lower FA values in the affected CST because of the beginning of Wallerian degeneration.^{32,35-37} These integrity alterations measured by FA asymmetry have a particular impact in the subacute and chronic stages because they are associated with the persistence of motor deficit.^{36,38} In the present study, the grade of CST alterations of peripheral infarcts early after mechanical recanalization was shown to correlate with the functional outcome of patients after 90 days. These results give the first evidence for using the information of fiber integrity in the acute poststroke phase for outcome predictions. This could be helpful for the patients and relatives, eg, concerning post-inpatient management. Indeed, further studies about imaging biomarkers are necessary, especially with the aim of adapting rehabilitative and follow-up strategies in the long term.

To our knowledge, a subdivision in different stroke subtypes for structural analyses, especially in the acute poststroke phase, has not been reported. Similar FA indices of the CST within the PLIC are found for the BGI and peripheral infarcts, but the BGI do not show a correlation to the clinical parameters that are collected within the clinical routine. In contrast to peripheral infarcts with secondary disintegration of dependent fibers, BGIs do not show any gray matter infarction of the cortex regions representing the fiber origins (except possibly microstructural changes that were not assessed). FA alterations within the PLIC may be based on subtle direct white matter damage or perilesional edema, which cannot be visualized without DTI, or an increase in cellularity secondary to inflammation. These tract alterations with intact primary gray matter might be partially reversible or could constitute a better precondition for secondary brain plasticity processes in the reconstitution of motor regulation. This feature could explain the lack of correlation with clinical parameters and midterm functional outcome in the present study. However, the missing correlation might also be influenced by the structure of the underlying data: The subgroup of BGI

($n = 59$) is smaller, implying less statistical power than in the subgroup of peripheral infarcts ($n = 106$). Second, due to good clinical performance of patients with BGI, their mNIHSS scores have a small range, influencing the validity of a correlation analysis.

Both the interpretation and the limitations of the BGI analysis raise the challenge to further examine BGIs, their clinical presentation, and their pathophysiologic role in future studies, because the BGI entity presents with a wide interindividual variability and heterogeneity.³⁹

A limitation of the present study is that only common clinical parameters such as the NIHSS score, motor subindex scores, and the mRS were collected, but a large collective of almost all treated patients at a single comprehensive stroke center was included. These clinical parameters are assessed in the clinical routine for all patients independent of their condition or compliance, avoiding bias within the study cohort. However, especially the lack of motor assessment at 3 months reduces the validity concerning long-term outcome predictions. A further limitation is the lack of inclusion of patients with an incompatibility for an MR imaging examination. Additionally, these patients often present with extended ischemia or space-consuming hemorrhage, which makes a DTI analysis impossible. This subgroup of patients with distinctly worse outcome is missing in the analysis.

Further limitations of the study depend on the known technical limitations and validity of DTI, which cannot differentiate between direct white matter disintegration because of myelin sheath damage or axon collapse or processes that occur adjacent to the fibers such as inflammation or edema. These differences could impact the results of the present study that possibly differentiate these processes arising from pathophysiologic considerations of the different stroke subtypes. Additionally, DTI protocol could be improved for the future studies concerning b-values and the number of directions. The low b-value limits the accuracy of the DTI metrics and, secondarily, incurs the risk of imprecise measurements. The results should be verified in follow-up studies using the latest DTI technology and longitudinal examinations in the course of ischemia.

CONCLUSIONS

Microstructural CST alterations within the PLIC are already present in an early stage after mechanical recanalization of large intracranial vessel occlusions of the anterior circulation. For peripheral infarcts, these white matter changes can be interpreted as fiber disintegration and are associated with clinical outcome. These might be useful for the early adaptation of rehabilitative and follow-up strategies. In contrast, basal ganglia infarction showed a better clinical course, and also its distinct CST alterations were not associated with patient outcome. That association requires further and longitudinal exploration of fiber integrities to examine their reversibility and potential for neuroplasticity processes.

Disclosures: Johannes Kaesmacher—UNRELATED; Grants/Grants Pending: Swiss Academy of Medical Sciences through the Young Talents in Clinical Research program/Bangerter-Rhyner Foundation, Swiss Stroke Society.* *Money paid to institution.

REFERENCES

1. Roger VL, Go AS, Lloyd-Jones DM, et al; American Heart Association Statistics Committee and Stroke Statistics Subcommittee. **Heart disease and stroke statistics—2012 update: a report from the**

- American Heart Association. *Circulation* 2012;125:e2–20 CrossRef Medline
2. Hendricks HT, van Limbeek J, Geurts AC, et al. **Motor recovery after stroke: a systematic review of the literature.** *Arch Phys Med Rehabil* 2002;83:1629–37 CrossRef Medline
 3. Prabhakaran S, Zarahn E, Riley C, et al. **Inter-individual variability in the capacity for motor recovery after ischemic stroke.** *Neurorehabil Neural Repair* 2008;22:64–71 CrossRef Medline
 4. Bach-y-Rita P, Bach-y-Rita EW. **Biological and psychosocial factors in recovery from brain damage in humans.** *Can J Psychol* 1990;44:148–65 CrossRef Medline
 5. Puig J, Pedraza S, Blasco G, et al. **Acute damage to the posterior limb of the internal capsule on diffusion tensor tractography as an early imaging predictor of motor outcome after stroke.** *AJNR Am J Neuroradiol* 2011;32:857–63 CrossRef Medline
 6. Shelton FD, Volpe BT, Reding M. **Motor impairment as a predictor of functional recovery and guide to rehabilitation treatment after stroke.** *Neurorehabil Neural Repair* 2001;15:229–37 CrossRef Medline
 7. Feys H, Hetebrij J, Wilms G, et al. **Predicting arm recovery following stroke: value of site of lesion.** *Acta Neurol Scand* 2000;102:371–77 CrossRef Medline
 8. Kwakkel G, Kollen BJ, van der Grond J, et al. **Probability of regaining dexterity in the flaccid upper limb: impact of severity of paresis and time since onset in acute stroke.** *Stroke* 2003;34:2181–86 CrossRef Medline
 9. Chen CL, Tang FT, Chen HC, et al. **Brain lesion size and location: effects on motor recovery and functional outcome in stroke patients.** *Arch Phys Med Rehabil* 2000;81:447–52 CrossRef Medline
 10. Stinear CM, Byblow WD, Ackerley SJ, et al. **Proportional motor recovery after stroke: implications for trial design.** *Stroke* 2017;48:795–98 CrossRef Medline
 11. Smith MC, Byblow WD, Barber PA, et al. **Proportional recovery from lower limb motor impairment after stroke.** *Stroke* 2017;48:1400–03 CrossRef Medline
 12. Nijland RH, van Wegen EE, Harmeling-van der Wel BC, et al; Early Prediction of Functional Outcome After Stroke Investigators. **Accuracy of physical therapists' early predictions of upper-limb function in hospital stroke units: the EPOS Study.** *Phys Ther* 2013;93:460–69 CrossRef Medline
 13. Zhu LL, Lindenberg R, Alexander MP, et al. **Lesion load of the corticospinal tract predicts motor impairment in chronic stroke.** *Stroke* 2010;41:910–15 CrossRef Medline
 14. Lindenberg R, Renga V, Zhu LL, et al. **Structural integrity of corticospinal motor fibers predicts motor impairment in chronic stroke.** *Neurology* 2010;74:280–87 CrossRef Medline
 15. Nucifora PG, Verma R, Lee SK, et al. **Diffusion-tensor MR imaging and tractography: exploring brain microstructure and connectivity.** *Radiology* 2007;245:367–84 CrossRef Medline
 16. Puig J, Blasco G, Schlaug G, et al. **Diffusion tensor imaging as a prognostic biomarker for motor recovery and rehabilitation after stroke.** *Neuroradiology* 2017;59:343–51 CrossRef Medline
 17. Thomalla G, Glauche V, Koch MA, et al. **Diffusion tensor imaging detects early Wallerian degeneration of the pyramidal tract after ischemic stroke.** *Neuroimage* 2004;22:1767–74 CrossRef Medline
 18. Puig J, Pedraza S, Blasco G, et al. **Wallerian degeneration in the corticospinal tract evaluated by diffusion tensor imaging correlates with motor deficit 30 days after middle cerebral artery ischemic stroke.** *AJNR Am J Neuroradiol* 2010;31:1324–30 CrossRef Medline
 19. Leander Rimmele D, Frey BM, Cheng B, et al. **Association of extrapyramidal tracts' integrity with performance in fine motor skills after stroke.** *Stroke* 2018;49:2928–32 CrossRef Medline
 20. Lin DJ, Cloutier AM, Erler KS, et al. **Corticospinal tract injury estimated from acute stroke imaging predicts upper extremity motor recovery after stroke.** *Stroke* 2019;50:3569–77 CrossRef Medline
 21. Albers GW, Marks MP, Kemp S, et al; DEFUSE 3 Investigators. **Thrombectomy for stroke at 6 to 16 hours with selection by perfusion imaging.** *N Engl J Med* 2018;378:708–18 CrossRef Medline
 22. Nogueira RG, Jadhav AP, Haussen DC, et al; DAWN Trial Investigators. **Thrombectomy 6 to 24 hours after stroke with a mismatch between deficit and infarct.** *N Engl J Med* 2018;378:11–21 CrossRef Medline
 23. Zaidat OO, Yoo AJ, Khatri P, et al; STIR Thrombolysis in Cerebral Infarction (TICI) Task Force. **Recommendations on angiographic revascularization grading standards for acute ischemic stroke: a consensus statement.** *Stroke* 2013;44:2650–63 CrossRef Medline
 24. Barber PA, Hill MD, Eliasziw M, et al; ASPECTS Study Group. **Imaging of the brain in acute ischaemic stroke: comparison of computed tomography and magnetic resonance diffusion-weighted imaging.** *J Neurol Neurosurg Psychiatry* 2005;76:1528–33 CrossRef Medline
 25. Fahed R, Lecler A, Sabben C, et al. **DWI-ASPECTS (Diffusion-Weighted Imaging-Alberta Stroke Program Early Computed Tomography Scores) and DWI-FLAIR (Diffusion-Weighted Imaging-Fluid Attenuated Inversion Recovery) mismatch in thrombectomy candidates: an intrarater and interrater agreement study.** *Stroke* 2018;49:223–27 CrossRef Medline
 26. Jenkinson M, Beckmann CF, Behrens TE, et al. **FSL.** *Neuroimage* 2012;62:782–90 CrossRef Medline
 27. Byblow WD, Stinear CM, Barber PA, et al. **Proportional recovery after stroke depends on corticomotor integrity.** *Ann Neurol* 2015;78:848–59 CrossRef Medline
 28. Puig J, Blasco G, Daunis IE, et al. **Decreased corticospinal tract fractional anisotropy predicts long-term motor outcome after stroke.** *Stroke* 2013;44:2016–18 CrossRef Medline
 29. Stinear CM, Barber PA, Petoe M, et al. **The PREP algorithm predicts potential for upper limb recovery after stroke.** *Brain* 2012;135:2527–35 CrossRef Medline
 30. Kumar P, Kathuria P, Nair P, et al. **Prediction of upper limb motor recovery after subacute ischemic stroke using diffusion tensor imaging: a systematic review and meta-analysis.** *J Stroke* 2016;18:50–59 CrossRef Medline
 31. Lindenberg R, Zhu LL, Ruber T, et al. **Predicting functional motor potential in chronic stroke patients using diffusion tensor imaging.** *Hum Brain Mapp* 2012;33:1040–51 CrossRef Medline
 32. Stinear CM, Barber PA, Smale PR, et al. **Functional potential in chronic stroke patients depends on corticospinal tract integrity.** *Brain* 2007;130:170–80 CrossRef Medline
 33. Schaechter JD, Fricker ZP, Perdue KL, et al. **Microstructural status of ipsilesional and contralesional corticospinal tract correlates with motor skill in chronic stroke patients.** *Hum Brain Mapp* 2009;30:3461–74 CrossRef Medline
 34. Doughty C, Wang J, Feng W, et al. **Detection and predictive value of fractional anisotropy changes of the corticospinal tract in the acute phase of a stroke.** *Stroke* 2016;47:1520–26 CrossRef Medline
 35. Werring DJ, Toosy AT, Clark CA, et al. **Diffusion tensor imaging can detect and quantify corticospinal tract degeneration after stroke.** *J Neurol Neurosurg Psychiatry* 2000;69:269–72 CrossRef Medline
 36. Moller M, Frandsen J, Andersen G, et al. **Dynamic changes in corticospinal tracts after stroke detected by fibretracking.** *J Neurol Neurosurg Psychiatry* 2007;78:587–92 CrossRef Medline
 37. Radlinska B, Ghinani S, Leppert IR, et al. **Diffusion tensor imaging, permanent pyramidal tract damage, and outcome in subcortical stroke.** *Neurology* 2010;75:1048–54 CrossRef Medline
 38. Watanabe T, Honda Y, Fujii Y, et al. **Three-dimensional anisotropy contrast magnetic resonance axonography to predict the prognosis for motor function in patients suffering from stroke.** *J Neurosurg* 2001;94:955–60 CrossRef Medline
 39. Kaesmacher J, Huber T, Lehm M, et al. **Isolated striatocapsular infarcts after endovascular treatment of acute proximal middle cerebral artery occlusions: prevalence, enabling factors, and clinical outcome.** *Front Neurol* 2017;8:272 CrossRef Medline

Diffusion Tensor Imaging for Predicting the Outcome of Large-Vessel Ischemic Stroke Treated with Mechanical Thrombectomy: Is This the Prime Time?

DTI uses the physical principles of random displacement of water molecules, also known as Brownian motion, to measure the degree and directionality of water molecule motion in the human body.¹ These measurements can be used to infer the microstructural integrity of the underlying tissue. In the brain healthy WM, cellular membranes, with some contribution from myelination and the packing of axons, skew the directionality of water diffusion, making it less uniform “i.e. anisotropic.”² Hence, lower fractional anisotropy (FA) measures have been found to reflect impairment of the WM microstructure.³ Since its introduction in the early 1990s, the rapid development of postprocessing techniques has led to widespread application of DTI in the various neurologic fields of study. For example, DTI has been successfully used to detect WM damage in traumatic brain injury,⁴ cerebral small-vessel disease,⁵ multiple sclerosis, and others.⁶ In the field of ischemic stroke, brain MR imaging, in particular DWI, has been instrumental in advancing the field with critical roles spanning from early detection of ischemic changes and patient selection for endovascular therapy to prognostication of functional outcome.⁷⁻⁹ Indeed, larger DWI infarct volume has been associated with worse functional outcome after acute ischemic stroke. The introduction of mechanical thrombectomy in the management of patients with acute ischemic stroke, however, has significantly improved the functional outcome of patients with stroke with reduction in the associated infarct volume.⁸ In particular, after mechanical thrombectomy, infarction of the basal ganglia, secondary to the involvement of the perforator arteries that originate from the middle cerebral artery with sparing of the peripheral cortex, is now frequently encountered. Recent work has confirmed the role of the corticospinal tract (CST) injury by stroke in predicting motor recovery of the upper extremity.¹⁰ In this previous work, however, CST was mapped through the existing brain templates without direct measurement of its microstructural integrity. Hence, there is a need in the current thrombectomy era to better understand the outcomes of these patients and to guide selection in rehabilitation studies. DTI offers a sensitive tool that can address this dilemma by mapping the WM tracts, particularly the CST. Preliminary evidence of

small studies suggests that DTI is suitable for this purpose.¹¹ However, there remains a knowledge gap regarding the role of DTI in patients with stroke who are treated with mechanical thrombectomy.

In the article by Berndt et al,¹² the authors aim to answer this question by addressing the role of DTI in predicting the 3-month functional outcomes of patients with acute ischemic stroke caused by large-vessel occlusion in the anterior circulation who underwent mechanical thrombectomy. The study sample included 165 patients who had DTI sequences acquired within 7 days of stroke (median, 3 days). Probabilistic tractography was used to map the CST bilaterally, and atlas-based ROIs were used to characterize the CST in the posterior limb of the internal capsule (PLIC) and cerebral peduncle. Subsequently, the FA index was calculated for the PLIC and cerebral peduncle of the infarcted brain compared with healthy, nonaffected CST. The brain infarct was divided into the basal ganglia infarction (BGI) subgroup without relevant involvement of the cortical structures and the peripheral infarct subgroup in which the infarct involved the surrounding cortical areas. The latter's severity was further classified as mild, middle, or high, based on the peripheral territory involvement by the stroke that was originated from the Alberta Stroke Program Early CT Score (ASPECTS) of the DWI sequences. Good clinical functional outcome was defined by modified Rankin Scale score ≤ 2 at 90 days.

The main results of this work confirm the lower FA index values of the CST on the stroke-affected side of the PLIC. Additionally, although there was no difference in the FA index of the CST between the BGI subgroup and the peripheral infarct subgroup, the latter subgroup showed a significantly higher FA index of the CST of the PLIC in those with mild infarction severity compared with middle or high infarction severity. Furthermore, in this subgroup, there were statistically significant negative correlations between the motor subindex of the National Institute of Health Stroke Scale (sum of arm and leg symptom value of the affected side) at the time of brain MR imaging and the FA index of the PLIC. From a long-term functional outcome standpoint, the FA index of the CST in the PLIC was significantly

associated with good clinical outcomes in the study cohort. Although this effect was not seen in the BGI subgroup, a strong effect of the FA index on clinical outcome existed in the peripheral infarct subgroup. Finally, in mediation analysis, the effect of the infarction severity in the peripheral infarction subgroup on the 90-day functional outcome was present but reduced when controlling for the FA index of the CST, indicating that the FA index mediated the relationship between infarction severity and clinical outcome.

There are several notable accomplishments of this study. First, the sample size is relatively large, and the study population is homogeneous by including only patients with large-vessel occlusion stroke who were treated with mechanical thrombectomy. Second, the study ascertained the sensitivity of the FA index of the PLIC as an early measure of acute injury of CST in the setting of stroke. Third, the FA index of CST in the PLIC was also found to be a measure of the magnitude of motor deficit in the acute stroke phase in those with peripheral cortical stroke involvement. Finally, the FA index of the CST was associated with long-term functional outcome of acute ischemic stroke. Taken together, these results suggest that the FA index of the PLIC is a sensitive marker for acute CST injury after stroke, and it may represent a marker of long-term functional recovery.

This study, however, has several limitations. First, it did not include an accurate measure of the motor function acutely or at 3 months. Second, the degree of involvement of the peripheral cortical areas was measured through a categoric score rather than accurately segmenting the stroke area to assess the degree of anatomic overlap with the CST. Third, the study did not include a repeat DTI scan at 3 months to assess whether the improvement of functional outcome coincided with improvement on the FA index of the CST. Finally, the underlying causes of impairment of the microstructural integrity of the CST cannot be ascertained; it is unknown whether it is caused by tissue necrosis from stroke, edema, or Wallerian degeneration. Knowing the cause is necessary to understand the reversibility of the CST injury.

In summary, although the current study is a step forward in incorporating DTI into the clinical care of patients with stroke, several important questions first need to be resolved in large prospective studies to achieve this goal. These include, among many others, determining the relevant WM tracts for recovery, defining the critical FA thresholds of the necessary tracts for motor and functional improvement, characterizing types and location of injury, and selecting patients who will benefit from rehabilitation. Addressing these important questions will bring DTI closer for application in the daily care of patients with ischemic stroke. When combined with other genetic and serologic biomarkers of recovery, this will enable physicians to accurately predict the

functional outcome of acute ischemic stroke through personalized medicine.¹³ Advanced imaging acquisition and analytics, including DTI, are at the forefront of these efforts, and they are ready to be tested in large multicenter clinical trials.

Conflict of Interest

Author reports no conflicts of interests in relationship to this work.

REFERENCES

1. Yang E, Nucifora PG, Melhem ER. **Diffusion MR imaging: basic principles.** *Neuroimaging Clin N Am* 2011;21:1–25, vii CrossRef Medline
2. O'Donnell LJ, Westin CF. **An introduction to diffusion tensor image analysis.** *Neurosurg Clin N Am* 2011;22:185–96, viii CrossRef Medline
3. Tournier JD, Mori S, Leemans A. **Diffusion tensor imaging and beyond.** *Magn Reson Med* 2011;65:1532–56 CrossRef Medline
4. Asken BM, DeKosky ST, Clugston JR, et al. **Diffusion tensor imaging (DTI) findings in adult civilian, military, and sport-related mild traumatic brain injury (mTBI): a systematic critical review.** *Brain Imaging Behav* 2018;12:585–612 CrossRef Medline
5. Hannawi Y, Yanek LR, Kral BG, et al. **Hypertension is associated with white matter disruption in apparently healthy middle-aged individuals.** *AJNR Am J Neuroradiol* 2018;39:2243–48 CrossRef Medline
6. Tae WS, Ham BJ, Pyun SB, et al. **Current clinical applications of diffusion-tensor imaging in neurological disorders.** *J Clin Neurol* 2018;14:129–40 CrossRef Medline
7. Bang OY, Li W. **Applications of diffusion-weighted imaging in diagnosis, evaluation, and treatment of acute ischemic stroke.** *Precis Future Med* 2019;3:69–76 CrossRef
8. Albers GW, Marks MP, Kemp S, et al. **Thrombectomy for stroke at 6 to 16 hours with selection by perfusion imaging.** *N Engl J Med* 2018;378:708–18 CrossRef Medline
9. Thomalla G, Simonsen CZ, Boutitie F, et al. **MRI-guided thrombolysis for stroke with unknown time of onset.** *N Engl J Med* 2018;379:611–22 CrossRef Medline
10. Lin DJ, Cloutier AM, Erler KS, et al. **Corticospinal tract injury estimated from acute stroke imaging predicts upper extremity motor recovery after stroke.** *Stroke* 2019;50:3569–77 CrossRef Medline
11. Puig J, Blasco G, Schlaug G, et al. **Diffusion tensor imaging as a prognostic biomarker for motor recovery and rehabilitation after stroke.** *Neuroradiology* 2017;59:343–51 CrossRef Medline
12. Berndt MT, Purner D, Maegerlein C, et al. **Basal ganglia versus peripheral infarcts: predictive value of early fiber alterations.** *AJNR Am J Neuroradiol* 2020;42:264–70 CrossRef Medline
13. Hinman JD, Rost NS, Leung TW, et al. **Principles of precision medicine in stroke.** *J Neurol Neurosurg Psychiatry* 2017;88:54–61 CrossRef Medline

Y. Hannawi

Division of Cerebrovascular Diseases and Neurocritical Care
Department of Neurology, The Ohio State University
Columbus, Ohio

<http://dx.doi.org/10.3174/ajnr.A7026>

Automated Cerebral Hemorrhage Detection Using RAPID

J.J. Heit, H. Coelho, F.O. Lima, M. Granja, A. Aghaebrahim, R. Hanel, K. Kwok, H. Haerian, C.W. Cereda, C. Venkatasubramanian, S. Dehkharghani, L.A. Carbonera, J. Wiener, K. Copeland, and F. Mont'Alverne



ABSTRACT

BACKGROUND AND PURPOSE: Intracranial hemorrhage (ICH) is an important event that is diagnosed on head NCCT. Increased NCCT utilization in busy hospitals may limit timely identification of ICH. RAPID ICH is an automated hybrid 2D–3D convolutional neural network application designed to detect ICH that may allow for expedited ICH diagnosis. We determined the accuracy of RAPID ICH for ICH detection and ICH volumetric quantification on NCCT.

MATERIALS AND METHODS: NCCT scans were evaluated for ICH by RAPID ICH. Consensus detection of ICH by 3 neuroradiology experts was used as the criterion standard for RAPID ICH comparison. ICH volume was also automatically determined by RAPID ICH in patients with intraparenchymal or intraventricular hemorrhage and compared with manually segmented ICH volumes by a single neuroradiology expert. ICH detection accuracy, sensitivity, specificity, positive predictive value, negative predictive value, and positive and negative likelihood ratios by RAPID ICH were determined.

RESULTS: We included 308 studies. RAPID ICH correctly identified 151/158 ICH cases and 143/150 ICH-negative cases, which resulted in high sensitivity (0.956, CI: 0.911–0.978), specificity (0.953, CI: 0.907–0.977), positive predictive value (0.956, CI: 0.911–0.978), and negative predictive value (0.953, CI: 0.907–0.977) for ICH detection. The positive likelihood ratio (20.479, CI 9.928–42.245) and negative likelihood ratio (0.046, CI 0.023–0.096) for ICH detection were similarly favorable. RAPID ICH volumetric quantification for intraparenchymal and intraventricular hemorrhages strongly correlated with expert manual segmentation (correlation coefficient $r = 0.983$); the median absolute error was 3 mL.

CONCLUSIONS: RAPID ICH is highly accurate in the detection of ICH and in the volumetric quantification of intraparenchymal and intraventricular hemorrhages.

ABBREVIATIONS: CNN = convolutional neural network; ICH = intracranial hemorrhage; LR = likelihood ratio; NPV = negative predictive value; PPV = positive predictive value

Intracranial hemorrhage (ICH) secondary to trauma, cerebrovascular disease, tumors, coagulation disorders, and other disorders results in significant morbidity and mortality.^{1–3} The volume and severity of ICH at presentation correlate with neurologic status and likelihood of survival,^{4,5} and prompt medical and surgical intervention have been shown to reduce the mortality

rate associated with ICH.^{6,7} Therefore, accurate and timely ICH diagnosis is essential for patient treatment, and prompt detection and interpretation of ICH on NCCT are necessary. Excluding acute ICH is also a critical component of the evaluation of patients with stroke for IV thrombolysis.

The presentation of ICH is often nonspecific, and ICH is most commonly diagnosed on head NCCT.² Prompt NCCT interpretation in busy emergency departments and hospitals remains challenging, and interpretation delays may result in patient care delays, which can lead to poor outcomes.⁸ Triage software that identifies ICH, estimates ICH volume, and alerts radiologists and clinicians would streamline patient care and

Received May 29, 2020; accepted after revision September 13.

From the Department of Radiology, Neuroimaging and Neurointervention Division (J.J.H.), Stanford University School of Medicine, Stanford, California; Interventional Radiology Service (H.C., F.M.) and Department of Neurology (F.O.L.), Hospital Geral de Fortaleza, R. Ávila Goulart, Fortaleza, Brazil; Baptist Neurological Institute (M.G., A.A., R.H.), Lyerly Neurosurgery/Baptist Health, Jacksonville, Florida; Diagnostic Imaging Department (M.G., A.A., R.H.), Fundación Santa Fe de Bogota University Hospital, Bogotá, Colombia; Department of Radiology (K.K.), Central Valley Imaging Medical Associates, Manteca, California; Department of Radiology (H.H.), LifeBridge Health, Baltimore, Maryland; Department of Neurology (C.W.C.), EOC Ospedale Regionale di Lugano, Lugano, Switzerland; Neurocritical Care and Stroke, Department of Neurology (C.V.), Stanford University, Palo Alto, California; Department of Radiology (S.D.), NY University Langone Health, New York, New York; Hospital das Clínicas de Porto Alegre (L.A.C.), Bairro Santa Cecilia, Brazil; Department of Radiology (J.W.), Boca Raton Regional Hospital, Boca Raton, Florida; and Boulder Statistics (K.C.), Steamboat Springs, Colorado.

Please address correspondence to Jeremy J. Heit, MD, PhD, 300 Pasteur Dr, Room S-047, Stanford, CA 94305; e-mail: jheit@stanford.edu; @JeremyHeitMDPHD

Indicates article with supplemental online tables.

Indicates article with supplemental online photo.

<http://dx.doi.org/10.3174/ajnr.A6926>

increase diagnostic confidence. Deep learning convolutional neural networks (CNNs) represent a technology for automated imaging interpretation that has shown promise in the detection of ICH and other cerebral emergencies.⁹⁻¹⁴ However, this technology has not yet been adopted in widespread clinical practice.

Table 1: Patient demographic details

	All	ICH-	ICH+	P Value ^a
Sex				
Female, n (%)	117 (38.0)	53 (33.5)	64 (42.7)	<.0002
Male, n (%)	164 (53.3)	81 (51.3)	83 (55.3)	
Unknown, n (%)	27 (8.8)	24 (15.2)	3 (2.0)	
Age				
20-39 years, n (%)	33 (10.9)	15 (9.9)	18 (12.0)	.5692
40-59 years, n (%)	78 (25.8)	43 (28.3)	35 (23.3)	
60+ years, n (%)	191 (63.3)	94 (61.8)	97 (64.7)	

^a For a Pearson chi-square test of independence.

Table 2: Performance of RAPID for ICH detection

RAPID vs Consensus Truth		Consensus = Truth		Total
n = 308		1 (positive)	0 (negative)	
RAPID	1 (positive)	151	7	158
	0 (negative)	7	143	150
	Total	158	150	308

RAPID ICH (iSchemaView) is an artificial intelligence software program developed to identify acute ICH and determine ICH on NCCT studies. RAPID ICH builds on the widely used RAPID software platform for the detection of cerebral ischemia in patients with large-vessel occlusions¹⁵⁻¹⁸ and is readily adaptable to the RAPID mobile triage platform, which is currently used for triage of patients with ischemic stroke to thrombectomy.

In this study, we tested whether RAPID ICH can accurately detect and volumetrically quantify ICH.

MATERIALS AND METHODS

The data that support the findings of this study are available from the corresponding author upon reasonable request.

Patient Cohort and Image Acquisition

This retrospective cohort study complied with the Health Insurance Portability and Accountability Act. Institutional review board approval was obtained at each site, and the need for informed consent was waived. NCCTs were obtained from 6 institutions. Only NCCTs that were free of significant motion artifact were included for analysis.

NCCT studies from multiple vendors (Online Table 1) were acquired in the axial plane with section thickness that ranged from 1 to 5 mm. Radiation doses varied by vendor and location, and these variables were not controlled for in this study, which was intended

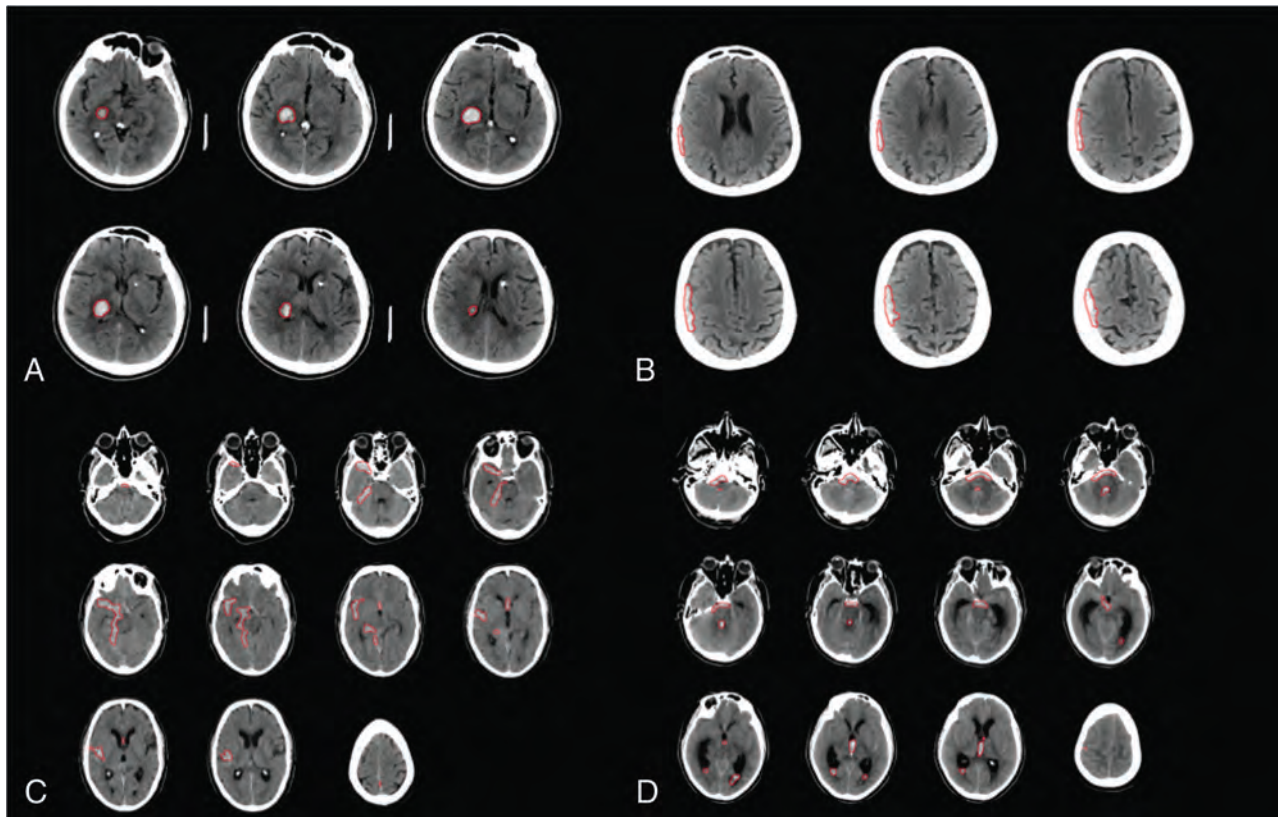


FIG 1. Representative imaging examples of ICH correctly detected by RAPID. A. Primary intraparenchymal hemorrhage within the right thalamus and posterior limb of the right internal capsule (red outline by RAPID). B. Small extra-axial subdural hematoma overlying the right cerebral hemisphere (red outline by RAPID). C. Subarachnoid hemorrhage (red outline by RAPID). D. Subarachnoid and intraventricular (right and left lateral, third, and fourth ventricles) hemorrhage (red outline by RAPID).

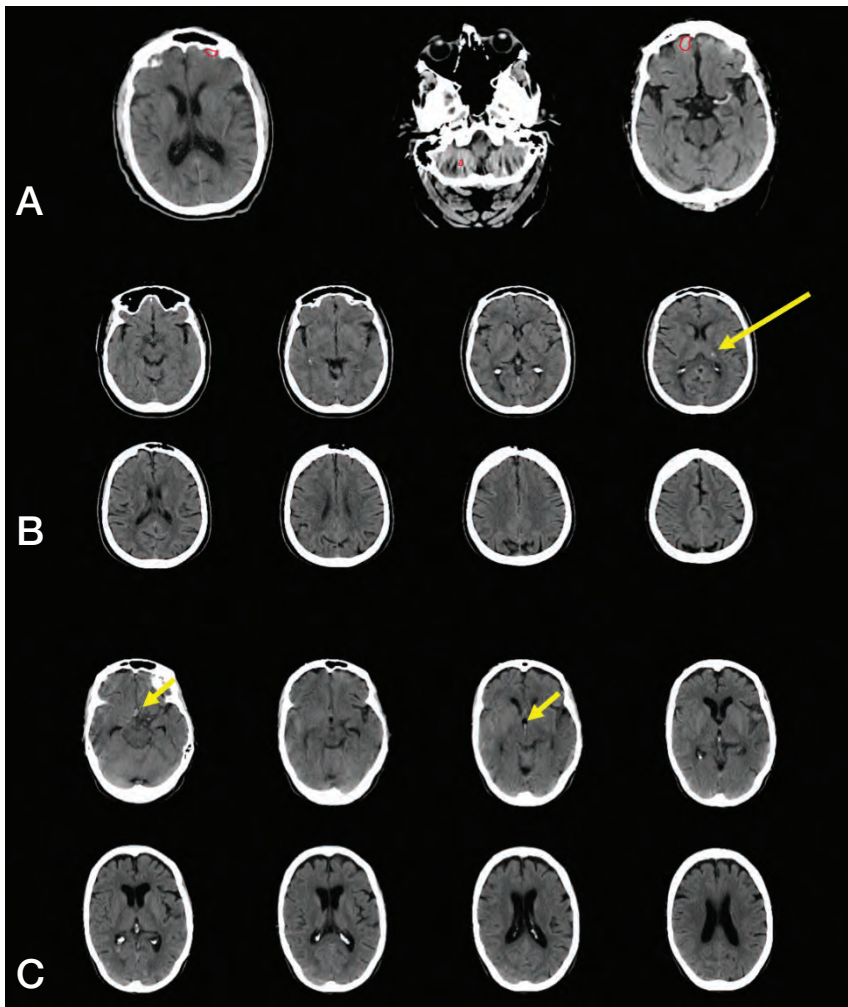


FIG 2. Representative false-positive and false-negative ICH examples. A. RAPID incorrectly detected ICH (false-positive result) in a patient with volume averaging in the anterior cranial fossa and beam-hardening artifact in the posterior fossa (red outlines by RAPID). B. RAPID failed to detect ICH (false-negative result) in a patient intraparenchymal hemorrhage in the left thalamus (yellow arrow). C. RAPID failed to detect ICH (false-negative result) in a patient with a small amount of subarachnoid and intraventricular hemorrhage (yellow arrows).

Table 3: RAPID ICH performance

Measure	Estimate	Lower 95% CI	Upper 95% CI
Prevalence	0.513	0.457	0.568
Sensitivity	0.956	0.911	0.978
Specificity	0.953	0.907	0.977
PPV	0.956	0.911	0.978
NPV	0.953	0.907	0.977
Positive LR	20.479	9.928	42.245
Negative LR	0.046	0.023	0.096

to sample variations in standard radiology practices. Images were not tilt corrected or otherwise manipulated before interpretation by the neuroradiologists in the study. Studies with significant metal or motion artifact were excluded from the analysis.

RAPID Machine Learning ICH Detection

A deep CNN with a hybrid 2D–3D architecture was trained on a cohort of 805 NCCT examinations. All head CTs analyzed by

RAPID ICH were postprocessed into 5-mm-thick axial slices, and 48 images per study were analyzed by the training dataset. If CT source data were acquired with a thickness of <5 mm, images were merged and averaged into 5-mm thickness before analysis. The training dataset included NCCT with intraparenchymal hemorrhage (245 cases; 30%), intraventricular hemorrhage (83 cases; 10%), extra-axial hemorrhage (70 cases, 9%), subarachnoid hemorrhage (67 cases, 8%), and no hemorrhage (457 cases, 57%). Regions of ICH were manually outlined by neuroradiology experts and stored as binary masks that were used as ground truth for the training analysis. Ground truth masks were randomly split into training (80%) and testing (20%) groups.

After training, the ICH detection module was prototyped in Python/Keras and implemented on a Linux server (4 CPUs) that was embedded on a larger imaging platform dedicated to ischemic stroke analysis (iSchemaView).

Additional details of the CNN are presented in Online Figure.

RAPID ICH Validation Study Design

The RAPID ICH module was validated in a different and independent dataset of 308 adult patients that included 158 patients with ICH (52%) and 150 patients without ICH (48%). The reference standard or truth was determined by consensus among 3 expert neuroradiologists who reviewed NCCT images via Horos (Horos Project, version 3.3) or Osirix (Pixmeo, version 11). Neuroradiologists had full control over window width and

levels for all images and were blinded to RAPID ICH results.

The primary end point was the detection of any ICH, which included intraparenchymal, subdural, epidural, subarachnoid, and intraventricular hemorrhages, and ICH presence was recorded in a binary manner (present [ICH+] or absent [ICH–]). Most subdural hemorrhages were acute, but some had subacute or chronic components. Epidural and subdural hemorrhage are collectively referred to as extra-axial hemorrhage.

The secondary end point was ICH volume for isolated intraparenchymal and intraventricular hemorrhages. The reference standard ICH volume was determined by manual segmentation by a single neuroradiologist and verification by a second neuroradiologist. Manual segmentation was performed on axial images. Regions of confluent hyperattenuation that were consistent with intraparenchymal or intraventricular hemorrhage were outlined on all images and volumetrically quantified in Osirix (Pixmeo, version 11).

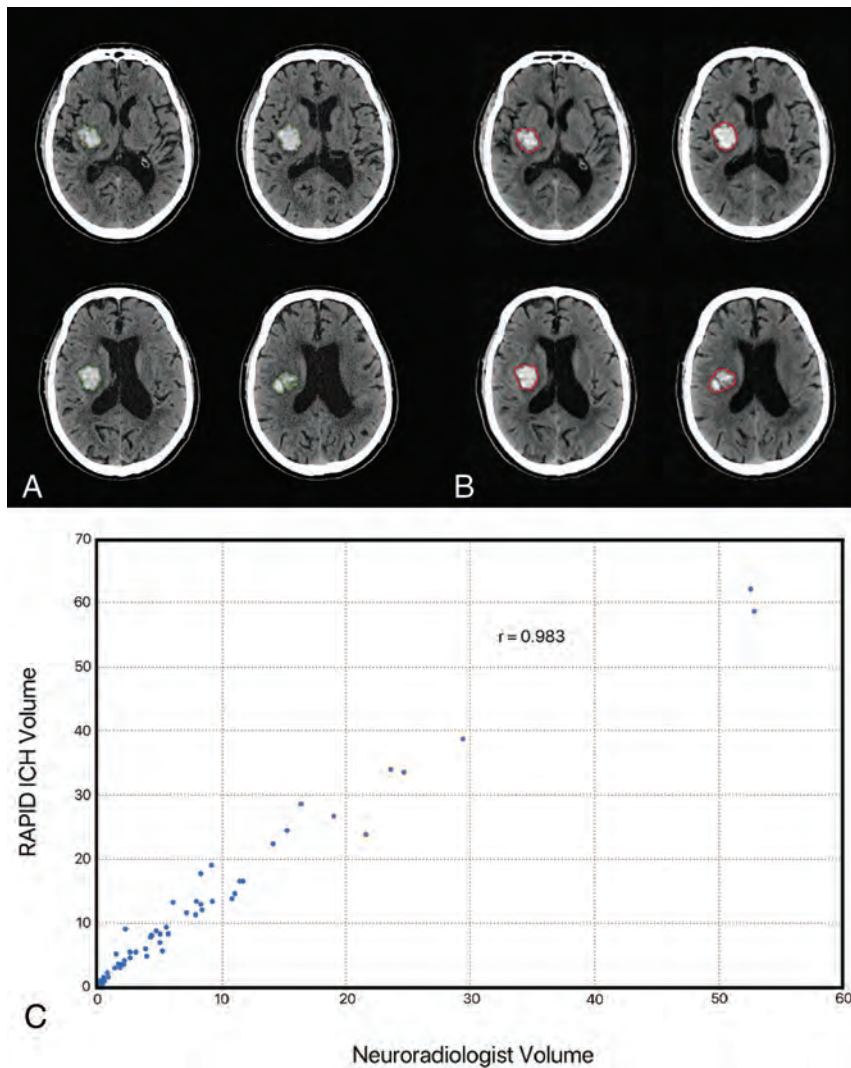


FIG 3. Intraparenchymal and intraventricular hemorrhage volumetric agreement between RAPID and expert interpretation. A and B, Representative example of an intraparenchymal hemorrhage in the right basal ganglia. Manual segmentation by a neuroradiologist (A, green outline) is well correlated with automated segmentation by RAPID ICH (B, red outline). C, Scatterplot denotes volumetric agreement between RAPID and expert evaluation for NCCT with isolated intraparenchymal or intraventricular hemorrhage.

Statistical Analysis

Sensitivity, specificity, positive predictive value (PPV), negative predictive value (NPV), positive likelihood ratio (LR), and negative LR were calculated by comparison of RAPID identification of ICH+ studies compared with the reference standard ICH+. All statistical analyses were performed using JMP Pro 15 (SAS Institute).

RESULTS

A total of 308 NCCTs were included in the validation study. NCCT was acquired from 5 CT vendors (Online Table 1), distributed across the ICH- and ICH+ studies. After training, the processing time for RAPID's ICH detection module was <3 minutes per study.

NCCT was derived from 117 female patients (38.0%) and 164 male patients (53.3%), and sex was unknown in 27 patients

(8.8%). Most patients were 60 years or older (63.3%), but young patients (ages 20–39 years) were well represented (33 patients, 10.9%). These demographic data are summarized in Table 1.

ICH was detected (ICH+) in 158 NCCT studies (51.2%) by neuroradiology experts, and the distribution of ICH is denoted in Online Table 2. Intraparenchymal hemorrhage was part of most ICH+ NCCT studies (79 cases, 50%), and extra-axial hemorrhage (39 cases, 25%), subarachnoid hemorrhage (25 cases, 16%), intraventricular hemorrhage (10 cases, 6%), and other hemorrhage (5 cases, 3%) were less common.

We compared ICH detection by RAPID with the consensus of 3 expert neuroradiologists (Table 2). RAPID correctly identified 151/158 ICH+ cases and 143/150 ICH- cases (Figs 1 and 2). Therefore, RAPID had a high sensitivity (0.956, CI: 0.911–0.978), specificity (0.953, CI: 0.907–0.977), PPV (0.956, CI: 0.911–0.978), and NPV (0.953, CI: 0.907–0.977) for ICH detection (Table 3). The positive LR (20.479, CI 9.928–42.245) and negative LR (0.046, CI 0.023–0.096) for ICH detection were similarly favorable. NCCT in which RAPID did not detect hemorrhage (false-negative cases) involved cases with small volumes of ICH (<1.5 mL in all instances) that were intraparenchymal, intraventricular, and subdural in location (Fig 2).

We then determined the accuracy of RAPID for ICH volumetric quantification. ICH volume was automatically quantified from the segmentation using Osirix. RAPID quantification of ICH volume demonstrated a strong correlation with the neuroradiology experts (correlation coefficient $r=0.983$, Fig 3). The mean volumes of ICH in this analysis were 12 mL (RAPID) and 8 mL (expert), and the median absolute error was 3 mL.

DISCUSSION

In this study, we found that the automated artificial intelligence RAPID ICH module is highly accurate for the detection of ICH on NCCT. Moreover, RAPID ICH volumetric quantification of ICH for intraparenchymal and intraventricular hemorrhage was highly accurate. These findings have important implications for the more widespread adoption of artificial intelligence ICH detection into clinical practice.

Other studies have used CNNs to detect the presence of ICH on NCCT.^{9-11,14} The high sensitivity (96%) and specificity (95%) of RAPID ICH compare favorably with these prior studies that found a sensitivity of 70%–98% and a specificity of 87%–95% for their individual CNN.^{9-11,14} All 7 false-negative RAPID ICH evaluations consisted of small ICHs that measured <1.5 mL in volume, and 6 of the 7 false-positive cases were attributable to volume averaging. The remaining false-positive study was read as a dural fold by an expert reader. Future iterations of this platform might improve the detection of these small volumes of ICH and the exclusion of false-positive ICHs with artifact reduction approaches. The use of studies from multiple centers and the use of neuroradiology expert interpretations as the criterion standard rather than radiology reports likely increase the generalizability and accuracy of our study compared with prior studies.

Computer-assisted detection of findings on imaging studies has been previously used for cancer detection in mammography, pulmonary nodule detection on chest CT, and colonic polyp detection,¹⁹⁻²¹ but these technologies are not based on CNNs and have limited utility in routine clinical practice. By contrast, CNN technology has been successfully applied to nonradiology studies, such as the detection of diabetic retinopathy²² and skin cancer detection,²³ which has prompted efforts to move this technology into routine medical practice.

The progressive and substantial increase in the amount of diagnostic imaging studies^{24,25} places particular stress on the timely interpretation of NCCT. Delays in interpretation may lead to delayed identification of ICH, resulting in nonexpedient patient care that could lead to poor patient outcomes.⁸ We speculate that the adoption of CNN technology for ICH detection into routine clinical practice will speed NCCT interpretations, which must still be performed by a board-certified radiologist, and patient treatment decisions. Future studies should be designed to test how this technology changes radiology workflows and patient care.

The use of automated image processing in acute ischemic stroke, which is another cerebrovascular emergency that relies on prompt diagnosis and treatment, is already in widespread clinical practice after several randomized studies demonstrated the effectiveness of this approach in selecting patients for endovascular thrombectomy treatment.¹⁵⁻¹⁸ We expect that the adoption of ICH detection in a manner similar to cerebral ischemia detection will lead to timely detection, resulting in improved care of patients with hemorrhagic stroke. In addition, the detection of ICH may also impact the treatment of patients with concomitant ischemic stroke because the presence of ICH is a contraindication to treatment with IV thrombolysis and, in some instances, endovascular thrombectomy.

Further studies are required to determine how automated ICH volume quantification may be best used in clinical practice. Other studies have found similar accuracy for CNN methods of ICH volume measurement^{9,13} as in our study, which suggests that application of these methods to the care of patients with intraparenchymal, intraventricular, and even subarachnoid hemorrhage may have a role in patient treatment and prognostication.

Our study has several limitations. The retrospective design may introduce bias, and the inclusion of studies from a limited number of CT vendors and locations may limit the generalizability of our findings. Future prospective studies that include a larger number of sites are required for further validation of our findings. It is also possible that beam-hardening artifact, particularly within the posterior fossa, may further limit the sensitivity of RAPID ICH. We also note that although RAPID ICH was highly accurate in this study, automated ICH detection should not preclude interpretation by a trained radiologist because even small undetected hemorrhages might impact outcomes in patients, such as those with ischemic strokes who are being considered for IV thrombolysis.

CONCLUSIONS

RAPID ICH is highly accurate in the detection of ICH and in the volumetric quantification of intraparenchymal and intraventricular hemorrhages. The overall robustness of this CNN approach suggests that automated ICH detection is sufficiently developed for introduction into routine clinical practice.

Disclosures: Jeremy Heit—RELATED: Consulting Fee or Honorarium: iSchemaView, Medtronic, Microvention, Comments: iSchemaView Medical and Scientific Advisory Board, Medtronic-minimal consulting fees, Microvention-modest consulting fees. Amin Aghaebrahim—UNRELATED: Consultancy: iSchemaView advisor. Ricardo Hanel—UNRELATED: Board Membership: Elum, Three Rivers Medical; Consultancy: Medtronic, Stryker, Microvention, Balt, Phenox, Cerenovus; Stock/Stock Options: Corindus. Keith Kwok—RELATED: Consulting Fee or Honorarium: Consultant for iSchemaView. Hafez Haerian—RELATED: Consulting Fee or Honorarium: iSchemaView. Carlo Cereda—UNRELATED: Consultancy: Member of the iSchemaView Scientific Board, Comments: Minor.* Chitra Venkatasubramanian—UNRELATED: Expert Testimony: Law firms; Grants/Grants Pending: NIH and industry grants as part of multi center trials; Stock/Stock Options: Ceribell. Seena Dehkharghani—UNRELATED: Grants/Grants Pending: Grant support from anonymous donor paid to institution, Comments: Grant on development of a device for collecting and analyzing brain electrical properties*; Patents (Planned, Pending or Issued): Patent pending for device to collect and analyze brain dielectric properties; Travel/Accommodations/Meeting Expenses Unrelated to Activities Listed: iSchemaView, Comments: Travel (2019) and research support for unrelated scientific collaboration. Leonardo Carbonera—UNRELATED: Consultancy: Allm Inc; Payment for Lectures Including Service on Speakers Bureaus: Boehringer Ingelheim, iSchemaView. Karen Copeland—RELATED: Fees for Participation in Review Activities Such as Data Monitoring Boards, Statistical Analysis, Endpoint Committees, and the Like: Boulder Statistics LLC, Comments: I (Karen Copeland, Boulder Statistics) was paid as a consultant to iSchemaView for statistical analysis and manuscript review; Payment for Writing or Reviewing the Manuscript: Boulder Statistics LLC, Comments: I (Karen Copeland, Boulder Statistics) was paid as a consultant to iSchemaView for statistical analysis and manuscript review; UNRELATED: Consultancy: Boulder Statistics, Comments: I (Karen Copeland, Boulder Statistics) am a paid consultant to iSchemaView. Francisco Mont'Alverne—UNRELATED: Consultancy: Medtronic; Payment for Lectures Including Service on Speakers Bureaus: Medtronic, Penumbra, Stryker. *Money paid to institution.

REFERENCES

1. van Asch CJ, Luitse MJ, Rinkel GJ, et al. **Incidence, case fatality, and functional outcome of intracerebral haemorrhage over time, according to age, sex, and ethnic origin: a systematic review and meta-analysis.** *Lancet Neurol* 2010;9:167–76 CrossRef Medline
2. Heit JJ, Iv M, Wintermark M. **Imaging of intracranial hemorrhage.** *J Stroke* 2017;19:11–27 CrossRef Medline
3. Zahuranec DB, Lisabeth LD, Sanchez BN, et al. **Intracerebral hemorrhage mortality is not changing despite declining incidence.** *Neurology* 2014;82:2180–86 CrossRef Medline

4. Broderick JP, Brott TG, Duldner JE, et al. **Volume of intracerebral hemorrhage. A powerful and easy-to-use predictor of 30-day mortality.** *Stroke* 1993;24:987–93 CrossRef Medline
5. Dengler NF, Sommerfeld J, Dising D, et al. **Prediction of cerebral infarction and patient outcome in aneurysmal subarachnoid hemorrhage: comparison of new and established radiographic, clinical and combined scores.** *Eur J Neurol* 2018;25:111–19 CrossRef Medline
6. Hemphill JC 3rd, Greenberg SM, Anderson CS, et al. **Guidelines for the management of spontaneous intracerebral hemorrhage: a guideline for healthcare professionals from the American Heart Association/American Stroke Association.** *Stroke* 2015;46:2032–60 CrossRef Medline
7. Goldstein JN, Gilson AJ. **Critical care management of acute intracerebral hemorrhage.** *Curr Treat Options Neurol* 2011;13:204–16 CrossRef Medline
8. Glover M 4th, Almeida RR, Schaefer PW, et al. **Quantifying the impact of noninterpretive tasks on radiology report turn-around times.** *J Am Coll Radiol* 2017;14:1498–1503 CrossRef Medline
9. Chang PD, Kuoy E, Grinband J, et al. **Hybrid 3D/2D convolutional neural network for hemorrhage evaluation on head CT.** *AJNR Am J Neuroradiol* 2018;39:1609–16 CrossRef Medline
10. Arbabshirani MR, Fornwalt BK, Mongelluzzo GJ, et al. **Advanced machine learning in action: identification of intracranial hemorrhage on computed tomography scans of the head with clinical workflow integration.** *NPJ Digit Med* 2018;1:9 CrossRef Medline
11. Chilamkurthy S, Ghosh R, Tanamala S, et al. **Deep learning algorithms for detection of critical findings in head CT scans: a retrospective study.** *Lancet* 2018;392:2388–96 CrossRef Medline
12. Titano JJ, Badgeley M, Schefflein J, et al. **Automated deep-neural-network surveillance of cranial images for acute neurologic events.** *Nat Med* 2018;24:1337–41 CrossRef Medline
13. Ye H, Gao F, Yin Y, et al. **Precise diagnosis of intracranial hemorrhage and subtypes using a three-dimensional joint convolutional and recurrent neural network.** *Eur Radiol* 2019;29:6191–01 CrossRef Medline
14. Ginat DT. **Analysis of head CT scans flagged by deep learning software for acute intracranial hemorrhage.** *Neuroradiology* 2020;62:335–40 CrossRef Medline
15. Saver JL, Goyal M, Bonafe A, et al. **Stent-retriever thrombectomy after intravenous t-PA vs. t-PA alone in stroke.** *N Engl J Med* 2015;372:2285–95 CrossRef Medline
16. Campbell BC, Mitchell PJ, Kleinig TJ, et al. **Endovascular therapy for ischemic stroke with perfusion-imaging selection.** *N Engl J Med* 2015;372:1009–18 CrossRef Medline
17. Albers GW, Marks MP, Kemp S, et al. **Thrombectomy for stroke at 6 to 16 hours with selection by perfusion imaging.** *N Engl J Med* 2018;378:708–18 CrossRef Medline
18. Nogueira RG, Jadhav AP, Haussen DC, et al. **Thrombectomy 6 to 24 hours after stroke with a mismatch between deficit and infarct.** *N Engl J Med* 2018;378:11–21 CrossRef Medline
19. Winsberg F, Elkin M, Macy J, et al. **Detection of radiographic abnormalities in mammograms by means of optical scanning and computer analysis.** *Radiology* 1967;89:211–15 CrossRef
20. Monnier-Cholley L, MacMahon H, Katsuragawa S, et al. **Computer-aided diagnosis for detection of interstitial opacities on chest radiographs.** *AJR Am J Roentgenol* 1998;171:1651–56 CrossRef Medline
21. Yoshida H, Masutani Y, MacEneaney P, et al. **Computerized detection of colonic polyps at CT colonography on the basis of volumetric features: pilot study.** *Radiology* 2002;222:327–36 CrossRef Medline
22. Gulshan V, Peng L, Coram M, et al. **Development and validation of a deep learning algorithm for detection of diabetic retinopathy in retinal fundus photographs.** *JAMA* 2016;316:2402–10 CrossRef Medline
23. Esteva A, Kuprel B, Novoa RA, et al. **Dermatologist-level classification of skin cancer with deep neural networks.** *Nature* 2017;542:115–18 CrossRef Medline
24. Sunshine JH, Burkhardt JH. **Radiology groups' workload in relative value units and factors affecting it.** *Radiology* 2000;214:815–22 CrossRef Medline
25. McDonald RJ, Schwartz KM, Eckel LJ, et al. **The effects of changes in utilization and technological advancements of cross-sectional imaging on radiologist workload.** *Acad Radiol* 2015;22:1191–98 CrossRef Medline

Serial Imaging of Virus-Associated Necrotizing Disseminated Acute Leukoencephalopathy (VANDAL) in COVID-19

 S. Agarwal,  J. Conway,  V. Nguyen,  S. Dogra,  P. Krieger,  D. Zagzag,  A. Lewis,  K. Melmed,  S. Galetta, and  R. Jain



ABSTRACT

BACKGROUND AND PURPOSE: Various patterns of leukoencephalopathy have been described in coronavirus disease 2019 (COVID-19). In this article, we aimed to describe the clinical and imaging features of acute disseminated leukoencephalopathy in critically ill patients with COVID-19 and the imaging evolution during a short-term follow-up.

MATERIALS AND METHODS: We identified and reviewed the clinical data, laboratory results, imaging findings, and outcomes for 8 critically ill patients with COVID-19 with acute disseminated leukoencephalopathy.

RESULTS: All patients demonstrated multiple areas of white matter changes in both cerebral hemispheres; 87.5% (7/8) of patients had a posterior predilection. Four patients (50%) had short-term follow-up imaging within a median of 17 days after the first MR imaging; they developed brain atrophy, and their white matter lesions evolved into necrotizing cystic cavitations. All (8/8) patients had inflammatory cytokine release syndrome as demonstrated by elevated interleukin-6, D-dimer, lactate dehydrogenase, erythrocyte sedimentation rate, C-reactive protein, and ferritin levels. Most (7/8; 87.5%) patients were on prolonged ventilator support (median, 44.5 days; interquartile range, 20.5 days). These patients had poor functional outcomes (6/8 [75%] patients were discharged with mRS 5) and high mortality (2/8, 25%).

CONCLUSIONS: Critically ill patients with COVID-19 can develop acute disseminated leukoencephalopathy that evolves into cystic degeneration of white matter lesions with brain atrophy during a short period, which we dubbed virus-associated necrotizing disseminated acute leukoencephalopathy. This may be the result of COVID-19-related endothelial injury, cytokine storm, or thrombotic microangiopathy.

ABBREVIATIONS: ADEM = acute disseminated encephalomyelitis; ARDS = acute respiratory distress syndrome; CRP = C-reactive protein; COVID-19 = coronavirus disease 2019; ESR = erythrocyte sedimentation rate; GCS = Glasgow Coma Scale; IL-6 = interleukin-6; INR = international normalized ratio; IQR = interquartile range; LDH = lactate dehydrogenase; PRES = posterior reversible encephalopathy syndrome; SARS-CoV-2 = Severe Acute Respiratory Syndrome coronavirus 2; VANDAL = Virus Associated Necrotizing Disseminated Acute Leukoencephalopathy; WM = white matter

Much of the focus regarding the global pandemic of coronavirus disease 2019 (COVID-19) has been on the cardiovascular, pulmonary, and hematologic complications. However, neurologic complications have become increasingly recognized sequelae, with associated high morbidity and mortality.¹⁻⁵ Although the current literature is limited regarding neuroimaging findings in patients with COVID-19,⁶⁻⁸ there have been recent reports of critically ill patients with leukoencephalopathy with

or without cerebral microhemorrhages.⁹⁻¹⁴ Different radiologic patterns of white matter (WM) injury have been described in critically ill patients with viral infections, including diffuse leukoencephalopathy with microhemorrhages, acute disseminated encephalomyelitis (ADEM), and posterior reversible encephalopathy syndrome (PRES).^{11,15-20} Due to a paucity of neuropathologic data, the pathophysiologic processes responsible for these imaging characteristics are not completely understood. A recent report on postmortem examination of 5 patients with COVID-19 did not reveal evidence of encephalitis or central nervous system vasculitis, but this series lacked neuroimaging.²¹ Another report suggested that the neuropathologic lesions in patients with COVID-19 had features resembling both vascular and demyelinating etiologies,²² but this report also lacked neuroimaging data to correlate with the neuropathologic findings.

In this article, we aimed to describe the clinical, laboratory, and functional outcomes of patients with COVID-19 with acute

Received August 11, 2020; accepted after revision September 16.

From the Departments of Neurology (S.A., J.C., A.L., K.M., S.G.), Radiology (V.N., S.D., P.K., R.J.), Pathology (D.Z.), and Neurosurgery (D.Z., A.L., K.M., R.J.), NYU Langone Health, New York, New York.

Please address correspondence to Rajan Jain, MD, NYU School of Medicine, 660 First Ave, 2nd Floor, NY, NY 10016; e-mail: rajan.jain@nyulangone.org; @CoolAsANeuroRad

 Indicates open access to non-subscribers at www.ajnr.org

 Indicates article with online supplemental data.

<http://dx.doi.org/10.3174/ajnr.A6898>

disseminated leukoencephalopathy on brain MR imaging, as well as the imaging evolution of these WM lesions. We examined possible underlying mechanisms for these findings.

MATERIALS AND METHODS

We performed a retrospective chart review of 115 adult patients positive for COVID-19 who underwent brain MR imaging at 3 tertiary care hospital sites of a single academic medical center from March 1, 2020, to May 10, 2020, and found 8 patients with acute disseminated leukoencephalopathy, 4 (50%) of whom had >1 MR imaging, 3/4 (75%) who had 2, and 1/4 (25%) who had 3 MR imagings. MR images obtained on a 3T MR imaging scanner included susceptibility-weighted imaging, while those scanned on a 1.5T scanner had gradient-echo imaging. Of the 8 patients, 4 patients had imaging performed on both 1.5T and 3T MR imaging scanners. MRIs were evaluated independently by 2 fellowship-trained neuroradiologists (R.J. and V.N.). Imaging data on the pattern of distribution of the WM lesions and microhemorrhages were collected. Follow-up MR imaging studies were evaluated for progression or evolution of WM lesions and evidence of subjective brain atrophy, defined as an interval increase in the prominence of the ventricles and sulcal spaces due to brain volume loss compared with the baseline study.

S.A., S.D., and P.K. reviewed charts and collected the following data: comorbidities, presenting symptoms, time from symptom onset to presentation, vital signs, ventilator days before brain MR imaging, total ventilator days, the total length of hospitalization, treatment received for COVID-19, occurrence of in-house cardiac arrest, Glasgow Coma Scale (GCS) score at MR imaging and 2 weeks post-MR imaging, acute respiratory distress syndrome (ARDS) severity score (calculated as the lowest partial pressure of oxygen/fraction of inspired oxygen ratio while intubated).²³ Functional outcomes included discharge mRS, discharge disposition, and death. Discharge mRS scores were calculated by trained physical therapists ≤ 5 days before discharge or determined by a neurology resident (S.A.) on the basis of the clinical notes when not otherwise documented. We collected laboratory variables including admission and nadir platelet count and fibrinogen levels and admission and peak D-dimer, lactate dehydrogenase (LDH), international normalized ratio (INR), erythrocyte sedimentation rate (ESR), C-reactive protein (CRP), interleukin-6 (IL-6), and ferritin levels.

This study was approved by the New York University Grossman School of Medicine Institutional Review Board, which granted a waiver of informed consent (IRB No. i20-00567).

RESULTS

All 8 patients with MR imaging findings of acute disseminated leukoencephalopathy were men, with a median age of 59.5 years (range, 38–69 years). Demographic and clinical features of individual patients are shown in the Online Supplemental Data. Although 2 patients had no known comorbidities, the remaining 6 had at least 3 comorbidities on admission. All patients presented with respiratory symptoms (fevers, chills, cough, and dyspnea) and had symptoms for a median of 7 days (range, 4–14 days) before presentation to the emergency department. All patients (100%) were treated with a combination of hydroxychloroquine and azithromycin,

62.5% (5/8) were also treated with tocilizumab, and 12.5% (1/8) were given lopinavir-ritonavir. Intubation was required for 87.5% of patients (7/8), and ventilator support was needed for a median of 44.5 days (range, 24–52 days). Of these 7 patients, 42.9% (3/7) had moderate and 42.9% (3/7) had severe ARDS. The peak systolic blood pressure before the first MR imaging ranged from 162 to 240 mm Hg. In-hospital cardiac arrest occurred in 37.5% (3/8) of patients, all of whom achieved a return of spontaneous circulation. Nearly all (87.5%; 7/8) patients developed acute kidney injury, and 62.5% (5/8) required continuous renal replacement therapy. At the time of the analysis of this study, 25% (2/8) of patients had died. There were no neuropathologic specimens available for analysis because postmortem examination was not performed.

These patients had cytokine storming as demonstrated by elevated median IL-6 (admission = 31 pg/mL [interquartile range (IQR) = 15.5 pg/mL]; peak = 49 pg/mL [IQR = 73.5 pg/mL]; normal IL-6 levels = ≤ 5 pg/mL); D-dimer (admission = 2003 ng/mL [IQR = 2980 ng/mL]; peak = 8645 ng/mL [IQR = 4751.25 ng/mL]; normal = D-dimer <230 ng/mL); LDH (admission = 492 U/L [IQR = 284 U/L]; peak = 970.5 U/L [IQR = 605.5 U/L]; normal LDH levels = 84–246 IU/L); ESR (admission = 83 mm/h [IQR = 60.5 mm/h]; peak = 117 mm/h [IQR = 27.75 mm/h]; normal ESR levels = 0–10 mm/h); CRP (admission = 113.5 mg/L [IQR = 106.43 mg/L]; peak = 336 mg/L [IQR 77.63 mg/L]; normal CFP levels = 0.0–3.0 mg/L); and ferritin (admission = 1070 ng/mL [IQR = 906.7 ng/mL]; peak = 4701.5 ng/mL [IQR = 11616.3 ng/mL]; normal ferritin levels = 8.0–388.0 ng/mL) (Online Supplemental Data).

Initial neuroimaging with brain MR imaging was performed at a median of 23.5 days (IQR = 5 days) since admission and, if intubated, 23 days (IQR = 6.5 days) after intubation. The indication for neuroimaging was persistent encephalopathy in nearly all (87.5%; 7/8) patients. Patients had a median GCS of 5 (IQR = 5.8) on the day of MR imaging, and there was no change in median GCS scores 2 weeks post-MR imaging. These patients had poor functional outcomes (75% of patients with discharge mRS of 5) and a high mortality rate (25%).

Neuroimaging showed multiple patchy areas of WM restricted diffusion/cytotoxic edema in both cerebral hemispheres, with a predilection for the posterior and subcortical regions in 87.5% (7/8) of patients. One of the 2 patients who received gadolinium demonstrated enhancement of the WM lesions suggesting BBB breakdown and evidence of central necrosis (Fig 1). Patchy lesions similar to WM lesions were also seen in the cerebellum (62.5%), brain stem (50%), and basal ganglia (25%) (Online Supplemental Data). Most (75%) patients also had microhemorrhages (Fig 1). Four patients underwent a follow-up MR imaging at a median of 35.5 days (IQR = 14.3 days) since admission and 17 days (IQR = 19.5 days) after the first MR imaging. Follow-up imaging in all 4 patients showed necrosis and development of small cystic cavitations in the WM lesions (which showed restricted diffusion/cytotoxic edema on the baseline study) and brain volume loss (Online Supplemental Data and Fig 2). Three patients also showed progression of WM lesions, which became more confluent (Fig 3). One patient who had 3 MR imaging studies showed sequential progression of the above WM findings on both follow-up studies.

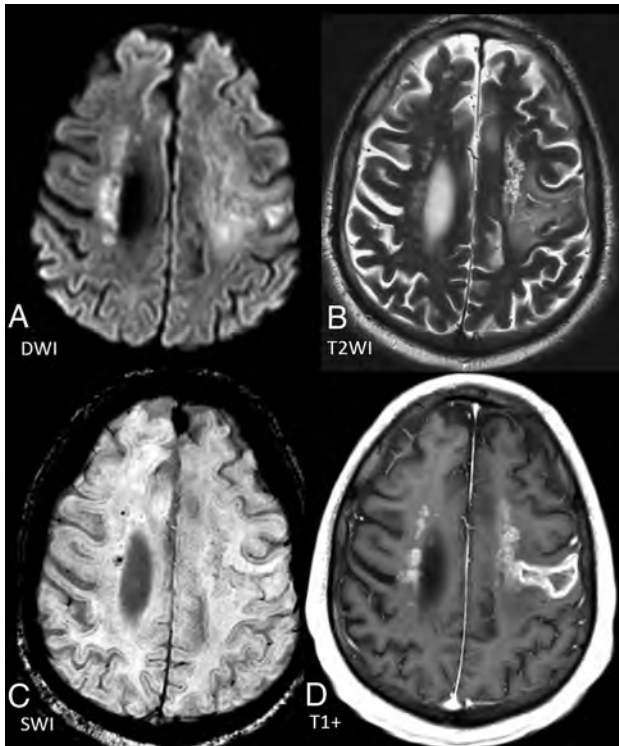


FIG 1. Axial DWI (A) and T2-weighted imaging (B) showing disseminated leukoencephalopathy with associated microhemorrhages (C) seen on the susceptibility-weighted imaging. D, Postcontrast T1-weighted imaging shows patchy enhancement of most WM lesions, with the larger lesion in the left cerebral hemisphere also showing central nonenhancement, suggestive of breakdown of the BBB and WM necrosis.

DISCUSSION

We identified 8 critically ill patients with COVID-19 with acute disseminated leukoencephalopathy. This is the first study, to our knowledge, to show imaging evolution of acute disseminated leukoencephalopathy in patients with COVID-19. All patients who underwent follow-up imaging showed necrosis and cavitation of initial WM cytotoxic lesions as well as brain atrophy during their hospital stay within a fairly short follow-up period. Our findings suggest that this necrotizing leukoencephalopathy leads to rather rapid progression of extensive and permanent white matter damage and brain atrophy in these critically ill patients, which correlate very well with the poor functional outcomes shown in these patients.

Most (87.5%) of our patients had lesions that were predominantly posterior, similar to lesions seen in PRES. There have been reports of PRES in COVID-19,^{24,25} and while the MRI findings for our patients appear similar to those in PRES, they differ from those in PRES in that these WM changes are more patchy and deep, rather than confluent²⁶ and progress rather than resolve on follow-up imaging.

Furthermore, while these lesions bear some similarity to other white matter lesions seen in patients with viral infections, such as acute necrotizing encephalitis^{27,28} or ADEM,^{29,30} they differ from these entities, as well. The WM lesions seen in patients in our study showed multiple diffuse confluent areas of T2/FLAIR hyperintensity, with diffusion restriction suggesting cytotoxic

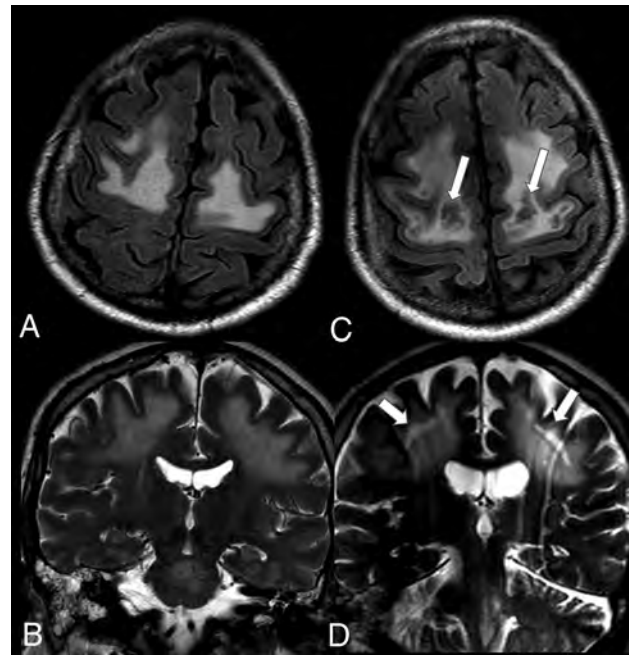


FIG 2. A and B, Axial FLAIR and coronal T2-weighted images at baseline MR imaging (day 25) showing multiple confluent areas of leukoencephalopathy. C and D, These lesions progressed to show development of cystic cavitations in the WM (arrows) as well as interval prominence of the lateral and third ventricles, suggesting brain atrophy on follow-up MR imaging on day 75.

edema, which appears to be different from ADEM, in which these lesions are seen more often in subcortical regions with surrounding vasogenic edema. Thus, it appears that these lesions represent a previously undescribed finding, which we have dubbed virus-associated acute necrotizing disseminated leukoencephalopathy, or VANDAL, for short.

There have been serial brain MR imaging studies among critically ill patients without COVID-19 that have demonstrated global brain atrophy with preferential involvement of the superior frontal gyri, thalami, cerebellum, and hippocampal regions. The 4 patients in our study who had follow-up imaging showed brain atrophy. Although there have been no prior studies in patients with COVID-19 with serial imaging showing any evidence of brain atrophy, the findings seen in our patients could be due to either critical illness, hypoxic injury, or cytokine storming.³¹⁻³³

Variable direct and indirect mechanisms of CNS injury due to COVID-19 could be responsible for these imaging findings.

COVID-19–Related Endothelial Injury

Viral infections have been noted to cause endothelial damage leading to increased permeability of the BBB.¹⁵ Some pathologic studies in patients with COVID-19 have shown direct viral invasion of endothelial cells and diffuse endothelial inflammation,³⁴ but more recent literature has suggested that these particles may have been misinterpreted as coronavirus and instead represent the rough endoplasmic reticulum.³⁵ Severe Acute Respiratory Syndrome coronavirus 2 (SARS-CoV-2) binds directly to angiotensin-converting enzyme 2 receptors, which can cause weakening of the endothelial layer,

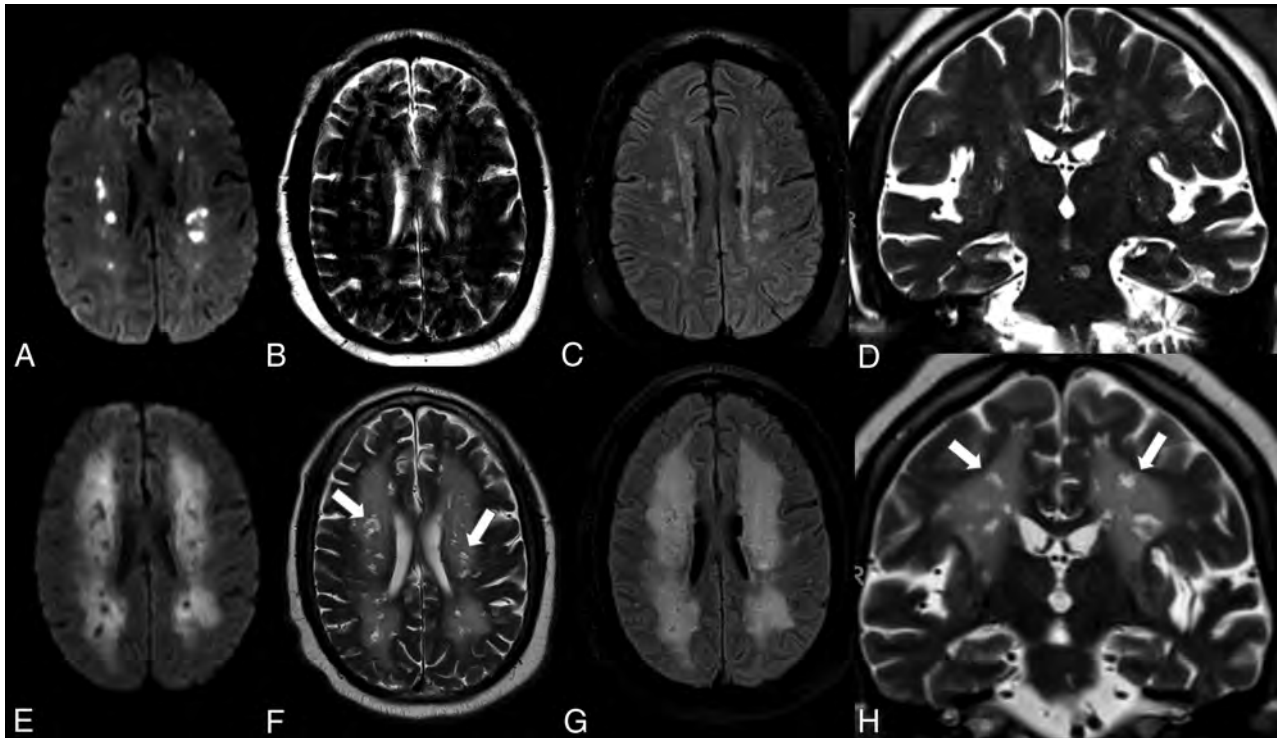


FIG 3. Axial DWI, T2-weighted, FLAIR (A–C), and coronal T2-weighted images (D) at baseline MR imaging (day 10) showing multiple patchy areas of restricted diffusion/cytotoxic edema in the WM. E–H, Axial corresponding follow-up MR imaging (day 75) demonstrates development of cystic cavitations in the previous patchy cytotoxic WM lesions (arrows) as well as interval prominence of the lateral and third ventricles, suggesting brain atrophy. Follow-up MR imaging also showed marked progression of more confluent WM lesions surrounding the patchy cystic lesions.

leading to a breakdown of the BBB and subsequent dysfunction of autoregulation.^{36,37} Additionally, SARS-CoV-2 could lead to inflammation of the endothelial lining due to the recruitment of immune cells or hypoxic injury.³⁸

PRES has been associated with endothelial dysfunction.³⁹ In PRES, peak systolic blood pressure usually is between 170 and 190 mm Hg, but 10%–30% of patients have normal or only mildly elevated blood pressure.^{40,41} The peak systolic blood pressures in our patients ranged from 162 to 240 mm Hg. Thus, the imaging changes in our patients may be related to PRES, despite the absence of prolonged hypertension. While PRES usually resolves with time, 4 of our patients who had follow-up imaging were found to have progression of their WM lesions, suggesting that while this process may be related to PRES, it is different. Some of these deep, patchy WM lesions were present in the middle cerebral artery–posterior cerebral artery overlap area and could represent watershed ischemia due to hypoperfusion resulting from hypotension during cardiac arrest (experienced by 37.5% [3/8] of our patients) or hypotension secondary to sepsis. However, the posterior predominance of these lesions and the presence of lesions in the brain stem and cerebellum, areas not typically associated with watershed ischemia, make this mechanism of injury less likely.

Cytokine Storm

Patients with COVID-19 who are critically ill have a massive inflammatory reaction believed to be due to accumulation of T-cells and macrophages, resulting in the release of a large number

of cytokines into the bloodstream aiming to destroy the offending pathogen and resulting in numerous clinical manifestations known commonly as cytokine release syndrome.^{42,43} Classic laboratory findings of cytokine release include decreased T-cells and natural killer cells and, most important, an increase in IL-6, which leads to fever and multiorgan dysfunction. Higher levels of cytokines and interleukins have been postulated to be related to findings of disseminated leukoencephalopathy in patients with septic shock.⁴⁴ These patients had laboratory evidence of cytokine storming, which could lead to BBB breakdown, promoting the development of acute disseminated leukoencephalopathy.

Thrombotic Microangiopathy

Microhemorrhages in the subcortical WM and corpus callosum have been reported in high-altitude exposure and ARDS,⁴⁵ and they are believed to be the result of disseminated intravascular coagulation. Microhemorrhages within afflicted posterior and subcortical WM may also be seen in PRES.^{26,46} In the population of critically ill patients with COVID-19, neuroimaging findings of diffuse leukoencephalopathy may be seen in conjunction with microhemorrhages, as is seen in some of our patients.^{7,10,11,47} The appearance of cotton wool spots and microhemorrhages on fundus examinations further suggests pathologic and ophthalmologic evidence of thrombotic microangiopathy in patients with COVID-19.⁴⁸

Thus, endothelial dysfunction, cytokine storming, and thrombotic microangiopathy may contribute to the development of the acute disseminated leukoencephalopathy seen in

patients with severe COVID-19 described herein. Of course, these factors could also lead to leukoencephalopathy with a variety of other imaging phenotypes. Acute disseminated necrotizing leukoencephalopathy appears to be a harbinger of poor outcome in patients with severe COVID-19, but it is unclear how patients with acute disseminated necrotizing leukoencephalopathy will compare with patients with other COVID-19-associated WM changes during a long period.

Limitations of the current report include a small sample size, retrospective data collection, and a lack of histopathologic data. Nevertheless, there have been other neuropathologic studies published recently that support our findings and provide insight into the neurotropism of SARS-CoV-2⁴⁹ and the potential parainfectious processes affecting the neural tissue in COVID-19.²² Further neuropathologic studies that include clinical and imaging data are needed to better understand these findings.

CONCLUSIONS

Critically ill patients with COVID-19 may develop extensive and disseminated leukoencephalopathy, which evolves into cystic/cavitary necrotizing lesions during a short time period with brain atrophy, correlating with the poor functional outcome in these patients. We believe that these lesions occur as a result of endothelial dysfunction, cytokine storming, and thrombotic microangiopathy. Because these findings appear to be inconsistent with any previously described neuropathology, we have dubbed this virus-associated necrotizing disseminated acute leukoencephalopathy (VANDAL). Histopathologic studies as well as long-term follow-up studies are needed to better understand this phenotype of leukoencephalopathy and determine if and how this is different from other WM changes in patients with COVID-19.

Disclosures: Ariane Lewis—UNRELATED: Expert Testimony; Other: Deputy Editor for *Neurology* and *Seminars in Neurology*. Steven Galetta—UNRELATED: Consultancy: Genentech, Biogen. Rajan Jain—UNRELATED: Consultancy: Cancer Panels; Royalties: Thieme.

REFERENCES

1. Bridwell R, Long B, Gottlieb M. **Neurologic complications of COVID-19.** *Am J Emerg Med* 2020;38:1549.e3–49.e7 CrossRef Medline
2. Ahmad I, Rathore FA. **Neurological manifestations and complications of COVID-19: a literature review.** *J Neurol Sci* 2020;77:8–12 CrossRef Medline
3. Carod-Artal FJ. **Neurological complications of coronavirus and COVID-19.** *Rev Neurol* 2020;70:311–22 CrossRef Medline
4. Helms J, Kremer S, Merdji H, et al. **Neurologic features in severe SARS-CoV-2 infection.** *N Engl J Med* 2020;382:2268–70 CrossRef Medline
5. Mao L, Jin H, Wang M, et al. **Neurologic manifestations of hospitalized patients with coronavirus disease 2019 in Wuhan, China.** *JAMA Neurol* 2020;77:683–90 CrossRef Medline
6. Nicholson P, Alshafai L, Krings T. **Neuroimaging findings in patients with COVID-19.** *AJNR Am J Neuroradiol* 2020;41:1380–83 CrossRef Medline
7. Jain R, Young M, Dogra S, et al. **COVID-19 related neuroimaging findings: a signal of thromboembolic complications and a strong prognostic marker of poor patient outcome.** *J Neurol Sci* 2020;414:116923 CrossRef Medline

8. Pons-Escoda A, Naval-Baudín P, Majós C, et al. **Neurological involvement in COVID-19: cause or coincidence? A neuroimaging perspective.** *AJNR Am J Neuroradiol* 2020;41:1365 CrossRef Medline
9. Kandemirli SG, Dogan L, Sarikaya ZT, et al. **Brain MRI findings in patients in the intensive care unit with COVID-19 infection.** *Radiology* 2020;297:E232–35 CrossRef Medline
10. Agarwal S, Jain R, Dogra S, et al. **Cerebral microbleeds and leukoencephalopathy in critically ill patients with COVID-19.** *Stroke* 2020;51:2649–55 CrossRef Medline
11. Radmanesh A, Derman A, Lui Y, et al. **COVID-19 associated diffuse leukoencephalopathy and microhemorrhages.** *Radiology* 2020;297:E223–27 CrossRef Medline
12. Sachs JR, Gibbs KW, Swor DE, et al. **COVID-19-associated leukoencephalopathy.** *Radiology* 2020;296:E184–85 CrossRef Medline
13. Huang H, Eichelberger H, Chan M, et al. **Pearls and oysters: leukoencephalopathy in critically ill patients with COVID-19.** *Neurology* 2020 Aug 11 [Epub ahead of print] CrossRef Medline
14. Lang M, Buch K, Li MD, et al. **Leukoencephalopathy associated with severe COVID-19 infection: sequela of hypoxemia?** *AJNR Am J Neuroradiol* 2020;41:1641–45 CrossRef Medline
15. Claveau JS, LeBlanc R, Ahmad I, et al. **Cerebral adenovirus endotheliitis presenting as posterior reversible encephalopathy syndrome after allogeneic stem cell transplantation.** *Bone Marrow Transplant* 2017;52:1457–59 CrossRef Medline
16. Ogunneye O, Hernandez-Montfort JA, Ogunneye Y, et al. **Parainfluenza virus infection associated with posterior reversible encephalopathy syndrome: a case report.** *J Med Case Rep* 2012;6:89 CrossRef Medline
17. Muco E, Hasa A, Rroji A, et al. **Posterior reversible encephalopathy syndrome in a patient with hemorrhagic fever with renal syndrome.** *Case Rep Infect Dis* 2020;2020:1017689 CrossRef Medline
18. Sasson SC, Oon A, Chagantri J, et al. **Posterior reversible encephalopathy syndrome (PRES) in an HIV-1 infected patient with disseminated varicella zoster virus: a case report.** *BMC Infect Dis* 2013;13:396 CrossRef Medline
19. Bartynski WS, Boardman JF, Zeigler ZR, et al. **Posterior reversible encephalopathy syndrome in infection, sepsis, and shock.** *AJNR Am J Neuroradiol* 2006;27:2179–90 Medline
20. Poyiadji N, Shahin G, Noujaim D, et al. **COVID-19-associated acute hemorrhagic necrotizing encephalopathy: CT and MRI features.** *Radiology* 2020;296:E119–20 CrossRef Medline
21. Schaller T, Hirschbuhl K, Burkhardt K, et al. **Postmortem examination of patients with COVID-19.** *JAMA* 2020;323:2518 CrossRef Medline
22. Reichard RR, Kashani KB, Boire NA, et al. **Neuropathology of COVID-19: a spectrum of vascular and acute disseminated encephalomyelitis (ADEM)-like pathology.** *Acta Neuropathol* 2020;140:1–6 CrossRef Medline
23. Ranieri VM, Rubenfeld GD, Thompson BT, et al; ARDS Definition Task Force. **Acute respiratory distress syndrome: the Berlin definition.** *JAMA* 2012;307:2526–33 CrossRef Medline
24. Rogg J, Baker A, Tung G. **Posterior reversible encephalopathy syndrome: a manifestation of COVID-19 cytokine storm.** *Interdiscip Neurosurg* 2020;22:100808 CrossRef Medline
25. Kishfy L, Casasola M, Banankhah P, et al. **Posterior reversible encephalopathy syndrome (PRES) as a neurological association in severe Covid-19.** *J Neurol Sci* 2020;414:116943 CrossRef Medline
26. McKinney AM, Sarikaya B, Gustafson C, et al. **Detection of microhemorrhage in posterior reversible encephalopathy syndrome using susceptibility-weighted imaging.** *AJNR Am J Neuroradiol* 2012;33:896–903 CrossRef Medline
27. Ormitti F, Ventura E, Summa A, et al. **Acute necrotizing encephalopathy in a child during the 2009 influenza A(H1N1) pandemic: MR imaging in diagnosis and follow-up.** *AJNR Am J Neuroradiol* 2010;31:396–400 CrossRef Medline
28. Wong AM, Simon EM, Zimmerman RA, et al. **Acute necrotizing encephalopathy of childhood: correlation of MR findings and clinical outcome.** *AJNR Am J Neuroradiol* 2006;27:1919–23 Medline

29. Rossi A. **Imaging of acute disseminated encephalomyelitis.** *Neuroimaging Clin N Am* 2008;18:149–61x CrossRef Medline
30. Honkaniemi J, Dastidar P, Kahara V, et al. **Delayed MR imaging changes in acute disseminated encephalomyelitis.** *AJNR Am J Neuroradiol* 2001;22:1117–24 Medline
31. Herridge MS, Moss M, Hough CL, et al. **Recovery and outcomes after the acute respiratory distress syndrome (ARDS) in patients and their family caregivers.** *Intensive Care Med* 2016;42:725–38 CrossRef Medline
32. Garbade SF, Boy N, Heringer J, et al. **Age-related changes and reference values of bicaudate ratio and sagittal brainstem diameters on MRI.** *Neuropediatrics* 2018;49:269–75 CrossRef Medline
33. Hopkins RO, Suchyta MR, Beene K, et al. **Critical illness acquired brain injury: Neuroimaging and implications for rehabilitation.** *Rehabil Psychol* 2016;61:151–64 CrossRef Medline
34. Varga Z, Flammer AJ, Steiger P, et al. **Endothelial cell infection and endotheliitis in COVID-19.** *Lancet* 2020;395:1417–18 CrossRef Medline
35. Goldsmith CS, Miller SE, Martines RB, et al. **Electron microscopy of SARS-CoV-2: a challenging task.** *Lancet* 2020;395:e99 CrossRef Medline
36. Wu Y, Xu X, Chen Z, et al. **Nervous system involvement after infection with COVID-19 and other coronaviruses.** *Brain Behav Immun* 2020;87:18–22 CrossRef Medline
37. Baig AM, Khaleeq A, Ali U, et al. **Evidence of the COVID-19 virus targeting the CNS: tissue distribution, host-virus interaction, and proposed neurotropic mechanisms.** *ACS Chem Neurosci* 2020;11:995–98 CrossRef Medline
38. Teuwen LA, Geldhof V, Pasut A, et al. **COVID-19: the vasculature unleashed.** *Nat Rev Immunol* 2020;20:389–91 CrossRef Medline
39. Marra A, Vargas M, Striano P, et al. **Posterior reversible encephalopathy syndrome: the endothelial hypotheses.** *Med Hypotheses* 2014;82:619–22 CrossRef Medline
40. Fugate JE, Claassen DO, Cloft HJ, et al. **Posterior reversible encephalopathy syndrome: associated clinical and radiologic findings.** *Mayo Clin Proc* 2010;85:427–32 CrossRef Medline
41. Roth C, Ferbert A. **The posterior reversible encephalopathy syndrome: what's certain, what's new?** *Pract Neurol* 2011;11:136–44 CrossRef Medline
42. Xie J, Tong Z, Guan X, et al. **Clinical characteristics of patients who died of coronavirus disease 2019 in China.** *JAMA Netw Open* 2020;3:e205619 CrossRef Medline
43. Mehta P, McAuley DF, Brown M, et al; HLH Across Speciality Collaboration, UK. **COVID-19: consider cytokine storm syndromes and immunosuppression.** *Lancet* 2020;395:1033–34 CrossRef Medline
44. Sharshar T, Gray F, Poron F, et al. **Multifocal necrotizing leukoencephalopathy in septic shock.** *Crit Care Med* 2002;30:2371–75 CrossRef Medline
45. Fanou EM, Coutinho JM, Shannon P, et al. **Critical illness-associated cerebral microbleeds.** *Stroke* 2017;48:1085–87 CrossRef Medline
46. Hefzy HM, Bartynski WS, Boardman JF, et al. **Hemorrhage in posterior reversible encephalopathy syndrome: imaging and clinical features.** *AJNR Am J Neuroradiol* 2009;30:1371–79 CrossRef Medline
47. Breit H, Jhaveri M, John S. **Concomitant delayed posthypoxic leukoencephalopathy and critical illness microbleeds.** *Neurol Clin Pract* 2018;8:e31–33 CrossRef Medline
48. Marinho PM, Marcos AA, Roman AC, et al. **Retinal findings in patients with COVID-19.** *Lancet* 2020;395:590–92 CrossRef Medline
49. Puelles VG, Lütgehetmann M, Lindenmeyer MT, et al. **Multiorgan and renal tropism of SARS-CoV-2.** *N Engl J Med* 2020;383:590–92 CrossRef Medline
50. Radmanesh A, Derman A, Ishida K. **COVID-10-associated delayed posthypoxic necrotizing leukoencephalopathy.** *J Neurol Sci* 2020;415:116945 CrossRef Medline

Quantifying Tissue Properties of the Optic Radiations Using Strategically Acquired Gradient Echo Imaging and Enhancing the Contrast Using Diamagnetic Susceptibility Weighted Imaging

P.K. Jella, Y. Chen, W. Tu, S. Makam, S. Beckius, E. Hamtaei, C.C.-T. Hsu, and E.M. Haacke

ABSTRACT

SUMMARY: Visualization of the optic radiations is of clinical importance for diagnosing many diseases and depicting their anatomic structures for neurosurgical interventions. In this study, we quantify proton density, T1, T2*, and susceptibility of the optic radiation fiber bundles in a series of 10 healthy control participants using strategically acquired gradient echo imaging. Furthermore, we introduce a novel means to enhance the contrast of the optic radiations using diamagnetic susceptibility weighted imaging.

ABBREVIATIONS: dSWI = diamagnetic susceptibility weighted imaging; ESS = external sagittal striatum; ISS = internal sagittal striatum; OR = optic radiation; STAGE = strategically acquired gradient echo; TAP = tapetum; HPF = high-pass-filtered; QSM = quantitative susceptibility map; PD = proton density

Some pathologies may benefit from studying the tissue properties of the optic radiations (ORs). The ORs are a common site for chronic small-vessel ischemic changes, especially in older adults.¹ Periventricular demyelinating plaques in multiple sclerosis also have a propensity to involve the ORs.² Wallerian degeneration of the OR fibers can occur from a wide range of injuries to the visual pathway such as traumatic optic neuropathy,³ compressive optic neuropathy, degeneration of the ORs in patients with glaucoma, restricted blood supply of the optic nerve followed by ischemic infarction, and various postoperative visual deficits. Infarcts in both middle and posterior cerebral artery territories can cause injury to the ORs, causing homonymous hemianopia. Finally, preoperative localization of the ORs can be important to ensure the ORs are not affected during neurosurgical procedures.⁴

Knowledge of the tissue properties of each structure is important to image the 3 bundles of the ORs (external sagittal striatum [ESS], internal sagittal striatum [ISS], and tapetum [TAP]) with adequate contrast. Therefore, we proposed using strategically acquired gradient echo (STAGE) imaging as a means to collect qualitative and quantitative information to study the tissue properties of the ORs.⁵ STAGE uses 2 contiguous double-echo gradient-

echo sequences with differing flip angles. STAGE provides a variety of different contrasts, including T1, proton density (PD), quantitative susceptibility map (QSM), and R2* maps. Finally, we propose using diamagnetic susceptibility weighted imaging (dSWI) to further improve visualization of the OR.

MATERIALS AND METHODS

All participants signed consent forms approved by the local institutional review board. Data were collected on a 3T scanner (Verio; Siemens) using a 32-channel head coil. STAGE imaging was used to acquire the data (imaging parameters are given in a previous work).⁵ Briefly, we used TR = 25 ms, flip angles = 6° and 24°, TEs = 7.5 and 17.5 ms, bandwidth = 270 Hz/pixel, and resolution = 0.67 × 0.67 × 2 mm³. With a parallel imaging acceleration factor of 2, STAGE acquisition time was 7 minutes each for these 2 high-resolution scans. They were repeated 3 times, co-registered using SPM,⁶ averaged to increase the signal-to-noise ratio, and processed using software described previously.⁵ In addition, instead of using a positive phase mask from the phase,⁷ we generated dSWI data using a negative phase mask. The following 8 images were evaluated: T2* PD-weighted (the B1 field variation corrected second echo magnitude of the low flip angle scan), PD map, T1 map, R2* map, pure-PD map (T2*-corrected PD map), high-pass-filtered (HPF) phase, dSWI, and QSM. The images were reviewed throughout the OR bundles over roughly 10–15 slices using SPIN software (SpinTech). Slices that demonstrated the best contrast and most uniform signals were used. Given the narrow width of the OR bundles and adjacent bands of WM, for quantification purposes, a line was drawn down the middle of the bundles for ESS, ISS, TAP, and outer and inner WM. Mean and standard deviation were calculated for each layer.

Received July 10, 2020; accepted after revision September 18.

From the Departments of Radiology (P.K.J., S.B., E.M.H.) and Neurology (Y.C.), Wayne State University School of Medicine, Detroit, Michigan; Shanghai World Foreign Language Academy, (W.T.), Shanghai, China; Detroit Medical Center, (S.M.), Detroit, Michigan; MR Innovations Inc. (E.H., E.M.H.), Bingham Farms, Michigan; and Division of Neuroradiology, Department of Medical Imaging (C.C.-T.H.), Gold Coast University Hospital, Southport, Australia.

P.K.J. and Y.C. contributed equally.

Please address correspondence to E. Mark Haacke, PhD, MR Research Core, Harper University Hospital, 3990 John R, Room #G030, Detroit, MI 48201, e-mail: nmrimging@aol.com

<http://dx.doi.org/10.3174/ajnr.A6897>

The PD values were normalized to the outer WM regions. These measurements were calculated for both the right and left ORs and averaged.

RESULTS

Ten healthy volunteers were imaged (mean age, 28.7 ± 5.3 years; range, 20–37 years; 6 female). The 3 bundles of the ORs can be seen clearly in the Figure, D–F. Each image type revealed a different contrast mechanism. 1) On the R2* map, the ESS is part of the bright band that appears to cover all 3 bundles. The 2 dark bands abutting each side of the ORs represent adjacent

subcortical WM. There are occasional medullary veins imaged orthogonal to the long axis of the OR. These appear as white bands on R2* and HPF images (Figure A, F) and dark bands on the dSWI and T2* PD-weighted images (Figure D, E) cutting across the 5 bundles. 2) On the QSM and HPF phase images (Figure C, F), the ESS is the darkest band. Often the ISS and TAP cannot be identified clearly on these 2 images, and the medullary veins appear bright. 3) On the PD map, the 5 layers (WM, ESS, ISS, TAP, and WM) can be identified with the 3 OR bundles appearing as “dark–bright–dark” bands in the images as “ESS–ISS–TAP.” The adjacent subcortical WM is the 2 white bands outside the ESS and lateral to the tapetum. 4) On the T1 map and pure-PD map images,

only the dark band representing ESS can be seen. Finally, 5) the dSWI and T2* PD-weighted images showed the best contrast depicting all 5 layers (Figure D, E). The dSWI provided the highest contrast between the 5 layers with the ESS being highlighted because of the intrinsic diamagnetic nature of the fiber bundles.

Our data show that tissues with the highest PD have the highest T1, lowest R2*, and susceptibility close to zero (Table). On the other hand, the most negative PD tissues (the ESS and tapetum) have the lowest T1, highest R2*, and most negative susceptibility (Table). Specifically, the WM had the highest T1 of 864.3 ± 23.4 (ms), the lowest R2* of 20.1 ± 1.3 (s^{-1}), and a susceptibility of -3.1 ± 11.3 ppb (effectively zero). The 3 bundles of the ORs showed relative PD about 0.911, T1 of about 784 ms, and R2* values of about 28/s. All of these are significantly different from WM ($P < .001$ for 1-way ANOVA followed by the Tukey-Kramer post hoc test).

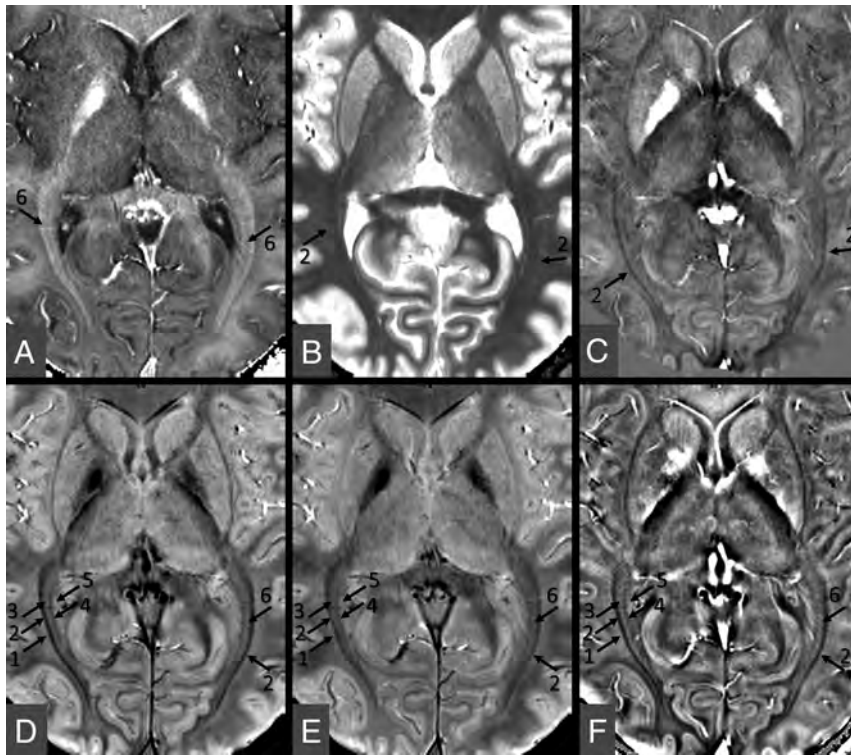


FIGURE. Example images used for evaluating the ORs from a representative case (a 32-year-old woman). A, R2* map. B, T1 map. C, QSM. D, dSWI. E, T2*-PD-weighted image. F, HPF phase image. The T2*-PD-weighted and dSWI show the best contrast for visualizing the ORs, in which the ESS and TAP (black arrows 2 and 4) and the ISS (arrow 3) can be identified. In D and E, one can see 5 bundles: the outer WM layer (arrow 1), the ESS (arrow 2), the ISS (arrow 3), the TAP (arrow 4), and the inner WM (arrow 5) layer. Also, for the T2*-PD-weighted (E), R2* (A), dSWI (D), and HPF phase data (F), there is evidence of veins cutting across the 5 bundles (arrow 6).

DISCUSSION AND CONCLUSIONS

In this work, the MR tissue properties of the layers of the OR bundles and the adjacent WM were quantitatively

Averaged results over all 10 participants showing the quantitative tissue properties of the 3 bundles of the ORs compared with adjacent WM

	R2* (1/s)	QSM (ppb)	Phase (SPU)	T1 (ms)	PDmap ⁺	dSWI ⁺	T2* PDW ⁺	Pure PD ⁺
	Mean ± SD	Mean ± SD	Mean ± SD	Mean ± SD	nMean ± nSD	nMean ± nSD	nMean ± nSD	nMean ± nSD
WM	20.1 ± 1.3	-3.1 ± 11.3	32.1 ± 26.8	864.3 ± 23.4	1	1	1	1
ESS	29.8 ± 1.6	-42.2 ± 10.1	-158.9 ± 32.8	780.3 ± 23.3	0.889 ± 0.017	0.725 ± 0.034	0.841 ± 0.022	0.928 ± 0.023
ISS	26.5 ± 1.6	-18.3 ± 8.7	-39.6 ± 28.5	791.2 ± 25.7	0.925 ± 0.017	0.859 ± 0.031	0.89 ± 0.023	0.958 ± 0.024
TAP	27.2 ± 1.7	-19.6 ± 9.5	-57.3 ± 32.1	779.4 ± 22.4	0.919 ± 0.018	0.834 ± 0.031	0.878 ± 0.024	0.954 ± 0.024
WM	20.3 ± 2.4	-0.8 ± 12.1	22.1 ± 42.4	870.6 ± 37.9	0.988 ± 0.024	0.99 ± 0.04	1.005 ± 0.035	0.998 ± 0.027

Note:—The ⁺ sign indicates that these values were normalized to adjacent WM values. Mean and standard deviation (SD) are given for each structure and each image type. The standard error of the mean can be obtained by dividing each SD by $\sqrt{10}$.

Phase is represented in Siemens phase units (SPU) ranging from -4096 to 4096 ($-\pi$ to π radians). To convert phase to radians, multiply the phase value with $\pi/4096$. nMean indicates normalized mean; nSD = normalized standard deviation; PDW, PD-weighted.

analyzed using STAGE. We found that T1 and R2* for different tissues behave as expected relative to water content with the highest PD tissues having the highest T1, lowest R2* and close to zero susceptibility and the lowest PD tissues having the lowest T1 and highest R2*. As expected, the diamagnetic fiber tracts, especially the ESS, which has the highest density of fibers, had the most negative susceptibility. Using the T2*-PD-weighted image along with SWI processing for diamagnetic structures, the best contrast was shown for the dSWI data. Although the OR bundles have been difficult to differentiate on conventional MR imaging, we have shown here that SWI and dSWI can exquisitely delineate the separate layers of the OR bundles based on their differences in susceptibility (Fig).^{8,9}

Compared with its neighboring fiber bundles, the ESS is the richest in myelin, demonstrating both the largest axons and thickest myelin sheaths.⁹ It is usually the easiest to visualize, but the ISS and TAP are often difficult to visualize. Not only does the diamagnetic susceptibility of the ESS help enhance its contrast, but it can also be used to predict the increase in R2*. Recent works have shown that changes in R2* (1/s) are roughly one-eighth changes in susceptibility (given in parts per billion) at 3T.¹⁰ With a change of roughly 30 ppb relative to WM in the ESS, this would predict a change of roughly 4/s in R2*, very close to the 5/s seen in our data. One could imagine using dSWI as a means to guide or constrain the fiber tracking in diffusion tensor imaging for the ORs.¹¹

There are several limitations to this study. First, the sample size is small and does not capture the potential alterations in tissue properties with age. Second, higher resolution imaging could provide even better definition of the different layers of the ORs but requires longer scanning time.

In summary, whereas STAGE is best suited to quantify the tissue properties and delineate the OR bundles, dSWI provides high-contrast images of the ORs and the surrounding subcortical WM layers.

Disclosures: Pavan Jella—UNRELATED: Employment: Wayne State University, Comments: I am an employee at Wayne State University, and I am paid for

performing my responsibilities as a research assistant and MRI technologist. Charlie Chia-Tsong Hsu—UNRELATED: Employment: Gold Coast University Hospital. E. Mark Haacke—UNRELATED: Board Membership: SpinTech Inc, Comments: Chief Scientific Officer; Employment: Wayne State University; Grants/Grants Pending: Wayne State University.

REFERENCES

1. Kitajima M, Korogi Y, Okuda T, et al. **Hyperintensities of the optic radiation on T2-weighted MR images of elderly subjects.** *AJNR Am J Neuroradiol* 1999;20:1009–14 Medline
2. Reich DS, Smith SA, Gordon-Lipkin EM, et al. **Damage to the optic radiation in multiple sclerosis is associated with retinal injury and visual disability.** *Arch Neurol* 2009;66:998–1006 CrossRef Medline
3. Steinsapir KD, Goldberg RA. *Traumatic optic Neuropathies.* In: *Walsh and Hoyt's Clinical Neuroophthalmology.* 5th ed. Baltimore: Williams and Wilkins; 1998
4. Nooij R, Hoving E, van Hulzen A, et al. **Preservation of the optic radiations based on comparative analysis of diffusion tensor imaging tractography and anatomical dissection.** *Front Neuroanat* 2015;9:96 CrossRef Medline
5. Chen Y, Liu S, Wang Y, et al. **Strategically Acquired Gradient Echo (STAGE) imaging, part I: Creating enhanced T1 contrast and standardized susceptibility weighted imaging and quantitative susceptibility mapping.** *Magn Reson Imaging* 2018;46:130–39 CrossRef Medline
6. Penny WD, Friston KJ, Ashburner JT, et al. *Statistical Parametric Mapping: The Analysis of Functional Brain Images.* Elsevier; 2011
7. Haacke EM, Xu Y, Cheng YC, et al. **Susceptibility weighted imaging (SWI).** *Magn Reson Med* 2004;52:612–18 CrossRef Medline
8. Ide S, Kakeda S, Korogi Y, et al. **Delineation of optic radiation and stria of Gennari on high-resolution phase difference enhanced imaging.** *Acad Radiol* 2012;19:1283–89 CrossRef Medline
9. Mori N, Miki Y, Kasahara S, et al. **Susceptibility-weighted imaging at 3 Tesla delineates the optic radiation.** *Invest Radiol* 2009;44:140–45 CrossRef Medline
10. Ghassaban K, Liu S, Jiang C, et al. **Quantifying iron content in magnetic resonance imaging.** *Neuroimage* 2019;187:77–92 CrossRef Medline
11. Hofer S, Karaus A, Frahm J. **Reconstruction and dissection of the entire human visual pathway using diffusion tensor MRI.** *Front Neuroanat* 2010;4:15 CrossRef Medline

Dural Venous Sinus Stenosis: Why Distinguishing Intrinsic-versus-Extrinsic Stenosis Matters

S.H. Sundararajan, A.D. Ramos, V. Kishore, M. Michael, R. Doustaly, F. DeRusso, and A. Patsalides



ABSTRACT

BACKGROUND AND PURPOSE: Dural venous sinus stenosis has been associated with idiopathic intracranial hypertension and isolated venous pulsatile tinnitus. However, the utility of characterizing stenosis as intrinsic or extrinsic remains indeterminate. The aim of this retrospective study was to review preprocedural imaging of patients with symptomatic idiopathic intracranial hypertension and pulsatile tinnitus, classify the stenosis, and assess a trend between stenosis type and clinical presentation while reviewing the frequencies of other frequently seen imaging findings in these conditions.

MATERIALS AND METHODS: MRVs of 115 patients with idiopathic intracranial hypertension and 43 patients with pulsatile tinnitus before venous sinus stent placement were reviewed. Parameters recorded included the following: intrinsic or extrinsic stenosis, prominent emissary veins, optic nerve tortuosity, cephalocele, sella appearance, poststenotic fusiform enlargement versus saccular venous aneurysm, and internal jugular bulb diverticula. χ^2 cross-tabulation statistics were calculated and recorded for all data.

RESULTS: Most patients with idiopathic intracranial hypertension (75 of 115 sinuses, 65%) had extrinsic stenosis, and most patients with pulsatile tinnitus (37 of 45 sinuses, 82%) had intrinsic stenosis. Marked optic nerve tortuosity was more common in idiopathic intracranial hypertension. Cephaloceles were rare in both cohorts, with an increased trend toward the presence in idiopathic intracranial hypertension. Empty sellas were more common in idiopathic intracranial hypertension. Cerebellar tonsils were similarly located at the foramen magnum level in both cohorts. Saccular venous aneurysms were more common in pulsatile tinnitus. Internal jugular bulb diverticula were similarly common in both cohorts.

CONCLUSIONS: In this cohort, most patients with idiopathic intracranial hypertension had extrinsic stenosis, and most patients with pulsatile tinnitus had intrinsic stenosis. Awareness and reporting of these subtypes may reduce the underrecognition of potential contributory stenoses in a given patient's idiopathic intracranial hypertension or pulsatile tinnitus.

Idiopathic intracranial hypertension has undergone several name changes since the 1890s, previously referred to pseudotumor cerebri, followed by benign intracranial hypertension, and, most recently, idiopathic intracranial hypertension. While the term “idiopathic” is used to describe this pathology, there has been continued emergence of research pointing to idiopathic

intracranial hypertension stemming from a neurovascular etiology. The redistribution pathway of CSF involves absorption from brain and spinal subarachnoid spaces into the systemic circulation via arachnoid granulations located within the walls of the dural venous sinuses. Thus, blockage or severe stenoses of the dural venous sinuses responsible for draining intracranial venous circulation has the potential to limit CSF re-absorption, therefore leading to gradual intracranial CSF buildup with subsequent elevations of intracranial pressure and resultant symptomatology as reported in the literature.¹⁻⁴

Although pulsatile tinnitus has been associated with idiopathic intracranial hypertension, its unique manifestation in either the setting of idiopathic intracranial hypertension or in isolation remains a clinical enigma. This vascular somatosound has been reported in the setting of venous sinus stenosis, lateral sinus wall dehiscence with associated venous sinus aneurysms, and prominent collateral circulation via mastoid, condylar, or occipital emissary veins.^{5,6}

Dural venous sinus stenosis can be characterized as either intrinsic or extrinsic stenosis. Intrinsic stenosis refers to internal

Received June 8, 2020; accepted after revision September 4.

From the Department of Neurosurgery (S.H.S., A.D.R., M.M., F.D.), Division of Interventional NeuroRadiology, NY Presbyterian Hospital Weill Cornell Medicine, New York, New York; GE Healthcare (V.K., R.D.), Buc, France; and Department of Neuro-Interventional Surgery (A.P.), North Shore University Hospital, Northwell Health, Manhasset, New York.

Data from this article were first presented as an ePoster and recorded lecture at: Annual Meeting of the American Society of Neuroradiology, May 30 to June 4, 2020; Virtual.

Please address correspondence to Athos Patsalides, MD, MPH, Neuro-Interventional Surgery, North Shore University Hospital, Northwell Health, 300 Community Dr, Manhasset, NY 11030; e-mail: apatsalides@northwell.edu; @radiolosri

Indicates open access to non-subscribers at www.ajnr.org

<http://dx.doi.org/10.3174/ajnr.A6890>

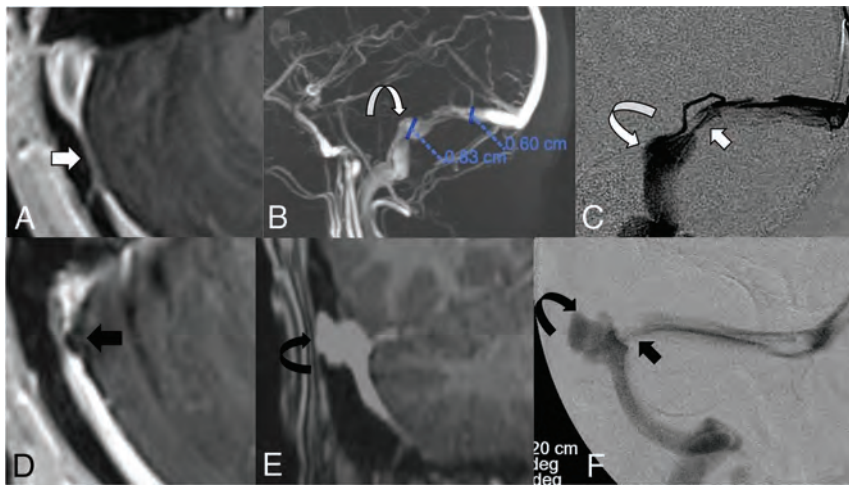


FIG 1. A, Axial postcontrast MRV demonstrating extrinsic stenosis from the overlying cerebellum (short white arrow). B, Contrast-enhanced 3D-MRV image shows poststenotic sigmoid sinus enlargement (curved white arrow). C, Accompanying lateral venography confirms stenosis (white arrow) and sinus enlargement (curved white arrow) seen on the corresponding MRV. D, Separate axial postcontrast MRV shows intrinsic stenosis from arachnoid granulations (black arrow). E, A coronal postcontrast MRV sequence shows lateral sinus dehiscence with a venous aneurysm (curved black arrow). F, Accompanying frontal venography confirms stenosis (short black arrow) and a saccular aneurysm (curved black arrow) seen on the corresponding MRV.

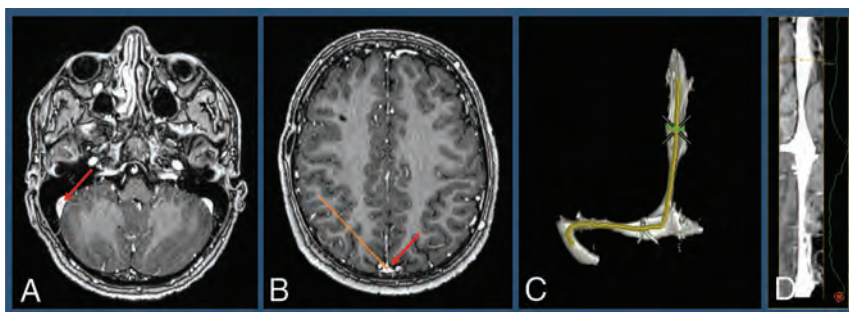


FIG 2. A, 2-Click automatic vessel analysis start point selection in the sigmoid sinus (short arrow). B, 2-Click automatic vessel analysis end point selection (long arrow) in the superior sagittal sinus. C, 3D volume-rendered vessel segmentation. D, Lumen view shows the straightened vessel segmentation.

filling defects such as prominent arachnoid granulations that narrow the sinus. Extrinsic stenosis involves external compression of the sinus by adjacent brain parenchyma.^{7,8} Despite the overlap of venous sinus stenosis in both idiopathic intracranial hypertension and isolated pulsatile tinnitus of venous etiology, the type of stenosis is seldom distinguished in clinical practice despite a pre-existing classification schema in the literature. The purpose of this study was to review preprocedural imaging of treated patients with symptomatic idiopathic intracranial hypertension and pulsatile tinnitus in our institution and classify the stenosis to assess the presence or absence of a trend between stenosis type and clinical presentation.

MATERIALS AND METHODS

Following institutional review board (Weill Cornell Medicine) approval, a retrospective review of patients treated with venous

sinus stent placement from January 2012 to January 2020 was performed. Two certified neuroradiologists reviewed, in consensus, MRV head imaging performed within 3 months of a planned intervention and conventional venography performed at the time of the subsequent intervention. All institutional MRV examinations were performed on 3T units (Magnetom Skyra; Siemens; and Signa Architect; GE Healthcare) with coronal 2D-TOF, sagittal 3D phase contrast, and 3D thin-section T1 pre- and postcontrast sequences (echo-spoiled gradient echo or MPRAGE). Contrast-enhanced sequences were acquired following weight-based intravenous administration of gadobutrol (Gadavist; Bayer Schering Pharma). Classification schemas were implemented for all recorded imaging findings to allow the objective recording of parameters and subsequent data evaluation. χ^2 cross-tabulation statistics were calculated and recorded for all data, with an α of .05 used for all computations.

Patients were categorized into the idiopathic intracranial hypertension and isolated venous pulsatile tinnitus cohorts before planned interventions. Eligibility for idiopathic intracranial hypertension cohort categorization required a diagnosis of idiopathic intracranial hypertension as per pre-established criteria, including a lumbar puncture opening pressure of ≥ 25 cm H₂O in the left lateral decubitus position and preprocedural clinical evaluation for papilledema by an ophthalmologist.³

Categorization into the pulsatile tinnitus cohort consisted of several strict criteria. Patients with clinical findings consistent with pulsatile tinnitus from a venous origin and imaging findings of lateral venous sinus stenosis of at least 50% either ipsilateral to the pulsatile tinnitus or within the dominant sinus were included in the pulsatile tinnitus cohort. Patients with causes of pulsatile tinnitus other than lateral sinus stenosis were excluded. An otorhinolaryngologist evaluated all patients within 6 months of planned interventions. Patients with otologic disorders, nonpulsatile tinnitus, or spontaneous CSF leak were excluded. Similarly, an ophthalmologist evaluated all patients within 6 months of planned interventions. The presence of papilledema of any degree was considered an exclusion criterion. Patients with venous pulsatile tinnitus symptomatology yet with opening pressure of 25 cm H₂O or higher were excluded from the pulsatile tinnitus cohort and instead were included in the idiopathic intracranial hypertension cohort. Patients with opening pressure between 20 and 24 cm H₂O were

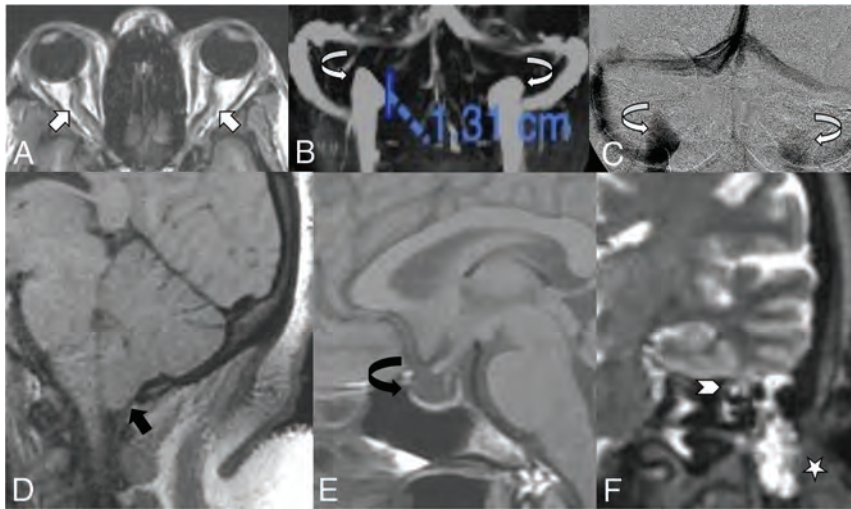


FIG 3. Objective parameters implemented in recording corollary findings of both idiopathic intracranial hypertension and pulsatile tinnitus cohorts. *A*, Marked optic nerve tortuosity, with >50% of optic sheath width deviation noted relative to its expected straight path along the optic canal (white arrows). *B*, Bilateral ≥ 5 -mm internal jugular bulb diverticula, as seen on MRV (*B*) and catheter venography (*C*) images (curved white arrows). *D*, Cerebellar tonsil projecting 1–3 mm below the foramen magnum, referred to as ectopia (black arrow). *E*, Empty sella recorded if there is >75% loss of pituitary height (curved black arrow). *F*, Coronal T2 MR imaging demonstrates a left temporal lobe cephalocele through the tegmen tympani (arrowhead) and CSF in mastoid air cells (star).

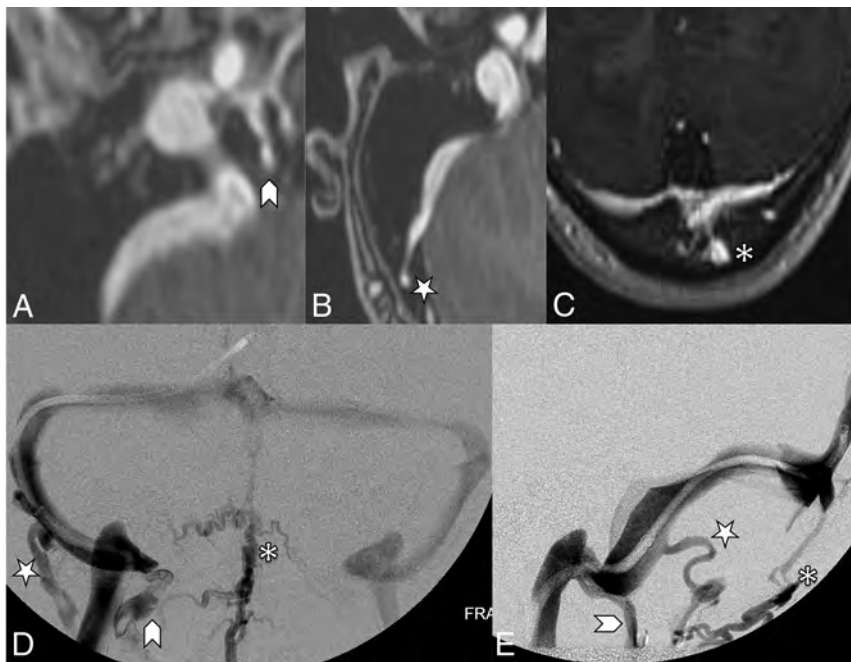


FIG 4. Contrast-enhanced MRV images (*A*, *B*, and *C*) highlighting features of the emissary veins categorized in this study. *A*, A condylar vein is seen arising from the internal jugular vein bulb extending through the condylar canal (arrowhead). *B*, A mastoid emissary vein is seen arising from the sigmoid sinus traversing the mastoid foramen (star). *C*, An occipital emissary vein is seen arising from the torcula extending through the calvaria (asterisk). Conventional venography frontal (*D*) and lateral (*E*) images showcase the 3 emissary vein types categorized in this study. The condylar vein (arrowhead) extends inferiorly toward the vertebral plexus. The mastoid emissary vein (star) extends posteriorly and inferiorly to join the suboccipital plexus and external jugular vein. The occipital emissary vein (asterisk) drains inferiorly into the suboccipital plexus.

initially medically managed with acetazolamide for 4 weeks with subsequent inclusion in the pulsatile tinnitus cohort if there was no major improvement of pulsatile tinnitus. The severity of pulsatile tinnitus was assessed with a standardized questionnaire, the Tinnitus Handicap Inventory.⁹ A minimum score of 38, consistent with moderate severity, was required for inclusion in the pulsatile tinnitus cohort.

All venous sinus stenoses included were considered severe at the time of initial and retrospective study review. The location and type of stenosis were recorded on the basis of findings made from MRV examinations. However, because all cohort patients underwent venous sinus stent placement, conventional venography images were available for review and useful in corroborating the stenosis subtype characterized on MRV. Stenosis lengths were not recorded. Stenosis caused by intraluminal processes such as prominent arachnoid granulations were classified as intrinsic stenosis. Stenosis caused by compression of the venous sinus from brain parenchyma against the adjacent calvaria was classified as extrinsic stenosis. In the event of intrinsic stenoses preceding segments of extrinsic stenosis, the overall stenosis was still categorized as extrinsic stenosis. The presence of poststenotic dilation of the lateral sinus was classified as “fusiform” if it had the appearance of a shallow, wide-neck aneurysm with a 25%–50% increase in size relative to its expected diameter. The term “saccular” was used if it had the appearance of a discrete dome with the depth larger than the neck dimensions. Examples of these findings are shown in Fig 1.

Straight-vessel views and 3D reconstructions of both TOF and contrast-enhanced images were created and reviewed to better characterize venous sinus anatomy and stenosis, as shown in Fig 2. The straightened vessel view was achieved using 2-click automatic vessel analysis (Vessel ASSIST; GE Healthcare). After the user selected the start and end points in the sigmoid sinus and superior sagittal sinus, the software automatically tracked the vessel and computed its centerline. The resulting vessel segmentation could be displayed

Table 1: Idiopathic intracranial hypertension and pulsatile tinnitus cohort demographics

Demographic	Idiopathic Intracranial Hypertension	Pulsatile Tinnitus
No. of patients	115	43
Age (yr)	Mean = 32.8 Min = 4 Max = 66	Mean = 38.1 Min = 20 Max = 67
No. of females	107 (90%)	41 (95%)
No. of males	8 (10%)	2 (5%)
No. of sinuses:	115	45 sinuses ^a
Right	90	29
Left	25	16

Note:—Min indicates minimum; Max, maximum.

^aTwo patients were stented bilaterally.

Table 2: Breakdown of intrinsic and extrinsic stenosis relative to the total number of sinuses and distribution of additional corollary findings noted in the idiopathic intracranial hypertension and pulsatile tinnitus cohorts^a

Imaging Finding	IIH	PT
Stenosis type		
Extrinsic stenosis	58	8
Mixed extrinsic and intrinsic	17	0
Intrinsic stenosis	40	37
Total	115	45
$\chi^2 P$ value $\leq .001^b$		
Saccular venous aneurysm		
Yes	4	11
No	111	34
Total	115	45
$\chi^2 P$ value $\leq .001$		
Sella appearance		
Partially empty	49	18
Empty	61	15
Normal	5	11
NA (adenoma)	0	1
Total	115	45
$\chi^2 P$ value $\leq .001$		
Optic nerve tortuosity		
Minimal	46	31
Marked	69	14
Total	115	45
$\chi^2 P$ value = .001		

Note:—NA indicates not applicable; IIH, idiopathic intracranial hypertension; PT, pulsatile tinnitus.

^a χ^2 cross-tabulation *P* values were calculated for each variable. Eighty-two percent of pulsatile tinnitus sinuses had intrinsic stenosis, and 65% of idiopathic intracranial hypertension sinuses had extrinsic stenosis (*P* value $< .001$). Statistically significant differences were noted when comparing the distribution of optic nerve tortuosity, sella appearance, and saccular aneurysm presence between the 2 groups (*P* values $\leq .001$).

^bExtrinsic and mixed subgroups summed for χ^2 calculation.

as a 3D volume-rendered model or a lumen view (D). The lumen view is obtained by transforming the 3D vessel centerline into a straight line and displaying the corresponding perpendicular plane for each point on the line. For each position, minimum, mean, and maximum diameters were automatically computed.

The other recorded imaging findings included the presence or absence of prominent emissary veins, optic nerve tortuosity, cephalocele, sella appearance, sinus enlargement versus aneurysm, and internal jugular bulb diverticula as shown in Fig 3. The presence of prominent emissary veins was initially detected on MRV and corroborated on subsequent conventional venography.

Table 3: Continued breakdown of intrinsic and extrinsic stenosis relative to the total number of sinuses and distribution of additional corollary findings noted in the idiopathic intracranial hypertension and pulsatile tinnitus cohorts^a

Imaging Finding	IIH	PT
Internal jugular bulb diverticulum size		
<5 mm	47	26
≥ 5 mm	68	19
Total	115	45
$\chi^2 P$ value = .053		
Cerebellar tonsil location		
Above	22	11
At	54	23
Ectopia	35	11
Above (prior Chiari I surgery)	4	0
Total	115	45
$\chi^2 P$ value = .522		
Cephalocele presence		
No	110	44
Yes	5	1
Total	115	45
$\chi^2 P$ value = .525		
Emissary vein prominence		
Condylar	52	19
Occipital and condylar	28	11
Mastoid	6	1
Mastoid and condylar	5	3
Occipital, condylar, and mastoid	1	2
None	23	9
Total	115	45
$\chi^2 P$ value = 1		

Note:—IIH indicates idiopathic intracranial hypertension; PT, pulsatile tinnitus.

^aNo significant differences were noted when comparing the distribution of internal jugular bulb diverticulum size, cerebellar tonsil location, cephalocele presence, or emissary vein prominence (*P* values $\geq .053$).

The 3 subtypes classified were condylar arising from the internal jugular bulb, mastoid arising from the sigmoid sinus, and occipital arising from the torcula as shown in Fig 4.

Optic nerve tortuosity was evaluated on axial thin-section T1- and T2-weighted images when available. Tortuosity was classified as marked if the optic sheath width deviated $>50\%$ of its diameter relative to its expected straight path from the optic canal and minimal if $<50\%$ of its diameter. Cephaloceles were characterized as being either present or absent.

The degree of mass effect on the sella was graded in reference to the noncompressed posterior pituitary gland relative to the expected pituitary gland height in each case. The sella was characterized as empty if $>75\%$ of pituitary parenchymal height was lost on sagittal plane imaging and partially empty if anywhere between 25% and 75% loss of pituitary height was identified. The cerebellar tonsils were graded according to location on sagittal plane imaging. ‘Above’ was used when both cerebellar tonsils were above the foramen magnum, noting 4 separate patients with prior Chari 1 surgical intervention were separately categorized. ‘At’ was used when one or both cerebellar tonsils were at the foramen magnum. ‘Ectopia’ was used when one or both cerebellar tonsils were projecting below the foramen magnum by 1–3 mm. Internal jugular bulb diverticula were evaluated on coronal plane MRV imaging, with sizes graded according to height projecting above a line drawn perpendicular to the distal sigmoid sinus insertion into the internal jugular vein. Diverticula were

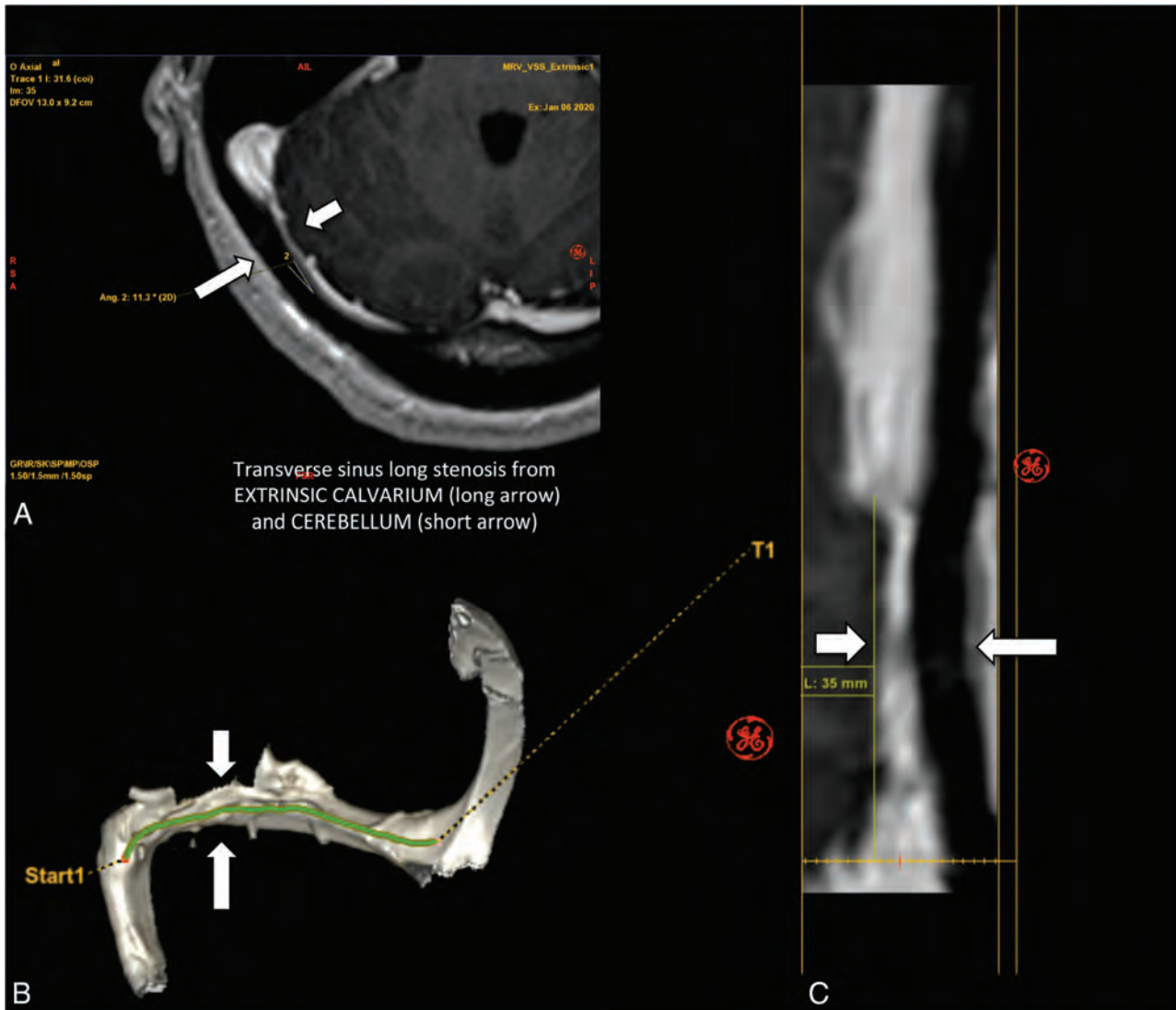


FIG 5. MR images showing extrinsic stenosis of the right transverse sinus. The *short arrows* point to right cerebellar parenchyma location, and the *long arrows* points to the occipital calvaria location. **A**, An axial contrast-enhanced MRV image. **B**, A 3D reconstruction image. **C**, A straight-vessel reformat of the right transverse-to-proximal sigmoid sinus from source contrast-enhanced axial images.

categorized as either being small (<5 mm in height) or prominent (≥ 5 mm in height).

RESULTS

The imaging of 115 patients with idiopathic intracranial hypertension (107 women; mean, 32.8 years age of age) and 43 with pulsatile tinnitus (41 women; mean, 38.1 years of age) who underwent subsequent endovascular intervention was reviewed. Forty-five sinuses were counted in the pulsatile tinnitus cohort because 2 patients were bilaterally stented (Tables 1–3). Regardless of the cohort, all patients with intrinsic stenosis had either a single arachnoid granulation or a cluster of prominent arachnoid granulations located at the transverse-sigmoid sinus junction. Similarly, all patients with extrinsic stenosis in both cohorts were from overlying brain parenchyma extending from the transverse sinus to the sigmoid sinus.

In both idiopathic intracranial hypertension and pulsatile tinnitus cohorts, most patients similarly had prominence of the

emissary veins ($P = 1$). The 2 most commonly seen were condylar and occipital subtypes. Marked optic nerve tortuosity was more common in the idiopathic intracranial hypertension cohort compared with the pulsatile tinnitus cohort ($P = .001$). Cephaloceles were infrequently present in both cohorts, with an increased trend toward their presence in the idiopathic intracranial hypertension cohort relative to the pulsatile tinnitus cohort ($P = .525$). Empty sellas were more common in the idiopathic intracranial hypertension cohort compared with the pulsatile tinnitus cohort ($P < .001$). Cerebellar tonsils were frequently located at the foramen magnum level in both cohorts ($P = .522$). Sacular aneurysms were more common in the pulsatile tinnitus cohort relative to the idiopathic intracranial hypertension cohort ($P < .001$). Internal jugular bulb diverticula were similarly common in distribution across both cohorts, regardless of <5 or ≥ 5 mm size ($P = .053$). Specifics regarding these findings are noted in Fig 4.

Seventy-five of 115 (65%) sinuses in the idiopathic intracranial hypertension cohort had extrinsic stenosis related to

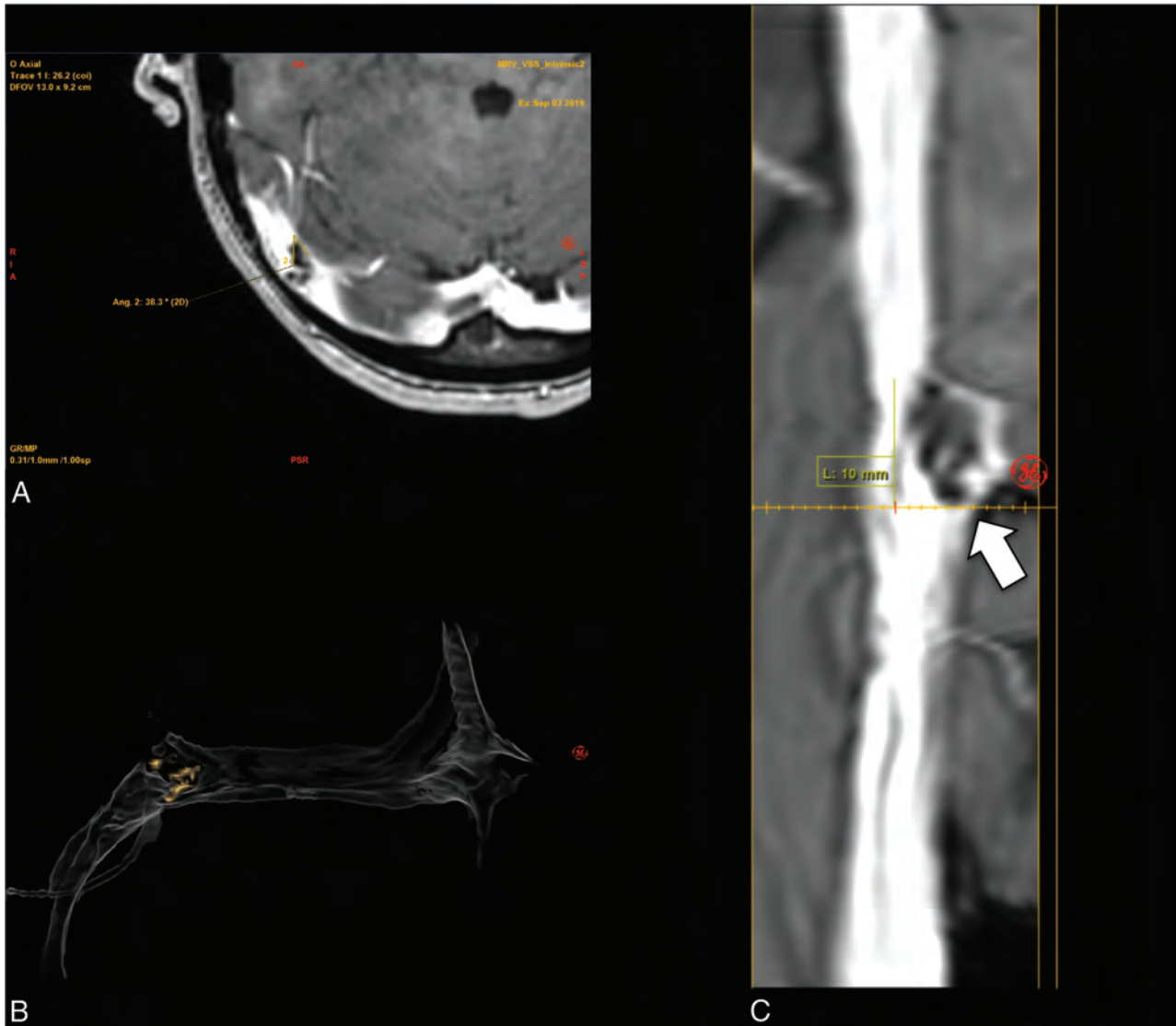


FIG 6. MR images showing intrinsic stenosis of the right transverse sinus. The *short arrow* points to a prominent arachnoid granulation situated inside the sinus. *A*, An axial contrast-enhanced MRV image, *B*, A 3D reconstruction image. *C*, A straight-vessel reformat of the right transverse-to-proximal sigmoid sinus from source contrast-enhanced axial images, noting orange shading of the arachnoid granulation and transparency of the remaining dural venous sinus.

narrowing from adjacent parenchyma. Seventeen of these sinuses were in patients with dominant extrinsic stenosis and superimposed prominent arachnoid granulations flanking either end of the extrinsic stenosis. The remaining 58 sinuses had extrinsic stenosis alone. Forty patients in the idiopathic intracranial hypertension cohort (35%) had intrinsic stenosis related to arachnoid granulations.

Thirty-seven of 45 (82%) sinuses in the pulsatile tinnitus cohort had intrinsic stenosis related to arachnoid granulations. In the remaining 8 patients in the pulsatile tinnitus cohort, all 8 (18%) had extrinsic stenosis related to adjacent brain parenchyma. As noted above, 11 of 45 (24%) had saccular venous aneurysms of the transverse/sigmoid junction. The remaining 34 of 45 (76%) had poststenotic fusiform sinus enlargement.

The proportion of patients with idiopathic intracranial hypertension presenting with extrinsic stenosis relative to those with pulsatile tinnitus presenting with intrinsic stenosis was a statistically significant difference (P value < .001). These results are summarized in Tables 2 and 3.

DISCUSSION

In this cohort, review of neuroimaging demonstrated intrinsic and extrinsic stenosis presence in the transverse sinus, transverse-sigmoid sinus junction, and proximal sigmoid sinus in patients with both idiopathic intracranial hypertension and isolated pulsatile tinnitus clinical symptomatology. Extrinsic and intrinsic stenoses alike were best detected on thin-section contrast-enhanced axial MRV images, reconstructed straight-vessel views of the affected dural venous sinus, and 3D reconstructions of either TOF or contrast-enhanced MRV imaging (Figs 5 and 6). Within the idiopathic intracranial hypertension cohort, 65% of the sinuses had extrinsic stenosis about the margins of the transverse and sigmoid sinuses. This finding is in contrast to the pulsatile tinnitus cohort in which 82% of the sinuses had intrinsic stenosis related to arachnoid granulations, noting that the presence or absence of superimposed webbing may contribute to stenosis as well. The imaging features of webbing or intraluminal synechia are ill-defined on cross-sectional imaging modalities, noting that

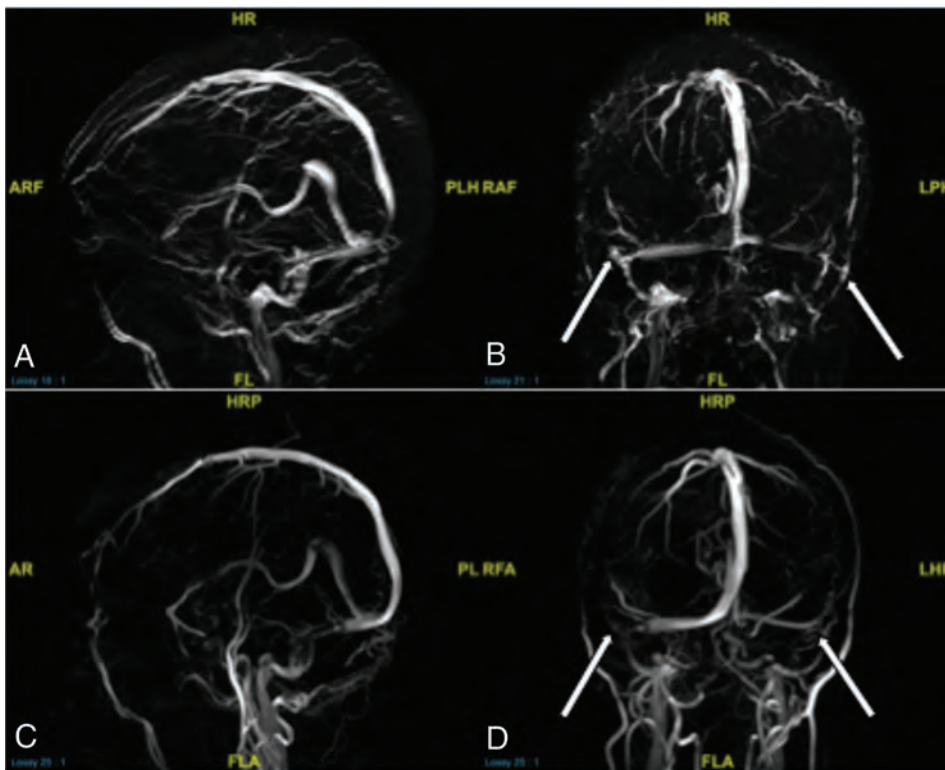


FIG 7. Comparing TOF sagittal and coronal 3D reconstructions (A and B) and contrast-enhanced sagittal and coronal 3D reconstructions (C and D) from MRV in a patient with idiopathic intracranial hypertension. Note how the TOF images show the patient's physiologic venous drainage due to properties of TOF imaging, showing only blood draining back to the patient's heart (veins). Contrast-enhanced imaging, though crisper, shows arteries and veins in the same image. B and D. Arrows point to severe extrinsic stenoses in the bilateral transverse sinus-sigmoid sinus junctions, a common location for idiopathic intracranial hypertension stenosis. Such short-segment severe stenoses appear to simulate the abrupt narrowing commonly seen in short-segment intrinsic stenoses on these 3D reconstructions. However, review of source imaging would demonstrate brain parenchymal narrowing rather than primary arachnoid granulations producing the stenoses. HRP indicates head right posterior; PLH, posterior left head; RAF, right anterior foot; RA, right anterior; FL, foot left; PL, posterior left; RFA, right foot anterior; LHP, left head posterior; LPH, left posterior head; ARF, anterior right foot; AR, anterior right; FLA, foot left anterior; AF, anterior foot.

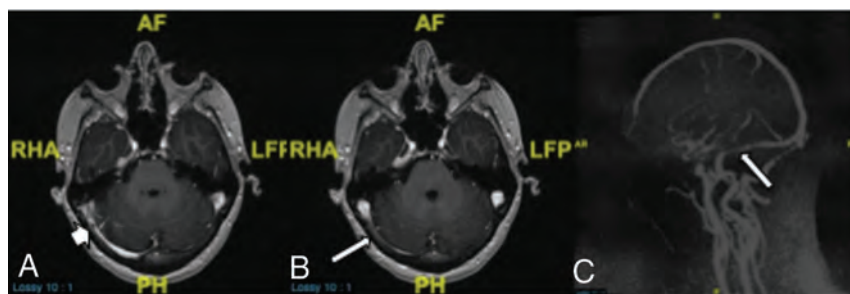


FIG 8. MR images demonstrating focal intrinsic stenosis just proximal to dominant extrinsic stenosis in this patient with idiopathic intracranial hypertension. The *short arrow* in A demonstrates focal arachnoid granulation. The *long arrows* in B and C demonstrate a primary extrinsic stenosis pattern. Despite the mixed presence of intrinsic and extrinsic stenoses, this was categorized as primary extrinsic stenosis. RHA indicates right head anterior; PH, posterior head; LFP, left foot posterior; AF, anterior foot; AR, anterior right; PL, posterior left; H, head; F, foot.

their presence can be detected with the use of intravascular ultrasound.¹⁰ However, in our experience, knowledge of the presence or absence of webbing with an otherwise MR imaging-evident stenosis produced by arachnoid granulation or brain parenchyma

was not beneficial in procedural planning. Thus, the use of intravascular ultrasound during venous sinus procedures is no longer routinely performed at our institution.

MRV without contrast involves the use of TOF techniques that image the flow of blood in a specific direction, therefore allowing its specificity in looking at the venous system rather than the arteries. TOF allows a physiologic approximation of the dural venous sinus caliber in relation to venous flow through the sinus that can better approximate the true degree of stenosis in a given segment. By administering contrast, one can better characterize a stenosis as the sinus lining and can inspect luminal content with a high spatial resolution compared with flow-related techniques alone. Contrast-enhanced images also provide the true sinus caliber relative to surrounding calvarial demarcations, an important distinction compared with flow when measuring for hardware sizes, depending on the dural venous sinus segment to be stented. Volume-rendered and 3D reconstructed images from source TOF and contrast-enhanced images were of equal importance in demonstrating a global understanding of the type and location of stenosis (Fig 7).^{10,11}

Confounders in the dichotomous characterization of intrinsic-versus-extrinsic stenosis can be seen. For instance, the degree of extrinsic stenosis can be so severe and short-segmented as to remove the typically seen feature of extrinsic stenosis tapering, giving a false appearance of a rounded filling defect on 3D reconstructions (Fig 7).

However, source images would reveal an abrupt change in caliber related to brain parenchyma and not primary intrinsic stenosis lead points. One useful means of distinguishing severe extrinsic-versus-intrinsic stenosis is the continuity of the stenosis in question.

Specifically, extrinsic stenosis is typically continuous in length owing to its uniform brain parenchymal extension into the sinus. In contrast, intrinsic stenosis may manifest as discontinuous points of stenosis, depending on the distribution and number of contributory arachnoid granulations.

Some patients may have features of both intrinsic and extrinsic stenosis. This was seen in 17 of the patients in the idiopathic intracranial hypertension cohort, noting that such a mixed appearance was not identified in any of the patients in the pulsatile tinnitus cohort. All these cases had the appearance of clustered arachnoid granulations located either proximal or distal to the area of otherwise-prominent extrinsic stenosis. Arachnoid granulations can demonstrate compensatory enlargement to promote further reabsorption of CSF in the setting of an underlying dural venous sinus stenosis.¹² Thus, in patients with arachnoid granulations about the margins of a prominent sinus narrowing from overlying parenchyma, the authors considered these sinuses as having overall extrinsic stenosis (Fig 8).

The presence of internal jugular vein diverticula or prominent emissary veins was uniformly distributed across both cohorts, presumably related to pressure-induced vessel dilation and collateral redistribution in the setting of stenosis. The prominence of emissary veins may not be uniquely specific to the diagnosis of idiopathic intracranial hypertension, given their similar prominence in patients with both idiopathic intracranial hypertension and isolated venous pulsatile tinnitus, as previously reported with regard to the occipital emissary vein.¹³ In the pulsatile tinnitus cohort, management of the underlying transstenotic gradient with stent placement alone was sufficient in resolving patients' tinnitus symptomatology without the need for additional internal jugular bulb diverticulum or emissary vein embolization. Given the similar distribution of emissary vein prominence and internal jugular bulb diverticula across both cohorts, the resolution of tinnitus following transstenotic gradient resolution adds support to stent placement while avoiding unnecessary embolization of prominent emissary veins, especially in the absence of an associated saccular venous aneurysm. Nevertheless, in the authors' experience, a subset of patients not included in this study in whom the absence of a notable venous sinus stenosis or pressure gradient was recorded demonstrated benefit from embolization of such collateral findings if the side of pulsatile tinnitus corroborated with the side of the diverticulum or emissary vein.

Cerebellar tonsils were either at or slightly below the foramen magnum level in a similar distribution across both cohorts. A notably increased presence of marked optic nerve tortuosity, empty sella, and cephalocele identification in the idiopathic intracranial hypertension cohort relative to the pulsatile tinnitus cohort suggests that these imaging manifestations are more specific to idiopathic intracranial hypertension rather than their incidental presence in the setting of lateral sinus stenosis, as previously reported with regard to the empty sella.¹⁴ Similarly, a notably increased prevalence of saccular venous aneurysm in the pulsatile tinnitus cohort relative to idiopathic intracranial hypertension suggests that aneurysm formation may be more specific to pulsatile tinnitus. Despite such trends, the overlapping of all

collateral findings assessed in this study between both cohorts adds further credence to the notion that a clinical spectrum between pulsatile tinnitus and idiopathic intracranial hypertension exists. On the basis of the results of this study, the authors propose that the evaluation of stenosis subtype be considered a similarly important diagnostic finding alongside the other collateral imaging findings discussed in this study.

CONCLUSIONS

In this cohort, most patients with idiopathic intracranial hypertension had extrinsic venous sinus stenosis, and most patients with pulsatile tinnitus had intrinsic venous sinus stenosis. The authors propose that the reporting of venous sinus stenosis subtype as either intrinsic or extrinsic be considered in standardized MRV reporting. Awareness and reporting of these subtypes on diagnostic imaging may reduce underrecognition of potentially symptomatic venous sinus stenoses. This, in turn, may allow improved multidisciplinary discussions and appropriately tailored management in patients with idiopathic intracranial hypertension and pulsatile tinnitus, accordingly.

Disclosures: Vaishnavi Kishore—UNRELATED: Employment: GE Healthcare. Raphael Doustaly—UNRELATED: Employment: GE Healthcare. Athos Patsalides—UNRELATED: Consultancy: MicroVention, Penumbra, money paid to Weill Cornell Medical College.

REFERENCES

1. Dinkin MJ, Patsalides A. **Venous sinus stenting for idiopathic intracranial hypertension: where are we now?** *Neurol Clin* 2017;35:59–81 CrossRef Medline
2. Patsalides A, Oliveira C, Wilcox J, et al. **Venous sinus stenting lowers the intracranial pressure in patients with idiopathic intracranial hypertension.** *J Neurointerv Surg* 2019;11:175–78 CrossRef Medline
3. Toscano S, Lo Fermo S, Reggio E, et al. **An update on idiopathic intracranial hypertension in adults: a look at pathophysiology, diagnostic approach and management.** *J Neurol* 2020 May 27. [Epub ahead of print] CrossRef Medline
4. Johnston I. **The historical development of the pseudotumor concept.** *Neurosurg Focus* 2001;11:E2 CrossRef Medline
5. Hewes D, Morales R, Raghavan P, et al. **Pattern and severity of transverse sinus stenosis in patients with pulsatile tinnitus associated with sigmoid sinus wall anomalies.** *Laryngoscope* 2020;130:1028–33 CrossRef Medline
6. Pekcevik R, Pekcevik Y. **Anatomy of the posterior fossa emissary veins and their clinical importance.** In: Proceedings of the Annual Meeting of the European Congress of Radiology, Vienna, Austria. June 7–11, 2013
7. Bergman RA, Tubbs RS, Shoja MM, et al. Dural venous sinuses. In: Bergman RA, Tubbs RS, Shoja MM, et al. *Bergman's Comprehensive Encyclopedia of Human Anatomic Variation*. John Wiley & Sons; 2019:775–99
8. Sivasankar R, Pant R, Indrajit IK, et al. **Imaging and interventions in idiopathic intracranial hypertension: a pictorial essay.** *Indian J Radiol Imaging* 2015;25:439–44 CrossRef Medline
9. Newman CW, Jacobson GP, Spitzer JB. **Development of the Tinnitus Handicap Inventory.** *Arch Otolaryngol Head Neck Surg* 1996;122:143–48 CrossRef Medline
10. Boddu SR, Gobin P, Oliveira C, et al. **Anatomic measurements of cerebral venous sinuses in idiopathic intracranial hypertension patients.** *PLoS One* 2018;13:e0196275 CrossRef Medline

11. Lenck S, Vallee F, Labeyrie MA, et al. **Stenting of the lateral sinus in idiopathic intracranial hypertension according to the type of stenosis.** *Neurosurgery* 2017;80:393–400 CrossRef Medline
12. Mondejar V, Patsalides A. **The role of arachnoid granulations and the lymphatic system in the pathophysiology of idiopathic intracranial hypertension.** *Curr Neurol Neurosci Rep* 2020;20:20 CrossRef Medline
13. Hedjoudje A, Piveteau A, Gonzalez-Campo C, et al. **The occipital emissary vein: a possible marker for pseudotumor cerebri.** *AJNR Am J Neuroradiol* 2019;40:973–78 CrossRef Medline
14. Zetchi A, Labeyrie M-A, Nicolini E, et al. **Empty sella is a sign of symptomatic lateral sinus stenosis and not intracranial hypertension.** *AJNR Am J Neuroradiol* 2019;40:1695–1700 CrossRef Medline

Cerebral Venous Wall Diseases: The Other Side of the Picture

Traditionally, the attention of the neurovascular community has been on the arterial system. Even when looking at venous cerebral pathology, most attention has to date focused on cerebral venous thrombosis. More recently, parallel developments in both medical imaging and neurointerventional techniques have focused more attention on the cerebral veins and venous sinuses. Our knowledge of venous and arteriovenous physiology and pathology is improving significantly, thanks to the anatomic and physiologic data we are gleaning from both modern MR imaging techniques and venous endovascular techniques. Despite this, however, our knowledge of the cerebral venous physiology is still significantly lacking compared with our grasp of the arterial system, meaning that this represents a fascinating research avenue.

The discovery in the past decade of the glymphatic system has cast new light on CSF clearance pathways in the brain and raised intriguing new possibilities regarding diseases that have thus far been called idiopathic.¹⁻³ In recent years, many studies have demonstrated that “idiopathic” stenoses could affect the dural sinuses and can be associated with several clinical symptoms such as pulsatile tinnitus (PT) or idiopathic intracranial hypertension (IIH).⁴⁻⁶ This alone represents a major paradigm shift in neurovascular diseases because the concept of “cerebral venous wall disease” has hitherto not been well-addressed. Unlike the arteries and veins, the dural sinuses are not surrounded by their own “wall.” Instead, the venous blood of the dural sinuses is surrounded by the dura mater. This thick envelope surrounds the brain, the CSF spaces, and the venous blood. Far from being an inert fibrous membrane, however, the dura is now recognized to be a metabolically and immunologically active membrane, with arteries, veins, and lymphatics.^{7,8} It also appears to be actively involved in regulation of CSF clearance.^{9,10}

Given these anatomic observations, the mechanisms of formation of venous sinuses are probably more complex than previously suspected.¹¹ Although the relationships between intracranial pressure (ICP) and transverse sinus stenoses (TSSs) has long been a matter of debate,¹²⁻¹⁴ we now realize that these stenoses may play an intrinsic role in maintaining and/or triggering the so-called vicious circle of IIH. The effectiveness of venous sinus stent placement to relieve the symptoms related to ICP has probably been the best proof of this theory.¹⁵ Thus, TSSs lead to an increase in the cerebral venous pressure, thereby interrupting the passive resorption

of CSF from the subarachnoid space to the venous blood of the dural sinuses. However, the mechanisms of formation of these TSSs are still poorly understood.

Accordingly, it is crucial that we improve our knowledge of venous sinus stenoses. With this in mind, Sundararajan et al¹⁶ provide a very good radiologic observation of patients with symptomatic TSSs. In one of the largest series published so far, they report that most patients with IIH possessed extrinsic TSSs, and most patients with PT were found to have intrinsic TSSs. Whereas an extrinsic stenosis is usually defined as a long segment of sinus stenosis without an endoluminal component, an intrinsic stenosis is usually defined as the presence of one (or several) granulation projecting into the sinus. Although the dichotomization of stenoses into these types appears to have some relevance to clinical practice and to neurointerventions,¹⁷ it is probably a crude approximation of the underlying morphology of the stenosis. Indeed, many stenoses may have both intrinsic and extrinsic components. Furthermore, some patients may have an extrinsic stenosis on one side and an intrinsic one on the other side. Despite these limitations, we believe that a continuum between extrinsic and intrinsic stenoses seems to arise over time, a supposition that is based on our clinical and radiologic observations. Although both types of TSS seem to preferentially affect overweight women, their clinical impact and morphology seem to evolve with age.¹⁸ Extrinsic stenoses are more commonly diagnosed in younger patients, and IIH is by far the most common primary clinical presentation in these patients. The severity and risk of recurrence of IIH after venous sinus stent placement are significantly higher in these patients than in older patients with intrinsic stenoses. On the other hand, intrinsic stenoses are more frequently observed in older patients who present with more benign IIH or even with isolated pulsatile tinnitus.

Despite the limitations of this dichotomy, distinguishing between extrinsic and intrinsic stenoses appears to be helpful in clinical practice; it may represent the best we have for now. But outside of these practical considerations, these observations should prompt us to keep exploring the underlying pathophysiological mechanisms of TSS and to improve our knowledge of the venous physiology and better understand how it relates to CSF circulation. We now have to go on the other side of the neurovascular picture, keeping in mind that “All photos are accurate. None of them is the truth” (Richard Avedon).

REFERENCES

1. Rasmussen MK, Mestre H, Nedergaard M. **The glymphatic pathway in neurological disorders.** *Lancet Neurol* 2018;17:1016–24 CrossRef Medline
2. Iliff JJ, Goldman SA, Nedergaard M. **Implications of the discovery of brain lymphatic pathways.** *Lancet Neurol* 2015;14:977–79 CrossRef Medline
3. Iliff JJ, Wang M, Zeppenfeld DM, et al. **Cerebral arterial pulsation drives paravascular CSF-interstitial fluid exchange in the murine brain.** *J Neurosci* 2013;33:18190–99 CrossRef Medline
4. Farb RI, Vanek I, Scott JN, et al. **Idiopathic intracranial hypertension: the prevalence and morphology of sinovenous stenosis.** *Neurology* 2003;60:1418–24 CrossRef Medline
5. Lenck S, Labeyrie MA, Vallee F, et al. **Stent placement for disabling pulsatile tinnitus caused by a lateral sinus stenosis: a retrospective study.** *Oper Neurosurg (Hagerstown)* 2017;13:560–65 CrossRef Medline
6. Higgins JN, Cousins C, Owlser BK, et al. **Idiopathic intracranial hypertension: 12 cases treated by venous sinus stenting.** *J Neurol Neurosurg Psychiatry* 2003;74:1662–66 CrossRef Medline
7. Kierdorf K, Masuda T, Jordao MJC, et al. **Macrophages at CNS interfaces: ontogeny and function in health and disease.** *Nat Rev Neurosci* 2019;20:547–62 CrossRef Medline
8. Louveau A, Smirnov I, Keyes TJ, et al. **Structural and functional features of central nervous system lymphatic vessels.** *Nature* 2015;523:337–41 CrossRef Medline
9. Da Mesquita S, Louveau A, Vaccari A, et al. **Functional aspects of meningeal lymphatics in ageing and Alzheimer's disease.** *Nature* 2018;560:185–91 CrossRef Medline
10. Vinje V, Eklund A, Mardal KA, et al. **Intracranial pressure elevation alters CSF clearance pathways.** *Fluids Barriers CNS* 2020;17:29 CrossRef Medline
11. Lenck S, Radovanovic I, Nicholson P, et al. **Idiopathic intracranial hypertension: The veno glymphatic connections.** *Neurology* 2018;91:515–22 CrossRef Medline
12. Scoffings DJ, Pickard JD, Higgins JN. **Resolution of transverse sinus stenoses immediately after CSF withdrawal in idiopathic intracranial hypertension.** *J Neurol Neurosurg Psychiatry* 2007;78:911–12 CrossRef Medline
13. Bono F, Giliberto C, Mastrandrea C, et al. **Transverse sinus stenoses persist after normalization of the CSF pressure in IIH.** *Neurology* 2005;65:1090–93 CrossRef Medline
14. Chan W, Neufeld A, Maxner C, et al. **Irreversibility of transverse venous sinus stenosis and optic nerve edema post-lumbar puncture in idiopathic intracranial hypertension.** *Can J Ophthalmol* 2019;54:e57–59 CrossRef Medline
15. Nicholson P, Brinjikji W, Radovanovic I, et al. **Venous sinus stenting for idiopathic intracranial hypertension: a systematic review and meta-analysis.** *J Neurointerv Surg* 2019;11:380–85 CrossRef Medline
16. Sundararajan SH, Ramos AD, Kishore V, et al. **Dural sinus venous sinus stenosis: why distinguishing intrinsic versus extrinsic stenosis matters.** *AJNR Am J Neuroradiol* 2021 in press
17. Kumpe DA, Seinfeld J, Huang X, et al. **Dural sinus stenting for idiopathic intracranial hypertension: factors associated with hemodynamic failure and management with extended stenting.** *J Neurointerv Surg* 2017;9:867–74 CrossRef Medline
18. Lenck S, Vallee F, Labeyrie MA, et al. **Stenting of the lateral sinus in idiopathic intracranial hypertension according to the type of stenosis.** *Neurosurgery* 2017;80:393–400 CrossRef Medline

© S. Lenck

Department of Neuroradiology
Groupe Hospitalier Pitié Salpêtrière
Paris, France

Groupe de Recherche Clinique (GRC) 31 E-HTIC
Sorbonne Université
Paris, France

© P. Nicholson

Department of Neuroradiology
Toronto Western Hospital
Toronto, Canada

<http://dx.doi.org/10.3174/ajnr.A6914>

Endovascular Recanalization of Symptomatic Nonacute Intracranial Internal Carotid Artery Occlusion: Proposal of a New Angiographic Classification

F. Gao, X. Sun, X. Guo, D. Li, G.D. Xu, and Z.R. Miao



ABSTRACT

BACKGROUND AND PURPOSE: The optimal treatment for symptomatic nonacute intracranial ICA occlusion is uncertain, and endovascular recanalization remains a technical challenge. Our purpose was to report multicenter clinical results of endovascular recanalization for medically refractory, nonacute, intracranial ICA occlusion and to propose a new angiographic classification to explore which subgroups of patients are most amenable to this treatment.

MATERIALS AND METHODS: From January 2015 to December 2019, thirty-six consecutive patients who underwent endovascular recanalization for refractory, nonacute, atherosclerotic intracranial ICA occlusion at 3 stroke centers were analyzed retrospectively. The patients were divided into 3 types according to an angiographic classification. Rates of technical success, periprocedural complications, and any stroke or death within 30 days along with follow-up results were evaluated.

RESULTS: The overall technical success rate was 80.6% (29/36), and the rate of any stroke or death within 30 days was 16.7% (6/36). The recanalization success rate gradually decreased from type I to type III in the 3 classification groups (92.9%, 81.3%, and 50%, $P = .038$), and the opposite was true of the perioperative complication rates (7.1%, 18.8%, and 50%, $P = .038$). Type I lesions showed favorable recanalization effects, 92.9% technical success rates, and 7.1% perioperative complications.

CONCLUSIONS: Endovascular recanalization for nonacute atherosclerotic intracranial ICA occlusion is technically feasible, especially in patients with type I lesions, and could offer an alternative option for patients with recurrent ischemic symptoms despite aggressive medical therapy. The angiographic classification proposed is conducive to the selection of suitable patients and difficulty in grading.

ABBREVIATIONS: AcomA = anterior communicating artery; ILAO = intracranial large-artery occlusion; IQR = interquartile range; PcomA = posterior communicating artery

Intracranial large-artery occlusion (ILAO) is a common cause of ischemic stroke.¹ Previous randomized studies have shown an overwhelming benefit of endovascular therapy for selected patients with acute ILAO during the extended 24-hour therapeutic window.^{2,3} A subset of patients with ILAO can tolerate the initial acute occlusion and enter the nonacute phase (including subacute-to-chronic occlusion). Studies have shown that a

considerable number of these patients will continue to be at higher risk for subsequent stroke despite aggressive medical therapy.⁴⁻⁶ However, the optimal treatment for medically refractory, nonacute ILAO remains unclear. Extracranial-intracranial artery bypass surgery failed to prove benefit in preventing ischemic attacks or stroke.^{7,8} Some small-sample case series studies have reported that endovascular recanalization appeared to be feasible and may be a promising therapeutic option.^{9,10} However, there was heterogeneity of outcomes and perioperative complications for endovascular recanalization, and it is believed that there are differences in the difficulty and risk at different sites of ILAO.¹⁰

Endovascular recanalization for nonacute occlusion of the intracranial vertebral artery, middle cerebral artery, and basilar artery has been reported in previous studies.¹¹⁻¹³ However, there are few reports on endovascular recanalization for nonacute intracranial intradural ICA occlusion.¹⁴ In this study, we retrospectively analyzed 36 consecutive patients with nonacute intracranial intradural ICA occlusion of presumed atherosclerotic etiology who underwent endovascular recanalization at 3 comprehensive

Received August 6, 2020; accepted after revision September 19.

From the Departments of Interventional Neuroradiology (F.G., X.S., Z.R.M.), Beijing Tiantan Hospital, and Interventional Neurology (X.G.), Beijing Anzhen Hospital, Capital Medical University, Beijing, China; Department of Neurointervention (D.L.), Dalian Municipal Central Hospital affiliated with Dalian Medical University, Dalian City, Liaoning Province, China; and Department of Neurointervention (G.D.X.), Hebei General Hospital, Shijiazhuang City, Hebei Province, China.

This study was funded by the National Key R&D Program (2018AAA0102600).

Please address correspondence to Feng Gao, MD, Department of Interventional Neuroradiology, Beijing Tiantan Hospital, Capital Medical University, No.119 South 4th Ring West Rd, Fengtai District, Beijing, China, 100070; e-mail: gaofengletter@sina.com

Indicates open access to non-subscribers at www.ajnr.org

<http://dx.doi.org/10.3174/ajnr.A6928>

stroke centers (Department of Interventional Neuroradiology, Beijing Tiantan Hospital; Department of Neurointervention, Dalian Municipal Central Hospital; Department of Neurointervention, Hebei General Hospital); we also propose a new angiographic classification. The aim of the study was to explore the technical feasibility and safety of endovascular recanalization and to provide a reference for the selection of patients and difficulty of grading.

MATERIALS AND METHODS

Study Population

From January 2015 to December 2019, thirty-six consecutive patients with symptomatic, nonacute, intracranial ICA occlusion treated with endovascular recanalization at 3 comprehensive stroke centers were reviewed. Twenty-four patients were men, with an average age of 53.83 years (range, 41–75 years). In this study, intracranial ICA occlusion was defined as occlusion beyond the ophthalmic artery segment—that is, the intracranial intradural segment including the ophthalmic artery segment and the communicating segment according to the ICA classification proposed by Bouthillier et al.¹⁵ Nonacute occlusion was defined as occlusion with a time window of >24 hours from the onset (TIA or stroke). After intracranial ICA occlusion was diagnosed by CTA or MRA, patients were treated with aggressive medical therapy (dual-antiplatelet therapy plus statins and management of risk factors).¹⁶ The patients were clinically observed and followed up, and endovascular treatment was considered if they still experienced recurrent TIAs or stroke related to an occluded ICA. Informed consent for endovascular treatment was obtained from all patients. Beijing Tiantan Hospital institutional review board approved this retrospective study, and the requirement for patient informed consent was waived for review of patient records and images.

Inclusion Criteria

The inclusion criteria were as follows: 1) nonacute intracranial ICA occlusion diagnosed by CTA or MRA and confirmed by DSA; 2) recurrent TIA or stroke related to the occluded ICA despite aggressive medical treatment; 3) preoperative CTP revealing hypoperfusion in the occluded ICA territory;¹⁷ 4) a preoperative mRS score of equal to or less than three; 5) >1 risk factor for atherosclerosis (eg, hypertension, diabetes mellitus, hyperlipidemia, coronary artery disease, and cigarette smoking); and 6) patient refusal to undergo bypass surgery.

Exclusion Criteria

The exclusion criteria were as follows: 1) clinical, laboratory, or imaging findings not suspicious for atherosclerotic lesions, such as vasculitis, Moyamoya syndrome, arterial dissection; 2) a coexisting cardioembolic source (eg, atrial fibrillation, mitral stenosis, prosthetic valve, Myocardial infarction within 6 weeks, intracardiac clot, ventricular aneurysm, and bacterial endocarditis); 3) a concomitant intracranial aneurysm or any bleeding disorder; 4) large infarct core, defined as an ASPECTS of <6 points; and 5) life expectancy of <1 year due to other medical conditions.

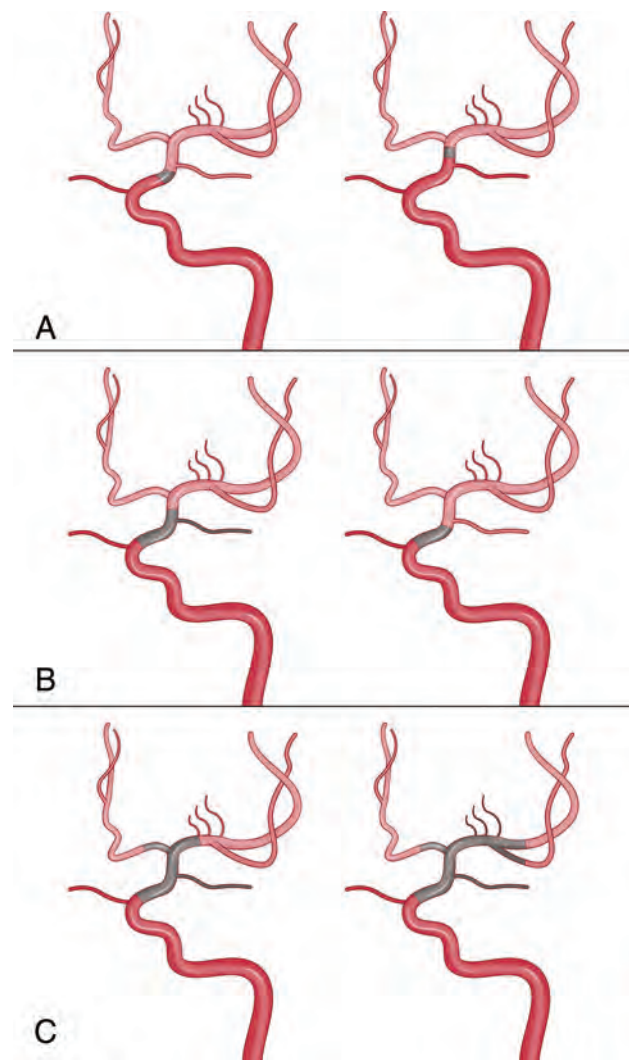


FIG 1. Schematic diagram for the angiographic classification of nonacute intracranial ICA occlusion. *A*, Type I: the intracranial ICA is occluded, with an occlusion length of ≤ 10 mm and established collateral filling to the distal intracranial ICA via the PcomA or AcomA. *B*, Type II: the intracranial ICA is occluded, with an occlusion length of >10 mm and established collateral filling to the distal intracranial ICA via the AcomA or PcomA. *C*, Type III: the intracranial ICA is occluded, with an uncertain occlusion length or involving the middle MCA with no established collateral filling to the distal intracranial ICA via the PcomA or AcomA.

Angiographic Classification of Nonacute Intracranial ICA Occlusion

Angiographic classification of intracranial ICA occlusion was based on standard cerebral angiography, including the bilateral internal carotid and vertebral arteries with sufficient contrast medium and a prolonged run, which emphasizes opacification of the posterior communicating artery (PcomA), anterior communicating artery (AcomA), or leptomeningeal collateral vessels. The length of occlusion was determined by the distance between proximal occlusion and the reconstruction of distal collateral vessels, which was categorized as ≤ 10 or >10 mm.¹⁸ On the basis of angiographic characteristics, intracranial ICA occlusion was divided into the following 3 types (Fig 1).

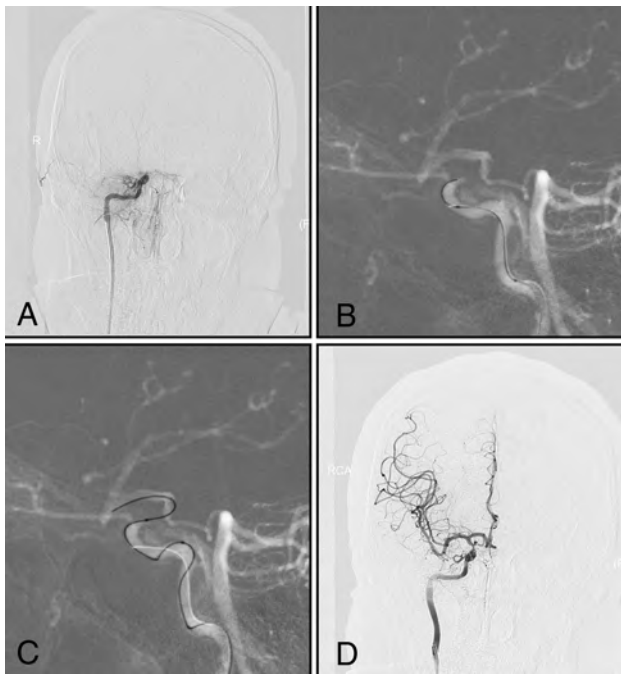


FIG 2. A man with left-sided weakness for 15 days. *A*, DSA shows that the right intracranial internal carotid artery is occluded, with an occlusion length of ≤ 10 mm and established collateral filling to the distal intracranial ICA via the PcomA (type I). *B* and *C*, Under dual-roadmap guidance, the microwire in combination with a microcatheter passes through the occluded segment. *D*, Successful recanalization.

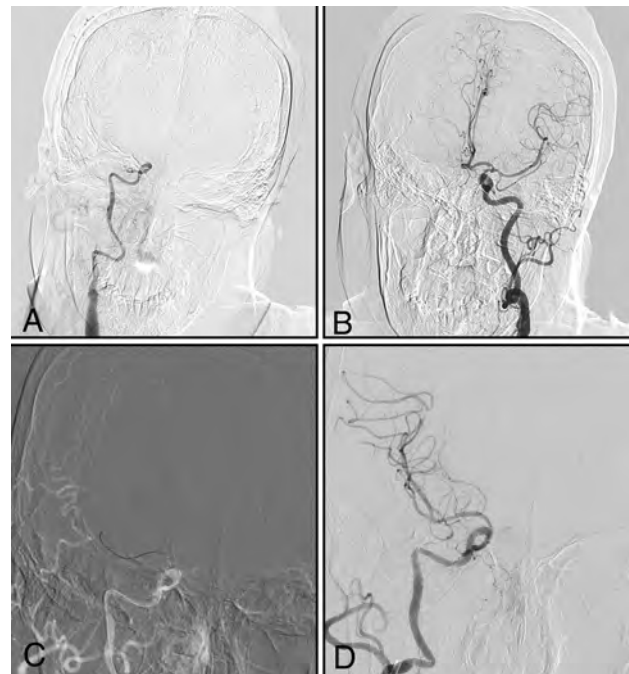


FIG 4. A man with left-sided weakness for 20 days. *A* and *B*, DSA shows that the right intracranial internal carotid artery is occluded, with uncertain occlusion length and no established collateral filling to the distal right intracranial ICA via the AcomA or PcomA (type III). *C*, The microwire, in combination with a microcatheter, passes through the occluded segment. *D*, Successful recanalization.

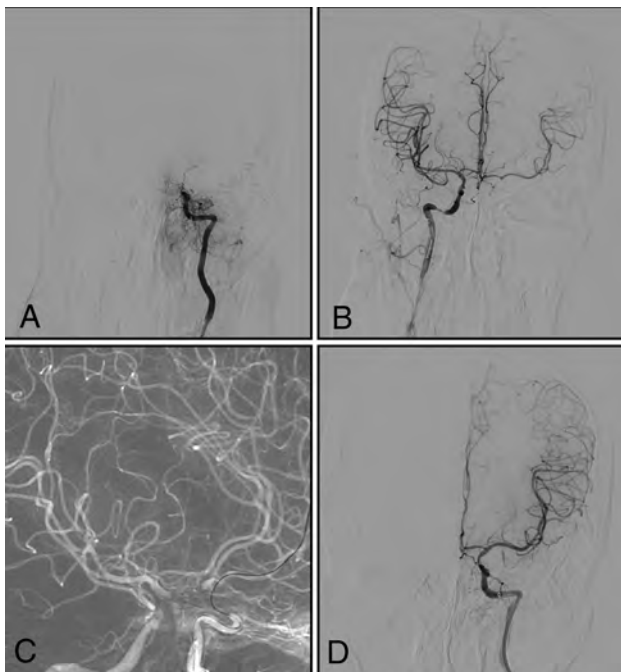


FIG 3. A man with right-sided weakness for 30 days, with increasingly slurred speech for 10 days. *A* and *B*, DSA shows that the left intracranial internal carotid artery is occluded, with an occlusion length of > 10 mm and established collateral filling to the distal right intracranial ICA via the AcomA (type II). *C*, Under dual-roadmap guidance, the microwire, in combination with a microcatheter, passes through the occluded segment. *D*, Successful recanalization.

- Type I (Figs 1A and 2): The intracranial ICA is occluded, with an occlusion length of ≤ 10 mm and established collateral filling to the distal intracranial ICA via the PcomA or AcomA.
- Type II (Figs 1B and 3): The intracranial ICA is occluded, with an occlusion length of > 10 mm and established collateral filling to the distal intracranial ICA via the AcomA or PcomA.
- Type III (Figs 1C and 4): The intracranial ICA is occluded, with an uncertain occlusion length or involving the MCA and no established collateral filling to the distal intracranial ICA via the PcomA or AcomA.

Endovascular Recanalization Procedure

All procedures were performed with the patient under general anesthesia. After we placed the sheath introducer, heparin was administered intravenously to keep the activated clotting time between 200 and 300 seconds. A 6F guiding catheter was advanced into the cervical segment of the ICA.

For type I and II lesions with a patent PcomA or AcomA, we used dual-roadmap guidance with simultaneous 2-vessel injections to map the course of the occlusion site (Figs 2 and 3). The microwire (Synchro, Stryker Neurovascular; Transend EX 014/205 soft tip, Stryker) was used in combination with a microcatheter (Echelon-10, Medtronic; Excelsior SL-10, Stryker) to carefully pass through the occluded segment. If the attempts were repeated and the microwire and microcatheter could not pass the occluded segment and enter the distal true lumen, the procedure was stopped. If the microwire was successfully steered through the occluded segment, then microcatheter injection confirmed the position distal to occlusion in the distal true lumen.

Table 1: Baseline characteristics

	Overall (n = 36)	Type I (n = 14)	Type II (n = 16)	Type III (n = 6)	P Value
Mean age (yr)	53.83 [SD, 10.47]	55.57 [SD, 7.98]	52.31 [SD, 11.78]	53.83 [SD, 13.01]	.708
Men (No.) (%)	24 (66.7)	10 (71.4)	11 (68.8)	3 (50.0)	.722
Risk factors (No.) (%)					
Diabetes mellitus	13 (36.1)	6 (42.9)	4 (25.0)	3 (50.0)	.469
Hypertension	26 (72.2)	11 (78.6)	11 (68.8)	4 (66.7)	.789
Hyperlipidemia	6 (16.7)	3 (21.4)	3 (18.8)	0	.708
Cardiac disease	3 (8.3)	1 (7.1)	2 (12.5)	0	1
Smoking	14 (38.9)	6 (42.9)	7 (43.8)	1 (16.7)	.541
Qualifying event (No.) (%)					
Recurrent stroke	33 (91.7)	11 (78.6)	16 (100.0)	6 (100.0)	.117
Recurrent TIA	3 (8.3)	3 (21.4)	0	0	
Imaging occlusion-to-recanalization time (median) (IQR) (day)	45.00 (30.50–68.50)	52.50 (32.00–90.00)	41.00 (30.00–60.00)	54.50 (19.50–90.00)	.387
Last symptom-to-recanalization time (median) (IQR) (day)	14.00 (10.00–17.75)	13.50 (10.00–20.25)	13.00 (10.00–17.75)	14.50 (13.25–17.00)	.72
Preoperative NIHSS score (median) (IQR)	2.00 (2.00–4.00)	2.00 (1.00–4.00)	2.00 (2.00–4.00)	2.00 (1.75–4.00)	.266
Preoperative mRS score (median) (IQR)	2.00 (1.00–3.00)	1.00 (1.00–2.00)	2.00 (1.00–2.00)	2.00 (1.00–3.00)	.317

Subsequently, an exchange-length microwire (Transend ES 014/300 Floppy; Stryker) was placed in the appropriate anchoring position, and the microcatheter was removed. A 2- to 2.5-mm Gateway angioplasty balloon (Stryker) was advanced to predilate the lesion. On the basis of measurement of the proximal and distal diameters as well as the length of the occluded segment after balloon dilation, a self-expandable stent (Wingspan stent, Stryker; Neuroform EZ, Stryker; or Enterprise, Codman & Shurtleff) was introduced and deployed according to the operator's preference.

Postoperative angiography was performed to confirm the patency. Successful revascularization was defined as a modified TIC1 grade 3 antegrade flow and residual stenosis of $\leq 50\%$. Brain CT immediately after the operation was performed to rule out intracranial hemorrhage. Then, all patients were typically monitored in Neurocritical Care Units for 24 hours postprocedure with a goal of systolic blood pressure within 20 mmHg Torr of the patient's baseline blood pressure to reduce the risk of reperfusion hemorrhage.¹⁹

Combination treatment with oral aspirin (100 mg) and clopidogrel (75 mg) was started at least 5 days before the endovascular procedure. Thromboelastography was used to evaluate platelet reactivity.²⁰ No aspirin resistance was observed, and the 6 patients who showed clopidogrel resistance were treated with ticagrelor, 90 mg twice a day. Dual-antiplatelet therapy was maintained for 6 months, with life-long aspirin or clopidogrel monotherapy maintained thereafter.

Data Collection and Follow-Up

Cases were identified through a search of prospectively acquired endovascular databases of 3 comprehensive stroke centers. We collected the following baseline and treatment variables: demographic, clinical, procedural, imaging, and follow-up data. All image assessments were performed by 2 independent neuroradiologists, and discrepancies were resolved by consensus. Restenosis was defined as $>50\%$ stenosis within the implanted stent and $>20\%$ absolute luminal loss on CTA or DSA.²¹

Statistical Analysis

All normally distributed continuous quantitative variables were expressed as means [SDs]; nonnormally distributed continuous variables, as median and interquartile range; and categorical variables, as proportions. Comparisons between groups were performed using the Student *t* test or the approximate χ^2 test when the variances of comparison between groups were quite different. The comparison among the 3 groups was performed using the χ^2 test for trend. Differences were considered statistically significant with $P \leq .05$. All statistical analyses were performed with SPSS 25.0 (IBM).

RESULTS

Baseline Characteristics

All 36 patients underwent endovascular recanalization for symptomatic, nonacute, intracranial ICA occlusion. The median time from last symptom onset to endovascular treatment was 14 days (interquartile range [IQR] = 10.00–17.75 days). These patients were classified into 3 types according to the angiographic classification. There was no significant difference in the patients' demographic characteristics, risk factors, or clinical characteristics. See Table 1 for the detailed baseline information.

Perioperative Outcome

The overall technical success rate was 80.6% (29/36). The perioperative complication rate was 19.4% (7/36), and the overall rate of stroke or death within 30 days was 16.7% (6/36). The recanalization success rate gradually decreased from type I to type III in the 3 classification groups (92.9%, 81.3%, and 50%; $P = .038$), and the opposite was true of the overall perioperative complication rates (7.1%, 18.8%, and 50%, $P = .038$). Table 2 presents the detailed clinical and angiographic outcomes. Two patients experienced vessel perforation with subarachnoid hemorrhage during attempts to traverse the occluded segment with a microwire. After coiling, 1 patient presented with a mild headache, which was relieved 2 days later. The other patient had new neurologic symptoms (NIHSS 5). Two patients had reperfusion hemorrhage

Table 2: Clinical and angiographic outcomes

	Overall (n = 36)	Type I (n = 14)	Type II (n = 16)	Type III (n = 6)	P Value
Technical success (No.) (%)	29 (80.6)	13 (92.9)	13 (81.3)	3 (50.00)	.038
Periprocedural complication (No.) (%)	7 (19.4)	1 (7.1)	3 (18.8)	3 (50.00)	.038
Perforation	2 (5.6)	0	0	2 (33.3)	.027
Dissection	2 (5.6)	0	1 (6.25)	1 (16.7)	.145
Thrombosis	1 (2.8)	1 (7.1)	0	0	.274
Reperfusion hemorrhage	2 (5.6)	0	2 (12.5)	0	.654
Stroke within 30 days (No.) (%)	6 (16.7)	1 (7.1)	2 (12.5)	3 (50.00)	.039
Ischemic stroke	2 (5.6)	1 (7.1)	0	1 (16.7)	.654
Hemorrhagic stroke	4 (11.1)	0	2 (12.50)	2 (33.3)	.034
Death within 30 days (No.) (%)	2 (5.6)	0	2 (12.5)	0	.654
mRS score at 90 days (median) (IQR)	1.00 (1.00–2.00)	1.00 (0.00–2.00)	1.00 (1.00–2.00)	1.00 (1.00–2.00)	.218
Clinical follow-up (median) (IQR) (mo)	12.00 (6.00–24.00)	9.00 (6.00–14.25)	24.00 (7.50–34.50)	9.00 (8.00–9.00)	.267
Imaging follow-up (median) (IQR) (mo)	12.00 (3.00–12.00)	6.00 (3.00–12.00)	12.00 (3.00–12.00)	24.00 (6.00–24.00)	.28
Stroke and death beyond 30 days (No.) (%)	2/27 (7.40)	1/12 (8.33)	1/12 (8.33)	0/3	1
Restenosis (No.) (%)	4/26 (15.38)	1/11 (9.09)	3/12 (25.00)	0/3	.757

3 and 4 hours after successful recanalization; their symptoms deteriorated rapidly, and they died. Two patients underwent vascular dissection, and the operation was terminated because the guidewire could not pass through the occlusion to the distal vascular true lumen. One patient had mild ischemic stroke (NIHSS 3) after the operation, and the other one was asymptomatic. One patient experienced left-limb weakness (NIHSS 4) five days after successful recanalization, and transcranial Doppler showed patency of the treated right ICA.

Follow-Up Outcome

The median clinical follow-up period was 12 months (IQR = 6.00–24.00). Stroke or death occurred at a rate of 7.4% (2/27) during follow-up. One patient each experienced ipsilateral ischemic stroke at 3 and 6 months after the operation, and CTA revealed in-stent restenosis; the symptoms improved after drug and rehabilitation treatment (mRS 1). The median imaging follow-up period was 12 months (IQR = 3.00–12.00 months). Four patients (15.4%, 4/26) developed in-stent restenosis: Two were symptomatic, and the other 2 were asymptomatic.

DISCUSSION

In previous studies of intracranial ICA stenosis or occlusive diseases, the intracranial ICA usually refers to the C2–C7 segment (beyond the petrous segment).^{22,23} When the primary occlusion occurs at the proximal-to-ophthalmic artery orifice (C2–C5 segment), due to the lack of an ophthalmic artery outflow tract, it is often accompanied by proximal blood flow stagnation or secondary thrombus extension involving the extracranial cervical ICA. In this case, it is very difficult to identify the primary occlusion point using angiography alone, and the occlusion is usually ambiguously referred to as an ICA occlusion or cervical ICA occlusion. Previous research by Lee et al²⁴ suggested that the difficulty and risk of endovascular recanalization for ICA occlusion involving the intradural segment were increased due to the difference in the anatomic structures between the intradural and epidural segments.

In this study, we report, for the first time, the multicenter preliminary results of endovascular recanalization for nonacute, intracranial, intradural ICA occlusion. The results show that the overall recanalization rate was 80.6% and the perioperative complication rate was 19.4%. Patients with type I occlusions had

higher revascularization rates than those with type II or III occlusions (92.9%, 81.3%, and 50%, respectively), and the opposite was true of overall perioperative complication rates (7.1%, 18.8%, and 50%, respectively), which indicated that different patient selection may lead to different recanalization outcomes.

When intracranial ICA occlusion occurs, the distal collateral pathway mainly originates from the PcomA, AcomA, or leptomeningeal collateral vessels. The length of occlusion judged is mainly based on the distance between the proximal occlusion and reconstruction of distal collateral vessels, which may be longer than the true length of underlying atherosclerotic lesions.²⁵ In our study, the occlusion length of type I lesions was <10 mm, which was equivalent to the length of type B stenosis according to the classification of Mori et al.¹⁸ In types II and III, when the primary occlusion was located in the ophthalmic artery segment, the occlusion may extend beyond the PcomA due to hypoplasia or absence of a PcomA.

Good reconstruction of distal collateral vessels is a favorable factor for endovascular recanalization because it increases the visibility of distal vessels.²⁶ Given the opening of the PcomA or AcomA, for type I and type II lesions, the dual-roadmap technique can be used to inject contrast into the proximal and distal vessels through the bilateral ICA or the ICA combined with the vertebral artery at the same time so that these vessels can be visualized simultaneously in roadmap mode. This procedure can extrapolate the course of the occluded site, define the length of the occlusion, and provide a “landing point” and distal vascular navigation for the guidewire to pass through smoothly. In the current series, type I lesions showed a high recanalization rate (92.9%) and a low incidence of perioperative complications (7.1%) because of the relatively short occlusion (≤ 10 mm) and good reconstruction of distal collateral vessels from the PcomA or AcomA, which may be the best candidates for endovascular recanalization. Type II lesions were more difficult to recanalize than type I lesions because of their longer occlusion length (>10 mm), but due to collateral reconstruction from the AcomA, occlusions were still relatively limited between the origin of the ophthalmic artery and the distal bifurcation of the ICA. Although there was an acceptable success rate of recanalization (81.3%), it was accompanied by a high perioperative complication rate (18.8%). Therefore, for patients of type II lesion, endovascular

therapy, as an alternative treatment for medically refractory patients, needs to be comprehensively weigh the risks and benefits in this group.

For type III lesions, this study showed a low recanalization rate (50%) and a high incidence of perioperative complications (50%). Because of involvement or absence of the AcomA or PcomA, the uncertainty of occlusion length and course significantly increased the operational risk of endovascular recanalization. The incidence of operation-related complications such as vascular perforation was significantly higher in type III, which may suggest that endovascular recanalization should be performed with caution in these patients. In fact, in type III, the distal collateral pathway mainly comes from the leptomeningeal anastomosis between the middle and anterior cerebral arteries or the posterior cerebral arteries, and angiography may show late retrograde opacification of the distal MCA M1 trunk or M2–3 branches. According to different distal collateral reconstructions, type III can be divided into subtypes a and b: In subtype a, retrograde filling of the distal collateral can be seen in the distal MCA M1 trunk; in subtype b, retrograde filling of the distal collateral can be seen only in the M2–3 branches. Because of the small sample size, we did not have separate statistics. Further study with a larger case number is warranted.

Intracranial hemorrhagic complication, including subarachnoid hemorrhage and parenchymal hematoma, can be caused by microwire perforation, reperfusion injury, or hemorrhagic transformation. The use of soft-tipped hydrophilic-coated microwires and dual-roadmap guidance by experienced operators can help reduce the incidence of operation-related complications such as guidewire perforation. Reperfusion hemorrhage is still a potentially devastating complication after recanalization. The frequency of reperfusion hemorrhage has been reported to range from 0.3% to 1.2% following carotid endarterectomy and 0.67%–2.3% following carotid stent placement in different series,^{27,28} though there are scant data on the risk following endovascular recanalization for nonacute intracranial occlusion.^{9,12} In the present study, we report that the incidence of reperfusion hemorrhage was 5% (2/40) after endovascular recanalization for nonacute, intracranial, intradural ICA occlusion. The mechanism of reperfusion hemorrhage may be related to cerebral autoregulation and blood-brain barrier damage caused by long-term chronic ischemia, and it can be reduced by intensive treatment of perioperative hypertension.²⁸

Another concern is thromboembolic complications. Secondary thrombosis may occur proximal or distal to the ICA occlusion, which may displace and cause distal embolism during endovascular recanalization. In this group, no thromboembolism occurred during the operation, considering that it was related to the degree of organization of secondary thrombosis. The stent was placed after balloon dilation to scaffold the occlusion; perioperative, dual-antiplatelet therapy and intraoperative heparinization were helpful in reducing the occurrence of thromboembolic events. It has been reported in some cases that proximal balloon occlusion and a flow-reversal device were used to prevent distal embolization.²³

The clinical symptoms of the patients in this group were relatively mild, which may be mainly related to the following factors: 1) Some patients with large-core infarction and severe clinical

symptoms were excluded; 2) in some patients with recurrent stroke, the pattern of infarction was watershed infarction with mild clinical symptoms; and 3) the median time from last ischemic symptom onset to endovascular treatment was 14 days (IQR = 10.00–17.75), and some patients recovered somewhat before the operation.

Our study has some limitations. First, this study was a retrospective study with a modest sample size, and further prospective studies are needed to confirm the results. Second, the lack of long-term follow-up imaging data in some patients may limit the evaluation of the overall restenosis rate. Finally, this study lacked a medically managed control arm, and it remains unknown whether endovascular recanalization compares favorably with the best medical therapies. However, before a controlled study, it is important to carefully explore which subgroups of patients are most amenable to endovascular treatment.

CONCLUSIONS

Endovascular recanalization for nonacute atherosclerotic, intracranial, intradural ICA occlusion is technically feasible, especially in patients with type I, and could offer an alternative option for patients with recurrent ischemic symptoms despite aggressive medical therapy. The angiographic classification proposed is conducive to the selection of suitable patients and difficulty in grading. Endovascular recanalization of nonacute intracranial ICA occlusion is still a high-risk procedure; therefore, selecting the subgroup of patients who could benefit from this treatment is critical.

REFERENCES

1. Smith WS, Lev MH, English JD, et al. **Significance of large vessel intracranial occlusion causing acute ischemic stroke and TIA.** *Stroke* 2009;40:3834–40 CrossRef Medline
2. Berkhemer OA, Majoie CB, Dippel DW, MR CLEAN Investigators. **Endovascular therapy for ischemic stroke.** *N Engl J Med* 2015;372:2363 CrossRef Medline
3. Nogueira RG, Jadhav AP, Haussen DC, et al; DAWN Trial Investigators. **Thrombectomy 6 to 24 hours after stroke with a mismatch between deficit and infarct.** *N Engl J Med* 2018;378:11–21 CrossRef Medline
4. Yamauchi H, Higashi T, Kagawa S, et al. **Chronic hemodynamic compromise and cerebral ischemic events in asymptomatic or remote symptomatic large-artery intracranial occlusive disease.** *AJNR Am J Neuroradiol* 2013;34:1704–10 CrossRef Medline
5. Kuroda S, Houkin K, Kamiyama H, et al. **Long-term prognosis of medically treated patients with internal carotid or middle cerebral artery occlusion: can acetazolamide test predict it?** *Stroke* 2001;32:2110–16 CrossRef Medline
6. Yamauchi H, Fukuyama H, Nagahama Y, et al. **Evidence of misery perfusion and risk for recurrent stroke in major cerebral arterial occlusive diseases from PET.** *J Neurol Neurosurg Psychiatry* 1996;61:18–25 CrossRef Medline
7. EC/IC Bypass Study Group. **Failure of extracranial-intracranial arterial bypass to reduce the risk of ischemic stroke: results of an international randomized trial.** *N Engl J Med* 1985;313:1191–1200 CrossRef Medline
8. Powers WJ, Clarke WR, Grubb RL Jr, et al; COSS Investigators. **Extracranial-intracranial bypass surgery for stroke prevention in hemodynamic cerebral ischemia: the Carotid Occlusion Surgery Study randomized trial.** *JAMA* 2011;306:1983–92 CrossRef Medline

9. Aghaebrahim A, Jovin T, Jadhav AP, et al. **Endovascular recanalization of complete subacute to chronic atherosclerotic occlusions of intracranial arteries.** *J Neurointerv Surg* 2014;6:645–48 CrossRef Medline
10. Yao YD, Liu AF, Qiu HC, et al. **Outcomes of late endovascular recanalization for symptomatic non-acute atherosclerotic intracranial large artery occlusion.** *Clin Neurol Neurosurg* 2019;187:105567 CrossRef Medline
11. Gao P, Wang Y, Ma Y, et al. **Endovascular recanalization for chronic symptomatic intracranial vertebral artery total occlusion: experience of a single center and review of literature.** *J Neuroradiol* 2018;45:295–304 CrossRef Medline
12. Zheng M, Song Y, Zhang J, et al. **Endovascular recanalization of non-acute symptomatic middle cerebral artery total occlusion and its short-term outcomes.** *Front Neurol* 2019;10:484 CrossRef Medline
13. Dashti SR, Park MS, Stiefel MF, et al. **Endovascular recanalization of the subacute to chronically occluded basilar artery: initial experience and technical considerations.** *Neurosurgery* 2010;66:825–31; discussion 831–32 CrossRef Medline
14. Wang X, Wang Z, Ji Y, et al. **Enterprise stent in recanalizing non-acute atherosclerotic intracranial internal carotid artery occlusion.** *Clin Neurol Neurosurg* 2017;162:47–52 CrossRef Medline
15. Bouthillier A, van Loveren HR, Keller JT. **Segments of the internal carotid artery: a new classification.** *Neurosurgery* 1996;38:425–42; discussion 432–33 CrossRef Medline
16. Chimowitz MI, Lynn MJ, Derdeyn CP, et al; SAMMPRIS Trial Investigators. **Stenting versus aggressive medical therapy for intracranial arterial stenosis.** *N Engl J Med* 2011;365:993–1003 CrossRef Medline
17. Murphy BD, Fox AJ, Lee DH, et al. **Identification of penumbra and infarct in acute ischemic stroke using computed tomography perfusion-derived blood flow and blood volume measurements.** *Stroke* 2006;37:1771–77 CrossRef Medline
18. Mori T, Fukuoka M, Kazita K, et al. **Follow-up study after intracranial percutaneous transluminal cerebral balloon angioplasty.** *AJNR Am J Neuroradiol* 2000;6(Suppl 1):243–49 CrossRef Medline
19. Alexander MJ, Zauner A, Chaloupka JC, et al; WEAVE Trial Sites and Interventionalists. **WEAVE trial: final results in 152 on-label patients.** *Stroke* 2019;50:889–94 CrossRef Medline
20. Sun X, Tong X, Lo WT, et al. **Risk factors of subacute thrombosis after intracranial stenting for symptomatic intracranial arterial stenosis.** *Stroke* 2017;48:784–86 CrossRef Medline
21. Levy EI, Turk AS, Albuquerque FC, et al. **Wingspan in-stent restenosis and thrombosis: incidence, clinical presentation, and management.** *Neurosurgery* 2007;61:644–50; discussion 650–51 CrossRef Medline
22. Ko JK, Choi CH, Cha SH, et al. **Percutaneous transluminal angioplasty and stenting for severe stenosis of the intracranial extracranial internal carotid artery causing transient ischemic attack or minor stroke.** *Interv Neuroradiol* 2015;21:511–19 CrossRef Medline
23. Komiyama M, Yoshimura M, Honnda Y, et al. **Percutaneous angioplasty of a chronic total occlusion of the intracranial internal carotid artery: case report.** *Surg Neurol* 2006;66:513–18; discussion 518 CrossRef Medline
24. Lee CW, Lin YH, Liu HM, et al. **Predicting procedure successful rate and 1-year patency after endovascular recanalization for chronic carotid artery occlusion by CT angiography.** *Int J Cardiol* 2016;221:772–76 CrossRef Medline
25. He Y, Wang Z, Li T, et al. **Preliminary findings of recanalization and stenting for symptomatic vertebrobasilar artery occlusion lasting more than 24h: a retrospective analysis of 21 cases.** *Eur J Radiol* 2013;82:1481–86 CrossRef Medline
26. Stone GW, Reifart NJ, Moussa I, et al. **Percutaneous recanalization of chronically occluded coronary arteries: a consensus document: Part II.** *Circulation* 2005;112:2530–37 CrossRef Medline
27. Ouriel K, Shortell CK, Illig KA, et al. **Intracerebral hemorrhage after carotid endarterectomy: incidence, contribution to neurologic morbidity, and predictive factors.** *J Vasc Surg* 1999;29:82–87; discussion 87–89 CrossRef Medline
28. Abou-Chebl A, Yadav JS, Reginelli JP, et al. **Intracranial hemorrhage and hyperperfusion syndrome following carotid artery stenting: risk factors, prevention, and treatment.** *J Am Coll Cardiol* 2004;43:1596–1601 CrossRef Medline

Distal Vessel Imaging via Intra-arterial Flat Panel Detector CTA during Mechanical Thrombectomy

T. Nozaki, M. Noda, T. Ishibashi, K. Otani, M. Kogiku, K. Abe, H. Kishi, and A. Morita



ABSTRACT

BACKGROUND AND PURPOSE: Obtaining information on invisible vasculature distal to the occlusion site helps to deploy a stent retriever safely during mechanical thrombectomy for large-vessel occlusion. It is essential to reduce the amount of contrast used for detecting the vessels distal to the occlusion site because acute ischemic stroke patients tend to have chronic kidney disease and patients with severe chronic kidney disease are at an increased risk of contrast-associated acute kidney injury. We assessed whether vessels distal to the occlusion site during acute ischemic stroke with large-vessel occlusion could be visualized on angiographic images using flat panel detector CT acquired following intra-arterial diluted contrast injection, compared with MRA findings.

MATERIALS AND METHODS: Between May 2019 and January 2020, we enrolled 28 consecutive patients with large-vessel occlusions of the anterior circulation eligible for mechanical thrombectomy following MR imaging. The patients underwent CBV imaging using flat panel detector CT with an intra-arterial diluted contrast injection instead of intravenous injection. Flat panel detector CT angiographic images reconstructed from the same dataset were evaluated for image quality, collateral status of the MCA territory, and visualization of the vessels distal to the occlusion site. These findings were compared with MRA findings.

RESULTS: Twenty-two patients were retrospectively examined. Flat panel detector CT angiographic image quality in 20 patients (91%) was excellent or good. The distal portion of the occluded vessel segment was visualized in 14 patients (70%), while the proximal portion of the segment adjacent to the occluded vessel in 3 (15%) was visualized. No visualization was observed in only 1 patient (5%) with no collateral supply. Flat panel detector CT angiographic images were shown to evaluate vessels distal to the occlusion site more accurately than MRA.

CONCLUSIONS: In acute ischemic stroke with large-vessel occlusion, flat panel detector CT angiographic images could successfully visualize vessels distal to the occlusion site with a small amount of contrast material.

ABBREVIATIONS: AIS = acute ischemic stroke; cICA = cervical ICA; FPD = flat panel detector; ICA-T = ICA terminal; LVO = large-vessel occlusion; MT = mechanical thrombectomy

Mechanical thrombectomy (MT) using a stent retriever is an effective treatment strategy for acute ischemic stroke (AIS) with large-vessel occlusion (LVO).¹⁻⁴ Obtaining information on invisible vasculature distal to the occlusion site helps to select appropriate devices and guides them safely because MT, using a stent retriever, requires a microguidewire and microcatheter to

pass through the occlusion site and be guided to an invisible vessel distal to the occlusion site. Furthermore, a stent retriever must be deployed, usually in an invisible vessel. Approximately 20%–35% of patients with AIS have chronic kidney disease,⁵ and patients with severe chronic kidney disease are at an increased risk of contrast-associated acute kidney injury.^{6,7} Therefore, it is essential to reduce the amount of contrast used for diagnostic imaging. Pial collaterals can be assessed using CTA.⁸⁻¹⁰ Similarly, flat panel detector (FPD) CT angiography in the angiography suite¹¹ following intravenous contrast injection allows detecting vessels distal to the occlusion site. Furthermore, FPD CT has also been used to generate FPD CBV images with an intravenous contrast injection,¹² which are potentially useful for prediction of the final infarct volume in patients with AIS with LVO¹³⁻¹⁵ and of hemorrhagic infarction post-MT.¹⁶ The image reconstruction of FPD CBV datasets provides FPD CT

Received June 27, 2020; accepted after revision September 5.

From the Department of Neurosurgery (T.N., M.N., M.K., K.A., H.K.), Yokohama Shin-Midori General Hospital, Kanagawa, Japan; Department of Neurological Surgery (T.N., A.M.), Nippon Medical School Hospital, Tokyo, Japan; Department of Neurosurgery (T.I.), Jikei University School of Medicine, Tokyo, Japan; and Siemens Healthcare K.K. (K.O.), Tokyo, Japan.

Please address correspondence to Toshiki Nozaki, MD, Department of Neurological Surgery, Nippon Medical School Hospital, 1-1-5 Sendagi, Bunkyo-ku, Tokyo 113-8603, Japan; e-mail: tonod03sm069@gmail.com

Indicates article with supplemental online photos.

<http://dx.doi.org/10.3174/ajnr.A6906>

angiographic images that are comparable with CTA with regard to the visualization of LVO, collateral state, and clot extent.¹² Moreover, FPD CBV images can be obtained using an intra-arterial diluted contrast injection,^{16,17} which requires less contrast material. However, it remains unclear whether the vessels distal to the occlusion site in patients with stroke can be evaluated on the FPD CT angiographic images with intra-arterial diluted contrast injection.

Therefore, in our study, we assessed whether FPD CT angiographic images, generated during FPD CBV imaging with an intra-arterial diluted contrast injection, could visualize vessels distal to the occlusion site in patients with AIS compared with MRA findings.

MATERIALS AND METHODS

This study was approved by the ethics committee of Yokohama Shin-Midori General Hospital (permission No. 19001-2) and was performed using the opt-out method described on our hospital Web site.

Subjects and Methods

Between May 2019 and January 2020, we enrolled all patients with AIS with LVO of the anterior circulation (ICA and MCA) who were eligible for MT. An MR imaging-based protocol was used to select patients for reperfusion therapy (Online Fig 1). All patients, except those for whom MR imaging was contraindicated, were assessed using MR imaging and MRA to diagnose AIS and LVO. Nonenhanced CT was used to evaluate AIS and exclude hemorrhage or large demarcated infarction in patients contraindicated for MR imaging. Following assessment using MR imaging/MRA or a nonenhanced CT, all patients were treated with IV rtPA therapy in the angiography suite, when eligible. An 8F sheath was inserted into the femoral artery following groin puncture. Then, an 8F balloon guide catheter and a 6F diagnostic catheter coaxial system were used, and FPD CBV images were acquired. The extent of tissue damage was assessed on MR imaging before the procedure. We used the FPD CBV images to confirm the extent of damaged brain tissue and to assess risks of hyperperfusion and hemorrhagic infarction following the procedure, and we used the FPD CT angiography images as reference vessel images for performing MT.

FPD CBV and MRA Imaging Protocols

MRA imaging was performed with a 1.5T MR imaging scanner (EXCELRT Vantage; Canon Medical Systems) using a TOF-MRA sequence (TE = 6.8 ms, TR = 21 ms, flip angle = 18°, FOV = 200 × 200 mm, section thickness = 1 mm, pixel spacing = 1.3 × 0.8, resulting in an acquisition time = 4 minutes and 12 seconds).

We used a biplanar flat panel detector angiographic system (Artis zee biplane VD11C; Siemens) for all angiographic imaging. FPD CBV imaging was performed with 2 rotations of the flat panel detector system. Mask images (mask run) were first acquired and fill images (fill run) were acquired post-contrast injection. We applied the following protocol:^{16,18} acquisition time, 6 seconds; x-ray tube voltage, 70 kV; total angle, 200°; projections, 400; dose, 0.36 mGy/

frame; and x-ray delay, 9 seconds. We used contrast medium with an iodine concentration of 300 mg/mL. A solution of 30% diluted contrast medium was injected using a power injector at a rate of 6.0 mL/s through a 6F diagnostic catheter placed just above the aortic valve in the ascending aorta. The total contrast dose was 25.2 mL (total injection volume was 84 mL). Two types of images were generated simultaneously: angiographic images reconstructed from the fill run (FPD CT angiographic images), and color-coded FPD CBV images from the mask and fill runs (Fig 1A) using the application software of the workstation of the system (syngo DynaPBV Neuro; Siemens). The color-coded FPD CBV images provided an approximation of the CBV and a real-time overview on the extension of irreversibly damaged brain tissue. The additional FPD CT angiographic images depicted intracranial vessels post-contrast flow in the brain parenchyma reached a steady-state, and were used for detecting LVO and vessels distal to the occlusion site, evaluating the collateral status of the occluded MCA territory during MT.

Image Analysis

All images were anonymized before analysis and evaluated by 2 board-certified and experienced neurosurgeons (H.K. and M.N.) blinded to clinical information. Vessels proximal to the occlusion site were identified on FPD CT angiographic images and initial MRA and described as follows: cervical ICA (cICA); ICA terminal (ICA-T); MCA M1 segment (M1) proximal/distal; and MCA M2 segment (M2) proximal/distal. Previously published scales of angiographic assessment were used.

First, we evaluated the image quality of FPD CT angiographic images on a 4-point scale:¹⁹ 1) poor image quality, blurring of the vessel contours; 2) fair image quality, suboptimal arterial enhancement for confident diagnosis; 3) good image quality and arterial enhancement, adequate for confident diagnosis; and 4) excellent image quality and arterial enhancement.

We evaluated the visualization of vessels distal to the occlusion site on the basis of retrograde contrast opacification of vessels within the occluded territory on FPD CT angiographic images and MRA.²⁰ The visualization score, used to assess the degree of visualization of vessels distal to the occlusion site, consisted of 5 categories describing which part of the collateral vessels could be visualized: 1) distal portion of the occluded vessel segment, 2) proximal portion of the segment adjacent to the occluded vessel, 3) distal portion of the segment adjacent to the occluded vessel, 4) vessels 2 segments distal to the occluded vessel, and 5) little-or-no significant visualization of the territory of the occluded vessel. For example, in the case of M1 proximal occlusion, if M1 distal was visualized, a score of 1 was assigned. Similarly, if the M2 proximal, M2 distal, or MCA M3 segment was visualized, a score of 2, 3, or 4 was, respectively, assigned. Online Fig 2 shows the visualization score rating, for example, in the case of right ICA-T occlusion.

Finally, the collateral status of the occluded MCA territory was evaluated semiquantitatively on the same FPD CT angiographic images and scored on a 4-point scale:²¹ 0) absent collateral supply

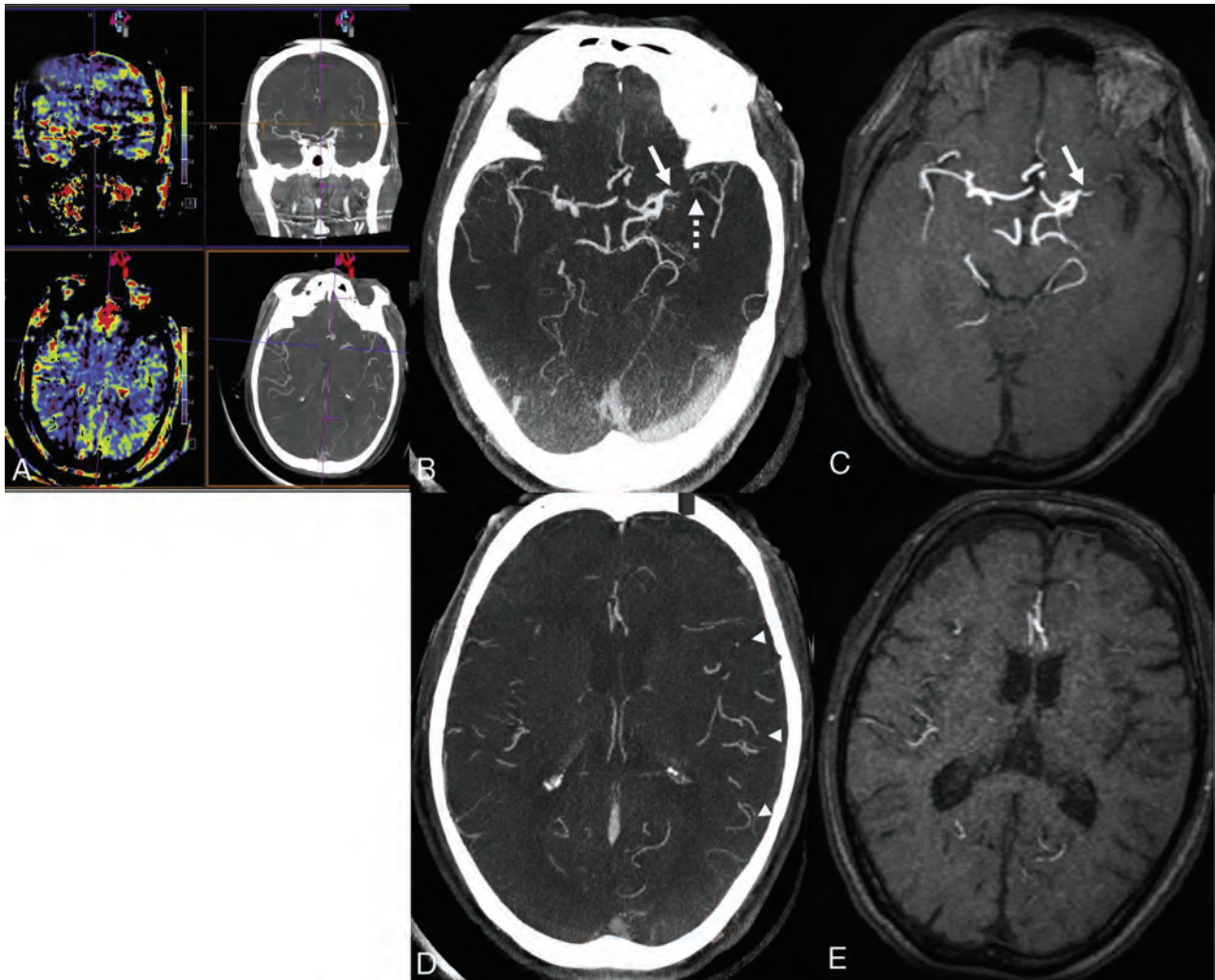


FIG 1. Representative case 1. A patient presented with a left M1 segment occlusion. A, FPD CBV imaging includes FPD CBV images and FPD CT angiographic images. B, The axial FPD CT angiographic images could visualize the occlusion site (M1 proximal, *white continuous arrow*) and its distal vessel (M1 distal, *white dashed arrow*) by the filling of collaterals. The visualization score is 1. C, MRA could visualize the occlusion site but not its distal vessel (visualization score = 5). D, *White arrowheads* in the FPD CT angiographic image show the filling of the MCA territory via leptomeningeal anastomosis. The collateral score is 3 for 100% collateral supply of the occluded MCA territory. E, The filling of the MCA territories is not confirmed on the MRA. MIP thickness is set to 10 mm for B and C and 5 mm for D and E.

to the occluded MCA territory, 1) collateral supply filling $\leq 50\%$ but $>0\%$ of the occluded MCA territory, 2) collateral supply filling $>50\%$ but $<100\%$ of the occluded MCA territory, and 3) 100% collateral supply of the occluded MCA territory.

MIP thickness of FPD CT angiographic images was changed from 1 to 99 mm according to the rater's intention when assessing the visualization score and fixed to 5 mm when assessing the collateral score.

Statistical Analysis

Intrater agreement was analyzed using the quadratic weighted κ statistic (≤ 0.4 , poor agreement; 0.4–0.75, fair to good agreement; ≥ 0.75 , excellent agreement²²). The Spearman rank correlation coefficient, the Mann-Whitney *U* test, and the Kruskal-Wallis test followed by the Steel-Dwass post hoc test were used to assess associations of the visualization score with the collateral score, the occlusion site, TICI grade, and the 90-day mRS. The Mann-Whitney *U* test was used to assess the difference in the visualization

scores between FPD CT angiographic images and MRA. The level of statistical significance was set to $P < .05$. Data from the more experienced of the 2 raters have been used in the text, tables, and figures. Statistical software (Easy R [EZ]; Saitama Medical Center, Jichi Medical University) was used for all statistical analyses.

RESULTS

We performed MT for 28 consecutive patients with AIS with LVO of the anterior circulation. Six of them did not undergo FPD CBV imaging because 2 were treated in the other angiography suite where we could not perform FPD CBV imaging, and 4 were excluded owing to a protocol violation. Therefore, the remaining 22 patients underwent FPD CBV imaging and were retrospectively analyzed.

Patient Characteristics

Table 1 shows the baseline characteristics of the 22 patients who fulfilled the inclusion criteria. Twenty patients were

initially assessed by MR imaging and MRA. The remaining 2 patients with cardiac pacemaker implantation were initially assessed by nonenhanced CT. Of the 22 patients, 2 patients (9%) had a cerebral aneurysm: One had an aneurysm at the bifurcation of M1–M2 distal to the occlusion site (ICA-T), which was not depicted owing to its fair image quality caused by motion artifacts, while the other had an aneurysm at the bifurcation of M1–M2 proximal to the occlusion site (M2 proximal), which was visualized using FPD CT angiographic images.

Evaluation of FPD CT Angiographic Images

Table 2 shows the results of the FPD CT angiographic image evaluation of all patients. The proximal occluded sites identified on

FPD CT angiographic images and initial MRA were ICA-T ($n = 7$), M1 proximal ($n = 4$), M1 distal ($n = 2$), M2 proximal ($n = 6$), M2 distal ($n = 1$), cICA and M2 proximal (tandem occlusions) ($n = 2$). In 2 cases of tandem occlusions with cICA and M2 proximal, vessels distal to the occlusion site (M2 proximal) were observed on FPD CT angiographic images only, not on MRA. The FPD CT angiographic images of 20 patients (91%) had good or excellent image quality, and the FPD CT angiographic images of 2 patients (9%) had poor or fair image quality owing to motion artifacts.

The vessels distal to the occlusion site were visualized only in the 20 patients with good or excellent image quality as follows: the distal portion of the occluded vessel segment (visualization score = 1) in 14 patients (70%), the proximal portion of the segment adjacent to the occluded vessel (visualization score = 2) in 3 patients (15%), and the distal portion of the segment adjacent to the occluded vessel (visualization score = 3) in 2 patients (10%). Only 1 patient (5%) who had no collateral supply (collateral score = 0) had no significant visualization of the territory of the occluded vessel (visualization score = 5).

Evaluation of the Visualization Score Using MRA

We evaluated the MRA scans of 20 patients; 2 patients contraindicated for MR imaging were excluded. The visualization scores were 2 in 1 patient (5%), 3 in 2 patients (10%), 4 in 2 patients (10%), and 5 in 15 patients (75%).

Statistical Analyses for Visualization Score

FPD CT angiographic images were shown to evaluate the visualization score more accurately than MRA (median scores, FPD CT versus MRA = 1 and 5, $P < .001$) in 19 patients with good- or excellent-quality FPD CT angiographic images. Vessels distal to the

occlusion site were significantly more clearly visualized in patients with MCA M1 and M2 occlusion than in patients with ICA occlusion (median scores, M1 = 1, M2 = 1, ICA = 2; M1 versus ICA, $P = .01$; M2 versus ICA, $P = .007$). There was a significant correlation between the visualization scores and collateral scores ($r = -0.61$, $P = .004$) and between the visualization scores and the 90-day mRS after MT ($r = 0.49$, $P = .03$). In contrast, the TICI grade did not significantly correlate with the visualization scores ($P = .39$).

Interrater agreement analyzed by the quadratic weighted κ statistic was excellent for image quality, visualization score, and collateral scores (0.85, 0.90, and 0.80, respectively).

Representative Cases

Case 1: M1 Occlusion, Patient No. 8. A patient presented with a left M1

Table 1: Baseline characteristics^a

Characteristics	
Patient background	
Age (yr)	74.9 [SD, 13.1]
Atrial fibrillation	16 (72.7%)
Hypertension	13 (59.1%)
Diabetes mellitus	2 (9.1%)
Dyslipidemia	12 (54.5%)
Chronic kidney disease	11 (50%)
Clinical status and treatment	
NIHSS at arrival	13.9 [SD, 5.9]
Sedation (midazolam)	6 (27.3%)
IV rtPA therapy	8 (40.9%)
TICI Grade 2a	1 (4.5%)
Grade 2b	5 (22.7%)
Grade 3	16 (72.7%)
Puncture-to-recanalization time (min)	66.2 [SD, 25.2]
Total contrast dose (mL)	130.3 [SD, 39.4]
mRS pre-onset	0.6 [SD, 1.2]
90-day post-MT	2.7 [SD, 1.9]

^aData are presented as mean [SD] or No. (%).

Table 2: Results of FPD CT angiographic image and MRA evaluation

Patient No.	Occlusion Site	Image Quality	Collateral Score	Visualization Score	
				FPD CT	MRA
1	ICA-T	Excellent	1	3	3
2	ICA-T	Excellent	3	2	5
3	ICA-T	Poor	—	—	—
4	ICA-T	Excellent	1	3	5
5	ICA-T	Excellent	1	2	—
6	ICA-T	Fair	—	—	5
7	ICA-T	Excellent	0	5	5
8	M1 proximal	Excellent	3	1	5
9	M1 proximal	Excellent	2	1	5
10	M1 proximal	Excellent	2	1	5
11	M1 proximal	Excellent	2	1	4
12	M1 distal	Excellent	3	1	5
13	M1 distal	Good	2	1	3
14	M2 proximal	Excellent	3	1	4
15	M2 proximal	Good	1	1	2
16	M2 proximal	Excellent	2	1	5
17	M2 proximal	Excellent	2	1	5
18	M2 proximal	Excellent	2	1	5
19	M2 proximal	Good	2	1	5
20	M2 distal	Excellent	3	1	5
21	cICA, M2 proximal	Good	3	1	5
22	cICA, M2 proximal	Good	1	2	5

Note:— indicates unevaluable.

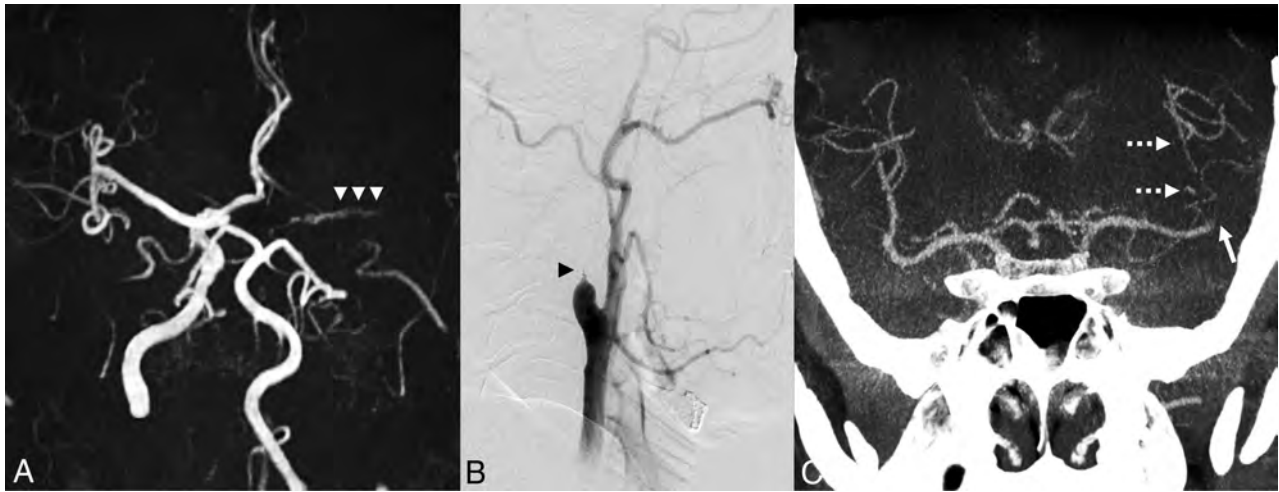


FIG 2. Representative case 2. A patient presented with tandem occlusions (cICA and M2 segment proximal occlusions). A, The left intracranial ICA is not visualized on MRA, suggesting left cICA occlusion. White arrowheads show slightly depicted M1 segment probably via the anterior communicating artery. Left M2 occlusion could not be identified on MRA. B, FPD CBV imaging before percutaneous transluminal angioplasty followed by conventional angiography at the left common carotid artery identifies left cICA occlusion (black arrowhead). C, The occlusion site (M2 proximal, white continuous arrow) and its distal vessel (M2 distal, white dashed arrows) on the coronal image by the fillings of collaterals. The visualization score is 1. MIP thickness is set to 20 mm.

proximal occlusion at 85 minutes with an NIHSS score of 29 (Fig 1). Concurrent with IV rtPA, MT using the stent retriever and reperfusion catheter was performed. TICI 3 recanalization was achieved 32 minutes post-groin puncture. FPD CT angiographic images could visualize the occlusion site (M1 proximal) and its distal vessel (M1 distal) by the filling of collaterals. We evaluated the visualization score as 1 and the collateral score as 3.

Case 2: cICA and M2 Occlusions, Patient No. 21. A patient presented with tandem occlusions with cICA and M2 proximal occlusion at 177 minutes, with an NIHSS score of 6 (Fig 2). MRA showed that left cICA occlusion was suspected; thus, we subsequently performed FPD CBV imaging in the angiography suite. FPD CT angiographic images revealed an M2 proximal occlusion. Concurrent with IV rtPA, percutaneous transluminal angioplasty using an angioplasty balloon for the cICA occlusion and MT using a stent retriever for the M2 occlusion were performed sequentially. The groin puncture to target recanalization time for M2 occlusion was 70 minutes, and TICI 3 recanalization was achieved. Contrast medium for FPD CBV imaging was administered from the ascending aorta just above the aortic valve before percutaneous transluminal angioplasty. FPD CT angiographic images could visualize the occlusion site (M2 proximal) and its distal vessel (M2 distal) by the filling of collaterals, though initial MRA did not show the occlusion site (M2 proximal). We evaluated the visualization score as 1. The images allowed planning for target recanalization (M2 occlusion) early during the procedure. Therefore, conventional angiography with contrast injection could be reduced, and some selective guidance of the catheter to specific vessels could be omitted.

DISCUSSION

In this study, we investigated whether vessels distal to the occlusion site in patients with AIS with LVO can be detected before MT on FPD CT angiographic images acquired post-intra-arterial diluted contrast injection. We found that the image quality of the FPD CT angiographic images was adequate for diagnosis, except in 2 cases affected by motion artifacts. These cases showed that movement and motion artifacts could not always be avoided, even in sedated patients. We could delineate the vessels distal to the occlusion site of the anterior circulation, including aneurysms in 2 patients, on all FPD CT angiographic images that had good or excellent image quality, except in 1 patient with no collateral supply (collateral score = 0). Interrater agreement for image quality, visualization score, and collateral score was excellent.

Vessels distal to the occlusion site tended to be more clearly visualized in patients with MCA occlusion than in patients with ICA-T occlusion but could be detected in all patients who had at least slight collateral flow (more than collateral score 1). Our result, therefore, suggests that even if there is only slight collateral supply in vessels distal to the occlusion site, they can be seen on FPD CT angiographic images using an intra-arterial contrast injection.

We used MR imaging as the first choice in treating patients with stroke because it allowed us to correctly differentiate between stroke and nonstroke conditions. However, MRA could not visualize collateral blood flow because it may have been too subtle to be detected. FPD CT angiographic images were also better at depicting vessels distal to the occlusion site than MRA.

The visualization score, using FPD CT angiographic images, was significantly correlated with the collateral score

and 90-day mRS post-MT. This finding suggested that FPD CT angiographic images may be useful for predicting clinical outcome of patients with AIS.

Patients with AIS eligible for MT have a higher prevalence of cerebral aneurysm (3.7%) than a healthy reference population.²³⁻²⁵ FPD CT angiographic imaging thus appeared useful for the planning of appropriate treatment strategies, considering anatomic details that need careful attention.

The results of our study suggested that FPD CT angiographic imaging using an intra-arterial injection may reduce the contrast dose used for visualization of vessels distal to the occlusion site compared with other modalities. This is important because the prevalence of chronic kidney disease in patients with AIS tends to be higher than in the general population,⁵ and the total contrast dose required for the MT procedure is difficult to predict in individual patients. In our hospital, whenever possible, the patients with AIS do not receive contrast medium for diagnostic imaging outside the angiography suite. The contrast dose required to obtain FPD CT angiographic images in our study was only 25.2 mL. This compares with 187–189 mL of contrast (converted to iodine concentrations of 300 mg/mL) used during a CT-based protocol (CTA or CTP) including MT^{6,7,26} and 80 mL of contrast used for FPD CT with intravenous injection.^{11,12} The effective radiation dose of FPD CBV imaging is less than that of CTA and CTP.^{27,28}

Our study has some limitations. First, it was a retrospective study with a small sample size, which has selection bias. Therefore, larger prospective studies are warranted to validate our results. Second, we could not compare our results with those from CTA/CTP or FPD CT with an intravenous contrast injection because we used an MR imaging–based protocol for selection of patients for reperfusion therapy.

CONCLUSIONS

FPD CT angiographic images acquired post-intra-arterial contrast injection could visualize vessels distal to the occlusion site for patients with AIS with LVO of the anterior circulation using a small amount of contrast material.

ACKNOWLEDGMENTS

The authors thank Masayuki Arakawa (Chief Radiologic Technologist, Yokohama Shin-Midori General Hospital) for the technical assistance. We also thank Editage (<https://www.editage.jp>) for English language editing.

Disclosures: Katharina Otani—RELATED: Other: Siemens Healthcare K.K., Comments: Employee.

REFERENCES

1. Albers GW, Marks MP, Kemp S, et al. **Thrombectomy for stroke at 6 to 16 hours with election by perfusion imaging.** *N Engl J Med* 2018;378:708–18 CrossRef Medline
2. Van Den Berg LA, Dijkgraaf MG, Berkhemer OA, et al; MR CLEAN Investigators. **Two-year outcome after endovascular treatment for acute ischemic stroke.** *N Engl J Med* 2017;376:1341–49 CrossRef Medline
3. Berkhemer OA, Fransen PS, Beumer D, et al; MR CLEAN Investigators. **A randomized trial of intraarterial treatment for acute ischemic stroke.** *N Engl J Med* 2015;372:11–20 CrossRef Medline
4. Nogueira RG, Jadhav AP, Haussen DC, et al. **Thrombectomy 6 to 24 hours after stroke with a mismatch between deficit and infarct.** *N Engl J Med* 2018;378:11–21 CrossRef Medline
5. Toyoda K, Ninomiya T. **Stroke and cerebrovascular diseases in patients with chronic kidney disease.** *Lancet Neurol* 2014;13:823–33 CrossRef Medline
6. Loh Y, McArthur DL, Vespa P, et al. **The risk of acute radiocontrast-mediated kidney injury following endovascular therapy for acute ischemic stroke is low.** *AJNR Am J Neuroradiol* 2010;31:1584–87 CrossRef Medline
7. Diprose WK, Sutherland LJ, Wang MTM, et al. **Contrast-associated acute kidney injury in endovascular thrombectomy patients with and without baseline renal impairment.** *Stroke* 2019;50:3527–31 CrossRef Medline
8. Smit EJ, Vonken EJ, Van Seeters T, et al. **Timing-invariant imaging of collateral vessels in acute ischemic stroke.** *Stroke* 2013;44:2194–99 CrossRef Medline
9. Maas MB, Lev MH, Ay H, et al. **Collateral vessels on CT angiography predict outcome in acute ischemic stroke.** *Stroke* 2009;40:3001–05 CrossRef Medline
10. Puetz V, Dzialowski I, Hill MD, et al. **Intracranial thrombus extent predicts clinical outcome, final infarct size and hemorrhagic transformation in ischemic stroke: the clot burden score.** *Int J Stroke* 2008;3:230–06 CrossRef Medline
11. Blanc R, Pistocchi S, Babic D, et al. **Intravenous flat-detector CT angiography in acute ischemic stroke management.** *Neuroradiology* 2012;54:383–91 CrossRef Medline
12. Hoelter P, Goelitz P, Lang S, et al. **Visualization of large vessel occlusion, clot extent, and collateral supply using volume perfusion flat detector computed tomography in acute stroke patients.** *Acta Radiol* 2019;60:1504–11 CrossRef Medline
13. Ava L, Berkefeld J, Lauer A, et al. **Predictive value of pooled cerebral blood volume mapping for final infarct volume in patients with major artery occlusions. a retrospective analysis.** *Clin Neuroradiol* 2017;27:435–42 CrossRef Medline
14. Fiorella D, Turk A, Chaudry I, et al. **A prospective, multicenter pilot study investigating the utility of flat detector derived parenchymal blood volume maps to estimate cerebral blood volume in stroke patients.** *J Neurointerv Surg* 2014;6:451–56 CrossRef Medline
15. Wagner M, Kyriakou Y, du Mesnil de Rochemont R, et al. **Does preinterventional flat-panel computer tomography pooled blood volume mapping predict final infarct volume after mechanical thrombectomy in acute cerebral artery occlusion?** *Cardiovasc Intervent Radiol* 2013;36:1132–38 CrossRef Medline
16. Moriya M, Itokawa H, Fujimoto M, et al. **Evaluation of patients with acute ischemic stroke using angiographic C-arm cerebral blood volume (C-arm CBV) measurements.** *Journal of Neuroendovascular Therapy* 2018;12:57–62 CrossRef
17. Kuriyama T, Sakai N, Beppu M, et al. **Optimal dilution of contrast medium for quantitating parenchymal blood volume using a flat-panel detector.** *J Int Med Res* 2018;46:464–74 CrossRef Medline
18. Ikemura A, Yuki I, Otani K, et al. **Evaluation of balloon test occlusion before therapeutic carotid artery occlusion: flat detector computed tomography cerebral blood volume imaging versus single-photon emission computed tomography.** *World Neurosurg* 2020; 133:e522–28 CrossRef Medline
19. Hinkmann FM, Voit HL, Anders K, et al. **Ultra-fast carotid CT-angiography: low versus standard volume contrast material protocol for a 128-slice CT-system.** *Invest Radiol* 2009;44:257–64 CrossRef Medline
20. Christoforidis GA, Mohammad Y, Kehagias D, et al. **Angiographic assessment of pial collaterals as a prognostic indicator following intra-arterial thrombolysis for acute ischemic stroke.** *AJNR Am J Neuroradiol* 2005;26:1789–97 Medline
21. Tan IY, Demchuk AM, Hopyan J, et al. **CT angiography clot burden score and collateral score: correlation with clinical and radiologic**

- outcomes in acute middle cerebral artery infarct. *AJNR Am J Neuroradiol* 2009;30:525–31 CrossRef Medline
22. McCluggage WG, Bharucha H, Caughley LM, et al. **Interobserver variation in the reporting of cervical colposcopic biopsy specimens: comparison of grading systems.** *J Clin Pathol* 1996;49:833–35 CrossRef Medline
 23. Zhou T, Li T, Zhu L, et al. **Endovascular thrombectomy for large-vessel occlusion strokes with preexisting intracranial aneurysms.** *Cardiovasc Intervent Radiol* 2018;41:1399–403 CrossRef Medline
 24. Zibold F, Kleine JF, Zimmer C, et al. **Aneurysms in the target vessels of stroke patients subjected to mechanical thrombectomy: prevalence and impact on treatment.** *J Neurointerv Surg* 2016;8:1016–20 CrossRef Medline
 25. Vlak MH, Algra A, Brandenburg R, et al. **Prevalence of unruptured intracranial aneurysms, with emphasis on sex, age, comorbidity, country, and time period: a systematic review and meta-analysis.** *Lancet Neurol* 2011;10:626–36 CrossRef Medline
 26. Jia ZY, Wang SX, Zhao LB, et al. **Risk of acute kidney injury with consecutive, multidose use of iodinated contrast in patients with acute ischemic stroke.** *AJNR Am J Neuroradiol* 2019;40:652–54 CrossRef Medline
 27. Struffert T, Deuerling-Zheng Y, Kloska S, et al. **Flat detector CT in the evaluation of brain parenchyma, intracranial vasculature, and cerebral blood volume: a pilot study in patients with acute symptoms of cerebral ischemia.** *AJNR Am J Neuroradiol* 2010;31:1462–69 CrossRef Medline
 28. Struffert T, Deuerling-Zheng Y, Kloska S, et al. **Dynamic angiography and perfusion imaging using flat detector CT in the angiography suite: a pilot study in patients with acute middle cerebral artery occlusions.** *AJNR Am J Neuroradiol* 2015;36:1964–67 CrossRef Medline

Transradial Approach for Neuroendovascular Procedures: A Single-Center Review of Safety and Feasibility

 D.T. Goldman,  D. Bageac,  A. Mills,  B. Yim,  K. Yaeger,  S. Majidi,  C.P. Kellner, and  R.A. De Leacy



ABSTRACT

BACKGROUND AND PURPOSE: In recent years, the transradial approach has become more widely adopted for neuroendovascular procedures. The purpose of this study was to evaluate the safety and feasibility of a transradial approach and distal transradial access for neuroendovascular procedures in a single center.

MATERIALS AND METHODS: Retrospective analysis was performed for all patients who underwent transradial approach or distal transradial access neuroendovascular procedures from January 2016 to August 2019 at a single center. Exclusion criteria included a Barbeau D waveform, a radial artery of <2 mm on sonographic evaluation, and known radial artery occlusion. Procedures were evaluated for technical success (defined as successful radial artery access and completion of the intended procedure without crossover to an auxiliary access site), complications, and adverse events during follow-up at 30 days.

RESULTS: The transradial approach or distal transradial access was attempted in 279 consecutive patients (58.1% women; median age, 57.7 years) who underwent 328 standard or distal transradial approach procedures. Two-hundred seventy-nine transradial approach and 49 distal transradial approach procedures were performed (cerebral angiography [$n = 213$], intracranial intervention [$n = 64$], head and neck intervention [$n = 30$], and stroke intervention [$n = 21$]). Technical success was 92.1%. Immediate adverse events (2.1%) included radial access site hematoma ($n = 5$), radial artery occlusion ($n = 1$), and acute severe radial artery spasm ($n = 1$). Thirty-day adverse events (0.3%) included a radial artery pseudoaneurysm ($n = 1$). Twenty-six cases (7.9%) required crossover to transfemoral access.

CONCLUSIONS: The transradial approach for neuroendovascular procedures is safe and feasible across a wide range of neuroendovascular interventions.

ABBREVIATIONS: dTRA = distal transradial approach; TFA = transfemoral approach; TRA = transradial approach

The transradial approach (TRA) is well-established within interventional cardiology and is recommended as first-choice access by the American Heart Association.¹⁻⁶ Large, randomized, multicenter trials from the cardiology literature show that TRA is associated with lower rates of access site morbidity and mortality compared with the transfemoral approach (TFA).⁷⁻¹¹ Additional

evidence supports the use of TRA in peripheral vascular interventions.¹²

Given the associated benefits to patient safety, satisfaction, and decreased recovery time, a first-line transradial approach for endovascular surgery has gained traction in both peripheral and neurointerventional radiology.¹³⁻¹⁵ Matsumoto et al^{16,17} published the earliest study of TRA for cerebral angiography in 2000, demonstrating the technical feasibility and safety of this approach. Since then, further studies have added to the neuroendovascular literature on TRA.¹⁸⁻²¹ Nevertheless, the common femoral artery remains the primary access site for cerebral angiography and neurointerventional procedures.

The distal transradial approach (dTRA) is a further modification by which the radial artery is accessed distal to the flexor retinaculum as the radial branch courses superficial to the scaphoid bone within the anatomic snuffbox. This access site allows

Received June 16, 2020; accepted after revision September 5.

From the Departments of Radiology (D.T.G., R.A.D.L.), Neurosurgery (D.B., B.Y., K.Y., S.M., C.P.K., R.A.D.L.), Icahn School of Medicine at Mount Sinai (A.M.), New York, New York.

Please address correspondence to Reade A. De Leacy, MD, Departments of Neurosurgery & Radiology, Icahn School of Medicine at Mount Sinai, Cerebrovascular Center, 1450 Madison Ave, KCC 1-North, New York, NY, 10075; e-mail: reade.deleacy@mountsinai.org; @Daryl_Goldman; @rdeleacymd

 Indicates article with supplemental online table.

<http://dx.doi.org/10.3174/ajnr.A6971>

Table 1: Procedure characteristic (n = 328)

Characteristic	Value
Age (yr)	57.7 [SD, 15.9] (48–68)
Sex	
Male	41.9 (137/327)
Female	58.1 (190/327)
Height (cm)	165.2 [SD, 10.1] (157.5–172.7)
Weight (kg)	77.3 [SD, 21.7] (63.0–88.5)
BMI (kg/m ²)	28.3 [SD, 7.4] (23.4–31.7)
Procedure	
Cerebral angiography	64.9 (213/328)
Head and neck	9.1 (30/328)
Intracranial intervention	19.5 (64/328)
Acute stroke intervention/mechanical thrombectomy	6.4 (21/328)
dTRA access	14.9 (49/328)
Prior TRA	15.5 (51/328)
Technique failure	7.9 (26/328)
Sheath size (Fr)	
4	50.6 (166/328)
5	35.7 (117/328)
6	12.5 (41/328)
Arm accessed	
Left	4.3 (14/328)
Right	94.5 (310/328)
Coagulopathy	10.7 (35/328)
Crossover	7.9 (26/328)
Vessel accessed	
Right common carotid artery	64.9 (213/328)
Right internal carotid artery	50.3 (165/328)
Right external carotid artery	19.8 (65/328)
Left common carotid artery	62.8 (206/328)
Left internal carotid artery	47.6 (156/328)
Left external carotid artery	19.2 (63/328)
Right vertebral artery	55.8 (183/328)
Left vertebral artery	35.7 (117/328)

Note:—BMI indicates body mass index.

preservation of the more proximal radial artery for future interventions or access requirements.

Here we present our initial institutional experience performing TRA and dTRA for diagnostic neuroangiography and neurointerventions.

MATERIALS AND METHODS

Study Design and Exclusion Criteria

This single-center retrospective study was approved by the local institutional review board, and all study activities followed Health Insurance Portability and Accountability Act regulations. A retrospective analysis was performed of 279 patients evaluated for 328 consecutive TRA or dTRA neuroendovascular procedures from January 2016 to December 2019.

All neurointerventional procedures, both diagnostic and interventional, were included and separated into 4 groups: cerebral angiography, head and neck interventions, intracranial interventions, and acute stroke intervention/mechanical thrombectomy.

All patients were given the option of TRA and consented appropriately. Testing for ulnar-palmar arch patency was performed using a technique previously described by Barbeau et al.²² This practice was abandoned in 2019 following updated

guidelines from the Society of Neuro-Interventional Surgery Standards and Guidelines Committee highlighting the limitations of the test in predicting ischemic complications.²³ Before these updated guidelines exclusion criteria for TRA included a Barbeau D waveform (when Barbeau test was performed), a radial artery diameter <2 mm on initial sonographic evaluation, and known radial artery occlusion. Radial artery diameter <2 mm is treated as a relative contraindication to radial access at our institution due to the reported association between a smaller radial artery diameter and an increased risk of radial artery occlusion following TRA procedures.²⁴ Distal TRA was specifically considered in patients with limited supination of the arm, though the decision to proceed with dTRA was ultimately made by the operator.

Additional patient demographic data were collected retrospectively using the electronic medical record system, Epic Systems (Verona, Wisconsin) and the Mount Sinai Data Warehouse (Table 1).

TRA Access

Standard radial artery access technique, previously described by Posham et al¹² and Snelling et al,²¹ was used for all procedures. Under sonographic guidance, the radial artery was localized with compression on B-mode and color Doppler flowmetry, confirming patency.

Local anesthesia (1% lidocaine) was infiltrated in the subdermal layer. A single-wall puncture of the radial artery was performed at the level of the radial epiphysis on the volar radial surface under real-time sonographic guidance. Using the modified Seldinger technique, the proceduralist inserted an access sheath into the radial artery.

dTRA Access

The patient was positioned with the access arm partially pronated at his or her side in a thumbs-up position. Under sonographic guidance, the metacarpals of the thumb and index finger were identified first, followed by the trapezium and the scaphoid bones below the distal radial artery. A single-wall puncture of the artery was performed through the anatomic snuffbox under real-time sonographic visualization. Using the modified Seldinger technique, the proceduralist inserted an access sheath into the radial artery.

Procedural Technique

A 4F or 5F Glidesheath Slender (Terumo) sheath was used for diagnostic studies, and a 5F or 6F Glidesheath Slender sheath was used for most head and neck and intracranial interventions. For stroke interventions and select aneurysm treatments using flow diversion, a 0.088-inch-long guide sheath was used without a

short sheath. Maintenance of the radial access sheath on continuous heparinized flush was left to the proceduralist's discretion. Following sheath insertion, a radial artery access cocktail consisting of 3000 U of heparin, 200 µg of nitroglycerin, and 2.5 mg of verapamil was mixed with 10 mL of the patient's blood and slowly infused through the sheath for 5–10 minutes to induce vasodilation. Administration of the access cocktail was omitted during the stroke intervention to expedite the procedure and avoid inducing hypotension.

Equipment selection was dependent on the procedure type. For diagnostic angiography, a 5F Simmons 2 Glidecath catheter (Terumo) was advanced over a Bentson guidewire and formed within the aortic arch before selectively catheterizing the vessels of interest. For most nonstroke interventions, a 0.071-inch guide catheter was advanced over a 125-cm Select catheter (Penumbra) and guidewire into the vessel of interest. For stroke interventions and selected flow-diverter cases, a 0.088-inch guide catheter was used without a sheath and advanced over a selecting catheter and stiff guidewire for added support. Once the guide catheter was positioned, the procedure followed a similar vessel-selection technique used during femoral access.

Following the procedure, a radial artery compression device was placed over the arteriotomy site for a minimum of 60 minutes. The band was removed after arterial hemostasis and pulse were reconfirmed. Similar closure techniques were followed for both TRA and dTRA procedures. Repeat evaluation of the access site and radial pulse was performed for all patients before discharge and during the 30 day follow-up outpatient visit.

Technical Success and Complications

Technical success was defined as successful radial artery access and completion of the intended procedure without crossover to an auxiliary access site.

Major complications included the need for prolonged hospitalization, an unplanned increase in the level of care, permanent adverse sequelae, and death. Minor complications included the need for additional nominal therapy, overnight admission for observation, loss of a radial pulse without evidence of distal ischemia, and hematoma or blood loss not requiring transfusion or open surgical repair. In addition to the periprocedural data, the access site was evaluated for bleeding and neurologic events before and after the procedure with additional evaluations up to 30 days postprocedure.

Statistical Analysis

Data are presented as mean and range for continuous variables and frequency for categorical variables. Univariate and multivariate analyses of complications and crossover were performed using logistic regression. A *P* value of $\leq .05$ was considered statistically significant. SPSS Statistics for Windows, Version 23.0 (IBM) was used for statistical analyses.

RESULTS

Procedure

A total of 328 radial procedures were performed during the study period, including cerebral angiography ($n = 213$), intracranial interventions ($n = 64$), head and neck interventions ($n = 30$), and

Table 2: Adverse events

Adverse Event	No. (%)
Early complications	
Hematoma	1.5 (5/328)
Radial artery spasm	0.3 (1/328)
Radial artery occlusion	0.3 (1/328)
30-Day complications	
Radial artery pseudoaneurysm	0.3 (1/328)

stroke interventions ($n = 21$) (Table 1). Of the 328 procedures, 279 procedures used the TRA and 49 procedures used the dTRA. A total of 51 procedures were performed in patients who had undergone prior TRA, and 8 cases were transitioned to TRA after failed TFA. Crossover to the TRA was most often necessary due to tortuous vascular anatomy preventing supra-aortic vessel selection from the femoral artery. Radial artery micropuncture and vessel access were successful in all cases. Completion of the intended procedure via TRA was achieved in 255 of 279 cases (91.3%), while it was via the dTRA in 47 of 49 cases (95.9%). Composite success in completing the intended procedure via TRA or dTRA was achieved in 302 of 328 cases (92.1%).

Crossover to TFA

Crossover to TFA was required to successfully complete 26 of 328 (7.9%) cases. Of all TRA crossovers, 19 (73.1%) were attributed to vascular anomalies or severe tortuosity of the subclavian artery ($n = 7$), aortic arch ($n = 7$), or carotid artery ($n = 5$), which undermined stability and/or prevented navigation of the catheter system. An additional 6 failures (23.1%) were related to radial artery vasospasm ($n = 3$), severe radial and brachial artery tortuosity secondary to hypertensive vasculopathy ($n = 1$), and an aberrant right subclavian artery morphology that prevented target artery access ($n = 2$). In 1 patient, crossover to TFA was performed due to patient discomfort.

Analysis of TFA crossover is presented in the Online Table. There were no significant predictors of crossover from TRA to TFA.

The Barbeau test was performed for assessment of collateral circulation to the hand in 306 cases (93.3%) and was stopped in 2019 following guidelines that highlight the inability of the test to predict ischemic complications.²⁵ All tested patients had favorable Barbeau test outcomes (grade A and B), and no correlation was demonstrated between the test result and access site complication or crossover to TFA.

Complications

A total of 8 adverse events (2.4%) were recorded among all radial artery cases: 7 in the TRA group (2.5%, 7/279) and 1 in the dTRA group (2.0%, 1/49). Seven of these events were immediate, and 1 was delayed (noted at 30-day follow-up). Immediate adverse events included hematoma ($n = 5$), radial artery occlusion ($n = 1$), and severe radial artery spasm ($n = 1$). The delayed adverse event was a radial artery pseudoaneurysm measuring < 2 mm that was managed conservatively with observation. An analysis of the TRA adverse events is presented in Table 2. Larger sheath size (≥ 6 F) was a significant predictor of adverse events ($P < .001$).

Table 3: Analysis of total adverse events

Predictor/Category	OR (95% CI)	P
Age (yr)		
60 or older	1.00	
Younger than 60	0.53 (0.12–2.25)	.39
Sex		
Male	1.00	
Female	2.20 (0.44–11.1)	.34
Height (cm)		
≥165.1	1.00	
<165.1	0.36 (0.07–1.80)	.21
Weight (kg)		
≥74.3	1.00	
<74.3	1.70 (0.40–7.23)	.47
BMI (kg/m ²)		
≥27.4	1.00	
<27.4	7.37 (0.90–60.6)	.06
Procedure		
Cerebral angiogram	1.00	
Head and neck intervention	11.7 (1.87–73.3)	.05
Intracranial intervention	3.40 (0.47–24.7)	.86
Acute stroke intervention/ mechanical thrombectomy	5.28 (0.46–60.8)	.69
Prior TRA		
No	1.00	
Yes	1.84 (0.36–9.4)	.46
Sheath size (Fr)		
4	1.00	
5	0.71 (0.06–7.89)	.19
6	8.87 (1.57–50.2)	.004
Coagulopathy		
No	1.00	
Yes	0.76 (0.09–6.52)	.80

DISCUSSION

The success and widespread adoption of the TRA in cardiology has highlighted the benefits of radial access. Unlike traditional femoral access, TRA is associated with a decreased risk of bleeding and arterial damage, both of which are critical for patients on anticoagulant or antiplatelet therapy.¹² TRA has been associated with lower access site infection rates, expedited postprocedural ambulation, reduced postprocedure nursing care, and shorter hospital stay.²¹ Patient preference for TRA over TFA has been demonstrated previously.²⁶

The present study describes data from 328 TRA neuroendovascular procedures performed in 279 patients. Both diagnostic and interventional procedures were included from a practice of 8 neurointerventionalists, each having varying levels of TRA case experience. Two interventionalists performed most procedures (40% and 30%, respectively). Six interventionalists performed between 11 and 28 procedures each (median, 13.5).

Our overall success rate, defined as successful completion of the intended procedure from the initial radial access, was 92.2% (302/328 cases). The success rate of TRA neuroendovascular procedures in the literature is reportedly 92.7%–99%.¹⁸ A dedicated analysis of TRA to TFA crossover in the current study showed that the primary factors contributing to crossover included the following: vascular anomalies and tortuosity of the subclavian artery ($n = 7$), aortic arch ($n = 7$), and carotid artery ($n = 5$); radial artery spasm ($n = 3$); severe radial artery tortuosity ($n = 1$); variant arch anatomy ($n = 2$); and excessive arm pain ($n = 1$). A combination

of factors led to the high crossover rate (7.9%) in the current study, including operator experience, position on the TRA learning curve, availability of access catheters, and case selection.

Various studies have examined the relationship between operator volume and procedural outcomes, suggesting 30–50 cases as the general learning curve.^{27,28} We separately analyzed the 100 most recent cases and demonstrated a technical success rate of 95% with 5 crossover cases (5%). While the operator's learning curve was not directly studied, this is a likely contributor to the overall crossover rate of 7.9% for the entire cohort. To that end, this study was performed at an academic teaching hospital with neurointerventional trainees of varying experience in performing transradial neurointerventional procedures.

Although our study did not elucidate significant predictors for conversion from TRA to TFA, other, non-neurointervention-focused studies have identified such predictors. Posham et al¹² noted procedural type, female sex, and height of <1.7 m as significant predictors of radial-to-femoral crossover using univariate analysis. However, these were not significant by multivariate analysis. Additionally, Carvalho et al²⁹ reported short sheaths, female sex, multivessel disease, body surface area, and age older than 66 years as independent predictors of conversion from radial to femoral access. To our knowledge, no prior studies on TRA neuroendovascular procedures have examined the predictors of conversion from radial to femoral access.

The radial artery is easily compressible against the volar radial surface, permitting easy hemostasis. Titano et al³⁰ showed that TRA was associated with a low incidence of bleeding complications in patients with an elevated international normalized ratio (>1.5) undergoing below-neck interventions. Our study reaffirms this finding in a neurointerventional population with no significant difference in adverse events between patients with and without coagulopathy.

The overall adverse event rate in our study was 2.4%, including 7 immediate adverse events (access site hematoma [$n = 5$], radial artery occlusion [$n = 1$], severe radial artery spasm [$n = 1$], and one 30-day adverse event (radial artery pseudoaneurysm of <2 mm). No major access site complications occurred. This complication rate of 2.4% is similar to those published for TRA in visceral interventions and TRA in neurointerventions.^{12,31} All immediate adverse events were managed conservatively. An analysis of the total adverse events is presented in Table 3. Significantly higher adverse events rates were observed for procedures that used 6F sheaths ($P < .001$). All access site hematomas were small and resolved following conservative management. One of the 5 patients who developed an access site hematoma had been placed on dual-antiplatelet therapy following intracranial stent placement.

Four of the 8 total adverse events occurred when a 6F sheath was used (access site hematoma [$n = 3$] and severe radial artery spasm [$n = 1$]). The significant association observed between larger sheath size and access site complications is in keeping with

previous studies examining both transfemoral and transradial procedures.³²⁻³⁴ This association is thought to arise from larger radial arteriotomy size, increased potential for intimal damage, and longer procedure times associated with interventional cases in which 6F sheaths are common. dTRA was used in 49 cases with a procedural completion rate without crossover to TFA of 95.6% (47/49). This outcome measure and the reported adverse events are comparable with those in the TRA cohort and previously reported dTRA data. dTRA allows preservation of the more proximal radial artery, which may be required for other interventions/therapies, enhanced operator and patient comfort, and easy hemostasis.

Direct comparison of complication rates of TRA and TFA cannot be made from the current study. However, comparison of complication rates for TRA versus TFA have been described previously.^{35,36} Stone et al³⁵ performed a prospective comparison of TFA to TRA for diagnostic cerebral angiography and demonstrated no significant difference in complication rates between the 2 groups.

Our study did not demonstrate a relationship between repeat catheterization and adverse events. Repeat TRA was performed in 51 cases (15.5%) and accounted for 2 of the 8 total minor adverse events (25%): 1 hematoma and 1 radial artery occlusion. These findings are consistent with the previously published literature, describing same-site repeat TRA success rates of >94% with up to 6 prior TRA procedures.²⁵

The primary limitation of the present study is the retrospective design and lack of a comparator control arm, making it difficult to appreciate subtle differences in procedural success and complication rates. Additionally, patient selection for TRA was based on both operator and patient preference in addition to the specific procedure performed.

CONCLUSIONS

Our institution's initial experience using TRA for diagnostic angiography and neurointerventional procedures was comparable with that of previously reported TRA studies. No major complications were noted, and the rate of femoral crossovers will likely continue to improve with technical familiarity and case selection. Furthermore, favorable outcomes were observed in patients on anticoagulation, mirroring findings from the coronary/cardiac literature. The transition of practice to a radial first approach is a safe and worthwhile endeavor that may substantially improve the morbidity and mortality of select patients.

Disclosures: Ariana Mills—UNRELATED: Stock/Stock Options: Vanguard Health Care exchange traded funds, Comments: I own various health care-related exchange traded funds from which I receive dividends in the ordinary course. Christopher P. Kellner—UNRELATED: Grants/Grants Pending: Penumbra and Siemens.* *Money paid to the institution.

REFERENCES

1. Archbold RA, Robinson NM, Schilling RJ. **Radial artery access for coronary angiography and percutaneous coronary intervention.** *BMJ* 2004;329:443-46 CrossRef Medline
2. Caputo RP, Tremmel JA, Rao S, et al. **Transradial arterial access for coronary and peripheral procedures: executive summary by the Transradial Committee of the SCAI.** *Cathet Cardiovasc Interv* 2011;78:823-39 CrossRef Medline

3. Hamon M, Pristipino C, Di Mario C, et al; Working Group on Thrombosis on the European Society of Cardiology. **Consensus document on the radial approach in percutaneous cardiovascular interventions: position paper by the European Association of Percutaneous Cardiovascular Interventions and Working Groups on Acute Cardiac Care** and Thrombosis of the European Society of Cardiology.** *EuroIntervention* 2013;8:1242-51 CrossRef Medline
4. Mann JT 3rd, Cubeddu MG, Schneider JE, et al. **Right radial access for PTCA: a prospective study demonstrates reduced complications and hospital charges.** *J Invasive Cardiol* 1996;8 (Suppl D):40d-44 Medline
5. Mason PJ, Shah B, Tamis-Holland JE, et al; American Heart Association Interventional Cardiovascular Care Committee of the Council on Clinical Cardiology; Council on Cardiovascular and Stroke Nursing; Council on Peripheral Vascular Disease; and Council on Genomic and Precision Medicine. **An update on radial artery access and best practices for transradial coronary angiography and intervention in acute coronary syndrome: a Scientific Statement From the American Heart Association.** *Circ Cardiovasc Interv* 2018;11:e000035 CrossRef Medline
6. Mitchell MD, Hong JA, Lee BY, et al. **Systematic review and cost-benefit analysis of radial artery access for coronary angiography and intervention.** *Circ Cardiovasc Qual Outcomes* 2012;5:454-62 CrossRef Medline
7. Bernat I, Horak D, Stasek J, et al. **ST-segment elevation myocardial infarction treated by radial or femoral approach in a multicenter randomized clinical trial: the STEMI-RADIAL trial.** *J Am Coll Cardiol* 2014;63:964-72 CrossRef Medline
8. Jolly SS, Yusuf S, Cairns J, et al. **Radial versus femoral access for coronary angiography and intervention in patients with acute coronary syndromes (RIVAL): a randomised, parallel group, multi-centre trial.** *Lancet* 2011;377:1409-20 CrossRef Medline
9. Mehta SR, Jolly SS, Cairns J, et al; RIVAL Investigators. **Effects of radial versus femoral artery access in patients with acute coronary syndromes with or without ST-segment elevation.** *J Am Coll Cardiol* 2012;60:2490-99 CrossRef Medline
10. Romagnoli E, Biondi-Zoccai G, Sciahbasi A, et al. **Radial versus femoral randomized investigation in ST-segment elevation acute coronary syndrome: the RIFLE-STEACS (Radial Versus Femoral Randomized Investigation in ST-Elevation Acute Coronary Syndrome) study.** *J Am Coll Cardiol* 2012;60:2481-89 CrossRef Medline
11. Valgimigli M, Gagnor A, Calabró P, et al; MATRIX Investigators. **Radial versus femoral access in patients with acute coronary syndromes undergoing invasive management: a randomised multi-centre trial.** *Lancet* 2015;385:2465-76 CrossRef Medline
12. Posham R, Biederman DM, Patel RS, et al. **Transradial approach for noncoronary interventions: a single-center review of safety and feasibility in the first 1,500 cases.** *J Vasc Interv Radiol* 2016;27:159-66 CrossRef Medline
13. Kumar AJ, Jones LE, Kollmeyer KR, et al. **Radial artery access for peripheral endovascular procedures.** *J Vasc Surg* 2017;66:820-25 CrossRef Medline
14. Ruzsa Z, Nemes B, Pinter L, et al. **A randomised comparison of transradial and transfemoral approach for carotid artery stenting: RADCAR (RADial access for CARotid artery stenting) study.** *EuroIntervention* 2014;10:381-91 CrossRef Medline
15. Zussman BM, Tonetti DA, Stone J, et al. **A prospective study of the transradial approach for diagnostic cerebral arteriography.** *J Neurointerv Surg* 2019;11:1045-49 CrossRef Medline
16. Matsumoto Y, Hokama M, Nagashima H, et al. **Transradial approach for selective cerebral angiography: technical note.** *Neurol Res* 2000;22:605-08 CrossRef Medline
17. Matsumoto Y, Hongo K, Toriyama T, et al. **Transradial approach for diagnostic selective cerebral angiography: results of a consecutive series of 166 cases.** *AJNR Am J Neuroradiol* 2001;22:704-08 Medline

18. Jo KW, Park SM, Kim SD, et al. **Is transradial cerebral angiography feasible and safe? A single center's experience.** *J Korean Neurosurg Soc* 2010;47:332–37 CrossRef Medline
19. Levy EI, Boulos AS, Fessler RD, et al. **Transradial cerebral angiography: an alternative route.** *Neurosurgery* 2002;51:335–42 Medline
20. Park JH, Kim DY, Kim JW, et al. **Efficacy of transradial cerebral angiography in the elderly.** *J Korean Neurosurg Soc* 2013;53:213–17 CrossRef Medline
21. Snelling BM, Sur S, Shah SS, et al. **Transradial cerebral angiography: techniques and outcomes.** *J Neurointerv Surg* 2018;10:874–81 CrossRef Medline
22. Barbeau GR, Arseneault F, Dugas L, et al. **Evaluation of the ulnopalmar arterial arches with pulse oximetry and plethysmography: comparison with the Allen's test in 1010 patients.** *Am Heart J* 2004;147:489–93 CrossRef Medline
23. Starke RM, Snelling B, Al-Mufti F, et al. **Transarterial and transvenous access for neurointerventional surgery: report of the SNIS Standards and Guidelines Committee.** *J Neurointerv Surg* 2020;12:733–41 CrossRef Medline
24. Rashid M, Kwok CS, Pancholy S, et al. **Radial artery occlusion after transradial interventions: a systematic review and meta-analysis.** *J Am Heart Assoc* 2016;5:e002686 CrossRef Medline
25. Chen SH, Brunet MC, Sur S, et al. **Feasibility of repeat transradial access for neuroendovascular procedures.** *J Neurointerv Surg* 2020;12:431–34 CrossRef Medline
26. Khanna O, Sweid A, Mouchtouris N, et al. **Radial artery catheterization for neuroendovascular procedures.** *Stroke* 2019;50:2587–90 CrossRef Medline
27. Hess CN, Peterson ED, Neely ML, et al. **The learning curve for transradial percutaneous coronary intervention among operators in the United States: a study from the National Cardiovascular Data Registry.** *Circulation* 2014;129:2277–86 CrossRef Medline
28. Sur S, Snelling B, Khandelwal P, et al. **P-005 adoption of the transradial approach for cerebral angiography: learning curve and early experience.** *J Neurointerv Surg* 2017;9:A24 CrossRef
29. Carvalho MS, Calé R, de Araújo Gonçalves P, et al. **Predictors of conversion from radial into femoral access in cardiac catheterization [in Portuguese].** *Arq Bras Cardiol* 2015;104:401–08 CrossRef Medline
30. Titano JJ, Biederman DM, Zech J, et al. **Safety and outcomes of transradial access in patients with international normalized ratio 1.5 or above.** *J Vasc Interv Radiol* 2018;29:383–88 CrossRef Medline
31. Brunet M-C, Chen SH, Peterson EC. **Transradial access for neurointerventions: management of access challenges and complications.** *J Neurointerv Surg* 2020;12:82–86 CrossRef Medline
32. Levin SR, Farber A, Bertges DJ, et al. **Larger sheath size for infrainguinal endovascular intervention is associated with minor but not major morbidity or mortality.** *Ann Vasc Surg* 2019;60:327–34 CrossRef Medline
33. Chung R, Weller A, Morgan R, et al. **Are complication rates lower with 4-Fr versus 6-Fr transfemoral arterial access: prospective audit at a single interventional radiology centre.** *CVIR Endovasc* 2018;1:15 CrossRef Medline
34. Uhlemann M, Möbius-Winkler S, Mende M, et al. **The Leipzig prospective vascular ultrasound registry in radial artery catheterization: impact of sheath size on vascular complications.** *JACC Cardiovasc Interv* 2012;5:36–43 CrossRef Medline
35. Stone JG, Zussman BM, Tonetti DA, et al. **Transradial versus transfemoral approaches for diagnostic cerebral angiography: a prospective, single-center, non-inferiority comparative effectiveness study.** *J Neurointerv Surg* 2020;12:993–98 CrossRef Medline
36. Chen SH, Snelling BM, Sur S, et al. **Transradial versus transfemoral access for anterior circulation mechanical thrombectomy: comparison of technical and clinical outcomes.** *J Neurointerv Surg* 2019;11:874–78 CrossRef Medline

Periprocedural Safety and Feasibility of the New LVIS EVO Device for Stent-Assisted Coiling of Intracranial Aneurysms: An Observational Multicenter Study

D.F. Vollherbst, A. Berlis, C. Maurer, L. Behrens, S. Sirakov, A. Sirakov, S. Fischer, V. Maus, M. Holtmannspötter, R. Rautio, M. Sinisalo, W. Poncyłjusz, H. Janssen, F. Wodarg, C. Kabbasch, J. Trenkler, C. Herweh, M. Bendszus, and M.A. Möhlenbruch

ABSTRACT

BACKGROUND AND PURPOSE: Stent-assisted treatment techniques can be an effective treatment option for intracranial aneurysms. The aim of this study was to evaluate the periprocedural feasibility and safety of the new LVIS EVO stent for the treatment of intracranial aneurysms.

MATERIALS AND METHODS: Patients with intracranial aneurysms treated with the LVIS EVO in 11 European neurovascular centers were retrospectively reviewed. Patient and aneurysm characteristics, procedural parameters, immediate grade of occlusion, and technical and clinical complications were assessed.

RESULTS: Fifty-seven patients with 59 aneurysms were treated with the LVIS EVO device; 57.6% of the aneurysms were incidental; 15.3% were acutely ruptured; 15.3% were recanalized or residual aneurysms; and 11.9% were treated for symptoms other than acute hemorrhage. The most frequent aneurysm locations were the middle cerebral artery (25.4%) and the anterior communicating artery (22.0%). The rate of immediate successful deployment was 93.2%. In 6.8% ($n = 4$) of cases, additional in-stent angioplasty was needed. The immediate complete occlusion rate was 54.2%, while there was a residual aneurysm in 35.6% and a residual neck in 10.2%. Periprocedural technical complications occurred in 7/59 treatments (11.9%; the most frequent technical complication [$n = 3$] was thrombus formation), which all resolved completely without clinical sequelae. Postprocedural neurologic complications occurred after 4/59 treatments (6.8%; 2 transient ischemic attacks, 1 minor stroke, 1 major stroke), of which only 1 persistent complication was directly related to the procedure (minor stroke in the vascular territory distal to the stent).

CONCLUSIONS: The LVIS EVO stent is a safe, feasible device for the treatment of intracranial aneurysms.

ABBREVIATIONS: ACA = anterior cerebral artery; AcomA = anterior communicating artery; ASA = acetylsalicylic acid; BA = basilar artery; DFT = drawn filled tube; SAC = stent-assisted coiling

Stent-assisted coiling (SAC) is a well-established endovascular technique for the treatment of intracranial aneurysms.¹⁻⁴ Implantation of a stent can have several advantages, such as prevention of coil protrusion into the parent vessel and the ability to increase the coil packing density, ultimately aiming to enhance the safety of the procedure and improve the long-term stability of

coil occlusion of intracranial aneurysms.^{2,5,6} SAC is specifically indicated for wide-neck aneurysms, anatomically complex aneurysms, and aneurysms situated at vessel bifurcations. Various stents with differences in material, composition, and structure are currently available for SAC.^{4,7-10} The LVIS EVO (MicroVention) is a new stent, specifically designed for SAC, which has recently been introduced to the market. Compared with other braided stents, such as the LVIS Jr (MicroVention), potential differences of the LVIS EVO include enhanced visibility, shorter flared ends, and a smaller cell size. The aim of this study was to investigate the periprocedural feasibility and safety of this new device for the endovascular treatment of intracranial aneurysms.

Received May 13, 2020; accepted after revision September 7.

From the Department of Neuroradiology (D.F.V., C.H., M.B., M.A.M.), Heidelberg University Hospital, Heidelberg, Germany; Department of Diagnostic and Interventional Radiology and Neuroradiology (A.B., C.M., L.B.), Universitätsklinikum Augsburg, Augsburg, Germany; Radiology Department (S.S., A.S.), University Hospital Saint Ivan Rilski, Sofia, Bulgaria; Department of Neuroradiology (S.F., V.M.), Knappschafts Krankenhaus, Recklinghausen, Germany; Institute of Radiology and Neuroradiology (M.H.), Klinikum Nuernberg Sued, Paracelsus Medical University, Nuernberg, Germany; Department of Interventional Radiology (R.R., M.S.), Turku University Hospital, Turku, Finland; Department of Diagnostic Imaging and Interventional Radiology (W.P.), Pomeranian Medical University, Szczecin, Poland; Department of Neuroradiology (H.J.), Ingolstadt General Hospital, Ingolstadt, Germany; Department of Radiology and Neuroradiology (F.W.), University Hospital Schleswig-Holstein, Kiel, Germany; Institute for Diagnostic and Interventional Radiology (C.K.), Faculty of Medicine, University Hospital Cologne, Cologne, Germany; and Institute of Neuroradiology (J.T.), Kepler University Hospital, Linz, Austria.

Please address correspondence to Markus A. Möhlenbruch, MD, Department of Neuroradiology, Heidelberg University Hospital, INF 400, 69120 Heidelberg, Germany; e-mail: Markus.Moehlenbruch@med.uni-heidelberg.de
<http://dx.doi.org/10.3174/ajnr.A6887>

Table 1: Patient and aneurysm characteristics

Characteristic	Data ^a
Age (yr)	58.5 [SD, 12.0] (25–81)
Clinical presentation	Incidental (<i>n</i> = 34) (57.6%), recanalization (<i>n</i> = 7) (11.9%), SAH (<i>n</i> = 9) (15.3%), symptomatic ^b (<i>n</i> = 5) (8.5%), ischemic stroke ^c (<i>n</i> = 2) (3.4%), residual aneurysm (<i>n</i> = 2) (3.4%)
Aneurysm location	MCA (<i>n</i> = 15) (25.4%), AcomA (<i>n</i> = 13) (22.0%), BA (<i>n</i> = 9) (15.3%), ICA (<i>n</i> = 7) (11.9%), ACA (<i>n</i> = 6) (10.2%), Others (<i>n</i> = 9) (15.3%)
Aneurysm size (maximal diameter) (mm)	6.2 [SD, 3.9] (1.0–18.0)
Aneurysm type	Saccular (<i>n</i> = 55) (93.2%), dissecting (<i>n</i> = 3) (5.1%), blisterlike (<i>n</i> = 1) (1.7%)
Neck diameter (mm)	4.2 [SD, 1.8] (1.0–9.5)
Dome-to-neck ratio	1.5 [SD, 0.7] (0.3–4.5)
Diameter of the parent artery proximal to the aneurysm (mm)	2.8 [SD, 0.8] (1.0–4.3)
Diameter of the parent artery distal to the aneurysm (mm)	2.4 [SD, 0.8] (1.2–4.0)
Angulation of the parent artery at the site of the aneurysm	102.6° [SD, 44.1°] (23.0°–180.0°)

^aData are mean [SD] (minimum to maximum) or absolute number of cases (relative frequency in %).

^bSymptoms not caused by SAH or ischemic stroke, including headaches (*n* = 3), dizziness (*n* = 1), and double vision (*n* = 1).

^cRelated to the aneurysm.

MATERIALS AND METHODS

Study Design

This work is a retrospective, multicenter, observational study at 11 European neurovascular centers. The clinical and radiologic records of patients with intracranial aneurysms who were treated with the LVIS EVO stent between September 2019 and April 2020 were systematically reviewed on the basis of a dedicated survey that was completed by the interventionalists who had used the device. Institutional ethics committees approved this study.

Patient and Aneurysm Characteristics

The collected patient data included the patient's age, sex, clinical presentation, and the pretreatment mRS score. For patients presenting with ruptured intracranial aneurysms, the severity of the subarachnoid hemorrhage was assessed according to the Hunt and Hess scale.

The assessed characteristics of the treated aneurysms included aneurysm location, type, size (maximal diameter), neck diameter, the diameter of the parent vessel proximal and distal to the aneurysm, and the degree of angulation of the parent vessel at the site of the aneurysm. Wide-neck aneurysms were defined as aneurysms with a neck diameter of ≥ 4 mm or a dome-to-neck ratio of < 2 .

Device Characteristics

The LVIS EVO consists of drawn filled tubes (DFTs) consisting of an inner platinum wire and an outer nitinol wire. The platinum core makes every wire of the device x-ray-visible. Additionally, 4 radiopaque markers are attached to short (0.5 mm) flared ends at each end of the device. The metal coverage of the LVIS EVO ranges from 17% to 28%, depending on factors such as the diameter and the configuration of the deployed stent and the parent vessel. Without packing the stent, the stent cell size ranges from approximately 0.4 to 1.0 mm. The recommended delivery systems are the Headway 17 microcatheter (MicroVention) and the Scepter C or XC dual-lumen balloon catheters (MicroVention).

Two other braided low-profile stents are currently available: the LVIS Jr and the Leo+ Baby (Balt Extrusion). The most important difference in the LVIS EVO to these devices is the material of the stent, which is DFT for the LVIS EVO and nitinol for

the LVIS Jr and Leo+ Baby. While every DFT wire is inherently visible, the stent body of the LVIS Jr and the Leo+ Baby is made visible by 3 (LVIS Jr) or 2 (Leo+ Baby) additional tantalum wires. Other special features are the relatively high metal coverage and the small cell size of 0.4–1.0 mm, which is much higher for the LVIS Jr (1.5 mm) and slightly higher for the Leo+ Baby (0.9 mm).

Treatment

The indication for choosing the LVIS EVO, the treatment technique, and the peri-interventional medical treatment were recorded. The ease of deployment and the radiopacity of the device were rated by the treating interventionalist on a 5-point scale: 1, very poor; 2, poor; 3, intermediate; 4, good; 5, very good. Successful deployment was defined as complete opening of the stent without the need for additional techniques such as in-stent angioplasty.

Safety and Feasibility

Periprocedural technical complications were assessed by the neurointerventionalist on fluoroscopy, DSA, and, in some cases, additionally with 3D-DSA and/or flat panel CT. Post-procedural clinical complications until discharge were assessed. Clinical evaluation was performed by a board-certified neuroradiologist, neurosurgeon, or neurologist before the procedure, immediately after the procedure, 24 (± 6 hours) after the procedure, and at discharge. The patient's clinical status was assessed with the mRS. The grade of occlusion immediately after treatment was reported according to the modified Raymond-Roy classification.¹¹

RESULTS

Patient and Aneurysm Characteristics

Fifty-nine aneurysms in 57 patients were treated in 11 European centers between September 2019 and April 2020. Patient and aneurysm characteristics are summarized in Table 1.

The patient age was 58.5 [SD, 12.0] years; 73.7% of the patients were female; and 26.3% were male. The pretreatment mRS was 0.6 [SD, 1.2] (mRS 0 in *n* = 42, 71.2%; mRS 1 in *n* = 11, 18.6%; mRS 2 in *n* = 2, 3.4%; mRS 3 in *n* = 1, 1.7%; and mRS 5 in *n* = 3, 5.1%). All patients with an mRS of > 2 had acute aneurysmal subarachnoid hemorrhage or ischemic stroke. 57.6%

Table 2: Treatment characteristics, safety, and feasibility

Characteristics, Safety, and Feasibility ^a						
Treatment parameter						
Reason for choosing LVIS EVO	Wide neck (n = 56) (94.9%)		Flow diversion (n = 2) (3.4%)		Bailout (n = 1) (1.7%)	
Ease of deployment	Very poor (n = 0) (0%)	Poor (n = 0) (0%)	Intermediate (n = 0) (0%)		Good (n = 4) (6.8%)	Very good (n = 55) (93.2%)
Radiopacity	Very poor (n = 0) (0%)	Poor (n = 0) (0%)	Intermediate (n = 1) (1.7%)		Good (n = 28) (47.5%)	
Treatment technique	Jailing technique (n = 52) (88.1%)		WEB and stent (n = 3) (5.1%)		Stent only (n = 2) (3.4%)	
Safety						
Technical complications	Thrombus formation (n = 3) (5.1%)		Stent shortening (n = 1) (1.7%)	Incomplete stent opening (n = 1) (1.7%)	Coil protrusion (n = 1) (1.7%)	Unrelated to LVIS EVO (n = 1) (1.7%)
Clinical complications ^b	TIA (n = 2) (3.4%)		Major stroke ^c (n = 1) (1.7%)	Minor stroke ^d (n = 1) (1.7%)	GIT bleeding (n = 1) (1.7%)	Leg ischemia (n = 1) (1.7%)
Feasibility						
Occlusion immediately after treatment ^e	I: Complete occlusion (n = 32) (54.2%)		II: Residual neck (n = 6) (10.2%)		IIIa: Residual neck with contrast within coil interstices (n = 18) (30.5%)	
					IIIb: Residual neck with contrast along aneurysm wall (n = 3) (5.1%)	

Note:—GIT indicates gastrointestinal tract.

^a Data are mean [SD], (minimum to maximum), or absolute number of cases (relative frequency in %).

^b Two patients had 2 clinical complications, respectively.

^c Not related to the intervention (most likely caused by vasospasm).

^d Related to the intervention (stroke in vascular territory of stented artery).

^e Reported according to the modified Raymond-Roy classification.

of the aneurysms were incidental; and 27.1% were symptomatic (15.3% acute subarachnoid hemorrhage, 3.4% ischemic stroke related to the aneurysm, and 8.5% other symptoms). In 15.3%, the treatment indication was a recanalized or residual aneurysm. For 11.9% of the aneurysms, treatment was indicated because of recanalization after previous coiling; 3.4% were treated because of a residual aneurysm after a previous treatment. The 9 patients with acutely ruptured aneurysms (15.3%) presented with a Hunt and Hess scale score of 1.9 [SD, 1.2].

Most of the aneurysms were located in the MCA (25.4%), followed by the anterior communicating artery (AcomA; 22.0%), the basilar artery (BA; 15.3%), the supraophthalmic ICA (11.9%), and the anterior cerebral artery (ACA; 10.2%). Most aneurysms (93.2%) had a saccular configuration, 5.1% were dissecting aneurysms, and 1.7% were blisterlike aneurysms. The maximal diameter of the treated aneurysms was 6.2 [SD, 3.9] mm, ranging from 1 to 18 mm. Fifty-five aneurysms (93.2%) were wide-neck with a neck diameter of 4.2 [SD, 1.8] mm and a dome-to-neck ratio of 1.5 [SD, 0.7] mm. The diameter of the parent vessel was 2.8 [SD, 0.8] mm proximal to the aneurysm and 2.4 [SD, 0.8] mm distal to the aneurysm. The angulation of the parent vessel at the site of the aneurysm was 102.6° [SD, 44.1°], ranging from 23.0° (sharp angle) to 180° (straight vessel). In 28.8% of the

aneurysms, there was a sharp angle of the parent vessel (<90°) at the site of the aneurysm.

Treatment

Treatment characteristics are summarized in Table 2. Example cases are illustrated and described in Figs 1 and 2. The most frequent indication for choosing the LVIS EVO device was a wide aneurysm neck (94.9%). In 2 patients (3.4%), the reason was flow diversion, and in 1 patient (1.7%), the LVIS EVO device was used as a bailout technique after failure of conventional coiling. The ease of deployment was rated as very good in 93.2% and good in 6.8% of cases. Most of the interventionalists rated the radiopacity of the LVIS EVO as good (47.5%) or very good (50.8%).

Jailing was the predominant treatment technique (88.1%), while the LVIS EVO was used in combination with a Woven EndoBridge device (WEB; MicroVention) in 3 cases (5.1%) and alone without coiling or a WEB in 2 cases (3.4%). In the 3 cases in which a WEB was combined with the LVIS EVO, there was an acute angulation of the aneurysm in relation to the parent vessel, explaining why the WEB was primarily combined with stent implantation. In the 2 cases in which the LVIS EVO device was used alone, the aim was to achieve a flow-diverting effect by the implanted stent. In the first case, coiling with the jailing

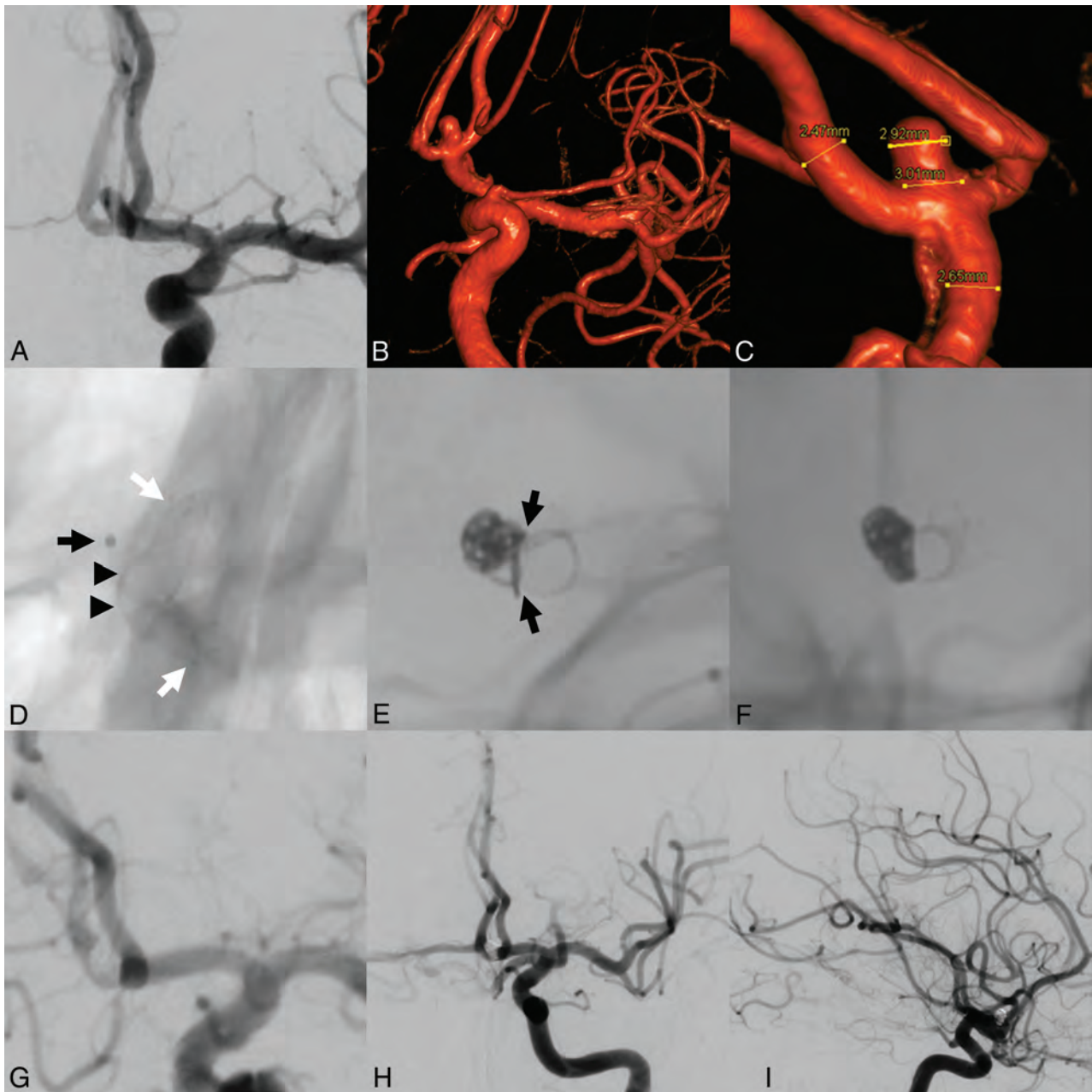


FIG 1. Stent-assisted coiling of an incidental aneurysm of the Acoma. DSA (A) and 3D reconstructions of rotational angiography (B and C) show a wide-neck aneurysm of the Acoma. After positioning of a microcatheter within the aneurysm (black arrow in D), a 3 × 18 mm LVIS EVO stent was deployed in the A1 and A2 segments of the left ACA (stent ends marked with white arrows). Shouldering of the stent at the base of the aneurysm (black arrowheads) enabled protection of the aneurysmal neck. Subsequently, the aneurysm was coiled (E and F). The shouldered stent enabled complete protection of the parent artery at the aneurysmal neck (black arrows in E) and remodeling of the parent artery. DSAs after treatment (G–I) show complete occlusion of the aneurysm.

technique of an aneurysm of the superior cerebellar artery was intended but not possible because a severe stenosis at the entry of the fusiform aneurysm impeded the navigation of a second microcatheter into the aneurysm before implantation of the LVIS EVO. In the second case, treatment of a residual ACA aneurysm was intended after previous SAC using a Neuroform Atlas stent (Stryker Neurovascular). Because jailing of a microcatheter into the residual aneurysm was impeded by the previously implanted stent, the LVIS EVO was used alone. Coiling passing through the stent struts was performed in 2 cases (3.4%). In-stent

angioplasty was performed in 4 treatments (6.8%). The reason for in-stent angioplasty was incomplete wall apposition (>75% stent opening) in 3 cases and incomplete opening of the stent (50% stent opening) in 1 case.

Antiplatelet Therapy

The most frequently administered preinterventional therapy was acetylsalicylic acid (ASA) in combination with clopidogrel (79.7%), followed by ASA combined with ticagrelor (11.9%). In 5 patients with ruptured aneurysms (8.5%), no

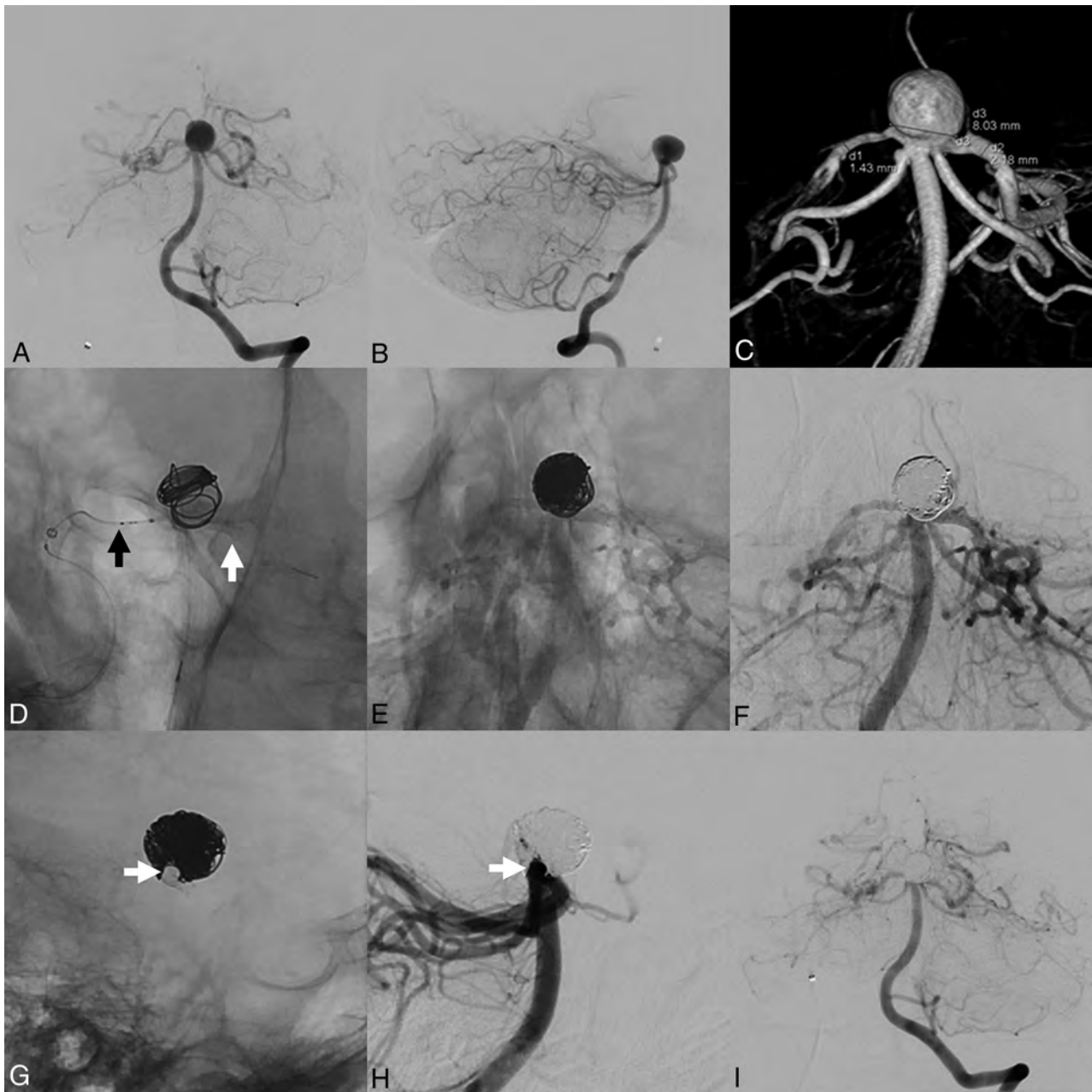


FIG 2. Stent-assisted coiling of an incidental aneurysm of the basilar artery. Digital subtraction angiography (A and B) and 3D reconstructions of rotational angiography (C) show a wide-neck aneurysm of the tip of the basilar artery. After positioning of a microcatheter within the aneurysm, a Headway 17 microcatheter was positioned in the left posterior cerebral artery via the right posterior cerebral artery (black arrow in D), the right posterior communicating artery, and the right ICA. Subsequently, a 2.5 × 17 mm LVIS EVO stent (distal end marked with a white arrow in D) was deployed horizontally over the aneurysmal neck, followed by coiling of the aneurysm (E and F). The stent ensured protection and remodeling of the parent artery (white arrow in G and H). DSAs after treatment (F, H, and I) show complete occlusion of the aneurysm.

preinterventional antiplatelet therapy was used. Peri-interventional glycoprotein IIb/IIIa antagonists (tirofiban or abciximab) were given in 13.6% of the cases. Postinterventional antiplatelet therapy consisted of ASA combined with ticagrelor in 45.8%, ASA combined with clopidogrel in 42.4%, ASA combined with prasugrel in 6.8%, and cilostazol combined with clopidogrel in 3.4% of cases. Platelet function testing was performed in 43 patients (72.9%).

Safety and Feasibility

Safety and feasibility parameters are summarized in Table 2.

The LVIS EVO stent could be successfully deployed in 55 of 59 treatment procedures (93.2%). As stated above, in-stent angioplasty was needed in the remaining 4 cases without immediate complete stent opening. The total number of periprocedural technical complications was 7 (11.9%), 2 of which occurred during the treatment of acutely ruptured aneurysms. All except 1 of these

technical complications were directly related to the LVIS EVO and included thrombus formation within the stent lumen in 3 cases as well as coil protrusion into the parent vessel, shortening of the stent, and insufficient stent opening in 1 case each.

Unsuccessful stent deployment occurred during the treatment of an aneurysm of the ICA. The proximal stent only opened incompletely (50% of the vessel lumen), which was most probably related to a 180° curve of the vessel at the site of the proximal stent. Navigation with a balloon catheter into the stent and following in-stent angioplasty caused slight compression of the proximal half of the stent without any flow disruption.

Thrombus formation occurred during the treatment of aneurysms of the MCA (unruptured), AcomA (ruptured), and ICA (ruptured), respectively, and was successfully treated by intravenous abciximab infusion, which led to complete resolution of the thrombus. In one of these cases (an MCA aneurysm), thrombus formation was observed in a second stent (Neuroform Atlas), which was positioned in an MCA M2 branch for Y-stent placement. The thrombosis in this second stent might have resulted from the interaction of the 2 stents (constraining full opening of the second stent and/or increased metal density within the vessel). This patient received ASA in combination with clopidogrel before the treatment, both of which showed an adequate effect in the preinterventional platelet function test. The 2 patients with ruptured aneurysms and periprocedural in-stent thrombosis received periprocedural intravenous abciximab and heparin.

Coil protrusion occurred in an aneurysm of the AcomA in the direction of the nonstented A2 segment and was successfully treated by stent placement (Acclino flex; Acandis) in the contralateral ACA. Slight stent shortening occurred during modeling of an 18 × 4 mm LVIS EVO with a 6 × 9 mm Eclipse 2L balloon (Balt Extrusion). A technical complication that was not directly related to the LVIS EVO consisted of coil dislocation, which did not lead to any angiographic or clinical consequences. All of these technical complications resolved without clinical sequelae. In 1 case, full opening of the stent was reported to occur only after removing the jailed microcatheter, which we did not classify as a technical complication.

In 4 patients (6.8%), neurologic complications were reported before hospital discharge. Of these complications, 2 were transient (TIAs) and 2 were permanent (minor and major stroke), while 1 occurred after the treatment of a ruptured aneurysm (major stroke) and 3 occurred after the treatment of unruptured aneurysms. Two neurologic complications were directly related to the LVIS EVO: 1 minor stroke in the vascular territory distal to the stent and 1 TIA. Both of these complications occurred after the treatment of unruptured aneurysms in patients who received pre- and postinterventional antiplatelet therapy using ASA and clopidogrel with positive antiplatelet function test results. The neurologic complications, which were persistent until discharge, included a major stroke not restricted to the territory of the stented artery due to vasospasms in a patient with a ruptured ICA aneurysm, and the above-mentioned minor stroke in the territory of the stented artery, which became clinically apparent as dizziness. Both of these ischemic strokes led to an increase in the mRS score (2–5 for the major stroke and 1–2 for the minor stroke). Apart from these 2 complications, no increase in mRS

scores was observed when comparing the preinterventional mRS and the mRS at discharge. Two patients (3.4%) had transient postprocedural headache, which was not classified as a clinical complication.

Postprocedural non-neurologic complications occurred in 3 patients (5.1%) and included upper gastrointestinal bleeding, puncture site bleeding, and acute ischemia of the leg contralateral to the puncture site in a patient with known peripheral arterial occlusive disease.

Immediately after the treatment, “complete occlusion” was observed in 54.2%; “residual neck,” in 10.2%; “residual aneurysm with contrast within coil interstices,” in 30.5%; and “residual aneurysm with contrast along the aneurysm wall,” in 5.1%.

DISCUSSION

This multicenter study, reporting the experience of 11 European neurovascular centers, demonstrates acceptable periprocedural safety and feasibility of the new LVIS EVO stent for the treatment of intracranial aneurysms.

Endovascular treatment has become the first-line therapy for most intracranial aneurysms.¹² For aneurysms with a wide neck, aneurysms with complex anatomy, or aneurysms situated at vessel bifurcations, it was shown that SAC provides better occlusion rates and anatomic results, compared with coiling only or balloon remodeling.^{1,2} The advantages of this treatment technique include the possibility of increasing the density of coil packing, the impediment of coil protrusion into the parent artery, the forming of a scaffold for endothelialization, and the generation of a flow-diverting effect past the aneurysm.^{1,2,13,14} All these factors ultimately aim to improve the immediate and long-term occlusion rates of ruptured and unruptured intracranial aneurysms and to enhance the safety of the treatment procedure.

For the new LVIS EVO stent, as initially indicated, the major innovation is the structure of the wires of the stent. While established braided stents, such as the Leo+ and Leo+ Baby or the LVIS and LVIS Jr, predominantly consist of pure nitinol wires, the LVIS EVO consists of DFT wires with a platinum core and an outer nitinol coating. In addition to these structural differences, the wires of the LVIS EVO are arranged in a specific braiding pattern, which is based on the specific behavior of the DFT wires. These technical features aim to improve the visibility and enhance the opening ability and formability of the stent. The results of this study are in line with these promoted features. In all except one of the treatments (98.2%), the visibility of the device was rated as good or very good. The LVIS EVO stent was deployed successfully in most of the treatment procedures, while the ease of deployment was rated as good in 6.8% and very good in 93.2% of the cases.

The metal coverage of the LVIS EVO device, which depends on the size of the implanted stent and its configuration within the parent vessel, is relatively high and can range up to 28%. This maximum metal coverage is equal to the minimum metal coverage of the Flow-Redirection Endoluminal Device (FRED Jr; MicroVention) stent, which features a metal coverage ranging from 28% to 33%.¹⁵ Accordingly, it is likely that the LVIS EVO stent also offers a certain flow-diverting effect. In this study, the LVIS EVO was used for flow diversion in 2 cases (without

additional coiling). In both cases, stasis within the aneurysm but not complete occlusion was observed immediately after the procedure. Mid- and long-term follow-up data are needed to assess the value of the flow-diverting effects of the LVIS EVO stent.

Compared with other braided stents, the LVIS EVO has a relatively small cell size. This smaller cell size can be a disadvantage because it may impede passing through the stent with a micro-wire/microcatheter for coiling. Therefore, we recommend jailing as the first-line treatment technique with the LVIS EVO. However, crossing the stent with a microcatheter is also possible, while its ease depends on the anatomy, the outer diameter of the stent, and the degree of stent packing. Nevertheless, the small cell size might impede crossing-stent techniques, such as Y- and X-stent placement. In such cases, T-stent placement could be an alternative treatment option.

Despite these very positive results, no statement with regard to the superiority of the LVIS EVO stent over other stents can be made on the basis of this study because we only investigated the periprocedural results of the LVIS EVO without comparison with any other device. However, the high rate of technical feasibility is similar to that in other comparable devices, such as the Leo+ Baby, LVIS, LVIS Jr, Neuroform Atlas, or Acclino stents.^{4,8,16-18}

In this study, periprocedural technical complications occurred in 11.9% of treatments. However, all of these technical complications resolved without clinical sequelae. The rate of neurologic complications until discharge was 6.8%, of which only 2 complications were directly related to the LVIS EVO stent (1 minor ischemic stroke in the vascular territory of the stented artery and 1 TIA). One major stroke, which was unrelated to the procedure, was observed. The low rate of symptomatic and persistent complications in this study is in line with results reported in the literature.^{2,4}

The rate of immediate aneurysm occlusion in this study was 54.2%, which is in accordance with immediate occlusion results after SAC reported in the literature.^{19,20} A systematic review and meta-analysis by Hong et al²⁰ reported an immediate occlusion rate of 57.6%. A substantial angiographic improvement in occlusion during follow-up can be expected after SAC.^{1,20,21}

We acknowledge that this study has some noteworthy limitations. Because this is a retrospective, observational study based on a dedicated survey, which was completed by the interventionalists themselves, without additional data analysis by a core lab, there is inherent selection and reporting bias associated with it. The number of patients and aneurysms in this study is relatively small, the data are quite heterogeneous, and a control group is lacking. However, this is a multicenter study and, to our knowledge, it is the only study reporting on the clinical use of the LVIS EVO stent to date. No follow-up data are available for this study yet. To assess the effectiveness of this device in particular, long-term follow-up data are necessary. However, the focus of this study was the periprocedural safety and feasibility of the LVIS EVO device. Furthermore, this device was introduced only recently, and accordingly, to the best of our knowledge, comprehensive follow-up results are not yet available.

CONCLUSIONS

The LVIS EVO stent is a safe and feasible device for the treatment of intracranial aneurysms. Further studies are needed to assess

the mid- and long-term effectiveness as well as potential advantages of this new device over other available stents.

Disclosures: Dominik F. Vollherbst—UNRELATED: Travel/Accommodations/Meeting Expenses Unrelated to Activities Listed: MicroVention and Stryker Neurovascular, Comments: travel support.* Ansgar Berlis—RELATED: Consulting Fee or Honorarium: proctor for MicroVention; UNRELATED: Consultancy: proctor for Stryker Neurovascular and Medtronic; Payment for Lectures Including Service on Speakers Bureaus: Penumbra; Other: Clinical ethics committee for phenox. Christoph Maurer—UNRELATED: Grants/Grants Pending: MicroVention, Comments: educational grant. Sebastian Fischer—UNRELATED: Consultancy: MicroVention, Comments: proctoring and consultancy agreement; Payment for Lectures Including Service on Speakers Bureaus: MicroVention. Markus Holtmannspötter—UNRELATED: Consultancy: MicroVention, Medtronic, Stryker Neurovascular, phenox, Mentice, Rapid Medical, Comments: proctoring and consulting. Riitta Rautio—UNRELATED: Consultancy: Stryker Neurovascular, MicroVention, Medtronic. Wojciech Poncyjusz—UNRELATED: Consultancy: proctoring for MicroVention. Fritz Wodarg—UNRELATED: Consultancy: MicroVention, Cerus Endovascular, Acandis; Payment for Lectures Including Service on Speakers Bureaus: MicroVention, Cerus Endovascular, Acandis; Travel/Accommodations/Meeting Expenses Unrelated to Activities Listed: MicroVention, Cerus Endovascular, Acandis, Stryker Neurovascular. Christoph Kabbasch—UNRELATED: Consultancy: proctor for MicroVention, consultant for Acandis. Johannes Trenkler—RELATED: Support for Travel to Meetings for the Study or Other Purposes: MicroVention. Markus A. Möhlenbruch—UNRELATED: Consultancy: Medtronic, MicroVention, Stryker Neurovascular, phenox*; Grants/Grants Pending: Balt, MicroVention*; Payment for Lectures Including Service on Speakers Bureaus: Medtronic, MicroVention, Stryker Neurovascular.* Martin Bendzus—UNRELATED: Board Membership: Vascular Dynamics, B. Braun Medical, Boehringer Ingelheim Pharma; Consultancy: Guerbet; Grants/Grants Pending: European Union, German Research Foundation, Hopp Foundation, Siemens, Novartis, Stryker Neurovascular*; Payment for Lectures Including Service on Speakers Bureaus: Merck, Teva Pharmaceutical Industries, Novartis, Bayer AG, Grifols. Christian Herweh—UNRELATED: Consultancy: Brainomix. *Money paid to the institution.

REFERENCES

1. Piotin M, Blanc R, Spelle L, et al. **Stent-assisted coiling of intracranial aneurysms: clinical and angiographic results in 216 consecutive aneurysms.** *Stroke* 2010;41:110–15 CrossRef Medline
2. Wang F, Chen X, Wang Y, et al. **Stent-assisted coiling and balloon-assisted coiling in the management of intracranial aneurysms: a systematic review and meta-analysis.** *J Neurol Sci* 2016;364:160–06 CrossRef Medline
3. Shankar JJS, Quateen A, Weill A, et al. **Canadian Registry of LVIS Jr for Treatment of Intracranial Aneurysms (CaRLA).** *J Neurointerv Surg* 2017;9:849–53 CrossRef Medline
4. Iosif C, Piotin M, Saleme S, et al; TRAIL Investigators. **Safety and effectiveness of the Low Profile Visualized Intraluminal Support (LVIS and LVIS Jr) devices in the endovascular treatment of intracranial aneurysms: results of the TRAIL multicenter observational study.** *J Neurointerv Surg* 2018;10:675–81 CrossRef Medline
5. Bendok BR, Parkinson RJ, Hage ZA, et al. **The effect of vascular reconstruction device-assisted coiling on packing density, effective neck coverage, and angiographic outcome: an in vitro study.** *Neurosurgery* 2007;61:835–40; discussion 40–41 CrossRef Medline
6. Mokin M, Primiani CT, Ren Z, et al. **Stent-assisted coiling of cerebral aneurysms: multi-center analysis of radiographic and clinical outcomes in 659 patients.** *J Neurointerv Surg* 2020;12:289–97 CrossRef Medline
7. Ulfert C, Pham M, Sonnberger M, et al. **The Neuroform Atlas stent to assist coil embolization of intracranial aneurysms: a multi-centre experience.** *J NeuroIntervent Surg* 2018;10:1192–96 CrossRef Medline
8. Aydin K, Arat A, Sencer S, et al. **Stent-assisted coiling of wide-neck intracranial aneurysms using low-profile LEO Baby stents: initial and midterm results.** *AJNR Am J Neuroradiol* 2015;36:1934–41 CrossRef Medline
9. Möhlenbruch M, Herweh C, Behrens L, et al. **The LVIS Jr. micro-stent to assist coil embolization of wide-neck intracranial aneurysms: clinical study to assess safety and efficacy.** *Neuroradiology* 2014;56:389–95 CrossRef Medline

10. Herweh C, Nagel S, Pfaff J, et al. **First experiences with the new Enterprise2[®] stent.** *Clin Neuroradiol* 2018;28:201–07 CrossRef Medline
11. Mascitelli JR, Moyle H, Oermann EK, et al. **An update to the Raymond-Roy Occlusion Classification of intracranial aneurysms treated with coil embolization.** *J NeuroIntervent Surg* 2015;7:496–502 CrossRef Medline
12. Molyneux AJ, Kerr RS, Yu LM, et al; International Subarachnoid Aneurysm Trial (ISAT) Collaborative Group. **International subarachnoid aneurysm trial (ISAT) of neurosurgical clipping versus endovascular coiling in 2143 patients with ruptured intracranial aneurysms: a randomised comparison of effects on survival, dependency, seizures, rebleeding, subgroups, and aneurysm occlusion.** *Lancet* 2005;366:809–17 CrossRef Medline
13. Wakhloo AK, Mandell J, Gounis MJ, et al. **Stent-assisted reconstructive endovascular repair of cranial fusiform atherosclerotic and dissecting aneurysms: long-term clinical and angiographic follow-up.** *Stroke* 2008;39:3288–96 CrossRef Medline
14. Kono K, Terada T. **Hemodynamics of 8 different configurations of stenting for bifurcation aneurysms.** *AJNR Am J Neuroradiol* 2013;34:1980–86 CrossRef Medline
15. Möhlenbruch MA, Kizilkilic O, Killer-Oberpfalzer M, et al. **Multicenter experience with FRED Jr Flow Re-Direction Endoluminal Device for intracranial aneurysms in small arteries.** *AJNR Am J Neuroradiol* 2017;38:1959–65 CrossRef Medline
16. Goyal RK, Kato Y, Kawase T, et al. **Comparative outcome analysis of Enterprise and Neuroform stent-assisted coiling of cerebral aneurysms: a review of the literature.** *Asian J Neurosurg* 2020;15:4–9 CrossRef Medline
17. Fiorella D, Boulos A, Turk AS, et al; LVIS investigators. **The safety and effectiveness of the LVIS stent system for the treatment of wide-necked cerebral aneurysms: final results of the pivotal US LVIS trial.** *J Neurointerv Surg* 2019;11:357–61 CrossRef Medline
18. Goertz L, Smyk MA, Mpotsaris A, et al. **Long-term angiographic results of the low-profile Acandis Acclino stent for treatment of intracranial aneurysms: a multicenter study.** *Clin Neuroradiol* 2019 Nov 15. [Epub ahead of print] CrossRef Medline
19. Dietrich P, Gravius A, Mühl-Benninghau R, et al. **Single center experience in stent-assisted coiling of complex intracranial aneurysms using low-profile stents: the ACCLINO[®] stent versus the ACCLINO[®] flex stent.** *Clin Neuroradiol* 2020 Feb 12. [Epub ahead of print] CrossRef Medline
20. Hong Y, Wang YJ, Deng Z, et al. **Stent-assisted coiling versus coiling in treatment of intracranial aneurysm: a systematic review and meta-analysis.** *PLoS One* 2014;9:e82311 CrossRef Medline
21. Jahshan S, Abla AA, Natarajan SK, et al. **Results of stent-assisted vs non-stent-assisted endovascular therapies in 489 cerebral aneurysms: single-center experience.** *Neurosurgery* 2013;72:232–39 CrossRef Medline

Outcome of Flow Diverters with Surface Modifications in Treatment of Cerebral Aneurysms: Systematic Review and Meta-analysis

Y.-L. Li, A. Roalfe, E.Y.-L. Chu, R. Lee, and A.C.O. Tsang



ABSTRACT

BACKGROUND: Newer flow diverters are enhanced with antithrombogenic surface modifications like the Pipeline Embolization Device with Shield Technology and the Derivo Embolization Device and are purported to facilitate deployment and reduce ischemic events.

PURPOSE: Our aim was to review the safety and efficacy of surface-modified flow diverters in treating patients with cerebral aneurysms.

DATA SOURCES: We used Preferred Reporting Items for Systematic Reviews and Meta-Analyses–compliant systematic review and meta-analysis covering 3 major data bases and gray literature between 2014 and 2019.

STUDY SELECTION: Two reviewers independently reviewed human studies of surface-modified flow diverters for eligibility based on predetermined criteria.

DATA ANALYSIS: The random effects model and Freeman-Tukey arcsine transformation were used to pool efficacy outcomes (technical success, aneurysm occlusion at 6 and 12 months) and safety outcomes (mortality, morbidity, all ischemia, and serious ischemia). Subgroup analysis was performed to compare outcomes between 2 different flow diverters.

DATA SYNTHESIS: Eight single-arm case series involving 911 patients and 1060 aneurysms were included. The median follow-up was 8.24 months. Pooled estimate for technical success was 99.6%, while the aneurysm occlusion at 6 and 12 months were 80.5%, and 85.6%, respectively. Pooled estimates for mortality, morbidity, total ischemia, and serious ischemia rates were 0.7%, 6.0%, 6.7%, and 1.8%, respectively. Most studies were of good quality, and no significant heterogeneity was observed.

LIMITATIONS: Limitations include a retrospective, observational design in some studies; heterogeneous and underreported antiplatelet therapy; and potential performance and ecologic bias.

CONCLUSIONS: Early-to-midterm safety and efficacy for surface-modified flow diverters appear comparable with older devices, especially for small, unruptured anterior circulation aneurysms. Long-term clinical data are required to further corroborate these results.

ABBREVIATIONS: DAPT = dual antiplatelet therapy; FD = flow diverter; HPC = hydrophilic polymer coating; SM = surface modification; SPED = Pipeline Flex Embolization Device with Shield Technology; DED = Derivo Embolization Device

Since their introduction in 2007, flow diverters (FDs) have revolutionized the endovascular treatment of cerebral aneurysms with expanding indications. Previously uncoilable aneurysms (wide-neck, giant, fusiform, tiny, blister, distally located) are increasingly treated with FDs.¹ The efficacy and long-term safety of first-generation FDs have been proved in several meta-analyses.²⁻⁶

A major limitation of flow diversion is ischemic stroke associated with stent thrombogenicity, necessitating dual-antiplatelet therapy and its associated risk. Since 2014, different manufacturers have incorporated surface modifications (SMs) to reduce FD thrombogenicity. Currently available devices include the Pipeline Flex Embolization Device with Shield Technology (SPED; Medtronic), the Derivo Embolization Device (DED; Acandis), and

Received August 2, 2020; accepted after revision September 8.

From the Division of Neuroradiology, Department of Radiology (Y.-L.L., E.Y.-L.C., R.L.), Queen Mary Hospital, Hong Kong, China; Division of Neurosurgery, Department of Surgery (A.C.O.T.), University of Hong Kong, Hong Kong, China; and Nuffield Department of Primary Care Health Sciences (A.R.), University of Oxford, Oxford, UK.

Please address correspondence to Anderson Chun On Tsang, FRCS, FCSHK, Department of Neurosurgery, Room 701, Administrative Block, Queen Mary Hospital, 102 Pokfulam Rd, Hong Kong; e-mail: acotsang@hku.hk

Indicates article with online supplemental data.

<http://dx.doi.org/10.3174/ajnr.A6919>

Table 1: Overview of surface-modified flow diverters

	Device		
	SPED	DED	p64/p48 MW HPC
Manufacturer	Medtronic	Acandis	phenox
Year of release	2014	2016	2017
Stent structure	Permanent mesh cylinder braided from platinum, tungsten, and cobalt-chromium-nickel alloy wires	24 Nitinol wires with radiopaque platinum core looped at the end, with a 48-wire braid	Drawn filled tubing wires with platinum core and nitinol coating
Diameter	2.5–5 mm	3.5–6 mm	p64: 2.5 × 5 mm p48 MW: 1.75–2 mm
Length	10–35 mm	15–50 mm	p64: 9–30 mm p48 MW: 9–18 mm
Previous versions	1) PED; original device available since 2008 2) FPED: resheathable and available since 2014	A non-BlueXide (Acandis)-coated version was available briefly	p64/P48 MW non-HPC versions
Surface modifier Description	PC polymer (Shield technology) <3-nm PC polymer covalently bonded to stent braids	BlueXide 50-nm titanium oxide and titanium oxynitride surface finishing	pHPC Covalent bonding of the proprietary pHPC to the stent braids
Proposed mechanism	PC is a constituent of the red cell membranes, thus reduces platelet adhesion and activation	Reduces friction during delivery and expansion, thus reducing thrombogenicity	Mimics glycocalyx on the vessel wall to inhibit platelet plug formation

Note:—PC indicates phosphorylcholine; pHPC, phenox Hydrophilic Polymer Coating; FPED, Pipeline Flex without Shield coating.

p64 and p48 MW hydrophilic polymer coating (HPC) Flow Modulation Device (phenox) (Table 1). Although laboratory studies have demonstrated lower thrombogenicity compared with older FDs, their clinical efficacy and safety have not been extensively tested.⁷

This study synthesizes the current evidence regarding the clinical and radiologic outcomes of patients with cerebral aneurysms treated by these SM-FDs.

MATERIALS AND METHODS

This is a Preferred Reporting Items for Systematic Reviews and Meta-Analyses–compliant systematic review and meta-analysis.⁸ The protocol was prospectively enrolled in the International Prospective Register of Systematic Reviews register.

Search Strategy

A search was conducted in major online data bases (MEDLINE, EMBASE, Cochrane) for studies published between January 2014 (when the first SM-FD was introduced) and September 2019. Gray literature sources, including Web sites of manufacturers, major journals and conferences in interventional neuroradiology, and bibliographies of screened full texts were reviewed to identify additional studies. The following keywords and their combinations and permutations were used in the search: “intracranial aneurysm,” “cerebral aneurysm,” “flow diverter,” “pipeline shield,” “derive,” “p64,” and “p48mw.” Detailed search strategy and results are given in the Online Supplemental Data.

Eligibility Criteria

Recognizing that most studies on novel neurointerventional devices are nonrandomized, uncontrolled, and observational, we did not limit eligibility by study design.

We included studies meeting the following inclusion criteria:

1. Evaluated use of SM-FDs in intracranial aneurysms in humans
2. Enrolled at least 15 subjects

3. Reported on outcomes described below
4. Followed up subjects for at least 6 months
5. Article published in English.

We excluded studies meeting the following exclusion criteria:

1. Laboratory and cadaveric studies
2. Narrative review or opinion articles
3. Novel series evaluating off-label use in challenging cases not representative of typical clinical scenarios
4. Disaster series highlighting complications
5. Intermixed studies in which outcomes of SM-FD cannot be extracted.

Data Collection and Analysis

Search results were pooled, and duplicates were removed. The titles and abstracts were screened independently by 2 investigators, and full texts of potentially eligible studies were perused. A list of demographic-, aneurysm-, treatment-, and outcome-related data was extracted. Conflicts were resolved by consensus. We subsequently performed a meta-analysis of the following efficacy and safety outcomes:

Efficacy outcomes:

1. Technical successful rate (%)
2. Aneurysm occlusion rate at 6 months (%)
3. Aneurysm occlusion rate at 12 months (%).

Aneurysm occlusion is defined by cerebral angiography showing Raymond-Roy class I or O’Kelly-Marotta class D results.

Safety outcomes were the following:

1. Mortality rate (%), including any death occurring during the study
2. Morbidity rate (%), including any treatment-related significant clinical symptoms during the study
3. Total ischemia rate (%), including all ischemic events, both clinical and radiologic, during the study

4. Serious ischemia rate (%), including only permanent neurologic deficits attributed to an ischemic mechanism during the study.

Result Synthesis and Reporting

Risk-of-bias assessment was performed by 2 investigators for each study. The National Institutes of Health Quality Assessment Tool for Observational Cohort and Cross-Sectional Studies was used, and studies were classified into good, fair, or poor quality.⁹

Random effects model was adopted because neurointerventional procedures were highly variable and the effect was expected to be different depending on the patient, clinical setting, and neurointerventionalist.

Because all the main outcome events were binary and denoted in proportions, they were pooled with results denoted in a summary point estimate with 95% CIs. Outcomes available in less than half of all studies would not undergo pooling. Confidence intervals for individual studies were calculated with the score method. Because the studies included were single-arm with event rates close to 0 or 1, the Freeman-Tukey double arcsine method was used for transformation and pooling.¹⁰

Subgroup analysis was performed for the type of FD (DED versus SPED) for all outcomes. Heterogeneity was evaluated using the I^2 statistic and the Cochrane Q test. We followed the Cochrane Collaboration's interpretation for statistical heterogeneity. P values $< .05$ were considered significant for the Q test. For the I^2 statistic, 0%–40%, 30%–60%, 50%–90%, and 75%–100% were considered little, moderate, substantial, and considerable heterogeneity, respectively.¹¹

Meta-regression, funnel plots, and the Egger test were not performed because the results would not be valid if the number of eligible studies was < 10 .¹¹

Data entry and review were performed with Excel (Microsoft). Forest plotting and meta-analysis were performed in STATA/IC 16 (StataCorp, 2019) using the metaprop function (Online Supplemental Data).¹²

RESULTS

Study Selection and Characteristics

Our search yielded 2119 entries; 1580 records were screened, and 93 full texts were perused to assess eligibility. After exclusion, 8 studies were eventually included for meta-analysis.^{13–24} The Preferred Reporting Items for Systematic Reviews and Meta-Analyses flow chart is given in the Online Supplemental Data.

All 8 studies were single-arm case series, 4 of which studied DED, and 4, SPED. Five were retrospective, and 3 were prospective. There was no eligible study for the p64 and p48 MW HPC. The number of participants per study ranged from 24 to 294, with a total of 911 patients and 1060 aneurysms. Results from individual studies are provided in the Online Supplemental Data.

Participant and Aneurysm Characteristics

Participants ranged from 17 to 82 years of age and were treated in centers in Europe, America, and Australia. The proportion of females in each study ranged from 58.3% to 82%.

The eligible studies evaluated various types of aneurysms, but most were treated in an elective setting. Unruptured aneurysms constituted 66.2%–100% of each study. Most aneurysms were

small (< 10 mm, 75.9%) with a mean sac size ranging from 7.0 to 9.0 mm.

Most aneurysms were in the anterior circulation (90.2%), with the paraophthalmic internal carotid artery being the most common location (50.7%). Distal vessels such as the anterior cerebral artery (5%) and middle cerebral artery (7.5%) accounted for small proportions. Most aneurysms were saccular in morphology (88.1%).

Treatment Characteristics

All interventions were performed with the patient under general anesthesia using transfemoral access with perioperative heparinization. Hemostasis was achieved either by manual compression or a closure device.

The neurointerventional technique was variable, but authors generally adopted a triaxial technique with a long sheath, an intracranial support catheter, and a microcatheter for delivery. The choice of catheter and the use of conebeam CT, balloon angioplasty, resheathing, platelet function testing, or branch artery coverage were not well-reported to allow statistical description.

A total of 1086 flow diverters were placed (1.02 per aneurysm), of which 455 were DED (41.9%) and 631 were SPED (58.1%). The mean proportion of stent-assisted coiling procedures varied greatly from 6.4% to 88.9%.

The periprocedural and postprocedural dual-antiplatelet therapy (DAPT) protocol was poorly documented overall, and statistical analysis was not possible. Compliance with DAPT on follow-up was not reported by all except 1 study.^{13,14}

Among those with available data, DAPT was generally prescribed for at least 4 months (aspirin, 75–325 mg daily, plus a second agent, clopidogrel, 75–150 mg daily; prasugrel, 5–10 mg daily; ticagrelor, 90 mg twice daily; or ticlopidine, 250 mg twice daily) followed by variably dosed aspirin for at least 6 months to indefinitely.

Risk of Bias Characteristics

Most studies (6 of 8) received a “good” grade for overall study quality. Two studies scored “fair” because they did not report on consecutive enrollment and used inappropriate outcome measurements and statistical methods.^{15,19}

Most studies (6 of 8) lacked adequate follow-up, which was explicable because the devices are novel. Overall, we consider most studies well-conducted with a clearly expressed study question, appropriate case definitions, and consecutive enrollment of comparable subjects. The interventions, outcome measurements, and results were generally clearly described. The overall risk of bias is therefore low. The overall study rating and details are given in the Online Supplemental Data.

Results of Meta-Analysis and Subgroup Analysis

A summary of the results of meta-analysis is given in Table 2.

Efficacy Outcomes. The overall technical success rate for device placement was 99.6% (95% CI, 98.6%–99.8%) with no significant difference between DED and SPED ($P = .33$).

Among cases of technical failure, 5 cases of improper DED expansion were seen and solved by angioplasty, device substitution, and placement of an additional overlapping stent. There

Table 2: Results of meta-analysis^a

	Overall	DED	SPED	Intergroup Heterogeneity
Efficacy outcomes				
Technical success	99.6% (98.6%–99.8%) $I^2 = 33.0\%$ $P = .165$	100% (99.2%–100%) $I^2 = 0.00\%$ $P = .487$	99.2% (97.2%–100%) $I^2 = 54.4\%$ $P = .087$	$P = .165$
Aneurysm occlusion rate (6 mo)	80.5% ^b (74.5%–86.0%) $I^2 = 70.8\%$ $P = .000$	78.9% (74.3%–83.1%) $I^2 = 0.00\%$ $P = .559$	82.7% ^b (73.4%–90.4%) $I^2 = 75.3\%$ $P = .000$	$P = .420$
Aneurysm occlusion rate (12 mo)	85.6% (80.6%–90.0%) $I^2 = 0.00\%$ $P = .744$	87.8% (80.9%–93.5%) NA	83.2% (75.8%–89.6%) NA	$P = .329$
Safety outcomes				
Mortality rate	1.0% (0.3%–1.9%) $I^2 = 0.00\%$ $P = .608$	1.3% (0.2%–3.1%) $I^2 = 5.47\%$ $P = .366$	0.8% (0.1%–1.9%) $I^2 = 0.00\%$ $P = .675$	$P = .410$
Morbidity rate	6.0% (4.5%–7.7%) $I^2 = 0.00\%$ $P = .857$	6.3% (3.9%–9.1%) $I^2 = 0.00\%$ $P = .618$	5.8% (3.9%–8.1%) $I^2 = 0.00\%$ $P = .710$	$P = .725$
Total ischemia rate	6.7% ^b (4.1%–10.1%) $I^2 = 61.9\%$ $P = .010$	8.3% ^b (2.9%–15.7%) $I^2 = 75.1\%$ $P = .007$	6.3% (3.2%–10.2%) $I^2 = 50.1\%$ $P = .111$	$P = .548$
Serious ischemia rate	1.8% (0.8%–3.0%) $I^2 = 12.1\%$ $P = .335$	2.5% (1.0%–4.6%) $I^2 = 0.00\%$ $P = .685$	1.2% (0.1%–3.2%) $I^2 = 37.0\%$ $P = .190$	$P = .240$

Note:—NA indicates not applicable.

^a Table shows pooled point estimate, 95% confidence intervals, heterogeneity (I^2 statistic and P value for the Cochrane Q test) and intergroup heterogeneity for all outcomes of the meta-analysis.

^b Significant heterogeneity.

were 3 cases of incomplete deployment of the SPED, with all stents resheathed without sequelae. There were 3 cases of failed cannulation, including 1 case of off-label use in treating a distal aneurysm.

There was considerable difference in the follow-up period, imaging technique, and imaging scale across studies. To pool data, we discounted longer follow-ups: For example, 9-month follow-up DSA results were pooled under 6 months. As indicated in the protocol, aneurysm obliteration is defined when filling is completely absent in the angiogram (ie, Raymond-Roy I and O’Kelly-Marotta D classification).

The overall median follow-up interval was 8.24 months (interquartile range, 6.67–12 months). Imaging data were available for 825 (90.6%) and 231 (25.4%) patients at 6- and 12-month follow-up, respectively.

The overall pooled aneurysm occlusion rates at 6 and 12 months were 80.5% (95% CI, 74.5%–86.0%) and 85.6% (95% CI, 80.6%–90.0%), respectively, with no significant difference between DED and SPED ($P = .42$ and $P = .33$).

Safety Outcomes. There was considerable heterogeneity in the definition and reporting of complications. The definitions described under Materials and Methods were adopted, and individual events were reclassified when possible. Events with insufficient detail were treated conservatively. For example, an adverse event labelled as “thromboembolism” without further detail was classified under “serious ischemia,” which indicated a permanent neurologic deficit observed in the patient.

The overall pooled morbidity and mortality rates were 6.0% (95% CI, 4.5%–7.7%) and 1.0% (95% CI, 0.3–1.9%), respectively, with no significant difference between DED and SPED ($P = .73$ and $P = .41$). Among the 10 deaths, 7 were related to early and late rebleeding, 1 patient died of perforation in DED-assisted coiling, and 1 patient died of stent occlusion from self-discontinuation of antiplatelets shortly after the operation. The cause of death in 1 case was not specified.

The overall pooled ischemic and serious ischemic event rates were 6.7% (95% CI, 4.1%–10.1%) and 1.8% (95% CI, 0.8%–3.0%), respectively, with no significant difference between DED and SPED ($P = .55$ and $P = .24$).

Details of technical challenges during intervention and unsuccessful placements and mortality, morbidity, and ischemic events are listed in the Online Supplemental Data. Forest plots of all meta-analysis outcomes are available in the Online Supplemental Data.

A table showcasing results of the present and previous meta-analyses on older FDs treating different types of aneurysms is shown in the Online Supplemental Data.^{3–6,25–30}

DISCUSSION

This is the first meta-analysis examining clinical outcomes of surface-modified flow diverters since the release of SPED in 2014. As these devices become more available in angiosuites worldwide, it is important for interventionists to understand their properties, differences, therapeutic efficacy, and safety profile to select the best device for patients.

Surface modifications are designed to reduce platelet activation, adhesion, and clot formation to prevent clinical ischemic events. Our results appear to confirm this claim. Serious ischemic event rates were uniformly low across studies (0.8% to 3.0%) and compare favorably with meta-analyses performed between 2012 and 2017 on older devices including the Pipeline Embolization Device (PED; Medtronic), the Silk flow diverter (Balt Extrusion), the Flow-Redirection Endoluminal Device (FRED; MicroVention), the Surpass stent (Stryker Neurovascular), and the Tubridge flow diverter (MicroPort Medical Company) (4.1%–7.5%).^{2,3,5,6}

The significant heterogeneity observed in “total ischemic events” in the present study is accountable by methodologic variation, specifically in 1 study that included ischemic lesions seen on MR imaging immediately postprocedure (Table 2).²³ These lesions are very common and normally not associated with

clinical sequelae.²³ The serious ischemic event rate in that particular study was not inordinately high (4.2%) compared with others.

The overall mortality was low (1.0%) compared with older stents (2.8%–4%), attesting to the *in vivo* safety of these new devices. Cerebral hemorrhage remains the most common cause of mortality in FD treatment of aneurysms (80%) as in a previous meta-analysis.⁴ The cause of hemorrhage after flow diversion is not always clear. In patients with ruptured aneurysms, early rebleeds can be explained by the inability of the FD to immediately obliterate the aneurysm. In other patients, bleeding may be facilitated by DAPT. Giant aneurysms are more prone to delayed rupture, and this may be the result of increased intraneurysm pressure after flow diversion.^{31,32} Hemodynamic disturbance caused by the FD may explain rare instances of bizarre delayed parenchymal hemorrhage.³³ In our study, surface modifications do not appear to mitigate the risk of bleeding. Three of 8 fatal hemorrhages occurred in patients with giant aneurysms (37.5%). Whether this is causative would require further investigation.

Clinical outcomes of aneurysm treatment are affected by various factors other than the FD, such as aneurysm characteristics. Previous studies have shown higher morbidity and mortality rates in giant, acutely ruptured, blood-blister, posterior circulation, and nonsaccular aneurysms (Online Supplemental Data).²⁷⁻³⁰ Because most patients in the present analysis had unruptured (91.6%), anterior circulation (90.8%), and small (<10 mm) aneurysms, perhaps a more appropriate comparison is with the recent studies by Fiorella et al²⁵ and Bhatia et al,²⁶ who examined aneurysms with similar characteristics treated by older FDs. They found a 12-month aneurysm occlusion rate of 74.6% compared with our 85.6% and a total morbidity rate of 7.81%–10.1% compared with our 6.0%. While meta-analyses are not meant to be compared directly, this finding would suggest that SM-FDs are noninferior and potentially superior to previous-generation FDs in terms of efficacy and safety.

Our results also corroborate manufacturers' claims of better apposition and improved deliverability. The technical success rate was excellent (99.6%), improved from older stents (90.6%–91.7%), and similar to that of the Pipeline Flex without Shield coating (Medtronic; 99.3%). For cases of technical failure, no significant adverse consequences were seen, with stents resheathed and removed or improper expansion solved with other endovascular techniques. These findings indicate that SM-FDs are robust and highly deliverable devices.

While coiling and clipping may occlude an aneurysm instantly, flow diverters are designed to hemodynamically remodel the parent artery, causing gradual aneurysm occlusion. Hence, occlusion rates at 6 and 12 months may not reflect the eventual obliteration rate, which tends to be higher in the long run. For example, in a study examining long-term outcome for older stents (Silk, PED, and FRED), occlusion rates were found to progress from 76.2% at 6 months to 94.2% at 5 years.³⁴

SM-FDs are novel devices, and there are only studies with 6–12 months of follow-up at present. Nevertheless, they appear comparable with older FDs and coiling. The 6-month occlusion is 80.5% compared with 74.5%–77.9% in older FDs⁴⁻⁶ and slightly

lower than that of coiling (86.1%).³⁵ Limited data on 12-month occlusion give a pooled estimate of 85.6%, which is slightly lower than that of older FDs (89.6%).⁵ Of note, the 6-month aneurysm occlusion rate is significantly higher in the Safety and Clinical Effectiveness of Pipeline Shield Devices for Intracranial Aneurysm (SCOPE-AUS) study than in other studies (90.3% versus pooled estimate of 80.5%, $I^2 = 75.3%$, $P = .007$). Because only intermediate results were presented at the World Federation of Interventional and Therapeutic Neuroradiology conference in 2019, we eagerly anticipate the full article, which may shed more light on its superior results.²⁰

Another concern regarding SM-FDs is the effect of neointimal hyperplasia. *In vivo* animal studies using optic coherence tomography showed conflicting results in the early formation of neointimal hyperplasia in the SPED compared with conventional PED, raising concern for in-stent stenosis after FD placement.^{7,36} Clinical studies included in this review did not routinely analyze this phenomenon, and its effect on patient outcome remains unclear.

Trivelato et al²¹ observed, in their DED cohort, that a branch vessel arising from the aneurysm led to higher rates of persistence, with an odds ratio of 6.36. This finding is consistent with those of previous studies on flow diversion.³⁷ However, because other authors did not report this detail and the number of studies included was too small, meta-regression was not possible.

Summarizing the present findings, SM-FDs appear to be as efficacious and safe as older FDs and coiling in the early and mid-term results. No significant clinical difference was seen between the SPED and DED.

Limitations, Criticisms, and Future Research Directions

Most included studies were retrospective, uncontrolled, non-randomized case series lacking long-term (>1 year) outcome. Nonetheless, within the limitations of the study design, the authors produced high-quality research. Assessment of aneurysm occlusion was not blinded except for 1 study in which the aneurysm occlusion was determined by an independent radiology laboratory.^{13,14} The other studies were prone to performance bias.

Most patients included had unruptured, small, anterior circulation saccular aneurysms, which tend to be the easiest to treat. This feature can cause ecologic bias leading to better outcomes reported than those encountered in real-life clinical practice.

DAPT was a major confounder in ischemic and hemorrhagic events. The regimen, compliance, and platelet function testing were poorly reported for all except 1 study.^{13,14} The possibility that the difference in outcome only reflected a variable effect from different antiplatelet therapy cannot be excluded.

There was significant heterogeneity in endovascular techniques, such as the use of stent-assisted coiling, follow-up and imaging protocols, and the definition of treatment success and complications. In particular, adjunctive coiling occurred in 6.0%–47.1% of participants in the included studies. Because some studies did not report this detail and the overall number of studies is small, meta-regression is not feasible. Instead, we adopted the random effects model to minimize the effects of this clinical heterogeneity.

Aneurysm factors such as rupture status, location, branch vessel coverage, and adverse events were not adequately reported to allow analysis. Further individual-patient-data meta-analysis may be helpful in teasing out which patients are more prone to adverse effects.

Because the present findings indicate that SM-FDs are, indeed, less thrombogenic in vivo, future research should be directed to determine the optimal antiplatelet regimen for these stents. There are already initial reports of using a single agent in selected cases.^{38,39} If the bleeding risk of DAPT can be mitigated by SM-FD, flow diversion may be posited as an acceptable treatment for ruptured aneurysms, which is currently an off-label use.

Looking forward, 2 prospective observational cohorts on SPED are in progress (Pipeline Flex With Shield Technology Embolization [SHIELD], NCT02719522, and Pipeline Vantage Embolization Device With Shield Technology for Wide-Necked Intracranial Aneurysms [ADVANCE], NCT03873714) as is an Italian registry on DED, and these may add further evidence to this evolving area in the near future.

CONCLUSIONS

Surface-modified flow diverters appear as efficacious in closing aneurysms as older FDs and coiling in the early- and midterm outcomes. A uniformly high technical success rate is reported for both SPED and DED. Lower mortality and serious ischemic events are observed compared with previous meta-analyses on older FDs. No significant difference was demonstrated between the SPED and DED. Our results may better apply to small, unruptured saccular aneurysms in the anterior circulation. The long-term clinical outcomes of these devices remain to be seen.

Larger scale prospective studies with a standardized DAPT regimen; follow-up protocol; and more detailed reporting of patient, aneurysm, and treatment characteristics can permit further analysis to identify the best fit patients for these newer devices and predict treatment failure.

REFERENCES

1. Limbucci N, Leone G, Renieri L, et al. **Expanding indications for flow diverters: distal aneurysms, bifurcation aneurysms, small aneurysms, previously coiled aneurysms and clipped aneurysms, and carotid cavernous fistulas.** *Neurosurgery* 2020;86:S85–94 CrossRef Medline
2. Leung GK, Tsang AC, Lui WM. **Pipeline Embolization Device for intracranial aneurysm: a systematic review.** *Clin Neuroradiol* 2012;22:295–303 CrossRef Medline
3. Zhou G, Zhu YQ, Su M, et al. **Flow-diverting devices versus coil embolization for intracranial aneurysms: a systematic literature review and meta-analysis.** *World Neurosurg* 2016;88:640–45 CrossRef Medline
4. Brinjikji W, Murad MH, Lanzino G, et al. **Endovascular treatment of intracranial aneurysms with flow diverters: a meta-analysis.** *Stroke* 2013;44:442–47 CrossRef Medline
5. Briganti F, Leone G, Marseglia M, et al. **Endovascular treatment of cerebral aneurysms using flow-diverter devices: a systematic review.** *Neuroradiol J* 2015;28:365–75 CrossRef Medline
6. Ye G, Zhang M, Deng L, et al. **Meta-analysis of the efficiency and prognosis of intracranial aneurysm treated with flow diverter devices.** *J Mol Neurosci* 2016;59:158–67 CrossRef Medline

7. Matsuda Y, Chung J, Lopes DK. **Analysis of neointima development in flow diverters using optical coherence tomography imaging.** *J Neurointerv Surg* 2018;10:162–67 CrossRef Medline
8. Moher D, Liberati A, Tetzlaff J, et al; PRISMA Group. **Preferred reporting items for systematic reviews and meta-analyses: the PRISMA statement.** *BMJ* 2009;339:b2535 CrossRef Medline
9. National Institutes of Health, National Heart, Lung, and Blood Institute. **Study Quality Assessment Tools.** <https://www.nhlbi.nih.gov/health-topics/study-quality-assessment-tools>. Accessed October 1, 2019
10. Rousseau MJ, Evans JC. **Key statistical assumptions and methods in one-arm meta-analyses with binary endpoints and low event rates, including a real-life example in the area of endoscopic colonic stenting.** *Cogent Medicine* 2017;4:13343318 CrossRef
11. Higgins JP, Thomas J, Chandler J, et al, eds. *Cochrane Handbook for Systematic Reviews of Interventions, Version 5.1.0.* The Cochrane Collaboration and John Wiley & Sons Ltd.; 2011
12. Nyaga VN, Arbyn M, Aerts M. **Metaprop: a Stata command to perform meta-analysis of binomial data.** *Arch Public Health* 2014;72:39 CrossRef Medline
13. Martínez-Galdámez M, Lamin SM, Lagios KG, et al. **Periprocedural outcomes and early safety with the use of the Pipeline Flex Embolization Device with Shield Technology for unruptured intracranial aneurysms: preliminary results from a prospective clinical study.** *J Neurointerv Surg* 2017;9:772–76 CrossRef Medline
14. Martínez-Galdámez M, Lamin SM, Lagios KG, et al. **Treatment of intracranial aneurysms using the Pipeline Flex Embolization Device with Shield technology: angiographic and safety outcomes at 1-year follow-up.** *J Neurointerv Surg* 2019;11:396–99 CrossRef Medline
15. Daglioglu E, Akmgangit İ, Acik V, et al. **The experience of the Derivo® Embolisation Device in intracranial aneurysms.** *Turk Neurosurg* 2020;30:30–37 CrossRef Medline
16. Goertz L, Dorn F, Kraus B, et al. **Improved occlusion rate of intracranial aneurysms treated with the Derivo Embolization Device: one-year clinical and angiographic follow-up in a multicenter study.** *World Neurosurg* 2019;126:e1503–09 CrossRef Medline
17. Goertz L, Dorn F, Kraus B, et al. **Safety and efficacy of the Derivo Embolization Device for the treatment of ruptured intracranial aneurysms.** *J Neurointerv Surg* 2019;11:290–95 CrossRef Medline
18. Kraus B, Goertz L, Turowski B, et al. **Safety and efficacy of the Derivo Embolization Device for the treatment of unruptured intracranial aneurysms: a multicentric study.** *J Neurointerv Surg* 2019;11:68–73 CrossRef Medline
19. Kaschner MG, Petridis A, Turowski B. **Single center experience with the new generation Derivo embolization device for ruptured and unruptured intracranial aneurysms.** *J Neurosurg Sci* 2020;64:353–63 CrossRef Medline
20. Owusu MA, Rice HA, De Villiers LE, et al. **SCOPE-AUS: the safety and clinical effectiveness of Pipeline™ Flex Embolization Devices with Shield Technology™ in patients with intracranial aneurysms: a multicentre retrospective study of an Australian cohort.** In: *Proceedings of the Annual Meeting of the World Federation of Interventional and Therapeutic Neuroradiology*, Naples, Italy. December 1–24, 2019
21. Trivelato FP, Abud DG, Ulhoa AC, et al. **Derivo Embolization Device for the treatment of intracranial aneurysms.** *Stroke* 2019;50:2351–58 CrossRef Medline
22. Trivelato FP, Wajnberg E, Rezende MTS, et al. **Safety and effectiveness of the Pipeline Flex Embolization Device with Shield Technology for the treatment of intracranial aneurysms: midterm results from a multicenter study.** *Neurosurgery* 2020;87:104–11 CrossRef Medline
23. Akgul E, Onan HB, Akpinar S, et al. **The DERIVO Embolization Device in the treatment of intracranial aneurysms: short- and midterm results.** *World Neurosurg* 2016;95:229–40 CrossRef Medline

24. Atasoy D, Kandasamy N, Hart J, et al. **Outcome study of the Pipeline Embolization Device with Shield Technology in Unruptured Aneurysms (PEDSU).** *AJNR Am J Neuroradiol* 2019; 40:2094–2101 CrossRef Medline
25. Fiorella D, Gache L, Frame D, et al. **How safe and effective are flow diverters for the treatment of unruptured small/medium intracranial aneurysms of the internal carotid artery? Meta-analysis for evidence-based performance goals.** *J Neurointerv Surg* 2020;12: 869–73 CrossRef Medline
26. Bhatia KD, Kortman H, Orru E, et al. **Periprocedural complications of second-generation flow diverter treatment using Pipeline Flex for unruptured intracranial aneurysms: a systematic review and meta-analysis.** *J Neurointerv Surg* 2019;11:817–24 CrossRef Medline
27. Cagnazzo F, Mantilla D, Rouchaud A, et al. **Endovascular treatment of very large and giant intracranial aneurysms: comparison between reconstructive and deconstructive techniques—a meta-analysis.** *AJNR Am J Neuroradiol* 2018;39:852–58 CrossRef Medline
28. Cagnazzo F, di Carlo DT, Cappucci M, et al. **Acutely ruptured intracranial aneurysms treated with flow-diverter stents: a systematic review and meta-analysis.** *AJNR Am J Neuroradiol* 2018;39:1669–75 CrossRef Medline
29. Zhu D, Yan Y, Zhao P, et al. **Safety and efficacy of flow diverter treatment for blood blister-like aneurysm: a systematic review and meta-analysis.** *World Neurosurg* 2018;118:e79–86 CrossRef Medline
30. Kiyofuji S, Graffeo CS, Perry A, et al. **Meta-analysis of treatment outcomes of posterior circulation non-saccular aneurysms by flow diverters.** *J Neurointerv Surg* 2018;10:493–99 CrossRef Medline
31. Cebal JR, Mut F, Raschi M, et al. **Aneurysm rupture following treatment with flow-diverting stents: computational hemodynamics analysis of treatment.** *AJNR Am J Neuroradiol* 2011;32:27–33 CrossRef Medline
32. Rouchaud A, Brinjikji W, Lanzino G, et al. **Delayed hemorrhagic complications after flow diversion for intracranial aneurysms: a literature overview.** *Neuroradiology* 2016;58:171–77 CrossRef Medline
33. Mitha AP, Mynard JP, Storwick JA, et al. **Can the Windkessel hypothesis explain delayed intraparenchymal haemorrhage after flow diversion? A case report and model-based analysis of possible mechanisms.** *Heart, Lung Circ* 2015;24:824–30 CrossRef Medline
34. Korkmazer B, Kocak B, Islak C, et al. **Long-term results of flow diversion in the treatment of intracranial aneurysms: a retrospective data analysis of a single center.** *Acta Neurochir* 2019;161:1165–73 CrossRef Medline
35. Naggara ON, White PM, Guilbert F, et al. **Endovascular treatment of intracranial unruptured aneurysms: systematic review and meta-analysis of the literature on safety and efficacy.** *Radiology* 2010;256:887–97 CrossRef Medline
36. Caroff J, Tamura T, King RM, et al. **Phosphorylcholine surface modified flow diverter associated with reduced intimal hyperplasia.** *J Neurointerv Surg* 2018;10:1097–101 CrossRef Medline
37. Chiu AH, Cheung AK, Wenderoth JD, et al. **Long-term follow-up results following elective treatment of unruptured intracranial aneurysms with the Pipeline embolization device.** *AJNR Am J Neuroradiol* 2015;36:1728–34 CrossRef Medline
38. Hanel RA, Aguilar-Salinas P, Brasiliense LB, et al. **First US experience with Pipeline Flex with Shield Technology using aspirin as antiplatelet monotherapy.** *BMJ Case Rep* 2017;2017:bcr2017219406 CrossRef Medline
39. Orlov K, Kisilitsin D, Strelnikov N, et al. **Experience using Pipeline Embolization Device with Shield Technology in a patient lacking a full postoperative dual antiplatelet therapy regimen.** *Interv Neuroradiol* 2018;24:270–73 CrossRef Medline

WEB Device Shape Changes in Elastase-Induced Aneurysms in Rabbits

Y. Ding, D. Dai, A. Rouchaud, K. Janot, S. Asnafi, D.F. Kallmes, and R. Kadirvel



ABSTRACT

BACKGROUND AND PURPOSE: While WEB devices have been shown to be safe and effective for aneurysm treatment, WEB-shape modification compression has been associated with incomplete aneurysm occlusion. We explored the relationship between occlusion rates and WEB-shape modification in different WEB device types in an experimental aneurysm model.

MATERIALS AND METHODS: Elastase-induced aneurysms were created in rabbits and treated with dual-layer ($n=12$), single-layer ($n=12$), or single-layer sphere ($n=12$) WEB devices. Aneurysms were followed up either at 3 or 12 months. Angiographic occlusion was graded using the WEB Occlusion Scale: grade I, complete; grade II, complete but recess filling; grade III, residual neck; or grade IV, residual aneurysm. WEB-shape modification and histologic features were also analyzed.

RESULTS: Grade I or II occlusion was seen in 16 (44%) aneurysms, and grade I, II, or III (“adequate”) occlusion was observed in 22 (61.1%) aneurysms at follow-up. WEB-shape modification was observed in 22 (61.1%) aneurysms. WEB-shape modification was higher in single-layer (9/12) and dual-layer (10/12) devices compared with single-layer sphere devices (3/12). Aneurysms with WEB-shape modification had a higher level of thrombus organization in the dome compared with those without WEB-shape modification (68% [15/22] versus 50% [7/14]). WEB-shape modification was not correlated with angiographic or histologic outcomes but was significantly correlated with levels of fibrosis and smooth muscle cells in the aneurysm.

CONCLUSIONS: WEB-shape modification is not associated with incomplete aneurysm occlusion of WEB devices in the rabbit model but may be related to connective tissue formation and the healing response to WEB device implantation.

ABBREVIATIONS: FD = flow diverter; SMA = smooth muscle actin; WSM = WEB-shape modification; DL = dual-layer; SL = single-layer; SLS = single-layer sphere

During the past 2 decades, the treatment of intracranial aneurysms has rapidly evolved from the single option of open skull surgical clipping to the increasingly common use of minimally invasive endovascular techniques. While endovascular coiling has been shown to offer significant advantages over an open surgical approach, it is still associated with significant limitations. These include treatment-associated morbidity of at least 5%–7%,

a high aneurysm recurrence rate (as high as 20%–30% in some series), and low aneurysm occlusion rates.¹

Flow diverters (FDs) are innovative and promising devices used to treat complex and/or wide-neck aneurysms.^{2,3} They divert blood away from aneurysms, and their use has expanded since inception.^{4,5} Use of endoluminal FDs, however, necessitates the use of antiplatelet therapy, which can be problematic for ruptured aneurysms. Unfortunately, the use of FDs does not eliminate the possibility of delayed aneurysm rupture, a thromboembolic event, and parent artery stenosis.⁶

The Woven EndoBridge (WEB) device (MicroVention) is a completely intrasaccular FD device, which was designed to treat challenging, wide-neck bifurcation aneurysms that are difficult to embolize safely and effectively with other existing treatment approaches.^{7,8} From the original dual-layer (DL) to current single-layer (SL) design, WEB devices have shown a good safety profile and a high rate of adequate occlusion both in experimental and clinical studies.^{9–16} In the meantime, WEB-shape modification (WSM) has been reported in the literature and could

Received March 27, 2018; accepted after revision September 5, 2020.

From the Department of Radiology (Y.D., D.D., S.A., D.F.K., R.K.), Mayo Clinic, Rochester, Minnesota; Department of Interventional Neuroradiology (A.R.), University Hospital, Limoges, France; Neuroradiology Department (K.J.), University Hospital of Tours, Tours, France; and Department of Radiology (S.A.), Emory University, Atlanta, Georgia.

This study was supported, in part, by National Institutes of Health grant No. NS076491 (R. Kadirvel).

Please address correspondence to Ramanathan Kadirvel, PhD, Department of Radiology, Mayo Clinic, 200 First ST SW, Rochester, MN 55905; e-mail: kadir@mayo.edu

Indicates open access to non-subscribers at www.ajnr.org

<http://dx.doi.org/10.3174/ajnr.A6899>

potentially be associated with the approximately 15% rate of incomplete/inadequate aneurysm occlusion observed in the published WEB Intracascular Therapy (WEB-IT) trial.¹⁷ However, this phenomenon has not been well-understood until now because other researchers have reported that this shape change did not impact the anatomic outcome after WEB deployment.¹⁸ In this study, we compared the occlusion rates of DL, SL, and single-layer sphere (SLS) WEBs in rabbit elastase (Worthington Biochemical)-induced aneurysm models and evaluated the relationship between WSM using histologic results and angiographic occlusion rates.

MATERIALS AND METHODS

Aneurysm Creation

Elastase-induced aneurysms were created in 36 New Zealand white rabbits. Animal procedures were approved by the Institutional Animal Care and Use Committee at Mayo Clinic. Aneurysm-creation procedures were performed using an elastase-induction model as previously described.¹⁹ Endovascular treatment of each aneurysm was undertaken at least 3 weeks after aneurysm creation.²⁰

Devices

WEB devices are classified according to shape and the number of mesh layers each one contains. DL devices consist of 2 layers of braided, nitinol wire mesh. SL and SLS devices consist of a single layer of braided, nitinol/platinum wire mesh; however, SLS implants have a more rounded 3D shape than the “barrel-like” SL and DL devices. The specific qualities of the WEB devices have been previously described.^{21,22}

Device Deployment

The WEB device deployment procedure has been reported previously.^{7,8} The right femoral artery was briefly exposed. A 5F sheath (Envoy; Cordis) was inserted, 500 U of heparin was injected, and a 5F catheter was then advanced into the brachiocephalic trunk from the aortic arch. DSA was performed through the guide catheter. A 0.027-inch ID (interior diameter) microcatheter (VIA-27; Sequent Medical) was advanced into the aneurysm lumen over a microguidewire (Transend-14; Stryker). Appropriately sized devices were placed in the aneurysm cavity for each device ($n = 12$ [DL], $n = 12$ [SL], $n = 12$ [SLS]). DSA was performed immediately following device placement. No animals received antiplatelet therapy during the course of the study.

Follow-Up and Euthanasia

Angiographic evaluation was completed immediately after device implantation and again at follow-up. The cohort was divided into 2 subgroups preselected for euthanasia at 3 months ($n = 6$ [DL], $n = 6$ [SL], $n = 6$ [SLS]) and 12 months ($n = 6$ [DL], $n = 6$ [SL], $n = 6$ [SLS]), respectively, by intravenous injection with a lethal dose of pentobarbital through the ear vein. Following euthanasia, aneurysm tissue was harvested and placed in a 10% formalin solution.

Aneurysm Grading and WSM Assessment

The degree of angiographic aneurysm occlusion at follow-up was graded as follows: grade I, complete; grade II, complete but with recess filling; grade III, residual neck; or grade IV, residual

aneurysm.^{23,24} Two reviewers independently evaluated the angiographic occlusion, and disagreements were resolved by a third reviewer. Angiographic occlusion outcome was dichotomized into either complete occlusion (grade I or II) or incomplete occlusion (grade III or IV). Grades I, II, and III were considered adequate. The distance between proximal and distal device markers was measured on unsubtracted angiographic images. WSM was defined as a change in distance ($\leq -10\%$ to $\geq 10\%$) between markers at follow-up compared with immediate postdevice deployment.

Histopathologic Processing and Analysis

A histopathologist who was blinded to the angiographic results did the processing and analysis for healing evaluation. Aneurysm samples were processed at 1000- μm intervals in a coronal orientation, permitting long-axis sectioning of the aneurysm neck, with use of an IsoMet Low Speed Saw (Buehler). After the device segments were removed under a dissecting microscope, the samples were then re-embedded in paraffin, sectioned at 4 μm , and stained with hematoxylin-eosin.

Histologic healing of aneurysms was assessed using an ordinal scale.²⁵ The extent of blood clot organization within the aneurysm and the neointimal coverage of the aneurysm neck were evaluated. Tissue compaction, seen as a concave surface of clot tissue toward the aneurysm dome, was also analyzed. The degree of inflammation within each aneurysm was scored as 0 (no inflammatory cell infiltration); 1 (minimal or mild: scant, scattered inflammatory cell infiltration); 2 (moderate: patchy-but-localized or limited inflammatory cell infiltration); or 3 (marked: attenuated, diffuse inflammatory cell infiltration).

Masson trichrome staining was performed to evaluate collagen deposition within the aneurysm; collagen deposition within the aneurysm dome was segmented and quantified using the previously described method.²⁶ The fibrosis ratio (total area of fibrosis within the aneurysmal cavity divided by the total area of the aneurysmal cavity) was calculated for each aneurysm.

Immunohistochemical staining of smooth muscle cells in tissue sections was performed with smooth muscle actin (SMA).²⁷ The SMA-positive area was segmented and quantified with the same method used for collagen deposition as described above.

Statistical Analysis

Continuous variables were described as mean [SD] and compared using a Student *t* test. Categorical variables were presented as number (percentage) and compared using the Fisher exact test. The correlation between WSM and aneurysm occlusion was assessed by the Spearman rank correlation. The correlation between WSM and aneurysm geometries, histologic healing, fibrosis, and smooth muscle actin levels was evaluated by simple linear regression. A *P* value $< .05$ was considered statistically significant.

RESULTS

Angiographic Findings

All aneurysms were implanted with appropriately sized devices. No morbidity or mortality was observed throughout the study.

In the group of rabbits selected for euthanasia at 3 months ($n = 18$), grade I or II occlusion was achieved in 9 (50%)

aneurysms at follow-up. Within this group, 6 rabbits were treated with the DL device: 1 (16.7%) showed grade I occlusion, 3 (50.0%) showed grade II occlusion, 1 (16.7%) showed grade III occlusion, and 1 (16.7%) showed grade IV occlusion. For the 6 rabbits treated with the SL device, 1 (16.7%) showed grade I occlusion, 2 (33.3%) showed grade III occlusion, and 3 (50.0%) showed grade IV occlusion. In the final subgroup ($n = 6$) treated with the SLS device, 3 (50.0%) rabbits showed grade I occlusion,

1 (16.7%) showed grade II occlusion, and 2 (33.3%) showed grade IV occlusion.

In the 12-month group at follow-up ($n = 18$), 7 (38.9%) aneurysms had grade I or 2 occlusion. Of the 6 rabbits treated with the DL device, 3 (50.0%) showed grade I occlusion, 1 (16.7%) showed grade II occlusion, and 2 (33.3%) showed grade IV occlusion. For the 6 rabbits treated with the SL device, 1 (16.7%) showed grade I occlusion, 2 (33.3%) showed grade III occlusion, and 3 (50.0%) showed grade IV occlusion. For the rabbits treated with the SLS device, 1 (16.7%) showed grade I occlusion, 1 (16.7%) showed grade II occlusion, 1 (16.7%) showed grade III occlusion, and the remaining 3 (50.0%) showed grade IV occlusion (Table 1).

In a pooled angiographic analysis, 16 (44%) aneurysms (9 at 3 months and 7 at 12 months) demonstrated complete occlusion and 22 (61.1%) aneurysms (12 at 3 months, and 10 at 12 months) showed adequate occlusion. No significance was found in complete or adequate occlusion rates between the 3- and 12-month groups ($P = .74$). DL (75%, 9/12) devices demonstrated a higher percentage of adequate aneurysm occlusion compared with SLS (58.3%, 7/12; $P = .68$) and SL (50%, 6/12; $P = .04$) devices.

WEB-Shape Modification

WSM was observed in 22 (61%) aneurysms (Fig 1), of which half (5 with complete occlusion, 6 with incomplete occlusion) were in the 3-month group and the remaining half (4 with complete occlusion, 7 with incomplete occlusion) were in the 12-month group (Table 2). WSM was not statistically associated with aneurysm neck width or height (Fig 2). There were no significant differences in occlusion grades in aneurysms with or without WSM (9 with complete occlusion, 13 with incomplete occlusion versus 7 with complete occlusion and 7 with incomplete occlusion; $P = .73$) (Fig 1). Furthermore, no correlation was found between the percentage of WSM and the occlusion grade. Most interesting, SLS had significantly less WSM (25%, 3/12) compared with the DL (83%, 10/12; $P = .012$) and SL (75%, 9/12; $P = .039$) devices.

Histologic Findings

The mean histologic healing score was not significantly different between the 3- and 12-month groups (5.6 [SD, 2.6] versus 4.2 [SD, 2.5]; $P = .11$), but it was significantly higher in aneurysms with complete occlusion compared with those with incomplete occlusion (6.39 [SD, 2.07] versus 2.80 [SD, 1.75]). Histologic evaluation of aneurysm sacs showed a combination of loose connective tissue and thrombus (unorganized, organized, and poorly organized).

Table 1: Aneurysm occlusion grading summary

Group ^a	DL, No. (%)	SL, No. (%)	SLS, No. (%)	Total, No. (%)
3-Month group				
Grade I	1 (16.7)	1 (16.7)	3 (50.0)	5 (27.8)
Grade II	3 (50.0)	0 (0)	1 (16.7)	4 (22.2)
Grade III	1 (16.7)	2 (33.3)	0 (0)	3 (16.7)
Grade IV	1 (16.7)	3 (50.0)	2 (33.3)	6 (33.3)
Total	6	6	6	18
12-Month group				
Grade I	3 (50.0)	1 (16.7)	1 (16.7)	5 (27.8)
Grade II	1 (16.7)	0 (0)	1 (16.7)	2 (11.1)
Grade III	0 (0)	2 (33.3)	1 (16.7)	3 (16.7)
Grade IV	2 (33.3)	3 (50.0)	3 (50.0)	8 (44.4)
Total	6	6	6	18

^a Grade I represents complete occlusion; grade II, complete occlusion with recess filling; grade III, residual neck; grade IV, residual aneurysm.

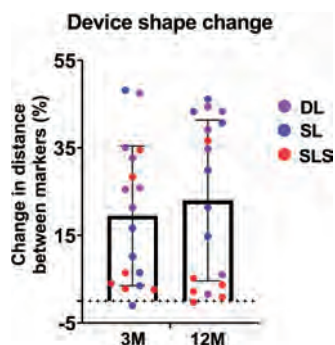


FIG 1. Range of WEB device shape change by time and device configuration. The change in distance between the distal and proximal markers of the device at follow-up compared with that immediately posttreatment. Positive values denote device shortening; negative values represent device elongation. Device elongation is seen in only 2 cases, both of which have device elongation of <2%. 3M indicates 3 months; 12M, 12 months.

Table 2: WSM and aneurysm occlusion by device type

Follow-Up, Occlusion Group ^a	DL ($n = 12$)		SL ($n = 12$)		SLS ($n = 12$)		Total ($n = 36$)	
	With WSM, No. (%)	Without WSM, No. (%)	With WSM, No. (%)	Without WSM, No. (%)	With WSM, No. (%)	Without WSM, No. (%)	With WSM, No. (%)	Without WSM, No. (%)
3 Months								
Grade I or II	4 (33.3)	0	0	1 (8.3)	1 (8.3)	3 (25.0)	5 (13.9)	4 (11.1)
Grade III or IV	2 (16.7)	0	3 (25.0)	2 (16.7)	1 (8.3)	1 (8.3)	6 (16.7)	3 (8.3)
12 Months								
Grade I or II	3 (25.0)	1 (8.3)	1 (8.3)	0	0	2 (16.7)	4 (11.1)	3 (8.3)
Grade III or IV	1 (8.3)	1 (8.3)	5 (41.7)	0	1 (8.3)	3 (25.0)	7 (19.4)	4 (11.1)
Total	10 (83.3)	2 (16.7)	9 (75.0)	3 (25.0)	3 (25.0)	9 (33.3)	22 (61.1)	14 (38.9)

^a Grade I represents complete occlusion; grade II, complete occlusion with recess filling; grade III, residual neck; grade IV, residual aneurysm.

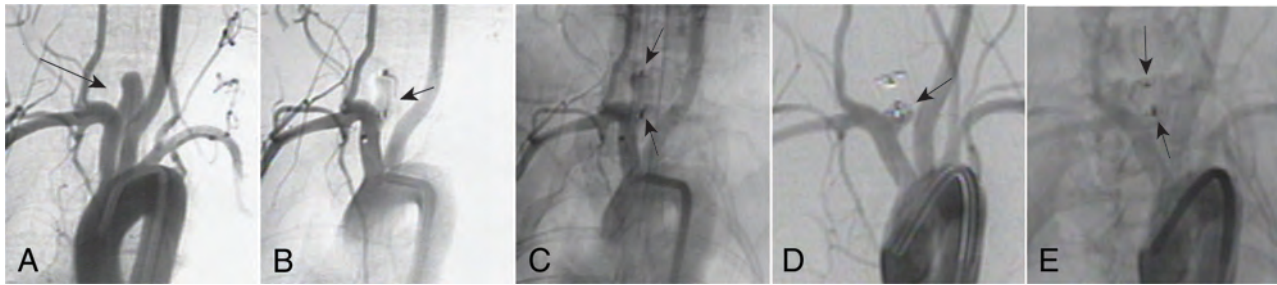


FIG 2. WEB shape changes at 3 months following device implantation. *A*, Anteroposterior DSA image before device implantation shows an aneurysm cavity (arrow). *B*, The DSA image immediately after SL device deployment shows complete aneurysm occlusion (arrow). *C*, Unsubtracted image of *B* shows proximal and distal markers (arrows) of the WEB device. *D*, DSA image at 3-month follow-up shows a residual neck (arrow). *E*, Unsubtracted image of *D* shows device compression. Note that the distance between the proximal and distal markers (arrows) is reduced compared with that in *C*, indicating a change in shape.

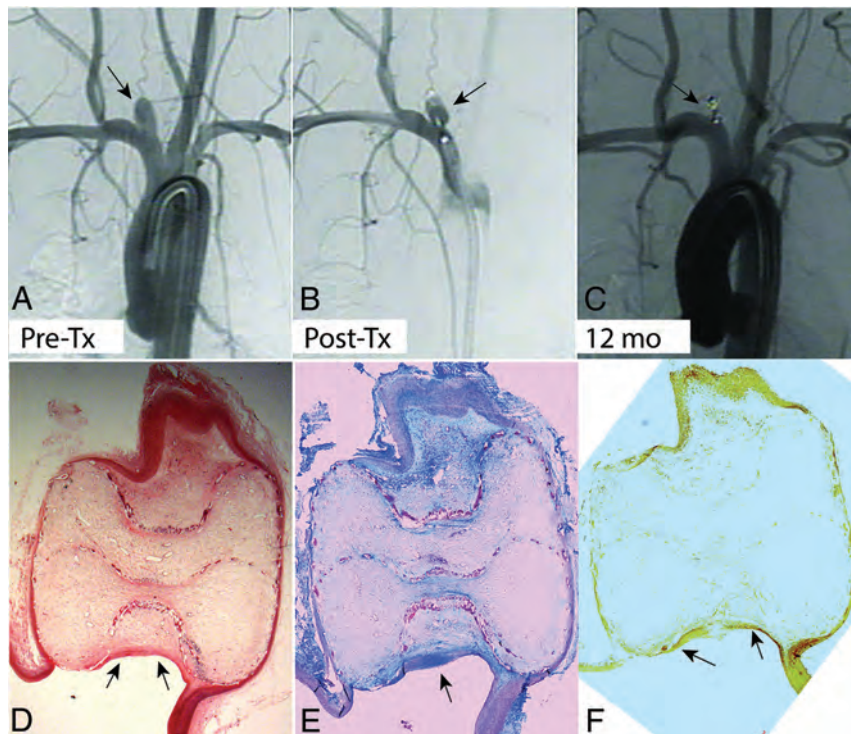


FIG 3. *A*, Anteroposterior DSA before aneurysm treatment (arrow). *B*, A DSA image immediately after DL device deployment shows residual aneurysm (arrow). *C*, A DSA image at 12 months shows complete occlusion (arrow) with substantial shortening of the device. *D*, Photomicrograph of a section (hematoxylin-eosin, original magnification $\times 12.5$) demonstrates an aneurysm sac filled with loose connective tissue, except for a small neck remnant. A neointimal layer completely traverses the neck interface near the proximal device markers (arrows). *E*, Photomicrograph of a section shows moderate collagen deposition throughout the aneurysm cavity (Masson trichrome stain, original magnification $\times 2.3$). Relatively high collagen content was noted near the proximal marker (arrow). *F*, Photomicrograph of a section shows the presence of smooth muscles throughout the aneurysm dome, as well as in the neointimal lining bridging the neck (arrows) (SMA immunostain, original magnification $\times 2.0$). Tx indicates treatment.

Aneurysms that demonstrated complete occlusion had more organized thrombus (76%, 16/21), while aneurysms that exhibited incomplete occlusion had unorganized thrombus (60%, 9/15) in the aneurysm dome. Most aneurysms showed open areas with no tissue filling and a neck remnant with a concave surface toward the dome (75% [12/16] in the complete occlusion group versus 90%

[18/20] in the incomplete occlusion group). Inflammation within the aneurysm lumen was absent or mild.

Aneurysms with the WSM showed a high level of organized thrombus compared with those without WSM (68% [15/22] versus 50% [7/14], $P = .09$) (Fig 3). The mean histologic healing score, inflammation score, fibrosis percentage, and SMA percentage was 5.0 [SD, 2.3], 1.5 [SD, 0.6], 15.9 [SD, 14.8], and 12.6 [SD, 9.6], respectively, in aneurysms with WSM, and 4.7 [SD, 3.2], 1.2 [SD, 0.8], 9.6 [SD, 8.0], and 9.5 [SD, 8.2], respectively, in aneurysms without WSM. There were no statistically significant differences in histologic healing, inflammation, fibrosis, and SMA between aneurysms with and without WSM. However, the percentage of WSM was moderately correlated with both fibrosis ($r = 0.37$, $P = .02$) and SMA levels ($r = 0.36$, $P = .032$) (Fig 4). WSM was not significantly correlated with either total histologic healing or inflammation.

DISCUSSION

Our study, which aimed to delineate the underlying mechanisms of WSM in WEB devices, demonstrates that WSM does not correlate with angiographic aneurysm occlusion or total histologic healing outcomes in the rabbit aneurysm model. However, WSM is positively associated with collagen and SMA levels, supporting the hypothesis that WSM is likely more related to aneurysm healing than external (eg, hemodynamic) compression alone.

The underlying mechanisms of WSM or compression could be multifaceted (eg, device size and construction, exact anatomic

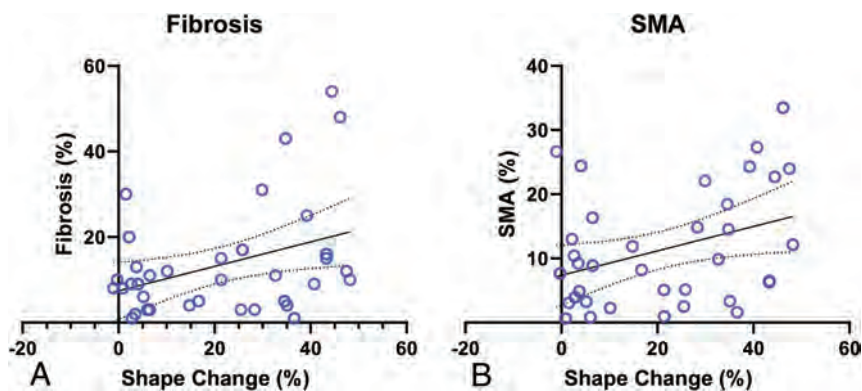


FIG 4. Correlation of the degree of device shape change with histologic features. Linear regression shows a significant positive correlation between the percentage of device length change and fibrosis (A) and SMA (B). Straight lines indicate regression; bowed lines indicate 95% CI.

configuration of aneurysm geometry and surrounding vessels, parent artery, aneurysm neck). Computational fluid dynamics simulations have shown that WEB device compression was positively correlated with computational fluid dynamics-derived inflow into the aneurysm.²⁸ In endoluminal FDs, pore density has been positively associated with aneurysm occlusion. Pore density at the proximal WEB device marker is relatively high compared with that in endoluminal devices,^{29,30} and it is highly unlikely that device compression would lead to reduced pore density at the neck. Rouchaud et al³¹ demonstrated, in coiled aneurysms, that a higher level of collagen in the aneurysm dome could trigger coil retraction from the neck orifice into the aneurysm cavity, resulting in aneurysm recurrence. Our findings suggest that WEB devices could behave like coils in the vascular microenvironment and result in device compression, and the contractile properties of connective tissue components in WEB-implanted aneurysms could lead to WSM. Proper endothelial cell growth across the pores of FDs in the aneurysm neck is also considered critical for aneurysm occlusion, in addition to the change in blood hemodynamics, for the mechanistic action of FDs. Endoluminal FDs placed in the healthy parent artery act as scaffolds for endothelial cell migration and neointima formation. In contrast, intrasaccular FDs are implanted in the aneurysm cavity, which represent a nonfunctional endothelium and a smooth-muscle layer and could explain the lack of neointimal coverage at the neck.

The observed WSM rate of 62% in the rabbit model is similar to that reported in clinical studies for the WEB device.³²⁻³⁶ Although DL WEB devices had higher adequate occlusion rates compared with SL devices in this study, the DL devices also demonstrated higher WSM. Given the small sample sizes and the difference of a single result providing statistical significance, taken together, these results suggest that WSM is not well-correlated with either device type.

Our study has several limitations. First, the variation in the angiographic working projection angle resulted in inaccurate measurements of the distance between device markers. Second, we arbitrarily defined 10% of the device as a threshold for WSM.

A high stringent limit may provide different results. Third, we did not evaluate numerous other factors, including mechanical and hemodynamic factors, which could influence the device shape changes.

CONCLUSIONS

WSM is not associated with incomplete aneurysm occlusion in the rabbit model but may be related to connective tissue formation and collagen deposition after WEB implantation.

Disclosures: Yonghong Ding—RELATED: Grant: National Institutes of Health NS071766, NS09-7038.* David F. Kallmes—RELATED: Grant: ev3/Covidien*; Consulting Fee or Honorarium: ev3/Covidien.* UNRELATED: Sequent Medical, Codman Neurovascular, National Institutes of Health, Surmodics, Benvenue Medi-cal, and MicroVention.* *Money paid to the institution.

REFERENCES

- De Leacy RA, Fargen KM, Mascitelli JR, et al. **Wide-neck bifurcation aneurysms of the middle cerebral artery and basilar apex treated by endovascular techniques: a multicentre, core lab adjudicated study evaluating safety and durability of occlusion (BRANCH).** *J Neurointerv Surg* 2019;11:31-36 CrossRef Medline
- Duman E, Coven I, Yildirim E, et al. **Endovascular treatment of wide necked ruptured saccular aneurysms with flow-diverter stent.** *Turk Neurosurg* 2017;27:362-67 CrossRef Medline
- Simgen A, Junk D, Reith W. **Flow diverter: a new therapy option for intracranial aneurysms.** *Radiologe* 2012;52:1118-24 CrossRef Medline
- Pumar JM, Mosqueira A, Cuellar H, et al. **Expanding the use of flow diverters beyond their initial indication: treatment of small unruptured aneurysms.** *J Neurointerv Surg* 2018;10:245-48 CrossRef Medline
- Kallmes DF, Ding YH, Dai D, et al. **A new endoluminal, flow-disrupting device for treatment of saccular aneurysms.** *Stroke* 2007;38:2346-52 CrossRef Medline
- Lubicz B, Collignon L, Raphaelli G, et al. **Flow-diverter stent for the endovascular treatment of intracranial aneurysms: a prospective study in 29 patients with 34 aneurysms.** *Stroke* 2010;41:2247-53 CrossRef Medline
- Ding YH, Lewis DA, Kadirvel R, et al. **The Woven EndoBridge: a new aneurysm occlusion device.** *AJNR Am J Neuroradiol* 2011;32:607-11 CrossRef Medline
- Ding YH, Dai D, Schroeder D, et al. **Experimental testing of the dual-layer Woven EndoBridge device using an elastase-induced aneurysm model in rabbits.** *Interv Neuroradiol* 2016;22:299-303 CrossRef Medline
- Papagiannaki C, Spelle L, Januel AC, et al. **WEB intrasaccular flow disruptor—prospective, multicenter experience in 83 patients with 85 aneurysms.** *AJNR Am J Neuroradiol* 2014;35:2106-11 CrossRef Medline
- Pierot L, Gubucz I, Buhk JH, et al. **Safety and efficacy of aneurysm treatment with the WEB: results of the WEBCAST 2 study.** *AJNR Am J Neuroradiol* 2017;38:1151-55 CrossRef Medline
- Pierot L, Klisch J, Liebig T, et al. **WEB-DL endovascular treatment of wide-neck bifurcation aneurysms: long-term results in a European series.** *AJNR Am J Neuroradiol* 2015;36:2314-19 CrossRef Medline
- Pierot L, Arthur A, Spelle L, et al. **Current evaluation of the safety and efficacy of aneurysm treatment with the WEB device.** *AJNR Am J Neuroradiol* 2016;37:586-87 CrossRef Medline
- Lescher S, Du Mesnil de Rochemont R, Berkefeld J. **Woven EndoBridge (WEB) device for endovascular treatment of complex**

- unruptured aneurysms: a single center experience. *Neuroradiology* 2016;58:383–90 CrossRef Medline
14. van Rooij WJ, Peluso JP, Bechan RS, et al. **WEB treatment of ruptured intracranial aneurysms.** *AJNR Am J Neuroradiol* 2016;37:1679–83 CrossRef Medline
 15. Sivan-Hoffmann R, Gory B, Riva R, et al. **One-year angiographic follow-up after WEB-SL endovascular treatment of wide-neck bifurcation intracranial aneurysms.** *AJNR Am J Neuroradiol* 2015;36:2320–24 CrossRef Medline
 16. Gherasim DN, Gory B, Sivan-Hoffmann R, et al. **Endovascular treatment of wide-neck anterior communicating artery aneurysms using WEB-DL and WEB-SL: short-term results in a multicenter study.** *AJNR Am J Neuroradiol* 2015;36:1150–54 CrossRef Medline
 17. Cognard C, Januel AC. **Remnants and recurrences after the use of the WEB intrasaccular device in large-neck bifurcation aneurysms.** *Neurosurgery* 2015;76:522–30 CrossRef Medline
 18. Herbreteau D, Bibi R, Narata AP, et al. **Are anatomic results influenced by WEB shape modification? Analysis in a prospective, single-center series of 39 patients with aneurysms treated with the WEB.** *AJNR Am J Neuroradiol* 2016;37:2280–86 CrossRef Medline
 19. Altes TA, Cloft HJ, Short JG, et al. **1999 ARRS Executive Council Award: creation of saccular aneurysms in the rabbit—a model suitable for testing endovascular devices.** *American Roentgen Ray Society. AJR Am J Roentgenol* 2000;174:349–54 CrossRef Medline
 20. Fujiwara NH, Cloft HJ, Marx WF, et al. **Serial angiography in an elastase-induced aneurysm model in rabbits: evidence for progressive aneurysm enlargement after creation.** *AJNR Am J Neuroradiol* 2001;22:698–703 Medline
 21. Caroff J, Mihalea C, Klisch J, et al. **Single-layer WEBS: intrasaccular flow disrupters for aneurysm treatment—feasibility results from a European study.** *AJNR Am J Neuroradiol* 2015;36:1942–46 CrossRef Medline
 22. Pierot L, Moret J, Turjman F, et al. **WEB treatment of intracranial aneurysms: feasibility, complications, and 1-month safety results with the WEB DL and WEB SL/SLS in the French Observatory.** *AJNR Am J Neuroradiol* 2015;36:922–27 CrossRef Medline
 23. Fiorella D, Arthur A, Byrne J, et al. **Interobserver variability in the assessment of aneurysm occlusion with the WEB aneurysm embolization system.** *J Neurointerv Surg* 2015;7:591–95 CrossRef Medline
 24. Rouchaud A, Brinjikji W, Ding YH, et al. **Evaluation of the angiographic grading scale in aneurysms treated with the WEB device in 80 rabbits: correlation with histologic evaluation.** *AJNR Am J Neuroradiol* 2016;37:324–29 CrossRef Medline
 25. Dai D, Ding Y-H, Lewis DA, et al. **A proposed ordinal scale for grading histology in elastase-induced, saccular aneurysms.** *AJNR Am J Neuroradiol* 2006;27:132–38 Medline
 26. Fitzgerald S, Wang S, Dai D, et al. **Orbit image analysis machine learning software can be used for the histological quantification of acute ischemic stroke blood clots.** *PLoS One* 2019;14:e0225841 CrossRef Medline
 27. Dai D, Ding YH, Danielson MA, et al. **Histopathologic and immunohistochemical comparison of human, rabbit, and swine aneurysms embolized with platinum coils.** *AJNR Am J Neuroradiol* 2005;26:2560–68 Medline
 28. Caroff J, Mihalea C, Da Ros V, et al. **A computational fluid dynamics (CFD) study of WEB-treated aneurysms: can CFD predict WEB “compression” during follow-up?** *J Neuroradiol* 2017;44:262–68 CrossRef Medline
 29. Klisch J, Sychra V, Strasilla C, et al. **The Woven EndoBridge cerebral aneurysm embolization device (WEB II): initial clinical experience.** *Neuroradiology* 2011;53:599–607 CrossRef Medline
 30. Maragos GA, Dmytriw AA, Salem MM, et al. **Overview of different flow diverters and flow dynamics.** *Neurosurgery* 2020;86:521–34 CrossRef Medline
 31. Rouchaud A, Brinjikji W, Dai D, et al. **Autologous adipose-derived mesenchymal stem cells improve healing of coiled experimental saccular aneurysms: an angiographic and histopathological study.** *J Neurointerv Surg* 2018;10:60–65 CrossRef Medline
 32. Pierot L, Moret J, Turjman F, et al. **WEB treatment of intracranial aneurysms: clinical and anatomic results in the French Observatory.** *AJNR Am J Neuroradiol* 2016;37:655–59 CrossRef Medline
 33. Armoiry X, Turjman F, Hartmann DJ, et al. **Endovascular treatment of intracranial aneurysms with the WEB device: a systematic review of clinical outcomes.** *AJNR Am J Neuroradiol* 2016;37:868–72 CrossRef Medline
 34. Behme D, Berlis A, Weber W. **Woven EndoBridge Intrasaccular flow disrupter for the treatment of ruptured and unruptured wide-neck cerebral aneurysms: report of 55 cases.** *AJNR Am J Neuroradiol* 2015;36:1501–06 CrossRef Medline
 35. Arthur AS, Molyneux A, Coon AL, et al. **WEB-IT Study investigators. The safety and effectiveness of the Woven EndoBridge (WEB) system for the treatment of wide-necked bifurcation aneurysms: final 12-month results of the pivotal WEB Intrasaccular Therapy (WEB-IT) Study.** *J Neurointerv Surg* 2019;11:924–30 CrossRef Medline
 36. Pierot L, Moret J, Barreau X, et al. **Safety and efficacy of aneurysm treatment with WEB in the cumulative population of three prospective, multicenter series.** *J Neurointerv Surg* 2018;10:553–62 CrossRef Medline

Assessment of 4D MR Angiography at 3T Compared with DSA for the Follow-up of Embolized Brain Dural Arteriovenous Fistula: A Dual-Center Study

 B. Dissaux,  F. Eugène,  J. Ognard,  J.-Y. Gauvrit,  J.-C. Gentric, and  J.-C. Ferré

ABSTRACT

BACKGROUND AND PURPOSE: 4D contrast-enhanced MRA in the follow-up of treated dural arteriovenous fistulas has rarely been evaluated. Our aim was to evaluate its diagnostic performance at 3T in the follow-up of embolized dural arteriovenous fistulas using DSA as the standard of reference.

MATERIALS AND METHODS: Patients treated for dural arteriovenous fistulas in 2 centers between 2008 and 2019 were included if they met the following criteria: 1) dural arteriovenous fistula embolization, and 2) follow-up imaging with <6 months between DSA and 4D contrast-enhanced MRA. Two readers reviewed the 4D contrast-enhanced MRA images, first independently, then in consensus to detect any residual/recurrent dural arteriovenous fistula and to grade cases according to the Cognard classification system. Interobserver and intermodality agreement for the detection of a residual dural arteriovenous fistula and stratification of bleeding risk (0-I-IIa; IIb-IIa+b-III-IV-V) was calculated using κ coefficients.

RESULTS: A total of 51 pairs of examinations for 44 patients (median age, 65 years; range, 25–81 years) were analyzed. Interobserver agreement for the detection and stratification of bleeding risk was, respectively, $\kappa = 0.8$ (95% CI, 0.6–1) and $\kappa = 0.8$ (95% CI, 0.5–1). After consensus review, the sensitivity and specificity of 4D contrast-enhanced MRA for the detection of residual/recurrent dural arteriovenous fistula was 63.6% (95% CI, 40.7%–82.8%) and 96.6% (95% CI, 82.2%–99.9%), respectively. The positive and negative predictive values of 4D contrast-enhanced MRA were 93.3% (95% CI, 68.1%–99.8%) and 77.8% (95% CI, 60.8%–89.9%). Intermodality agreement for the detection and stratification of bleeding risk was good, with $\kappa = 0.60$ (95% CI, 0.3–0.8).

CONCLUSIONS: 4D contrast-enhanced MRA at 3T is of interest in the follow-up of treated dural arteriovenous fistulas but lacks the sensitivity to replace arteriography.

ABBREVIATIONS: DAVF = dural arteriovenous fistula; 4D-MRA = 4D contrast-enhanced magnetic resonance angiography

Dural arteriovenous fistulas (DAVFs) are abnormal arteriovenous connections between dural vessels. The risk of intracranial hemorrhage is variable according to the venous drainage patterns.^{1–5} There are several treatment options, including surgical resection and endovascular embolization, which can be attempted to achieve a cure. The risk of bleeding persists as long as an anatomic cure is not completely achieved, with risk depending on the residual venous drainage pattern. Therefore, it is

necessary to confirm that the DAVF has been effectively cured after treatment.

Due to its high sensitivity and specificity, DSA is the current method of choice in the diagnosis and follow-up of DAVFs despite several disadvantages, such as radiation exposure for patients and medical staff, injection risk of iodinated contrast agent (including allergy and nephrotoxicity), and neurologic procedural risks (0.30%–2.63%).^{1,6} The technique has very good spatial and, especially, temporal resolution, allowing precise evaluation of a potential residual shunt.

Several noninvasive cross-sectional imaging techniques such as 3D-TOF-MRA and 3D contrast-enhanced MRA have been used to reduce the risk of invasive procedures for patients who otherwise would undergo repeat angiography during treatment planning or follow-up. The diagnostic accuracy of these techniques has proved to be relatively good, but not sufficient to replace DSA due to limited spatial resolution and a static temporal view without temporal hemodynamic information, such as arterial

Received March 19, 2020; accepted after revision September 27.

From the Department of Neuroradiology (B.D., F.E., J.-Y.G., J.-C.F.), Centre Hospitalier Universitaire Rennes, Rennes, France; Department of Medical Imaging (B.D., J.O., J.-C.G.), Centre Hospitalier Universitaire La Cavale Blanche, Brest, France; GETBO group EA3878 (B.D., J.-C.G.), Université de Bretagne Occidentale, Brest, France; LATIM U1101 (J.O.), INSERM, Université de Bretagne Occidentale, Brest, France; Empenn Unit U1228 (J.-Y.G., J.-C.F.), INSERM, INRIA, Université Rennes 1, Rennes, France.

Please address correspondence to Brieg Dissaux, MD, Service d'Imagerie Médicale, CHU de la Cavale Blanche, Boulevard Tanguy-Prigent, 29609 Brest cedex, France; e-mail: brieg.dissaux@chu-brest.fr
<http://dx.doi.org/10.3174/ajnr.A6903>

phase venous filling.³ 4D contrast-enhanced MRA (4D-MRA) was conceived to solve this problem and provide better temporal resolution while also preserving spatial resolution. With improving technology, it became a widely used technique with the advantage of a dynamic DSA-like evaluation of DAVFs. Previous studies report time-resolved 3T MR angiography as an appropriate tool for DAVF diagnosis and monitoring. However, the value of 4D-MRA for the follow-up of patients with treated DAVFs has rarely been evaluated.

We hypothesized that this technique could be valuable for the follow-up and posttherapeutic assessment of DAVFs. With DSA images as the standard of reference, the purpose of this study was to evaluate the performance of 4D-MRA at 3T in the follow-up of patients with treated DAVFs.

MATERIALS AND METHODS

Study Design

Institutional review board approval was granted (No. 19.87), and informed consent was waived due to the study design. All patients treated for DAVFs in 2 university hospital departments (Rennes and Brest, France) were included in a data base. For this study, patients imaged between August 2008 and May 2019 were included if they met the following criteria:

1. They had a DAVF treated with embolization
2. They underwent both 4D-MRA at 3T and DSA during follow-up
3. Both examinations were performed within a 6-month interval without treatment between them.

Treatment Strategy

For all patients, the indication and strategy of treatment were based on multidisciplinary decisions involving neurologists, neurosurgeons, and neuroradiologists.

MR Imaging

All MRA examinations were performed on a 3T MR imaging system (Achieva and Ingenia, Philips Healthcare, Best, Netherlands). All contrast-enhanced 4D-MRA examinations consisted of coronal, sagittal, and axial MIP subtraction images derived from a sagittal time-resolved 3D T1-weighted fast gradient-echo sequence. Several acquisition schemes were used according to the brain coverage (full or two-thirds). At least 20 dynamic acquisitions were performed with a temporal resolution of 0.9–1.7 seconds per volume and a native spatial resolution from $0.8 \times 0.8 \times 1.6 \text{ mm}^3$ to $1.1 \times 1.1 \times 2.8 \text{ mm}^3$ and, after interpolation, ranging from $0.5 \times 0.5 \times 0.9 \text{ mm}^3$ to $0.94 \times 0.94 \times 1.4 \text{ mm}^3$. The 15-mL macrocyclic gadolinium bolus was administered intravenously at a minimum rate of 3 mL/s.⁷

DSA Technique

DSA was performed on a biplane angiography system (Allura, Philips Healthcare, Best, Netherlands and Artis, Siemens Healthineers, Erlangen, Germany). DSA images involved selective injection of internal and external carotid and vertebral arteries with anterior-posterior and lateral projections, supplemented by additional views when necessary. Each projection was acquired with a frequency of 2–3 images per second. For each

projection, a 6- to 10-mL bolus of nonionic iodinated contrast material was injected with a power injector.

End Points

The primary end point was to evaluate the diagnostic reproducibility and performance of 4D-MRA for detecting any residual/recurrent shunts in patients with treated DAVFs using DSA as the standard of reference. The secondary end point was to evaluate the diagnostic reproducibility and performance of 4D-MRA for detecting any high-bleeding-risk residual/recurrent shunts in patients with treated DAVFs using DSA as the standard of reference.

Interpretation

Readers were blinded to all clinical data except the original location of the treated DAVF. Only the 3 MIPs were used to read the 4D-MRA. One reader (J.-C.F., reader 3) with 17 years' experience in neuroradiology reviewed the DSA images. Two readers (F.E., reader 1, and B.D., reader 2) with 9 and 5 years' experience in neuroradiology, respectively, reviewed the 4D-MRA images. First, readers 1 and 2 assessed the quality of the 4D-MRA images. 4D MRA image-quality scores ranged among 0 (no vascular study possible), 1 (vascular study possible with low diagnostic confidence), 2 (vascular study possible with adequate diagnostic confidence), and 3 (vascular study possible with high diagnostic confidence). The readers independently assessed the presence of residual/recurrent DAVFs on the 4D-MRA and DSA images. Then, when present, each DAVF was graded according to the Cognard classification scheme and divided into 2 groups based on bleeding risk: low-bleeding-risk DAVFs (types I and IIa) and high-bleeding-risk DAVFs (types IIb, IIa + b, III, IV, and V).⁵ Second, a consensus reading (readers 1 and 2) of the 4D-MRA images was conducted to solve any discrepancies. Third, a retrospective explanatory analysis was performed in consensus by the 3 readers to explain intermodality (4D-MRA and DSA) differences.

Data Analysis and Sample Size

Baseline characteristics, including age and fistula type, were summarized using descriptive statistics. The intervals among DSA and 4D-MRA, treatment, and the first imaging technique (DSA or 4D-MRA) were recorded. 4D-MRA interobserver and intermodality agreement was assessed using κ for the following: 1) residual/recurrent DAVF detection, and 2) bleeding-risk grading with a 2×2 contingency table (low-risk: absence of a shunt and Cognard types I–IIa; high-risk: Cognard types IIb, III, IV, and V) and on a 3-tier modified scale (comprising absence of a shunt; Cognard types I–IIa; and Cognard types IIb, III, IV, and V). The Cohen κ coefficient was calculated using quadratic weighting (for bleeding-risk grading with the 3-tier modified scale). The 95% confidence intervals for κ were estimated with the bootstrap method. κ statistics were interpreted as suggested by Landis and Koch ($\kappa < 0$, poor agreement; 0.01–0.20, slight agreement; 0.21–0.40, fair agreement; 0.41–0.60, moderate agreement; 0.61–0.80, substantial agreement; and 0.81–1, almost perfect agreement).

The binary decision regarding the presence of a residual/recurrent DAVF and a residual high-bleeding-risk DAVF (low

risk: absence of a shunt and Cognard types I-IIa; high risk: Cognard types IIb, III, IV, and V) was used to determine the diagnostic performance of 4D-MRA (sensitivity, specificity, positive predictive value, negative predictive value, the area under the ROC curve), and 95% confidence intervals were estimated with generalized estimating equations.

All statistical analyses were performed using STATA software (STATA/MP 16.0; StataCorp).

RESULTS

We included 51 examination pairs (4D-MRA and DSA within 6 months) for 44 patients with a median age of 65 years (range, 25–81 years). No examination (neither 4D-MRA nor DSA) was included >1 time. Nineteen (43%) of the 44 patients were women. Pretreatment DAVF grading was as follows—type I: $n = 1$ (2.3%), type IIa: $n = 2$ (4.6%), type IIb: $n = 13$ (29.5%), type IIa + b: $n = 0$ (0%), type III: $n = 13$ (29.5%), type IV: $n = 12$ (27.3%), and type V: $n = 3$ (6.8%). Thirty-nine (88.6%) patients underwent 1 embolization session, and 5 patients (11.4%) underwent 2 sessions. The corresponding flowchart is shown in Fig 1. The median interval between 4D-MRA and DSA was 49 days (range, 0–155 days). 4D-MRA was performed before DSA in 31 (70.4%) examination pairs. The median interval between DAVF treatment and the first examination was 124 days (range, 2–730 days). The DSA images yielded the following results—no residual/

recurrent DAVF: 29/51 (56.9%), type I: $n = 4$ (7.9%), type IIa: $n = 4$ (7.9%), type IIb: $n = 1$ (1.9%), type IIa + b: $n = 0$ (0%), type III: $n = 11$ (21.6%), type IV: $n = 1$ (1.9%), and type V residual/recurrent DAVF: $n = 1$ (1.9%). Twelve examination pairs were obtained from 5 patients: After the first follow-up ($n = 5$), 4 examination pairs were obtained after a new treatment and 3 later in the follow-up of the first treatment.

4D-MRA Image Quality

After reaching a consensus, all images were given a minimum score of 1. The median quality score was 3. One (1.9%) 4D-MRA examination scored 1, seven (13.7%) scored 2, and 43 (84.4%) scored 3 on the 4-point grading scale, respectively.

4D-MRA Interobserver Agreement

One reader assigned 1 examination a score of zero (no vascular study possible). Fifty examinations were assessed for interobserver agreement. Interobserver agreement was considered substantial for residual/recurrent DAVF detection, with an agreement of 92% and $\kappa = 0.8$ (95% CI, 0.6–1). Disagreement among readers (readers 1 and 2) is shown in Table 1. Interobserver agreement was considered substantial in terms of the ability to detect a fistula at risk of hemorrhage, with an agreement of 92% and $\kappa = 0.8$ (95% CI, 0.5–1) in a 2×2 contingency table (low-risk: absence of a shunt and types I–IIa; high-risk: types IIb, III, IV, and V) and an agreement of 92% and $\kappa = 0.8$ (95% CI, 0.8–0.9) on a 3-tier modified scale (comprising absence of a shunt; types I–IIa; and IIb, III, IV, and V).

Intermodality Agreement

After reaching a 4D-MRA reading consensus, 51 comparisons were available. Table 2 provides the results for the 2 modalities. Disagreement between readers 1 and 2 is shown in Table 3.

Intermodality agreement was considered substantial for residual/recurrent DAVF detection, with an agreement of 82.4% and $\kappa = 0.6$ (95% CI, 0.4–0.8). Intermodality agreement

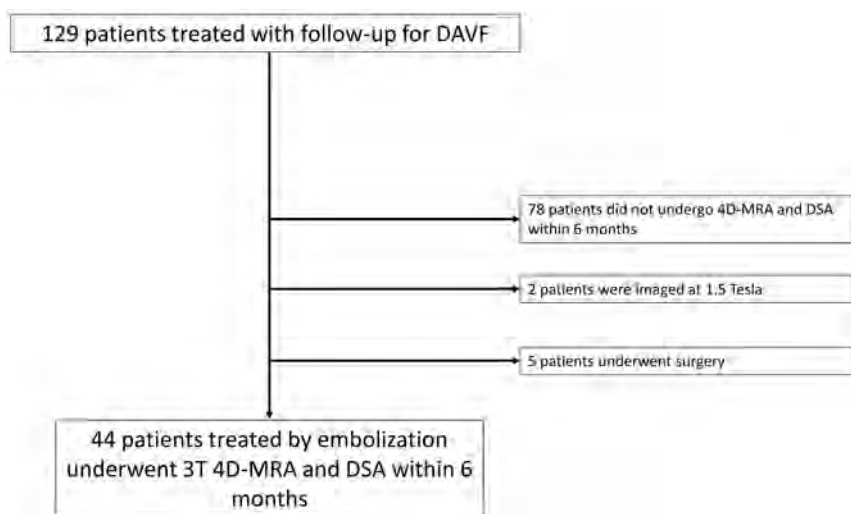


FIG 1. Flow chart.

Table 1: Interreader disagreement in 4D-MRA residual/recurrent DAVF classification

Dural Fistula Location	4D-MRA Classification Reader 1	4D-MRA Classification Reader 2	4D-MRA Classification Consensus	DSA Classification	4D-MRA Consensus Quality Score
Hemispheric right	0	III	III	III	3
Parasagittal right	0	III	0	0	3
SSS	0	IIa	0	0	1
Epiphyseal	0	III	III	III	3
Sinus lateralis left	I	0	I	I	3
Medulla	III	0	0	V	3

Note:—SSS indicates superior sagittal sinus.

Table 2: Contingency table of residual/recurrent DAVF grading according to technique (4D-MRA and DSA)^a

DSA	4D-MRA							
	No Shunt	Type I ^b	Type IIa ^b	Type IIb ^c	Type IIa+b ^c	Type III ^c	Type IV ^c	Type V ^c
No shunt	28	0	0	0	1	0	0	0
Type I ^b	1	3	0	0	0	0	0	0
Type IIa ^b	1	0	3	0	0	0	0	0
Type IIb ^c	0	0	1	0	0	0	0	0
Type IIa + b ^c	0	0	0	0	0	0	0	0
Type III ^c	4	0	0	0	0	4	3	0
Type IV ^c	1	0	0	0	0	0	0	0
Type V ^c	1	0	0	0	0	0	0	0

^a Consensus grading according to Cognard et al.⁵^b Low bleeding risk.^c High bleeding risk.**Table 3: Intermodality discrepancy in residual/recurrent dural arteriovenous fistula detection and classification^a**

Location	Pretreatment Grading	4D-MRA/DSA		4D-MRA Consensus Grading	4D-MRA Reader Disagreement (Yes/No)	Year	4D-MRA Consensus Quality Score	Possible Explanation
		Interval (Days)	DSA Grading					
Parasagittal right	III	65	IV	0	No	2010	3	Confusion between occipital artery and a cortical vein
Cavernous sinus right	III	59	III	0	No	2015	2	Cortical vein visible but missed by 4D-MRA readers
Transverse sinus left	IIb	112	I	0	No	2017	2	Artery and vein overlay
SSS	IIb	129	0	IIa + b	No	2012	3	Early drainage due to a meningioma
Cavernous sinus left	III	0	III	0	No	2015	3	Cortical vein visible but missed by 4D-MRA readers
Posterior fossa right	IV	43	III	0	No	2009	3	Early opacification of all dural sinuses; shunt missed due to misinterpretation of time sequence in 4D-MRA
Sigmoid sinus left	III	2	IIa	0	No	2011	2	Cortical vein visible but missed by 4D-MRA readers
Medulla	V	3	V	0	Yes (III/0)	2011	3	Not visible in the FOV
Parieto-occipital left	III	85	III	0	No	2018	2	Cortical vein visible but missed by 4D-MRA readers

Note:—SSS indicates superior sagittal sinus.^a Grading according to Cognard et al.⁵

was considered moderate in terms of the ability to detect a fistula at risk of hemorrhage, with an agreement of 84.3% and $\kappa = 0.6$ (95% CI, 0.3–0.8) in a 2 × 2 contingency table (low-risk: absence of a shunt and types I–IIa; high-risk: types IIb, III, IV, and V) and an agreement of 83.3% and $\kappa = 0.6$ (95% CI, 0.5–0.7) on a 3-tier modified scale (comprising absence of a shunt; types I–IIa; types IIb, III, IV, and V).

Diagnostic Value of 4D-MRA Compared with DSA

The diagnostic accuracy of 4D-MRA in terms of residual/recurrent DAVF detection yielded a sensitivity of 63.6% (95% CI, 40.7%–82.8%), specificity of 96.6% (95% CI, 82.2%–99.9%), positive predictive value of 93.3% (95% CI,

68.1%–99.8%), and negative predictive value of 77.8% (95% CI, 60.8%–89.9%). The area under curve score was 0.8 (95% CI, 0.7–0.9).

The diagnostic accuracy of 4D-MRA in terms of bleeding-risk grading yielded a sensitivity of 50% (95% CI, 23%–77%), specificity of 97.3% (95% CI, 85.8%–99.9%), positive predictive value of 87.5% (95% CI, 47.3%–99.7%), and negative predictive value of 83.7% (95% CI, 69.3%–93.2%). The area under the curve score was 0.7 (95% CI, 0.6–0.8).

Retrospective Review of Intermodality Disagreement

As described in Table 3, intermodality disagreement involved 8 false-negatives and 1 false-positive result. There were several

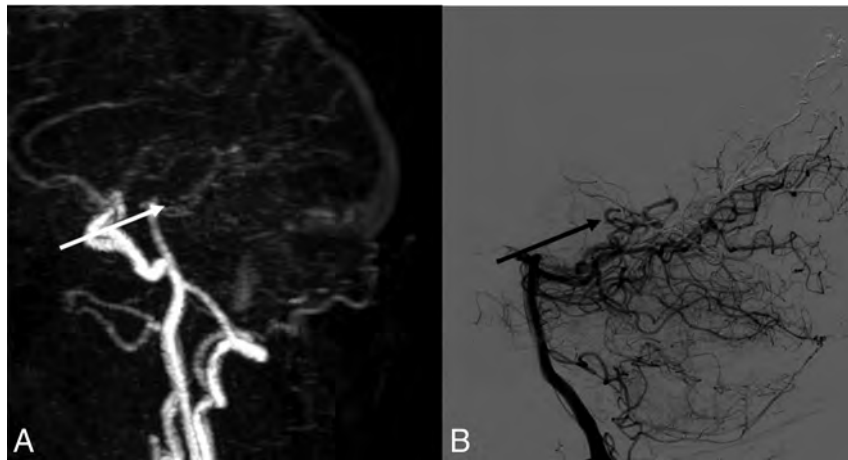


FIG 2. A, Sagittal MIP of 4D-MRA at arterial phase. B, Cerebral arteriography through the left vertebral artery in a sagittal view. The white arrow in A and the black arrow in B show early opacification of an epiphyseal vein, before the superior sagittal sinus, confirming an arteriovenous shunt. This examination was rated type III on both imaging modalities.

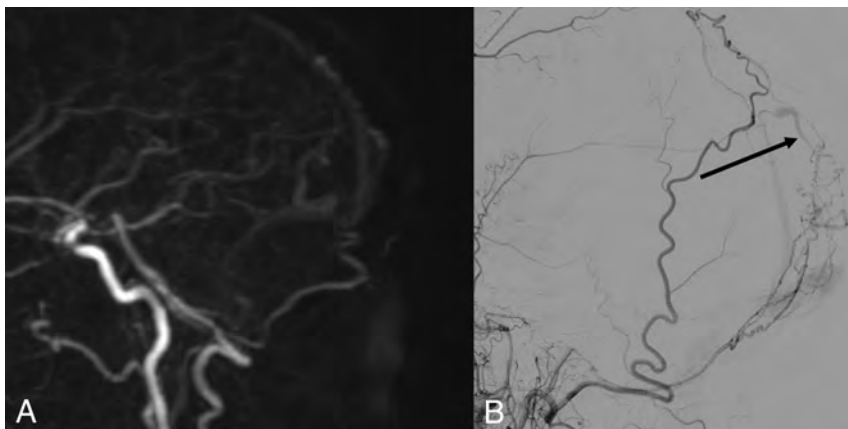


FIG 3. A, Sagittal MIP of 4D-MRA at late arterial phase. B, Cerebral arteriography through the left external carotid artery in a sagittal view. The black arrow in B shows early opacification of an occipital vein, confirming an arteriovenous shunt not found in A.

DAVF locations: supra- or infra tentorial, near the midsagittal plane, or more laterally. Figs 2 and 3 provide examples of a true-positive result and a false-negative result of 4D-MRA. Only 1 intermodality disagreement was also an interobserver disagreement. The false-positive case was due to a concomitant condition (early venous drainage due to a meningioma in the vicinity of the DAVF). Six of the 8 false-negative cases involved types III, IV, or V DAVFs, ie, DAVFs with cortical (small) veins. In 4 cases, the cortical vein was shown to be retrospectively present but was missed by all 3 readers.

DISCUSSION

This study assessed the diagnostic accuracy of 4D-MRA at 3T for detecting any recurrent/residual shunts in treated DAVFs. The sensitivity and specificity of the technique were, respectively, 63.6% (95% CI, 40.7%–82.8%) and 96.6% (95% CI, 82.2%–99.9%), with substantial intermodality agreement compared with

DSA, which yielded agreement of 82.4% and $\kappa = 0.6$ (95% CI, 0.4%–0.8%).

4D contrast-enhanced MRA is widely used to detect, characterize, and monitor brain vascular malformations and conditions, especially brain arteriovenous malformations.^{6,8} Previous studies reported the diagnostic performance of 4D-MRA for detection and grading of DAVFs. Contrary to brain arteriovenous malformations, only a few studies documented treated DAVFs, and they concerned limited numbers of patients.^{3,6,9-11} The value of 4D-MRA in posttreatment follow-up is, therefore, currently not well-defined. Meckel et al⁹ evaluated the diagnostic performance of MRA using a time-resolved 3D contrast-enhanced technique with 18 examination pairs (9 in a diagnosis group and 9 in a post-treatment follow-up group). On initial diagnosis, both readers identified signs indicative of a DAVF in all 9 cases of angiographically proved fistulas. In the follow-up group (post-embolization or surgery), both readers were able to differentiate between complete occlusion of a fistula and a patent residual fistula. However, DAVF occlusion was complete in 5 of the 9 patients. The readers could also use subtracted volumes in addition to 3-plane MIP images, which may have improved diagnostic accuracy.⁹ Bink et al¹⁰ reported diagnostic accuracy with 3T MR imaging, with sensitivities and specificities ranging from 84% to 100% for 3 readers tasked with detecting DAVFs in 38 patients (19 with DAVFs and 19 without). The readers assessed 4D-MRA in addition to 3D-TOF-MRA and 3D-MPRAGE. One patient had undergone endovascular therapy, and 1 patient had undergone surgical closure.¹⁰ In a consensus reading, Ertl et al¹¹ reported excellent intermodality agreement ($\kappa = 1$) for the pretreatment Cognard classification of lateral DAVFs in 24 patients using additional anatomic images such as TOF-MRA, contrast-enhanced T1-, axial T2-, and axial T2*-weighted images. However, there were no type III DAVFs and just 3 type IV DAVFs according to the Cognard classification. Farb et al¹² compared 4D-MRA at 3T with DSA for the diagnosis and classification of DAVFs in 42 cases, which included surveillance of a previously cured fistula in 15 cases. In 93% (39/42) of DAVFs, 3 readers were unanimous and correct in identifying or excluding them. However, all examinations performed for surveillance were negative for DSA, thus limiting the generalizability of the results in this population.

Unlike in previous studies, we chose to assess 4D-MRA alone without additional morphologic images.^{10,11} This could partly explain the lower performance in this context. Also, post-therapeutic changes, such as embolization product artifacts or anatomic changes, could partly explain these results. Another explanation might be the higher proportion of Cognard type III and IV DAVFs in our study compared with that of Ertl et al.¹¹ Indeed, direct drainage into a cortical vein might reduce DAVF detection with 4D-MRA.

The sensitivity and specificity of the technique in terms of the ability to detect a fistula at risk of hemorrhage was, respectively, 50% (95% CI, 23%–77%) and 97.3% (95% CI, 85.8%–99.9%), with an agreement of 84.3% and $\kappa = 0.6$ (95% CI, 0.3–0.8) in a 2×2 contingency table (low-risk: absence of a shunt and types I–IIa; high-risk: types IIb, III, IV, and V) and an agreement of 83.3% and $\kappa = 0.6$ (95% CI, 0.5–0.7) on a 3-tier modified scale (comprising absence of a shunt; types I–IIa; and IIb, III, IV, and V). Detecting the bleeding risk of a residual/recurrent DAVF is crucial in determining further treatment (false-negative rate of 0.5). Six of 8 false-negatives on 4D-MRA were types III–V DAVFs. We note that the cortical vein was shown to be retrospectively present but was missed by all 3 readers in 4 cases. For 1 patient, the cortical veins were not included in the FOV. In addition to this acquisition defect, discrepancies could be explained by the lack of spatial or temporal resolution. Also, we might speculate that 3-plane MIP image reading was perhaps not the optimal method. Multiplanar, thin MIP reconstructions could help to alleviate confusion between arteries and veins, though the existing literature on the method for reading 4D-MRA images for DAVF (thick MIP, thin MIP, MPR) is limited.

Interobserver agreement was considered substantial for residual/recurrent DAVF detection, with an agreement of 92% and $\kappa = 0.8$ (95% CI, 0.6–1). Farb et al¹² reported agreement among 3 readers of 0.94 [SD, 0.04] ($P < .001$). In our study, 4 of 6 cases of disagreement involved type III DAVFs, ie, DAVFs with direct drainage into a cortical vein. All except 1 disagreement involved high-quality (score = 3) 4D-MRA images.

Limitations

Limitations of our study include its retrospective design and the relatively small number of patients. However, to the best of our knowledge, this is the largest series of patients in the particular case of postembolization evaluation. Indeed, DAVF is a rare disease, and we focused on patients with embolized DAVFs who had undergone DSA and 4D-MRA within a 6-month interval during their follow-up, and this focus reduced the number of eligible patients, possibly resulting in a selection bias because patients with negative findings on DSA or who were asymptomatic but with a residual low-risk DAVF with DSA were less likely to benefit from both modalities within 6 months. The reason for this focus was because it is the first line of treatment for most DAVFs, and surgical treatment may involve the use of materials that can cause artifacts.¹ Second, different 4D-MRA techniques were used due to the study length and the 2 centers involved. Although Lin et al¹³ reported a trend toward better performance in newer MR imaging studies, in our cases, intermodality discrepancies involved recent and older examinations, as shown in Table

3. Furthermore, we graded image quality to overcome this limitation.⁷ Third, we read only the 4D-MRA images without any other sequences. This may seem artificial, but it was essential for assessing the diagnostic accuracy of the technique (4D-MRA). Fourth, the statistical distribution of the DAVF types based on the Cognard classification with a higher proportion of true-negative results (DSA, 0; 4D-MRA, 0) was expected but may have influenced the κ values.

As previously shown, the use of consensus reading for 4D-MRA in our study improved the diagnostic accuracy and might, therefore, be recommended.¹² Also, several publications have described novel tools that can further improve 4D-MRA efficacy, opening up new prospects for DAVF assessment before and after treatment.^{14–17} Indeed, venous arterial spin-labeling has shown high sensitivity and specificity in detecting dural arteriovenous fistulas;^{15,16} and the novel temporal spatial acceleration method, HYPRFlow, has also been reported to provide accurate delineation of DAVF vasculature.¹⁴

CONCLUSIONS

4D-MRA is a useful noninvasive technique for the follow-up of treated DAVFs. However, given its current limitations, it is not sufficient to confirm an effective cure but can be used as a diagnostic confirmation test. DSA remains mandatory for ensuring optimum bleeding-risk assessment in cases of residual/recurrent DAVF.

Disclosures: François Eugène—UNRELATED: Consultancy: Biomodex. Jean-Christophe Gentic—UNRELATED: Consultancy: Medtronic, Stryker, Balt; Stock/Stock Options: INTRADYS.

REFERENCES

1. Reynolds MR, Lanzino G, Zipfel GJ. **Intracranial dural arteriovenous fistulae.** *Stroke* 2017;48:1424–31 CrossRef Medline
2. Borden JA, Wu JK, Shucart WA. **A proposed classification for spinal and cranial dural arteriovenous fistulous malformations and implications for treatment.** *J Neurosurg* 1995;82:166–79 CrossRef Medline
3. Nishimura S, Hirai T, Sasao A, et al. **Evaluation of dural arteriovenous fistulas with 4D contrast-enhanced MR angiography at 3T.** *AJNR Am J Neuroradiol* 2010;31:80–85 CrossRef Medline
4. Van Dijk JM, TerBrugge KG, Willinsky RA, et al. **Clinical course of cranial dural arteriovenous fistulas with long-term persistent cortical venous reflux.** *Stroke* 2002;33:1233–36 CrossRef Medline
5. Cognard C, Gobin YP, Pierot L, et al. **Cerebral dural arteriovenous fistulas: clinical and angiographic correlation with a revised classification of venous drainage.** *Radiology* 1995;194:671–80 CrossRef Medline
6. Soize S, Bouquigny F, Kadziolka K, et al. **Value of 4D MR angiography at 3T compared with DSA for the follow-up of treated brain arteriovenous malformation.** *AJNR Am J Neuroradiol* 2014;35:1903–09 CrossRef Medline
7. Raoult H, Ferré JC, Morandi X, et al. **Quality-evaluation scheme for cerebral time-resolved 3D contrast-enhanced MR angiography techniques.** *AJNR Am J Neuroradiol* 2010;31:1480–87 CrossRef Medline
8. Hadizadeh DR, Kukuk GM, Steck DT, et al. **Noninvasive evaluation of cerebral arteriovenous malformations by 4D-MRA for preoperative planning and postoperative follow-up in 56 patients: comparison with DSA and intraoperative findings.** *AJNR Am J Neuroradiol* 2012;33:1095–101 CrossRef Medline

9. Meckel S, Maier M, San Millan Ruiz D, et al. **MR angiography of dural arteriovenous fistulas: diagnosis and follow-up after treatment using a time-resolved 3D contrast-enhanced technique.** *AJNR Am J Neuroradiol* 2007;28:877–84 Medline
10. Bink A, Berkefeld J, Wagner M, et al. **Detection and grading of dAVF: prospects and limitations of 3T MRI.** *Eur Radiol* 2012;22:429–38 CrossRef Medline
11. Ertl L, Brückmann H, Kunz M, et al. **Assessment and treatment planning of lateral intracranial dural arteriovenous fistulas in 3 T MRI and DSA: a detailed analysis under consideration of time-resolved imaging of contrast kinetics (TRICKS) and ce-MRA sequences.** *Eur Radiol* 2016;26:4284–92 CrossRef Medline
12. Farb RI, Agid R, Willinsky RA, et al. **Cranial dural arteriovenous fistula: diagnosis and classification with time-resolved MR angiography at 3T.** *AJNR Am J Neuroradiol* 2009;30:1546–51 CrossRef Medline
13. Lin YH, Lin HH, Liu HM, et al. **Diagnostic performance of CT and MRI on the detection of symptomatic intracranial dural arteriovenous fistula: a meta-analysis with indirect comparison.** *Neuroradiology* 2016;58:753–63 CrossRef Medline
14. Clark Z, Johnson KM, Wu Y, et al. **Accelerated time-resolved contrast-enhanced magnetic resonance angiography of dural arteriovenous fistulas using highly constrained reconstruction of sparse cerebrovascular data sets.** *Invest Radiol* 2016;51:365–71 CrossRef Medline
15. Amukotuwa SA, Marks MP, Zaharchuk G, et al. **Arterial spin-labeling improves detection of intracranial dural arteriovenous fistulas with MRI.** *AJNR Am J Neuroradiol* 2018;39:669–77 CrossRef Medline
16. Iryo Y, Hirai T, Kai Y, et al. **Intracranial dural arteriovenous fistulas: evaluation with 3-T four-dimensional MR angiography using arterial spin labeling.** *Radiology* 2014;271:193–99 CrossRef Medline
17. Edjlali M, Roca P, Rabrait C, et al. **MR selective flow-tracking cartography: a postprocessing procedure applied to four-dimensional flow MR imaging for complete characterization of cranial dural arteriovenous fistulas.** *Radiology* 2014;270:261–68 CrossRef Medline

Applications of a Novel Microangioscope for Neuroendovascular Intervention

 V.M. Srinivasan,  T.T. Lazaro,  A. Srivatsan,  P. Cooper,  M. Phillips,  R. Garcia,  S.R. Chen,  J.N. Johnson,  J.-K. Burkhardt,  D.E. Collins, and  P. Kan



ABSTRACT

BACKGROUND AND PURPOSE: Visualization in neuroendovascular intervention currently relies on biplanar fluoroscopy and contrast administration. With the advent of endoscopy, direct visualization of the intracranial intravascular space has become possible with microangioscopes. We analyzed the efficacy of our novel microangioscope to enable direct observation and inspection of the cerebrovasculature, complementary to a standard fluoroscopic technique.

MATERIALS AND METHODS: Iterations of microangioscopes were systematically evaluated for use in neurodiagnostics and neurointerventions in both live animal and human cadaveric models. Imaging quality, trackability, and navigability were assessed. Diagnostic procedures assessed included clot identification and differentiation, plaque identification, inspection for vessel wall injury, and assessment of stent apposition. Interventions performed included angioscope-assisted stent-retriever thrombectomy, clot aspiration, and coil embolization.

RESULTS: The microangioscope was found helpful in both diagnosis and interventions by independent evaluators. Mean ratings of the imaging quality on a 5-point scale ranged from 3.0 (clot identification) to 4.7 (Pipeline follow-up). Mean ratings for clinical utility ranged from 3.0 (aspiration thrombectomy) to 4.7 (aneurysm treatment by coil embolization and WEB device).

CONCLUSIONS: This fiber optic microangioscope can safely navigate and visualize the intravascular space in human cadaveric and in vivo animal models with satisfactory resolution. It has potential value in diagnostic and neurointerventional applications.

ABBREVIATIONS: ICAD = intracranial atherosclerotic disease; IVUS = intravascular ultrasound; OCT = optical coherence tomography

Modern endovascular technique relies on fluoroscopy and contrast agents to guide visualization of the vasculature and deploy interventional devices. Even advanced techniques using conebeam CT are limited to this type of indirect visualization of the intravascular space—that is, that the operator cannot see what is not shown by the contrast or inherent radio-opacity. Matched with challenging anatomy, this indirect visualization

can lead to suboptimal clinical and radiologic outcomes, as well as complications.^{1,2}

Methods of direct intravascular visualization have been studied for neuroendovascular application, namely, intravascular ultrasound (IVUS) and optical coherence tomography (OCT). IVUS uses an ultrasound microcatheter and provides real-time cross-sectional images from inside the artery; it has been studied in stent placement for cervical atherosclerotic disease.^{3,4}

OCT involves using a fiber optic wire that emits near-infrared light that produces a signal based on the scattered or reflected light off the surrounding tissue and has been used to evaluate atherosclerotic disease and flow-diversion device placement.⁵⁻⁷ Nonetheless, both IVUS and OCT face notable challenges because they offer neither direct visualization of intravascular pathology nor the miniaturization necessary to be compatible with the intracranial vasculature.

Prior studies of “angioscopes” (intravascular endoscope)⁸⁻¹⁰ have focused on larger vessels (cervical carotid artery). These were 7F and 5F guide catheters, again too large and inflexible for intracranial vessels.¹¹

Received July 6, 2020; accepted after revision September 5.

From the Department of Neurosurgery (V.M.S., T.T.L., A.S., R.G., J.N.J., J.-K.B., P.K.) and Center for Comparative Medicine (D.E.C.), Baylor College of Medicine, Houston, Texas; Vena Medical (P.C., M.P.), Kitchener, Ontario, Canada; and Department of Interventional Radiology (S.R.C.), The MD Anderson Cancer Center, Houston, Texas.

Funding for the experiments was from Vena Medical, the manufacturer of the devices used in this study.

Paper previously presented as an oral presentation for an “Innovator of the Year” award at: Congress of Neurological Surgeons Annual Meeting, October 19–23, 2019; San Francisco, California.

Please address correspondence to Peter Kan, MD, Department of Neurosurgery, Baylor College of Medicine, 7200 Cambridge St, Suite 9B, Houston, TX 77030; e-mail: ptkan@utmb.edu; @PeterKa80460001

 Indicates article with online supplemental data.

<http://dx.doi.org/10.3174/ajnr.A6900>

Our group has recently described the development of a novel microangioscope for neurointerventional application.¹¹ The goal of this device is to provide direct, in vivo intravascular imaging of pathology and neurointerventional devices to augment the view by traditional fluoroscopy. In initial development, the device was tested in an in vivo porcine model, and several adjustments were made.

In this follow-up study, we aimed to develop this high-resolution microangioscope for clinical application in the human cerebrovasculature. The goals were to assess the compatibility of the device with the human cerebrovasculature (based on the interaction with the delivery system and flexibility) and its diagnostic utility and validity in assisting neurointerventions in animal models (based partially on image quality/resolution).

MATERIALS AND METHODS

The study was approved by the institutional animal care and use committee (AN-5442). Several prototype microangioscopes, not yet commercially available, were used for intravascular visualization (Vena Medical). The development of the microangioscope and technologic background have been previously described.¹¹ The first aim of this study was to improve on the resolution, flexibility, depth of view, and ergonomics of the previous microangioscope.

As previously described, continuous high-flow irrigation (50 mL/min) was performed via a balloon guide catheter or balloon distal access catheter (not commercially available). The combination of flow arrest and irrigation allowed visualization up to 3 cm distal to the distal access catheter or guide catheter.¹¹

Three independent evaluators assessed the image quality for diagnostic utility of the live camera feed and processed procedural videos. Compatibility with the human cerebrovasculature was assessed by a separate cadaver study. Finally, the perceived utility of the microangioscope for diagnostic and interventional applications was graded by the same 3 independent evaluators, again using live camera intraprocedural feed and processed operative videos from cadaver and animal experiments. Procedures were performed by a fellowship-trained neurointerventionalist, and assessments were performed independently by 3 other neurointerventionalists. Videos were assessed using a 5-point qualitative scale (1 = poor, nondiagnostic; 2 = limited diagnostic value; 3 = average, some restricted visibility; 4 = good quality, minimal restrictions on visibility; 5 = excellent) based on prior similar radiographic analysis.¹² The clinical utility for the interventions was rated on a similar-but-separate 5-point qualitative scale based on the added information and the likelihood of using the microangioscope in the clinical setting. A structured debriefing session was then conducted between the engineering team and the clinicians following each experiment to allow iterative improvement of the microangioscope.

Periprocedural animal care (porcine and rabbit) was provided by a veterinary team, according to previously published protocols.¹³ On completion of the study, the animals were euthanized under anesthesia.

Red and white thrombi were prepared using autologous porcine blood. Red thrombi were prepared by mixing autologous blood with bovine thrombin. White thrombi were obtained after centrifuge separation of autologous whole blood. Thrombus

preparation and the model for large-vessel occlusion have been previously described.¹³

The cadaver model was a formalin-fixed whole body. Standard surgical exposure was performed of the cervical carotid artery, which was transected. The distal access catheter was placed within the arterial lumen, and a suture was placed to close the artery around the catheter.

Last, a fusiform aneurysm with intimal injury was created using a rabbit survival model, in which the right common carotid artery was exposed and a 1-cm segment was trapped with 2 aneurysm clips. Elastase (12.5 U; Worthington Biochemical) was injected into the isolated segment and incubated for 20 minutes before reperfusion. The rabbits underwent follow-up angiography 4 weeks later to assess the device and vessel again. Further details about animal research methodology (according to ARRIVE guidelines; <https://arriveguidelines.org/>) are described in the Online Supplemental Data.

Statistical analysis was performed in Excel (Microsoft) for typical descriptive statistics; mean ratings are displayed as mean [SD].

RESULTS

Technologic Iterations and Improvement

Since the first generation of the microangioscope, considerable effort has been made to improve the device in 4 major areas: resolution, flexibility, FOV, and depth of view. Resolution was improved by increasing the number of pixels from 1600 to 3000. This resulted in more resolving power. With this addition, the FOV also increased from 33.3° to 50°, which made it capable of capturing more of the intravascular environment.

Flexibility was the next important factor, especially for the application to the human cerebrovasculature. This was improved by thinning the image bundle, increasing flexibility by >50% and by selecting more malleable materials for the outer sheath. The overall outer diameter was reduced from 2.1F to 1.7F, increasing flexibility by >100%. In silicone model testing (not shown), the minimum bend radius was determined to be <3.1 mm, which was corroborated by the models tested here. Ultimately, these improvements resulted in a marked reduction in stiffness and allowed the device to traverse into the tortuous anatomy of the human cerebrovasculature. Finally, a greater depth of view was important to advance or retract the device.

Three-watt battery-powered LED light sources were used in our initial experiments, but these only illuminated surfaces within 3 mm of the tip of the device. The light source was upgraded to a L9000 LED Light Source (Stryker Endoscopy), improving the depth of view to between 5 and 10 mm. However, due to poor white balancing with this iteration, the final version included a Stryker X7000 Xenon Light Source (Stryker Endoscopy). This 300-watt xenon lamp provided a white light source with even greater illumination at the tip of the device. By improving the light source as well as the number of illuminating fibers, we were able to increase the light intensity by >20%, which ultimately allowed a greater depth of view.

Much of the focus has also been on improving the human factors associated with the use of the microangioscope. Moving from a battery-powered light source to a standard endoscopy

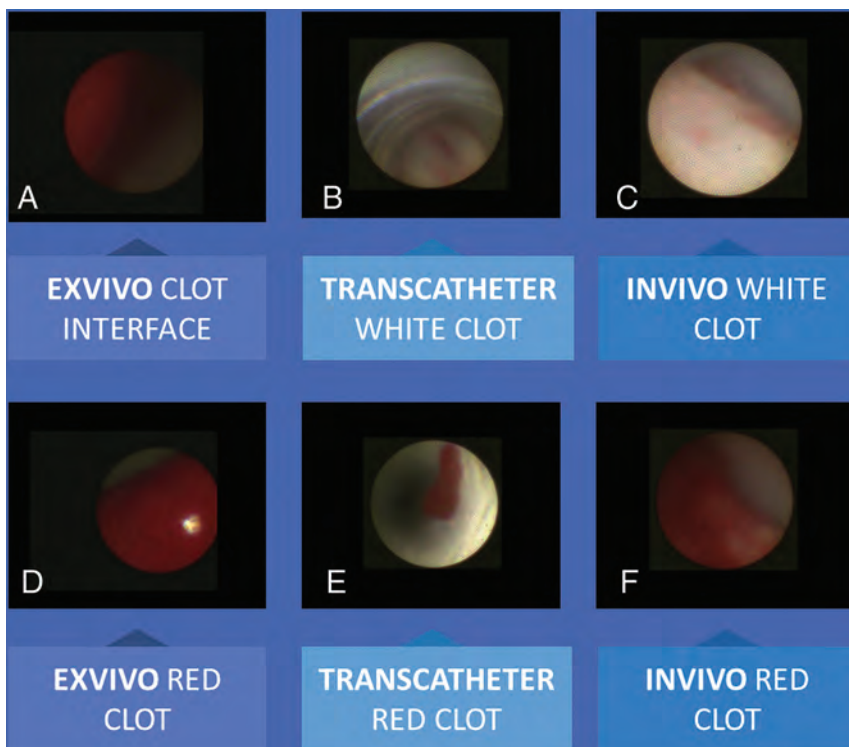


FIG 1. Clot identification and differentiation. A, Clot interface seen ex vivo with a red clot. A white clot is seen through the catheter (B) and in vivo in a porcine model (C). Red clots are seen clearly ex vivo (D), within the distal access catheter (E), and in vivo lodged in the porcine vessel (F).

light source meant that the light source did not need to be changed midway through a procedure. This feature naturally improved the workflow by extending the continuous viewing time of the camera. In addition, the display unit was changed from a cart-based one in which the physician must intermittently look away from the fluoroscope images to see the microangiography images to an “integrated” display so that both fluoroscopic and angiographic images can be seen side by side on the Artis zeego monitor (Siemens) (Online Supplemental Data). The microangiography also originally had a threaded attachment to the proximal assembly that was cumbersome and slow to couple. That was refined to a quick-disconnect system that takes 1 easy motion to replace the scope intraoperatively if necessary. Along with an increased working length of 150 cm and extended cables from the microangiography to the control console, these improvements provide physicians and nurses with added flexibility and ease of operation. The overall advances between the first-generation and the current generation have resulted in a clinically acceptable device that can now be used to practically image the intravascular space (Online Supplemental Data).

Diagnostic Utility: Clot Identification and Differentiation

Autologous porcine blood clots were created and injected into the porcine external carotid circulation. Distinct clots (“red clot” or “white clot”) were made by separation of whole-blood

products to mimic the red cell-rich or fibrin-rich clots. The mean rating for clot identification by video and static images was 3.0 [SD, 1]. Clots were viewed in both ex vivo and in vivo settings. The clarity of the images was sufficient to differentiate the color of the clots as a proxy for their composition (Fig 1). The individual ratings are shown in the Table.

Compatibility with Human Cerebrovasculature

Because our initial proof-of-concept study¹¹ was in an animal model and prior studies with an angiography had evaluated only up to the human cervical carotid artery, we expanded the angiography into the human intracranial vasculature using a cadaver model. After gaining access via the common carotid artery, the microangiography was successfully navigated to the MCA with acceptable force within a distal access catheter using conventional angiography (Catalyst 5; Stryker Neurovascular). This deliverability was compared at the time of procedure with other deployed devices (stent retriever) and was comparable with the deployment of a stent retriever in stiffness/tracking. At the most distal aspect, the microangiography was positioned in the distal M1 to visualize the MCA bifurcation. No untoward events such as vessel dissection or perforation were noted.

Diagnostic Utility: Carotid Disease and Intracranial Atherosclerotic Disease

The mean rating for the carotid disease and intracranial atherosclerotic disease (ICAD) was 4.0 [SD, 1] in the human cadaver model. In the procedure, a plaque was noted in the proximal internal carotid artery, just past the carotid bifurcation (Online Supplemental Data). This was visualized clearly as a plaque via the microangiography but was missed on subsequent conventional angiography. Going further distally into the intracranial circulation, we identified an intracranial plaque within the artery (Online Supplemental Data), which was also not visualized on subsequent angiography.

Diagnostic Utility: Vessel Wall Injury

In the rabbit model, a fusiform aneurysm was created by incubation of the arterial segment with elastase. The mean rating for the microangiography video visualizing the diseased intima of this segment was 3.3 [SD, 1.2]. In this in vivo model, the differentiation of the intima between this segment and the normal segment proximally was seen as a luminal irregularity within the diseased segment. The irregularity was visualized by both angiography

Ratings of microangioscope image quality and interventional utility

Ratings	MD 1	MD 2	MD 3	Mean
Image-quality rating ^a				
Video clip				
Diagnostic, cadaver carotid	3	4	5	4.0
Diagnostic, clot identification	2	3	4	3.0
Diagnostic, vessel wall injury	2	4	4	3.3
Diagnostic, PED follow-up	4	5	5	4.7
Diagnostic, PED initial	3	5	5	4.3
Interventional, aspiration	2	4	3	3.0
Interventional, stent retriever	3	4	3	3.3
Interventional, coil embolization	3	5	5	4.3
Interventional, WEB deployment	2	5	3	3.3
Utility rating ^a				
Interventional application				
Aspiration	2	4	3	3.0
Stent retriever	3	4	3	3.3
Coil embolization	4	5	5	4.7
WEB deployment	4	5	5	4.7

Note:—MD indicates independent neurointerventionalist evaluator.

^a One worst; 5 best. Image quality rating scale described first, followed by device interventional utility rating scale:

- 1) Poor, no diagnostic value; not useful at all for intervention.
- 2) Limited diagnostic value; minimally useful, just of research value/interest.
- 3) Average quality, of possible clinical utility; moderately useful, adds to procedure quality/safety.
- 4) Good quality, minimal restrictions on visibility, probably adds benefit beyond angiography; significantly useful, should strongly consider for this indication.
- 5) Excellent quality, adds benefit beyond angiography, could definitely use as an adjunct; extremely useful, would definitely use in most/all such procedures.

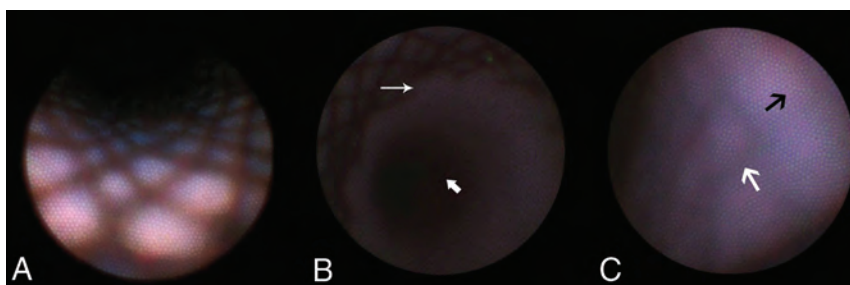


FIG 2. Visualization of a flow-diverting device by the microangioscope. *A*, The fine-woven mesh of the PED is seen. *B*, The interface between the PED and the distal vessel is seen (*thin arrow*), and the distal vessel is dark (*thick arrow*) and beyond the illumination of the microangioscope, giving depth perception. Thrombus formation is excluded, and good wall apposition is confirmed. *C*, After 1 month post-procedure, the device is partially endothelialized, with struts less visible (*medium white arrow*) and endothelium more prominent (*medium black arrow*).

and microangiography (Online Supplemental Data: Video showing the diseased vessel in a rabbit model).

Diagnostic Utility: Device Follow-Up

The fusiform aneurysm created in the prior experiment was then treated with flow diversion using the Pipeline Embolization Device (PED; Medtronic). The aneurysm and device were visualized immediately after device deployment to assess apposition (Fig 2A, -B) and 4 weeks later to assess endothelialization (Fig 2C). The mean rating for the new device placement was 4.3 [SD, 1.2], and the rating at follow-up was 4.7 [SD, 0.6]. Immediately after deployment, all stent tines and the interface between the stent and the normal vessel were well-visualized, and the ability to assess apposition was excellent. No thrombus was seen on the device surface. At follow-up, the same stent tines were visualized in only some areas, though less distinct, and in others, there was complete tissue coverage. We expect that this is secondary to the

desired endothelialization response, though it could also be a combination of fibrin deposition, smooth-muscle cell proliferation, or immune-cell attachment. This was deemed clinically relevant and useful in the follow-up of flow-diversion treatment by all independent evaluators.

Interventional Utility: Stroke Thrombectomy

The feasibility and utility of the microangioscope as an adjunct in stroke thrombectomy was tested with the 2 main thrombectomy techniques: aspiration (A Direct Aspiration First Pass Technique [ADAPT] technique, Catalyst 5) and stent-retriever thrombectomy (Trevor, Stryker; and Embotrap II, Cerenovus) (Fig 3). Experiments were conducted across 3 porcine subjects. The mean rating for the ADAPT image quality was 3.0 [SD, 1], while the rating of visualization of the stent retriever thrombectomy was 3.3 [SD, 0.6]. The expected clinical utility was separately assessed, with a mean rating of 3.0 [SD, 1] for aspiration and 3.3 [SD, 0.6] for the stent retriever. These fall between 3, moderately useful, adds to procedure quality/safety and 4, significantly useful, should strongly consider for this indication.

In the aspiration experiment (3 attempts), a clot was delivered at a bifurcation and the microangioscope was positioned within the aspiration catheter as the pump was turned on. Distal fluid was seen flowing backward toward the camera. Once sufficient force was generated, the clot was aspirated toward the catheter tip and was “corked.” A “red out” was seen on the microangioscope as it was obscured by the face of the clot. A few seconds later, the

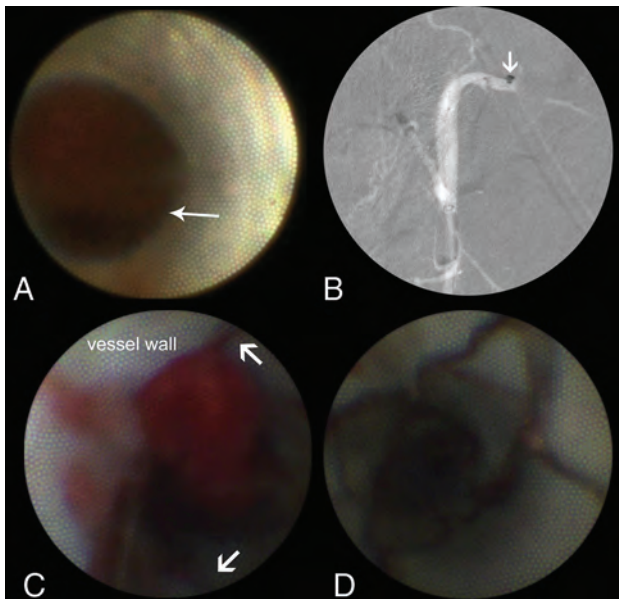


FIG 3. Visualization of mechanical thrombectomy. *A*, A clot is visualized by the microangioscope, and an aspiration catheter is positioned at the face of the clot. The interface between the artery and the clot is seen (*thin arrow*). *B*, Corresponding view on roadmap fluoroscopy shows the positioning of the aspiration catheter at the sharp cutoff point. *C*, A red thrombus is seen during removal by stent-retriever thrombectomy. *D*, The struts of the device can be clearly seen, as can the endothelium, with clear color differentiation (*thick arrows*).

clot was then ingested into the inner lumen of the aspiration catheter past the microangioscope, again giving clear visualization and confirming successful clot evacuation. The microangioscope then traversed outside the aspiration catheter and could visualize the newly recanalized segment. The camera was able to visualize small residual clot in the aspiration catheter, and this small clot was successfully aspirated by a second attempt (Online Supplemental Data: Data/Videos).

In the stent-retriever experiments (5 attempts), both Trevo and Embotrap II stent retriever thrombectomy was performed (Fig 3). In these cases, the tines and expansion of each device were clearly seen, regardless of their radio-opacity on fluoroscopy. Furthermore, the interface between the clot and the device could be visualized as the clot was retrieved. As in aspiration thrombectomy, the microangioscope could later adequately inspect the vessel after recanalization to confirm total revascularization.

All 8 vessels were recanalized after the first pass.

Interventional Utility: Aneurysm Treatment

The feasibility and utility of the microangioscope as an adjunct in aneurysm treatment were tested with multiple devices, including coil embolization and intrasaccular flow disruption (Woven EndoBridge, WEB; MicroVention).

Aneurysm coiling was simulated in an in vivo porcine model. The microangioscope and the coiling microcatheter were simultaneously placed in a balloon guide catheter. The coils were deployed with the camera positioned at the origin of a vessel to simulate aneurysm coiling. The mean rating for this video was 4.3 [SD, 1.2]. The vessel origin, a surrogate of the aneurysm neck,

was well-visualized with the microangioscope. The distal vessel, however, as a surrogate for the aneurysm fundus, was better seen with conventional angiography. The mean rating for the clinical utility was 4.7 [SD, 1.2], which ranges between 4, significantly useful and 5, extremely useful, would definitely use in most/all such procedures.

Finally, an intrasaccular flow-disruption device (WEB), deployed at a vessel origin, was visualized with the microangioscope. The fine mesh of the device, very similar to the lattice of the PED, was visualized clearly, as was the interface between the device and the normal vessel as a surrogate for the aneurysm neck. The mean rating for this video was 3.3 [SD, 1.5]. The mean rating for the clinical utility was 4.7 [SD, 1.2].

DISCUSSION

Shortcomings of Diagnostic Angiography

DSA is the criterion standard for all modern neuroendovascular interventions but has notable disadvantages. Namely, high cumulative radiation doses, contrast usage, and poor visualization over bony anatomy limit its safety and utility. Furthermore, the proper visualization of devices with DSA relies largely on their radio-opacity. To this end, there has been interest in using IVUS and OCT as adjuncts to DSA. However, these methods have their own limitations, chiefly their cumbersome size and stiffness that limit safe neurovascular navigation.

From Angioscope to Microangioscope

Angioscopy, as described in previous iterations, has been limited by visualization through blood in vivo, camera size, and image quality. In this study, we demonstrate the utility of a further-improved¹¹ high-resolution microangioscope. The miniaturization of the angioscopic technology is truly transformative and allows access into the distal intracranial vasculature (MCA bifurcation), as seen in the human cadaver experiments. In the iterative process used between our proof-of-concept study and the current version, the microangioscope optics have also been improved with better diagnostic quality. Specifically, improvement in the fiberoptic light source allowed better image resolution (increased image fibers) as well as intravascular illumination and depth of view (improved light source and increased illumination fibers). Additional improvements were also made to the flexibility and FOV of the device. Each successive iteration made for a quantitatively improved experience.

Diagnostic Applications

Four discrete diagnostic applications were evaluated in this study: clot identification/differentiation, plaque identification, inspection of vessel wall injury, and flow-diverter apposition and endothelialization. The mean rating for these all reached above 3/5, qualifying for potential clinical benefit/use per the clinicians viewing the video.

The clot identification and differentiation have clear implications for mechanical thrombectomy. The ability to identify vessel wall injury and inspect the vessel wall surface is important for identifying subtle vascular dissection and differentiating vasculitis/vasospasm from diffuse atherosclerotic disease. These entities are often difficult to diagnose and differentiate on angiography,

and a microangiogram can clarify these diagnoses with direct visual inspection.

The uses of other intravascular visualization technologies (IVUS, OCT) have been studied in the context of flow-diversion follow-up.^{5,7} In follow-up angiograms, usually obtained at 3- to 12-month intervals after aneurysm treatment, the neurointerventionalist evaluates parent artery patency, aneurysm occlusion, branch vessel patency, and in-stent stenosis. The goal of flow diversion is to achieve durable aneurysm occlusion by endothelialization of the stent across the aneurysm neck. However, complete aneurysm occlusion is only inferred by angiography in these experiments. In this study, the microangiogram was able to clearly identify the tissue response across the fine struts of the PED. With this technology, the successful treatment with a device can be monitored and could then dictate the necessary duration of antiplatelet therapy.

Interventional Applications: Stroke

Various interventional applications were evaluated in this study, namely aneurysm treatment by several modalities (flow diversion with the PED, intrasaccular flow disruption with WEB, and aneurysm coiling) and stroke thrombectomy. In all interventions, device adjustments were made on the basis of real-time feedback to increase workflow and accuracy in a clinical setting. Overall, there is potential for assistance in thrombectomy as per the clinician ratings.

Practically, we envision the potential use of the microangiogram in stroke thrombectomy as an adjunct to the current treatment paradigm, which is meant to be performed swiftly^{14,15} and with a high first-pass efficacy.¹⁶ First, given the ability of the microangiogram to directly visualize and differentiate between white clot (high fibrin content, firm, recalcitrant) and red clot (high red blood cell content, softer, easier to remove), the optimal thrombectomy strategy could be chosen (aspiration versus stent retriever). If using aspiration, as in the case of a fibrin clot, the microangiogram can help identify when corking or when contact has been established and can identify any uncaptured/residual clot to be ingested. If using a stent retriever, in the case of a red thrombus, the microangiogram can visualize clot integration and identify residual, especially because some thrombi were not seen on conventional angiography. In this sense, the microangiogram shows up-close what was previously seen only in clear silicone flow models with simulated clots. The microangiogram practically gives us a “new set of eyes” in the angiography suite. Future translational research is certainly needed to corroborate some of the potential applications in our models and bring them to the angiography suite. Most important, these applications are limited by visualization just to the clot face (and not distal to it) and the flow-arrest requirement.

In another scenario, when there is re-occlusion, the microangiogram can be used to evaluate and differentiate between intracranial atherosclerosis and vasospasm/vasculitis and can help guide additional treatment such as rescue stent placement¹⁷ in the case of ICAD or antispasmodics in case of vasospasm. From the perspective of carotid disease and stroke work-up, microangiography could potentially identify high-risk plaques (eg, thrombus or ulceration) in the setting of mild or normal-appearing

angiographic stenosis for patients with an otherwise unremarkable stroke work-up. This could be a key development in identifying the embolic source in this clinically challenging group of patients.¹⁸

Interventional Applications: Aneurysm Treatment

The clinical utility ratings for the 2 aneurysm treatments (coil embolization and WEB deployment) were both very high, 4.7 [SD, 1.2]. In both of these treatments, visualization of the neck of the aneurysm is critical to ensure complete coverage and treatment and to prevent encroachment of the implant into the parent artery or branch artery. In standard fluoroscopy, oblique views are often needed to optimize visualization of the aneurysm neck and the normal artery. However, this can be challenging, depending on patient anatomy and aneurysm projection. Therefore, the ability of the microangiogram to directly visualize this critical area of the neck to ensure complete and safe device deployment is clinically significant.

Workflow

The imagined workflow of angiography and microangiography is demonstrated in the Online Supplemental Data. These are complementary technologies. Generally, the microangiogram helps visualize proximal pathology and is somewhat limited distally, given the 3-cm tether from the balloon catheter. Thus, the distal anatomy is well-seen with angiography, which also provides a roadmap to go further with the microangiogram. Practically, this is similar to what neuroendoscopy has done in operative micro-neurosurgery; bringing the light source and visualization closer to the pathology has been revolutionary.¹⁹ The ergonomics of where to position the operating instruments (microcatheter and microwire device) relative to the endoscope (microangiogram) are quite similar. Thus, in the aneurysm experiments, fluoroscopy and the microangiogram each had their own distinct advantages and were quite complementary. Overall, standard angiography demonstrates the distal aneurysm fundus and the walls well, whereas the neck of the aneurysm can be well-visualized with the microangiogram.

Future Directions

This technology has myriad potential applications in neuroendovascular surgery and for both clinical and translational research to further our understanding of cerebrovascular diseases. For example, further quantitative studies should be performed to truly assess its value in microangiogram-assisted thrombectomy. In this study, we were able to visualize intracranial atherosclerotic disease in a cadaver experiment, but the results should be validated in further cadaveric and possibly in vivo human subjects. Our thrombectomy experiments suggest that direct visualization of thrombi could help the clinician with revascularization, and more quantitative revascularization outcomes should be tested.

Other types of vascular injury (intimal flaps/dissections, webs) can also be difficult to assess by angiography alone. In the assessment of its use in aneurysm treatment, these experiments were only a proof-of-concept and also deserve future study using well-established aneurysm models to explore the visualization of

device apposition, intraprocedural clot detection, and aneurysm neck healing with time.

Limitations

The limitations of this technology were discussed in our prior proof-of-concept study.¹¹ Briefly, these are the inability to see distally beyond the pathology and the necessity for flow arrest. The duration of flow arrest could theoretically vary from procedure to procedure but certainly carries potential morbidity with the use of balloons and increased ischemic time during device manipulation.

The study itself additionally has limitations. This study has established the feasibility of its use in a human cadaver and a porcine model. The cadaver model had no flowing blood and did not require the ability to obtain intracranial flow arrest, and the external carotid artery of the porcine model had limited tortuosity and was of large diameter. Additionally, the outcome measures used to assess imaging quality and device compatibility are not validated.

CONCLUSIONS

Current neuroendovascular imaging relies on fluoroscopy-based DSA. We used a recently developed fiber optic microangiography to visualize the intravascular space in human cadaveric and in vivo animal models. In this series of experiments, we demonstrate its feasibility in diagnostic and neurointerventional applications. An independent rating of video capture suggested satisfactory visualization and potential utility, particularly in aneurysm embolization procedures. Further studies are needed to evaluate its potential in this and other applications, including diagnosis, device deployment, and treatment monitoring.

ACKNOWLEDGMENT

We appreciate the excellent care of animal subjects by Dr Collins' veterinary team.

Disclosures: Tyler T. Lazaro—RELATED: Grant: Vena Medical, Comments: provided money to fund the experiments in this study. No money paid to the individual authors. Phillip Cooper—UNRELATED: Board Membership: Vena Medical, Comments: I am a board member at my startup, Vena Medical; Employment: Vena Medical; Stock/Stock Options: I own stock in my startup, Vena Medical; Travel/Accommodations/Meeting Expenses Unrelated to Activities Listed: Vena Medical pays for my travel. Michael Phillips—UNRELATED: Board Membership: Vena Medical, Comments: I am on the board of Vena Medical; Employment: Vena Medical; Patents (Planned, Pending or Issued): Vena Medical, Comments: I am an inventor of several pending patents assigned to Vena Medical; Stock/Stock Options: Vena Medical; Travel/Accommodations/Meeting Expenses Unrelated to Activities Listed: Vena Medical, Comments: travel and accommodations to conferences such as the World Live Neurovascular Conference, the Society of Neurointerventional Surgery, and so forth to represent Vena Medical. Jan-Karl Burkhardt—UNRELATED: Board Membership: Longevity Neuro Solutions, Comments: Advisory Board member. Peter Kan—UNRELATED: Stock/Stock Options, Vena Medical.

REFERENCES

1. Ketteler ER, Brown KR. Radiation exposure in endovascular procedures. *J Vasc Surg* 2011;53:35S–38S CrossRef Medline
2. Wong JM, Ziewacz JE, Panchmatia JR, et al. Patterns in neurosurgical adverse events: endovascular neurosurgery. *Neurosurg Focus* 2012;33:E14 CrossRef Medline
3. Kan P, Mokin M, Abla AA, et al. Utility of intravascular ultrasound in intracranial and extracranial neurointerventions: experience at University at Buffalo Neurosurgery-Millard Fillmore Gates Circle Hospital. *Neurosurg Focus* 2012;32:E6 CrossRef Medline
4. Tobis JM, Mallery J, Mahon D, et al. Intravascular ultrasound imaging of human coronary arteries in vivo: analysis of tissue characterizations with comparison to in vitro histological specimens. *Circulation* 1991;83:913–26 CrossRef Medline
5. Caroff J, Tamura T, King RM, et al. Phosphorylcholine surface modified flow diverter associated with reduced intimal hyperplasia. *J Neurointerv Surg* 2018;10:1097–1101 CrossRef Medline
6. King RM, Marosfoi M, Caroff J, et al. High frequency optical coherence tomography assessment of homogenous neck coverage by intrasaccular devices predicts successful aneurysm occlusion. *J Neurointerv Surg* 2019;11:1150–54 CrossRef Medline
7. King RM, Brooks OW, Langan ET, et al. Communicating malapposition of flow diverters assessed with optical coherence tomography correlates with delayed aneurysm occlusion. *J Neurointerv Surg* 2018;10:693–97 CrossRef Medline
8. Tanemura H, Hatazaki S, Asakura F, et al. Angioscopic observation during carotid angioplasty with stent placement. *AJNR Am J Neuroradiol* 2005;26:1943–48 Medline
9. Savastano LE, Chaudhary N, Murga-Zamalloa C, et al. Diagnostic and interventional optical angiography in ex vivo carotid arteries. *Oper Neurosurg (Hagerstown)* 2017;13:36–46 CrossRef Medline
10. Savastano LE, Zhou Q, Smith A, et al. Multimodal laser-based angiography for structural, chemical and biological imaging of atherosclerosis. *Nat Biomed Eng* 2017;1:0023 CrossRef Medline
11. Lazaro T, Srinivasan VM, Cooper P, et al. A new set of eyes: development of a novel microangiography for neurointerventional surgery. *J Neurointerv Surg* 2019;11:1036–39 CrossRef Medline
12. Srinivasan VM, Chintalapani G, Camstra KM, et al. Fast acquisition cone-beam computed tomography: initial experience with a 10 s protocol. *J Neurointerv Surg* 2018;10:916–20 CrossRef Medline
13. Srinivasan VM, Chen SR, Camstra KM, et al. Development of a recalcitrant, large clot burden, bifurcation occlusion model for mechanical thrombectomy. *Neurosurg Focus* 2017;42:E6 CrossRef Medline
14. Huang X, Cai Q, Xiao L, et al. Influence of procedure time on outcome and hemorrhagic transformation in stroke patients undergoing thrombectomy. *J Neurol* 2019;266:2560–70 CrossRef Medline
15. Saver JL, Goyal M, van der Lugt A, et al; HERMES Collaborators. Time to treatment with endovascular thrombectomy and outcomes from ischemic stroke: a meta-analysis. *JAMA* 2016;316:1279–88 CrossRef Medline
16. Zaidat OO, Castonguay AC, Linfante I, et al. First pass effect: a new measure for stroke thrombectomy devices. *Stroke* 2018;49:660–66 CrossRef Medline
17. Maingard J, Phan K, Lamanna A, et al. Rescue intracranial stenting after failed mechanical thrombectomy for acute ischemic stroke: a systematic review and meta-analysis. *World Neurosurg* 2019;132:e235–45 CrossRef Medline
18. Goyal M, Singh N, Marko M, et al. Embolic stroke of undetermined source and symptomatic nonstenotic carotid disease. *Stroke* 2020;51:1321–25 CrossRef Medline
19. Torres-Corzo JG, Rangel-Castilla L, Nakaji P. *Neuroendoscopic Surgery*. Thieme Publishers; 2016

Correlation of Technical and Adjunctive Factors with Quantitative Tumor Reduction in Children Undergoing Selective Ophthalmic Artery Infusion Chemotherapy for Retinoblastoma

T. Abruzzo, K. Abraham, K.B. Karani, J.I. Geller, S. Vadivelu, J.M. Racadio, B. Zhang, and Z.M. Correa



ABSTRACT

BACKGROUND AND PURPOSE: Selective ophthalmic artery infusion chemotherapy has improved ocular outcomes in children with retinoblastoma. Our aim was to correlate quantitative tumor reduction and dichotomous therapeutic response with technical and adjunctive factors during selective ophthalmic artery infusion chemotherapy for retinoblastoma. An understanding of such factors may improve therapeutic efficacy.

MATERIALS AND METHODS: All patients with retinoblastoma treated by selective ophthalmic artery infusion chemotherapy at a single center during a 9-year period were reviewed. Only first-cycle treatments for previously untreated eyes were studied. Adjunctive factors (intra-arterial verapamil, intranasal oxymetazoline external carotid balloon occlusion) and technical factors (chemotherapy infusion time, fluoroscopy time) were documented by medical record review. Quantitative tumor reduction was determined by blinded comparison of retinal imaging acquired during examination under anesthesia before and 3–4 weeks after treatment. The dichotomous therapeutic response was classified according to quantitative tumor reduction as satisfactory ($\geq 50\%$) or poor ($<50\%$).

RESULTS: Twenty-one eyes met the inclusion criteria. Patients ranged from 2 to 59 months of age. Adjuncts included intra-arterial verapamil in 15, intranasal oxymetazoline in 14, and external carotid balloon occlusion in 14. Quantitative tumor reduction ranged from 15% to 95%. Six showed poor dichotomous therapeutic response. A satisfactory dichotomous therapeutic response was correlated with intra-arterial verapamil ($P = .03$) in the aggregate cohort and in a subgroup undergoing treatment with single-agent melphalan at a dose of <5 mg ($P = .02$). In the latter, higher average quantitative tumor reduction correlated with intra-arterial verapamil ($P < .01$).

CONCLUSIONS: Intra-arterial verapamil during selective ophthalmic artery infusion chemotherapy is correlated with an improved therapeutic response, particularly when treating with lower doses of single-agent melphalan.

ABBREVIATIONS: CIT = chemotherapeutic infusion time; DTR = dichotomous therapeutic response; ECBO = external carotid artery balloon occlusion; FT = fluoroscopy time; IAV = intra-arterial verapamil; INA = intra-nasal Afrin; OA = ophthalmic artery; SOAIC = selective ophthalmic artery infusion chemotherapy; QTR = quantitative tumor reduction

Selective ophthalmic artery infusion chemotherapy (SOAIC) has emerged as an important approach to ocular salvage in children with intermediate-to-advanced intraocular retinoblastoma. Numerous variations in neuroendovascular technique have been reported. Temporary or permanent occlusion of the external

carotid artery, infusion of verapamil into the ophthalmic artery (OA), and intranasal oxymetazoline or (Afrin) (INA) have all been described as adjunctive methods to optimize ocular hemodynamics.^{1,2} Known factors associated with failure of intravenous chemotherapy for retinoblastoma include older patient age, greater tumor thickness, vitreal seeds, and subretinal fluid at

Received June 25, 2020; accepted after revision September 4.

From the Departments of Radiology (T.A., J.M.R.), Epidemiology and Biostatistics (B.Z.), Ophthalmology (Z.M.C.), Neurosurgery (S.V.) and Oncology (J.I.G.), Cincinnati Children's Hospital Medical Center, Cincinnati, Ohio; Departments of Neurosurgery (T.A.), Radiology (K.A., K.B.K., T.A.), Epidemiology and Biostatistics (B.Z.), and Ophthalmology (Z.M.C.), University of Cincinnati Medical Center, Cincinnati, Ohio; Department of Neurosciences (T.A.), Barrow Neurological Institute at Phoenix Children's Hospital, Phoenix, Arizona; Departments of Radiology and Child Health (T.A.), University of Arizona College of Medicine, Phoenix, Arizona; and Department of Ophthalmology (Z.M.C.), Wilmer Eye Institute, Johns Hopkins University Medical Center, Baltimore, Maryland.

Paper previously presented, in part, at: Annual Meeting of the Society of Interventional Radiology, March 17–22, 2018; Los Angeles, California, abstract No. 527.

Please address correspondence to Todd Abruzzo, MD, Phoenix Children's Hospital, 1919 East Thomas Rd, Phoenix, AZ 85016; e-mail: tabruzzo@phoenixchildrens.com

Indicates article with supplemental online tables.

<http://dx.doi.org/10.3174/ajnr.A6905>

presentation.³ Tumor response to SOAIC is proportional to the product of tissue chemotherapeutic concentration and the duration of chemotherapeutic exposure.^{4,5} Each of these factors is influenced by variations in the neuroendovascular technique, particularly by adjuncts that modulate ocular blood flow and introduce variations in chemotherapeutic dilution and reflux.

We sought to determine the impact of technical and adjunctive factors on quantitative tumor reduction (QTR) and dichotomous therapeutic response (DTR) as biomarkers of SOAIC therapeutic efficacy. We also evaluated the association of chemotherapeutic infusion time (CIT), a correlate of drug exposure duration, and fluoroscopy time (FT), a surrogate of the difficulty of OA catheterization, with specific therapeutic adjuncts, QTR and DTR.

MATERIALS AND METHODS

The clinical material for this study comprises patients with retinoblastoma who were evaluated and treated at Cincinnati Children's Hospital Medical Center. This study was approved by the institutional review board at Cincinnati Children's Hospital Medical Center. Records of all patients with retinoblastoma treated by SOAIC at Cincinnati Children's Hospital Medical Center during a 9-year period (December 2008 to July 2017) were evaluated. Only the first SOAIC cycles for previously untreated eyes in chemo-naïve patients were studied to avoid the confounding effects of prior treatment. This approach also optimized our chances of observing measurable changes in QTR because the largest tumor reduction is known to occur with the first SOAIC.⁶

Baseline tumor features and treatment response were documented by the senior author during ophthalmic examination under anesthesia. During this examination, retinal photographs were obtained with a wide-field retinal imaging system (Retcam; Clarity Medical Systems). All SOAICs were performed by the senior neurointerventionist. SOAIC was conducted by placing the tip of a steam-shaped 1.5F microcatheter (Marathon; Medtronic) directly into the ostium of the OA.¹ If a stable ostial microcatheter position could not be established after multiple attempts with alternate microcatheter tip shapes, midsegment OA catheterization was performed with a 1.2F microcatheter (Magic FM; Balt).

Steam-shaping of microcatheter tips was accomplished by inserting a malleable wire template into the microcatheter tip and then shaping the wire template to conform to a curved line drawn through the infraophthalmic internal carotid artery lumen into the OA origin on lateral projections of simultaneously acquired carotid angiograms. The reconfigured microcatheter tip and coaxial wire template were placed into a steam jet for 1–2 minutes. Before removal of the wire template, the microcatheter tip was submerged into and flushed with room temperature saline. Microcatheter tips steam-shaped in this manner generally retained patient-specific curvatures that would support a stable ostial microcatheter position.

In the initial phase of this experience, intra-arterial verapamil (IAV) was selectively administered to patients with a small or constricted OA. In the later phase, IAV was administered to all patients. IAV consisted of 20 µg per kilogram of verapamil (in

2 mL) infused into the internal carotid artery for 2 minutes and 80 µg per kilogram of verapamil (in 8 mL) infused into the OA for 8 minutes. Also, in the initial phase, INA, comprising 2 puffs ipsilateral to the OA, was administered to all patients after establishing general anesthesia. In the latter phase, INA was selectively administered to patients with robust OA perfusion of the nasal mucosa. External carotid artery balloon occlusion (ECBO) was performed as previously described.¹ Patients were selected for ECBO if carotid or OA angiography showed continuous or intermittent retrograde OA flow. Patients undergoing SOAIC with a single agent were treated with melphalan or topotecan. SOAIC with single-agent topotecan was performed according to an investigational protocol (NCT01466855). Patients undergoing triple-agent SOAIC were treated with melphalan, topotecan, and carboplatin. Chemotherapeutics and dosing schemes were selected as reported previously.⁷

Patient age, sex, International Classification of Intraocular Retinoblastoma group, tumor laterality, history of familial retinoblastoma, date of SOAIC, procedure-related adverse events, and chemotherapeutics were documented by electronic medical record review. The date of SOAIC was used to divide cases into early (before May 2015) and late (subsequent to May 2015) epochs. Epochs were defined according to a time point that divided the study period into halves according to the number of the first-cycle SOAICs. Adjunctive (IAV, INA, ECBO) and technical (CIT, FT) factors were documented by electronic medical record review. CIT intervals were designated as brief (<20 minutes), intermediate (20–38 minutes), or prolonged (\geq 39 minutes). FT intervals were designated as brief (<20 minutes), intermediate (20–35 minutes), or prolonged (> 35 minutes).

QTR was determined by retrospective estimation of changes in overall tumor size judged by comparison of retinal photographs, fundus maps, and sonographic examinations acquired by ophthalmic examination under anesthesia before and 3–4 weeks after first-cycle SOAIC (Fig 1). All QTR determinations were made by the senior author, an ophthalmologist with fellowship training in vitreoretinal surgery and ocular oncology and >20 years of clinical practice experience. Each QTR determination was made by masking patient identifiers in the presented images. Furthermore, no information about treatment-related technical or adjunctive factors was provided at the time of QTR determination. Consequently, QTR determinations were considered to be blinded with respect to study end points. DTR was categorized as satisfactory (QTR \geq 50%) or poor (QTR < 50%).

Preliminary analysis to estimate the potential confounding effect of prior exposure to systemic multiagent chemotherapy was conducted on the entire population of patients undergoing SOAIC treated at the study center during the study period. DTR for first-cycle SOAIC was compared between patients previously exposed to systemic multiagent chemotherapy and patients not previously exposed to systemic multiagent chemotherapy.

For the primary analysis, only first-cycle SOAIC for each enrolled eye was considered. Study inclusion criteria were the following: 1) previously untreated eye, 2) chemo-naïve patient, and 3) adequate records to retrospectively determine QTR. SOAICs complicated by microcatheter migration during chemoinfusion were excluded. In the primary analysis, primary outcome

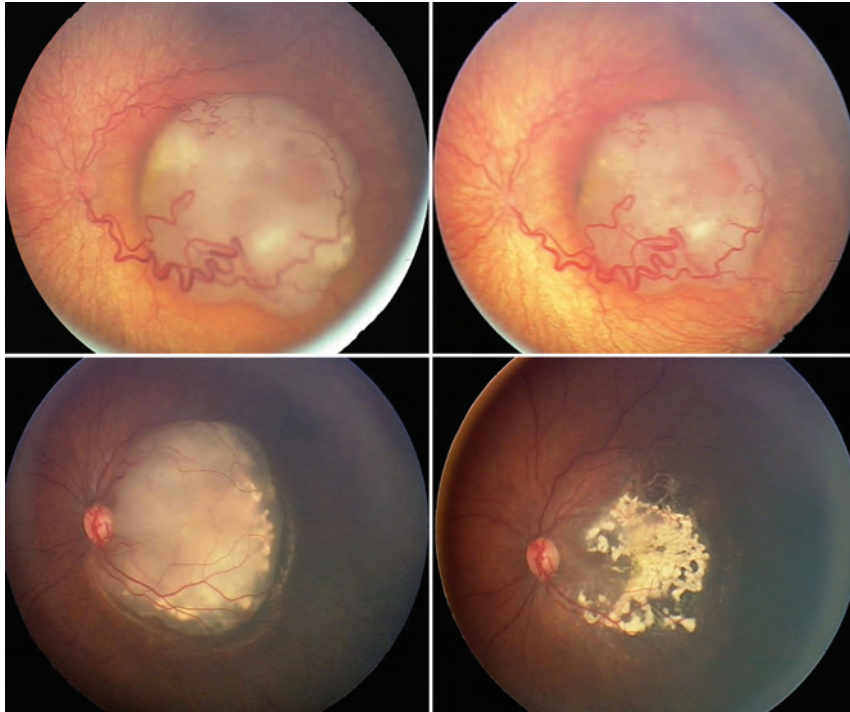


FIG 1. Composite photograph shows 2 eyes of 2 individual patients with macular retinoblastoma displaying substantially different QTRs at 3–4 weeks after the first cycle of selective ophthalmic artery infusion chemotherapy. Analysis of the top pair of photos gives a QTR of 15% and a DTR classified as poor (QTR < 50%). Analysis of the bottom pair of photos gives a QTR of 95% and DTR classified as satisfactory (QTR > 50%).

measures (QTR and DTR) were analyzed in relation to adjunctive factors (IAV, INA, ECBO) and technical factors (CIT, FT) for the aggregate study population and 2 subgroups of first-cycle SOAIC performed with different doses of single-agent melphalan (any dose and <5mg). Secondary analyses included correlation of primary outcome measures (QTR and DTR) with epoch, correlation of technical factors (CIT, FT) with adjunctive factors (IAV, INA, ECBO), and assessment of procedure-related adverse events.

Descriptive analysis was performed to summarize patient demographics, tumor characteristics, and chemotherapeutics. Correlation between categorical variables was evaluated by χ^2 or Fisher exact tests. A 2-sample *t* test or 1-way ANOVA was used to detect differences in average QTR, CIT, and FT between different adjunctive treatment groups and epochs or to assess differences in average QTR between different CIT and FT intervals. Correlation between continuous variables was assessed using the Pearson correlation coefficient. All analyses were performed using SAS software, Version 9.4 (SAS Institute). A *P* value < .05 was considered statistically significant.

Procedure-related adverse events were assessed for all first-cycle SOAICs performed during the study period.

RESULTS

During December 2008 to July 2017, forty eyes of 35 patients with intraocular retinoblastoma were treated by SOAIC at the study center. Two eyes were excluded because fundus views precluded determination of QTR. Preliminary analysis of the

remaining 38 eyes confirmed correlation of prior systemic multiagent chemotherapy with poor DTR (*P* = .02).

Fifteen eyes previously exposed to systemic multiagent chemotherapy were excluded. One eye was excluded because SOAIC was complicated by microcatheter migration during chemoinfusion. One eye was excluded because of prior local therapy. The remaining 21 eyes of 20 patients composed the aggregate study population. These patients ranged from 2 to 59 months of age (median, 12 months). One of these 20 patients had bilateral retinoblastoma, and both eyes of this patient were enrolled in the study. The single patient with bilateral retinoblastoma was also the only patient in the study with familial retinoblastoma. Laterality was evenly distributed (11 left, 10 right). Eleven eyes were treated in the early epoch, and 10, in the late epoch. The OA was the chemoinfusion artery for all SOAIC treatments. Fourteen first-cycle SOAICs were performed with ECBO, and 7 were performed without ECBO. In 1 case,

ECBO was performed because super selective OA angiography demonstrated retrograde OA flow throughout the angiographic cycle. In the remaining 13 cases, ECBO was performed because fluoroscopic monitoring of contrast media injected through the treating microcatheter or superselective OA angiography demonstrated competitive retrograde inflow of unopacified blood into the OA from external carotid artery collaterals as the contrast injection pressure decreased.

The Table and Online Table 1 summarize patient and tumor characteristics. There is a trend toward younger age and male sex in patients achieving satisfactory DTR. Patients treated with ECBO (*P* < .01) were younger. Low-grade tumors (group B) accounted for a small minority in all comparison groups. Triple-agent chemotherapy had a negative association with INA (*P* = .03), and single-agent topotecan had a positive association with IAV (*P* = .04).

QTR for the aggregate population ranged from 15% to 95% (average, 59.0%). DTR was poor in 6 and satisfactory in 15 (Online Tables 2–4). DTR and QTR were not significantly associated with sex or age. One-third of patients with poor DTR were cases with single-agent melphalan; one-third, with single-agent topotecan; and one-third, with triple-agent chemotherapy. In the aggregate population, FT ranged from 10 to 76 minutes (average, 29 minutes), and CIT ranged from 12 to 60 minutes (average, 31 minutes).

Online Tables 2 and 3 compare primary outcome measures (QTR and DTR, respectively) between treatment groups differentiated according to adjunctive factors (\pm IAV, \pm INA, \pm ECBO).

Age, sex, history of familial retinoblastoma, and tumor laterality

		Average Patient Age (mo) [SD]	Female Sex (Fraction of Total Patients)	Familial Retinoblastoma (Fraction of Total Eyes)	Tumor Laterality		
					Bilateral Tumors (Fraction of Total Eyes)	Right-Sided Tumors (Fraction of Total Eyes)	Left-Sided Tumors (Fraction of Total Eyes)
Aggregate study population <i>n</i> = 21 eyes, <i>n</i> = 20 patients		19.5 [SD, 14.7]	12 (0.60)	2 (0.09)	2 (0.09)	10 (0.48)	11
Eyes treated with IAV	+ (<i>n</i> = 15 eyes)	15.4 [SD, 11.1]	8 (0.53)	2 (0.13)	2 (0.13)	6 (0.40)	9 (0.60)
	– (<i>n</i> = 6 eyes)	29.7 [SD, 16.5]	4 (0.67)	0 (0.0)	0 (0.0)	4 (0.67)	2 (0.33)
Eyes treated with INA	+ (<i>n</i> = 14 eyes)	17.7 [SD, 15.1]	8 (0.57)	2 (0.14)	2 (0.14)	8 (0.57)	6 (0.43)
	– (<i>n</i> = 7 eyes)	23.1 [SD, 14.0]	4 (0.57)	0 (0.0)	0 (0.0)	2 (0.29)	5 (0.71)
Eyes treated with adjunctive ECBO	+ (<i>n</i> = 14 eyes)	14.3 [SD, 9.5]	8 (0.57)	2 (0.14)	1 (0.07)	5 (0.36)	9 (0.64)
	– (<i>n</i> = 7 eyes)	30.0 [SD, 18.2]	4 (0.57)	0 (0.0)	1 (0.14)	5 (0.71)	2 (0.29)
Eye status according to DTR	Satisfactory (<i>n</i> = 15 eyes)	16.4 [SD, 10.0]	7 (0.47)	1 (0.07)	2 (0.13)	7 (0.47)	8 (0.53)
	Poor (<i>n</i> = 6 eyes)	27.3 [SD, 21.8]	5 (0.83)	1 (0.17)	0 (0.0)	3 (0.50)	3 (0.50)

Note: + indicates receiving; –, not receiving.

Online Table 4 compares CIT and FT between treatment groups differentiated according to adjunctive factors (\pm IAV, \pm INA, \pm ECBO). In the aggregate population, IAV was correlated with satisfactory DTR ($P = .03$) (Fig 2) but not QTR. Notably, IAV correlated with a late epoch ($P = .01$), but DTR was not associated with an epoch (Online Table 5). There were 14 first-cycle SOAICs with single-agent melphalan. Five milligrams of melphalan was used in 2 first cycle SOAIC treatments. Analysis of first-cycle SOAIC performed with single-agent melphalan shows correlation of IAV with satisfactory DTR ($P = .01$) (Online Table 3 and Fig 2) and higher average QTR ($P < .01$) (Online Table 2) for a melphalan dose of <5 mg. When any melphalan dose is considered, the correlation of IAV with DTR falls just short of statistical significance ($P = .06$) (Fig 2). In the aggregate population, FT correlated with INA ($P < .01$) and ECBO ($P = .04$) (Online Table 4). The difference in average FT between patients with and without ECBO was 11 minutes. The difference in average FT between patients with and without INA was 16 minutes.

The average CIT was 30.2 and 31.7 minutes in patients with satisfactory and poor DTRs, respectively (Online Table 6). Average FT was 31.9 and 23.3 minutes in patients with satisfactory and poor responses, respectively (Online Table 6). Higher average QTR and satisfactory DTR were associated with decreasing CIT, but differences between CIT intervals were not significant (Fig 3). Similarly, higher average QTR and a satisfactory DTR were associated with increasing FT, but differences between FT intervals were not significant.

Adverse events for 40 first-cycle SOAICs in 35 patients (median age, 16 months) are detailed in Online Table 7. There were no strokes, subclinical cerebral infarctions on brain imaging, or ischemic retinal events. There were 2 transient, subclinical neurovascular events involving reversible vasoconstriction (1 cerebral and 1 ophthalmic) in infants receiving INA.

Transient periorbital erythema secondary to hyperemia was common after IAV and was not counted as an adverse event. Symptomatic periocular edema requiring oral steroids occurred after SOAIC twice, once after IAV. In 2 different cases, ocular

hemorrhages were found on ophthalmic examination under anesthesia at 3–4 weeks (1 subretinal and 1 retinal). In both cases, IAV was administered. Neither was associated with prolonged CIT or a wedge microcatheter position, but the retinal hemorrhage was associated with midsegment OA catheterization (Online Table 7).

There were 2 instances of hypotension in infants receiving IAV. Both necessitated resuscitation with blood products. One patient was treated with calcium gluconate to counteract verapamil. There were also 2 instances of bronchospasm, which resolved with microcatheter repositioning and endotracheal albuterol. Postextubation laryngospasm required reintubation in 1 case.

There were 2 access site complications including 1 groin hematoma and 1 transient external iliac artery thrombosis treated by short-term lovenox without sequelae. Both occurred in infants requiring bifemoral arterial access for SOAIC with ECBO.

DISCUSSION

To our knowledge, this is the first study that describes QTR and its derivative DTR, as metrics of SOAIC therapeutic efficacy. QTR uniquely enables one to measure the effect of individual treatments differentiated by technical factors (ie, CIT). In contrast, the ocular salvage rate is determined by the cumulative effect of multiple treatments with variations in technical factors that are difficult or impossible to control. Our focus on first-cycle SOAIC in previously untreated patients allowed us to eliminate confounding effects of prior treatment and isolate the impact of the neuroendovascular technique.

Our study reveals a correlation of IAV with satisfactory DTR. This correlation was significant for the aggregate population and a subgroup treated by SOAIC with <5 mg of single-agent melphalan (Fig 2). Furthermore, the average QTR was higher for first-cycle SOAIC performed with IAV ($P < .01$) in the latter subgroup. These associations eliminate doubt that the benefit of IAV was due to unequal distribution of differentially effective chemotherapeutics. Although IAV was associated with the late epoch,

we found no correlation between DTR and epoch to suggest that the benefit of IAV was attributable to increasing experience of the operating team.

IAV enhancement of therapeutic efficacy could be related to augmentation of ocular perfusion, chemosensitization, or both. Verapamil has potent long-lasting vasodilator actions when administered by the arterial route.⁸ Because the tumoricidal effect is proportional to tumoral perfusion with chemotherapeutics, vasodilation in target tissue may enhance therapeutic efficacy. Laboratory and clinicopathologic studies have demonstrated that verapamil inhibits membrane-associated glycoproteins, conferring multidrug resistance to retinoblastoma cells and that expression of these glycoproteins by retinoblastoma is associated with treatment failure.⁹⁻¹² Biochemical studies show that these verapamil-sensitive glycoproteins actively export melphalan, rendering retinoblastoma cells resistant to the chemotherapeutic activity of melphalan.¹³ Owing to this mechanism, the chemosensitizing potency of verapamil is blunted at higher melphalan doses.^{14,15} The results of our study are consistent with that paradigm (Fig 2).

The chemosensitizing tissue concentration of verapamil cannot be safely established by oral or intravenous routes, but the pharmacokinetics of superselective intra-arterial administration make it achievable. Others have leveraged intra-arterial administration strategies to commission the chemosensitizing properties of IAV.^{16,17} Another property of verapamil underlies an anatomically specific advantage unique to the retina. Extensive research has demonstrated that verapamil is actively transported across the blood-retina barrier by retinal pigment epithelium proteins.^{18,19} Thus, a combination of pharmacokinetic and molecular transport effects may enable chemosensitization with IAV during SOAIC.

In the current series, 2 of 25 children treated with IAV experienced hypotension. Both were infants younger than 12 months of age. Notably, some authors advise against intravenous verapamil administration in infants younger than 12 months of age due to a paucity of safety data.²⁰ Despite such recommendations, intravenous verapamil dosed at 100–200 µg per kilogram for 2 minutes remains the preferred treatment for some types of cardiac dysrhythmia in infants.²⁰ While most agree that the risk of verapamil toxicity is very high during the first 6 weeks of life, there is no evidence that the use of intravenous verapamil in older infants is unsafe.^{20,21} The incidence of hypotension in this series is substantially lower than that reported in other series of SOAIC.²² In those series, IAV was not given, and procedural hypotension was related to autonomic reflexes associated with OA catheterization.²² It is possible that intraoperative hypotension in the current series was at least partially related to autonomic responses.

INA was not correlated with a therapeutic response in this study. INA has been used to limit perfusion of the sinonasal mucosa with chemotherapeutics during SOAIC. Theoretically, perfusion of the sinonasal mucosa through ethmoidal branches of the OA can cause a steal that reduces delivery of chemotherapeutics to the retina and may cause mucosal injury resulting in epistaxis.²³ Two infants receiving INA in the current study experienced procedure-related adverse events related to vasoconstriction (1 cerebral and 1 ophthalmic). Although OA spasm during SOAIC is primarily related to mechanical stimulation, the

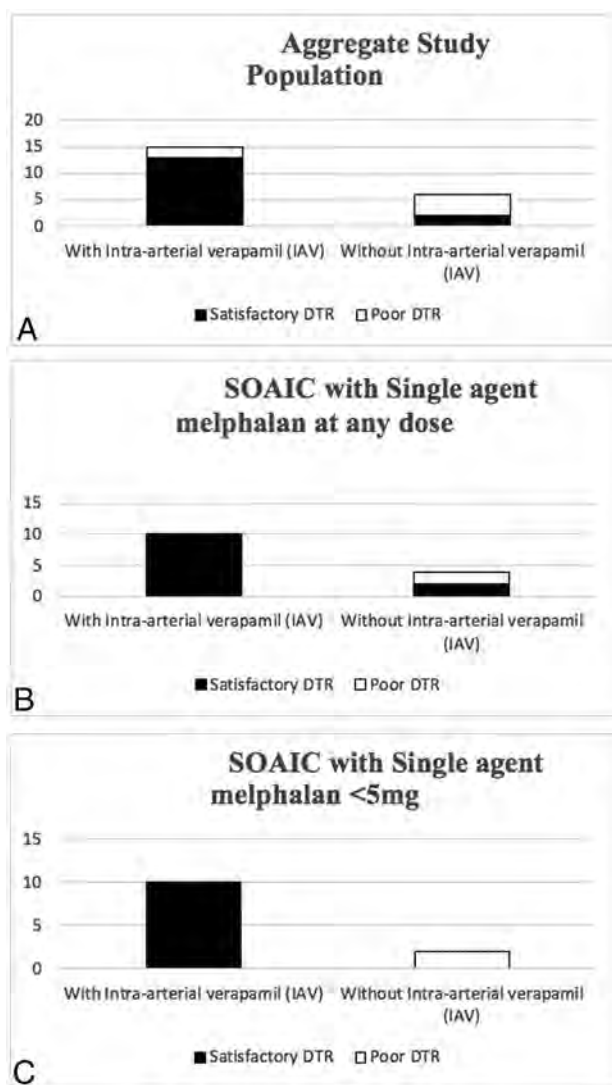


FIG 2. The absolute number of satisfactory (black) or poor (white) DTRs for first cycle of SOAIC treatments performed with or without adjunctive IAV is presented for the aggregate study population (A), SOAIC treatments performed with single-agent melphalan at any dose (B), and SOAIC treatments performed with single-agent melphalan at doses of <5 mg (C).

striking association of INA with increased FT in this study raises the possibility that INA may be a contributory factor and that off-target vasoconstriction caused by INA may interfere with OA catheterization. One patient in the current study demonstrated findings concerning for reversible cerebral vasoconstriction after administration of INA, which cannot be attributed to vessel instrumentation. Reversible cerebral vasoconstriction associated with concomitant administration of oxymetazoline and phenylephrine-containing eye drops during SOAIC has been reported in another patient.²⁴

ECBO is used to optimize ocular hemodynamics during SOAIC because it ensures continuous anterograde OA flow throughout the entire period of chemotherapeutic administration, regardless of microcatheter injection pressure or the patient's blood pressure.¹ The direction of OA flow during SOAIC is assessed by angiography and by subtracted

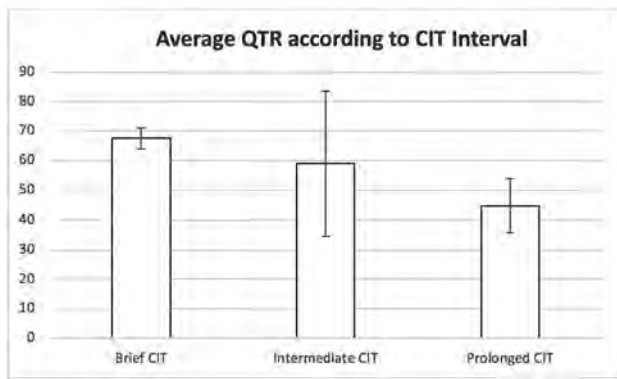


FIG 3. The average QTR is presented for the first cycle of selective ophthalmic artery infusion chemotherapy treatment differentiated into brief (<20 minutes), intermediate (20–38 minutes), and prolonged (≥ 39 minutes) CIT intervals. Error bars indicate ± 1 SD.

fluoroscopic monitoring of contrast media injected through the treating microcatheter in a manner that simulates chemotherapy administration.¹ In children with well-developed external carotid artery-to-OA collaterals, OA flow may be frankly retrograde throughout the entire angiographic cycle. Alternatively, competitive retrograde inflow from external carotid artery collaterals may only be transiently revealed in the delayed phase of angiography as the angiographic injection pressure falls. Under these circumstances, all or some of the administered chemotherapeutic misses the tumor target and refluxes into the cerebral circulation. Another approach intended to overcome competitive flow from external carotid artery collaterals involves administration of chemotherapeutics through the dominant competing external carotid artery collateral, which is frequently the orbital branch of the ipsilateral middle meningeal artery. Advancing a microcatheter deep into such a collateral vessel often produces a pressure gradient that promotes blood flow in the collateral vessel to move toward the external carotid artery, away from the OA. Under these conditions, chemotherapeutic infusion is administered against the direction of arterial flow in the microcatheter-bearing collateral vessel. Moreover, external carotid artery anastomoses with the OA are often distal to the origin of the retinociliary trunk (parent vessel of the central retinal artery and posterior ciliary arteries). This anatomy makes a chemoinfusion administered through the external carotid artery branch countercurrent with blood flow entering the ostium of the OA origin from the internal carotid artery. In order for the chemotherapeutic to reach the retinal circulation under these circumstances, it must overcome a potentially stronger countercurrent flow from the internal carotid artery. As a result, administration of chemotherapy through external carotid artery collaterals trades one source of competitive countercurrent flow with alternative sources of countercurrent flow. We favor ECBO for the management of competitive countercurrent flow encountered during SOAIC because it completely suppresses all sources of countercurrent flow, without introducing new ones. Nonetheless, if the orbital branch of the middle meningeal artery is highly dominant and OA catheterization is challenging,

administration of chemotherapy through the orbital branch of the middle meningeal artery may be preferable.

ECBO was not correlated with QTR or DTR in this study. However, because our practice was to perform ECBO in patients with intermittent or continuous OA flow reversal, selection bias likely masked the benefit. ECBO was associated with 11 minutes of additional FT in this study due to the need for fluoroscopy guidance during balloon catheter positioning, inflation, re-adjustment of the balloon during chemoinfusion, and deflation. This amount of added FT may not be significant, depending on the advantage provided by ECBO in any given case. Although there were no adverse events directly attributable to ECBO, our only 2 access site complications occurred in patients undergoing ECBO (Online Table 7). Notably, our method of ECBO relies on bifurcated arterial sheath placement, and patients undergoing ECBO were notably younger. These features raise the possibility that there is a tendency toward retrograde OA flow in younger patients because the ratio of extracranial vascular resistance to cerebrovascular resistance is elevated in early childhood. Indeed, transcranial Doppler studies provide indirect evidence of this.²⁵ It is also possible that age-related changes in OA anatomy may contribute to hemodynamic variations encountered in children. Perhaps expansion of the calvaria and bony orbit in early childhood cause physical displacement of OA anastomoses from corresponding external carotid artery feeders, resulting in developmental involution of anastomoses with maturation of the cranial skeleton. In any case, additional study is warranted to further investigate the safety and potential therapeutic advantage of ECBO.

As reported by others, our approach to SOAIC involves manual infusion of the total chemotherapy dose in a volume of 30 mL.^{1,23} Although most operators strive to administer the infusion for 30 minutes, adjustment of infusion parameters is often necessary to prevent chemotherapeutic reflux into the internal carotid artery and maximally flood the anterograde target-tissue blood volume. Consequently, CIT varies. Although tumor killing during SOAIC is proportional to the duration of tumor chemotherapeutic exposure, higher average QTR and satisfactory DTR were associated with decreasing CIT in this study, albeit the associations were not statistically significant (Fig 3). It is possible that prolonged CIT with a fixed infusion volume diminishes the therapeutic potency by allowing chemotherapeutics entering the OA to be diluted by a larger volume of inflowing blood.

All except one of the ocular, neurovascular, and cardiovascular adverse events in this series were associated with prolonged FT, and these were predominantly in infants younger than 12 months of age (Online Table 7). The findings emphasize that longer and technically more difficult cases are associated with a generalized increase in procedure-related risks and that infants younger than 12 months of age are particularly at risk. In our study, satisfactory DTR correlated more closely with prolonged FT than brief FT. The results suggest that even children presenting with significant technical challenges realize the full therapeutic benefit of SOAIC. It is notable that the only procedure-related retinal hemorrhage in this series complicated an SOAIC treatment involving midsegment OA catheterization. In our approach to SOAIC, midsegment OA catheterization is generally avoided

because we believe that it carries a higher risk of bronchospasm, bradycardia, hypotension, OA spasm, OA dissection, retinal hemorrhage, and retinal ischemia relative to ostial catheterization. Even in the absence of OA spasm, long-segment obturation of the OA by an indwelling microcatheter (as in midsegment catheterization) may create a “wedge dynamic” that pressurizes the retinal circulation during chemoinfusion (leading to retinal hemorrhage) or restricts retinal perfusion (leading to retinal ischemia). Furthermore, procedure-related OA microdissections or intramural hematomas created by excessive OA instrumentation may evolve into a stenosis that thwarts future treatment attempts.

One weakness of this study lies in the retrospective nature of data collection and analysis. Because the details of treatment were obtained by electronic medical record review rather than imaging review, the results are susceptible to documentation inaccuracies and omissions. Another weakness is that most patients received a mixture of different adjunctive therapies, making it difficult to isolate the effect of individual adjuncts. Furthermore, some potentially confounding variations of anatomy and technique (ostial-versus-midsegment OA catheterization) were not considered in our analysis.²⁶ Because midsegment OA catheterization is rarely performed in our practice, we do not think that variations in the OA catheterization technique contributed significantly to our results. Although only 1 case of midsegment catheterization was known to occur, our study methodology did not allow us to systematically classify cases according to catheterization technique. Investigation of the catheterization technique would have required analysis of OA angiograms rather than review of reports contained in the electronic medical record. Future studies should address the potential impact of the OA catheterization technique. Although the current study suggests IAV enhancement of therapeutic efficacy, the study cohort is small and further study is necessary to determine whether the added therapeutic benefit outweighs the increased risks of drug-induced hypotension.

CONCLUSIONS

In children undergoing SOAIC for intraocular retinoblastoma, IAV is safe and may increase the probability of a satisfactory therapeutic response, particularly in those treated with <5 mg single-agent melphalan. Procedural hypotension occurs in a minority of infants and is correctable with calcium gluconate and/or volume resuscitation. INA is not associated with measurable benefit and may produce off-target vasoconstrictive effects that lead to adverse events, particularly in infants. Although ECBO did not demonstrate a therapeutic advantage in this study, selection bias may have confounded our assessment.

Disclosures: Sudhakar Vadivelu—UNRELATED: Consultancy: Alcyone Lifesciences. Zelia M. Correa—UNRELATED: Consultancy: Castle Biosciences.

REFERENCES

1. Abruzzo TA, Geller J, Kimbrough D, et al. **Adjunctive techniques for optimization of ocular hemodynamics and biological response to therapy in children undergoing ophthalmic artery infusion chemotherapy.** *J Neurointerv Surg* 2015;7:770–76 CrossRef Medline
2. Bertelli E, Leonini S, Galimberti D, et al. **Hemodynamic and anatomic variations require an adaptable approach during intra-arterial chemotherapy for intra-ocular retinoblastoma: alternative routes, strategies and follow up.** *AJNR Am J Neuroradiol* 2016;37:1289–95 CrossRef Medline
3. Gündüz K, Günalp I, Yalçındağ N, et al. **Causes of chemoreduction failure in retinoblastoma and analysis of associated factors leading to eventual treatment with external beam radiotherapy and enucleation.** *Ophthalmology* 2004;111:1917–24 CrossRef Medline
4. Eckman WW, Patlack CS, Fenstermacher JD. **A critical evaluation of the principles governing the advantages of intra-arterial infusion.** *J Pharmakinet Biopharm* 1974;2:257–85 CrossRef Medline
5. Fenstermacher JD, Cowles AL. **Theoretic limitations of intracarotid infusions in brain tumor chemotherapy.** *Cancer Treat Rep* 1977;61:519–26 Medline
6. Shields CL, Kaliki S, Shah SU, et al. **Minimal exposure (one or two cycles) of intra-arterial chemotherapy in the management of retinoblastoma.** *Ophthalmol* 2012;119:188–92 CrossRef Medline
7. Michaels ST, Abruzzo TA, Augsburger JJ, et al. **Selective ophthalmic artery infusion chemotherapy for advanced intraocular retinoblastoma: CCHMC early experience.** *J Pediatr Hematol Oncol* 2016;38:65–69 CrossRef Medline
8. Feng L, Fitzsimmons BF, Young WL, et al. **Intraarterially administered verapamil as adjunct therapy for cerebral vasospasm: safety and 2-year experience.** *AJNR Am J Neuroradiol* 2002;23:1284–90 Medline
9. Krishnakumar S, Mallikarjuna K, Desai N, et al. **Multidrug resistant proteins: P-glycoprotein and lung resistance protein expression in retinoblastoma.** *Br J Ophthalmol* 2004;88:1521–26 CrossRef Medline
10. Kamburoğlu G, Kiratlı H, Söylemezoğlu F, et al. **Clinicopathological parameters and expression of P-glycoprotein and MRP-1 in retinoblastoma.** *Ophthalmic Res* 2007;39:191–97 CrossRef Medline
11. Seigel GM, Campbell LM, Narayan M, et al. **Basic and clinical research on the therapeutic effect of intervention in primary liver cancer by targeted intra-arterial verapamil infusion.** *Cell Biochem Biophys* 2012;62:59–67 CrossRef Medline
12. Filho JP, Correa ZM, Odashiro AN, et al. **Histopathological features and P-glycoprotein expression in retinoblastoma.** *Invest Ophthalmol Vis Sci* 2005;46:3478–83 CrossRef Medline
13. Kuhne A, Tzvetkov MV, Hagos Y, et al. **Influx and efflux as determinants of melphalan cytotoxicity: resistance to melphalan in MDR1 overexpressing tumor cell lines.** *Biochem Pharmacol* 2009;78:45–53 CrossRef Medline
14. Larrivee B, Averill DA. **Melphalan resistance and photoaffinity labelling of P-glycoprotein in multidrug-resistant Chinese hamster ovary cells: reversal of resistance by cyclosporin A and hyperthermia.** *Biochem Pharmacol* 1999;58:291–302 CrossRef Medline
15. Raaijmakers HG, Izquierdo MA, Lokhorst HM, et al. **Lung-resistance-related protein expression is a negative predictive factor for response to conventional low but not to intensified dose alkylating chemotherapy in multiple myeloma.** *Blood* 1998;91:1029–36 Medline
16. Huang J, Duan Q, Fan P, et al. **Clinical evaluation of targeted arterial infusion of verapamil in the interventional chemotherapy of primary hepatocellular carcinoma.** *Cell Biochem Biophys* 2011;59:127–32 CrossRef Medline
17. Cairo MS, Siegel S, Anas N, et al. **Clinical trial of continuous infusion verapamil, bolus vinblastine, and continuous infusion VP-16 in drug-resistant pediatric tumors.** *Cancer Res* 1989;49:1063–66 Medline
18. Han YH, Sweet DH, Hu DN, et al. **Characterization of a novel cationic drug transporter in human retinal pigment epithelial cells.** *J Pharmacol Exp Ther* 2001;296:450–57 Medline
19. Chapy H, Saubamea B, Tournier N, et al. **Blood-brain and retinal barriers show dissimilar ABC transporter impacts and concealed effect of P glycoprotein on a novel verapamil influx carrier.** *Br J Pharmacol* 2016;173:497–510 CrossRef Medline
20. LaPage MJ, Bradley DJ, Dick M. **Verapamil in infants: an exaggerated fear?** *Pediatr Cardiol* 2013;34:1532–34 CrossRef Medline

21. Kehr J, Binfield A, Maxwell F, et al. **Fascicular tachycardia in infancy and the use of verapamil: a case series and literature review.** *Arch Dis Child* 2019;104:789–92 CrossRef Medline
22. Phillips TJ, McGuirk SP, Chahal HK, et al. **Autonomic cardio-respiratory reflex reactions and superselective ophthalmic arterial chemotherapy for retinoblastoma.** *Paediatr Anaesth* 2013;23:940–55 CrossRef Medline
23. Abramson DH, Daniels AB, Marr BP, et al. **Intra-arterial chemotherapy (ophthalmic artery chemosurgery) for group D retinoblastoma.** *PLoS One* 2016;11:e0146582 CrossRef Medline
24. Abruzzo TA, Patino M, Leach J, et al. **Cerebral vasoconstriction triggered by sympathomimetic drugs during chemotherapy.** *Pediatr Neurol* 2013;48:139–42 CrossRef Medline
25. Bode H, Wais U. **Age dependence of flow velocities in basal cerebral arteries.** *Arch Dis Child* 1988;63:606–11 CrossRef Medline
26. Area C, Yen CJ, Chevez-Barrios P, et al. **Technical and anatomical factors affecting intra-arterial chemotherapy fluoroscopy time and radiation dose for intraocular retinoblastoma.** *J Neurointerv Surg* 2019;11:1273–76 CrossRef Medline

Cone-beam CT versus Multidetector CT in Postoperative Cochlear Implant Imaging: Evaluation of Image Quality and Radiation Dose

R.A. Helal, R. Jacob, M.A. Elshinnawy, A.I. Othman, I.M. Al-Dhamari, D.W. Paulus, and T.T. Abdelaziz

ABSTRACT

BACKGROUND AND PURPOSE: Cone-beam CT is being increasingly used in head and neck imaging. We compared cone-beam CT with multidetector CT to assess postoperative implant placement and delineate finer anatomic structures, image quality, and radiation dose used.

MATERIALS AND METHODS: This retrospective multicenter study included 51 patients with cochlear implants and postoperative imaging via temporal bone cone-beam CT ($n = 32$ ears) or multidetector CT ($n = 19$ ears) between 2012 and 2017. We evaluated the visualization quality of single electrode contacts, the scalar position of the electrodes, cochlear walls, mastoid facial canal, metallic artifacts (using a 4-level visual score), and the ability to measure the insertion angle of the electrodes. The signal-to-noise ratio and radiation dose were also evaluated.

RESULTS: Cone-beam CT was more sensitive for visualizing the scalar position of the electrodes ($P = .046$), cochlear outer wall ($P = .001$), single electrode contacts ($P < .001$), and osseous spiral lamina ($P = .004$) and had fewer metallic artifacts ($P < .001$). However, there were no significant differences between both methods in visualization of the modiolus ($P = .37$), cochlear inner wall ($P > .99$), and mastoid facial canal wall ($P = .07$) and the ability to measure the insertion angle of the electrodes ($P > .99$). The cone-beam CT group had significantly lower dose-length product ($P < .001$), but multidetector CT showed a higher signal-to-noise ratio in both bone and air ($P = .22$ and $P = .001$).

CONCLUSIONS: Cone-beam CT in patients with cochlear implants provides images with higher spatial resolution and fewer metallic artifacts than multidetector CT at a relatively lower radiation dose.

ABBREVIATIONS: CBCT = cone-beam CT; CI = cochlear implant; MDCT = multidetector CT

A cochlear implant (CI) as a treatment option for profound sensorineural hearing loss has increased remarkably in recent years. This increase can be partly attributed to the innovative diagnostic radiologic procedures. These procedures facilitate preoperative and intraoperative processes and enhance postoperative outcomes.¹ Preoperative assessment of the temporal bone and inner ear structures is crucial to check the feasibility of implantation and predict the outcome. Usually both MR imaging and multidetector CT (MDCT) are used for assessment.² Intraoperative imaging is usually reserved for cases with severe anatomic abnormalities and during minimally invasive procedures to guide the

electrode placement and reduce the duration of the operation using fluoroscopy or mobile radiography.³

As in most cases, the use of MR imaging after a CI must be limited, so the electrode position is usually assessed using conventional x-ray or MDCT.³ An important postoperative assessment is to ensure the proper positioning of the electrode inside the cochlea and check its insertion depth (which are important factors for the first activation and follow-up) as well as to assess the scalar position (the proper location being in the scala tympani near the nerve endings), distance of the first contact from the round window (optimal, 3–4 mm), and distance from the electrode to the modiolus or lateral wall. Any complications such as electrode kinking, looping, or dislocation; presence of extracochlear electrodes; inner ear trauma; or osseous spiral lamina injury should be also assessed.^{4–6}

These assessments post-CI require optimal imaging techniques. Conventional x-ray can localize the implant position but does not provide much detail and is, therefore, inadequate. MDCT provides more anatomic details; however, it has remarkable metallic artifacts.³

Received April 17, 2020; accepted after revision September 15.

From the Radiodiagnosis Department (R.A.H., M.A.E., A.I.O., T.T.A.), Ain Shams University, Cairo, Egypt; HNOplus (R.J.), Höhr-Grenzhausen, Germany; and Institute for computational visualistics (I.M.A.-D., D.W.P.), Koblenz University, Koblenz, Germany.

Please address correspondence to Rania Helal, MD, Radiodiagnosis Department, Faculty of Medicine, Ain Shams University, 38 Ramsis street, Abbassia Square, PO Box 11381, Cairo, Egypt; e-mail: raniahelal@med.asu.edu.eg; @20f81fe9c71b44c
<http://dx.doi.org/10.3174/ajnr.A6894>

Cone-beam CT (CBCT) is becoming increasingly popular for head and neck imaging despite its low contrast resolution, which precludes the examination of soft-tissue pathology, because of its high spatial resolution and relatively low radiation dose. In the field of CIs, the importance of CBCT is increasing due to its provision of more accurate details and fewer metallic artifacts.⁷⁻¹⁴

CBCT involves a rotating gantry to which an x-ray source (with a divergent cone-shaped radiation) and flat panel detector are fixed. During complete/partial rotation of the gantry, multiple sequential planar projection images of the FOV are obtained, which differ from the helical progression of the fan-shaped radiation used in MDCT devices. Thus, CBCT imaging requires a relatively longer duration compared with MDCT, which increases the overall risk of motion artifacts.¹⁵

The accuracy of radiologic implant assessment is also important for improving surgical skills (correct electrode positioning) and CI fitting procedures. Auditory outcome depends on the correct scalar position of the electrode in the scala tympani, without scalar translocation. Furthermore, these data help in the development of new devices, more accessible surgical techniques, and better follow-up of patients.¹⁶ Recently, the combination of post-operative CBCT with preoperative MR imaging has shown very good results in the assessment of electrode position.¹⁷

The purpose of this study was to compare CBCT with MDCT post-CI for radiologic evaluation of important finer anatomic details around the implant, electrode radiologic assessment, and assessment of metallic artifacts, signal-to-noise ratio, and radiation doses used.

MATERIALS AND METHODS

Study Design and Population

This was a retrospective multicenter study approved by Ain Shams University institutional review board (approval number MD237/2017). We conducted a retrospective review from January 2012 to December 2017 using our institution's CI data base and a public human cochlea data base to retrieve the postoperative imaging data of patients who underwent CI surgery and postoperative MDCT (from our institution) or CBCT (from the public data base). Exclusion criteria were the presence of a morphologically abnormal cochlea, severe motion artifacts distorting the image quality, and inadequate data about the type of electrode inserted. For patients undergoing bilateral CI, only the right ear was included (for statistical reasons). Fifty-one patients were identified and included, regardless of their age or sex. Patients' demographic data and data about the types of electrodes inserted were collected.

Radiologic Examination and Analysis

CBCT Group. This group was scanned using the CBCT 3D Accutomo 170 (J. Morita). Each ear was imaged separately using 90-kV tube voltage and 5-mA current, with a high-resolution mode (Hi-Res J.Morita) with a rotation of 180°. A voxel size of 0.125 mm and an ROI of 80 × 80 × 80 mm were used. Images were reconstructed with filtered back-projection using the G_001 reconstruction algorithm.

MDCT Group. The MDCT group was scanned using the MDCT Somatom Definition Flash (dual-source 64-detector row scanner; Siemens) with single-energy automated tube-

voltage selection (CARE kV; Siemens). The quality reference tube voltage was 120 kV, providing an acquisition of 100 kV. Automated tube modulation (CARE Dose4D; Siemens) was used, with a quality reference tube current of 375 mAs. Images were obtained using a beam collimation = 0.5 mm, rotation time = 1 second, FOV = 240 mm, section thickness = 0.6 mm, section interval = 0.3 mm, and pitch = 0.8. Reconstruction was performed using the Hr60 kernel.

The obtained images were anonymized and examined by 2 experienced neuroradiologists with 5 and 15 years of experience until consensus was reached. The images were processed in the coronal, sagittal, and cochlear views. The window width and level were 3500 and 500, which were adjusted according to the observers' preferences for optimal visualization of the cochlear structures near the metallic artifacts.

Qualitative Image Analysis and Analysis of Electrode Positions

Image sharpness was defined by identification of important anatomic details, such as the cochlear inner and outer walls, osseous spiral lamina, modiolus, and the mastoid facial nerve canal wall. Each image was also evaluated for the precise scalar localization of the inserted electrode, its insertion angle, and visualization of single electrode contacts. The electrode insertion angle was measured using the method suggested by Pearl et al¹⁸ (Fig 1). Its measurement ability was categorized into a 2-level score (0 = not measurable; 1 = measurable). The quality of visualization of the other details was reported according to a 4-level score (0 = not visualized, 1 = barely visualized, 2 = well-visualized, 3 = perfectly visualized). Scoring of metallic artifacts was also performed (ranging from 0 = markedly affecting the diagnosis to 3 = minimal metallic artifacts).

Quantitative Image-Quality Analysis

The signal-to-noise ratio was calculated for each group; for calculation, 2 ROIs measuring approximately 4 mm² were used. One was at the bone surrounding the cochlea (posterior-medial to the basal turn), and the other was in the air in the external auditory canal. The signal was defined as the mean ROI value, while the SD was defined as image noise; the signal-to-noise ratio was calculated as the mean ROI signal value divided by the SD.¹⁹

Patient Dose Analysis. The dose-length product was analyzed; the calculation was according to the manufacturer-specific protocols, and the output was via the device. Separate measurements were not performed.

Statistical Analysis. Data were coded and processed using the Statistical Package for the Social Sciences (SPSS Statistics for Windows, Version 23.0; IBM). Quantitative data were presented mainly as medians with interquartile ranges, when not normally distributed. Qualitative variables were presented as numbers and percentages. The χ^2 test was used for comparison of ≥ 2 groups of categorical variables. The Monte Carlo test was used as correction for the χ^2 test when $>20\%$ of the cells had a count of <5 in the tables. For comparison of the dose measurements and signal-to-noise ratio (quantitative data with nonparametric distribution), the Mann-Whitney test was used. A P value $\leq .05$ was considered statistically significant, with a confidence interval of 95%.

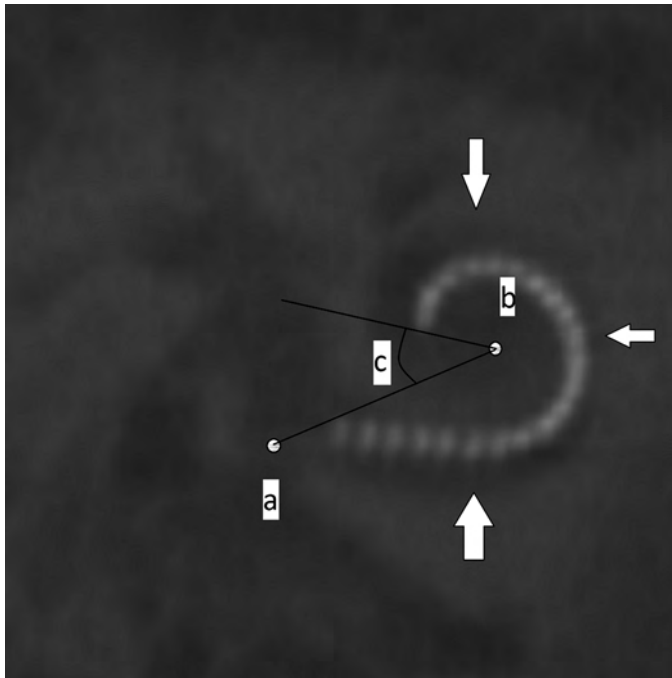


FIG 1. Coronal oblique (cochlear view with thick MPR=5 mm) CBCT image showing the measurement of the angle of insertion between the deepest electrode and the reference line joining the insertion point (round window/cochleostomy center) (a) and the center of a circle formed by the 3 most apical electrodes (b). The insertion angle = 360° (c). The cochlear lateral wall is also well-visualized in this thick MPR coronal view (white arrows).

Table 1: Different electrodes with intercontact distancing

Electrodes	Intercontact Distancing (mm)	CBCT Group (n = 32)	MDCT Group (n = 19)
Widely spaced contacts			
FLEX28 ^a	2.1	3	0
FLEX-Synchrony-Medium ^a	1.9	2	2
HiRes MIDSCALA ^b	0.975	3	1
CI422 ^{*c}	0.85–0.95	1	0
Narrowly spaced contacts			
CI24RE-CA ^c	Nonuniform 0.4–0.8	9	0
CI512-CA ^c	Nonuniform 0.4–0.8	3	0
CI532-CA ^c	0.6	11	1
CI24RE-ST ^c	0.75	0	15

Note:—CA indicates contour advance; ST, straight electrode.

^a MED-EL.

^b Advanced Bionics.

^c Cochlear.

All distances were obtained from the portfolios of the electrodes (* except for CI422 cited from Bennink et al.²⁹)

RESULTS

A total of 51 ears that received CIs were included in the final analysis. Thirty-two patients underwent postoperative CBCT (females = 13 [40.6%], males = 19 [59.4%] with median age = 56 years [interquartile range, 46–0.5 years] and range = 13–84 years), and 19 patients underwent postoperative MDCT (females = 11 [57.9%], males = 8 [42.1%] with median age = 4 years [interquartile range, 3–6 years] and range = 1–17 years). The average exposure time for the CBCT protocol was 15.8 seconds, while that for MDCT was 4 seconds. Details of the implanted electrodes are shown in Table 1.

Qualitative Image Analysis and Analysis of Electrode Positions

The results of comparison between both groups regarding visualization of the finer anatomic details and electrode positioning are shown in Tables 2 and 3 (Fig 2). Scalar positioning of electrodes inside the cochlea was identified in both groups, except for 1 ear in the MDCT group (strong metallic artifacts). In the CBCT group (n = 32), electrodes in 63% of ears (n = 20) were inserted in the scala tympani (2 were barely visualized), 9% (n = 3) were in the scala vestibuli (1 was barely visualized), and 28% (n = 9) had scalar dislocation (1 was barely visualized), whereas in the MDCT group (n = 19), 79% (n = 15) were inserted in the scala tympani (1 was barely visualized), 11% (n = 2) were in the scala vestibuli (1 was barely visualized), 5% (n = 1) had scalar dislocation, and 5% were nonassessable (n = 1). The electrodes with widely spaced contacts showed perfectly visualized contacts (n = 3) in the MDCT group, despite the higher metallic artifacts and were perfectly to well-visualized (n = 7 and n = 2, respectively) in the CBCT group. The narrowly spaced contacts were barely visualized (n = 6) and were not visualized (n = 10) in the MDCT group compared with those in the CBCT group: well-visualized (n = 9), barely visualized (n = 13), and not visualized (n = 1). The barely-to-nonvisualized electrodes in the CBCT group were mainly Cochlear CI532 and CI512.

Quantitative Image-Quality Analysis

The results of comparison of the signal-to-noise ratio between both

groups are shown in Table 4.

Dose Analysis

There was a statistically significant difference between both groups in terms of the dose-length product values. The median (interquartile range) in the CBCT group was 93 (47.6–93) with a range of 47.6–93 mGy*cm, while in the MDCT group, the median was (interquartile range) = 387.5 (206–527.75) with a range of 179–650 mGy*cm (P < .001). The difference between the maximum doses encountered in both groups was 557 mGy*cm, representing 85.7% of the maximum dose encountered in the MDCT group.

Table 2: Qualitative image scoring results for fine anatomic structures and metallic artifacts

Scale Points	CBCT Group (n = 32)	MDCT Group (n = 19)	P Value
Cochlear inner wall			
Not visualized (0)	1 (3%)	0 (0%)	>.99
Barely visualized (1)	3 (9%)	2 (10.5%)	
Well-visualized (2)	6 (19%)	3 (15.8%)	
Perfectly visualized (3)	22 (69%)	14 (73.7%)	
Cochlear lateral wall			
Not visualized (0)	0 (0%)	1 (5%)	.001
Barely visualized (1)	0 (0%)	0 (0%)	
Well-visualized-(2)	2 (6%)	8 (42%)	
Perfectly visualized (3)	30 (94%)	10 (53%)	
Modiolus			
Not visualized (0)	0 (0%)	0 (0%)	.37
Barely visualized (1)	2 (6%)	0 (0%)	
Well-visualized (2)	5 (16%)	1 (5%)	
Perfectly visualized (3)	25 (78%)	18 (95%)	
Osseous spiral, lamina			
Not visualized (0)	18 (56%)	19 (100%)	.002
Barely visualized (1)	10 (31%)	0 (0%)	
Well -visualized (2)	4 (13%)	0 (0%)	
Perfectly visualized (3)	0 (0%)	0 (0%)	
Mastoid facial, canal wall			
Not visualized (0)	4 (13%)	4 (21%)	.07
Barely visualized (1)	10 (31%)	6 (32%)	
Well-visualized (2)	9 (28%)	9 (47%)	
Perfectly visualized (3)	9 (28%)	0 (0%)	
Metallic artifacts			
Very strong artifact (0)	0 (0%)	0 (0%)	<.001
Strong artifacts (1)	6 (18.8%)	14 (74%)	
Moderate artifacts (2)	22 (68.8%)	5 (26%)	
Weak artifacts (3)	4 (12.5%)	0 (0%)	

Table 3: Qualitative image scoring results for electrode evaluation

Scale Points	CBCT Group (n = 32)	MDCT Group (n = 19)	P Value
Electrode scalar position			
Not visualized (0)	0 (0%)	0 (0%)	.046
Barely visualized (1)	4 (13%)	3 (16%)	
Well-visualized (2)	3 (9%)	7 (37%)	
Perfectly visualized (3)	25 (78%)	9 (47%)	
Single electrode contact visibility			
Not visualized (0)	1 (3%)	10 (52.6%)	<.001
Barely visualized (1)	13 (41%)	6 (31.6%)	
Well-visualized (2)	11 (34%)	0 (0%)	
Perfectly visualized (3)	7 (22%)	3 (15.8%)	
Insertion angle of electrode			
Not measurable (0)	0 (0%)	0 (0%)	>.99
Measurable (1)	32 (100%)	19 (100%)	
	Mean, 437.7° [SD, 120.8°]	Mean, 329.4° [SD, 80°]	

DISCUSSION

The number of CI operations has increased notably in recent years; however, there is still a wide spectrum of postoperative outcomes. Hence, more improvement in the electrode design, surgical approaches, and evaluation of the related detailed cochlear anatomy is necessary.^{5,20} Conventional radiography and MDCT have long been used for postoperative evaluation. CBCT imaging is a relatively new technique in the imaging of CIs and is reported to have a better spatial resolution than MDCT, with fewer metallic artifacts affecting the implant evaluation.^{3,21}

High-resolution images are necessary for the proper visualization of single electrode contacts. Verbist et al²² compared 4 different MDCT devices in the evaluation of CIs. They used an in-plane resolution (x and y axis) of 0.48–0.68 mm and a longitudinal resolution (z-axis) of 0.7–0.98 mm, obtaining images with the high resolution necessary to adequately discriminate among the different electrode contacts. However, the use of flat panel detectors in CBCT devices provides images with higher isotropic resolution using a submillimeter detector size ranging from 0.09 to 0.4 mm.¹⁵ In the current study, the voxel size used in the CBCT group was 0.125 mm (in all dimensions), which provided an isotopic image with high spatial resolution, thus allowing good-to-perfect visualization of single electrode contacts in 56% of patients (including widely spaced and narrowly spaced electrode contacts) compared with only 16% in the MDCT group (including only widely spaced contacts).

The metallic artifacts were also significantly lower in the CBCT group than in the MDCT group ($P < .001$). However, some of the patients undergoing CBCT implanted with CI532 (intercontact distance of 0.6 mm) and CI512 (nonuniform intercontact distance ranging from 0.4 to 0.8) had high to-moderate metallic artifacts, leading to poor visualization of electrode contacts. The signal-to-noise ratio was significantly lower in the CBCT group; this finding can be explained by the higher scattered radiation of CBCT, which is one of its main disadvantages, which decreases the contrast resolution and increases image noise.⁸ The other disadvantage of CBCT was the relatively longer exposure time, which may increase the risk of motion artifacts. However, in

patients with dizziness, shortened techniques with slightly lower resolution can be used to overcome this.

Some studies have examined the role of CBCT in the assessment of postoperative CIs in vitro.^{12,13} These studies compared the results of image analysis, including scalar positioning of the electrode, the presence of kinking, the number of intracochlear electrode contacts, and proper overall insertion using CBCT with those of histopathologic examinations in temporal bone specimens and concluded that CBCT as a noninvasive approach yielded results comparable with

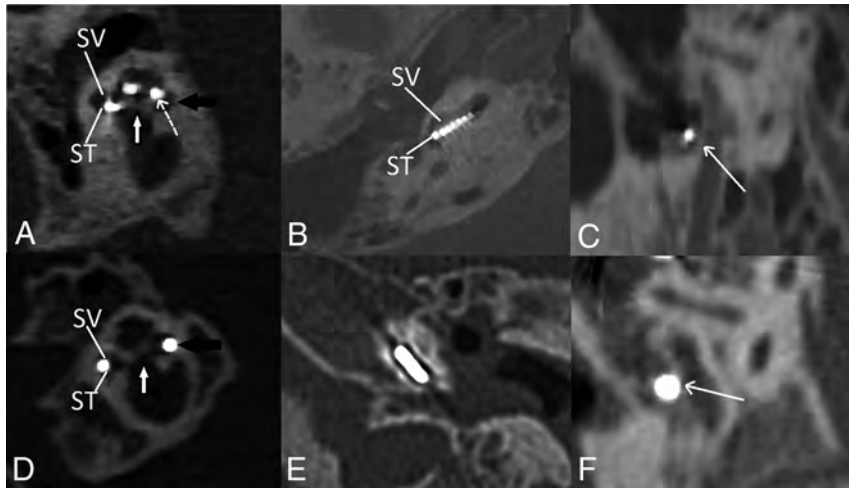


FIG 2. CBCT group. *A*, Midmodiolar view (cochlea) shows the modiolus (*white arrow*), the perfectly visualized cochlear lateral wall (*black arrow*), and the scalar translocation from ST to SV at the pars ascendens (*dashed arrow*). *B*, Axial view (cochlea) shows good visualization of single electrode contacts. *C*, Sagittal oblique view shows good visualization of the facial nerve canal wall (*arrow*). *D*, In the MDCT group, the midmodiolar view (cochlea) shows the modiolus (*white arrow*), nonvisualized cochlear lateral wall (artifacts) (*black arrow*), and the difficult scalar localization of the electrode (mostly ST). *E*, Axial view (cochlea) shows difficult identification of single electrode contacts and the osseous spiral lamina. *F*, Sagittal oblique view shows difficult identification of the facial nerve canal wall (*arrow*). ST indicates scala tympani; SV, scala vestibuli.

Table 4: SNR comparison

	CBCT Group	MDCT Group	P Value ^a
SNR in bone (median) (IQR)	8.31 (3.8)	10.77 (4.25)	.02
SNR in air (median) (IQR)	6.58 (3.85)	11.97 (5.53)	.001

Note:—IQR indicates interquartile range.

^aMann-Whitney U test.

those of histopathologic analyses, encouraging its clinical use. Razafindranaly et al¹⁴ compared the role of CBCT with that of MDCT in 9 patients in terms of scalar localization, insertion depth, and radiation doses. They concluded that there was good agreement between the 2 modalities in the evaluation of insertion depth; however, CBCT could be superior to MDCT in determining the scalar location of electrodes with lower doses.

Our results are in line with these previous studies because perfect visualization of the scalar position of the electrode was successful in 78% of cases in the CBCT group compared with 47% in the MDCT group. There was no statistically significant difference between both groups in the ability to measure the electrode insertion angle. Nevertheless, Jia et al²³ had difficulty in assessing the scalar position of electrode or interscalar translocation using the mobile intraoperative CBCT device compared with previously obtained images using MDCT in the same patients; however, this issue could be attributed to the differences between mobile and fixed CBCT devices and the lack of specialized neuroradiologists during the operation.

The assessment of cochlear walls is essential for electrode localization, scalar position, and evaluation of postimplant inner ear trauma. Verbist et al²² concluded that the outer (lateral) cochlear wall could be better evaluated than the inner wall, a result attributed to the thick outer wall being a part of the otic capsule (dense bone), which provides a

better contrast with the cochlear lumen, unlike the inner wall, which contains neural elements with lower density.

Our study revealed a statistically significant difference between the 2 groups regarding the visualization of the cochlear outer wall ($P < .001$), with it being perfectly visualized in 94% of the patients of the CBCT group compared with 53% in the MDCT group; however, there was no significant difference in the visualization of the cochlear inner wall ($P > .99$) and the modiolus ($P = .37$). Perfectly visualized cochlear inner walls and modioli were reported in 69% and 78% of patients in the CBCT group, respectively, compared with 73.7% and 95% in the MDCT group. This finding could be attributed to the larger number of lateral wall electrodes used in the MDCT group compared with the more perimodiolar and midscalar electrodes used in the CBCT group in our study population. The proximity of the electrode to the lateral cochlear wall or the modiolus can degrade the image quality by metallic artifacts. Furthermore, the osseous spiral lamina could be identified in only the CBCT group, in which 31% were barely visualized and 13% were well-visualized. The visualization of the spiral lamina could be further used for

better evaluation of electrode translocation and inner ear trauma after CI.

The facial nerve canal, though an extracochlear anatomic structure, is an important surgical landmark in the CI field.²⁴ In the current study, the good-to-perfect visualization of the facial canal bony wall was higher in the CBCT group than in the MDCT group. Although the difference was nonsignificant, this finding might allow a better radiologic evaluation of postoperative complications such as facial nerve injury or stimulation.

Many studies have compared the radiation dose of MDCT and CBCT in the assessment of CIs.²⁵ Guberina et al²⁶ compared CBCT with MDCT with 3 different machines (128-, 256-, and 384-multislice CT scanners) by imaging 4 temporal bone specimens and concluded that the dose-length product of a CBCT examination was 9%–15% of the dose-length product used during MDCT. In another study, this mean value was 200 [SD, 53.4] mGy*cm for CBCT compared with 605 [SD, 57.2] mGy*cm for MDCT.²¹ Our results also revealed significant radiation dose differences between the 2 groups. The dose-length product for the CBCT group ranged from 47.6 to 93 mGy*cm, while it was 179–650 mGy*cm for the MDCT group, indicating a reduction of about 85.7% of the maximum dose with CBCT compared with MDCT. However, the low radiation dose is associated with a decreased signal-to-noise ratio, which makes CBCT

unsuitable for soft-tissue imaging and limits its use for visualizing bone details.⁷

Other studies examined the possibility of using low-dose CT in the cadaveric lamb model for assessment of the electrode position.^{27,28} They succeeded in evaluating the electrode position using a reduced tube current of 50% without an increase in the artifacts. They stated that the use of low-dose CT protocols might have results comparable with those of CBCT, both in terms of image quality and radiation dose. However, further prospective studies are needed to substantiate this possibility.

The main limitations of our study were the heterogeneity in the age, the differences in the types of implanted electrodes, and the 2 imaging modalities not being compared in the same group of patients because of the risk of radiation exposure.

CONCLUSIONS

CBCT imaging in postoperative patients with CIs can provide images with high spatial resolution and fewer metallic artifacts compared with MDCT, with a relatively lower radiation dose.

Disclosures: Ibraheem M. Al-Dhamari—UNRELATED: Employment: Koblenz University.

REFERENCES

1. Vaid S, Vaid N. **Imaging for cochlear implantation: structuring a clinically relevant report.** *Clin Radiol* 2014;69:e307–22 CrossRef Medline
2. Fishman AJ. **Imaging and anatomy for cochlear implants.** *Otolaryngol Clin North Am* 2012;45:1–24 CrossRef Medline
3. Vogl TJ, Tawfik A, Emam A, et al. **Pre-, intra- and post-operative imaging of cochlear implants.** *Rofa* 2015;187:980–89 CrossRef Medline
4. Abd El Aziz TT, El Fiky L, Shalaby MH, et al. **Radiological evaluation of inner ear trauma after cochlear implant surgery by cone beam CT (CBCT).** *Eur Arch Otorhinolaryngol* 2019;276:2697–2703 CrossRef Medline
5. Diogo I, Walliczek U, Taube J, et al. **Possibility of differentiation of cochlear electrodes in radiological measurements of the intracochlear and chorda-facial angle position.** *Acta Otorhinolaryngol Ital* 2016;36:310–16 CrossRef Medline
6. Dhanasingh A, Jolly C. **An overview of cochlear implant electrode array designs.** *Hear Res* 2017;356:93–103 CrossRef Medline
7. Miracle AC, Mukherji SK. **Cone beam CT of the head and neck, Part 2: clinical applications.** *AJNR Am J Neuroradiol* 2009;30:1285–92 CrossRef Medline
8. Miracle AC, Mukherji SK. **Conebeam CT of the head and neck, Part 1: physical principles.** *AJNR Am J Neuroradiol* 2009;30:1088–95 CrossRef Medline
9. Wanna GB, Noble JH, McRackan TR, et al. **Assessment of electrode placement and audiological outcomes in bilateral cochlear implantation.** *Otol Neurotol* 2011;32:428–32 CrossRef Medline
10. Güldner C, Weiss R, Eivazi B, et al. **Intracochlear electrodeposition: evaluation after deep insertion using cone-beam computed tomography [in German].** *HNO* 2012;60:817–22 CrossRef Medline
11. Cushing SL, Daly MJ, Treaba CG, et al. **High-resolution cone-beam computed tomography: a potential tool to improve atraumatic electrode design and position.** *Acta Otolaryngol* 2012;132:361–68 CrossRef Medline
12. Marx M, Risi F, Escudé B, et al. **Reliability of cone-beam computed tomography in scalar localization of the electrode array: a radio histological study.** *Eur Arch Otorhinolaryngol* 2014;271:673–79 CrossRef Medline
13. Saeed S, Selvadurai D, Beale T, et al. **The use of cone-beam computed tomography to determine cochlear implant electrode position in human temporal bones.** *Otol Neurotol* 2014;35:1338–44 CrossRef Medline
14. Razafindranaly V, Truy E, Pialat JB, et al. **Cone Beam CT versus multislice CT: radiologic diagnostic agreement in the postoperative assessment of cochlear implantation.** *Otol Neurotol* 2016;37:1246–54 CrossRef Medline
15. Scarfe WC, Farman AG. **What is cone-beam CT and how does it work?** *Dent Clin North Am* 2008;52:707–30 CrossRef Medline
16. Diogo I, Franke N, Steinbach-Hundt S, et al. **Differences of radiological artifacts in cochlear implantation in temporal bone and complete head.** *Cochlear Implants Int* 2014;15:112–17 CrossRef Medline
17. Dragovic AS, Stringer AK, Campbell L, et al. **Co-registration of cone beam CT and preoperative MRI for improved accuracy of electrode localization following cochlear implantation.** *Cochlear Implants Int* 2018;19:147–52 CrossRef Medline
18. Pearl MS, Roy A, Limb CJ. **High-resolution secondary reconstructions with the use of flat panel CT in the clinical assessment of patients with cochlear implants.** *AJNR Am J Neuroradiol* 2014;35:1202–08 CrossRef Medline
19. Tada A, Sato S, Masaoka Y, et al. **Imaging of the temporal bone in children using low-dose 320-row area detector computed tomography.** *J Med Imaging Radiat Oncol* 2017;61:489–93 CrossRef Medline
20. Whiting BR, Holden TA, Brunnsden BS, et al. **Use of computed tomography scans for cochlear implants.** *J Digit Imaging* 2008;21:323–28 CrossRef Medline
21. Merklen F, Piron J, Sicard M, et al. **Cone-beam computed tomography in children with cochlear implants: the effect of electrode array position on ECAP.** *Int J Pediatr Otorhinolaryngol* 2017;92:27–31 CrossRef Medline
22. Verbist BM, Joemai RM, Teeuwisse WM, et al. **Evaluation of 4 multi-section CT systems in postoperative imaging of a cochlear implant: a human cadaver and phantom study.** *AJNR Am J Neuroradiol* 2008;29:1382–88 CrossRef Medline
23. Jia H, Torres R, Nguyen Y, et al. **Intraoperative cone-beam CT for assessment of intracochlear positioning of electrode arrays in adult recipients of cochlear implants.** *AJNR Am J Neuroradiol* 2018;39:768–74 CrossRef Medline
24. Young JY, Ryan ME, Young NM. **Preoperative imaging of sensorineural hearing loss in pediatric candidates for cochlear implantation.** *Radiographics* 2014;34:E133–49 CrossRef Medline
25. Rafferty MA, Siewerdsen JH, Chan Y, et al. **Intraoperative cone-beam CT for the guidance of temporal bone surgery.** *Otolaryngol Head Neck Surg* 2006;134:801–08 CrossRef Medline
26. Guberina N, Dietrich U, Arweiler-Harbeck D, et al. **Comparison of radiation doses imparted during 128, 256, 384 multislice CT-scanners and cone beam computed tomography for intra and perioperative cochlear implant assessment.** *Am J Otolaryngol* 2017;38:649–53 CrossRef Medline
27. Weisstanner C, Mantokoudis G, Huth M, et al. **Radiation dose reduction in postoperative computed position control of cochlear implant electrodes in lambs: an experimental study.** *Int J Pediatr Otorhinolaryngol* 2015;79:2348–54 CrossRef Medline
28. Theunisse HJ, Joemai RMS, Maal TJJ, et al. **Cone-beam CT versus multi-slice CT systems for postoperative imaging of cochlear implantation: a phantom study on image quality and radiation exposure using human temporal bones.** *Otol Neurotol* 2015;36:592–99 CrossRef Medline
29. Bennink E, Peters JP, Wendrich AW, et al. **Automatic localization of cochlear implant electrode contacts in CT.** *Ear Hear* 2017;38:e376–84 CrossRef Medline

MR Imaging Characteristics of Intraocular Perfluoro-n-Octane

 M.T. Williams,  J.E. Williams,  B.A. Winegar,  R.F. Carmody, and  J.B. Christoforidis

ABSTRACT

SUMMARY: We describe the unique MR imaging characteristics of intraocular perfluoro-n-octane, a liquid used for intraoperative and postoperative tamponade in the context of complex retinal detachment repair, and contrast it with other intraocular pathologies. Because trace amounts of perfluoro-n-octane may be left in the globe postoperatively, it may be confused for other abnormalities, such as foreign bodies or tumors.

ABBREVIATION: PFO = perfluoro-n-octane

Perfluoro-n-octane (PFO) is a low-viscosity perfluorocarbon liquid used for intraoperative retinal tamponade in complex retinal detachments.¹ Its high specific gravity makes it useful for stabilizing and flattening the retina intraoperatively.¹ PFO is thought to exert a long-term toxic effect on the retina, depending on the amount left in the eye, and typically at the end of the surgical procedure, it is exchanged with a perfluorocarbon gas or silicone oil for postoperative tamponade.¹ The fluid-air exchange process is not perfect, and trace amounts of PFO may be left in the eye without consequence, except in rare cases when trace amounts of the liquid may be trapped in the subretinal space.² There have been reports, however, of trace amounts of PFO mimicking intraocular foreign bodies on CT, thus prompting further unnecessary work-up when its history of use was unrecognized.^{3,4} Although its CT characteristics have been reported, its MR imaging characteristics have not been described to our knowledge.

In some cases, PFO may be intentionally left in the globe short term postoperatively for tamponade in eyes at high risk of re-detachment because of proliferative vitreoretinopathy or in patients with giant retinal tears or multiple inferior breaks who cannot tolerate face-down positioning.⁵ We describe here the MR imaging characteristics of PFO in a patient with a history of recurrent retinal detachments of the left eye requiring postoperative PFO tamponade

who subsequently underwent MR imaging for unrelated vision loss of the right eye.

A 64-year-old male patient with a history of repair 2 weeks earlier of a recurrent rhegmatogenous retinal detachment of the left eye, complicated by proliferative vitreoretinopathy requiring PFO for postoperative tamponade, underwent MR imaging of the orbits (Figure) after presenting with vision loss of unclear cause of the right eye.

FINDINGS

PFO liquid demonstrates signal void on conventional fast spin-echo MR imaging, appearing hypointense on T1-weighted sequences, fat-suppressed T2-weighted sequences, and STIR sequences. In large quantities, the signal void of PFO on MR imaging resembles air. However, the high specific gravity of PFO accounts for its dependent layering when placed in the posterior segment, which is opposite of the nondependent layering of air and gaseous compounds.

DISCUSSION

The appearance of PFO on MR imaging results from its high specific gravity and lack of proton spins within the substance, leading to dependent layering and signal void on all sequences. The lack of proton spins owes to its chemical composition, C₈F₁₈, consisting entirely of carbon and fluorine atoms without any hydrogen atoms. In clinical contexts, PFO is most likely to be encountered in trace quantities. In these trace amounts, PFO could be mistaken for subhyaloid or retinal hemorrhage, air bubbles, dystrophic calcification, intraocular masses, or foreign bodies. Of the 5 substances injected into the globe for retinal tamponade, including filtered air, sulfur hexafluoride gas, perfluoropropane gas, silicone oil, and PFO, PFO is the only substance

Received July 1, 2020; accepted after revision September 18.

From the Departments of Ophthalmology and Vision Science (M.T.W., J.B.C.) and Medical Imaging (R.F.C.), University of Arizona College of Medicine, Tucson, Arizona; Ira A. Fulton Schools of Engineering (J.E.W.), Arizona State University, Tempe, Arizona; Department of Radiology & Imaging Sciences (B.A.W.) University of Utah School of Medicine, Salt Lake City, Utah; and Retina Specialists of Southern Arizona (R.F.C.), Tucson, Arizona.

Please address correspondence to Mark T. Williams, MD, University of Arizona, Department of Ophthalmology and Vision Science; 655 N. Alvernon Way, Suite 204, Tucson, AZ 85711; e-mail: mtwilli588@gmail.com
<http://dx.doi.org/10.3174/ajnr.A6901>

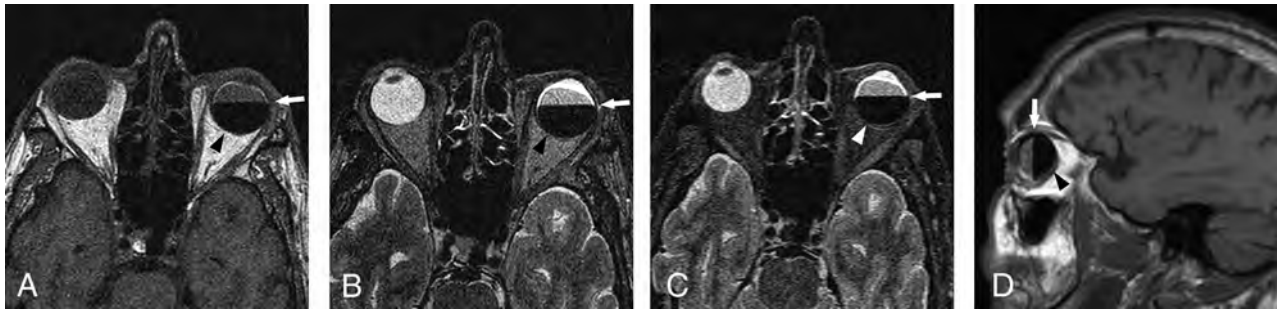


FIGURE. Axial T1-weighted (A), axial fat-suppressed T2-weighted (B), axial STIR (C), and sagittal T1-weighted (D) MR imaging of the orbits demonstrate hypointense PFO layering dependently within the posterior segment of the left globe (arrowheads) with fluid–fluid level (arrows). Note that the attenuation of PFO is greater than that of water, causing it to layer dependently within the left globe in this supine patient.

with a specific gravity higher than water and would be the only substance of the 5 expected to settle in a dependent manner. Silicone oil has been described as appearing similar to hemorrhage, demonstrating hyperintensity to vitreous on T1-weighted imaging and hypointensity on T2-weighted imaging.⁶

Intraocular masses, including uveal melanoma, intraocular metastases, retinoblastoma, and retinal capillary hemangioma, all demonstrate hypointensity to vitreous on T2-weighted images but are distinguishable from PFO by hyperintensity to vitreous on T1-weighted sequences or isointensity to vitreous on T1-weighted images in the case of metastases.⁷ Calcifications, which may be seen in phthisis bulbi, retinoblastoma, and optic disc drusen, would not feature fluid–fluid levels and typically take on a more disorganized or scattered appearance in the case of phthisis bulbi and retinoblastoma.⁸

Depending on their physical properties, intraocular foreign bodies can demonstrate a wide range of signal characteristics on MR imaging. Nonmetallic foreign bodies typically demonstrate low T1-weighted and T2-weighted signal intensity and may appear similar to PFO, especially if they are small.⁹ However, nonmetallic intraocular foreign bodies of larger size typically demonstrate geometric shapes without the fluid–fluid level appearance of PFO.⁹ Most nonmetallic intraocular foreign bodies also typically demonstrate a thin high-intensity rim most notable on T1-weighted images, with some foreign bodies, particularly certain types of glass and wood, also demonstrating variable blooming artifacts not seen with PFO.⁹

CONCLUSIONS

PFO may be differentiated from other intraocular entities by its signal void on all sequences, fluid–fluid levels when present in sufficient quantity, and dependent layering in the globe, owing to its high specific gravity. Multiple cases have been reported of trace amounts being confused for intraocular foreign bodies on CT, and if unrecognized, it may prompt further unnecessary work-up.^{3,4} In cases of repair of ocular trauma, both silicone oil droplets and PFO droplets have been reported to migrate intracranially, potentially

leading to further diagnostic confusion.^{10,11} Knowledge of its MR imaging characteristics compared with other intraocular entities is important to avoid incorrect diagnosis.

REFERENCES

1. Chang S, Sparrow JR, Iwamoto T, et al. **Experimental studies of tolerance to intravitreal perfluoro-n-octane liquid.** *Retina* 1991;11:367–74 Medline
2. Garcia-Valenzuela E, Ito Y, Abrams GW. **Risk factors for retention of subretinal perfluorocarbon liquid in vitreoretinal surgery.** *Retina* 2004;24:746–52 CrossRef Medline
3. Christoforidis JB, Caruso PA, Curtin HD, et al. **CT characteristics of intraocular perfluoro-N-octane.** *AJNR Am J Neuroradiol* 2003;24:1769–71 Medline
4. Baskaran P, Ganne P, Krishnappa NC. **Perfluoro-n-octane mimicking an intraocular foreign body.** *GMS Ophthalmol Cases* 2017;7: Doc30 CrossRef Medline
5. Rush R, Sheth S, Surka S, et al. **Postoperative perfluoro-N-octane tamponade for primary retinal detachment repair.** *Retina* 2012;32:1114–20 CrossRef Medline
6. Mathews VP, Elster AD, Barker PB, et al. **Intraocular silicone oil: in vitro and in vivo MR and CT characteristics.** *AJNR Am J Neuroradiol* 1994;15:343–47 Medline
7. Peyster RG, Augsburger JJ, Shields JA, et al. **Intraocular tumors: evaluation with MR imaging.** *Radiology* 1988;168:773–79 CrossRef Medline
8. Grech R, Cornish KS, Galvin PL, et al. **Imaging of adult ocular and orbital pathology—a pictorial review.** *J Radiol Case Rep* 2014;8:1–29 CrossRef Medline
9. Modjtahedi BS, Rong A, Bobinski M, et al. **Imaging characteristics of intraocular foreign bodies: a comparative study of plain film X-ray, computed tomography, ultrasound, and magnetic resonance imaging.** *Retina* 2015;35:95–104 CrossRef Medline
10. Malin DR, Aulino JM, Recchia FM. **Intracranial hyperdense subarachnoid perfluorocarbon droplets after attempted retinal detachment treatment.** *Emerg Radiol* 2007;14:261–63 CrossRef Medline
11. Eller AW, Friberg TR, Mah F. **Migration of silicone oil into the brain: a complication of intraocular silicone oil for retinal tamponade.** *Am J Ophthalmol* 2000;129:685–88 CrossRef Medline

Vestibular Implant Imaging

A. Hedjoudje, D.P. Schoo, B.K. Ward, J.P. Carey, C.C. Della Santina, and M. Pearl



ABSTRACT

SUMMARY: Analogous to hearing restoration via cochlear implants, vestibular function could be restored via vestibular implants that electrically stimulate vestibular nerve branches to encode head motion. This study presents the technical feasibility and first imaging results of CT for vestibular implants in 8 participants of the first-in-human Multichannel Vestibular Implant Early Feasibility Study. Imaging characteristics of 8 participants (3 men, 5 women; median age, 59.5 years; range, 51–66 years) implanted with a Multichannel Vestibular Implant System who underwent a postimplantation multislice CT ($n = 2$) or flat panel CT ($n = 6$) are reported. The device comprises 9 platinum electrodes inserted into the ampullae of the 3 semicircular canals and 1 reference electrode inserted in the common crus. Electrode insertion site, positions, length and angle of insertion, and number of artifacts were assessed. Individual electrode contacts were barely discernible in the 2 participants imaged using multislice CT. Electrode and osseous structures were detectable but blurred so that only 12 of the 18 stimulating electrode contacts could be individually identified. Flat panel CT could identify all 10 electrode contacts in all 6 participants. The median reference electrode insertion depth angle was 9° (range, -57.5° to 45°), and the median reference electrode insertion length was 42 mm (range, -21 –66 mm). Flat panel CT of vestibular implants produces higher-resolution images with fewer artifacts than multidetector row CT, allowing visualization of individual electrode contacts and quantification of their locations relative to vestibular semicircular canals and ampullae. As multichannel vestibular implant imaging improves, so will our understanding of the relationship between electrode placement and vestibular performance.

ABBREVIATIONS: FF = full-field; FPCT = flat panel CT; HR = high-resolution; MSCT = multislice CT; SCC = semicircular canal; MVI = Multichannel Vestibular Implant System

Although individuals with a unilateral vestibular deficit and 1 normal labyrinth usually compensate well via rehabilitation exercises and adaptation, those with bilateral vestibular hypofunction often have degraded visual acuity during head movement, postural instability, and chronic disequilibrium.^{1–3} When bilateral vestibular hypofunction results from ototoxic drug exposure, Ménière disease, genetic defects, or other inner ear dysfunction sparing the vestibular nerve and central pathways, an

implantable neuroelectronic prosthesis that measures 3D head rotation and stimulates the vestibular nerve with motion-modulated electrical pulse trains could substantially improve quality of life.^{4,5}

Vestibular implants are similar to commercially available cochlear implants in that they include an external unit that powers and communicates with an implanted inner ear stimulator via a transcutaneous inductive link.^{4,5} The external unit includes a head-worn unit (for sensing head motion and delivering power and signals to the implanted stimulator) and a power and control unit containing a battery and microprocessor. As in cochlear implant systems, the head-worn unit and implanted stimulator each contain at least 1 magnet to hold the head-worn unit on the scalp over the implant. Unlike cochlear implant systems, vestibular implant systems sometimes include ≥ 1 additional magnet on each component to facilitate retention of the head-worn unit. Vestibular implant electrode arrays typically are much smaller than cochlear implant electrode arrays and are implanted in the semicircular canal (SCCs) near the ampullae, where the vestibular nerves branches terminate.⁴ Variations on this approach have included an

Received May 30, 2020; accepted after revision September 10.

From the Department of Otolaryngology–Head and Neck Surgery (A.H., D.P.S., B.K.W., J.P.C., C.C.D.S.), Division of Interventional Neuroradiology (A.H., M.P.), and Department of Biomedical Engineering (C.C.D.S.), Johns Hopkins University School of Medicine, Baltimore, Maryland; Neuroradiology Unit (A.H.), Service of Diagnostic and Interventional Imaging, Sion Hospital, Sion, Valais, Switzerland; and Labyrinth Devices (C.C.D.S.), Baltimore, Maryland.

This work was supported by the National Institute on Deafness and Other Communication Disorders R01DC013536 and 2T32DC000023, Labyrinth Devices, and MED-EL.

Please address correspondence to Abderrahmane Hedjoudje, MD, MSE, Department of Interventional Neuroradiology, Johns Hopkins School of Medicine, 601 North Caroline St, Suite 6253, Baltimore, MD 21287; e-mail: ahedjou1@jhmi.edu

Indicates open access to non-subscribers at www.ajnr.org

<http://dx.doi.org/10.3174/ajnr.A6991>

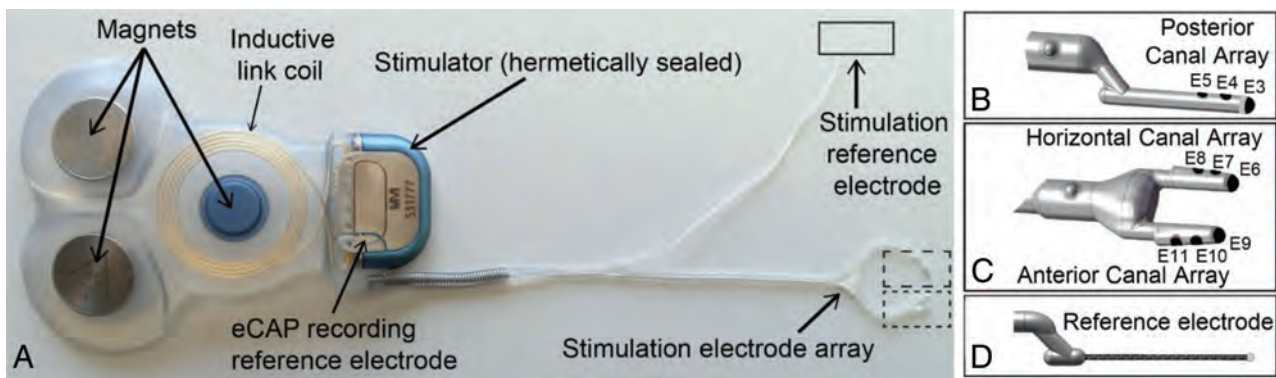


FIG 1. A, The MVI stimulator comprises 3 fixation magnets, an inductive coil link, electrical current stimulator circuitry, a stimulation electrode array, a stimulation reference electrode, and a recording reference electrode. The electrode array includes a 3-electrode shank for the posterior canal (B, E3–E5), a forked subarray with 2 shanks for the horizontal (C, E6–E8) and anterior (C, E9–E11) canals, and a stimulation reference electrode (D). eCAP indicates electrically evoked compound action potential. Reprinted with permission from Labyrinth Devices, LLC, 2019.

extraluminal approach (in which the surgeon attempts to expose and place electrodes near vestibular nerve branches in the distal-most aspect of the internal auditory canal and singular nerve canal); implantation of electrode arrays near the utricle and saccule; simultaneous or delayed placement of a separate electrode array in the cochlea; and variations in location of the stimulation reference electrode, which can be implanted in the labyrinth or a subperiosteal pocket (as an alternative surgical procedure) or integrated with the stimulator housing.

Empiric studies in animals and finite element models of current flow in the labyrinth indicate that electrode distances to target and nontarget nerve branches are key determinants of the strength and selectivity of stimulation. Therefore, precise knowledge of electrode location, as provided by high-resolution postoperative imaging, can provide information helpful for both prognosis and guiding the choice of which electrodes to activate and which stimulus parameters to use. Postoperative imaging performed as a part of a vestibular implant operation is useful to confirm the location of implanted electrode arrays, measure the depth of insertion and electrode position relative to vestibular nerve branches, and detect kinking, damage, or displacement. MR imaging is unsuitable for assessing electrode location because of field interactions that distort images and can displace the magnet of the implant, poor air-bone contrast within the temporal bone, and the inability of MR imaging to directly image the platinum/iridium wires and silicone that make up electrode arrays (other than by imaging displacement of inner ear fluids). Multislice CT (MSCT) is the better technique for characterizing cochlear implant position and is the current de facto standard, given its greater spatial resolution and better contrast among bone, air, metal, and fluid.^{6,7} Metal artifacts, however, can significantly degrade image quality. Flat panel CT (FPCT), a relatively new imaging technique that yields tomographic reconstructions from images acquired using a C-arm x-ray system with flat panel image detectors, provides excellent visualization of high-contrast structures with better spatial resolution than MSCT.^{8,9} In particular, FPCT produces images with sufficient resolution to precisely quantify cochlear electrode contact locations in a clinical setting.^{6,7,9,10}

The purpose of this study was to present the very first imaging results of CT in vestibular implant imaging. In this report,

we present the technical aspects and imaging performance of MSCT and FPCT in assessing the intravestibular position of implanted electrode arrays in 8 participants in the first-in-human Multichannel Vestibular Implant Early Feasibility Study (clinicaltrials.gov, NCT02725463), and we suggest important features that should be reported in post-vestibular implantation imaging studies as well as a protocol for FPCT imaging of vestibular implants.¹¹

MATERIALS AND METHODS

This study was conducted under a protocol approved by the Johns Hopkins institutional review board (No. NA_00051349) and was registered on the clinicaltrials.gov data base (NCT02725463).

Vestibular Implant Electrode Array Design and Implantation

The implanted stimulator component of the Multichannel Vestibular Implant System (MVI; Labyrinth Devices) is a CONCERTO cochlear implant stimulator (MED-EL), modified for implantation in the SCCs (Fig 1A). It includes an electrode array with stimulation electrodes, a stimulation return and recording reference electrode, hermetically encapsulated electronics, 3 magnets, and an antenna coil for transcutaneous inductive transmission of power and control signals that the implant receives from the external system component.

The MVI is implanted via a postauricular incision and transmastoid approach similar to that typically used for cochlear implantation or labyrinthectomy, except that no entry is made into the cochlea and the SCCs are identified but not destroyed. Instead openings are made into the labyrinth for electrode array insertion (in the superior SCC ampulla, horizontal SCC ampulla, posterior SCC thin segment, and near the common crus). The electrode array (Fig 1B, C, and D) consists of a silicone carrier and comprises 10 platinum/iridium electrodes: 2 linear arrays of 3 electrodes each, joined to form a forked array inserted into the horizontal and superior ampullae; 3 on a linear array implanted in the posterior canal; and a braided platinum/iridium wire reference/return electrode inserted either into the common crus or in a subperiosteal pocket outside the temporal bone. Electrodes are spaced 0.2 mm apart in the silicone carrier for the forked array for the horizontal and

Table 1: Demographic information for participants with vestibular implants

Participants	Date Implanted	Date Imaged	Age (yr), ^a Sex	Imaging Protocol	Implant Side	Reference Location
1	12 Aug 2016	Sep 2016	62, M	MSCT	Left	CC
2	4 Nov 2016	Nov 2016	57, M	MSCT	Left	CC
3	3 Feb 2017	Feb 2017	63, F	FPCT, HR mode	Left	CC
4	15 Dec 2017	Jan 2018	62, F	FPCT, FF mode	Left	CC
5	24 Aug 2018	Sep 2018	51, F	FPCT, HR mode	Right	CC
6	31 Aug 2018	Sep 2018	66, F	FPCT, FF mode	Right	CC
7	14 Jan 2019	Feb 2019	53, F	FPCT, HR mode	Left	CC
8	13 Sep 2019	Oct 2019	55, M	FPCT, HR mode	Right	SP

Note:—CC indicates common crus of the implanted labyrinth; SP, in a subperiosteal pocket outside the temporal bone; Aug, August; Jan, January; Sep, September; Dec, December; Feb, February; Nov, November.

^a Age in years at time of implantation.

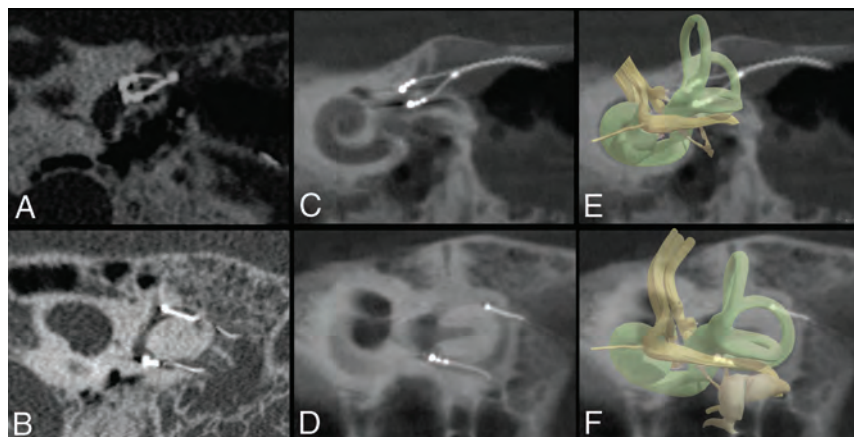


FIG 2. Method for generating MSCT (A and B) and FPCT (C and D) MPR. Two planes are generated. The first plane is approximately tangential to the thin segments of the superior and horizontal SCCs at their junctions with their ampullae and includes the 6 electrode contacts of the forked array inserted into the superior and horizontal ampullae. The second plane is in the posterior plane of the SCC and includes the 3 electrode contacts of the linear array implanted in the posterior canal and the tip of braided platinum/iridium wire inserted into the common crus. Section thickness was set to 2 mm to include all electrode contacts on 1 image for both planes. Window width and contrast level were adjusted as needed to optimize the visibility of electrode contacts. A 3D representation of the vestibular lumen and vestibular nerve is added in transparency (E and F) to help visualize the anatomy.

superior ampullae and 0.3 mm apart in the silicone carrier for the posterior SCC.

Participants

Eight participants (3 men, 5 women; median age, 59.5 years, range, 51–66 years) disabled by bilateral vestibular hypofunction were implanted unilaterally with the implanted receiver/stimulator of the MVI. Three participants were implanted in the right ear, and 5 participants, in the left ear. Table 1 summarizes demographic information.

Image Acquisition

After implantation, all subjects were scanned with either an MSCT (Somatom Sensation; Siemens) or a C-arm-based FPCT platform (Artis zee biplane; Siemens). MSCT was performed using standard clinical imaging parameters for temporal bone CT, with orientation of “axial” slices pitched to align with a plane through the horizontal SCC. Scanning was performed with 0.6-mm collimation, 120 kV, and 320 mAs. FPCT (DynaCT; Siemens) evaluation was performed using a flat panel angiography system (Axiom Artis zee;

Siemens) and commercially available software (syngo DynaCT; Siemens). The participant was placed supine on the angiography table, and the head was taped in place to limit participant motion. When we prepared the DynaCT acquisition, attention was paid to collimate the VOI to include only the temporal bones (craniocaudal collimation from just above the petrous ridges to just below the mastoid tip). A 20-second FPCT acquisition of the head was performed using the following parameters: 109 kV, small focus, 200° rotation angle, and angulation step of 0.4° per frame. FPCT was performed in 2 modes: full-field (FF) and high-resolution (HR). The FF mode uses top and bottom collimation, whereas the HR mode has collimation in all planes, allowing focal acquisition of the temporal bone of interest. Four participants underwent FPCT imaging with the HR mode, and 2 participants, with the FF mode.

Reconstruction Parameters

The MSCT dataset was reformatted with 0.6-mm slices every 0.2 mm using a 512 × 512 matrix and a 65–70 mm FOV. FPCT secondary reconstructions were created with the following parameters: manually generated VOI to include only the electrode array; isotropic voxel size, 0.08 mm; 512 × 512 section matrix; sharp image characteristics.

Multiplanar Images

We used MPR to generate 2 oblique 2D images. The first image was in the plane of the posterior SCC and included the 3 electrode contacts of the linear array implanted in the posterior canal and the tip of the braided platinum/iridium wire reference electrode inserted into the common crus. The second image was in a plane that was approximately tangential to the thin segments of the superior and horizontal canals and their junctions with their respective ampullae. This second image included the 6 electrode contacts of the forked array inserted into the superior and horizontal ampullae. Section thickness was set to 2 mm to include all

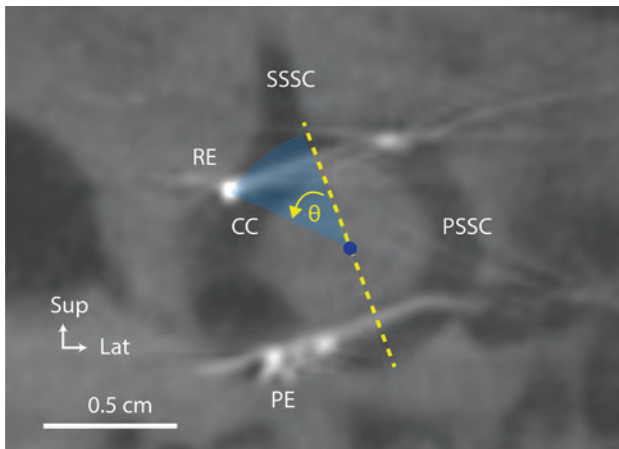


FIG 3. Subject: Participant 7. Method for calculating the angle (θ) of the angular insertion depth of the common crus reference electrode. CC indicates common crus of the implanted labyrinth; PE, posterior electrode array; PSSC, posterior semicircular canal; SSSC, superior semicircular canal; RE, reference electrode; Sup, superior; Lat, lateral.

electrode contacts on 1 image. Window width and contrast level were adjusted as needed to optimize the visibility of the electrode contacts (Fig 2).

Measuring Common Crus Reference Electrode Insertion Depth

To see the tip of the braided platinum/iridium wire reference electrode inserted into the common crus, we reduced the MPR section thickness to 0.1 mm for an oblique section in the plane of the posterior canal. The crest of bone at the junction of the common crus, superior canal, and posterior canal was designated as the first reference point for measuring angular insertion depth of the reference electrode. A line drawn from the first reference point to the center of the circle formed by the posterior canal served as the reference (zero degree) line. The angle between the line joining the tip of the reference electrode and the center of the posterior SCC and the reference line was then calculated (Fig 3) and defined as the insertion depth angle. The angle was positive when the reference electrode tip was inserted deeper than the junction of the superior and posterior canal (deep insertion) and negative otherwise (short insertion). We also reported the length inserted by measuring the wire distance from the point of insertion in the posterior SCC to the tip of the reference electrode. All measures were individually performed by 2 radiologists; the mean result was obtained and reported if measures did not exceed a 10% error.

Visualization of Electrode Contacts

Vestibular implant electrode array and single-electrode contacts were rated on a 3-point scale (0 = not visible; 1 = blurred, no single electrodes distinguishable; and 2 = clearly visible with single electrodes distinguishable).

RESULTS

Visualization of Individual Electrode Contacts

Individual electrode contacts were barely discernible in the 2 participants imaged using MSCT. Contacts and osseous structures were

detectable but blurred enough so that only 12 of the 18 stimulation electrode contacts could be individually identified (not visible, $n = 0$; blurred, $n = 6$; clearly visible, $n = 12$). A blooming-type artifact (Fig 2A), in which the electrode array appears larger than its actual size, was identified on the MSCT images both between contacts and at the level of individual electrode contacts. Electrode arrays appeared to occupy most of the ampullae space, making it challenging to identify precisely each electrode contact.

FPCT was able to identify individually all 9 stimulating electrode contacts of the MVI arrays in all 6 participants, as well as all 6 reference electrodes inserted in the common crus (not visible, $n = 0$; blurred, $n = 0$; clearly visible, $n = 60$). A linear sunburst streak artifact (Fig 2C) was observed in all FPCT images and was noticeable at the level of individual electrode contacts but was reduced between electrode contacts. The use of the HR mode when obtaining FPCT images ($n = 4$ participants) produced the clearest images of the electrode array and surrounding labyrinthine structures. After we used the FF mode ($n = 2$ participants), all individual electrode contacts could be identified, but electrodes and surrounding osseous structures were less well-resolved compared with the HR mode. MPR reconstructions for all subjects are shown in Fig 4.

Common Crus Insertion Depth

The median reference electrode insertion depth angle was 9° (range, -57.5° to 45°). The median reference electrode insertion length was 42 mm (range, 21–66 mm). The reference electrode tip was within the common crus in 3 participants, in the superior canal proximal to the common crus in 1 patient, in the posterior canal in 3 participants, and in a subperiosteal pocket in one. Results are summarized in Table 2.

DISCUSSION

Accurately positioning each electrode array near the nerve branch of the SCCs that it is intended to stimulate can maximize the strength and selectivity of the prosthetic stimulation because it reduces the current intensity required to achieve and excite a given proportion of neurons in the targeted nerve branch and also reduces current spread to adjacent neurons in other vestibular nerve branches. Vestibular implant outcomes can vary considerably depending on the strength and selectivity of the electrode-nerve interface, as indicated by variation in the magnitude and direction of reflex eye movements driven by stimuli meant to target each nerve branch individually.⁴ Electrode distances to target and nontarget nerve branches are key determinants of the strength and selectivity of stimulation; changing electrode location by ~ 200 μm can change implant outcomes dramatically. Typically, 1 electrode on an electrode array of a given canal outperforms the others that are 250–500 μm away.¹²

Knowing vestibular implant array location, their insertion depth, and distance from target vestibular nerve branches can provide helpful information to choose the best electrodes to activate and define stimulus parameters to use, valuable insights that can drive iterative improvements in electrode array design and surgical technique. For example, electrode contact locations can be used as input to individualized finite element models that, once adequately validated via comparison with real data, can facilitate interpretation of empiric data, generation of testable

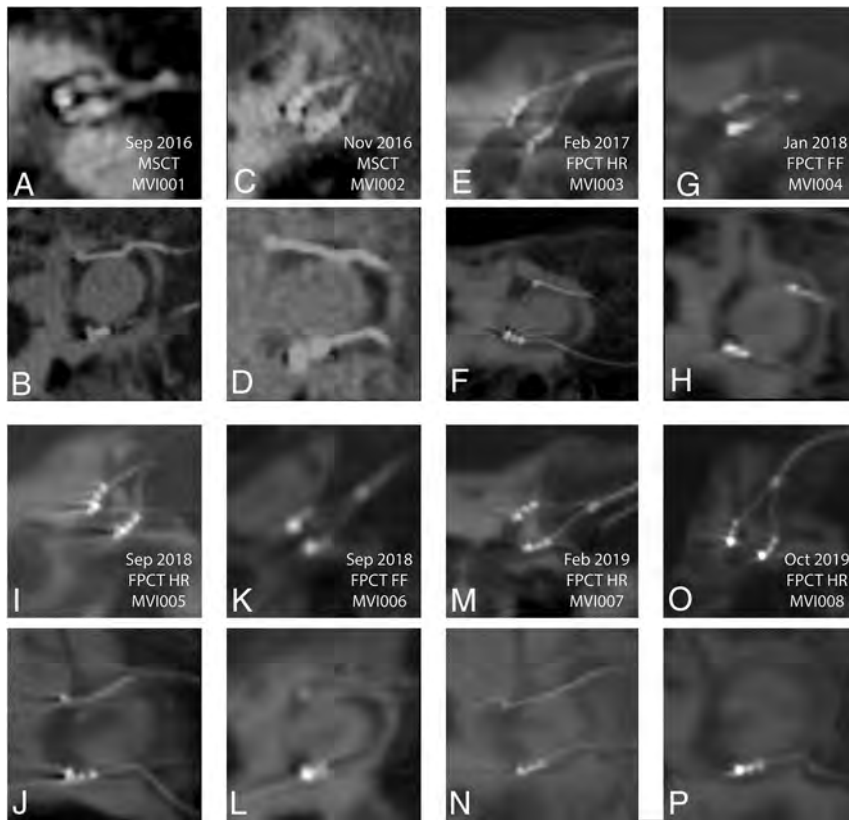


FIG 4. MSCT (A–D) and FPCT (E–P) multiplanar reconstructions for all participants. A and B, Participant 1 MSCT. C and D, Participant 2 MSCT. E and F, Participant 3 FPCT. G and H, Participant 4 FPCT. I and J, Participant 5 FPCT. K and L, Participant 6 FPCT, M and N, Participant 7 FPCT. O and P, Participant 8 FPCT. In every panel, the top of the image is superior and the left edge of the image is anteromedial. Sep indicates September; Feb, February; Oct, October; Nov, November; Jan, January.

Table 2: Common crus reference electrode angular depth and insertion length calculations and locations

Participant No.	CC Insertion Intended	Insertion Depth Angle	Insertion Length (mm)	Anatomic Location of the Reference Electrode Tip
1	Yes	−3°	39	Common crus
2	Yes	+26°	66	Superior canal
3	Yes	−30°	42	Posterior canal
4	Yes	−57°	21	Posterior canal
5	Yes	+21°	46	Common crus
6	Yes	−2°	41	Posterior canal
7	Yes	+45	51	Common crus
8	No	NA	NA	Outside temporal bone

Note:—NA indicates not applicable.

hypotheses, and optimization of electrode array designs through simulation.¹²

In the present study, we found that the locations of stimulating electrodes and their relation to vestibular bony structures can be depicted precisely with FPCT. All stimulating electrode arrays were close to their target end organs within the target ampullae; however, they varied with respect to location: adjacent to or far from the bone walls of each ampulla. Electrode contact with vestibular labyrinth walls may influence electrode impedance and the spatial pattern of current density, altering stimulation efficiency and

selectivity. We also found that reference electrode location varied significantly from case to case, likely because the surgical technique used (making as small an entry as possible in the posterior canal near the common crus, then sliding the reference electrode in with the intent of it reaching the common crus) does not permit direct intraoperative observation or steering of the electrode tip. In 2 cases, the reference electrode was inserted into the superior SCC instead of going down through the common crus. Intraoperative fluoroscopy or DynaCT may be helpful for guiding or confirming the electrode location.

FPCT versus MSCT

FPCT is a relatively new imaging technology that implements flat detectors to create volumetric reconstructions. Several advantages have been seen in angiography and temporal bone imaging for cochlear implantation.¹³ FPCT is a rapid imaging technique that obtains a full dataset of temporal bone images in approximately 20 seconds. The most clinically significant advantage of FPCT over MSCT is the ability for small voxel areas to be viewed with high resolution. Due to its higher spatial resolution, FPCT yields equal or higher image quality than MSCT when assessing bony structures of diagnostic interest for radiologists.^{7,8,14–16} Potential drawbacks to using FPCT for temporal bone imaging compared with MSCT include lack of widespread availability and poorer resolution of soft tissue with currently available FPCT systems.

A significant reduction in artifacts was appreciated on FPCT images over MSCT images. A blooming artifact, with the electrode array appearing larger than its actual size, was identified on the MSCT images. This smooth,

concentric artifact was identified both between and at the level of the individual electrode contacts, making it challenging to identify precisely each electrode contact. A beam artifact (linear streak bands) was noticeable on the FPCT images at the level of individual electrode contacts but was significantly reduced between electrode contacts. The position of the electrode contacts was better assessed on the FPCT images mainly because of the decrease in artifacts between them.

Previous authors have reported that an important advantage of FPCT is a reduced radiation dose compared with standard

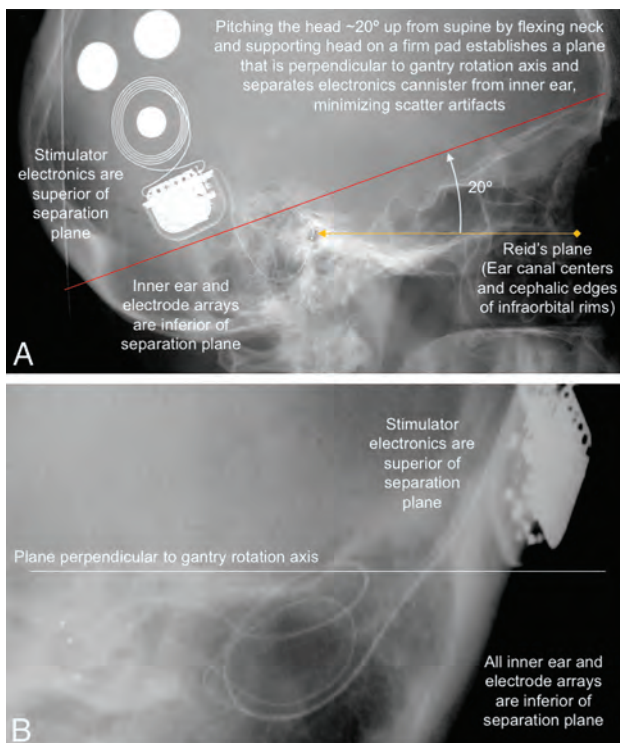


FIG 5. A, Lateral scout view showing electrode arrays visible through the external auditory canals (yellow arrowhead) and cephalic edges of the infraorbital rims (yellow diamond). Those palpable landmarks define the Reid plane (yellow line) and the plane of horizontal canals (red line). The plane of the horizontal semicircular canals, the standard “axial” plane for temporal bone CT reconstructions, is at a $\sim 20^\circ$ pitch from the Reid plane.¹⁷ By supporting the head on a firm wedge to pitch the head forward from supine (and flexing the neck until the Reid plane is pitched $\sim 20^\circ$ nose toward chest from Earth vertical), one can minimize scatter artifacts from the stimulator cannister to the inner ear by keeping them on opposite sides of a separation plane perpendicular to the gantry rotation axis (B).

temporal bone MSCT protocols.⁸ Depending on the clinical question, FPCT can reduce the radiation dose even more by imaging only the implanted ear. The collimation available in HR mode can direct the x-ray beam to the ear of interest, minimizing the dose received by the head.

Protocol for Vestibular Implant Imaging

Similar to imaging after cochlear implantation,^{7,9} FPCT imaging of postoperative vestibular implantation is easy to perform, produces high-resolution images, and can depict all individual electrode contacts. Patients should be positioned supine with the head pitched to prevent shadowing/overlap of the stimulator and/or magnets with the inner ear. Our imaging methods use a high-resolution secondary reconstruction algorithm with a manually generated small VOI (voxel size = 0.08 mm), Hounsfield unit kernel type, and sharp image characteristic. A 20-second FPCT acquisition of the head is performed using the following parameters: 109 kV, small focus, 200° rotation angle, and 0.4° per frame angulation step. Before image acquisition, the external components of the vestibular implant system are removed. The patient’s head is pitched forward $\sim 20^\circ$ by flexing the neck and

supporting the head on a firm wedge. The head is then taped in place. This positioning ensures that the Reid plane (which contains the center of the external auditory canals and the cephalic edges of the infraorbital rims, both easily palpable landmarks) is pitched $\sim 20^\circ$ from Earth-vertical, so that the horizontal SCC plane is approximately perpendicular to the gantry rotation axis and scatter artifacts from the magnets and stimulator electronics will not shadow the inner ear (Fig 5). Acquisition should include the entire implant, overlying scalp (to check scalp thickness over the magnets), inner ears, and at least the maxillary teeth (which are used to get canal orientation relative to a bite block for programming the alignment matrix of the processor).

Finally, multiplanar reconstructions are performed in the axial (horizontal plane of the SCC) and coronal planes, the planes of the superior and posterior canals (which also gives slices through the basal turn of the cochlea), and the plane that contains the superior and horizontal forked electrode array. This last plane should be tangential to the superior and horizontal canals at the junction of their ampullae as described in the Materials and Methods above. When reporting imaging findings of FPCT, we recommend that in addition to commenting on common temporal bone imaging findings, additional comments should be made on the quality of the examination, the number of metallic artifacts, the locations of stimulating electrode contacts relative to the ampullae, the location of the tip of the reference electrode if applicable; and scalp thickness over the implant.

This study has some limitations including a small sample size, lack of a control group, and lack of clinical information regarding correlation between vestibular function recovery and electrode contact positions. These topics are beyond the scope of this article, which aims to present the very first imaging results that are currently under investigation to be addressed in future studies in which imaging plays an important role.

Future development of vestibular imaging may lead to intraoperative DynaCT. DynaCT technology can be applied with acceptable additional time requirements without adding too much complexity to the surgical procedure. Intraoperative data acquisition by DynaCT may represent a suitable option for real-time surgical navigation during a vestibular implant operation. This imaging technology will encourage further advances in vestibular implant surgery and integrate functional aspects of imaging by applying individualized anatomy-based mathematic models that will help predict vestibular flow current spreading for each patient to further understand clinical outcomes of prosthesis implantation.

CONCLUSIONS

FPCT produces high-resolution images of vestibular implants, allowing identification of individual electrode contacts and quantification of their locations relative to vestibular SCC ampullae. Reduced artifacts were seen in FPCT images compared with MSCT images. Optimal FPCT imaging includes a high-resolution secondary reconstruction algorithm with a manually generated VOI that includes only the electrode array. As MVI imaging improves, so will our understanding of the relationships among vestibular anatomy, MVI electrode placement, vestibular performance, and hearing outcomes.

ACKNOWLEDGMENTS

We thank the 8 pioneering study subjects whose CT images are shown in this report; engineers on the MED-EL Vestibular Implant Systems team; Johns Hopkins School of Medicine trainees, faculty, and staff who facilitated this work; and members of the Data and Safety Monitoring Board (Drs David Eisenman, Frank Lin, and Charles Matthew Stewart).

Disclosures: Abderrahmane Hedjoudje—*RELATED: Grant: National Institute on Deafness and Other Communication Disorders R01DC013536 and 2T32DC000023, Labyrinth Devices, and MED-EL**; Desi P. Schoo—*RELATED: Grant: National Institutes of Health, Comments: My work/effort during this project was funded, in part, by the National Institutes of Health training grant Research Training in Otolaryngology (5T32DC000027-30)*; Support for Travel to Meetings for the Study or Other Purposes: MED-EL, Comments: MED-EL provided funding for expenses related to travel and lodging for the following meetings. 1) Implantable Vestibular Prosthesis Meeting, Innsbruck and Vienna, Austria, March 2017; 2) The 16th Hearing and Structure Preservation Workshop, Perth, Australia, November 2017; UNRELATED: Employment: Johns Hopkins Hospital, Comments: Resident Physician in the Department of Otolaryngology-Head and Neck Surgery. Bryan K. Ward—*RELATED: Grant: American Otological Society, Comments: Clinician Scientist Award*; UNRELATED: Patents (Planned, Pending or Issued): US 20180036549 A1, Comments: device for magnetic stimulation of the vestibular system*; Payment for Development of Educational Presentations: practical reviews, Comments: critically review recently-published studies in otolaryngology-head and neck surgery. John P. Carey—*RELATED: Grant: National Institutes of Health*; Support for Travel to Meetings for the Study or Other Purposes: Med-EL, Comments: MED-EL reimbursed me for 1 meeting in Austria to discuss this study and other ongoing vestibular implant studies; UNRELATED: Grants/Grants Pending: National Institutes of Health. Charles C. Della Santina—*RELATED: Grant: Labyrinth Devices, MED-EL, Comments: 1) clinical trial agreement between Labyrinth Devices and Johns Hopkins University, 2) research contract between MED-EL and Johns Hopkins University*; Support for Travel to Meetings for the Study or Other Purposes: MED-EL, Comments: travel support to investigator meeting; Provision of Writing Assistance, Medicines, Equipment, or Administrative Support: Labyrinth Devices, MED-EL, Comments: provision of equipment and devices for use in research*; UNRELATED: Grants/Grants Pending: Labyrinth Devices, MED-EL, Comments: 1) clinical trial agreement between Labyrinth Devices and Johns Hopkins University, 2) research contract between MED-EL and Johns Hopkins University*; Patents (Planned, Pending or Issued): System For Synchronously Sampled Binocular Video-Oculography Using A Single Head-Mounted Camera Publication number: 20150223683*; Other: Labyrinth Devices, Comments: equity, spouse employed part-time as administrator. *Money paid to the institution.****

REFERENCES

1. **LIVING without a balancing mechanism.** *N Engl J Med* 1952;246:458–60 CrossRef Medline
2. Ward BK, Agrawal Y, Hoffman HJ, et al. **Prevalence and impact of bilateral vestibular hypofunction.** *JAMA Otolaryngol Head Neck Surg* 2013;139:803–10 CrossRef Medline

3. Sun DQ, Ward BK, Semenov YR, et al. **Bilateral vestibular deficiency: quality of life and economic implications.** *JAMA Otolaryngol Head Neck Surg* 2014;140:527 CrossRef Medline
4. Boutros PJ, Schoo DP, Rahman M, et al. **Continuous vestibular implant stimulation partially restores eye-stabilizing reflexes.** *JCI Insight* 2019;4:e128397 CrossRef Medline
5. Sluydts M, Curthoys I, Vanspauwen R, et al. **Electrical vestibular stimulation in humans: a narrative review.** *Audiol Neurootol* 2020;25:6–24 CrossRef Medline
6. Jiam NT, Jiradejvong P, Pearl MS, et al. **The effect of round window vs cochleostomy surgical approaches on cochlear implant electrode position a flat-panel computed tomography study.** *JAMA Otolaryngol Head Neck Surg* 2016;142:873–80 CrossRef Medline
7. Jiam NT, Pearl MS, Carver C, et al. **Flat-panel CT imaging for individualized pitch mapping in cochlear implant users.** *Otol Neurotol* 2016;37:672–79 CrossRef Medline
8. Piergallini L, Scola E, Tuscano B, et al. **Flat-panel CT versus 128-slice CT in temporal bone imaging: assessment of image quality and radiation dose.** *Eur J Radiol* 2018;106:106–13 CrossRef Medline
9. Pearl MS, Roy A, Limb CJ. **High-resolution secondary reconstructions with the use of flat panel CT in the clinical assessment of patients with cochlear implants.** *AJNR Am J Neuroradiol* 2014;35:1202–08 CrossRef Medline
10. Roy AT, Penninger RT, Pearl MS, et al. **Deeper cochlear implant electrode insertion angle improves detection of musical sound quality deterioration related to bass frequency removal.** *Otol Neurotol* 2016;37:146–51 CrossRef Medline
11. **Multichannel Vestibular Implant Early Feasibility Study.** <https://clinicaltrials.gov/ct2/show/NCT02725463>. Accessed April 01, 2016
12. Hedjoudje A, Hayden R, Dai C, et al. **Virtual Rhesus Labyrinth Model predicts responses to electrical stimulation delivered by a vestibular prosthesis.** *J Assoc Res Otolaryngol* 2019;20:313–39 CrossRef Medline
13. Tunkel AE, Carey JP, Pearl M. **Flat panel computed tomography in the diagnosis of superior semicircular canal dehiscence syndrome.** *Otol Neurotol* 2019;40:213–17 CrossRef Medline
14. Liao D, Pearl MS, Ward BK. **Flat-panel CT imaging of a radiopaque shim for patulous eustachian tube dysfunction.** *Otol Neurotol* 2020;41:e412–13 CrossRef Medline
15. Mekabaty AE, Pross SE, Martinez M, et al. **Reducing radiation dose for high-resolution flat-panel CT imaging of superior semicircular canal dehiscence.** *Otol Neurotol* 2018;39:e683–90 CrossRef Medline
16. Kennedy TA, Connell N, Szczykutowicz T, et al. **Flat-panel CT for cochlear implant electrode imaging: comparison to multi-detector CT.** *Otol Neurotol* 2016;37:1646–53 CrossRef Medline
17. Della Santina CC, Potyagaylo V, Migliaccio AA, et al. **Orientation of human semicircular canals measured by three-dimensional multi-planar CT reconstruction.** *J Assoc Res Otolaryngol* 2005;6:191–206 CrossRef Medline

Assessment of the Membranous Labyrinth in Infants Using a Heavily T2-weighted 3D FLAIR Sequence without Contrast Agent Administration

G. Conte, S. Casale, L. Caschera, F.M. Lo Russo, C. Paoella, C. Cinnante, F. Di Berardino, D. Zanetti, D. Stocchetti, E. Scola, L. Bassi, and F. Triulzi



ABSTRACT

BACKGROUND AND PURPOSE: Imaging is fundamental to assessing the acoustic pathway in infants with congenital deafness. We describe our depiction of the membranous labyrinth in infants using the heavily T2-weighted 3D FLAIR sequence without a contrast agent.

MATERIALS AND METHODS: We retrospectively reviewed 10 infants (20 ears) (median term equivalent age: 2 weeks; IQR: 1–5 weeks) who had undergone brain MR imaging including a noncontrast heavily T2-weighted 3D FLAIR scan of the temporal bone. For each ear, 3 observers analyzed, in consensus, the saccule, the utricle, and the 3 ampullae, assessing the visibility (score 0, not appreciable; score 1, visible without well-defined boundaries; score 2, visible with well-defined boundaries) and morphology (“expected” or “unexpected” compared with adults). The heavily T2-weighted 3D FLAIR sequence was scored for overall quality (score 0, inadequate; score 1, adequate but with the presence of image degradation; score 2, adequate).

RESULTS: Six (60%) MR examinations were considered adequate (score 1 or 2). The saccule was visible in 10 ears (83.3%) with an expected morphology in 9 ears (90%). In 1 ear of an infant with congenital deafness, the saccule showed an unexpected morphology. The utricle was visible as expected in 12 ears (100%). The lateral ampulla was visible in 5 ears (41.6%), the superior ampulla was visible in 6 ears (50.0%), and the posterior ampulla was visible in 6 ears (50.0%), always with expected morphology (100%).

CONCLUSIONS: MR imaging can depict the membranous labyrinth in infants using heavily T2-weighted 3D FLAIR without an injected contrast agent, but the sequence acquisition time reduces its feasibility in infants undergoing MR studies during natural sleep.

ABBREVIATION: HT2W = heavily T2-weighted

Congenital bilateral permanent hearing loss is a chronic condition affecting approximately 1.33 per 1000 live births.^{1,2} Environmental and prenatal factors such as congenital infections, particularly cytomegalovirus, are common risk factors, most notably in low-income settings.³ Genetic causes account for most cases in developed countries and can lead to syndromic and nonsyndromic congenital hearing loss.^{4–6} Hearing during the critical periods of infancy and early childhood is necessary to develop spoken

language.⁷ Thus, hearing screening tests are performed no later than the first month of age.⁸ If congenital hearing loss is detected, understanding the cause is necessary to direct therapeutic decision making and guide prevention and (genetic) counseling.

Imaging plays a fundamental role in the assessment of the congenital hearing loss by detecting malformations, guiding genetic testing, helping to diagnose congenital cytomegalovirus infection, and providing preoperative information, including the feasibility of cochlear implantation and surgical risk factors.² Although CT is the imaging technique of choice for assessing the bony labyrinth and MR imaging is fundamental to evaluating the cochlear nerve and CNS in children and adults,^{9–11} no imaging study has been used to visualize the membranous labyrinth in infants.

Heavily T2-weighted (HT2W) 3D FLAIR images acquired 4 to 5 hours after IV contrast agent administration can assess the membranous labyrinth in adults.^{12,13} However, this imaging protocol may not be suitable for infants because of the need for contrast agent injection and to acquire the images during

Received May 16, 2020; accepted after revision September 1.

From the Neuroradiology Unit (G.C., S.C., L.C., F.M.L.R., C.C., D.S., E.S., F.T.), Audiology Unit (F.D.B., D.Z.), and NICU (L.B.), Fondazione IRCCS Ca' Granda Ospedale Maggiore Policlinico Milano, Università degli Studi di Milano, Milan, Italy; Department of Advanced Biomedical Sciences (C.P.), University of Naples “Federico II,” Naples, Italy; and Department of Pathophysiology and Transplantation (F.T.), University of Milan, Milan, Italy.

Please address correspondence to Luca Caschera, MD, Fondazione IRCCS Ca' Granda Ospedale Maggiore Policlinico, Neuroradiology Unit, Via Francesco Sforza 35, Milan, Italy; e-mail: luca.caschera@policlinico.mi.it; @caschera_luca; @GiorgioConte86

Indicates article with supplemental online photo.

<http://dx.doi.org/10.3174/ajnr.A6876>

separate sessions. In this study, we describe our experience in depicting the normal anatomy of the membranous labyrinth in a cohort of infants using the HT2W 3D FLAIR sequence with no contrast agent.

MATERIALS AND METHODS

Participants

This is a retrospective observational study approved by the institutional review board. Infants were recruited as clinical cases with ethical approval for review of clinical notes and MR images with consent from parents or legal guardians. The cohort consists of infants who underwent brain MR imaging with HT2W 3D FLAIR of the temporal bone at our neuroradiology department from September 2019 to January 2020. All brain MR imaging was performed for clinical purposes, and the HT2W 3D FLAIR sequence was acquired as part of the optimization of MR imaging protocols after the upgrade of the MR imaging scanner. Infants were not consecutively enrolled because the HT2W 3D FLAIR sequence was performed when a neuroradiologist with expertise in head and neck radiology (G.C.) was overseeing the MR imaging session. No exclusion criteria were adopted.

MR Imaging Acquisition

Each participant was imaged on a 3T Achieva scanner (Philips Healthcare) using a 32-channel phased-array coil. We applied a scan-specific energy dose corresponding to 0.5 kJ/kg that varied according to the baby's weight. Small infants (younger than 3 months of age) were scanned during natural sleep after feeding or under sedation with oral midazolam. One patient (23 months of age) was scanned under sedation with propofol. During the MR examination, infants were monitored by pulse oximetry and electrocardiography (Invivo-Expression Monitor MR200). Small infants (younger than 3 months of age) were also dressed in MR-compatible tracksuits; a warm blanket and a hat were used to prevent heat dispersion.¹⁴ Appropriate noise attenuators (MiniMuffs, Natus Medical) were used.

The imaging protocol consisted of sequences performed for whole-brain evaluation: T1-weighted 3D fast field-echo sequence, axial and coronal T2-weighted turbo spin-echo sequences, axial DWI sequence, and axial SWI sequence. The HT2W 3D FLAIR sequence was used to evaluate the membranous labyrinth with the following parameters: axial plane; TR: 6000 ms; TE: 350 ms; TI: 2350 ms; fat saturation: spectral presaturation with inversion recovery; TSE factor: 182; flip angle: 90 degrees; number of slices: 30; FOV: 230 × 190 mm²; matrix: 232 × 229; voxel size: 0.7 × 0.7 × 0.7 mm³; averages: 6; and scan time: 10 minutes and 6 seconds. Because MR examination was performed for clinical purposes, the HT2W 3D FLAIR sequence was acquired only at the end of the MR protocol. This guaranteed the best quality of MR images acquired for diagnostic purposes, an acceptable scanning time, and the shortest sedation time when applicable. Of note, sedation was never prolonged to obtain good-quality HT2W 3D FLAIR images. No contrast agent was injected during the examinations.

Image Analysis

Three observers (1 senior neuroradiologist with 10 years of experience in neuroimaging and 2 young neuroradiologists with 2 years

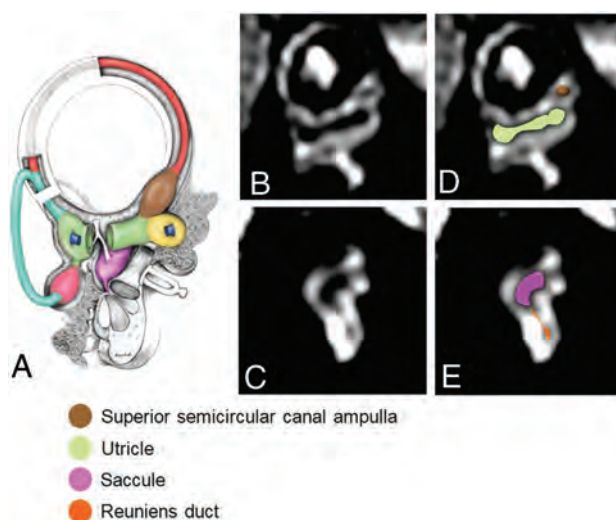


FIG 1. Schematic representation of the membranous labyrinth in the sagittal plane parallel to the superior semicircular canal (A, asterisk) and corresponding reformatted oblique sagittal MR images (B, intermediate sagittal plane; C, medial sagittal plane) with the corresponding colored representational structures (D and E). In E, the reunions duct connecting the inferior portion of the sacculle and the cochlear duct is highlighted in orange. The images were obtained from the same participant. (Reprinted from Conte G, Caschera L, Tuscano B, et al. Three-Tesla magnetic resonance imaging of the vestibular endolymphatic space: a systematic qualitative description in healthy ears. *Eur J Radiol* 2018; 109: 79. Copyright 2018, with permission from Elsevier.)

of experience in neuroimaging) assessed the HT2W 3D FLAIR images in consensus. MPRs were obtained using a local PACS viewer (section thickness: 0.33 mm). A systematic evaluation of the membranous labyrinth from each ear was performed following the method described by Conte et al.¹⁵ In particular, the analysis was performed by taking as a reference 2 main image reconstruction planes: 1) a short-axis oblique plane parallel to the superior semicircular canal (Fig 1 and 2) an axial plane parallel to the lateral semicircular canal (Fig 2).

The observers evaluated the sacculle, the utricle, and 3 ampullae of the semicircular canals as identified by Conte et al.¹⁵ Each structure was assessed using an ordinal visual scale: score 0, not appreciable; score 1, visible without well-delineable boundaries; and score 2, visible with well-delineable boundaries. In addition, for visible structures (score 1 or 2), the morphology was defined as “expected” or “unexpected” according to the normal radiologic anatomy described by Conte et al.¹⁵ Finally, the observers scored the quality of the MR examinations as follows: score 0, inadequate; score 1, adequate but with the presence of image degradation; and score 2, adequate.

Data Reporting

We reported a descriptive analysis of our data because the small numbers prevented us from obtaining reliable inferential statistics. Data were analyzed using an Excel spreadsheet (Microsoft).

RESULTS

We enrolled 10 infants (3 male, 7 female; median term equivalent age: 2 weeks [IQR: 1–5 weeks]). Five infants (50%) required

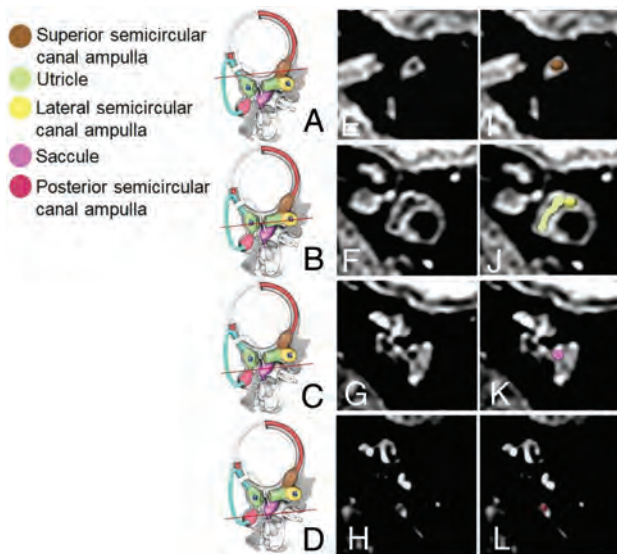


FIG 2. Reference working planes (A–D, asterisk) of the reformatted oblique axial MR images (E–H) parallel to the plane of the lateral semicircular canal with the corresponding colored representational images (I–L). The images were obtained from the same subject. (Reprinted from Conte G, Caschera L, Tuscano B, et al. Three-Tesla magnetic resonance imaging of the vestibular endolymphatic space: a systematic qualitative description in healthy ears. *Eur J Radiol* 2018;109:80. Copyright 2018, with permission from Elsevier.)

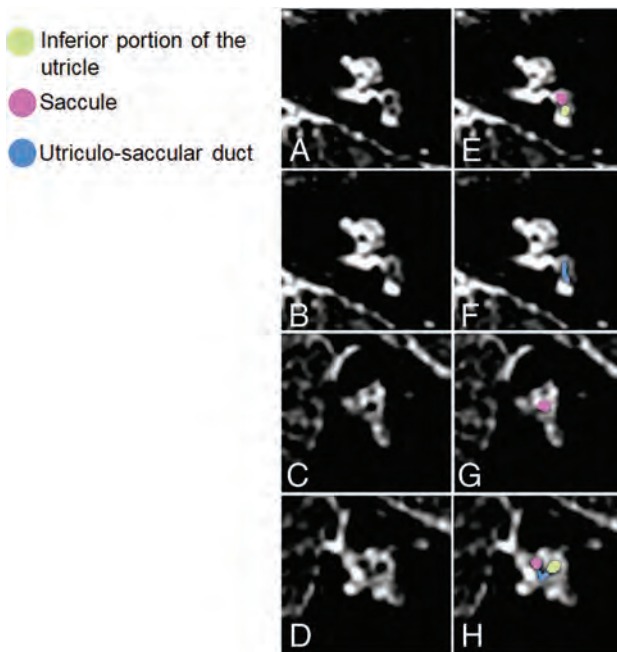


FIG 3. A 23-month-old female patient with extrapyramidal disorder and congenital sensorineural hearing deafness related to prematurity (born at 24 weeks of gestation). Reformatted oblique axial (A and B) and sagittal (C and D) MR images with corresponding colored representational images (E–H) showing the enlarged sacculle and an elongated structure connecting the utricle and the sacculle. This was interpreted as an enlarged utricular-saccular duct.

sedation during the MR imaging examination; the remaining infants were scanned during natural sleep after feeding. Nine infants were premature; congenital cytomegalovirus infection was

also diagnosed in 1 of them. Otoacoustic emissions at the neonatal hearing screening were present in all participants with the exception of 1 infant (female, 23 months old at MR imaging) who presented with extrapyramidal disorder and congenital deafness (bilateral moderately severe high-frequency sensorineural hearing loss) related to prematurity (gestational age at birth: 24 weeks).

In 4 (40%) of 10 cases, the MR examination was judged inadequate for analysis because of motion artifacts (all cases performed without sedation); 1 case (10%) was judged adequate but with the presence of image degradation (without sedation), and 5 cases (50%) were judged adequate (all cases performed with sedation). In total, 12 ears were ultimately analyzed.

The sacculle was visible with well-defined boundaries in 9 ears (75%), visible without well-delineable boundaries in 1 ear (8.3%), and not visible in the 2 ears (16.7%) in the MR examination with image degradation. The morphology of the sacculle was as expected in 9 (90%) of 10 ears. The sacculle was enlarged in both axial and short-axis oblique planes in the left ear of the infant with congenital bilateral sensorineural hearing loss (Fig 3) resembling a saccular hydrops grade I as described in adults.¹⁶ In addition, an elongated structure connecting the utricle and the sacculle was identified and interpreted as an enlarged utriculo-saccular duct.¹⁷ In this infant, the conventional sequences did not reveal pathologic ear and brain findings.

The utricle was visible with well-defined boundaries in 10 ears (83%) and visible without well-delineable boundaries in the 2 ears (17%) of the MR examination with image degradation. The morphology was as expected in the 12 visible utricles.

The lateral semicircular canal ampulla was visible with well-defined boundaries in 4 ears (33.3%), visible without well-defined boundaries in 1 ear (8.3%), and not visible in 7 ears (58.4%). The superior semicircular canal ampulla was visible with well-defined boundaries in 4 ears (33.3%), visible without well-defined boundaries in 2 ears (16.7%), and not visible in 6 ears (50%). The PSC ampulla was visible with well-defined boundaries in 4 ears (33.3%), visible without well-defined boundaries in 2 ears (16.7%), and not visible in 6 ears (50%). The morphology was as expected in the 17 visible ampullae.

DISCUSSION

In this study, we describe our experience in using the noncontrast HT2W 3D FLAIR sequence for assessing the membranous labyrinth in infants. The sequence could depict the membranous labyrinth when not degraded by motion artifact. Although the sequence's long scan time (>10 minutes) led to motion artifact, all inadequate HT2W 3D FLAIR images were acquired in small infants (younger than 3 months of age) during natural sleep.

In the literature, the 4-hour-delayed contrast-enhanced HT2W 3D FLAIR sequence has been demonstrated to depict the membranous labyrinth of adults with satisfactory anatomic details.¹⁸ The contrast agent gradually accumulates in the perilymph, where it reaches the maximum concentration at about 4.5 hours after IV administration. The use of 4-hour-delayed postcontrast HT2W 3D FLAIR allows for the visualization of the membranous labyrinth as a hypointense structure surrounded by the enhanced perilymph.¹⁵ This sequence has largely been used in adults to describe the normal vestibular membranous labyrinth anatomy and to assess inner ear

pathologies such as Ménière disease and sudden sensorineural hearing loss.¹⁹⁻²³ In recent years, various researchers have tried to image the vestibular membranous labyrinth with noncontrast MR techniques without achieving a good differentiation between the endolymph and perilymph.²⁴ Conversely, our study showed that the membranous labyrinth can be visualized using the noncontrast HT2W 3D FLAIR sequence in infants. This finding is of importance because the contrast agent is administered with caution in this population because of potential cellular toxicity and adverse reactions.²⁵ In particular, IV administration of contrast agents is not recommended for assessing patients with congenital deafness. The radiologic work-up often includes assessment of the temporal bone using a CT scan²⁶ and of the inner ear and the CNS with noncontrast MR imaging.⁹⁻¹¹ Augmenting the MR protocol with this sequence may reveal the presence of abnormalities of the membranous labyrinth in children screened for congenital deafness, especially when conventional imaging is normal as in 1 case we demonstrated. In fact, the only patient who underwent MR imaging for congenital deafness showed an unexpected morphology of the vestibular membranous labyrinth with a hydropic saccule and a dilation of the utricular-saccular duct.

It is difficult to explain why this sequence—which is identical to that used in adults in our department—allows for the visualization of the membranous labyrinth without the need for IV contrast agent administration. Indeed, even in adults, this noncontrast HT2W 3D FLAIR sequence shows a faint signal contrast between the perilymph and the endolymph. In fact, the perilymph shows high signal because of the HT2W, but the endolymph signal is suppressed by the selective inversion time pulse based on their differing compositions. However, the membranous labyrinth remains less defined because the intrinsic high noise of the sequence lowers the contrast-to-noise ratio. This leads to our rationale for administering the contrast agent—it increases the signal of the perilymph and, as consequence, the contrast-to-noise ratio. Thus, it improves the differentiation between perilymph and endolymph (Online Fig). We theorize that the contrast-to-noise ratio is spontaneously higher in infants than in adults on the noncontrast HT2W 3D FLAIR; thus, IV contrast agent administration is not necessary to delineate the membranous labyrinth.

Other findings may further validate our hypothesis. The temporal bone is much less mineralized in infants than in adults, and the head is smaller even if the inner ear size has already reached its maximum.²⁷ These 2 factors may reduce susceptibility artifact. We also speculate that the chemical composition of the labyrinthine fluids may be different between infants and adults and thus is responsible for the spontaneous increased contrast.²⁸ Furthermore, the spontaneous contrast between the perilymph and the endolymph was also detected in the nonsedated infant whose MR examination was degraded by motion artifact, excluding a role of the administered drugs (midazolam, propofol) in the signal changes of the perilymph.

This study does have limitations. We assessed a limited cohort of participants, potentially reducing the number of anatomic variants that we observed in the imaging assessment. However, the variability of the membranous labyrinth is limited as reported in the study of Conte et al¹⁵ in adults. An intraparticipant analysis comparing imaging findings before and after contrast agent

administration would have been useful for validating our results; however, the administration of a contrast agent would have been unethical without a clinical indication. There is also a study setting problem stemming from reimaging the infant after 4 hours from the base examination.

Finally, to avoid a longer scan time, we could not repeat the sequence more than once per infant, preventing us from optimizing MR parameters and addressing this critical point. Currently, the use of this sequence seems to be feasible only in sedated infants and appropriate only in the assessment of congenital sensorineural hearing loss to avoid the inappropriate prolongation of sedation; new MR technologies may overcome this drawback. Another limitation is that the 3D FLAIR MR assessment of the membranous labyrinth was performed without morphologic measurements because normal reference ranges are not available in the literature for both infants and adults.

It is well known that the bony labyrinth of the inner ear reaches its maximum in life at about 23 weeks of gestation,²⁷ and thus we supposed that the membranous labyrinth dimensions are comparable between infants and adults.

CONCLUSIONS

Our study demonstrates that the noncontrast HT2W 3D FLAIR sequence can depict the membranous labyrinth in infants though the susceptibility to motion artifact with the lengthy scan time limits the feasibility of the sequence when infants are scanned without sedation. Further optimization of the sequence to limit scan time and improve contrast resolution may encourage its routine use in clinical practice.

REFERENCES

1. Morton CC, Nance WE. **Newborn hearing screening—a silent revolution.** *N Engl J Med* 2006;354:2151–64 CrossRef Medline
2. Korver AMH, Smith RJH, Van Camp G, et al. **Congenital hearing loss.** *Nat Rev Dis Primers* 2017;3:16094 CrossRef Medline
3. Grosse SD, Ross DS, Dollard SC. **Congenital cytomegalovirus (CMV) infection as a cause of permanent bilateral hearing loss: a quantitative assessment.** *J Clin Virol* 2008;41:57–62 CrossRef Medline
4. Marazita ML, Ploughman LM, Rawlings B, et al. **Genetic epidemiological studies of early-onset deafness in the U.S. school-age population.** *Am J Med Genet* 1993;46:486–91 CrossRef Medline
5. Smith RJH, Bale JF Jr, White KR. **Sensorineural hearing loss in children.** *Lancet* 2005;365:879–90 CrossRef Medline
6. Snoeckx RL, Huygen PLM, Feldmann D, et al. **GJB2 mutations and degree of hearing loss: a multicenter study.** *Am J Hum Genet* 2005;77:945–57 CrossRef Medline
7. Yoshinaga-Itano C, Sedey AL, Coulter DK, et al. **Language of early- and later-identified children with hearing loss.** *Pediatrics* 1998;102:1161–71 CrossRef Medline
8. American Academy of Pediatrics, Joint Committee on Infant Hearing. **Year 2007 position statement: principles and guidelines for early hearing detection and intervention programs.** *Pediatrics* 2007;120:898–921 CrossRef Medline
9. Parry DA, Booth T, Roland PS. **Advantages of magnetic resonance imaging over computed tomography in preoperative evaluation of pediatric cochlear implant candidates.** *Otol Neurotol* 2005;26:976–82 CrossRef Medline
10. Casselman JW, Kuhweide R, Ampe W, et al. **Inner ear malformations in patients with sensorineural hearing loss: detection with**

- gradient-echo (3DFT-CISS) MRI.** *Neuroradiology* 1996;38:278–86 CrossRef Medline
11. Ellul S, Shelton C, Davidson HC, et al. **Preoperative cochlear implant imaging: is magnetic resonance imaging enough?** *Am J Otol* 2000;21:528–33 Medline
 12. Carfrae MJ, Holtzman A, Eames F, et al. **3 Tesla delayed contrast magnetic resonance imaging evaluation of Ménière's disease.** *Laryngoscope* 2008;118:501–05 CrossRef Medline
 13. Conte G, Lo Russo FM, Calloni SF, et al. **MR imaging of endolymphatic hydrops in Ménière's disease: not all that glitters is gold.** *Acta Otorhinolaryngol Ital* 2018;38:369–76 CrossRef Medline
 14. Fumagalli M, Cinnante CM, Calloni SF, et al. **Clinical safety of 3-T brain magnetic resonance imaging in newborns.** *Pediatr Radiol* 2018;48:992–98 CrossRef Medline
 15. Conte G, Caschera L, Tuscano B, et al. **Three-Tesla magnetic resonance imaging of the vestibular endolymphatic space: a systematic qualitative description in healthy ears.** *Eur J Radiol* 2018;109:77–82 CrossRef Medline
 16. Bernaerts A, Vanspauwen R, Blaivie C, et al. **The value of four stage vestibular hydrops grading and asymmetric perilymphatic enhancement in the diagnosis of Ménière's disease on MRI.** *Neuroradiology* 2019;61:421–29 CrossRef Medline
 17. Streeter GL. **On the development of the membranous labyrinth and the acoustic and facial nerves in the human embryo.** *Am J Anat* 1906;6:139–65 CrossRef
 18. Naganawa S, Kawai H, Sone M, et al. **Increased sensitivity to low concentration gadolinium contrast by optimized heavily T2-weighted 3D-FLAIR to visualize endolymphatic space.** *MRMS* 2010;9:73–80 CrossRef Medline
 19. Conte G, Caschera L, Calloni S, et al. **MR imaging in Ménière disease: is the contact between the vestibular endolymphatic space and the oval window a reliable biomarker?** *AJNR Am J Neuroradiol* 2018;39:2114–19 CrossRef Medline
 20. Sepahdari AR, Ishiyama G, Vorasubin N, et al. **Delayed intravenous contrast-enhanced 3D FLAIR MRI in Meniere's disease: correlation of quantitative measures of endolymphatic hydrops with hearing.** *Clin Imaging* 2015;39:26–31 CrossRef Medline
 21. Naganawa S, Yamazaki M, Kawai H, et al. **Visualization of endolymphatic hydrops in Ménière's disease with single-dose intravenous gadolinium-based contrast media using heavily T2-weighted 3D-FLAIR.** *Magn Reson Med Sci* 2010;9:237–42 CrossRef Medline
 22. Tagaya M, Teranishi M, Naganawa S, et al. **3 Tesla magnetic resonance imaging obtained 4 hours after intravenous gadolinium injection in patients with sudden deafness.** *Acta Otolaryngol* 2010;130:665–69 CrossRef Medline
 23. Nakashima T, Naganawa S, Teranishi M, et al. **Endolymphatic hydrops revealed by intravenous gadolinium injection in patients with Ménière's disease.** *Acta Otolaryngol* 2010;130:338–43 CrossRef Medline
 24. Lane JI, Witte RJ, Bolster B, et al. **State of the art: 3T imaging of the membranous labyrinth.** *AJNR Am J Neuroradiol* 2008;29:1436–40 CrossRef Medline
 25. Maloney E, Iyer RS, Phillips GS, et al. **Practical administration of intravenous contrast media in children: screening, prophylaxis, administration and treatment of adverse reactions.** *Pediatr Radiol* 2019;49:433–47 CrossRef Medline
 26. Conte G, Scola E, Calloni S, et al. **Flat panel angiography in the cross-sectional imaging of the temporal bone: assessment of image quality and radiation dose compared with a 64 section multisection CT scanner.** *AJNR Am J Neuroradiol* 2017;38:1998–2002 CrossRef Medline
 27. Richard C, Courbon G, Laroche N, et al. **Inner ear ossification and mineralization kinetics in human embryonic development—microtomographic and histomorphological study.** *Sci Rep* 2017;7:4825 CrossRef Medline
 28. Schmitt HA, Pich A, Schröder A, et al. **Proteome analysis of human perilymph using an intraoperative sampling method.** *J Proteome Res* 2017;16:1911–23 CrossRef Medline

Pediatric Head CT: Automated Quantitative Analysis with Quantile Regression

 K.A. Cauley,  Y. Hu, and  S.W. Fielden



ABSTRACT

BACKGROUND AND PURPOSE: Together with quantile regression methods, such a model would have the potential for clinical utility through automated quantitative comparison of individual cases relative to their age and gender-matched peer group. Our aim was to demonstrate the automated processing of digital clinical head CT data in the development of a clinically useful model of age-related changes of the brain in the first 2 decades of life.

MATERIALS AND METHODS: A total of 415 (209 female) consecutive, clinical head CTs with radiographically normal findings from patients from birth through 20 years of age were retrospectively selected and subjected to automated segmentation. Brain volume, brain parenchymal fraction, brain radiodensity, and brain radiomass were assessed as a function of patient age. Statistical modeling and quantile regression were performed.

RESULTS: Brain volume increased from 400 cm³ at birth to 1350 cm³ at 20 years of age (>3-fold). Males had a slightly steeper growth trajectory than females, with approximately 8% difference in volume between the sexes established in the first few years of life. Brain parenchymal fraction was variable at younger than 2 years of age, stabilizing between 0.85 and 0.92 at 2–3 years of age. Brain mean radiodensity was lower at birth (24 HU) and increased through 3 years of age, after which it stabilized near 30 HU, an approximately 25% increase. The product of brain volume and mean brain radiodensity (radiomass), increased from 700 HU × mL at birth to 3900 HU × mL, a 5.6-fold increase, with approximately 5% difference between males and females at 20 years. Quantile regression enables a given metric to be interpreted relative to an age- and sex-matched peer group.

CONCLUSIONS: Automated segmentation of clinical head CT images permitted the generation of a reference database for quantitative analysis of pediatric and adolescent brains. Quantile regression facilitates clinical application.

ABBREVIATION: BPF = brain parenchymal fraction

“... it became apparent that the conventional methods were not making full use of all the information the X-rays could give.”

G. Hounsfield, Nobel Lecture, 1979

CT is a highly calibrated and scaled imaging technique capable of volumetric and radiodensity assessment, though this capability is rarely used in the clinical setting. Concerns over

radiation exposure have limited prospective human subject research in CT and consequently have limited the investigation into the value of quantitative CT. Recent improvements in image quality and the availability of postprocessing software enable the generation of large reference databases from the existing clinical archives. Such databases facilitate research into quantitative CT by helping define the normal statistical variance, identify outliers, and correlate measurements with pathology.

In neuroimaging, brain volumetrics can have diagnostic value, as illustrated by prospective MR imaging studies of neurodegenerative diseases such as age-related dementia,¹ amyotrophic lateral sclerosis,² and multiple sclerosis.^{3,4} The volumetrics of CT imaging data have been less extensively researched, though a recent study of automated segmentation of clinical head CT data shows that the brain volume is statistically smaller in patients with Alzheimer disease.⁵ CT has the additional capability of voxel-based assessment of radiodensity, expressed in terms of Hounsfield units, a tissue

Received May 18, 2020; accepted after revision September 4.

From the Departments of Radiology (K.A.C.) and Biomedical and Translational Informatics (Y.H.), Geisinger Medical Center, Danville, Pennsylvania; and Geisinger Autism and Developmental Medicine Institute (S.W.F.), Lewisburg, Pennsylvania.

This work was funded by the Geisinger Clinical Research Fund to K.A.C. and S.W.F. (SRC-L-58).

Please address correspondence to Keith A. Cauley, MD, PhD, Geisinger Medical Center, Department of Radiology 100 N Academy Ave, Danville, PA 17822; e-mail: keithcauley@hotmail.com



Indicates article with supplemental online tables.



Indicates article with supplemental online photos.

<http://dx.doi.org/10.3174/ajnr.A6885>

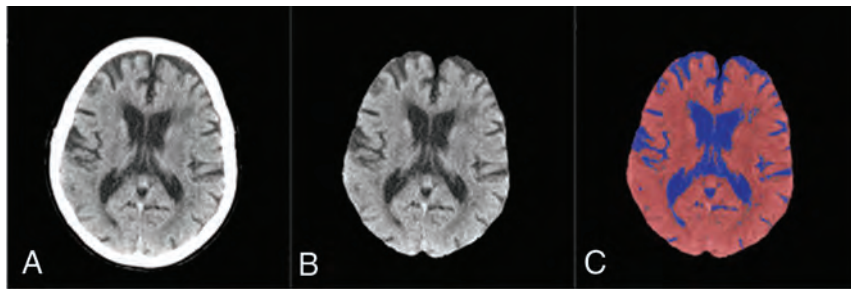


FIG 1. Products of automated head CT segmentation. Routine clinical head CT (A), brain-extracted image (B), and CSF eliminated (brain parenchyma) (C).

property measure that is unique to this technique. Because most brain imaging research has been conducted using MR imaging, there is little information on the diagnostic value of the brain radiodensity measure. It is well-established that mean brain radiodensity is abnormal in hypoxic-ischemic encephalopathy, for example, and quantitative assessment appears to have diagnostic and prognostic implications.⁶⁻⁸ Mean brain radiodensity is also abnormal in multiple sclerosis,⁹ and mean brain radiodensity shows a statistically significant decline as a function of aging.¹⁰ It would, therefore, appear reasonable that other forms of encephalopathy or neurodegenerative disease may also demonstrate abnormalities of brain radiodensity, and radiodensity measures may serve to identify disease or quantify disease progression. As with brain volume measures, these types of studies will also require a reference normative data base.

In this study, we focus on the pediatric age group and apply an automated segmentation algorithm to a large number of retrospectively identified head CTs with radiographically normal clinical findings to initiate the development of a clinical reference data base for brain volume, parenchymal fraction, brain radiodensity, and brain radiomass. Such a data base can be subject to quantile regression analysis because individual cases can be referenced against their clinical peer group.

MATERIALS AND METHODS

Study Design

This study was limited to a retrospective analysis of head CTs performed on patients who were identified from the clinical PACS. The study was approved by this institutional review board (Geisinger Medical Center), and a waiver of consent was granted.

Study Cohort

In total head CTs from 417 patients (209 females), 0–20 years of age, were included. Details regarding the imaging and data base for the neonates 0–2 years of age have been published previously.¹¹ The remaining cases were from a 2-year time interval (January 1, 2015, to December 31, 2016). Selected cases were scanned for trauma with no traumatic findings or nonspecific symptoms (headache, syncope, vertigo) without known systemic disease and were discharged without incident. All cases were interpreted as having normal findings (without acute or chronic abnormal findings) by 2 board-certified neuroradiologists. Patients older than 2 years of age were scanned in a single CT scanner (LightSpeed

VCT; GE Healthcare), which primarily serves the emergency department of a level 1 trauma center. The axial acquisition noncontrast head CT protocol was the following: 135kV(peak) and modulated milliampere, minimum 50 and maximum 290 mA, rotation time = 0.75 seconds, acquired from the foramen magnum through the vertex with a standard 512 × 512 matrix, 24-cm FOV at 5.0-mm section thickness. The scanner undergoes a daily quality-assurance procedure, which assesses the radiodensity of water. This value

must be within allowable limits, generally 0–5 HU. Drift or trending is rarely observed. In a typical month, the Hounsfield units of water or the tissue density plug is found to vary by <1 HU. In addition, scanners undergo an annual inspection by a medical physicist using the American College of Radiology phantom. Acceptable ranges of Hounsfield units for clinical scanners are broad (–7 to +7 for water, 110–135 for acrylic). This testing is extended to all kilovolt peaks used by the scanner. Additionally, service engineers routinely test the calibration at preventive maintenance.

Image Processing and Analysis

DICOM images were converted to the Neuroimaging Informatics Technology Initiative (NIfTI; <https://nifti.nimh.nih.gov/>) data format using MRICConvert-2.0.7 (<http://lcn.uoregon.edu/jolinda/MRICConvert/>). Images were first thresholded from –15 to 50 HU to grossly remove background and skull. Brain extraction was then applied by using FSL Brain Extraction Tool (<http://fsl.fmrib.ox.ac.uk/fsl/fslwiki/BET>)^{12,13} with a fractional intensity threshold of 0.01. All cases were carefully reviewed for integrity of brain extraction. For segmentation, FMRIB's Automated Segmentation Tool (FAST; <http://poc.vl-e.nl/distribution/manual/fsl-3.2/fast/index.html>) was used to generate a 3-tissue compartment segmentation with the resulting white matter and gray matter compartments combined into a single brain compartment (Fig 1). Brain radiomass was calculated as the product of mean brain radiodensity and total brain volume.

Statistical Methods

Statistical analysis was performed using GraphPad Prism software, Version 7.0c for Mac OS X (GraphPad Software). Scatterplots were generated in Excel (Microsoft) for Mac 2011, Version 14.2.3.

The overall polynomial regression of age was fitted on brain volume and brain parenchymal fraction (BPF) to evaluate the impact of sex on the outcomes. When stratified by sex, quantile regression models with the polynomial term of age were adopted to characterize brain volume and BPF, respectively. A 2-phase model enabled the best fit of the data. A natural inflection at 2 years was confirmed by 2D cluster analysis using a Gaussian mixture model (Online Fig 1). The Gaussian mixture model is a probabilistic model that comprises Gaussian distributions. Each Gaussian in the mixture is represented by a mean and covariance matrix. For ages 0–2, the linear term of age was fit, where 0.05 and 0.10 quantiles were presented.

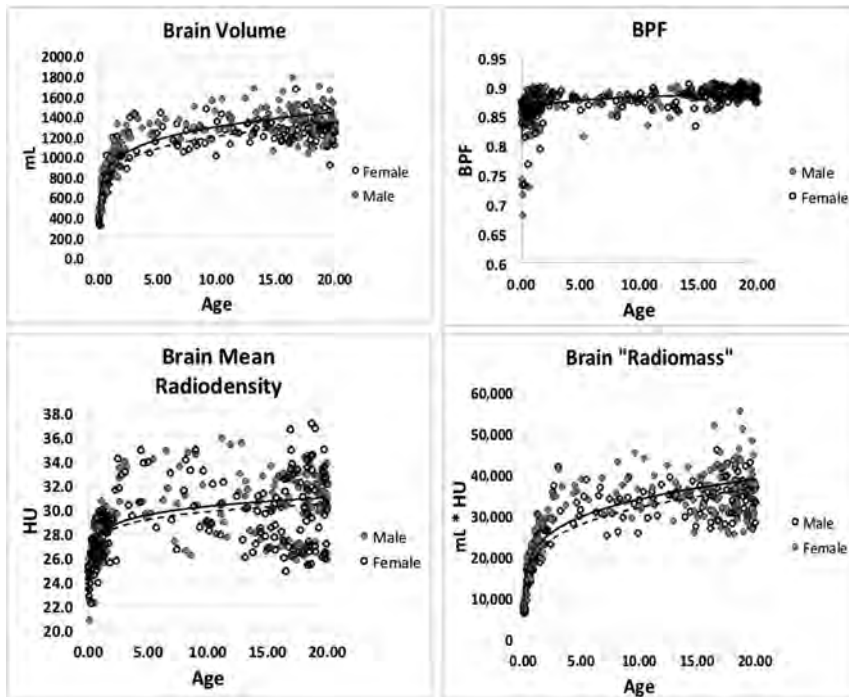


FIG 2. Scatterplots of computed brain metrics as a function of subject age: brain volume (A), BPF (B), mean brain radiodensity (C), and brain radiomass (D).

For ages 2–20, a quadratic term of age was fit, in which 0.05 and 0.10 quantiles were presented. A *P* value of < .05 was considered statistically significant. Quantile regression models were performed in R Studio (Version 1.2.1335; <http://rstudio.org/download/desktop>). Quantile regression quadratic coefficients for 2–20 years of age are included in Online Tables 1–4.

RESULTS

Brain Volume

Brain volume (Fig 2A) increases from approximately 400 mL at birth to 1350 mL at 20 years of age; males had a slightly steeper growth trajectory than females, with approximately 8% difference in volume established in the first few years of life. For 0–2 years of age, males had higher mean brain volumes than females (mean difference = 37.94; 95% CI, 0.07–75.81; *P* = .05). For 2–20 years of age, males again had higher mean brain volumes than females (mean difference = 94.81; 95% CI, 69.53–120.09; *P* < .001).

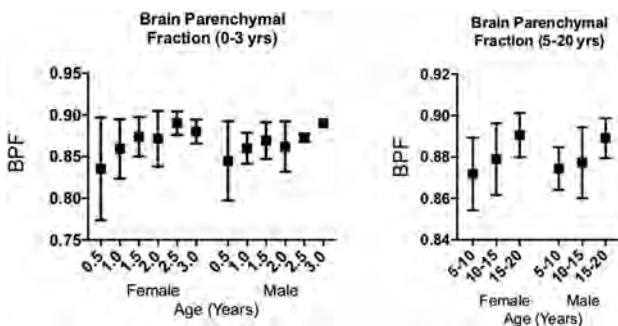


FIG 3. Box-and-whisker plots of BPF: 0–3 years (left) and 5–20 years (right). Tabular data below 0–3 years (Table 1). Data scatter is greater immediately after birth and decreases during the first 2 years, and the pattern is similar between the sexes. There is no significant difference between the mean BPF of the groupings. Table 2 shows statistically significant difference between the means of 5-year groupings.

Table 1: Brain parenchymal fraction 0–3.0 years

Age (yr)	Male			Female		
	Total	Mean	SD	Total	Mean	SD
0–0.5	20	0.845	0.047	17	0.84	0.062
0.5–1.0	15	0.86	0.018	23	0.86	0.035
1.0–1.5	12	0.87	0.022	13	0.87	0.024
1.5–2.0	10	0.86	0.030	7	0.87	0.033
2.0–2.5	4	0.87	0.005	2	0.89	0.014
2.5–3.0	2	0.89	0.000	4	0.88	0.014

Brain Parenchymal Fraction

The BPF value was variable in subjects younger than 2 years of age, with lower numbers in the immediate postpartum period (Fig 3), after which it stabilized as a largely age- and sex-independent variable between 0.85 and 0.92 (Table 1 and Fig 2B). During adolescence, the slight increase in brain size is reflected in a small, gradual increase in BPF. The mean BPF at 5–10 years of age was 0.87, and at 15–20 years of age, it was 0.89, with differences being statistically significant (*P* < .001) and virtually identical between the sexes (Table 2 and Fig 2B).

Brain Radiodensity

Brain tissue radiodensity was low at birth (mean, 24 HU) and increased through 3 years of age, after which it stabilized near 30 HU (Fig 2C). Although the data scatter is relatively large, there was no significant difference in mean density when comparing data between male and female cohorts. The mean radiodensity was not significantly changed among the age groups of 5–10, 10–15, and 15–20 years and was not significantly different between the sexes.

Brain Radiomass

The product of brain volume and radiodensity (the radiomass) increased from 7000 HU × cm³ at birth to 39,000 HU × cm³, a 5.6-fold increase, with an approximately 5% difference between males and females at 20 years of age (Fig 2D).

Direct comparison was made of changes in brain volume, brain radiodensity, and brain radiomass. Brain volume and brain

radiodensity increased along similar power trendlines in the first few years of life. Because the product of these 2 measures is the radiomass, we further investigated the correlation between these 2 variables by normalization and plotting on the same graph. When normalized for direct comparison, the radiodensity nearly plateaued at 3 years of age, whereas the volume continued to increase through early adulthood (Online Fig 2). The radiomass showed a small-but-consistent increase through adolescence and early adulthood. All 3 sets of curves are virtually identical between male and female patient groups. This high level of reproducibility between independent datasets (male and female patients) suggests that the trends are not significantly influenced by the presence of abnormal outliers and approximate normalcy.

Table 2: Brain parenchymal fraction 5–20 years

Age (yr)	Total	Mean	5–10 Years (P Value)	10–15 Years (P Value)
Male				
5–10	18	0.872		
10–15	20	0.879	NS	
15–20	72	0.891	<.001	.004
Female				
5–10	12	0.874		
10–15	20	0.877	NS	
15–20	70	0.889	.003	.003

Note:—NS indicates not significant.

Quantile Regression

Quantile regression provides a means to compare individual cases with their age- and sex-matched clinical peer group. Quantile regression of brain volume and BPF is shown in Fig 4. A linear regression is a best fit for the 0–2 age group, and a polynomial best fit is used for the 2–20 years-of-age grouping; quadratic coefficients are shown in Online Tables 1–4.

DISCUSSION

This study was motivated by a desire to bring quantitative methods to otherwise qualitative clinical head CT interpretation. The objectives of our study were the following: 1) to demonstrate automated data processing of clinical head CTs, 2) to demonstrate that these data can be used to develop a model of age-related changes in the first 2 decades of life that approaches normative data, and 3) to apply quantile regression methods to show how individual cases compare with their age- and sex-matched peer group.

Potential Value of Quantitative CT

CT is a very widely used first-line clinical imaging technique, though quantitative brain CT imaging has received considerably less research attention than MR imaging. CT can generate volumetrics and radiodensity measures. We know from MR imaging that brain volume and BPF have clinical implications.^{1–4} Because radiodensity is a measure that only CT can provide, there is currently little information regarding the use of the radiodensity measure to evaluate global brain parenchyma. It is well-established that

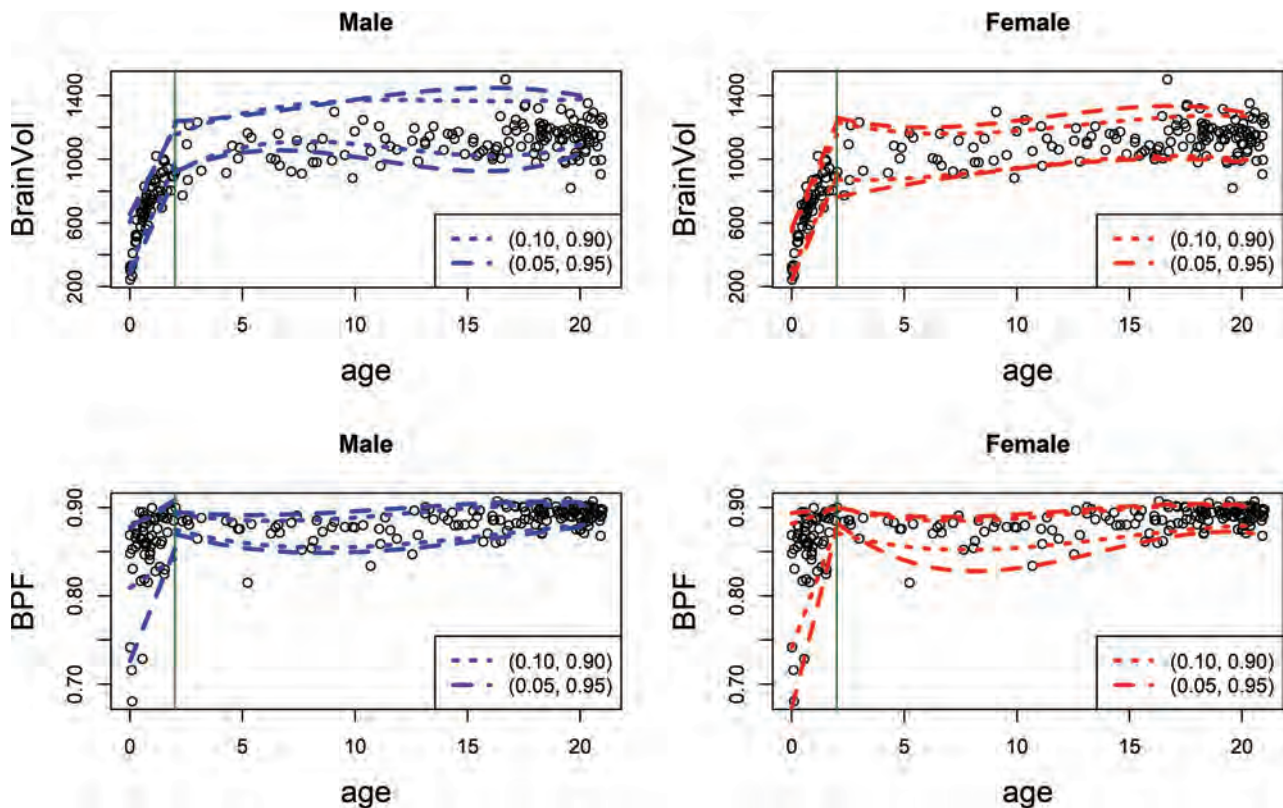


FIG 4. Quantile regression of brain volume (upper graphs) and BPF (lower graphs), male on the left, female on the right. The 5%–95% and 10%–90% quantiles are shown.

mean brain radiodensity is abnormal in hypoxic-ischemic encephalopathy following cardiac arrest, for example, and quantitative assessment appears to have diagnostic and prognostic implications.⁶⁻⁸ It may be reasonable to expect that other forms of encephalopathy may also be abnormal with respect to radiodensity. We have found that global brain radiodensity is abnormal in multiple sclerosis,⁹ and we have recently shown that mean brain radiodensity shows a statistically significant decline as a function of age in older adults.¹⁰ Thus, radiodensity may also be abnormal in other neurodegenerative diseases or in congenital neurologic conditions. These are topics for future investigation.

At imaging, tissue volume is a surrogate for tissue mass or weight because it might be obtained at postmortem examination. Because mass is the product of volume-by-density, the truer correlate of weight is volume-by-radiodensity, or radiomass, though this correlate has received little attention in the literature. Because we have evidence that both measured brain volume and radiodensity may have clinical significance, radiomass is a valid topic for investigation. In multiple sclerosis, for example, both brain volume^{3,4} and brain density⁹ are abnormal, and both mean brain radiodensity and brain volume decline as a function of age.¹⁰ Therefore the product of these measures may be abnormal in MS and potentially in other neurodegenerative diseases as well. This is a direction for future investigation.

Leveraging the Clinical Archive to Create a Reference Data Base for Head CT Imaging

Because CT entails a radiation dose, limiting prospective human subject research, we propose to leverage the existing clinical image archive to generate a reference data base. An argument against the use of clinical images is that patients are not truly healthy because they have been scanned for a clinical indication. We contend that large data bases generated from clinical scans with structurally normal findings will approximate normalcy. Additionally, the data base generated from clinical images reflects the clinical spectrum of interest to physicians, rather than a data base of cases with truly normal findings. We support this argument by comparing it with published data on subjects with normal findings (largely generated by MR imaging) and demonstrating statistical integrity by showing that our results are internally consistent, with relatively few outliers, with very similar findings between male and female patients.

Brain Volume and BPF

Regarding brain volume, we had previously shown that by means of clinical head CT data, brain volume increases from approximately 360 cm³ to 1072 cm³ at 2 years.¹¹ The current study shows a continued small increase in brain volume after 2 years of age, to reach a volume of 1350 cm³ at 20 years of age, an approximately 3.8-fold increase in volume from birth to early adulthood. Also, consistent with published findings, male brains are consistently larger than female brains, not correcting for body size, and this difference is seen very early in development and reaches an approximately 10% difference by 20 years of age,¹⁴ findings similar to those found at MR imaging.¹⁵

BPF is the ratio of the brain volume to the intracranial volume and has been widely used in the adult population as a means of measuring brain atrophy while normalizing for head size.^{16,17} An MR imaging study by Bartholomeusz et al¹⁸ investigated the BPF of children to find that the head circumference was an excellent predictor of brain volume in children 1.7 to 6 years of age. In further studies, BPF has been investigated in the preterm infant¹⁹ and younger pediatric¹⁵ populations using MR imaging, to find a wider range of normal CSF volumes occurring in children younger than 2 years of age. Our study also shows that the BPF is variable in the postnatal period and approaches adult values (0.85–0.90) at about 2 years of age, evidence that head circumference is a less accurate predictor of brain volume in this younger age group, similar to the findings reported for MR imaging.¹⁵ This pattern may suggest that the BPF is more variable before the closure of the fontanelles, which typically occurs within the first 2 years of life.²⁰

Because the brain volume continues to increase slightly through late adolescence and early adulthood, the BPF also continues to increase. The increase is statistically significant and not significantly different between the male and female cohorts (Table 2 and Fig 2B and Fig 3), as has been noted in an MR imaging study.¹⁵ Using statistical modeling methods, we found that brain growth, both in volume and BPF, exhibited 2 distinct phases of growth as identified by 2D cluster analysis using a Gaussian mixture model (Online Fig 1) and is best modeled using a linear regression from 0–2 years of age and a polynomial equation after 2 years. Other models are possible. Although there are relatively few studies modeling total brain growth through the adolescent and early adult periods, there are none using CT scans. Others have also noted that the most significant volume changes occur in the first 2 years, with a more linear growth and a nonlinear, flattening trajectory thereafter.^{14,15,21}

Radiodensity and Radiomass

CT measures radiodensity, an intrinsic tissue property, and automated segmentation can readily yield a mean brain radiodensity assessment. We had previously shown that the radiodensity of brain tissue is lower at birth and rises to stable, near-adult values within the first year of life.¹¹ Here, we show that this small increase in brain radiodensity continues throughout adolescence.

As Hounsfield had observed, at CT imaging, x-ray absorbance and the associated signal intensity reflect mainly 1 variable—density, but also a minor one—atomic number.²² When one compares like tissues of living persons, eg, the radiodensity values of the human brain, the contribution of differences in the mean atomic number is negligible, and the radiodensity is proportional to tissue density. We have found a strong correlation between the brain radiomass and the true brain weight as deduced from published postmortem examination values (data not shown). Published postmortem data show increasing brain weights throughout adolescence and early adulthood, with a peak brain weight reached at approximately 20 years of age.²³ These data evidence a brain weight of 369 g at birth and approximately 1300 g at 20 years of age. This 3.5-fold increase

in weight closely parallels the increase in brain radiomass observed in this study (3.8-fold).

Quantile Regression

Quantile regression provides a means of quantitatively comparing an individual measure with its reference data base and a means of putting a given metric into a statistical context. Using quantile regression, a study outcome is not judged to be “normal” or “abnormal” but rather “at the nth percentile for age and sex.” While an extreme percentile measure may be used to trigger or validate further clinical inquiry, all studies would have associated quantitative metrics that can be followed across time in the event of repeat imaging.

Study Limitations

For the current study, cases of patients older than 2 years of age were obtained from a single (LightSpeed VCT) CT scanner because we wished to investigate the variation among individuals as measured with a current standard clinical machine. Specifically, we wished to learn the variance among individuals in terms of brain volumes, BPF, and mean brain radiodensity and whether the variance was large enough to be detected with confidence above the variation in measure that can occur from a single, typical clinical scanner. Learning the answer to this question is an important first step in the investigation of the clinical use of quantitative CT.

We know from the literature that Hounsfield unit measures can vary with scan manufacturer,²⁴ with kilovolt (peak),^{24,25} and probably with scan protocol. The contribution of these factors as they affect the Hounsfield unit measure of human brain is a topic for future investigation. In an earlier study of mean brain radiodensity, we compared the results from 3 different clinical machines to find small differences in scan values, but the overall pattern of mean brain Hounsfield unit changes as a function of age from all 3 machines was very similar.¹¹ A universal reference data base likely represents a future goal that may be achievable through higher calibration standards or statistical normalization of datasets.

CONCLUSIONS

Clinical head CT images can be analyzed using automated segmentation algorithms to yield objective, reproducible, quantitative information about the pediatric brain. The existing clinical archive can be leveraged by processing previously acquired image datasets to generate reference data bases. Statistical methods such as quantile regression can be applied to a reference data base to compare individual patients with their age- and sex-matched peer group. These methods would facilitate quantitative reporting and have the potential to aid in the identification of pathology, though further research is needed.

REFERENCES

1. Fjell AM, McEvoy L, Holland D, et al; Alzheimer's Disease Neuroimaging Initiative. **Brain changes in older adults at very low risk for Alzheimer's disease.** *J Neurosci* 2013;33:8237–42 CrossRef Medline
2. Rajagopalan V, Piore EP. **Brain parenchymal fraction: a relatively simple MRI measure to clinically distinguish ALS phenotypes.** *Biomed Res Int* 2015;2015:693206 CrossRef Medline
3. Losseff NA, Wang L, Lai HM, et al. **Progressive cerebral atrophy in multiple sclerosis: a serial MRI study.** *Brain* 1996;119:2009–19 CrossRef Medline
4. Simon JH, Jacobs LD, Campion MK, et al. **A longitudinal study of brain atrophy in relapsing multiple sclerosis: the Multiple Sclerosis Collaborative Research Group (MSCRG).** *Neurology* 1999;53:139–48 CrossRef Medline
5. Adduru V, Baum SA, Zhang C, et al. **A method to estimate brain volume from head CT images and application to detect brain atrophy in Alzheimer disease.** *AJNR Am J Neuroradiol* 2020;41:224–30 CrossRef Medline
6. Choi SP, Park HK, Park KN, et al. **The density ratio of grey to white matter on computed tomography as an early predictor of vegetative state or death after cardiac arrest.** *Emerg Med J* 2008;25:666–69 CrossRef Medline
7. Lee BK, Jeung KW, Song KH, et al; Korean Hypothermia Network Investigators. **Prognostic values of gray matter to white matter ratios on early brain computed tomography in adult comatose patients after out-of-hospital cardiac arrest of cardiac etiology.** *Resuscitation* 2015;96:46–52 CrossRef Medline
8. Torbey MT, Selim M, Knorr J, et al. **Quantitative analysis of the loss of distinction between gray and white matter in comatose patients after cardiac arrest.** *Stroke* 2000;31:2163–67 CrossRef Medline
9. Cauley KA, Fielden SW. **A radiodensity histogram study of the brain in multiple sclerosis.** *Tomography* 2018;4:194–203 CrossRef Medline
10. Cauley KA, Hu Y, Fielden SW. **Aging and the brain: a quantitative study of clinical CT images.** *AJNR Am J Neuroradiol* 2020;41:809–14 CrossRef Medline
11. Cauley KA, Hu Y, Och J, et al. **Modeling early postnatal brain growth and development with CT: changes in the brain radiodensity histogram from birth to 2 years.** *AJNR Am J Neuroradiol* 2018;39:775–81 CrossRef Medline
12. Jenkinson M, Beckmann CF, Behrens TE, et al. **FSL.** *Neuroimage* 2012;62:782–90 CrossRef Medline
13. Muschelli J, Ullman NL, Mould WA, et al. **Validated automatic brain extraction of head CT images.** *Neuroimage* 2015;114:379–85 CrossRef Medline
14. Courchesne E, Chisum HJ, Townsend J, et al. **Normal brain development and aging: quantitative analysis at in vivo MR imaging in healthy volunteers.** *Radiology* 2000;216:672–82 CrossRef Medline
15. McAllister A, Leach J, West H, et al. **Quantitative synthetic MRI in children: normative intracranial tissue segmentation values during development.** *AJNR Am J Neuroradiol* 2017;38:2364–72 CrossRef Medline
16. Rudick RA, Fisher E, Lee JC, et al. **Use of the brain parenchymal fraction to measure whole brain atrophy in relapsing-remitting MS: Multiple Sclerosis Collaborative Research Group.** *Neurology* 1999;53:1698–1704 CrossRef Medline
17. Vagberg M, Granasen G, Svenningsson A. **Brain parenchymal fraction in healthy adults: a systematic review of the literature.** *PLoS One* 2017;12:e0170018 CrossRef Medline
18. Bartholomeusz HH, Courchesne E, Karns CM. **Relationship between head circumference and brain volume in healthy normal toddlers, children, and adults.** *Neuropediatrics* 2002;33:239–41 CrossRef Medline
19. Vanderhasselt T, Naeyaert M, Watte N, et al. **Synthetic MRI of preterm infants at term-equivalent age: evaluation of diagnostic image quality and automated brain volume segmentation.** *AJNR Am J Neuroradiol* 2020;41:882–88 CrossRef Medline
20. Aisenson MR. **Closing of the anterior fontanelle.** *Pediatrics* 1950;6:223–26 Medline

21. Zhang L, Thomas KM, Davidson MC, et al. **MR quantitation of volume and diffusion changes in the developing brain.** *AJNR Am J Neuroradiol* 2005;26:45–49 Medline
22. Hounsfield GN. **Computed medical imaging. Nobel lecture, December 8, 1979.** *J Comput Assist Tomogr* 1980;4:665–64 CrossRef Medline
23. Dekaban AS. **Changes in brain weights during the span of human life: relation of brain weights to body heights and body weights.** *Ann Neurol* 1978;4:345–56 CrossRef Medline
24. Cropp RJ, Seslija P, Tso D, et al. **Scanner and kVp dependence of measured CT numbers in the ACR CT phantom.** *J Appl Clin Med Phys* 2013;14:4417 CrossRef Medline
25. Pomerantz SR, Kamalian S, Zhang D, et al. **Virtual monochromatic reconstruction of dual-energy unenhanced head CT at 65-75 keV maximizes image quality compared with conventional polychromatic CT.** *Radiology* 2013;266:318–25 CrossRef Medline

Involvement of the Spinal Cord in Primary Mitochondrial Disorders: A Neuroimaging Mimicker of Inflammation and Ischemia in Children

C.A.P.F. Alves, A. Goldstein, S.R. Teixeira, J.S. Martin-Saavedra, I.P. de Barcelos, G. Fadda, L. Caschera, M. Kidd, F.G. Gonçalves, E.M. McCormick, M.J. Falk, Z. Zolkipli-Cunningham, A. Vossough, and G. Zuccoli



ABSTRACT

BACKGROUND AND PURPOSE: Little is known about imaging features of spinal cord lesions in mitochondrial disorders. The aim of this research was to assess the frequency, imaging features, and pathogenic variants causing primary mitochondrial disease in children with spinal cord lesions.

MATERIALS AND METHODS: This retrospective analysis included patients seen at Children's Hospital of Philadelphia between 2000 and 2019 who had a confirmed diagnosis of a primary (genetic-based) mitochondrial disease and available MR imaging of the spine. The MR imaging included at least both sagittal and axial fast spin-echo T2-weighted images. Spine images were independently reviewed by 2 neuroradiologists. Location and imaging features of spinal cord lesions were correlated and tested using the Fisher exact test.

RESULTS: Of 119 children with primary mitochondrial disease in whom MR imaging was available, only 33 of 119 (28%) had available spine imaging for reanalysis. Nineteen of these 33 individuals (58%) had evidence of spinal cord lesions. Two main patterns of spinal cord lesions were identified: group A (12/19; 63%) had white \pm gray matter involvement, and group B (7/19; 37%) had isolated gray matter involvement. Group A spinal cord lesions were similar to those seen in patients with neuromyelitis optica spectrum disorder, multiple sclerosis, anti-myelin oligodendrocyte glycoprotein-IgG antibody disease, and leukoencephalopathy with brain stem and spinal cord involvement and lactate elevation. Group B patients had spinal cord findings similar to those that occur with ischemia and viral infections. Significant associations were seen between the pattern of lesions (group A versus group B) and the location of lesions in cervical versus thoracolumbar segments, respectively ($P < .01$).

CONCLUSIONS: Spinal cord lesions are frequently observed in children with primary mitochondrial disease and may mimic more common causes such as demyelination and ischemia.

ABBREVIATIONS: mtDNA = mitochondrial DNA; NMOSD = neuromyelitis optica spectrum disorder; LBSL = leukoencephalopathy with brain stem and spinal cord involvement and lactate elevation; MOG = myelin oligodendrocyte glycoprotein; LHON = Leber hereditary optic neuropathy; AQP4-Ab = aquaporin 4 antibody

Primary mitochondrial disorders are a heterogeneous group of genetic diseases that can present in childhood and cause

multisystemic impairment, with particular involvement of the CNS.¹ Little is known about spinal cord lesions in individuals with mitochondrial disorders despite the high frequency of brain involvement and the several well-described cerebral imaging patterns. A recent review of original articles published between 1966 and 2017 focused on spinal cord findings in patients with mitochondrial disorders, concluding that the spinal cord may be involved in various mitochondrial disorders.² However, the different imaging patterns and the frequency of spinal cord lesions in these patients remain poorly defined. One exception is the

Received May 26, 2020; accepted after revision September 25.

From the Division of Neuroradiology, Department of Radiology (C.A.P.F.A., S.R.T., J.S.M.S., L.C., F.G.G., A.V., G.Z.), Division of Human Genetics, Department of Pediatrics (A.G., E.M.M., M.J.F., Z.Z.-C.), Mitochondrial Medicine Frontier Program, Division of Human Genetics (I. P.d.B.), Department of Pediatrics, Center for Applied Genomics, Children's Hospital of Philadelphia, Philadelphia, Pennsylvania; Departments of Neurology (G.F.) and Pediatrics (A.G., M.J.F., Z.Z.-C.), University of Pennsylvania Perelman School of Medicine, Philadelphia, Pennsylvania; Centre for Statistical Consultation (M.K.), University of Stellenbosch, Stellenbosch, South Africa; The Program for the Study of Neurodevelopment in Rare Disorders (G.Z.), Children's Hospital of Pittsburgh of UPMC, Pittsburgh, Pennsylvania; and Neuroradiology Unit (L.C.), Fondazione IRCCS Ca' Granda Ospedale Maggiore Policlinico, Via Francesco Sforza 35, Milan, Italy

This work was funded in part by The CHOP Mitochondrial Medicine Frontier Program and the National Institutes of Health (U24-HD093483 to M.J.F.) as the sources of research funding. The Institutional Development Fund (IDF) from the CHOP Center for Applied Genomics (CAG) supported I.-P.d.B.'s work. The content is solely the responsibility of the authors and does not necessarily represent the official views of the National Institutes of Health.

Please address correspondence to C.A.P.F. Alves, Division of Neuroradiology, Department of Radiology, Children's Hospital of Philadelphia, Philadelphia, PA; e-mail: alvesc@email.chop.edu

Indicates open access to non-subscribers at www.ajnr.org

Indicates article with online supplemental data.

<http://dx.doi.org/10.3174/ajnr.A6910>

well-described spinal cord involvement that occurs in individuals with leukoencephalopathy with brain stem and spinal cord involvement and lactate elevation (LBSL) that is caused by pathogenic variants in *DARS2*, which is characterized by cervical spinal lesions affecting the posterior columns and lateral corticospinal tracts.^{3,4}

Common mitochondrial disease phenotypes such as Leigh syndrome, Kearns-Sayre syndrome, and *POLG* (polymerase gamma)-related disorders and other pathogenic gene disorders have not had spinal cord imaging results described, with the exception of several small case reports and neuropathologic studies.^{5,6} To address this knowledge deficiency, the present study aimed to assess the frequency, MR imaging features, and clinical and genetic associations of spinal cord lesions that occur in children with primary (genetic-based) mitochondrial disease.

MATERIALS AND METHODS

Setting and Participants

This retrospective study was reported according to the Strengthening the Reporting of Observational Studies in Epidemiology statement.⁷ The study was conducted under an approval by the institutional review board of The Children's Hospital of Philadelphia (CHOP) #18-015488. Clinical cases were identified from the Mitochondrial Medicine Frontier Program in IRB-approved CHOP Study #08-6177 (M.J.F., Principal Investigator) and by electronic medical record data base search of brain MR imaging reports spanning January 2000 to January 2019 using the keywords "mitochondrial disease" or "mitochondrial disorder."

Included individuals had a genetically confirmed primary mitochondrial disorder identified by mitochondrial DNA sequencing, nuclear gene panel-based testing, or exome sequencing, with inheritance pattern confirmed when parental samples were available, and had undergone spinal MR imaging, with images available for review of at least the cervical segment. Patients older than 18 years of age at clinical onset and those with low-quality images were excluded. To avoid classification bias, 1 pediatric neurologist who specializes in mitochondrial disorders and 1 genetic counselor (20 and 8 years' clinical experience, respectively) reviewed medical records to confirm pathogenic genetic variants (mutations), clinical diagnosis, and the accuracy of the collected clinical data.

Collected Data

Clinical data were abstracted from the medical record for age at disease onset, sex, clinical presentation at onset, age and clinical presentation at time of imaging, and genotypes. Children were classified according to pathogenic variant, mitochondrial (mtDNA) or nuclear gene disorder, and mitochondrial pathway functional classifications.¹ Neurologic symptoms present at the time of spinal cord imaging study were recorded, as well as the results of testing for CSF oligoclonal bands, serum aquaporin 4 antibody (AQP4-Ab), and anti-myelin oligodendrocyte glycoprotein antibodies (anti-MOG), when available.

Spine MR imaging, previously performed for clinical purposes, was independently reviewed by 2 neuroradiologists with more than 5 years of experience in pediatric neuroradiology. Disagreements

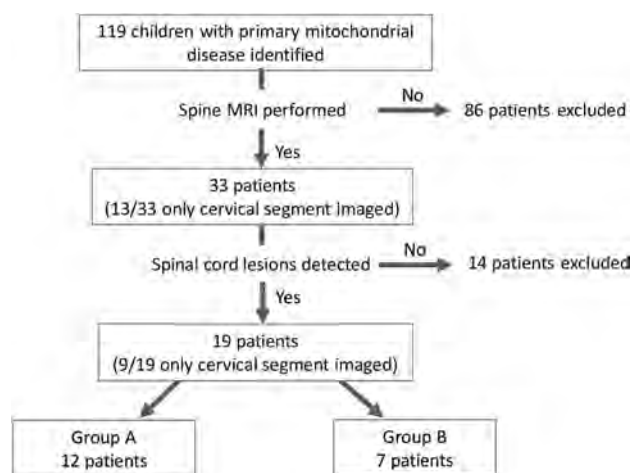


FIG 1. Flowchart of patient selection and inclusion criteria for our cohort.

were resolved by a third pediatric neuroradiologist (18 years of experience). MR imaging was done on a variety of 1.5T and 3T scanners (Siemens, GE Healthcare, Philips Healthcare). Studies included at least sagittal and axial fast spin-echo T2-weighted MR imaging: Axial T2—section thickness = 3–5 mm, section gap = 0–2.5 mm, TR = 2616–5720 ms, TE = 92–114 ms, flip angle = 90–160°, echo-train length = 14–29, acquisition matrix = 156–320 × 108–240; Sagittal T2—section thickness = 3 mm, section gap = 0–0.3 mm, TR = 2500–5150 ms, TE = 81–113 ms, flip angle = 90–180°, echo-train length = 16–35, acquisition matrix = 184–448 × 134–336.

MR imaging examinations were reviewed on a PACS and data were collected using a standardized form. Reviewers were blinded to patients' genetic diagnoses and clinical phenotypes.

Spinal cord MR imaging abnormalities were described according to the spinal cord segment involved (cervical, thoracolumbar, or both), their longitudinal extent (long if ≥3 vertebral bodies, or focal if <3 vertebral bodies), and the transverse distribution of the lesions (central, anterior, posterior, lateral columns, or whole cross-section). Spinal cord lesions were further classified into 2 main imaging categories, with group A having involvement of white matter (or both white and gray matter) and group B having exclusive involvement of gray matter.

Statistical Analysis

Data were analyzed using Statistica, version 13.5 (TIBCO Data Science). Numeric variables were described according to their distribution, with median and IQR. Categorical variables were expressed as percentage and frequency. Associations of the location of lesions with patterns of the lesion (group A versus group B) were tested using the Fisher exact test. Statistical significance was defined as $P < .05$.

RESULTS

Among 119 children identified with genetically confirmed primary mitochondrial disease who underwent CNS MR imaging studies, 33 had spine MR imaging performed of at least the cervical segment. Twenty of these 33 patients had MR imaging

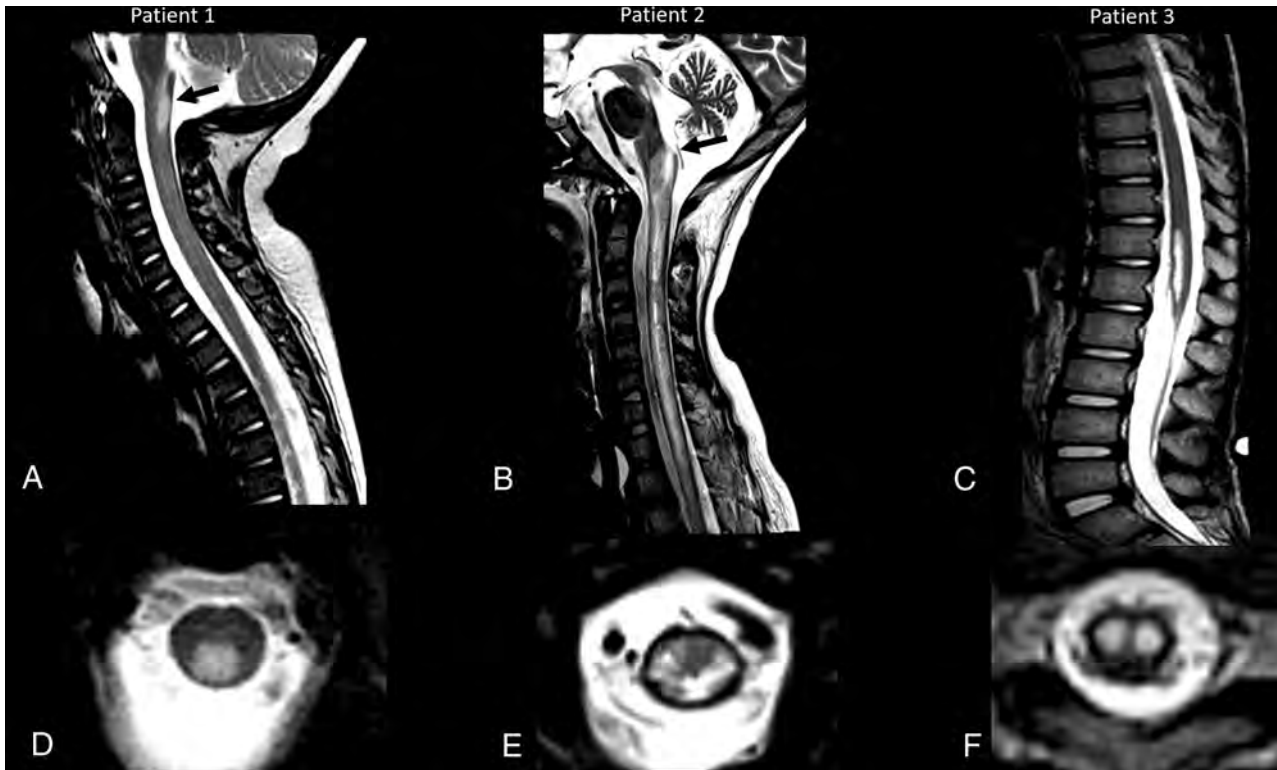


FIG 2. Segment distribution of the lesions and different appearances. Three patients with MR imaging spinal cord lesions in different segments of the spinal cord. Imaging in patient 1 (A and D) with an *NDUFS1* pathogenic variant (c.365C>T:p.Pro122Leu and c.155 + 1G>A) shows a lesion located in the cervical segment (arrow, A), at the level of C1, with a posterior and central distribution on the axial view (D) and extension to the area postrema. Imaging in patient 2 (B and E) with *MT-ND4* pathogenic variant (m.11777C>A) shows a spinal cord lesion with diffuse cross-sectional involvement (E), longitudinally extensive, and involving both cervical and thoracic levels, including the area postrema (arrow, B). Imaging in patient 3 (C and F) with *MT-ND5* pathogenic variant (m.13513G>A) shows a thoracolumbar lesion, extending to the conus medullaris, with isolated gray matter involvement and snake eyes appearance.

performed of the entire spine. Nineteen (19/119, 16% of all patients with primary mitochondrial disease; 19/33, 58% of those with spine MR imaging) demonstrated spinal cord lesions (Fig 1). The median age at onset of clinical symptoms was 1.76 years (IQR = 0.3–12.3 years), and the male:female ratio was 0.7:1.

Spine MR imaging studies were obtained for a variety of reasons: children demonstrating weakness (6/19, 32%), 3 of whom had acute onset respiratory failure and were found to have brain stem lesions extending to the spinal cord on brain MR imaging, changes in gait (4/19, 21%), acute bowel and bladder symptoms (4/19, 21%), scoliosis (2/19, 11%), and extremity tremor (2/19, 11%). Spinal myoclonus and vomiting were present in 1 child each (1/19, 5%), with lesions extending to the area postrema (Online Supplemental Data).

Sixteen (16/19, 84%) patients had lesions located at cervical levels, of whom 6 had lesions that extended to thoracic levels. Three (3/10, 30%) individuals had lesions restricted to the thoracolumbar levels that extended to the conus medullaris (Fig 2). Eight (8/19, 42%) of the spinal cord lesions were longitudinally extensive, and 11 (11/19, 58%) were focal in appearance. Six children (6/19, 32%) had lesions reaching the area postrema, and 3 (3/19, 16%) had lesions with a tumefactive appearance (with cord expansion). Clinical, genetic, and main radiologic findings of these cases with spinal cord involvement are

summarized in the Online Supplemental Data. Clinical and demographic features of all patients with a spine study are summarized in the Online Supplemental Data.

Involvement of the cross-sectional anatomy of the spinal cord varied. Lesions were most frequently distributed centrally around the central canal (11/19, 58%) followed by lesions involving the posterior columns (7/19, 37%).

Two main imaging patterns of spinal cord lesions were identified. The group A pattern was present in 12 patients (12/19, 63%), with involvement of the peripheral white matter with or without involvement of the central gray matter. This imaging pattern resembled that of demyelinating lesions.

Among the group A cohort, we further subdivided the lesions into 3 major subgroups based on their imaging appearance consistent with typical patterns of particular demyelinating disorders: neuromyelitis optica spectrum disorder (NMOSD)-like in 6 children, anti-MOG-like in 2 children, and MS-like in 2 children. In the group A NMOSD-like MR imaging presentation, spinal cord lesions were longitudinally extensive, mostly accompanied by tumefactive effect and involvement of the area postrema (Fig 3). No positive laboratory test results for AQP4-Ab were detected in these patients. Group A patients who had spinal cord lesions with anti-MOG-like imaging features demonstrated lesions that were longitudinally extensive with diffuse cross-sectional involvement,

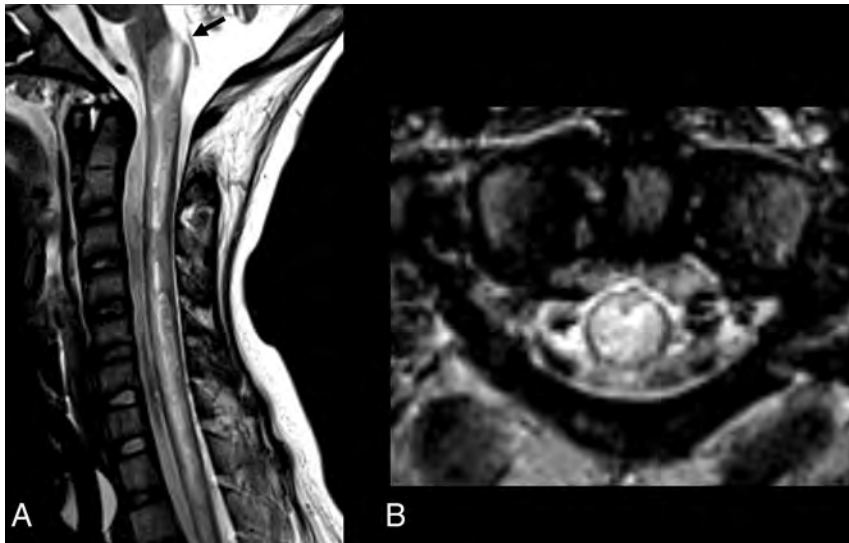


FIG 3. Group A, NMOSD appearance. A 12-year-old male patient with *MT-ND4* pathogenic variant (m.11777C>A) with a demyelination-like pattern of the spinal cord lesion and NMOSD-like appearance. Sagittal and axial T2 MR imaging of the cervical spine shows a longitudinal extensive hyperintense lesion in both cervical and thoracic segments with a tumefactive effect and involvement of the area postrema (arrow, A). The lesion has a diffuse cross-sectional involvement of the cord in the axial plane (B).

with more evident abnormalities in the central gray matter giving the “H sign” appearance (Fig 4). Of the 2 patients with anti-MOG-like MR imaging patterns, 1 child with *MT-TL1* variant was tested for anti-MOG antibodies because of a clinical presentation consistent with acute disseminated encephalomyelitis and had positive antibody results, leading to a final diagnosis of anti-MOG antibody associated disease in addition to the primary mitochondrial disorder. The other patient with an anti-MOG-like imaging pattern was not evaluated for the presence of serum antibodies. The 2 children with an MS-like imaging appearance demonstrated numerous lesions that were short in length, located at the cervical and thoracic levels, and distributed within the white matter at the periphery of the cord. No CNS oligoclonal bands were found in these children.

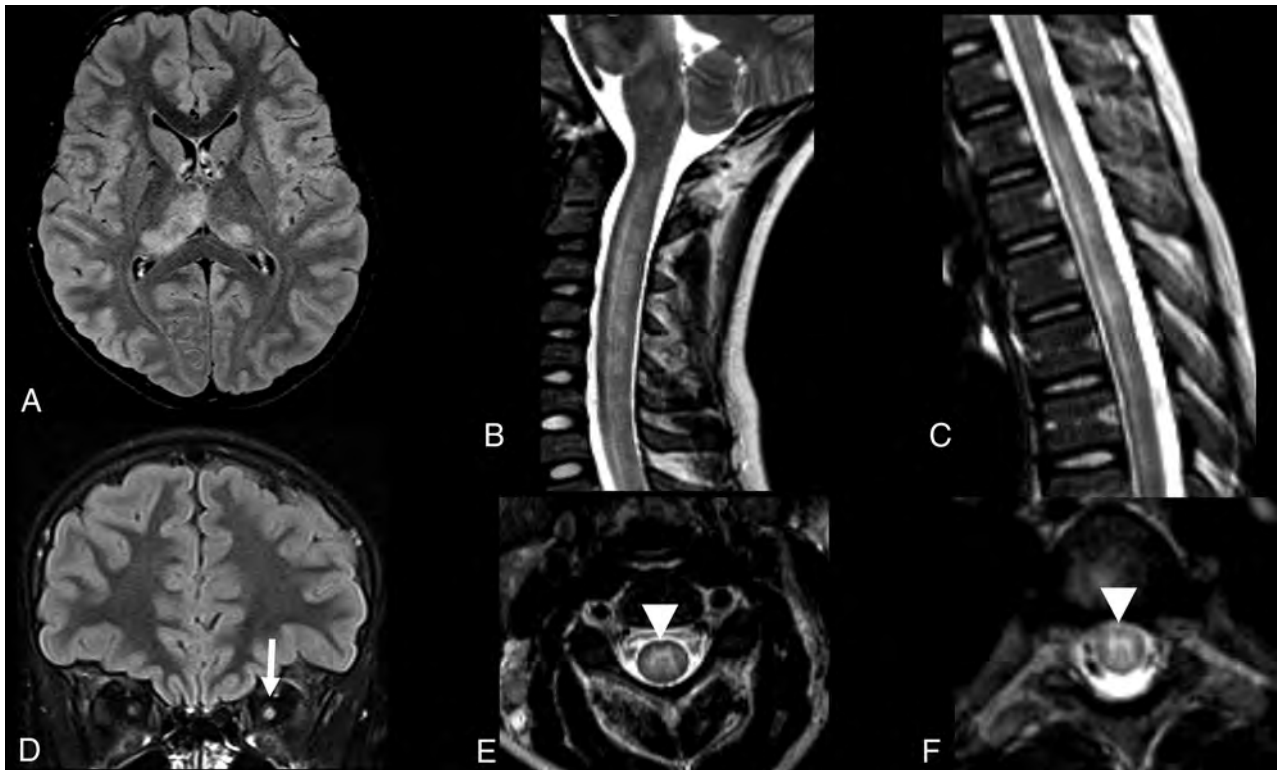


FIG 4. Group A, anti-MOG appearance. A 10-year-old female patient with a family diagnosis of LHON Leber’s hereditary optic neuropathy (heteroplasmic m.14484T>C and homoplasmic m.15256G>A mtDNA variants) and MOG+ demyelination. Brain MR imaging study axial and coronal FLAIR sequences show asymmetric hyperintense lesions in the thalami, more evident on the right side (A), and enlargement and hyperintensity of the intraorbital left optic nerve (arrow, D). Sagittal and axial spinal MR imaging of the cervical (B and E) and thoracic segments (C and F) show longitudinal extensive hyperintense lesions in both segments, with more evident involvement of the central gray matter, giving the “H sign” appearance on the axial planes (arrowheads, E and F).

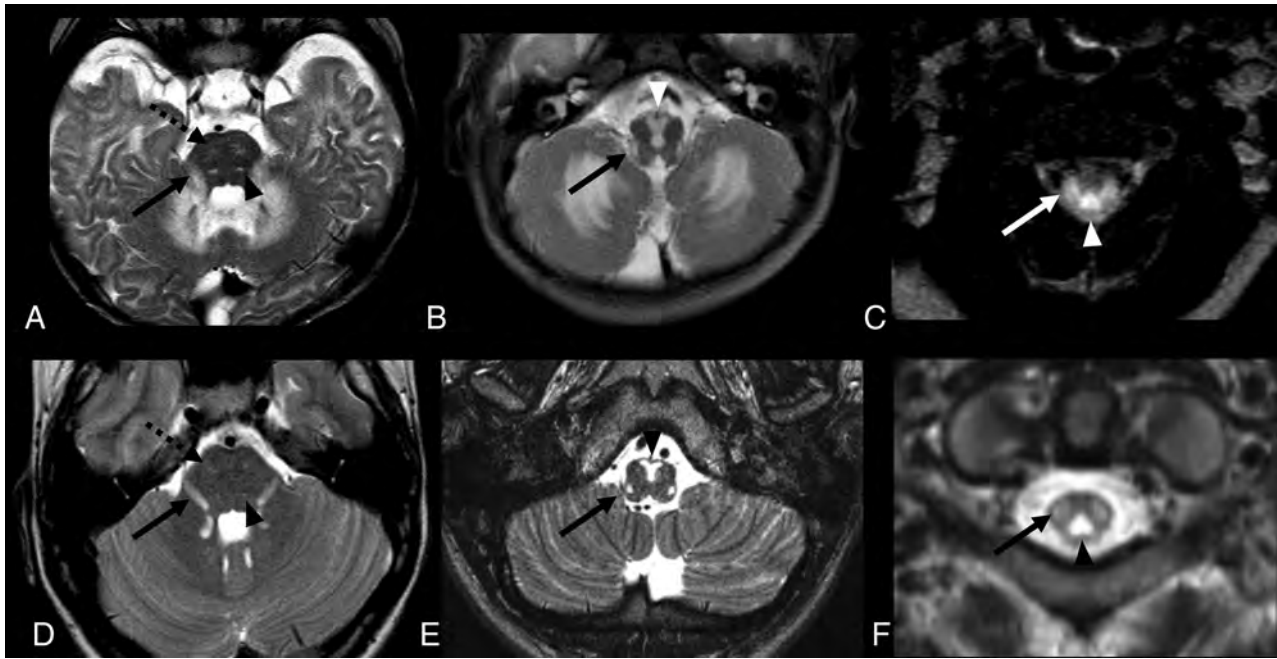


FIG 5. Group A, LBSL appearance. MR imaging of 2 patients with leukoencephalopathy with brain stem and spinal cord involvement and increased lactate (LBSL) appearance. Patient 1 (A–C) is a 6-month-old male patient with an *NDUF51* pathogenic variant. Patient 2 (D–F) is a 1-year-old male patient with a *DARS2* pathogenic variant. In both patients, axial T2 sequences show symmetric hyperintense lesions, affecting both corticospinal tracts, in the pons (dotted arrows, A and D). Hyperintense lesions are also observed along the intraparenchymal portions of the trigeminal nerves (arrows, A and D) and medial lemnisci (arrowheads, A and D). Lesions affecting the pyramids (arrowheads, B and E) and inferior cerebellar peduncles (arrows, B and E) are observed in the medulla. On axial T2-weighted cervical spinal MR imaging (C and F), hyperintense lesions are seen in the dorsal columns (arrowheads) and lateral corticospinal tracts (arrows).

Moreover, 2 patients who were included in group A and designated to have selective white matter involvement presented with imaging features of LBSL. These lesions involved the posterior and lateral columns of the spinal cord in the cervical segment. One of these children had pathogenic variants in *DARS2*, the commonly known cause of this phenotype, but the other child had *NDUF51* pathogenic variants that were not previously associated with this imaging phenotype. The brain MR imaging of these 2 patients was consistent with the imaging phenotype of LBSL, showing symmetric lesions affecting the bilateral corticospinal tracts, the intraparenchymal part of the trigeminal nerves, and the medial lemnisci (Fig 5).

The group B pattern was observed in 7 patients (7/19, 37%) with lesions limited to the spinal cord gray matter, resembling imaging features of spinal cord infarct or acute viral infections.

Regarding the clinical symptoms, whereas children in group A often demonstrated acute symptoms, children in group B showed gradually progressive symptoms, except for bowel and bladder changes that were always acute. A significant association was found between the pattern of lesions (group A versus group B) and lesions involving the cervical versus thoracolumbar segments ($P < .01$). Cervical lesions were more frequently observed in group A (12/12, 100%) as opposed to group B (4/7, 57%). Thoracolumbar lesions extending to the conus medullaris were observed in group B (3/7, 43%) but not in group A (0/12, 0%).

DISCUSSION

Although a few publications have reported spinal cord lesions may occur in very select mitochondrial disorders, limited evaluation has

been performed to characterize correlations between spinal cord imaging findings and clinical phenotypes in a broad range of patients with primary mitochondrial disease with well-defined pathogenic causes.^{3,8–14} Here, we performed a comprehensive retrospective review of all spine imaging in patients with confirmed primary mitochondrial disease over the past 2 decades, which has clearly demonstrated that a high frequency of spinal cord lesions occurs in children with primary mitochondrial disorders. Indeed, spinal cord lesions were observed in more than half of our pediatric patients with primary mitochondrial disease who underwent spine imaging.

A detailed description of the histopathologic features of spinal cord lesions in mitochondrial disorders has shown damage of motor, sensory, and autonomic fibers.^{2,3,6,8–10,15,16} Moreover, a variety of findings, including the presence of ischemia, necrosis, relative sparing of neurons, edema of the gray matter, vascular congestion, and demyelination around the central canal and dorsal columns of the cervical cord, have been reported in the neuropathologic literature.^{5,17} These data support our study's findings that imaging features resemble different forms of pediatric demyelination and that more frequent distribution of lesions occurs around the central canal and in the posterior columns of the spinal cord.

Studying the broad spectrum of imaging findings and patterns, we were able to classify the imaging appearance of the spinal cord lesions into 2 distinct patient subtypes, group A and group B. Group A patterns included individuals with overlapping imaging features of lesions observed in demyelinating disorders.

These lesions tend to be distributed in the cervical and thoracic segments and were restricted to the white matter or affected both white and gray matter. Group A patterns were present in half of the patients with imaging findings typical of NMOSD,¹⁸ including tumefactive effect, longitudinal extensive lesions, and involvement of the area postrema. These patients were clinically evaluated for demyelinating diseases but with negative results for AQP4-Ab. Possible associations linking NMOSD and mitochondrial disorders have been considered for many years, mainly based on a few patients who demonstrated imaging similarities of NMOSD in the context of having a diagnosis of Leber hereditary optic neuropathy (LHON).^{19,20} As one example, Hudson et al²¹ sequenced the mtDNA genes commonly known to cause LHON in patients with NMOSD, in addition to specific mtDNA haplogroups that are preferentially associated with pathogenic variants in complex I mtDNA gene that cause LHON, in both patients with NMOSD and control participants. The authors did not find any statistically significant association between these 2 disorders.²¹

However, in recent literature, mtDNA has been increasingly recognized as an agonist of the innate immune system. Its role in inflammasome activation as a damage-associated molecular pattern is shown by its ability to induce the secretion of interleukin-1 β from microglia.^{22,23} Interestingly, levels of CSF mtDNA have been noted to be higher in NMOSD AQP4-Ab-positive patients compared with those with other neurologic disorders. Moreover, transfected cells that express AQP4 when incubated with serum from NMOSD AQP4-Ab-positive patients were shown to release mtDNA.²⁴ NMOSD AQP4-Ab-negative patients may show similar imaging findings, including spinal cord features resembling positive AQP4-Ab.¹⁸ Furthermore, primary mitochondrial dysfunction may induce microglial activation. Microglial cells, in turn, can release reactive oxygen species and proinflammatory cytokines, which are able to damage essential components of the mitochondria such as mtDNA.²⁵

We postulate that the mtDNA insult and release may trigger neuroinflammation in predisposed individuals, as exemplified by specific case observations. Interestingly, 2 patients in group A who had lesions affecting the whole cross-section of the spinal cord that involved most pronounced signal abnormality in the central gray matter to give the “H sign” appearance were suspected in their differential diagnosis of having anti-MOG demyelination.²⁶ Indeed, 1 of these children harbored a heteroplasmic m.14484T>C known pathogenic variant and positive family history of LHON and had a confirmed anti-MOG Ab diagnosis. Although the spinal cord imaging features for the other patient were compatible for anti-MOG Ab phenotype, this child was not tested because there had been no other supporting clinical indication.

Two children had short-length spinal cord lesions that occurred in the periphery of the cord that involved only the white matter in the cervical and thoracic segments, mimicking MS. However, neither the brain imaging findings nor the laboratory results supported the imaging-based diagnosis of MS.²⁷ Reports from the scientific literature highlight the difficulty of a clinical

approach to patients affected by mitochondrial disorders who also present with brain lesions resembling demyelination.^{28,29} We believe that our study's focus on spinal cord MR imaging findings further supports the hypothesis of the mitochondrial cause of these MS-like cases, which also present with overlapping imaging features of autoimmunity.

Two other group A children from our cohort presented with the typical imaging findings of LBSL (following previously established features).⁸ These included 1 child with *DARS2* pathogenic variants (a gene that encodes mitochondrial aspartyl-tRNA synthetase described in association with this imaging pattern)⁸ and the other with *NDUFS1* pathogenic variants, a nuclear gene encoding a mitochondrial complex I subunit that has not previously been associated with this unique imaging phenotype. Further imaging characterization of larger prospective cohorts affected by these 2 pathogenic genes and related gene classes may be helpful to differentiate and optimize care for individuals with these genetic disorders.

The children in group B included patients who presented with features typical of spinal cord infarct, with all lesions localized within the gray matter. Even though other disorders, such as acute flaccid myelitis caused by viral infection, may present with similar findings,³⁰ there is indirect evidence that mitochondrial dysfunction that impairs cellular energy production may be a causal or contributing factor to ischemic tissue changes.³¹ Thus, we believe that ischemic lesions remain the primary pathogenic cause of isolated gray matter spinal cord lesions and accordingly should be excluded in this context. Indeed, some of the ischemic lesions that we identified in children with primary mitochondrial disease occurred within the lower thoracolumbar segment, extended to the conus medullaris, and had the classic ischemic “snake-eye” appearance.³²

Upon review of clinical phenotypes in our cohort with spinal cord lesions, Leigh syndrome was the most frequently observed; it was present in three-quarters of our cohort. Leigh syndrome cases with spinal cord lesions had diverse gene causes in both genomes, a range of pathogenic variants and lesions that could be grouped into both spinal cord imaging patterns (groups A and B).

Patients with primary mitochondrial disease and spinal cord lesions may present with several different neurologic symptoms, such as monoparesis, spasticity, autonomic dysfunction, or sensory or motor transverse syndrome. Less frequently, asymptomatic cases may occur. Spinal deformities are also commonly observed.² However, it has not previously been clear in the literature whether these neurologic symptoms are sufficiently common to support establishment of a standard MR imaging protocol or interval to routinely analyze the spinal segment for patients with primary mitochondrial disease. In our study, the most common clinical symptoms that led to performing spine MR imaging or brain MR imaging with subsequent spine evaluation (because of lesions depicted on brain imaging in the upper spine) were acute or progressive weakness and respiratory failure. Acute bowel or bladder incontinence or retention, change in gait, neuromuscular scoliosis, hyperreflexia, and myoclonus were also neurologic symptoms observed in our cohort. Moreover, individuals with acute weakness had a higher frequency of group A spinal cord lesions identified both at the cervical level and with longitudinally

extensive lesions. These data provide strong support to consider updating imaging protocols for children with mitochondrial disease when they have concerning neurologic manifestations. Further study will be needed to determine the potential utility of obtaining spinal MR imaging in patients with definite primary mitochondrial disease before the onset of severe neurologic evidence of spinal cord involvement.

The only statistically significant association observed was between the location of the lesions and the cross-sectional imaging pattern, with lesions involving the cervical segment more frequently observed in group A (demyelination features, white \pm gray matter involvement) and lower segment lesions (thoracic or thoracolumbar) more often observed in group B (ischemic features, selective gray matter involvement).

Ascertainment bias is a potential limitation of our study to estimate the frequency of spinal cord lesions in pediatric patients with primary mitochondrial disease because most individuals who had brain MR imaging performed during the 2 decades of the study period did not undergo full spine MR imaging. Indeed, all children evaluated in this study had MR imaging performed for at least part of the spinal cord because of pronounced neurologic signs or symptoms indicative of potential spinal cord involvement. Retrospective analysis of spinal cord images in this symptomatic cohort demonstrated the relatively high frequency of and value of clinical spine MR imaging to identify spinal cord lesions in patients with primary mitochondrial disorders who have concerning neurologic presentations. Despite the relatively low number of patients with definite mitochondrial disease who had spine MR imaging available for review, this study is the largest cohort reported to date and clearly demonstrates that spinal cord lesions are not an infrequent finding in children with a diverse array of primary mitochondrial diseases.

Furthermore, these analyses discovered that 2 main imaging patterns for spinal cord lesions occur in the context of primary mitochondrial disease, which may help to broaden the differential diagnosis of other common entities such as demyelination, ischemic, or viral disorders.

CONCLUSIONS

Spinal cord lesions are common in children with primary mitochondrial disorder who manifest with neurologic signs and symptoms. Spine imaging should be considered if spinal cord involvement is suspected based on the clinical associations described in this report. Moreover, spinal cord lesions related patients with primary mitochondrial disease may mimic demyelination, with features that overlap with those of NMOSD, anti-MOG antibody-associated demyelination, or MS, with a possible cervical predilection (group A, white \pm gray matter involvement), or they may mimic ischemia, with the classic snake-eye appearance and may have a predilection along the lower segments of the spinal cord (group B, selective gray matter involvement). The medical community should be aware that primary mitochondrial disorders affect the spinal cord with lesions similar to those observed in cord autoimmunity and ischemia.

ACKNOWLEDGMENTS

We are grateful to the patients with mitochondrial disease and their families for their involvement in this study. We also thank Lydia Sheldon, MEd, and Anthony Rosner, PhD, for helpful editing suggestions.

Disclosures: Amy Goldstein—RELATED: Consulting Fee or Honorarium: MitoAction, Comments: Grand rounds/family meeting support group travel fees, directly related to mitochondrial disease; Support for Travel to Meetings for the Study or Other Purposes: UMDF, Wellcome Trust, Comments: Honorarium speaker travel fees directly related to mitochondrial disease. Juan Martin-Saavedra—UNRELATED: Employment: The Children's Hospital of Philadelphia. Giulia Fadda—UNRELATED: Employment: University of Pennsylvania, Comments: I receive salary support from the clinical research training scholarship in multiple sclerosis from the American Academy of Neurology. Martin Kidd—RELATED: Consulting Fee or Honorarium: University of Stellenbosch, South Africa*; UNRELATED: Consultancy: University of Stellenbosch, South Africa*. Marni Falk—UNRELATED: Board Membership: Ribonova Inc, Khondrion, Luciole Pharma; Consultancy: Reneo Pharmaceuticals, Mission Therapeutics, Imel Therapeutics, Cylerion, Astellas, Neurovive Inc; Patents (Planned, Pending or Issued): Several patents; Royalties: Elsevier; Stock/Stock Options: RiboNova Inc, MitoCUREia; Travel/Accommodations/Meeting Expenses Unrelated to Activities Listed: United Mitochondrial Disease Foundation. Zarazuela Zolkipli-Cunningham—UNRELATED: Employment: Children's Hospital of Philadelphia. *Money paid to institution.

REFERENCES

1. Rahman J, Rahman S. Mitochondrial medicine in the omics era. *Lancet* 2018;391:2560–74 CrossRef Medline
2. Finsterer J, Zarrouk-Mahjoub S. Involvement of the spinal cord in mitochondrial disorders. *J Neurosci Rural Pract* 2018;9:245–51 CrossRef Medline
3. van der Knaap MS, van der Voorn P, Barkhof F, et al. A new leukoencephalopathy with brainstem and spinal cord involvement and high lactate. *Ann Neurol* 2003;53:252–58 CrossRef Medline
4. Lin T-K, Chang Y-Y, Lin H-Y, et al. Mitochondrial dysfunctions in leukoencephalopathy with brainstem and spinal cord involvement and lactate elevation (LBSL). *PLoS One* 2019;14:e0224173 CrossRef Medline
5. Cavanagh JB, Harding BN. Pathogenic factors underlying the lesions in Leigh's disease. *Brain* 1994;117:1357–76 CrossRef Medline
6. McKelvie P, Marotta R, Thorburn DR, et al. A case of myelopathy, myopathy, peripheral neuropathy and subcortical grey matter degeneration associated with recessive compound heterozygous POLG1 mutations. *Neuromuscul Disord* 2012;22:401–05 CrossRef Medline
7. von Elm E, Altman DG, Egger M, STROBE Initiative, et al. The Strengthening the Reporting of Observational Studies in Epidemiology (STROBE) statement: guidelines for reporting observational studies. *Lancet* 2007;370:1453–57 CrossRef Medline
8. Uluc K, Baskan O, Yildirim KA, et al. Leukoencephalopathy with brain stem and spinal cord involvement and high lactate: a genetically proven case with distinct MRI findings. *J Neurol Sci* 2008;273:118–22 CrossRef Medline
9. Yamashita S, Miyake N, Matsumoto N, et al. Neuropathology of leukoencephalopathy with brainstem and spinal cord involvement and high lactate caused by a homozygous mutation of DARS2. *Brain Dev* 2013;35:312–16 CrossRef Medline
10. Nikali K, Suomalainen A, Saharinen J, et al. Infantile onset spinocerebellar ataxia is caused by recessive mutations in mitochondrial proteins Twinkle and Twinky. *Hum Mol Genet* 2005;14:2981–90 CrossRef Medline
11. Bindu PS, Arvinda H, Taly AB, et al. Magnetic resonance imaging correlates of genetically characterized patients with mitochondrial disorders: a study from south India. *Mitochondrion* 2015;25:6–16 CrossRef Medline
12. Mauri E, Dilena R, Boccuzzi A, et al. Subclinical Leber's hereditary optic neuropathy with pediatric acute spinal cord onset: more than meets the eye. *BMC Neurol* 2018;18:220 CrossRef Medline

13. Miyauchi A, Osaka H, Nagashima M, et al. **Leigh syndrome with spinal cord involvement due to a hemizygous NDUFA1 mutation.** *Brain Dev* 2018;40:498–502 CrossRef Medline
14. Tenney JR, Prada CE, Hopkin RJ, et al. **Early spinal cord and brainstem involvement in infantile Leigh syndrome possibly caused by a novel variant.** *J Child Neurol* 2013;28:1681–85 CrossRef Medline
15. Sparaco M, Cavallaro T, Rossi G, et al. **Immunohistochemical demonstration of spinal ventral horn cells involvement in a case of “myoclonus epilepsy with ragged red fibers” (MERRF).** *Clin Neuropathol* 2000;19:200–07 Medline
16. Barz H, Henker J. **Pathological findings in subacute necrotizing encephalomyelopathy (Leigh’s disease) (author’s transl).** *Zentralbl Allg Pathol* 1975;119:488–94 Medline
17. Leigh D. **Subacute necrotizing encephalomyelopathy in an infant.** *J Neurol Neurosurg Psychiatry* 1951;14:216–21 CrossRef Medline
18. Wingerchuk DM, Banwell B, Bennett JL, et al. **International consensus diagnostic criteria for neuromyelitis optica spectrum disorders.** *Neurology* 2015;85:177–89 CrossRef Medline
19. Simão LM. **Neuromyelitis optica antibody in Leber hereditary optic neuropathy: case report.** *Arq Bras Oftalmol* 2012;75:280–82 CrossRef Medline
20. McClelland CM, Van Stavern GP, Tselis AC. **Leber hereditary optic neuropathy mimicking neuromyelitis optica.** *J Neuroophthalmol* 2011;31:265–68 CrossRef Medline
21. Hudson G, Mowbray C, Elson JL, et al. **Does mitochondrial DNA predispose to neuromyelitis optica (Devic’s disease)?** *Brain* 2008;131:e93–93 CrossRef Medline
22. Zhang Q, Raoof M, Chen Y, et al. **Circulating mitochondrial DAMPs cause inflammatory responses to injury.** *Nature* 2010;464:104–07 CrossRef Medline
23. West AP, Shadel GS. **Mitochondrial DNA in innate immune responses and inflammatory pathology.** *Nat Rev Immunol* 2017;17:363–75 CrossRef Medline
24. Yamashita K, Kinoshita M, Miyamoto K, et al. **Cerebrospinal fluid mitochondrial DNA in neuromyelitis optica spectrum disorder.** *Neuroinflammation* 2018;15:125 CrossRef Medline
25. Di Filippo M, Chiasserini D, Tozzi A, et al. **Mitochondria and the link between neuroinflammation and neurodegeneration.** *J Alzheimers Dis* 2010;20:S369–79 CrossRef Medline
26. Dubey D, Pittock SJ, Krecke KN, et al. **Clinical, radiologic, and prognostic features of myelitis associated with myelin oligodendrocyte glycoprotein autoantibody.** *JAMA Neurol* 2019;76:301–09 CrossRef Medline
27. De Angelis F, Brownlee WJ, Chard DT, et al. **New MS diagnostic criteria in practice.** *Pract Neurol* 2019;19:64–67 CrossRef Medline
28. Pfeffer G, Burke A, Yu-Wai-Man P, et al. **Clinical features of MS associated with Leber hereditary optic neuropathy mtDNA mutations.** *Neurology* 2013;81:2073–81 CrossRef Medline
29. Bittner F, Falardeau J, Spain RI. **Myelin oligodendrocyte glycoprotein antibody-associated demyelination comorbid with Leber hereditary optic neuropathy.** *JAMA Neurol* 2019;76:227–28 CrossRef Medline
30. Cheng H, Zeng J, Li H, et al. **Neuroimaging of HFMD infected by EV71.** *Radiol Infect Dis* 2015;1:103–08 CrossRef
31. Pathak D, Berthet A, Nakamura K. **Energy failure: does it contribute to neurodegeneration?** *Ann Neurol* 2013;74:506–16 CrossRef Medline
32. Vargas MI, Gariani J, Sztajzel R, et al. **Spinal cord ischemia: practical imaging tips, pearls, and pitfalls.** *AJNR Am J Neuroradiol* 2015;36:825–30 CrossRef Medline

Spinal CSF-Venous Fistulas in Morbidly and Super Obese Patients with Spontaneous Intracranial Hypotension

W.I. Schievink, M. Maya, R.S. Prasad, V.S. Wadhwa, R.B. Cruz, and F.G. Moser

ABSTRACT

BACKGROUND AND PURPOSE: Spinal CSF-venous fistulas are increasingly recognized as the cause of spontaneous intracranial hypotension. Here, we describe the challenges in the care of patients with CSF-venous fistulas who are morbidly or super obese.

MATERIALS AND METHODS: A review was undertaken of all patients with spontaneous intracranial hypotension and a body mass index of >40 who underwent digital subtraction myelography in the lateral decubitus position to look for CSF-venous fistulas.

RESULTS: Eight patients with spontaneous intracranial hypotension with a body mass index of >40 underwent lateral decubitus digital subtraction myelography. The mean age of these 5 women and 3 men was 53 years (range, 45 to 68 years). Six patients were morbidly obese (body mass indexes = 40.2, 40.6, 41, 41.8, 45.4, and 46.9), and 2 were super obese (body mass indexes = 53.7 and 56.3). Lumbar puncture showed an elevated opening pressure in 5 patients (26.5–47 cm H₂O). The combination of an elevated opening pressure and normal conventional spine imaging findings resulted in a misdiagnosis (midbrain glioma and demyelinating disease, respectively) in 2 patients. Prior treatment included surgical nerve root ligation for suspected CSF-venous fistula in 3 patients. Digital subtraction myelography demonstrated a CSF-venous fistula in 6 patients (75%). Rebound high-pressure headache occurred in all 6 patients following surgical ligation of the fistula, and papilledema developed in 3.

CONCLUSIONS: In our series, opening pressure was generally elevated in patients with morbid or super obesity. The yield of identifying CSF-venous fistulas with digital subtraction myelography in this patient population can approach that of the nonobese patient population. These patients may be at higher risk of developing rebound high-pressure headaches and papilledema.

ABBREVIATIONS: BMI = body mass index; DSM = digital subtraction myelography; SIH = spontaneous intracranial hypotension

Spontaneous intracranial hypotension (SIH) is an increasingly recognized cause of secondary headache and has also been associated with a wide variety of other neurologic disorders.¹⁻⁴ The cause of SIH is a spinal CSF leak; at least 3 distinct types have been identified.⁵ A direct communication between the subarachnoid space and a spinal epidural vein, a so-called CSF-venous fistula, is the most recently discovered type of spinal CSF leak and may be detected in up to one-fourth of patients with SIH.⁶ Since the first description of spontaneous spinal CSF-venous fistulas in 2014,⁷ several groups have confirmed their importance, but much remains unknown about these fistulas.⁶⁻¹⁵ The main reason that this type of CSF leak remained undiscovered for so long is that it is not associated with an extradural CSF collection and its

detection requires sophisticated imaging, eg, digital subtraction myelography (DSM) or dynamic CT myelography.⁶⁻¹⁵

Obesity has emerged as a major global and national health problem.¹⁶ Obesity is defined as a body mass index (BMI) of ≥ 30 and is associated with various diseases, such as diabetes, metabolic syndrome, and cardiovascular disease. The prevalence of obesity is increasing, and in the United States, it is among the highest in the world. According to the National Health and Nutrition Examination Survey 2015 and 2016 dataset, 39.8% of US adults live with obesity.¹⁷ Morbid obesity (BMI ≥ 40) and super obesity (BMI ≥ 50) have shown the most rapid rise in prevalence, and with data from the Behavioral Risk Factor Surveillance System, it was estimated that 6.6% of Americans had a BMI of >40 in 2010.¹⁸ Despite the importance of obesity, there is very limited information available on obesity in patients with spontaneous spinal CSF-venous fistulas. Actually, no information on BMI is available in any of the prior reports, including our own, on spontaneous spinal CSF-venous fistulas.⁶⁻¹⁵ We have noted that particularly morbid and super obesity can result in unique challenges in the diagnosis,

Received August 23, 2020; accepted after revision September 15.

From the Departments of Neurosurgery (W.I.S., R.B.C.) and Imaging (M.M., R.S.P., V.S.W., F.G.M.), Cedars-Sinai Medical Center, Los Angeles, California.

Please address correspondence to Wouter I. Schievink, MD, Department of Neurosurgery, Cedars-Sinai Medical Center, 127 S San Vicente Blvd, Suite A6600, Los Angeles, CA 90048; e-mail: schievinkw@cshs.org
<http://dx.doi.org/10.3174/ajnr.A6895>

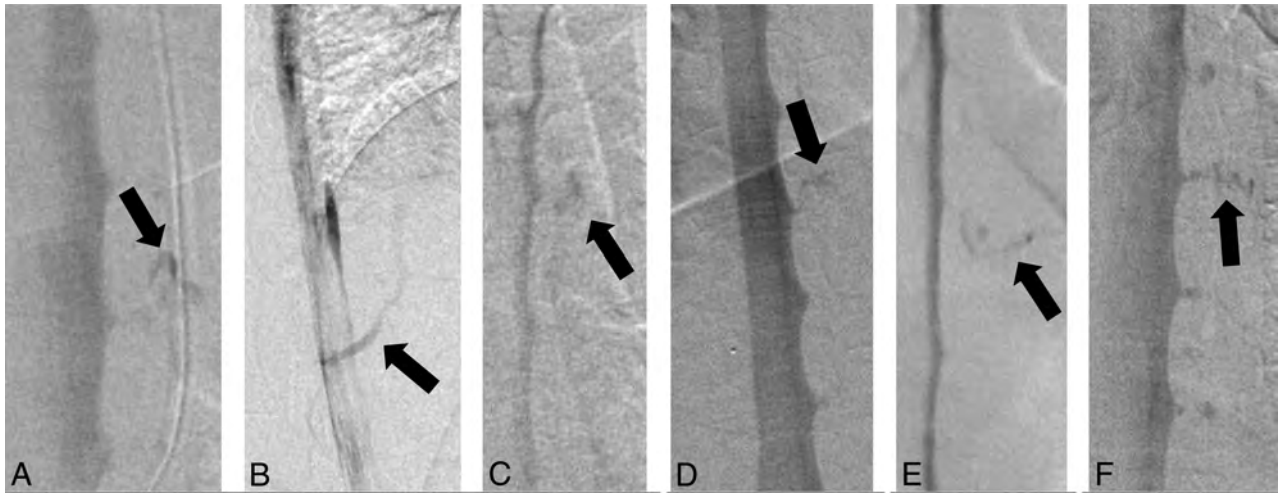


FIG 1. A, Anterior-posterior DSM demonstrates a CSF-venous fistula (BMI = 46.9 kg/m², weight 149 kg, height = 178 cm). B, Lateral DSM demonstrates a CSF-venous fistula (BMI = 40.6 kg/m², weight = 94.5 kg, height = 152 cm). C, Anterior-posterior DSM demonstrates a CSF-venous fistula (BMI = 40.2 kg/m², weight = 113 kg, height = 167 cm). D, Anterior-posterior DSM demonstrates a CSF-venous fistula (BMI = 53.7 kg/m², weight = 151 kg, height = 167 cm). E, Anterior-posterior DSM demonstrates a CSF-venous fistula (BMI = 41 kg/m², weight = 137 kg, height = 183 cm). F, Anterior-posterior DSM demonstrates a CSF-venous fistula (BMI = 45.4 kg/m², weight = 161 kg, height = 188 cm). In 2 other patients (BMI = 56.3 kg/m², weight = 149 kg, height = 163 cm and BMI = 41.8 kg/m², weight = 140 kg, height = 182 cm, respectively), DSM failed to demonstrate a CSF-venous fistula. Arrows indicates CSF-venous fistulas.

detection, and treatment of patients with SIH with spontaneous spinal CSF-venous fistulas; therefore, we reviewed our experience with this patient population.

MATERIALS AND METHODS

This study was approved by the Cedars-Sinai Medical Center institutional review board.

Using a prospectively maintained registry, we identified all patients with SIH and a BMI of ≥ 40 who underwent DSM in the lateral decubitus position to look for CSF-venous fistulas. The diagnosis of SIH was based on the criteria of the International Classification of Headache Disorders, third edition,¹⁹ with minor modifications. These criteria require objective evidence of SIH, consisting of brain MR imaging showing stigmata of SIH (ie, pachymeningeal enhancement, brain sagging, or subdural fluid collections), spinal imaging showing a CSF leak (ie, the presence of extradural CSF), or low CSF opening pressure (ie, < 6.0 cm H₂O). The modification consists of also including patients who do not have headaches but whose symptoms are best explained by SIH.

All patients underwent brain MR imaging and MR myelography (heavily T2-weighted MR imaging without intrathecal contrast). For DSM, the technique as described by Hoxworth et al²⁰ was used with some minor modifications.^{6,8} Briefly, DSM is performed with the patient under general endotracheal anesthesia with deep paralysis and suspended respiration for maximal detail and temporal resolution. Patients are positioned in the lateral decubitus position in a biplane angiography suite, with tilt-table capability. Pillows or foam padding are placed to optimize cervicothoracic alignment. A fluoroscopically guided lumbar puncture is performed at the L2–3 level with a 22-ga needle. An opening pressure is obtained at this time using standard manometry. Then, accurate needle position is confirmed with an injection of 0.5 mL of iohexol (Omnipaque; GE Healthcare). Patients are then

further positioned on the basis of the area of interest, and the table is tilted to achieve contrast flow to the cervicothoracic spine. Great care is taken, especially in these patients with obesity, to maximize contrast opacification of the lateral dural sac by adjusting the degree of tilting to patient-specific spinal curvature and anatomy. Finally, contrast is injected manually at 1 mL per second with suspended respiration for 40–100 seconds while acquiring biplane subtraction images at 2 frames per second. If the first DSM fails to identify a CSF-venous fistula, then the study is repeated on another day with the patient in the lateral decubitus position on the contralateral side.

Radiation exposure during DSM was calculated for these patients and for 2 age- and sex-matched controls, each with a BMI of < 40 .

RESULTS

Eight patients with SIH with a BMI of ≥ 40 underwent lateral decubitus DSM (Fig 1). The mean age of these 5 women and 3 men was 53 years (range, 45–68 years). Six patients were morbidly obese (BMI = 40.2, 40.6, 41, 41.8, 45.4, and 46.9), and 2 were super obese (BMI = 53.7 and 56.3). None of the patients had undergone bariatric surgery. Four patients presented with isolated orthostatic headaches; 3, with orthostatic headaches with Valsalva-induced worsening; and 1, with isolated Valsalva-induced headache. Fundoscopic examination findings were normal in all 8 patients. Brain MR imaging showed brain sagging in 7 patients and meningeal enhancement in 5 patients.

Before referral to our medical center, a lumbar puncture in the lateral decubitus position had been performed in 6 patients, showing a low opening pressure (< 6 cm H₂O) in 1 patient and an elevated opening pressure (26.5–36 cm H₂O) in 5 patients. A lumbar puncture performed with the patient in the prone position yielded a normal opening pressure (11.5 cm H₂O) in the remaining patient.

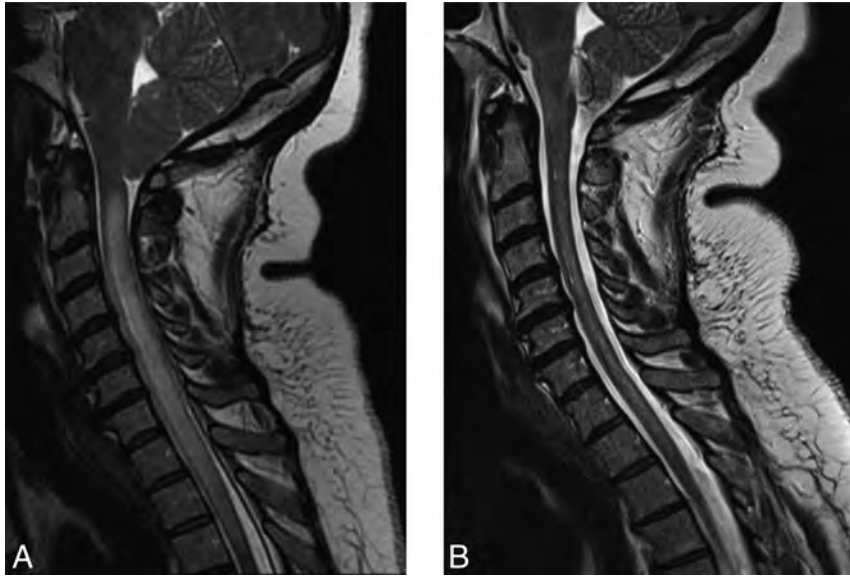


FIG 2. Sagittal T2-weighted MRIs showing brain sagging and T2 signal change within the cervical spinal cord (presyrinx) (A) and resolution of the presyrinx after surgical ligation of the thoracic CSF-venous fistula due to resolution of brain sagging and cerebellar tonsillar herniation (B).

All patients had undergone a spine MR imaging, 5 had undergone a conventional CT myelogram, 3 had undergone dynamic CT myelography, and 2 had undergone DSMs in the lateral decubitus position (using general or local anesthesia). None of these investigations had shown extradural CSF collections or a clear evidence of a CSF-venous fistula. The combination of an elevated opening pressure and normal spine imaging findings resulted in the diagnosis of SIH being discarded in 2 patients who were subsequently misdiagnosed with demyelinating disease (T2 signal abnormality of the spinal cord in the setting of severe brain sagging, Fig 2) and a midbrain glioma (T2 signal abnormality in the setting of severe brain sagging), respectively. Three patients had been treated with multiple epidural blood patches or fibrin glue injections as well as surgical ligation of thoracic nerve roots for the suspicion of a CSF-venous fistula. One patient had undergone an exploratory operation at the site of a disc herniation.

Using DSM with the patient in the lateral decubitus position, we were able to detect a CSF-venous fistula in 6 of the 8 patients (75%). All fistulas were located in the thoracic spine, 3 on the right side and 3 on the left side. All were associated with a spinal meningeal diverticulum. A normal opening pressure was found in 3 patients (13, 17, and 20 cm H₂O), a borderline elevated opening pressure was found in 2 patients (23 and 24 cm H₂O), and an elevated opening pressure was found in 3 patients (28, 29, and 47 cm H₂O). These opening pressure readings were obtained with the patient in the lateral decubitus position under general anesthesia. Radiation exposure was higher in these patients (mean, 1753 mGy; range, 1271–2314 mGy) than in controls (mean, 488 mGy; range, 167–979 mGy).

All 6 patients with a spinal CSF-venous fistula underwent an uneventful thoracic foraminotomy, with ligation of the fistula resulting in symptom resolution and normalization of the MR imaging findings. However, rebound high-pressure headache

requiring treatment with acetazolamide developed in all 6 patients, and this was complicated by visual blurring and papilledema in 3 patients. A lumbar puncture was performed with the patient in the lateral decubitus position in 2 of these patients with papilledema, and this showed an increase of opening pressure from 24 to 30 cm H₂O in one patient (spontaneous respirations) and from 47 to 51 cm H₂O in the other (at the time of repeat DSM with general anesthesia). Vision symptoms resolved with the acetazolamide treatment.

DISCUSSION

In this study of morbidly and super obese patients with spontaneous spinal CSF-venous fistulas, we found specific challenges in the diagnosis, imaging, and treatment.

Although it has been well-documented since the 1990s that patients with SIH often do not have abnormally low CSF pressure,^{21–23} the current study showed that opening pressure can be markedly elevated in these patients. This finding shows that just like the presence of a normal opening pressure, an abnormally high opening pressure does not preclude the diagnosis of SIH. Prior studies had already concluded that some patients with SIH may have borderline elevated CSF pressure,^{22,23} and a patient with SIH and an opening pressure of 31 cm H₂O was reported by Kranz et al.²³ The combination of an elevated opening pressure in addition to normal results of conventional spinal imaging, ie, the absence of any extradural CSF collection, caused the diagnosis of SIH to be discarded in some of the presently reported patients, despite the presence of the typical brain MR imaging findings. This step resulted in an erroneous diagnosis of demyelinating disease in one patient and of a midbrain glioma in another. The presence of elevated CSF pressure also has possible pathophysiologic implications for the development of spinal CSF-venous fistulas. Similar to spontaneous skull base CSF leaks in patients with idiopathic intracranial hypertension,^{24–27} chronically elevated CSF pressure could also predispose to spontaneous spinal CSF leaks. This possibility also had been reported in patients with pre-existing idiopathic intracranial hypertension who developed SIH.² The presently reported patients had normal fundoscopic examination findings on presentation and did not have idiopathic intracranial hypertension. Of note, none of the patients in the present study had undergone bariatric surgery, a risk factor for developing SIH.²⁸

The detection of CSF-venous fistulas requires sophisticated imaging, and we have been using lateral decubitus DSM with the patient under general anesthesia for this purpose with excellent results.⁶ Although the body habitus of morbidly and super obese patients may be intimidating, it should not result in a defeatist

attitude. In the present study, we detected CSF-venous fistulas in three-fourths of morbidly and super obese patients with SIH and no extradural CSF collections on spinal imaging, thus demonstrating that the yield of identifying such fistulas in this patient population can approach that of the nonobese patient population.⁶ In a prior study of 23 consecutive patients with SIH and the stigmata of SIH on brain MR imaging but no extradural CSF collections on spinal imaging who underwent lateral decubitus DSM, we found CSF-venous fistulas in 17 patients (74%).⁶

Postoperatively, rebound high-pressure headaches occurred in all 6 patients who underwent surgical ligation of the CSF-venous fistula, and this was complicated by papilledema and visual symptoms in 3 patients. The development of papilledema was associated with only a modest increase in opening pressure. This compares with a previous study in which about one-fourth of 113 patients developed rebound high-pressure headache requiring administration of acetazolamide following treatment of SIH, and papilledema was noted in only 2 patients.²⁹ Similarly, Wang et al³⁰ reported rebound high-pressure headaches requiring treatment with acetazolamide in 5 (25%) of 20 patients with SIH following surgical ligation of a spinal CSF-venous fistula. Although the number of patients in the current study is small, this suggests that morbidly and super obese patients with CSF-venous fistulas are at increased risk of developing rebound high-pressure headaches and papilledema postoperatively and that consideration should be given to pharmacologic prophylaxis with, for example acetazolamide, before treating the CSF-venous fistula and that careful ophthalmologic evaluation postoperatively is indicated.

CONCLUSIONS

In patients with SIH due to a spinal CSF-venous fistula who are morbidly or super obese, CSF pressure often is elevated and the risk of posttreatment rebound high-pressure headache and papilledema is increased. The yield of finding a CSF-venous fistula in this patient population using DSM is similar to that in patients who are not obese.

Disclosures: Wouter I. Schievink—UNRELATED: Board Membership: I am on the medical advisory board of the Spinal CSF Leak Foundation; this is a nonpaying position, and I have not received any funds toward this project. Marcel Maya—UNRELATED: Board Membership: I am on the medical advisory board of the Spinal CSF Leak Foundation; this is a nonpaying position, and I have not received any funds toward this project.

REFERENCES

- Schievink WI. Spontaneous spinal cerebrospinal fluid leaks and intracranial hypotension. *JAMA* 2006;295:2286–96 CrossRef Medline
- Mokri B. Spontaneous intracranial hypotension. *Continuum (Minneapolis)* 2015;21:1086–1108 CrossRef Medline
- Kranz PG, Malinzak MD, Amrhein TJ, et al. Update on the diagnosis and treatment of spontaneous intracranial hypotension. *Curr Pain Headache Rep* 2017;21:37 CrossRef Medline
- Robblee J, Secora KA, Alhilali LM, et al. Spontaneous intracranial hypotension. *Pract Neurol* 2020. <https://practicalneurology.com/articles/2020-may/spontaneous-intracranial-hypotension-1>. Accessed August 1, 2020
- Schievink WI, Maya MM, Jean-Pierre S, et al. A classification system of spontaneous spinal CSF leaks. *Neurology* 2016;87:673–79 CrossRef Medline
- Schievink WI, Maya MM, Moser FG, et al. Lateral decubitus digital subtraction myelography to identify spinal CSF-venous fistulas in spontaneous intracranial hypotension. *J Neurosurg Spine* 2019 Sept 13. [Epub ahead of print] CrossRef Medline
- Schievink WI, Moser FG, Maya MM. CSF-venous fistula in spontaneous intracranial hypotension. *Neurology* 2014;83:472–73 CrossRef Medline
- Schievink WI, Moser FG, Maya MM, et al. Digital subtraction myelography for the identification of spontaneous spinal CSF-venous fistulas. *J Neurosurg Spine* 2016;24:960–64 CrossRef Medline
- Kumar N, Diehn FE, Carr CM, et al. Spinal CSF venous fistula: a treatable etiology for CSF leaks in craniocervical hypovolemia. *Neurology* 2016;86:2310–12 CrossRef Medline
- Kranz PG, Amrhein TJ, Schievink WI, et al. The “hyperdense paraspinous vein” sign: a marker of CSF-venous fistula. *AJNR Am J Neuroradiol* 2016;37:1379–81 CrossRef Medline
- Kranz PG, Amrhein TJ, Gray L. CSF venous fistulas in spontaneous intracranial hypotension: imaging characteristics on dynamic and CT myelography. *AJR Am J Roentgenol* 2017;209:1360–66 CrossRef Medline
- Farb RI, Nicholson PJ, Peng PW, et al. Spontaneous intracranial hypotension: a systematic imaging approach for CSF leak localization and management based on MRI and digital subtraction myelography. *AJNR Am J Neuroradiol* 2019;40:745–53 CrossRef Medline
- Schievink WI, Maya MM, Moser FG, et al. Spontaneous spinal CSF-venous fistulas associated with venous/venolymphatic vascular malformations: report of 3 cases. *J Neurosurg Spine* 2019;32:305–10 CrossRef Medline
- Duval JR, Robertson CE, Cutsforth-Gregory JK, et al. Headache due to spontaneous spinal cerebrospinal fluid leak secondary to cerebrospinal fluid-venous fistula: case series. *Cephalalgia* 2019;39:1847–54 CrossRef Medline
- Chazen JL, Robbins MS, Strauss SB, et al. MR myelography for the detection of CSF-venous fistulas. *AJNR Am J Neuroradiol* 2020;41:938–40 CrossRef Medline
- NCD Risk Factor Collaboration (NCD-RisC). Trends in adult body-mass index in 200 countries from 1975 to 2014: a pooled analysis of 1698 population-based measurement studies with 19.2 million participants. *Lancet* 2016;387:1377–96 CrossRef Medline
- Health, United States, 2018—Data Finder. https://www.cdc.gov/nchs/healthdata/content/2018.htm#Table_021. Accessed June 9, 2020
- Sturm R, Hattori A. Morbid obesity rates continue to rise rapidly in the United States. *Int J Obes (Lond)* 2013;37:889–91 CrossRef Medline
- Headache Classification Committee of the International Headache Society: The International Classification of Headache Disorders, 3rd edition. *Cephalalgia* 2018 38:1–211 CrossRef Medline
- Hoxworth JM, Patel AC, Bosch EP, et al. Localization of a rapid CSF leak with digital subtraction myelography. *AJNR Am J Neuroradiol* 2009;30:516–19 CrossRef Medline
- Mokri B, Hunter SF, Atkinson JL, et al. Orthostatic headaches caused by CSF leak but with normal CSF pressures. *Neurology* 1998;51:786–90 CrossRef Medline
- Luetmer PH, Schwartz KM, Eckel LJ, et al. When should I do dynamic CT myelography? Predicting fast spinal CSF leaks in patients with spontaneous intracranial hypotension. *AJNR Am J Neuroradiol* 2012;33:690–94 CrossRef Medline
- Kranz PG, Tanpitukpongse TP, Choudhury KR, et al. How common is normal cerebrospinal fluid pressure in spontaneous intracranial hypotension? *Cephalalgia* 2016;36:1209–17 CrossRef Medline
- Brisman R, Hughes JE, Mount LA. Cerebrospinal fluid rhinorrhoea. *Arch Neurol* 1970;22:245–52 CrossRef Medline
- Aaron G, Doyle J, Vaphiades MS, et al. Increased intracranial pressure in spontaneous CSF leak patients not associated with papilledema. *Otolaryngol Head Neck Surg* 2014;151:1061–66 CrossRef Medline

26. Bidot S, Levy JM, Saindane AM, et al. **Do most patients with a spontaneous cerebrospinal fluid leak have idiopathic intracranial hypertension?** *J Neuroophthalmol* 2019;39:487–95 CrossRef Medline
27. Tam EK, Gilbert AL. **Spontaneous cerebrospinal fluid leak and idiopathic intracranial hypertension.** *Curr Opin Ophthalmol* 2019;30:467–71 CrossRef Medline
28. Schievink WI, Goseland A, Cunneen S. **Bariatric surgery as a possible risk factor for spontaneous intracranial hypotension.** *Neurology* 2014;83:1819–22 CrossRef Medline
29. Schievink WI, Maya MM, Jean-Pierre S, et al. **Rebound high-pressure headache after treatment of spontaneous intracranial hypotension: MRV study.** *Neurol Clin Pract* 2019;9:93–100 CrossRef Medline
30. Wang TY, Karikari IO, Amrhein TJ, et al. **Clinical outcomes following surgical ligation of cerebrospinal fluid–venous fistula in patients with spontaneous intracranial hypotension: a prospective case series.** *Oper Neurosurg (Hagerstown)* 2020;18:239–45 CrossRef Medline

Seeing What We Expect to See in COVID-19



I appreciate the effort among your staff that must be required to keep the articles in the *American Journal of Neuroradiology* current as we learn more about the potential for CNS involvement with coronavirus disease 2019 (COVID-19) infections.

The article in the September 2020 issue, “Anosmia in COVID-19 Associated with Injury to the Olfactory Bulbs Evident on MRI,” is certainly timely and of considerable interest because this symptom has been reported in many infected patients.¹ In this article, the authors report their experience with the imaging of 5 patients whom they believe demonstrated abnormalities of the olfactory bulbs, though 1 of these 5 did not have anosmia. While their article appears to support the suspicion of many that COVID-19 directly involves the olfactory bulbs, I think we should be careful that we are not seeing only what we expect to see. In Fig 1, where the authors point to presumed hemorrhage (microbleeding) into the left olfactory bulb, there is also high signal in both inferior rectus muscles and bilateral frontal lobes just lateral to the olfactory sulcus on the precontrast scan and in the inferior frontal lobes on the postcontrast scan. Because it is most likely that these other areas of symmetric high signal along brain-bone-air interfaces in the orbits and frontal fossa are susceptibility artifacts, one could argue that the high signal that appears to be in the olfactory bulb is also artifactual. In support of that contention, the left and right olfactory bulbs do not appear enlarged or asymmetric on the STIR scan, surprising with presumed hemorrhage.

It is entirely possible, however, that one or more of the other cases in which only postcontrast imaging is provided have real

enhancement of the olfactory bulbs. However, they do not appear to be enlarged, and this feature differs from a report in *Neurology*, in which transient enlargement without particularly evident signal change was illustrated in a patient with COVID-19 and anosmia,² albeit measured on MR imaging that appears to be acquired on different scanners or at least with different techniques.

This discrepancy among early reports supports the commentary in the same issue, “Level of Evidence during COVID-19 Pandemic: Making the Case for Case Series and Case Reports.”³ I agree that rapid publication of case reports of imaging findings with COVID-19 will, in time, benefit our patients, but in the meantime, we need to be particularly critical about the quality of these early reports and avoid reaching any conclusions until there is consistent and reliable evidence regarding CNS involvement from COVID-19 infection.

REFERENCES

1. Aragão MF, Leal MC, Filho OQ, et al. **Anosmia in COVID-19 associated with injury to the olfactory bulbs evident on MRI.** *AJNR Am J Neuroradiol* 2020;41:1703–06 CrossRef Medline
2. Laurendon T, Radulesco T, Mugnier J, et al. **Bilateral transient olfactory bulb edema during COVID-19-related anosmia.** *Neurology* 2020;95:224–25 CrossRef Medline
3. Ikuta I. **Level of evidence during COVID-19 pandemic: making the case for case series and case reports.** *AJNR Am J Neuroradiol* 2020;41:1646 CrossRef Medline

© A. Mamourian

Department of Radiology
Penn State Health Milton S. Hershey Medical Center,
Penn State College of Medicine
Hershey, Pennsylvania

Indicates open access to non-subscribers at www.ajnr.org
<http://dx.doi.org/10.3174/ajnr.A6912>

REPLY:



We are not always absolutely certain that what we see on MRI truly represents tissue injury, but there are consistent changes in the images of the olfactory bulbs in patients with coronavirus disease 2019 (COVID-19).

We understand the reason for Dr Alex Mamourian's questions and confess that initially, we also had the same doubts that he expressed in his letter, when for the first time, we were faced with the images of olfactory bulb injuries in these patients with COVID-19. The question arises about whether these are artifacts or do they truly represent an abnormality in the olfactory bulbs? To make sure that the findings we were identifying in the olfactory bulbs of patients with COVID-19 were real and abnormal, we reviewed healthy olfactory pathway of subjects from our data base with pre- and/or postcontrast fat-suppression T1WI and STIR of the orbit MRIs performed before the COVID-19 pandemic. We compared them with our data base because we did not find any article in the literature describing the normal aspect of the olfactory bulbs in pre- and postcontrast fat-suppression T1WI or on STIR.

We would like to reply to Dr Alex Mamourian, pointing out that all considerations regarding the difficulty of analyzing the olfactory bulbs were noted in our article in the last paragraph, which discusses the limitations¹ of our retrospective study during this terrible pandemic, which is still threatening humanity.

This region is difficult to analyze with fat-suppression T1WI because of the susceptibility artifacts in the interface with the air, and we spoke about these in the last paragraph of the Discussion in our article.¹ These artifacts are generally well-recognized by an experienced radiologist. In fact, if one reviews the image in Fig 1 of our article (case 1)¹ (referred to by Dr Mamourian as an artifact), it seems that it does not correspond to an artifact. It is unilateral, located in the left bulb, with well-defined margins (the susceptibility artifacts usually have ill-defined margins that vanish, and they are often bilateral). Another important argument against the possibility of an artifact is that besides being seen in pre- and postcontrast fat-suppression T1WI (where susceptibility artifacts often appear), it is also clearly identified on the STIR image; thus, it would seem that it corresponds to a real image. STIR is not a sequence that identifies this kind of artifact.² Moreover, if you read the legend, you will see that we stated "probable"¹ methemoglobin.

In the other 4 cases (Fig 2 of our article), the bulbs seemed to enhance on the postcontrast series, but because there were no precontrast series, the differential diagnosis would be made with the presence of methemoglobin (this is also very clear in the Materials and Methods).¹

The cases in our retrospective study did not have any coronal FLAIR, FIESTA, or CISS images because the olfactory bulbs and anosmia were not the reason for the investigation by brain MR imaging.¹ Thus, our study cannot be compared with the other studies about presence of edema or an increase of volume, and

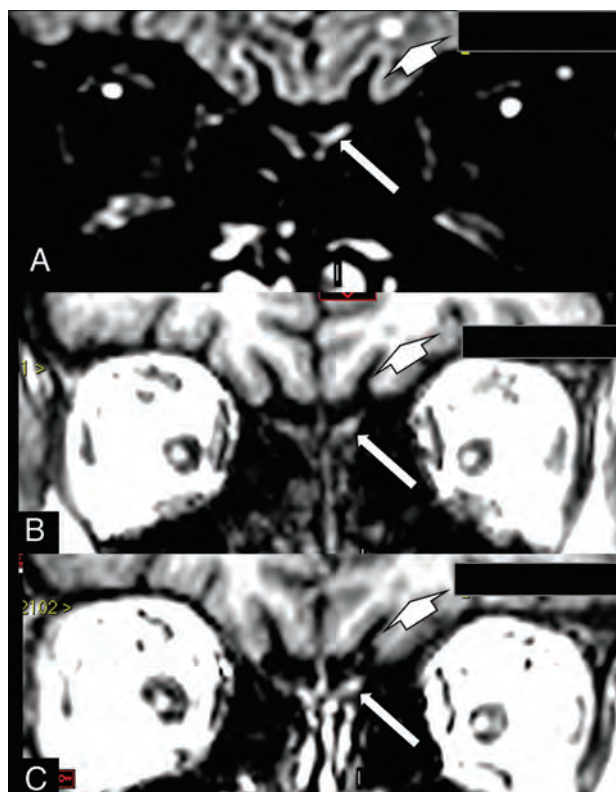


FIGURE. A woman in her 60s with confirmed COVID-19 for which MR imaging shows a hyperintense lesion on a coronal reconstruction of 3D-FLAIR (A, arrow) and also on pre- (B, arrow) and postcontrast SPGR T1WI (C, arrow). This is suggestive of a component of probably methemoglobin in this left olfactory bulb lesion, which seems to be a little larger and asymmetric compared with the apparently normal right olfactory bulb. This asymmetry is better seen on FLAIR. On FLAIR (A, short arrow), there is also a small round hyperintense lesion in the subcortical white matter in the left frontal lobe, which is hyperintense on T1WI (B, short arrow) and does not enhance on postcontrast T1WI (C, short arrow), being no specific lesion area probably corresponding to gliosis. This patient also had some areas of brain parenchymal bleeding and microbleeding, and had around 50% of the bilateral pulmonary parenchyma compromised with typical COVID-19 lesions on chest CT, not shown in this figure.

we also spoke about this in the introduction.¹ However, one of our new cases was also investigated using a 3D-FLAIR sequence, allowing clear evidence of damage to the olfactory bulb, corresponding to the alterations observed in the pre- and postcontrast spoiled gradient recalled (SPGR) T1WI, definitively ruling out the possibility of an artifact, at least in this particular case (Figure).

Regarding another comment, the only case reported in our publication (case 5) that did not mention anosmia presenting on the MR imaging had suggestive enhancement only in the left olfactory bulb, which is also described in the Results.¹ We also held a discussion about this and concluded (fourth paragraph), "The patient hardly perceives unilateral anosmia."¹ She probably had unilateral damage to the olfactory bulb that was not sufficient to clinically result in anosmia. The human olfactory pathway projects ipsilaterally to the brain, and the central processing of its information is initially also restricted to the same hemisphere. Later processing includes bilateral cortical activation.³ The clinical

Indicates open access to non-subscribers at www.ajnr.org

<http://dx.doi.org/10.3174/ajnr.A6943>

consequence of this is that unilateral olfactory deficits can remain asymptomatic and thus cannot be noticed. We did not use the olfactory test evaluation, only the patient's report, because our study was retrospective. However, even using smell tests measuring olfactory function mostly reflects the best side when testing bilaterally.

Unlike the pathologist who deals directly with the injured tissue, the radiologist tries to interpret on the image what may be happening in the tissue, evaluating a possible anatomofunctional correlation. Thus, it was not only in our study¹ that a relationship between anosmia and apparent alteration of the MR image was observed in patients with COVID-19 even if other MR imaging sequences have been performed and analyzed.^{4–6} Our obligation is to present to the scientific community what we believe as an interpretation of a possible lesion demonstrated by the imaging. Obviously, we agree that there is always the risk of seeing what we want to see and not seeing what we do not want to see. Moreover, we have to always remember that in science, there are false-positives and false-negatives beyond the artifacts.

We think all would agree that anatomopathologic studies are necessary to better define neuroradiologic interpretation.

REFERENCES

1. Aragão MF, Leal MC, Cartaxo Filho OQ, et al. **Anosmia in COVID-19 associated with injury to the olfactory bulbs evident on MRI.** *AJNR Am J Neuroradiol* 2020;41:1703–06 CrossRef Medline
2. Hong JH, Lee HY, Kang YH, et al. **Improvement of fat suppression and artifact reduction using IDEAL technique in head and neck MRI at 3T.** *Investig Magn Reson Imaging* 2016;20:44–52 CrossRef
3. Lascano AM, Hummel T, Lacroix JS, et al. **Spatio-temporal dynamics of olfactory processing in the human brain: an event-related source imaging study.** *Neuroscience* 2010;167:700–08 CrossRef Medline
4. Laurendon T, Radulesco T, Mugnier J, et al. **Bilateral transient olfactory bulb edema during COVID-19-related anosmia.** *Neurology* 2020;95:224–225 CrossRef Medline
5. Chetrit A, Lechien JR, Ammar A, et al. **Magnetic resonance imaging of COVID-19 anosmic patients reveals abnormalities of the olfactory bulb: preliminary prospective study.** *The Journal of Infection* 2020. CrossRef Medline
6. Strauss SB, Lantos JE, Heier LA, et al. **Olfactory bulb signal abnormality in patients with COVID-19 who present with neurologic symptoms.** *American Journal of Neuroradiology* 2020;41:1882–87 CrossRef

 **M.F.V.V. Aragão**

Universidade Federal de Pernambuco
Recife, Brazil

Centro Diagnostico Multimagem
Recife, Brazil

 **M.C. Leal**

Universidade Federal de Pernambuco
Recife, Brazil

Real Hospital Português de Beneficência em Pernambuco
Recife, Brazil

 **T.M. Fonseca**

Real Hospital Português de Beneficência em Pernambuco
Recife, Brazil

 **O.Q. Cartaxo Filho**

Universidade Federal de Pernambuco
Recife, Brazil

 **M.M. Valença**

COVID-19 Related Central Nervous System Vasculopathy: Beyond Vasculitis



I read with great interest the article by Hanafi et al¹ reporting the case of a patient with coronavirus disease 2019 (COVID-19) who developed multiple focal supra- and infratentorial ischemic lesions involving the periventricular white matter, basal ganglia, cerebellar peduncles, and the corpus callosum. The authors considered hypoxic-ischemic injury as an unlikely mechanism, given the temporal mismatch between hypoxemia and neurologic deterioration, as well as imaging studies excluding involvement of the striatum and brain cortex. They also excluded a prothrombotic state because coagulation panel findings were normal. Because there was an association between ischemic and hemorrhagic lesions with patchy enhancement after intravenous contrast administration, the possibility of injury to small intracranial vasculature in the distribution of distal perforating arteries in a pattern suggestive of vasculitis was suggested.

I would like to share some comments on this case, in the hope of adding some more useful insights.

In Severe Acute Respiratory Syndrome coronavirus 2 (SARS-CoV-2) infection, vascular injury can occur through 2 potentially complementary mechanisms: direct, resulting from the virus affinity to angiotensin-converting enzyme-2 expressed by endothelial cells;² and indirect, due to a misdirected host immune response inducing coagulopathy and vasoconstriction.³ Despite having a negative coagulation panel, the patient had elevated C-reactive protein (60 mg/L) and, very likely, a cytokine storm, as severely ill patients with COVID-19 typically present with it;⁴ these are known inflammatory markers that potentially induce hypercoagulability⁴ and endothelial cell injury per se. Moreover, Hanafi et al¹ could have stated which specific coagulation/inflammatory parameters were determined, as there are many described in the literature as

being abnormally high in patients with COVID-19, such as ferritin, D-dimer, or lactate dehydrogenase levels.

Simultaneously, to assertively diagnose vasculitis, one should document vessel lumen irregularities and, most important, vessel wall inflammation. Given the apparent small-vessel involvement, due to the topographic distribution of the aforementioned ischemic lesions, digital subtraction angiography could have been performed to characterize potential distal vessel irregularities (in this context, a more sensitive technique than 3D time-of-flight MRA); moreover, despite less sensitivity for small-vessel involvement, vessel wall MR imaging should ideally have been performed to search for concentric vessel wall enhancement, a known direct sign of regional mural inflammation. Therefore, in this case, the association of ischemic/hemorrhagic lesions and the patchy enhancement pattern is, in my opinion, insufficient to establish the diagnosis of vasculitis.

Therefore, I believe one should be cautious and more conservative and describe this condition as a COVID-19 related vasculopathy, potentially induced by a misdirected host immune response in a probable setting of a cytokine storm.

REFERENCES

1. Hanafi R, Roger PA, Perin B, et al. **COVID-19 neurologic complication with CNS vasculitis-like pattern.** *AJNR Am J Neuroradiol* 2020;41:1384–87 CrossRef Medline
2. Varga Z, Flammer AJ, Steiger P, et al. **Endothelial cell infection and endotheliitis in COVID-19.** *Lancet* 2020;395:1417–18 CrossRef Medline
3. Zhou F, Yu T, Du R, et al. **Clinical course of risk factors for mortality of adult inpatients with COVID-19 in Wuhan, China: a retrospective cohort study.** *Lancet* 2020;395:1054–62 CrossRef Medline
4. Zubair AS, McAlpine LS, Gardin T, et al. **Neuropathogenesis and neurologic manifestations of the coronaviruses in the age of coronavirus disease 2019: a review.** *JAMA Neurol* 2020;77:1018–27 CrossRef Medline

© M. Quintas-Neves
Neuroradiology Department
Hospital de Braga
Braga, Portugal

Indicates open access to non-subscribers at www.ajnr.org
<http://dx.doi.org/10.3174/ajnr.A6913>

REPLY:



We thank Dr Miguel Quintas-Neves for his interest in our article¹ and for his useful comments. As mentioned in Dr Quintas-Neves's commentary, and in our article, mechanisms of injury related to hypoxic-ischemic injury and a hypercoagulable state were confidently ruled out in our patient on solid clinical and biologic grounds. On the other hand, the patient clearly presented with signs and markers of inflammation.

In that patient, multiple, diffuse cerebral lesions were present, mostly ischemic, some hemorrhagic, in a wide distribution that included the deep white matter of both hemispheres, the corpus callosum, the deep gray matter structures, and the middle cerebellar peduncles. Restricted diffusion was present in all of those lesions, some of which demonstrated a "patchy" pattern of contrast uptake.

Such patterns of diffuse punctate deep white matter/gray matter restricted diffusion with postcontrast "patchy/punctate" enhancement have been shown to be associated with active small vessel wall inflammatory changes in primary and secondary CNS angiitis and in some presentations of the reversible cerebral vasoconstriction syndrome and posterior reversible encephalopathy syndrome complex.^{2,3} In those patients, hemorrhagic transformation has been speculated to possibly result from damage to the arterial wall in relation to a necrotizing pattern, allowing transmural passage of blood.⁴

Consequently and on the basis of the radiologic findings in that patient, we suspected and reported a vasculitis-like pattern. We further suggested that such a vasculitis-like picture may possibly be in relation to diffuse endotheliitis from the Severe Acute Respiratory Syndrome coronavirus 2 spike glycoprotein effect on the endothelial angiotensin-converting enzyme 2 (ACE-2) receptors. MRA demonstrated no evidence of large- or medium-sized vessel abnormalities. Although small, the potential risk of conventional cerebral angiography was not believed to be justified in

that patient, considering the lack of substantial impact on the patient's management.

Indeed, both mechanisms suggested by Quintas-Neves, ie, direct viral affinity for endothelial ACE-2 receptors and cytokine storm-related endothelial injury, are plausible mechanisms that are entirely in line with our description. Indeed, too, such a pattern of endothelial inflammation leading to microvascular ischemia/thrombosis may conceivably affect randomly any part of the body.

We further believe it likely that other, unforeseen mechanisms may be present to explain CNS injuries in patients with coronavirus disease 2019. Hopefully, new research will educate us all on the various molecular mechanisms through which this new virus can cause harm, until an effective vaccine is found.

REFERENCES

1. Hanafi R, Roger PA, Perin B, et al. **COVID-19 neurologic complication with CNS vasculitis-like pattern.** *AJNR Am J Neuroradiol* 2020;41:1384–87 CrossRef Medline
2. Boulouis G, de Boysson H, Zuber M, et al. **Primary angiitis of the central nervous system: magnetic resonance imaging spectrum of parenchymal, meningeal, and vascular lesions at baseline.** *Stroke* 2017;48:1248–55 CrossRef Medline
3. de Boysson H, Boulouis G, Aouba A, et al. **Adult primary angiitis of the central nervous system: isolated small-vessel vasculitis represents distinct disease pattern.** *Rheumatology (Oxford)* 2017;56:439–44 CrossRef
4. Salvarani C, Brown RD Jr, Calamia KT, et al. **Primary central nervous system vasculitis presenting with intracranial hemorrhage.** *Arthritis Rheum* 2011;63:3598–3606 CrossRef Medline

R. Hanafi

Department of Neuroradiology
Lille University Hospital
Lille, France

L. Hacein-Bey

Departments of Neuroradiology and Radiology
University of California Davis School of Medicine
Sacramento, California

G. Kuchcinski

Department of Neuroradiology
Lille University Hospital
Lille, France

Indicates open access to non-subscribers at www.ajnr.org

<http://dx.doi.org/10.3174/ajnr.A6944>

In the article “Secondary Oralgia: Referred Pain Pathways and Pathologies” by Norris CD and Koontz NA (*AJNR Am J Neuroradiol* 2020;41:2188–98), cervical nerves 2 and 3 were incorrectly printed as cranial nerves II and III.

The journal regrets the error.

<http://dx.doi.org/10.3174/ajnr.A7035>